

Methods in
ENZYMOLOGY

Volume 456
Mitochondrial Function,
Part A

Edited by
Bill Allison
Immo Scheffler



METHODS IN ENZYMOLOGY

Editors-in-Chief

JOHN N. ABELSON AND MELVIN I. SIMON

*Division of Biology
California Institute of Technology
Pasadena, California, USA*

Founding Editors

SIDNEY P. COLOWICK AND NATHAN O. KAPLAN

Academic Press is an imprint of Elsevier
525 B Street, Suite 1900, San Diego, CA 92101-4495, USA
30 Corporate Drive, Suite 400, Burlington, MA 01803, USA
32 Jamestown Road, London NW1 7BY, UK

First edition 2009

Copyright © 2009, Elsevier Inc. All Rights Reserved.

No part of this publication may be reproduced, stored in a retrieval system or transmitted in any form or by any means electronic, mechanical, photocopying, recording or otherwise without the prior written permission of the publisher

Permissions may be sought directly from Elsevier's Science & Technology Rights Department in Oxford, UK: phone (+44) (0) 1865 843830; fax (+44) (0) 1865 853333; email: permissions@elsevier.com. Alternatively you can submit your request online by visiting the Elsevier web site at <http://elsevier.com/locate/permissions>, and selecting *Obtaining permission to use Elsevier material*

Notice

No responsibility is assumed by the publisher for any injury and/or damage to persons or property as a matter of products liability, negligence or otherwise, or from any use or operation of any methods, products, instructions or ideas contained in the material herein. Because of rapid advances in the medical sciences, in particular, independent verification of diagnoses and drug dosages should be made

For information on all Academic Press publications visit our website at elsevierdirect.com

ISBN: 978-0-08-087776-1

ISSN: 0076-6879

Printed and bound in United States of America

09 10 11 12 10 9 8 7 6 5 4 3 2 1

Working together to grow
libraries in developing countries

www.elsevier.com | www.bookaid.org | www.sabre.org

ELSEVIER

BOOK AID
International

Sabre Foundation

CONTRIBUTORS

Boominathan Amutha

Department of Pharmacology and Physiology, UMDNJ, New Jersey Medical School, Newark, New Jersey, USA

Matthew C. Altman

The Medical Research Council Mitochondrial Biology Unit, Cambridge, United Kingdom

Nikolai P. Belevich

Institute of Biotechnology, University of Helsinki, Helsinki, Finland

Giancarlo A. Biagini

Liverpool School of Tropical Medicine, Pembroke Place, Liverpool, United Kingdom

Egbert J. Boekema

Department of Biophysical Chemistry, Groningen Biomolecular Sciences and Biotechnology Institute, University of Groningen, Groningen, The Netherlands

Ulrich Brandt

Molecular Bioenergetics Group, Cluster of Excellence Frankfurt “Macromolecular Complexes,” Medical School, Johann Wolfgang Goethe-University, Frankfurt am Main, Germany

Hans-Peter Braun

Institute for Plant Genetics, Faculty of Natural Sciences, Universität Hannover, Hannover, Germany

Christine A. Butler

Department of Molecular Biology and Genetics, Biotechnology Building, Cornell University, Ithaca, New York, USA

Roosevelt V. Campbell

Department of Neuroscience and Cell Biology, University of Texas Medical Branch, Galveston, Texas, USA

Joe Carroll

The Medical Research Council Mitochondrial Biology Unit, Cambridge, United Kingdom

Xiaowei Cen

Department of Biochemistry and Molecular Biology, Oklahoma State University, Stillwater, Oklahoma, USA

Jing Chen

Department of Pathology, Immunology, and Laboratory Medicine, College of Medicine, The University of Florida, Gainesville, Florida, USA

Helena M. Cochemé

Institute of Healthy Ageing, University College London, London, United Kingdom, and The Medical Research Council Mitochondrial Biology Unit, Cambridge, United Kingdom

Andrew Dancis

Department of Medicine, Division of Hematology-Oncology, University of Pennsylvania, Philadelphia, Pennsylvania, USA

Grazyna Debska-Vielhaber

Department of Neurology, University Magdeburg, Magdeburg, Germany, and Division of Neurochemistry, Department of Epileptology and Life & Brain Center, University Bonn, Bonn, Germany

Cindy E. J. Dieteren

Department of Paediatrics, Nijmegen Centre for Mitochondrial Disorders, and Department of Biochemistry, Nijmegen Centre for Molecular Life Sciences, Radboud University Nijmegen Medical Centre, Nijmegen, The Netherlands

Martina G. Ding

Department of Biochemistry, Dartmouth Medical School, Hanover, New Hampshire, USA

Jack E. Dixon

Departments of Pharmacology, Cellular and Molecular Medicine, and Chemistry and Biochemistry, and The Howard Hughes Medical Institute, University of California, San Diego, La Jolla, California, USA

Derek A. Drechsel

Department of Pharmaceutical Sciences, University of Colorado, Denver, Aurora, Colorado, USA

Stefan Dröse

Molecular Bioenergetics Group, Cluster of Excellence Frankfurt “Macromolecular Complexes,” Medical School, Johann Wolfgang Goethe-University, Frankfurt am Main, Germany

Bill Durham

Department of Chemistry and Biochemistry, University of Arkansas, Fayetteville, Arkansas, USA

Ian M. Fearnley

The Medical Research Council Mitochondrial Biology Unit, Cambridge, United Kingdom

Nicholas Fisher

Liverpool School of Tropical Medicine, Pembroke Place, Liverpool, United Kingdom

Thomas D. Fox

Department of Molecular Biology and Genetics, Biotechnology Building, Cornell University, Ithaca, New York, USA

Terrence G. Frey

Department of Biology, San Diego State University, San Diego, California, USA

Alexander Galkin

The Wolfson Institute for Biomedical Research, The Cruciform Building, University College London, London, United Kingdom

Lois Geren

Department of Chemistry and Biochemistry, University of Arkansas, Fayetteville, Arkansas, USA

François Godard

Institut de Biochimie et Génétique Cellulaires (CNRS), Université Victor Segalen, Bordeaux, France

Donna M. Gordon

Department of Biological Sciences, Mississippi State University, Mississippi State, Mississippi, USA

Aaron M. Gusdon

Department of Pathology, Immunology, and Laboratory Medicine, College of Medicine, The University of Florida, Gainesville, Florida, USA

Mark A. Hink

Max Planck Institute for Molecular Physiology, Dortmund, Germany

Gregory Holmes-Hampton

Department of Chemistry, Texas A&M University, College Station, Texas, USA

Thomas R. Hurd

The Medical Research Council Mitochondrial Biology Unit, Cambridge, United Kingdom

Andrew M. James

The Medical Research Council Mitochondrial Biology Unit, Cambridge, United Kingdom

Werner J. H. Koopman

Department of Biochemistry, and Microscopical Imaging Centre, Nijmegen Centre for Molecular Life Sciences, Radboud University Nijmegen Medical Centre, Nijmegen, The Netherlands

Roman Kouřil

Department of Biophysical Chemistry, Groningen Biomolecular Sciences and Biotechnology Institute, University of Groningen, Groningen, The Netherlands

Alexei P. Kudin

Division of Neurochemistry, Department of Epileptology and Life & Brain Center, University Bonn, Bonn, Germany

Wolfram S. Kunz

Division of Neurochemistry, Department of Epileptology and Life & Brain Center, University Bonn, Bonn, Germany

Michael Lazarou

Department of Biochemistry, La Trobe University, Melbourne, Australia

Yanchun Li

Department of Neurology, Baylor College of Medicine, Houston, Texas, USA

Roland Lill

Institut für Zytobiologie and Zytopathologie, Philipps-Universität, Marburg, Germany

Kathryn S. Lilley

Department of Biochemistry, Cambridge System Biology Centre, University of Cambridge, Cambridge, United Kingdom

Paul A. Lindahl

Department of Biochemistry and Biophysics, and Department of Chemistry, Texas A&M University, College Station, Texas, USA

Dominika Malinska

Laboratory of Intracellular Ion Channels, Nencki Institute of Experimental Biology, Warsaw, Poland, and Division of Neurochemistry, Department of Epileptology and Life & Brain Center, University Bonn, Bonn, Germany

Douglas Marshall

The Johnson Research Foundation and Department of Biochemistry and Biophysics, University of Pennsylvania, Philadelphia, Pennsylvania, USA

Clayton E. Mathews

Department of Pathology, Immunology, and Laboratory Medicine, College of Medicine, The University of Florida, Gainesville, Florida, USA

Matthew McKenzie

Department of Biochemistry, La Trobe University, Melbourne, Australia

Ren Miao

Department of Chemistry, Texas A&M University, College Station, Texas, USA

Francis Millett

Department of Chemistry and Biochemistry, University of Arkansas, Fayetteville, Arkansas, USA

Jessica Garber Morales

Department of Chemistry, Texas A&M University, College Station, Texas, USA

Michael P. Murphy

The Medical Research Council Mitochondrial Biology Unit, Cambridge, United Kingdom

Leo G. J. Nijtmans

Department of Paediatrics, Nijmegen Centre for Mitochondrial Disorders, Radboud University Nijmegen Medical Centre, Nijmegen, The Netherlands

Esther Nübel

Cluster of Excellence “Macromolecular Complexes,” Zentrum der Biologischen Chemie, Molekulare Bioenergetik, Goethe-Universität Frankfurt, Frankfurt, Germany

Debkumar Pain

Department of Pharmacology and Physiology, UMDNJ, New Jersey Medical School, Newark, New Jersey, USA

Manisha Patel

Department of Pharmaceutical Sciences, University of Colorado Denver, Aurora, Colorado, USA

Guy A. Perkins

National Center for Microscopy and Imaging Research, Center for Research in Biological Systems, University of California, San Diego, La Jolla, California, USA

Aparna Rachamalla

Department of Neuroscience and Cell Biology, University of Texas Medical Branch, Galveston, Texas, USA

Michael Radermacher

University of Vermont, Department of Molecular Physiology and Biophysics, Burlington, Vermont, USA

Jean-Paul di Rago

Institut de Biochimie et Génétique Cellulaires (CNRS), Université Victor Segalen, Bordeaux, France

Matthew J. Rardin

Gibson Lab, The Buck Institute for Age Research, Novato, California, USA

Peter R. Rich

Glynn Laboratory of Bioenergetics, Institute of Structural and Molecular Biology, University College London, London, United Kingdom

Michael T. Ryan

Department of Biochemistry, La Trobe University, Melbourne, Australia

Scott A. Saracco

Department of Molecular Biology and Genetics, Biotechnology Building, Cornell University, Ithaca, New York, USA

Hermann Schägger

Cluster of Excellence “Macromolecular Complexes,” Zentrum der Biologischen Chemie, Molekulare Bioenergetik, Goethe-Universität Frankfurt, Frankfurt, Germany

Alex D. Sheftel

Institut für Zytobiologie and Zytopathologie, Philipps-Universität, Marburg, Germany

Wim Sluiter

Department of Biochemistry, Mitochondrial Research Unit, Erasmus MC, Dr. Molewaterplein 50-60, Rotterdam, The Netherlands

Oliver Stehling

Institut für Zytobiologie and Zytopathologie, Philipps-Universität, Marburg, Germany

Rosemary A. Stuart

Department of Biological Sciences, Marquette University, Milwaukee, Wisconsin, USA

Mei G. Sun

Department of Biology, San Diego State University, San Diego, California, USA

Stephanie Sunderhaus

Institute for Plant Genetics, Faculty of Natural Sciences, Universität Hannover, Hannover, Germany

Herman G. Swarts

Department of Biochemistry, Nijmegen Centre for Molecular Life Sciences, Radboud University Nijmegen Medical Centre, Nijmegen, The Netherlands

Bernard L. Trumpower

Department of Biochemistry, Dartmouth Medical School, Hanover, New Hampshire, USA

Marina L. Verkhovskaya

Institute of Biotechnology, University of Helsinki, Helsinki, Finland

Michael I. Verkhovsky

Institute of Biotechnology, University of Helsinki, Helsinki, Finland

Stefan Vielhaber

Department of Neurology, University Magdeburg, Magdeburg, Germany

Tatyana V. Votyakova

Department of Pediatrics, School of Medicine, University of Pittsburgh, Pennsylvania, USA

John E. Walker

The Medical Research Council Mitochondrial Biology Unit, Cambridge, United Kingdom

Ting Wang

Department of Microbiology and Immunology, University of Texas Medical Branch, Galveston, Texas, USA

Stephen A. Ward

Liverpool School of Tropical Medicine, Pembroke Place, Liverpool, United Kingdom

Ashley J. Warman

Liverpool School of Tropical Medicine, Pembroke Place, Liverpool, United Kingdom

Stanley J. Watowich

Department of Biochemistry and Molecular Biology, University of Texas Medical Branch, Galveston, Texas, USA

Steven A. Weinman

Department of Internal Medicine, University of Kansas Medical Center, Kansas City, Kansas, USA

Sandra E. Wiley

Departments of Pharmacology, Cellular and Molecular Medicine, and Chemistry and Biochemistry, University of California, San Diego, La Jolla, California, USA

Peter H. G. M. Willems

Department of Biochemistry and Microscopical Imaging Centre, Nijmegen Centre for Molecular Life Sciences, Radboud University Nijmegen Medical Centre, Nijmegen, The Netherlands

L. Elly. A. de Wit

Department of Biochemistry, Mitochondrial Research Unit, Erasmus MC, Dr. Molewaterplein 50-60, Rotterdam, The Netherlands

Ilka Wittig

Cluster of Excellence “Macromolecular Complexes,” Zentrum der Biologischen Chemie, Molekulare Bioenergetik, Goethe-Universität Frankfurt, Frankfurt, Germany

Zibiernisha Wumaier

Cluster of Excellence “Macromolecular Complexes,” Zentrum der Biologischen Chemie, Molekulare Bioenergetik, Goethe-Universität Frankfurt, Frankfurt, Germany

Di Xia

Laboratory of Cell Biology, Center for Cancer Research, National Cancer Institute, National Institutes of Health, Bethesda, Maryland, USA

Yuanzheng Yang

Department of Neuroscience and Cell Biology, University of Texas Medical Branch, Galveston, Texas, USA

Shaoqing Yang

Department of Biochemistry and Molecular Biology, Oklahoma State University, Stillwater, Oklahoma, USA

Ying Yin

Department of Biochemistry and Molecular Biology, Oklahoma State University, Stillwater, Oklahoma, USA

Linda Yu

Department of Biochemistry and Molecular Biology, Oklahoma State University, Stillwater, Oklahoma, USA

Chang-An Yu

Department of Biochemistry and Molecular Biology, Oklahoma State University, Stillwater, Oklahoma, USA

Fei Zhou

Department of Biochemistry and Molecular Biology, Oklahoma State University, Stillwater, Oklahoma, USA

PREFACE

Two volumes of *Methods in Enzymology* devoted to methods in mitochondrial research were published in 1995 and 1996 under the editorship of the late Guisepe Attardi and Anne Chomyn. The emphasis of the earlier volumes was on mitochondrial biogenesis. Nevertheless, they also contained several articles describing methods for examining the structure and function of inner membrane complexes that participate in electron transport and ATP synthesis. In the intervening years, high-resolution crystal structures have been obtained for complexes II, III, and IV derived from the mitochondrial inner membrane. However, a crystal structure has yet to be obtained for a eukaryotic complex I (NADH: quinone oxidoreductase). Thus, several chapters in this volume of *Methods in Enzymology* describe alternative methods to characterize the structure and function of complex I. Other chapters are focused on the location and function of mitochondrial iron-sulfur complexes and the characterization of reactive oxygen species that are formed during mitochondrial electron transport in mammalian and yeast mitochondria.

Because a crystal structure has not been obtained for complex I isolated from mammalian or yeast mitochondria, several chapters in this volume (Chapters 1, 2, 6 and 7) describe methods that have been developed to examine structural characteristics of complex I. Other articles describe methods that have been developed to examine electron transport through complex I (Chapters 3 and 4) and to assay complex I in human cells (Chapter 9). Methods to characterize type II NADH: quinone oxidoreductases isolated from the parasites *Plasmodium falciparum* and *Mycobacterium tuberculosis* are described in Chapter 17. Three chapters describe methods for the isolation and characterization of electron transport super complexes from yeast (Chapters 10 and 11) and mammalian mitochondria (Chapter 8). Another chapter describes methods to examine the assembly of subunits encoded by mitDNA and nuclear DNA in the mitochondrial inner membrane of mammalian cells (Chapter 18). The use of ruthenium ion photooxidation and photoreduction to examine electron transfer in mitochondrial complex II and complex IV, respectively, are described in Chapters 5 and 28, respectively. Chapter 16 describes methods for examining mitochondrial mobility and protein diffusion within the mitochondrial matrix.

Although they were discovered in the 1970s, the biosynthesis and assembly iron-sulfur proteins have been examined more recently. Three chapters (Chapters 12, 14 and 15) describe methods to examine the

location, function, and assembly of iron-sulfur complexes in the mitochondrial inner membrane, whereas Chapter 13 describes the isolation and characterization an iron-sulfur protein located in the mitochondrial outer membrane.

Although they probably play a beneficial role at low concentrations, reactive oxygen species (ROS), which include superoxide anion ($O_2^{\bullet-}$) and hydrogen peroxide (H_2O_2), excessive ROS formation in mitochondria is invariably associated with pathologic conditions. Chapters 19 to 27 describe methods that have developed to detect, induce, or control formation of ROS during electron transport in mammalian and yeast mitochondria.

The methods described in this volume should provide investigators with techniques that can be used or modified to examine mitochondrial electron transport complexes, the location and function of iron-sulfur proteins, and the detection and control of reactive oxygen species that are formed during electron transport in mitochondria.

WILLIAM S. ALLISON AND IMMO E. SCHEFFLER

METHODS IN ENZYMOLOGY

VOLUME I. Preparation and Assay of Enzymes

Edited by SIDNEY P. COLOWICK AND NATHAN O. KAPLAN

VOLUME II. Preparation and Assay of Enzymes

Edited by SIDNEY P. COLOWICK AND NATHAN O. KAPLAN

VOLUME III. Preparation and Assay of Substrates

Edited by SIDNEY P. COLOWICK AND NATHAN O. KAPLAN

VOLUME IV. Special Techniques for the Enzymologist

Edited by SIDNEY P. COLOWICK AND NATHAN O. KAPLAN

VOLUME V. Preparation and Assay of Enzymes

Edited by SIDNEY P. COLOWICK AND NATHAN O. KAPLAN

VOLUME VI. Preparation and Assay of Enzymes (*Continued*)

Preparation and Assay of Substrates

Special Techniques

Edited by SIDNEY P. COLOWICK AND NATHAN O. KAPLAN

VOLUME VII. Cumulative Subject Index

Edited by SIDNEY P. COLOWICK AND NATHAN O. KAPLAN

VOLUME VIII. Complex Carbohydrates

Edited by ELIZABETH F. NEUFELD AND VICTOR GINSBURG

VOLUME IX. Carbohydrate Metabolism

Edited by WILLIS A. WOOD

VOLUME X. Oxidation and Phosphorylation

Edited by RONALD W. ESTABROOK AND MAYNARD E. PULLMAN

VOLUME XI. Enzyme Structure

Edited by C. H. W. HIRS

VOLUME XII. Nucleic Acids (Parts A and B)

Edited by LAWRENCE GROSSMAN AND KIVIE MOLDAVE

VOLUME XIII. Citric Acid Cycle

Edited by J. M. LOWENSTEIN

VOLUME XIV. Lipids

Edited by J. M. LOWENSTEIN

VOLUME XV. Steroids and Terpenoids

Edited by RAYMOND B. CLAYTON

VOLUME XVI. Fast Reactions

Edited by KENNETH KUSTIN

VOLUME XVII. Metabolism of Amino Acids and Amines (Parts A and B)

Edited by HERBERT TABOR AND CELIA WHITE TABOR

VOLUME XVIII. Vitamins and Coenzymes (Parts A, B, and C)

Edited by DONALD B. MCCORMICK AND LEMUEL D. WRIGHT

VOLUME XIX. Proteolytic Enzymes

Edited by GERTRUDE E. PERLMANN AND LASZLO LORAND

VOLUME XX. Nucleic Acids and Protein Synthesis (Part C)

Edited by KIVIE MOLDAVE AND LAWRENCE GROSSMAN

VOLUME XXI. Nucleic Acids (Part D)

Edited by LAWRENCE GROSSMAN AND KIVIE MOLDAVE

VOLUME XXII. Enzyme Purification and Related Techniques

Edited by WILLIAM B. JAKOBY

VOLUME XXIII. Photosynthesis (Part A)

Edited by ANTHONY SAN PIETRO

VOLUME XXIV. Photosynthesis and Nitrogen Fixation (Part B)

Edited by ANTHONY SAN PIETRO

VOLUME XXV. Enzyme Structure (Part B)

Edited by C. H. W. HIRS AND SERGE N. TIMASHEFF

VOLUME XXVI. Enzyme Structure (Part C)

Edited by C. H. W. HIRS AND SERGE N. TIMASHEFF

VOLUME XXVII. Enzyme Structure (Part D)

Edited by C. H. W. HIRS AND SERGE N. TIMASHEFF

VOLUME XXVIII. Complex Carbohydrates (Part B)

Edited by VICTOR GINSBURG

VOLUME XXIX. Nucleic Acids and Protein Synthesis (Part E)

Edited by LAWRENCE GROSSMAN AND KIVIE MOLDAVE

VOLUME XXX. Nucleic Acids and Protein Synthesis (Part F)

Edited by KIVIE MOLDAVE AND LAWRENCE GROSSMAN

VOLUME XXXI. Biomembranes (Part A)

Edited by SIDNEY FLEISCHER AND LESTER PACKER

VOLUME XXXII. Biomembranes (Part B)

Edited by SIDNEY FLEISCHER AND LESTER PACKER

VOLUME XXXIII. Cumulative Subject Index Volumes I-XXX

Edited by MARTHA G. DENNIS AND EDWARD A. DENNIS

VOLUME XXXIV. Affinity Techniques (Enzyme Purification: Part B)

Edited by WILLIAM B. JAKOBY AND MEIR WILCHEK

VOLUME XXXV. Lipids (Part B)

Edited by JOHN M. LOWENSTEIN

VOLUME XXXVI. Hormone Action (Part A: Steroid Hormones)

Edited by BERT W. O'MALLEY AND JOEL G. HARDMAN

VOLUME XXXVII. Hormone Action (Part B: Peptide Hormones)

Edited by BERT W. O'MALLEY AND JOEL G. HARDMAN

VOLUME XXXVIII. Hormone Action (Part C: Cyclic Nucleotides)

Edited by JOEL G. HARDMAN AND BERT W. O'MALLEY

VOLUME XXXIX. Hormone Action (Part D: Isolated Cells, Tissues,
and Organ Systems)

Edited by JOEL G. HARDMAN AND BERT W. O'MALLEY

VOLUME XL. Hormone Action (Part E: Nuclear Structure and Function)

Edited by BERT W. O'MALLEY AND JOEL G. HARDMAN

VOLUME XLI. Carbohydrate Metabolism (Part B)

Edited by W. A. WOOD

VOLUME XLII. Carbohydrate Metabolism (Part C)

Edited by W. A. WOOD

VOLUME XLIII. Antibiotics

Edited by JOHN H. HASH

VOLUME XLIV. Immobilized Enzymes

Edited by KLAUS MOSBACH

VOLUME XLV. Proteolytic Enzymes (Part B)

Edited by LASZLO LORAND

VOLUME XLVI. Affinity Labeling

Edited by WILLIAM B. JAKOBY AND MEIR WILCHEK

VOLUME XLVII. Enzyme Structure (Part E)

Edited by C. H. W. HIRS AND SERGE N. TIMASHEFF

VOLUME XLVIII. Enzyme Structure (Part F)

Edited by C. H. W. HIRS AND SERGE N. TIMASHEFF

VOLUME XLIX. Enzyme Structure (Part G)

Edited by C. H. W. HIRS AND SERGE N. TIMASHEFF

VOLUME L. Complex Carbohydrates (Part C)

Edited by VICTOR GINSBURG

VOLUME LI. Purine and Pyrimidine Nucleotide Metabolism

Edited by PATRICIA A. HOFFEE AND MARY ELLEN JONES

VOLUME LII. Biomembranes (Part C: Biological Oxidations)

Edited by SIDNEY FLEISCHER AND LESTER PACKER

VOLUME LIII. Biomembranes (Part D: Biological Oxidations)

Edited by SIDNEY FLEISCHER AND LESTER PACKER

VOLUME LIV. Biomembranes (Part E: Biological Oxidations)

Edited by SIDNEY FLEISCHER AND LESTER PACKER

VOLUME LV. Biomembranes (Part F: Bioenergetics)

Edited by SIDNEY FLEISCHER AND LESTER PACKER

VOLUME LVI. Biomembranes (Part G: Bioenergetics)

Edited by SIDNEY FLEISCHER AND LESTER PACKER

VOLUME LVII. Bioluminescence and Chemiluminescence

Edited by MARLENE A. DELUCA

VOLUME LVIII. Cell Culture

Edited by WILLIAM B. JAKOBY AND IRA PASTAN

VOLUME LIX. Nucleic Acids and Protein Synthesis (Part G)

Edited by KIVIE MOLDAVE AND LAWRENCE GROSSMAN

VOLUME LX. Nucleic Acids and Protein Synthesis (Part H)

Edited by KIVIE MOLDAVE AND LAWRENCE GROSSMAN

VOLUME 61. Enzyme Structure (Part H)

Edited by C. H. W. HIRS AND SERGE N. TIMASHEFF

VOLUME 62. Vitamins and Coenzymes (Part D)

Edited by DONALD B. MCCORMICK AND LEMUEL D. WRIGHT

VOLUME 63. Enzyme Kinetics and Mechanism (Part A: Initial Rate and Inhibitor Methods)

Edited by DANIEL L. PURICH

VOLUME 64. Enzyme Kinetics and Mechanism

(Part B: Isotopic Probes and Complex Enzyme Systems)

Edited by DANIEL L. PURICH

VOLUME 65. Nucleic Acids (Part I)

Edited by LAWRENCE GROSSMAN AND KIVIE MOLDAVE

VOLUME 66. Vitamins and Coenzymes (Part E)

Edited by DONALD B. MCCORMICK AND LEMUEL D. WRIGHT

VOLUME 67. Vitamins and Coenzymes (Part F)

Edited by DONALD B. MCCORMICK AND LEMUEL D. WRIGHT

VOLUME 68. Recombinant DNA

Edited by RAY WU

VOLUME 69. Photosynthesis and Nitrogen Fixation (Part C)

Edited by ANTHONY SAN PIETRO

VOLUME 70. Immunochemical Techniques (Part A)

Edited by HELEN VAN VUNAKIS AND JOHN J. LANGONE

VOLUME 71. Lipids (Part C)

Edited by JOHN M. LOWENSTEIN

VOLUME 72. Lipids (Part D)

Edited by JOHN M. LOWENSTEIN

VOLUME 73. Immunochemical Techniques (Part B)

Edited by JOHN J. LANGONE AND HELEN VAN VUNAKIS

VOLUME 74. Immunochemical Techniques (Part C)

Edited by JOHN J. LANGONE AND HELEN VAN VUNAKIS

VOLUME 75. Cumulative Subject Index Volumes XXXI, XXXII, XXXIV–LX

Edited by EDWARD A. DENNIS AND MARTHA G. DENNIS

VOLUME 76. Hemoglobins

Edited by ERALDO ANTONINI, LUIGI ROSSI-BERNARDI, AND EMILIA CHIANCONE

VOLUME 77. Detoxication and Drug Metabolism

Edited by WILLIAM B. JAKOBY

VOLUME 78. Interferons (Part A)

Edited by SIDNEY PESTKA

VOLUME 79. Interferons (Part B)

Edited by SIDNEY PESTKA

VOLUME 80. Proteolytic Enzymes (Part C)

Edited by LASZLO LORAND

VOLUME 81. Biomembranes (Part H: Visual Pigments and Purple Membranes, I)

Edited by LESTER PACKER

VOLUME 82. Structural and Contractile Proteins (Part A: Extracellular Matrix)

Edited by LEON W. CUNNINGHAM AND DIXIE W. FREDERIKSEN

VOLUME 83. Complex Carbohydrates (Part D)

Edited by VICTOR GINSBURG

VOLUME 84. Immunochemical Techniques (Part D: Selected Immunoassays)

Edited by JOHN J. LANGONE AND HELEN VAN VUNAKIS

VOLUME 85. Structural and Contractile Proteins (Part B: The Contractile Apparatus and the Cytoskeleton)

Edited by DIXIE W. FREDERIKSEN AND LEON W. CUNNINGHAM

VOLUME 86. Prostaglandins and Arachidonate Metabolites

Edited by WILLIAM E. M. LANDS AND WILLIAM L. SMITH

VOLUME 87. Enzyme Kinetics and Mechanism (Part C: Intermediates, Stereo-chemistry, and Rate Studies)

Edited by DANIEL L. PURICH

VOLUME 88. Biomembranes (Part I: Visual Pigments and Purple Membranes, II)

Edited by LESTER PACKER

VOLUME 89. Carbohydrate Metabolism (Part D)

Edited by WILLIS A. WOOD

VOLUME 90. Carbohydrate Metabolism (Part E)

Edited by WILLIS A. WOOD

VOLUME 91. Enzyme Structure (Part I)

Edited by C. H. W. HIRS AND SERGE N. TIMASHEFF

VOLUME 92. Immunochemical Techniques (Part E: Monoclonal Antibodies and General Immunoassay Methods)

Edited by JOHN J. LANGONE AND HELEN VAN VUNAKIS

VOLUME 93. Immunochemical Techniques (Part F: Conventional Antibodies, Fc Receptors, and Cytotoxicity)

Edited by JOHN J. LANGONE AND HELEN VAN VUNAKIS

VOLUME 94. Polyamines

Edited by HERBERT TABOR AND CELIA WHITE TABOR

VOLUME 95. Cumulative Subject Index Volumes 61–74, 76–80

Edited by EDWARD A. DENNIS AND MARTHA G. DENNIS

VOLUME 96. Biomembranes [Part J: Membrane Biogenesis: Assembly and Targeting (General Methods; Eukaryotes)]

Edited by SIDNEY FLEISCHER AND BECCA FLEISCHER

VOLUME 97. Biomembranes [Part K: Membrane Biogenesis: Assembly and Targeting (Prokaryotes, Mitochondria, and Chloroplasts)]

Edited by SIDNEY FLEISCHER AND BECCA FLEISCHER

VOLUME 98. Biomembranes (Part L: Membrane Biogenesis: Processing and Recycling)

Edited by SIDNEY FLEISCHER AND BECCA FLEISCHER

VOLUME 99. Hormone Action (Part F: Protein Kinases)

Edited by JACKIE D. CORBIN AND JOEL G. HARDMAN

VOLUME 100. Recombinant DNA (Part B)

Edited by RAY WU, LAWRENCE GROSSMAN, AND KIVIE MOLDAVE

VOLUME 101. Recombinant DNA (Part C)

Edited by RAY WU, LAWRENCE GROSSMAN, AND KIVIE MOLDAVE

VOLUME 102. Hormone Action (Part G: Calmodulin and Calcium-Binding Proteins)

Edited by ANTHONY R. MEANS AND BERT W. O'MALLEY

VOLUME 103. Hormone Action (Part H: Neuroendocrine Peptides)

Edited by P. MICHAEL CONN

VOLUME 104. Enzyme Purification and Related Techniques (Part C)

Edited by WILLIAM B. JAKOBY

VOLUME 105. Oxygen Radicals in Biological Systems

Edited by LESTER PACKER

VOLUME 106. Posttranslational Modifications (Part A)

Edited by FINN WOLD AND KIVIE MOLDAVE

VOLUME 107. Posttranslational Modifications (Part B)

Edited by FINN WOLD AND KIVIE MOLDAVE

VOLUME 108. Immunochemical Techniques (Part G: Separation and Characterization of Lymphoid Cells)

Edited by GIOVANNI DI SABATO, JOHN J. LANGONE, AND HELEN VAN VUNAKIS

VOLUME 109. Hormone Action (Part I: Peptide Hormones)

Edited by LUTZ BIRNBAUMER AND BERT W. O'MALLEY

VOLUME 110. Steroids and Isoprenoids (Part A)

Edited by JOHN H. LAW AND HANS C. RILLING

VOLUME 111. Steroids and Isoprenoids (Part B)

Edited by JOHN H. LAW AND HANS C. RILLING

VOLUME 112. Drug and Enzyme Targeting (Part A)

Edited by KENNETH J. WIDDER AND RALPH GREEN

VOLUME 113. Glutamate, Glutamine, Glutathione, and Related Compounds

Edited by ALTON MEISTER

VOLUME 114. Diffraction Methods for Biological Macromolecules (Part A)

Edited by HAROLD W. WYCKOFF, C. H. W. HIRS, AND SERGE N. TIMASHEFF

VOLUME 115. Diffraction Methods for Biological Macromolecules (Part B)

Edited by HAROLD W. WYCKOFF, C. H. W. HIRS, AND SERGE N. TIMASHEFF

VOLUME 116. Immunochemical Techniques

(Part H: Effectors and Mediators of Lymphoid Cell Functions)

Edited by GIOVANNI DI SABATO, JOHN J. LANGONE, AND HELEN VAN VUNAKIS

VOLUME 117. Enzyme Structure (Part J)

Edited by C. H. W. HIRS AND SERGE N. TIMASHEFF

VOLUME 118. Plant Molecular Biology

Edited by ARTHUR WEISSBACH AND HERBERT WEISSBACH

VOLUME 119. Interferons (Part C)

Edited by SIDNEY PESTRA

VOLUME 120. Cumulative Subject Index Volumes 81–94, 96–101

VOLUME 121. Immunochemical Techniques (Part I: Hybridoma Technology and Monoclonal Antibodies)

Edited by JOHN J. LANGONE AND HELEN VAN VUNAKIS

VOLUME 122. Vitamins and Coenzymes (Part G)

Edited by FRANK CHYTL AND DONALD B. MCCORMICK

- VOLUME 123. Vitamins and Coenzymes (Part H)
Edited by FRANK CHYTIL AND DONALD B. McCORMICK
- VOLUME 124. Hormone Action (Part J: Neuroendocrine Peptides)
Edited by P. MICHAEL CONN
- VOLUME 125. Biomembranes (Part M: Transport in Bacteria, Mitochondria, and Chloroplasts: General Approaches and Transport Systems)
Edited by SIDNEY FLEISCHER AND BECCA FLEISCHER
- VOLUME 126. Biomembranes (Part N: Transport in Bacteria, Mitochondria, and Chloroplasts: Protonmotive Force)
Edited by SIDNEY FLEISCHER AND BECCA FLEISCHER
- VOLUME 127. Biomembranes (Part O: Protons and Water: Structure and Translocation)
Edited by LESTER PACKER
- VOLUME 128. Plasma Lipoproteins (Part A: Preparation, Structure, and Molecular Biology)
Edited by JERE P. SEGREST AND JOHN J. ALBERS
- VOLUME 129. Plasma Lipoproteins (Part B: Characterization, Cell Biology, and Metabolism)
Edited by JOHN J. ALBERS AND JERE P. SEGREST
- VOLUME 130. Enzyme Structure (Part K)
Edited by C. H. W. HIRS AND SERGE N. TIMASHEFF
- VOLUME 131. Enzyme Structure (Part L)
Edited by C. H. W. HIRS AND SERGE N. TIMASHEFF
- VOLUME 132. Immunochemical Techniques (Part J: Phagocytosis and Cell-Mediated Cytotoxicity)
Edited by GIOVANNI DI SABATO AND JOHANNES EVERSE
- VOLUME 133. Bioluminescence and Chemiluminescence (Part B)
Edited by MARLENE DELUCA AND WILLIAM D. McELROY
- VOLUME 134. Structural and Contractile Proteins (Part C: The Contractile Apparatus and the Cytoskeleton)
Edited by RICHARD B. VALLEE
- VOLUME 135. Immobilized Enzymes and Cells (Part B)
Edited by KLAUS MOSBACH
- VOLUME 136. Immobilized Enzymes and Cells (Part C)
Edited by KLAUS MOSBACH
- VOLUME 137. Immobilized Enzymes and Cells (Part D)
Edited by KLAUS MOSBACH
- VOLUME 138. Complex Carbohydrates (Part E)
Edited by VICTOR GINSBURG

VOLUME 139. Cellular Regulators (Part A: Calcium- and Calmodulin-Binding Proteins)

Edited by ANTHONY R. MEANS AND P. MICHAEL CONN

VOLUME 140. Cumulative Subject Index Volumes 102–119, 121–134

VOLUME 141. Cellular Regulators (Part B: Calcium and Lipids)

Edited by P. MICHAEL CONN AND ANTHONY R. MEANS

VOLUME 142. Metabolism of Aromatic Amino Acids and Amines

Edited by SEYMOUR KAUFMAN

VOLUME 143. Sulfur and Sulfur Amino Acids

Edited by WILLIAM B. JAKOBY AND OWEN GRIFFITH

VOLUME 144. Structural and Contractile Proteins (Part D: Extracellular Matrix)

Edited by LEON W. CUNNINGHAM

VOLUME 145. Structural and Contractile Proteins (Part E: Extracellular Matrix)

Edited by LEON W. CUNNINGHAM

VOLUME 146. Peptide Growth Factors (Part A)

Edited by DAVID BARNES AND DAVID A. SIRBASKU

VOLUME 147. Peptide Growth Factors (Part B)

Edited by DAVID BARNES AND DAVID A. SIRBASKU

VOLUME 148. Plant Cell Membranes

Edited by LESTER PACKER AND ROLAND DOUCE

VOLUME 149. Drug and Enzyme Targeting (Part B)

Edited by RALPH GREEN AND KENNETH J. WIDDER

VOLUME 150. Immunochemical Techniques (Part K: *In Vitro* Models of B and T Cell Functions and Lymphoid Cell Receptors)

Edited by GIOVANNI DI SABATO

VOLUME 151. Molecular Genetics of Mammalian Cells

Edited by MICHAEL M. GOTTESMAN

VOLUME 152. Guide to Molecular Cloning Techniques

Edited by SHELBY L. BERGER AND ALAN R. KIMMEL

VOLUME 153. Recombinant DNA (Part D)

Edited by RAY WU AND LAWRENCE GROSSMAN

VOLUME 154. Recombinant DNA (Part E)

Edited by RAY WU AND LAWRENCE GROSSMAN

VOLUME 155. Recombinant DNA (Part F)

Edited by RAY WU

VOLUME 156. Biomembranes (Part P: ATP-Driven Pumps and Related Transport: The Na, K-Pump)

Edited by SIDNEY FLEISCHER AND BECCA FLEISCHER

VOLUME 157. Biomembranes (Part Q: ATP-Driven Pumps and Related Transport: Calcium, Proton, and Potassium Pumps)

Edited by SIDNEY FLEISCHER AND BECCA FLEISCHER

VOLUME 158. Metalloproteins (Part A)

Edited by JAMES F. RIORDAN AND BERT L. VALLEE

VOLUME 159. Initiation and Termination of Cyclic Nucleotide Action

Edited by JACKIE D. CORBIN AND ROGER A. JOHNSON

VOLUME 160. Biomass (Part A: Cellulose and Hemicellulose)

Edited by WILLIS A. WOOD AND SCOTT T. KELLOGG

VOLUME 161. Biomass (Part B: Lignin, Pectin, and Chitin)

Edited by WILLIS A. WOOD AND SCOTT T. KELLOGG

VOLUME 162. Immunochemical Techniques (Part L: Chemotaxis and Inflammation)

Edited by GIOVANNI DI SABATO

VOLUME 163. Immunochemical Techniques (Part M: Chemotaxis and Inflammation)

Edited by GIOVANNI DI SABATO

VOLUME 164. Ribosomes

Edited by HARRY F. NOLLER, JR., AND KIVIE MOLDAVE

VOLUME 165. Microbial Toxins: Tools for Enzymology

Edited by SIDNEY HARSHMAN

VOLUME 166. Branched-Chain Amino Acids

Edited by ROBERT HARRIS AND JOHN R. SOKATCH

VOLUME 167. Cyanobacteria

Edited by LESTER PACKER AND ALEXANDER N. GLAZER

VOLUME 168. Hormone Action (Part K: Neuroendocrine Peptides)

Edited by P. MICHAEL CONN

VOLUME 169. Platelets: Receptors, Adhesion, Secretion (Part A)

Edited by JACEK HAWIGER

VOLUME 170. Nucleosomes

Edited by PAUL M. WASSARMAN AND ROGER D. KORNBERG

VOLUME 171. Biomembranes (Part R: Transport Theory: Cells and Model Membranes)

Edited by SIDNEY FLEISCHER AND BECCA FLEISCHER

VOLUME 172. Biomembranes (Part S: Transport: Membrane Isolation and Characterization)

Edited by SIDNEY FLEISCHER AND BECCA FLEISCHER

VOLUME 173. Biomembranes [Part T: Cellular and Subcellular Transport: Eukaryotic (Nonepithelial) Cells]

Edited by SIDNEY FLEISCHER AND BECCA FLEISCHER

VOLUME 174. Biomembranes [Part U: Cellular and Subcellular Transport: Eukaryotic (Nonepithelial) Cells]

Edited by SIDNEY FLEISCHER AND BECCA FLEISCHER

VOLUME 175. Cumulative Subject Index Volumes 135–139, 141–167

VOLUME 176. Nuclear Magnetic Resonance (Part A: Spectral Techniques and Dynamics)

Edited by NORMAN J. OPPENHEIMER AND THOMAS L. JAMES

VOLUME 177. Nuclear Magnetic Resonance (Part B: Structure and Mechanism)

Edited by NORMAN J. OPPENHEIMER AND THOMAS L. JAMES

VOLUME 178. Antibodies, Antigens, and Molecular Mimicry

Edited by JOHN J. LANGONE

VOLUME 179. Complex Carbohydrates (Part F)

Edited by VICTOR GINSBURG

VOLUME 180. RNA Processing (Part A: General Methods)

Edited by JAMES E. DAHLBERG AND JOHN N. ABELSON

VOLUME 181. RNA Processing (Part B: Specific Methods)

Edited by JAMES E. DAHLBERG AND JOHN N. ABELSON

VOLUME 182. Guide to Protein Purification

Edited by MURRAY P. DEUTSCHER

VOLUME 183. Molecular Evolution: Computer Analysis of Protein and Nucleic Acid Sequences

Edited by RUSSELL F. DOOLITTLE

VOLUME 184. Avidin-Biotin Technology

Edited by MEIR WILCHEK AND EDWARD A. BAYER

VOLUME 185. Gene Expression Technology

Edited by DAVID V. GOEDDEL

VOLUME 186. Oxygen Radicals in Biological Systems (Part B: Oxygen Radicals and Antioxidants)

Edited by LESTER PACKER AND ALEXANDER N. GLAZER

VOLUME 187. Arachidonate Related Lipid Mediators

Edited by ROBERT C. MURPHY AND FRANK A. FITZPATRICK

VOLUME 188. Hydrocarbons and Methylotrophy

Edited by MARY E. LIDSTROM

VOLUME 189. Retinoids (Part A: Molecular and Metabolic Aspects)

Edited by LESTER PACKER

VOLUME 190. Retinoids (Part B: Cell Differentiation and Clinical Applications)

Edited by LESTER PACKER

VOLUME 191. Biomembranes (Part V: Cellular and Subcellular Transport: Epithelial Cells)

Edited by SIDNEY FLEISCHER AND BECCA FLEISCHER

VOLUME 192. Biomembranes (Part W: Cellular and Subcellular Transport: Epithelial Cells)

Edited by SIDNEY FLEISCHER AND BECCA FLEISCHER

VOLUME 193. Mass Spectrometry

Edited by JAMES A. MCCLOSKEY

VOLUME 194. Guide to Yeast Genetics and Molecular Biology

Edited by CHRISTINE GUTHRIE AND GERALD R. FINK

VOLUME 195. Adenylyl Cyclase, G Proteins, and Guanylyl Cyclase

Edited by ROGER A. JOHNSON AND JACKIE D. CORBIN

VOLUME 196. Molecular Motors and the Cytoskeleton

Edited by RICHARD B. VALLEE

VOLUME 197. Phospholipases

Edited by EDWARD A. DENNIS

VOLUME 198. Peptide Growth Factors (Part C)

Edited by DAVID BARNES, J. P. MATHER, AND GORDON H. SATO

VOLUME 199. Cumulative Subject Index Volumes 168–174, 176–194

VOLUME 200. Protein Phosphorylation (Part A: Protein Kinases: Assays, Purification, Antibodies, Functional Analysis, Cloning, and Expression)

Edited by TONY HUNTER AND BARTHOLOMEW M. SEFTON

VOLUME 201. Protein Phosphorylation (Part B: Analysis of Protein Phosphorylation, Protein Kinase Inhibitors, and Protein Phosphatases)

Edited by TONY HUNTER AND BARTHOLOMEW M. SEFTON

VOLUME 202. Molecular Design and Modeling: Concepts and Applications (Part A: Proteins, Peptides, and Enzymes)

Edited by JOHN J. LANGONE

VOLUME 203. Molecular Design and Modeling: Concepts and Applications (Part B: Antibodies and Antigens, Nucleic Acids, Polysaccharides, and Drugs)

Edited by JOHN J. LANGONE

VOLUME 204. Bacterial Genetic Systems

Edited by JEFFREY H. MILLER

VOLUME 205. Metallobiochemistry (Part B: Metallothionein and Related Molecules)

Edited by JAMES F. RIORDAN AND BERT L. VALLEE

VOLUME 206. Cytochrome P450

Edited by MICHAEL R. WATERMAN AND ERIC F. JOHNSON

VOLUME 207. Ion Channels

Edited by BERNARDO RUDY AND LINDA E. IVERSON

VOLUME 208. Protein–DNA Interactions

Edited by ROBERT T. SAUER

VOLUME 209. Phospholipid Biosynthesis

Edited by EDWARD A. DENNIS AND DENNIS E. VANCE

VOLUME 210. Numerical Computer Methods

Edited by LUDWIG BRAND AND MICHAEL L. JOHNSON

VOLUME 211. DNA Structures (Part A: Synthesis and Physical Analysis of DNA)

Edited by DAVID M. J. LILLEY AND JAMES E. DAHLBERG

VOLUME 212. DNA Structures (Part B: Chemical and Electrophoretic Analysis of DNA)

Edited by DAVID M. J. LILLEY AND JAMES E. DAHLBERG

VOLUME 213. Carotenoids (Part A: Chemistry, Separation, Quantitation, and Antioxidation)

Edited by LESTER PACKER

VOLUME 214. Carotenoids (Part B: Metabolism, Genetics, and Biosynthesis)

Edited by LESTER PACKER

VOLUME 215. Platelets: Receptors, Adhesion, Secretion (Part B)

Edited by JACEK J. HAWIGER

VOLUME 216. Recombinant DNA (Part G)

Edited by RAY WU

VOLUME 217. Recombinant DNA (Part H)

Edited by RAY WU

VOLUME 218. Recombinant DNA (Part I)

Edited by RAY WU

VOLUME 219. Reconstitution of Intracellular Transport

Edited by JAMES E. ROTHMAN

VOLUME 220. Membrane Fusion Techniques (Part A)

Edited by NEJAT DÜZGÜNEŞ

VOLUME 221. Membrane Fusion Techniques (Part B)

Edited by NEJAT DÜZGÜNEŞ

VOLUME 222. Proteolytic Enzymes in Coagulation, Fibrinolysis, and Complement Activation (Part A: Mammalian Blood Coagulation Factors and Inhibitors)

Edited by LASZLO LORAND AND KENNETH G. MANN

VOLUME 223. Proteolytic Enzymes in Coagulation, Fibrinolysis, and Complement Activation (Part B: Complement Activation, Fibrinolysis, and Nonmammalian Blood Coagulation Factors)

Edited by LASZLO LORAND AND KENNETH G. MANN

VOLUME 224. Molecular Evolution: Producing the Biochemical Data

Edited by ELIZABETH ANNE ZIMMER, THOMAS J. WHITE, REBECCA L. CANN, AND ALLAN C. WILSON

VOLUME 225. Guide to Techniques in Mouse Development

Edited by PAUL M. WASSARMAN AND MELVIN L. DEPAMPHILIS

VOLUME 226. Metallobiochemistry (Part C: Spectroscopic and Physical Methods for Probing Metal Ion Environments in Metalloenzymes and Metalloproteins)

Edited by JAMES F. RIORDAN AND BERT L. VALLEE

VOLUME 227. Metallobiochemistry (Part D: Physical and Spectroscopic Methods for Probing Metal Ion Environments in Metalloproteins)

Edited by JAMES F. RIORDAN AND BERT L. VALLEE

VOLUME 228. Aqueous Two-Phase Systems

Edited by HARRY WALTER AND GÖTE JOHANSSON

VOLUME 229. Cumulative Subject Index Volumes 195–198, 200–227

VOLUME 230. Guide to Techniques in Glycobiology

Edited by WILLIAM J. LENNARZ AND GERALD W. HART

VOLUME 231. Hemoglobins (Part B: Biochemical and Analytical Methods)

Edited by JOHANNES EVERSE, KIM D. VANDEGRIFF, AND ROBERT M. WINSLOW

VOLUME 232. Hemoglobins (Part C: Biophysical Methods)

Edited by JOHANNES EVERSE, KIM D. VANDEGRIFF, AND ROBERT M. WINSLOW

VOLUME 233. Oxygen Radicals in Biological Systems (Part C)

Edited by LESTER PACKER

VOLUME 234. Oxygen Radicals in Biological Systems (Part D)

Edited by LESTER PACKER

VOLUME 235. Bacterial Pathogenesis (Part A: Identification and Regulation of Virulence Factors)

Edited by VIRGINIA L. CLARK AND PATRIK M. BAVOIL

VOLUME 236. Bacterial Pathogenesis (Part B: Integration of Pathogenic Bacteria with Host Cells)

Edited by VIRGINIA L. CLARK AND PATRIK M. BAVOIL

VOLUME 237. Heterotrimeric G Proteins

Edited by RAVI IYENGAR

VOLUME 238. Heterotrimeric G-Protein Effectors

Edited by RAVI IYENGAR

- VOLUME 239. Nuclear Magnetic Resonance (Part C)
Edited by THOMAS L. JAMES AND NORMAN J. OPPENHEIMER
- VOLUME 240. Numerical Computer Methods (Part B)
Edited by MICHAEL L. JOHNSON AND LUDWIG BRAND
- VOLUME 241. Retroviral Proteases
Edited by LAWRENCE C. KUO AND JULES A. SHAFER
- VOLUME 242. Neoglycoconjugates (Part A)
Edited by Y. C. LEE AND REIKO T. LEE
- VOLUME 243. Inorganic Microbial Sulfur Metabolism
Edited by HARRY D. PECK, JR., AND JEAN LEGALL
- VOLUME 244. Proteolytic Enzymes: Serine and Cysteine Peptidases
Edited by ALAN J. BARRETT
- VOLUME 245. Extracellular Matrix Components
Edited by E. RUOSLAHTI AND E. ENGVALL
- VOLUME 246. Biochemical Spectroscopy
Edited by KENNETH SAUER
- VOLUME 247. Neoglycoconjugates (Part B: Biomedical Applications)
Edited by Y. C. LEE AND REIKO T. LEE
- VOLUME 248. Proteolytic Enzymes: Aspartic and Metallo Peptidases
Edited by ALAN J. BARRETT
- VOLUME 249. Enzyme Kinetics and Mechanism (Part D: Developments in Enzyme Dynamics)
Edited by DANIEL L. PURICH
- VOLUME 250. Lipid Modifications of Proteins
Edited by PATRICK J. CASEY AND JANICE E. BUSS
- VOLUME 251. Biothiols (Part A: Monothiols and Dithiols, Protein Thiols, and Thiyl Radicals)
Edited by LESTER PACKER
- VOLUME 252. Biothiols (Part B: Glutathione and Thioredoxin; Thiols in Signal Transduction and Gene Regulation)
Edited by LESTER PACKER
- VOLUME 253. Adhesion of Microbial Pathogens
Edited by RON J. DOYLE AND ITZHAK OFEK
- VOLUME 254. Oncogene Techniques
Edited by PETER K. VOGT AND IINDER M. VERMA
- VOLUME 255. Small GTPases and Their Regulators (Part A: Ras Family)
Edited by W. E. BALCH, CHANNING J. DER, AND ALAN HALL
- VOLUME 256. Small GTPases and Their Regulators (Part B: Rho Family)
Edited by W. E. BALCH, CHANNING J. DER, AND ALAN HALL

- VOLUME 257. Small GTPases and Their Regulators (Part C: Proteins Involved in Transport)
Edited by W. E. BALCH, CHANNING J. DER, AND ALAN HALL
- VOLUME 258. Redox-Active Amino Acids in Biology
Edited by JUDITH P. KLINMAN
- VOLUME 259. Energetics of Biological Macromolecules
Edited by MICHAEL L. JOHNSON AND GARY K. ACKERS
- VOLUME 260. Mitochondrial Biogenesis and Genetics (Part A)
Edited by GIUSEPPE M. ATTARDI AND ANNE CHOMYN
- VOLUME 261. Nuclear Magnetic Resonance and Nucleic Acids
Edited by THOMAS L. JAMES
- VOLUME 262. DNA Replication
Edited by JUDITH L. CAMPBELL
- VOLUME 263. Plasma Lipoproteins (Part C: Quantitation)
Edited by WILLIAM A. BRADLEY, SANDRA H. GIANTURCO, AND JERE P. SEGREST
- VOLUME 264. Mitochondrial Biogenesis and Genetics (Part B)
Edited by GIUSEPPE M. ATTARDI AND ANNE CHOMYN
- VOLUME 265. Cumulative Subject Index Volumes 228, 230–262
- VOLUME 266. Computer Methods for Macromolecular Sequence Analysis
Edited by RUSSELL F. DOOLITTLE
- VOLUME 267. Combinatorial Chemistry
Edited by JOHN N. ABELSON
- VOLUME 268. Nitric Oxide (Part A: Sources and Detection of NO; NO Synthase)
Edited by LESTER PACKER
- VOLUME 269. Nitric Oxide (Part B: Physiological and Pathological Processes)
Edited by LESTER PACKER
- VOLUME 270. High Resolution Separation and Analysis of Biological Macromolecules (Part A: Fundamentals)
Edited by BARRY L. KARGER AND WILLIAM S. HANCOCK
- VOLUME 271. High Resolution Separation and Analysis of Biological Macromolecules (Part B: Applications)
Edited by BARRY L. KARGER AND WILLIAM S. HANCOCK
- VOLUME 272. Cytochrome P450 (Part B)
Edited by ERIC F. JOHNSON AND MICHAEL R. WATERMAN
- VOLUME 273. RNA Polymerase and Associated Factors (Part A)
Edited by SANKAR ADHYA
- VOLUME 274. RNA Polymerase and Associated Factors (Part B)
Edited by SANKAR ADHYA

- VOLUME 275. Viral Polymerases and Related Proteins
Edited by LAWRENCE C. KUO, DAVID B. OLSEN, AND STEVEN S. CARROLL
- VOLUME 276. Macromolecular Crystallography (Part A)
Edited by CHARLES W. CARTER, JR., AND ROBERT M. SWEET
- VOLUME 277. Macromolecular Crystallography (Part B)
Edited by CHARLES W. CARTER, JR., AND ROBERT M. SWEET
- VOLUME 278. Fluorescence Spectroscopy
Edited by LUDWIG BRAND AND MICHAEL L. JOHNSON
- VOLUME 279. Vitamins and Coenzymes (Part I)
Edited by DONALD B. McCORMICK, JOHN W. SUTTIE, AND CONRAD WAGNER
- VOLUME 280. Vitamins and Coenzymes (Part J)
Edited by DONALD B. McCORMICK, JOHN W. SUTTIE, AND CONRAD WAGNER
- VOLUME 281. Vitamins and Coenzymes (Part K)
Edited by DONALD B. McCORMICK, JOHN W. SUTTIE, AND CONRAD WAGNER
- VOLUME 282. Vitamins and Coenzymes (Part L)
Edited by DONALD B. McCORMICK, JOHN W. SUTTIE, AND CONRAD WAGNER
- VOLUME 283. Cell Cycle Control
Edited by WILLIAM G. DUNPHY
- VOLUME 284. Lipases (Part A: Biotechnology)
Edited by BYRON RUBIN AND EDWARD A. DENNIS
- VOLUME 285. Cumulative Subject Index Volumes 263, 264, 266–284, 286–289
- VOLUME 286. Lipases (Part B: Enzyme Characterization and Utilization)
Edited by BYRON RUBIN AND EDWARD A. DENNIS
- VOLUME 287. Chemokines
Edited by RICHARD HORUK
- VOLUME 288. Chemokine Receptors
Edited by RICHARD HORUK
- VOLUME 289. Solid Phase Peptide Synthesis
Edited by GREGG B. FIELDS
- VOLUME 290. Molecular Chaperones
Edited by GEORGE H. LORIMER AND THOMAS BALDWIN
- VOLUME 291. Caged Compounds
Edited by GERARD MARRIOTT
- VOLUME 292. ABC Transporters: Biochemical, Cellular, and Molecular Aspects
Edited by SURESH V. AMBUDKAR AND MICHAEL M. GOTTESMAN
- VOLUME 293. Ion Channels (Part B)
Edited by P. MICHAEL CONN

VOLUME 294. Ion Channels (Part C)

Edited by P. MICHAEL CONN

VOLUME 295. Energetics of Biological Macromolecules (Part B)

Edited by GARY K. ACKERS AND MICHAEL L. JOHNSON

VOLUME 296. Neurotransmitter Transporters

Edited by SUSAN G. AMARA

VOLUME 297. Photosynthesis: Molecular Biology of Energy Capture

Edited by LEE MCINTOSH

VOLUME 298. Molecular Motors and the Cytoskeleton (Part B)

Edited by RICHARD B. VALLEE

VOLUME 299. Oxidants and Antioxidants (Part A)

Edited by LESTER PACKER

VOLUME 300. Oxidants and Antioxidants (Part B)

Edited by LESTER PACKER

VOLUME 301. Nitric Oxide: Biological and Antioxidant Activities (Part C)

Edited by LESTER PACKER

VOLUME 302. Green Fluorescent Protein

Edited by P. MICHAEL CONN

VOLUME 303. cDNA Preparation and Display

Edited by SHERMAN M. WEISSMAN

VOLUME 304. Chromatin

Edited by PAUL M. WASSARMAN AND ALAN P. WOLFFE

VOLUME 305. Bioluminescence and Chemiluminescence (Part C)

Edited by THOMAS O. BALDWIN AND MIRIAM M. ZIEGLER

VOLUME 306. Expression of Recombinant Genes in Eukaryotic Systems

Edited by JOSEPH C. GLORIOSO AND MARTIN C. SCHMIDT

VOLUME 307. Confocal Microscopy

Edited by P. MICHAEL CONN

VOLUME 308. Enzyme Kinetics and Mechanism (Part E: Energetics of Enzyme Catalysis)

Edited by DANIEL L. PURICH AND VERN L. SCHRAMM

VOLUME 309. Amyloid, Prions, and Other Protein Aggregates

Edited by RONALD WETZEL

VOLUME 310. Biofilms

Edited by RON J. DOYLE

VOLUME 311. Sphingolipid Metabolism and Cell Signaling (Part A)

Edited by ALFRED H. MERRILL, JR., AND YUSUF A. HANNUN

VOLUME 312. Sphingolipid Metabolism and Cell Signaling (Part B)

Edited by ALFRED H. MERRILL, JR., AND YUSUF A. HANNUN

VOLUME 313. Antisense Technology (Part A: General Methods, Methods of Delivery, and RNA Studies)

Edited by M. IAN PHILLIPS

VOLUME 314. Antisense Technology (Part B: Applications)

Edited by M. IAN PHILLIPS

VOLUME 315. Vertebrate Phototransduction and the Visual Cycle (Part A)

Edited by KRZYSZTOF PALCZEWSKI

VOLUME 316. Vertebrate Phototransduction and the Visual Cycle (Part B)

Edited by KRZYSZTOF PALCZEWSKI

VOLUME 317. RNA–Ligand Interactions (Part A: Structural Biology Methods)

Edited by DANIEL W. CELANDER AND JOHN N. ABELSON

VOLUME 318. RNA–Ligand Interactions (Part B: Molecular Biology Methods)

Edited by DANIEL W. CELANDER AND JOHN N. ABELSON

VOLUME 319. Singlet Oxygen, UV-A, and Ozone

Edited by LESTER PACKER AND HELMUT SIES

VOLUME 320. Cumulative Subject Index Volumes 290–319

VOLUME 321. Numerical Computer Methods (Part C)

Edited by MICHAEL L. JOHNSON AND LUDWIG BRAND

VOLUME 322. Apoptosis

Edited by JOHN C. REED

VOLUME 323. Energetics of Biological Macromolecules (Part C)

Edited by MICHAEL L. JOHNSON AND GARY K. ACKERS

VOLUME 324. Branched-Chain Amino Acids (Part B)

Edited by ROBERT A. HARRIS AND JOHN R. SOKATCH

VOLUME 325. Regulators and Effectors of Small GTPases (Part D: Rho Family)

Edited by W. E. BALCH, CHANNING J. DER, AND ALAN HALL

VOLUME 326. Applications of Chimeric Genes and Hybrid Proteins (Part A: Gene Expression and Protein Purification)

Edited by JEREMY THORNER, SCOTT D. EMR, AND JOHN N. ABELSON

VOLUME 327. Applications of Chimeric Genes and Hybrid Proteins (Part B: Cell Biology and Physiology)

Edited by JEREMY THORNER, SCOTT D. EMR, AND JOHN N. ABELSON

VOLUME 328. Applications of Chimeric Genes and Hybrid Proteins (Part C: Protein–Protein Interactions and Genomics)

Edited by JEREMY THORNER, SCOTT D. EMR, AND JOHN N. ABELSON

- VOLUME 329. Regulators and Effectors of Small GTPases (Part E: GTPases Involved in Vesicular Traffic)
Edited by W. E. BALCH, CHANNING J. DER, AND ALAN HALL
- VOLUME 330. Hyperthermophilic Enzymes (Part A)
Edited by MICHAEL W. W. ADAMS AND ROBERT M. KELLY
- VOLUME 331. Hyperthermophilic Enzymes (Part B)
Edited by MICHAEL W. W. ADAMS AND ROBERT M. KELLY
- VOLUME 332. Regulators and Effectors of Small GTPases (Part F: Ras Family I)
Edited by W. E. BALCH, CHANNING J. DER, AND ALAN HALL
- VOLUME 333. Regulators and Effectors of Small GTPases (Part G: Ras Family II)
Edited by W. E. BALCH, CHANNING J. DER, AND ALAN HALL
- VOLUME 334. Hyperthermophilic Enzymes (Part C)
Edited by MICHAEL W. W. ADAMS AND ROBERT M. KELLY
- VOLUME 335. Flavonoids and Other Polyphenols
Edited by LESTER PACKER
- VOLUME 336. Microbial Growth in Biofilms (Part A: Developmental and Molecular Biological Aspects)
Edited by RON J. DOYLE
- VOLUME 337. Microbial Growth in Biofilms (Part B: Special Environments and Physicochemical Aspects)
Edited by RON J. DOYLE
- VOLUME 338. Nuclear Magnetic Resonance of Biological Macromolecules (Part A)
Edited by THOMAS L. JAMES, VOLKER DÖTSCH, AND ULI SCHMITZ
- VOLUME 339. Nuclear Magnetic Resonance of Biological Macromolecules (Part B)
Edited by THOMAS L. JAMES, VOLKER DÖTSCH, AND ULI SCHMITZ
- VOLUME 340. Drug–Nucleic Acid Interactions
Edited by JONATHAN B. CHAIRES AND MICHAEL J. WARING
- VOLUME 341. Ribonucleases (Part A)
Edited by ALLEN W. NICHOLSON
- VOLUME 342. Ribonucleases (Part B)
Edited by ALLEN W. NICHOLSON
- VOLUME 343. G Protein Pathways (Part A: Receptors)
Edited by RAVI IYENGAR AND JOHN D. HILDEBRANDT
- VOLUME 344. G Protein Pathways (Part B: G Proteins and Their Regulators)
Edited by RAVI IYENGAR AND JOHN D. HILDEBRANDT
- VOLUME 345. G Protein Pathways (Part C: Effector Mechanisms)
Edited by RAVI IYENGAR AND JOHN D. HILDEBRANDT

- VOLUME 346. Gene Therapy Methods
Edited by M. IAN PHILLIPS
- VOLUME 347. Protein Sensors and Reactive Oxygen Species (Part A: Selenoproteins and Thioredoxin)
Edited by HELMUT SIES AND LESTER PACKER
- VOLUME 348. Protein Sensors and Reactive Oxygen Species (Part B: Thiol Enzymes and Proteins)
Edited by HELMUT SIES AND LESTER PACKER
- VOLUME 349. Superoxide Dismutase
Edited by LESTER PACKER
- VOLUME 350. Guide to Yeast Genetics and Molecular and Cell Biology (Part B)
Edited by CHRISTINE GUTHRIE AND GERALD R. FINK
- VOLUME 351. Guide to Yeast Genetics and Molecular and Cell Biology (Part C)
Edited by CHRISTINE GUTHRIE AND GERALD R. FINK
- VOLUME 352. Redox Cell Biology and Genetics (Part A)
Edited by CHANDAN K. SEN AND LESTER PACKER
- VOLUME 353. Redox Cell Biology and Genetics (Part B)
Edited by CHANDAN K. SEN AND LESTER PACKER
- VOLUME 354. Enzyme Kinetics and Mechanisms (Part F: Detection and Characterization of Enzyme Reaction Intermediates)
Edited by DANIEL L. PURICH
- VOLUME 355. Cumulative Subject Index Volumes 321–354
- VOLUME 356. Laser Capture Microscopy and Microdissection
Edited by P. MICHAEL CONN
- VOLUME 357. Cytochrome P450, Part C
Edited by ERIC F. JOHNSON AND MICHAEL R. WATERMAN
- VOLUME 358. Bacterial Pathogenesis (Part C: Identification, Regulation, and Function of Virulence Factors)
Edited by VIRGINIA L. CLARK AND PATRIK M. BAVOIL
- VOLUME 359. Nitric Oxide (Part D)
Edited by ENRIQUE CADENAS AND LESTER PACKER
- VOLUME 360. Biophotonics (Part A)
Edited by GERARD MARRIOTT AND IAN PARKER
- VOLUME 361. Biophotonics (Part B)
Edited by GERARD MARRIOTT AND IAN PARKER
- VOLUME 362. Recognition of Carbohydrates in Biological Systems (Part A)
Edited by YUAN C. LEE AND REIKO T. LEE

VOLUME 363. Recognition of Carbohydrates in Biological Systems (Part B)

Edited by YUAN C. LEE AND REIKO T. LEE

VOLUME 364. Nuclear Receptors

Edited by DAVID W. RUSSELL AND DAVID J. MANGELSDORF

VOLUME 365. Differentiation of Embryonic Stem Cells

Edited by PAUL M. WASSAUMAN AND GORDON M. KELLER

VOLUME 366. Protein Phosphatases

Edited by SUSANNE KLUMPP AND JOSEF KRIEGLSTEIN

VOLUME 367. Liposomes (Part A)

Edited by NEJAT DÜZGÜNEŞ

VOLUME 368. Macromolecular Crystallography (Part C)

Edited by CHARLES W. CARTER, JR., AND ROBERT M. SWEET

VOLUME 369. Combinational Chemistry (Part B)

Edited by GUILLERMO A. MORALES AND BARRY A. BUNIN

VOLUME 370. RNA Polymerases and Associated Factors (Part C)

Edited by SANKAR L. ADHYA AND SUSAN GARGES

VOLUME 371. RNA Polymerases and Associated Factors (Part D)

Edited by SANKAR L. ADHYA AND SUSAN GARGES

VOLUME 372. Liposomes (Part B)

Edited by NEJAT DÜZGÜNEŞ

VOLUME 373. Liposomes (Part C)

Edited by NEJAT DÜZGÜNEŞ

VOLUME 374. Macromolecular Crystallography (Part D)

Edited by CHARLES W. CARTER, JR., AND ROBERT W. SWEET

VOLUME 375. Chromatin and Chromatin Remodeling Enzymes (Part A)

Edited by C. DAVID ALLIS AND CARL WU

VOLUME 376. Chromatin and Chromatin Remodeling Enzymes (Part B)

Edited by C. DAVID ALLIS AND CARL WU

VOLUME 377. Chromatin and Chromatin Remodeling Enzymes (Part C)

Edited by C. DAVID ALLIS AND CARL WU

VOLUME 378. Quinones and Quinone Enzymes (Part A)

Edited by HELMUT SIES AND LESTER PACKER

VOLUME 379. Energetics of Biological Macromolecules (Part D)

Edited by JO M. HOLT, MICHAEL L. JOHNSON, AND GARY K. ACKERS

VOLUME 380. Energetics of Biological Macromolecules (Part E)

Edited by JO M. HOLT, MICHAEL L. JOHNSON, AND GARY K. ACKERS

VOLUME 381. Oxygen Sensing

Edited by CHANDAN K. SEN AND GREGG L. SEMENZA

VOLUME 382. Quinones and Quinone Enzymes (Part B)

Edited by HELMUT SIES AND LESTER PACKER

VOLUME 383. Numerical Computer Methods (Part D)

Edited by LUDWIG BRAND AND MICHAEL L. JOHNSON

VOLUME 384. Numerical Computer Methods (Part E)

Edited by LUDWIG BRAND AND MICHAEL L. JOHNSON

VOLUME 385. Imaging in Biological Research (Part A)

Edited by P. MICHAEL CONN

VOLUME 386. Imaging in Biological Research (Part B)

Edited by P. MICHAEL CONN

VOLUME 387. Liposomes (Part D)

Edited by NEJAT DÜZGÜNEŞ

VOLUME 388. Protein Engineering

Edited by DAN E. ROBERTSON AND JOSEPH P. NOEL

VOLUME 389. Regulators of G-Protein Signaling (Part A)

Edited by DAVID P. SIDEROVSKI

VOLUME 390. Regulators of G-Protein Signaling (Part B)

Edited by DAVID P. SIDEROVSKI

VOLUME 391. Liposomes (Part E)

Edited by NEJAT DÜZGÜNEŞ

VOLUME 392. RNA Interference

Edited by ENGELKE ROSSI

VOLUME 393. Circadian Rhythms

Edited by MICHAEL W. YOUNG

VOLUME 394. Nuclear Magnetic Resonance of Biological Macromolecules (Part C)

Edited by THOMAS L. JAMES

VOLUME 395. Producing the Biochemical Data (Part B)

Edited by ELIZABETH A. ZIMMER AND ERIC H. ROALSON

VOLUME 396. Nitric Oxide (Part E)

Edited by LESTER PACKER AND ENRIQUE CADENAS

VOLUME 397. Environmental Microbiology

Edited by JARED R. LEADBETTER

VOLUME 398. Ubiquitin and Protein Degradation (Part A)

Edited by RAYMOND J. DESHAIES

VOLUME 399. Ubiquitin and Protein Degradation (Part B)

Edited by RAYMOND J. DESHAIES

VOLUME 400. Phase II Conjugation Enzymes and Transport Systems

Edited by HELMUT SIES AND LESTER PACKER

VOLUME 401. Glutathione Transferases and Gamma Glutamyl Transpeptidases
Edited by HELMUT SIES AND LESTER PACKER

VOLUME 402. Biological Mass Spectrometry
Edited by A. L. BURLINGAME

VOLUME 403. GTPases Regulating Membrane Targeting and Fusion
Edited by WILLIAM E. BALCH, CHANNING J. DER, AND ALAN HALL

VOLUME 404. GTPases Regulating Membrane Dynamics
Edited by WILLIAM E. BALCH, CHANNING J. DER, AND ALAN HALL

VOLUME 405. Mass Spectrometry: Modified Proteins and Glycoconjugates
Edited by A. L. BURLINGAME

VOLUME 406. Regulators and Effectors of Small GTPases: Rho Family
Edited by WILLIAM E. BALCH, CHANNING J. DER, AND ALAN HALL

VOLUME 407. Regulators and Effectors of Small GTPases: Ras Family
Edited by WILLIAM E. BALCH, CHANNING J. DER, AND ALAN HALL

VOLUME 408. DNA Repair (Part A)
Edited by JUDITH L. CAMPBELL AND PAUL MODRICH

VOLUME 409. DNA Repair (Part B)
Edited by JUDITH L. CAMPBELL AND PAUL MODRICH

VOLUME 410. DNA Microarrays (Part A: Array Platforms and Web-Bench
Protocols)
Edited by ALAN KIMMEL AND BRIAN OLIVER

VOLUME 411. DNA Microarrays (Part B: Databases and Statistics)
Edited by ALAN KIMMEL AND BRIAN OLIVER

VOLUME 412. Amyloid, Prions, and Other Protein Aggregates (Part B)
Edited by INDU KHETERPAL AND RONALD WETZEL

VOLUME 413. Amyloid, Prions, and Other Protein Aggregates (Part C)
Edited by INDU KHETERPAL AND RONALD WETZEL

VOLUME 414. Measuring Biological Responses with Automated Microscopy
Edited by JAMES INGLESE

VOLUME 415. Glycobiology
Edited by MINORU FUKUDA

VOLUME 416. Glycomics
Edited by MINORU FUKUDA

VOLUME 417. Functional Glycomics
Edited by MINORU FUKUDA

VOLUME 418. Embryonic Stem Cells
Edited by IRINA KLIMANSKAYA AND ROBERT LANZA

VOLUME 419. Adult Stem Cells

Edited by IRINA KLIMANSKAYA AND ROBERT LANZA

VOLUME 420. Stem Cell Tools and Other Experimental Protocols

Edited by IRINA KLIMANSKAYA AND ROBERT LANZA

VOLUME 421. Advanced Bacterial Genetics: Use of Transposons and Phage for Genomic Engineering

Edited by KELLY T. HUGHES

VOLUME 422. Two-Component Signaling Systems, Part A

Edited by MELVIN I. SIMON, BRIAN R. CRANE, AND ALEXANDRINE CRANE

VOLUME 423. Two-Component Signaling Systems, Part B

Edited by MELVIN I. SIMON, BRIAN R. CRANE, AND ALEXANDRINE CRANE

VOLUME 424. RNA Editing

Edited by JONATHA M. GOTT

VOLUME 425. RNA Modification

Edited by JONATHA M. GOTT

VOLUME 426. Integrins

Edited by DAVID CHERESH

VOLUME 427. MicroRNA Methods

Edited by JOHN J. ROSSI

VOLUME 428. Osmosensing and Osmosignaling

Edited by HELMUT SIES AND DIETER HAUSSINGER

VOLUME 429. Translation Initiation: Extract Systems and Molecular Genetics

Edited by JON LORSCH

VOLUME 430. Translation Initiation: Reconstituted Systems and Biophysical Methods

Edited by JON LORSCH

VOLUME 431. Translation Initiation: Cell Biology, High-Throughput and Chemical-Based Approaches

Edited by JON LORSCH

VOLUME 432. Lipidomics and Bioactive Lipids: Mass-Spectrometry-Based Lipid Analysis

Edited by H. ALEX BROWN

VOLUME 433. Lipidomics and Bioactive Lipids: Specialized Analytical Methods and Lipids in Disease

Edited by H. ALEX BROWN

VOLUME 434. Lipidomics and Bioactive Lipids: Lipids and Cell Signaling

Edited by H. ALEX BROWN

VOLUME 435. Oxygen Biology and Hypoxia

Edited by HELMUT SIES AND BERNHARD BRÜNE

- VOLUME 436. Globins and Other Nitric Oxide-Reactive Proteins (Part A)
Edited by ROBERT K. POOLE
- VOLUME 437. Globins and Other Nitric Oxide-Reactive Proteins (Part B)
Edited by ROBERT K. POOLE
- VOLUME 438. Small GTPases in Disease (Part A)
Edited by WILLIAM E. BALCH, CHANNING J. DER, AND ALAN HALL
- VOLUME 439. Small GTPases in Disease (Part B)
Edited by WILLIAM E. BALCH, CHANNING J. DER, AND ALAN HALL
- VOLUME 440. Nitric Oxide, Part F Oxidative and Nitrosative Stress in Redox Regulation of Cell Signaling
Edited by ENRIQUE CADENAS AND LESTER PACKER
- VOLUME 441. Nitric Oxide, Part G Oxidative and Nitrosative Stress in Redox Regulation of Cell Signaling
Edited by ENRIQUE CADENAS AND LESTER PACKER
- VOLUME 442. Programmed Cell Death, General Principles for Studying Cell Death (Part A)
Edited by ROYA KHOSRAVI-FAR, ZAHRA ZAKERI, RICHARD A. LOCKSHIN, AND MAURO PIACENTINI
- VOLUME 443. Angiogenesis: *In Vitro* Systems
Edited by DAVID A. CHERESH
- VOLUME 444. Angiogenesis: *In Vivo* Systems (Part A)
Edited by DAVID A. CHERESH
- VOLUME 445. Angiogenesis: *In Vivo* Systems (Part B)
Edited by DAVID A. CHERESH
- VOLUME 446. Programmed Cell Death, The Biology and Therapeutic Implications of Cell Death (Part B)
Edited by ROYA KHOSRAVI-FAR, ZAHRA ZAKERI, RICHARD A. LOCKSHIN, AND MAURO PIACENTINI
- VOLUME 447. RNA Turnover in Bacteria, Archaea and Organelles
Edited by LYNNE E. MAQUAT AND CECILIA M. ARRAIANO
- VOLUME 448. RNA Turnover in Eukaryotes: Nucleases, Pathways and Analysis of mRNA Decay
Edited by LYNNE E. MAQUAT AND MEGERDITCH KILEDJIAN
- VOLUME 449. RNA Turnover in Eukaryotes: Analysis of Specialized and Quality Control RNA Decay Pathways
Edited by LYNNE E. MAQUAT AND MEGERDITCH KILEDJIAN
- VOLUME 450. Fluorescence Spectroscopy
Edited by LUDWIG BRAND AND MICHAEL L. JOHNSON

VOLUME 451. Autophagy: Lower Eukaryotes and Non-Mammalian Systems (Part A)

Edited by DANIEL J. KLIONSKY

VOLUME 452. Autophagy in Mammalian Systems (Part B)

Edited by DANIEL J. KLIONSKY

VOLUME 453. Autophagy in Disease and Clinical Applications (Part C)

Edited by DANIEL J. KLIONSKY

VOLUME 454. Computer Methods (Part A)

Edited by MICHAEL L. JOHNSON AND LUDWIG BRAND

VOLUME 455. Biothermodynamics (Part A)

Edited by MICHAEL L. JOHNSON, JO M. HOLT, AND GARY K. ACKERS (RETIRED)

VOLUME 456. Mitochondrial Function, Part A: Mitochondrial Electron Transport Complexes and Reactive Oxygen Species

Edited by WILLIAM S. ALLISON AND IMMO E. SCHEFFLER

VISUALIZING FUNCTIONAL FLEXIBILITY BY THREE-DIMENSIONAL ELECTRON MICROSCOPY: RECONSTRUCTING COMPLEX I OF THE MITOCHONDRIAL RESPIRATORY CHAIN

Michael Radermacher

Contents

1. Introduction	4
2. Random Conical Reconstruction	6
2.1. Digitization	7
2.2. Correction of the contrast transfer function	8
2.3. Particle selection	10
2.4. Processing of the 0° images	11
2.5. 3-D reconstruction by Radon inversion	15
2.6. Refinement	15
3. Application of the Techniques to Complex I From <i>Yarrowia Lipolytica</i>	16
3.1. Sample preparation for electron microscopy	16
3.2. Data collection	17
3.3. 2-D and 3-D data analysis	17
4. Conclusion	23
Acknowledgments	23
References	23

Abstract

Complex I is the major entry point in the bacterial and mitochondrial respiratory chain. Structural knowledge of the enzyme is still limited because of its large size and complicated architecture. Only the structure of the hydrophilic domain of a bacterial Complex I has been solved to high resolution by X-ray crystallography. To date, no X-ray structure of the complete enzyme has been reported, and most structural information of the holoenzyme has been obtained by 3-D electron microscopy. In this chapter the methods are described used for

University of Vermont, Department of Molecular Physiology and Biophysics, Burlington, Vermont, USA

Methods in Enzymology, Volume 456
ISSN 0076-6879, DOI: 10.1016/S0076-6879(08)04401-7

© 2009 Elsevier Inc.
All rights reserved.

determining the 3-D reconstruction of Complex I that revealed for the first time a detailed and reproducible domain structure. Complex I is a highly flexible molecule, and methods for calculating the 3-D reconstruction from electron micrographs must take into account this heterogeneity. The techniques described in this chapter can be modified and adapted for the study of more heterogeneous preparations, such as functionalized Complex I. In addition, these techniques are not restricted to the structure determination of Complex I but are appropriate for the 3-D reconstruction of macromolecular assemblies from electron micrographs when inhomogeneities may be present.

1. INTRODUCTION

Eukaryotic Complex I has more than 35 different subunits and a molecular mass of approximately 1 MDa, whereas the minimal bacterial Complex I has 14 subunits and a molecular mass of approximately 600 kDa. Additional subunits found in eukaryotic Complex I are referred to as accessory or supernumerary subunits, whereas subunits in common with the minimal bacterial Complex I are referred to as conserved subunits.

Large efforts have been undertaken over the past 20 years to determine the structure of Complex I from different species. Several medium resolution (16 to 35 Å) 3-D reconstructions determined by electron microscopy methods existed previously, three of *Neurospora crassa* Complex I (Guénebaut *et al.*, 1997; Hofhaus *et al.*, 1991; Leonard *et al.*, 1987), one of *Bos taurus* Complex I (Grigorieff, 1998), and two of *Escherichia coli* Complex I (Böttcher *et al.*, 2002; Guenebaut *et al.*, 1998). All, except the reconstruction reported in Böttcher *et al.* (2002) show Complex I as an L-shaped molecule: one arm is membrane bound, and the other arm reaches into the mitochondrial matrix. However, neither of these reconstructions, even though one was obtained from cryo preparations (Grigorieff, 1998), showed any detailed substructure. The Complex I structures determined in our laboratory since 2003 (from *Yarrowia lipolytica*, *B. taurus*, and *Aquifex aeolicus*) (Clason *et al.*, 2006; Radermacher *et al.*, 2006) show, for the first time, a distinct and reproducible domain structure conserved in different species.

Complex I is a large multi-subunit membrane protein. In the electron microscope, preparations of Complex I show a high degree of variation. Some of these variations can be expected to reflect part of the conformational spectrum of Complex I during its functional cycle. Other variations may originate from a destabilization of Complex I when it is removed from the membrane by detergent solubilization or during the preparation for electron microscopy. Given the lack of knowledge about the functional mechanism of Complex I, attempts to stabilize Complex I for electron microscopy by addition of inhibitors or substrates have been unsuccessful (Bostina, 2004).

Independently of the source of the variation, a reliable 3-D structure can only be obtained if the variations are carefully analyzed and reconstructions are calculated from subsets of particles that show the same conformation. At present, there are three techniques, random conical reconstruction (Radermacher, 1988; Radermacher *et al.*, 1986, 1987), orthogonal tilt reconstruction (Leschziner and Nogales, 2006; Leschziner *et al.*, 2007), and electron tomography (Forster *et al.*, 2008; Hoppe *et al.*, 1968, 1974, 1976; Knauer *et al.*, 1983; Walz *et al.*, 1997), that provide sufficiently sophisticated and proven classification schemes to accomplish this task.

We have used the random conical reconstruction technique for the reconstruction of Complex I. This technique developed in 1985/86 was the first technique that allowed the reconstruction of macromolecular complexes under true low-dose conditions (Radermacher *et al.*, 1986). Among many other applications, it has been used for the 3-D reconstruction of cryo samples of the ribosomes (Frank *et al.*, 1991; Morgan *et al.*, 2000), the calcium release channel (Radermacher *et al.*, 1994), the nuclear pore complex (Akey and Radermacher, 1993), and phosphofructokinase (Ruiz *et al.*, 2001).

Angular reconstitution (van Heel, 1987) and similar techniques, like 3-D reconstruction methods based on the alignment of projections to an initial model, have become very popular. These techniques work well for homogeneous samples, but their performance is questionable for heterogeneous data, even if a 3-D reference structure is available. With the increased awareness that many samples are not homogeneous, the random conical reconstruction technique has seen a revival, and major efforts are underway to automatize the data collection for this geometry (Yoshioka *et al.*, 2007). An essential step in the reconstruction process is the classification or sorting of particle images into homogeneous subgroups. Pattern analysis techniques used for this purpose are based on neural networks (self-organizing maps) (Kohonen, 1990; Marabini and Carazo, 1994), principle component analysis, and correspondence analysis (Lebart *et al.*, 1984), often followed by classification techniques. The type of analysis used is not irrelevant, because most—if not all—classification methods are based on heuristic approaches. Images are sorted according to a mathematical criterion, which is minimized. Although the techniques are “objective” in the sense that they minimize a mathematical criterion, they may not find the most optimum sorting for a specific set of images. The human brain in most instances is still unsurpassed in judging similarities and discrepancies of objects presented in images. This is limited, however, by the large size of the datasets and the extremely low signal-to-noise ratios. Any image classification should, whenever possible, be carefully supervised. If needed, several different classification strategies should be applied until the most convincing classification is found. For Complex I the best strategy for separating different conformations was the use of correspondence analysis in combination with

Diday's classification with moving centers (Diday, 1971, 1973) followed by hierarchical ascendant classification. In earlier tests we have observed that this combination of algorithms is one of the most effective methods for sorting electron microscopy images of single particles.

3-D reconstructions from heterogeneous samples are currently in the forefront of reconstruction problems and with each new reconstruction the methods are being improved, partially by making them easier to apply and partially by refining existing or developing new algorithms. Efforts are under way to extend the applicability of angular reconstitution techniques to heterogeneous samples. However, because of the lack of sufficiently large datasets recorded either with random conical or orthogonal tilting and reconstructed in two different ways, the validity of current attempts to separate inhomogeneity of samples without tilting has not yet been proven in practice (e.g., Fu *et al.* [2007] and Scheres *et al.* [2007]).

2. RANDOM CONICAL RECONSTRUCTION

Random conical reconstruction (Radermacher *et al.*, 1986, 1987, 1992; Yoshioka *et al.*, 2007) is a well-established technique, capable of reconstructing 3-D structures from heterogeneous samples. For simplicity of explanation, it is assumed that the sample contains identical particles, with a preferred orientation relative to the specimen support. These assumptions do not pose a limitation. When these conditions are not fulfilled, subgroups of molecules that fulfill these conditions are extracted from the dataset at a later stage in the processing.

The dataset for a random conical reconstruction consists of pairs of micrographs, the first image in each pair is recorded at a high tilt angle of the specimen, typically 55° to 60° (Fig. 1.1A), and a second image in each pair of the same specimen area is recorded at 0° (Fig. 1.1B). Under the assumption that all particles are identical and lie in a preferred orientation parallel to the sample support, every particle in the tilt image provides one view of the same molecule, however, each from a different direction. The viewing directions form a cone and, therefore, the set of tilt images form a conical tilt series (for an illustration of the technique see Radermacher *et al.* [1987]). Because the azimuthal angles are random, the technique is called random conical reconstruction technique. The 0° images serve two purposes; the first is the finding of the in-plane orientation of each particle, which, together with the tilt angle, specifies the viewing direction for each tilted particle. The second purpose, essential for the reconstruction from a heterogeneous sample, is the classification of the particles into groups that represent identical projections. After classification, each group of 0° images forms a homogeneous subset, with particles in the same in-plane orientation

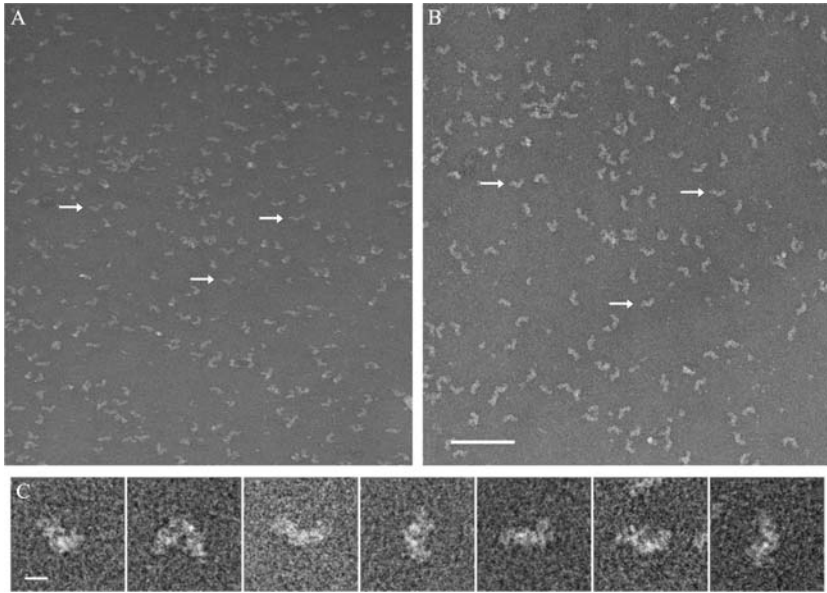


Figure 1.1 Tilt pair of *Y. lipolytica* Complex I. Top left, 0° image; top right, tilt image. Arrows point to particle pairs in the tilt and 0° image. Tilt axis horizontal. Scale bar 1000 Å. Bottom, Gallery of a few single particles boxed out of the 0° image. Scale bar 100 Å.

and the same conformation. Reconstructions are calculated for each group separately by use of the corresponding tilted views. The 3-D reconstructions of all classes are compared and those that differ only in the orientation in space are merged. Those that show different structures are left as separated classes.

2.1. Digitization

Images are digitized, usually with the best resolution of the scanner. The pixel size is increased by binning to an appropriate value for the following image processing, maintaining a balance between the best expected resolution and the dataset size. The factor between the final pixel size of the digitized images and the best resolution expected in the 3-D reconstruction should be at least 3, so that possible interpolation errors during image processing do not result in a loss of final resolution. Important in the scanning step is the conversion of film transparencies to optical densities. This conversion must be consistent throughout the dataset. The conversion is not linear, and inconsistencies can lead to loss of resolution when images are combined. For scanners with

a limited bit depth, like the SCAI scanner with a depth of only 10 bits, the best quality images are obtained by the following scanning procedure: First, an empty area of the film is scanned (e.g., the area that contains the image number) with the full range of the scanner. The maximum transparency of this area is used as the reference transparency T_0 . The entire image is scanned after adjustment of the transparency histogram, such that transparencies in the image as closely as possible fill the scanning range without cutting off any transparencies present in the image. If r is the range of the scanner values, and c_{\min} and c_{\max} are the minimum and maximum cutoffs for the histogram adjustments, we can define a scaling factor

$$s = \frac{r}{c_{\max} - c_{\min}} \quad (1.1)$$

and pixel values in the image t_i after the conversion from transparencies to densities I_i become:

$$I_i = -\log_{10} \left(\frac{s \cdot c_{\min} + t_i}{T_0 \cdot s} \right) \quad (1.2)$$

2.2. Correction of the contrast transfer function

The images of single particle preparations acquired in the electron microscope are, in good approximation, phase-contrast images. For obtaining visible image contrast, images are recorded in underfocus, and the combination of spherical aberration of the objective lens and the defocus used creates the phase contrast necessary for visualizing the sample. An image can be described as the perfect image, convoluted with the point-spread function of the microscope. The Fourier transform of the point-spread function is the transfer function, and the Fourier transform of the image is the Fourier transform of the perfect image multiplied with the phase-contrast transfer function (CTF). The equation of the CTF, as implemented in SPIDER 5.0 (Frank *et al.*, 1996), is:

$$f(\vec{r}^*) = \left[(1 - a)\sin(\gamma(\vec{r}^*)) + a\cos(\gamma(\vec{r}^*)) \right] \cdot E(\vec{r}^*) + b(\vec{r}^*) \quad (1.3)$$

with

$$\gamma(\vec{r}^*) = \frac{1}{2}\pi \cdot \left[C_s \lambda^3 \vec{r}^{*4} - \vec{r}^{*2} \lambda (2\Delta Z + \Delta Z_a \cos(2 \cdot \varphi - \varphi_a)) \right] \quad (1.4)$$

Where C_s is the spherical aberration of the objective lens, λ the electron wavelength, Δz the defocus, ΔZ_a the magnitude of the astigmatism, φ_a the direction of the astigmatism. a is a value depending on the amplitude contrast, $E(\vec{r}^*)$ is an envelope function that depends on the coherence and energy spread of the electron beam, and $b(\vec{r}^*)$ is a background function that depends on the noise in the image, the amount of inelastic scattering, and other factors (see e.g., [Toyoshima and Unwin \[1988\]](#)). An alternative equation for the contrast transfer function was developed by [Typke and Radermacher \(1982\)](#):

$$f(r^*) = \sin(\gamma - \eta) \cdot E(r^*) + b(r^*) \quad (1.5)$$

where γ , $E(r^*)$, and $b(r^*)$ are defined as above and η defines the amplitude contrast.

The CTF can be observed in the power spectrum of a micrograph ([Fig. 1.2](#)). The rings visible are Thon rings. The power spectrum is always positive; however, the complex transfer function changes its sign periodically. Therefore, in under focus the transfer function is negative until the first 0 transition, the next bright ring is positive and continues with alternating signs.

At 100 kV accelerating voltage, 1 to 1.5 μm is a typical defocus value used for the imaging of single particles, and the first 0-transition occurs at a radius corresponding to approximately 20 \AA to 25 \AA resolution. Therefore, image information up to 25 \AA is transferred with one sign, while the information in the next ring is subtracted, alternating for each ring. Without transfer function correction, only the information up to the first 0-transition can be used. To obtain higher resolution, the transfer function needs to be corrected.

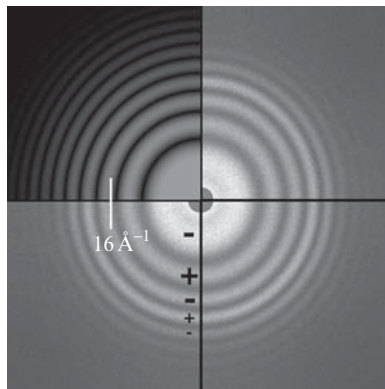


Figure 1.2 Typical power spectrum of an electron micrograph. Insert in upper left corner fitted CTF. The changing signs of the Fourier amplitudes are indicated.

Most importantly, the sign of the transfer function needs to be flipped in alternating rings, so that the information transfer occurs with the same sign throughout the full resolution range.

The CTF can be determined by use of a variety of fitting algorithms. We fit the defocus, astigmatism, and amplitude contrast by use of a cross-correlation approach, which is equivalent to a least squares fit. Although the fitting of the transfer function is simple for untilted images, the determination and correction of the transfer function in the tilt images is more elaborate (Radermacher *et al.*, 2001), because the defocus varies perpendicular to the tilt axis and can span a range of up to $2 \mu\text{m}$, depending on the image size, magnification, and tilt angle. The image is divided into 4×5 quadrants, and the CTF is fitted separately for each of the quadrants. A plane is fitted through the set of 20 defocus values, yielding the four parameters needed for the analytical description of a plane in space. From the equation of this plane, the defocus at any coordinate in the tilt image can be determined. The astigmatism is assumed to be the same for the complete micrograph, and an average value is determined. By use of the value for the astigmatism and the equation of the defocus plane, the image of every single particle in the tilt view is corrected by properly flipping the sign of the transfer function (Radermacher *et al.*, 2001). The correction is performed with a smooth function to avoid artifacts. When processing a large number of tilt images, it is important that the algorithm used works essentially without supervision. Many modern microscopes store a nominal defocus value with each image, which is used as a start value in the correlation procedure. Start values for each quadrant in a tilt image are calculated from the nominal defocus in the image center and the known tilt angle and tilt direction. Our algorithm is robust for start values that are within $0.5 \mu\text{m}$ of the true value, well within the accuracy of the values stored during image acquisition.

2.3. Particle selection

Images of single particles are selected from the tilt pairs, with the tilt-pair particle-picking program in WEB (Frank *et al.*, 1996). This program was developed in the framework of the original random conical reconstruction technique, aimed to make manual picking of image pairs as convenient as possible (unpublished at the time). It allows for interruptions during the picking process without loss of data, for correction of falsely picked particles at any stage of the particle picking, and it assists semiautomatically to find the position of each particle in the tilt micrograph from the location of its counterpart in the 0° micrograph. The first five matching pairs of particles are identified and picked manually from both micrographs viewed side by side. After this initial selection, the program calculates the geometric relation between both images and predicts the location of each newly selected

particle in the 0° micrograph in the tilt micrograph from its 0° location. The cursor automatically moves to the predicted location. The precise location of the tilt particle may be adjusted by hand, before confirming the selection.

The calculation of the geometric relation between the 0° image and the tilt image is divided into two parts. The tilt angle is calculated from the change in the area of triangles defined by any three particle coordinates. The relation between the area A_0 of a triangle in the 0° image and the area of the same triangle in the tilt image A_t changes as:

$$A_t = A_0 \cdot \cos(\vartheta), \quad (1.6)$$

where ϑ is the tilt angle. The number N of triangles that can be calculated from n picked particles is:

$$N = \frac{n!}{3!(n-3)!} \quad (1.7)$$

A parameter is provided to exclude those triangles whose area is too small and where inaccuracies of the picked particle coordinates would create large inaccuracies in the tilt angle calculation.

The rotational and translational parameters are calculated by a least squares fit, keeping ϑ fixed. The geometry calculations can be repeated at any time in the particle-picking process. At the end there are approximately 10,000 measurements for the angle ϑ and, even with some inaccuracies in the particle coordinates, the value of ϑ is correct to better than 0.1° .

During the particle-picking process care must be taken not to bias the particle selection. The only selection criterion that should be used is a sufficient separation between neighbors to avoid images with overlapping particles in the tilt micrograph. Only structures that obviously cannot represent the particle, for example substantially smaller particles, should be left out.

2.4. Processing of the 0° images

Processing of the Complex I dataset was carried out with the package SPIDER, version 5.0 with in-house extensions. The extensions comprise all techniques that are based on the use of Radon transforms and minor modifications to the calculation of the complex microscope transfer function. However, the 0° images can be processed with any good processing package that contains reliable 2-D image alignment algorithms and good pattern recognition and classification techniques (see, e.g., special issue *Journal of Structural Biology*, 1996, vol. 116, and 2007, vol. 157). When processing tilt pairs, it is crucial never to lose the correspondence between each 0° image and its tilted counterpart. In our processing setup this is

achieved by use of the same image number for the tilt images and their 0° counterparts. For systems with image stacks, an indexed stack should be used that enables a unique identification of every single image. Even if subsets of images are removed, the numbering is never changed. Without a system that uniquely links the tilted and untilted images throughout all the steps of processing, a 3-D reconstruction from random conical or orthogonal tilt data cannot be done.

The 0° images are processed first. This is the most critical part of the evaluation of a random conical tilt dataset, because in this step the particles are aligned and sorted into groups that show identical shapes in the 0° image. After classification, each group represents a set of identical particles in identical in-plane orientations. First, the images are aligned to a common reference. In highly noisy datasets, this reference can introduce a bias to the alignment. Therefore, the first reference is created by reference-free alignment as described in [Marco *et al.* \(1996\)](#). In essence, images in a series are aligned pairwise, in our implementation by simultaneous rotational translational alignment with Radon transforms ([Radermacher, 1997](#)). The pairs of aligned images are averaged, forming a new image series containing half the number of images. The algorithm continues with further pairwise alignments until only a single image, the average of all particles, is obtained. For a heterogeneous dataset this first average will contain a mixture of all the conformations and will not exhibit high-resolution detail. Therefore, it is not necessary to calculate the first reference-free average from the complete dataset; it is sufficient if 1000 to 2000 randomly selected images are used.

The reference-free average is used to align the complete set of images. Because of its speed and accuracy, we again use the Radon transform alignment techniques for these calculations. The reference in this alignment does not represent a motif common to all images, but the alignment minimizes the difference to the reference.

The aligned images are separated into groups showing different shapes by applying correspondence analysis ([Bretaudiere and Frank, 1986](#); [Frank and van Heel, 1982](#); [Lebart *et al.*, 1984](#); [van Heel and Frank, 1981](#)). Correspondence analysis is closely related to principle component analysis. The main difference is in the metric used in the scalar products. Principle component analysis uses the standard Euclidean metric, whereas correspondence analysis uses the χ^2 -metric, which makes it scaling invariant.

In correspondence analysis, a set of images with dimension $n \times m$ can be represented as vectors in an $n \cdot m$ -dimensional vector space $\mathfrak{R}^{n \cdot m}$. Identical images point to the same point in $\mathfrak{R}^{n \cdot m}$, very different images point to very different points. Therefore, the set of images forms a “point-cloud” in $\mathfrak{R}^{n \cdot m}$. Correspondence analysis determines a new orthogonal base-vector system for the images in the data cloud, such that the first base vector points along the largest extension of the cloud (i.e., in the direction of the largest variance

of the dataset). The next base vector is orthogonal to the first and points in the direction of the second largest variance, etc. Although the nomenclature for these new base vectors is not unique, in image processing for electron microscopy, the new base vectors are called factors. Typically 8 to 12 factors are sufficient to describe all major variations of electron microscopy datasets. Proper preparation of the data before applying the multivariate statistical analysis techniques is important for obtaining the best results. First, a sharp mask is created, and only the points of each image that fall inside the mask are used for the pattern recognition analysis. This prevents features that are present in the image background from influencing the analysis. The mask, however, must be sufficiently large to include all possible particle variations. In the first correspondence analysis a circular mask may be sufficient; in later steps a mask that follows the outline of the sum of all particles may be advantageous. Images should be low-pass filtered before performing correspondence analysis. A low-pass filter to 30 Å is appropriate in most cases, because these are single images and the signal-to-noise ratio at higher resolution is significantly below 1. Without a low-pass filter the results of correspondence analysis can easily be dominated by noise.

The reduced space (8 to 12 dimensions) in which the images are represented can be inspected by displaying 2-D maps, spanned by two eigenvector. For a complete understanding, all maps, 1 vs. 2, 2 vs. 3, etc until 11 vs. 12 should be inspected. Correspondence analysis reduces the dimensionality of the data but does not separate the data into classes. However, this data reduction serves two purposes: first the relation between the images can be visually assessed, important especially if the image variations are not discrete (i.e., do not form clear classes) but rather present a continuum, second, classification can be applied to a subset of significant features described by a subset of factors, speeding up the classification and reducing the influence of noise.

One of the very powerful classification techniques is Diday's method of moving centers (Diday, 1971, 1973) applied to the image coordinates in the reduced data space of correspondence analysis, followed by hierarchical ascendant classification (HAC). In many tests and comparisons with other methods, we have found that this technique produces the best image separation, especially in datasets with continuous variations that lack a clear class structure (unpublished results). The technique does not require one to predefine the desired number of classes (for details see Diday [1973]). The algorithm has three major parameters, the number of seed points for moving center classification, the number of iterations, and the number of repeats of the complete algorithm. The parameters for this classification are chosen such that the moving center algorithm results in less than but close to 100 classes. The most important parameter is the number of iterations. Higher iteration numbers result in fewer classes, lower iteration numbers in more classes. The resulting class averages are subsequently combined with HAC.

The class averages of all moving center classes and the dendrogram tree from the hierarchical classification are inspected. The number of final averages depends on the structure of this tree (Fig. 1.3). In the first analysis it is good to only merge the classes at the bottom of the tree, then visually inspect these averages and decide which of the averages show small enough differences that they could be merged. After cutting the tree at a higher level, the merging of these averages is checked. If the more extensive merging combines images that seem insufficiently similar, the tree again has to be cut lower, and should be left at this level, even if other averages do not show obvious differences.

Once class averages are available, they can be used as references in a multi reference alignment. In a multi reference alignment procedure each image of the dataset is aligned by cross-correlation to multiple references. The image is assigned to the reference that shows the highest cross-correlation. To exclude any residual misalignment from being perpetuated through the rest of the processing the class averages are first aligned to each other. In addition, they are low-pass and high-pass filtered to reduce the noise and remove long-range density differences from the images.

After multi reference alignment, the complete dataset is again analyzed by correspondence analysis and classification. The same rules apply as in the first round. This sequence, multi reference alignment, correspondence analysis, classification is iterated until the classes are stable. The final results should be closely inspected.

A good impression of the structural variations in the sample is obtained during all steps: data acquisition, particle picking, alignment, and classification. If a characteristic view of the particles has been observed during the processing, it should form a separate class after classification.

The alignment and classification of the 0° image produces lists that contain the in-plane rotation angle of each particle and the class membership of each image. Both are transferred to the set of corresponding tilt images. The in-plane orientation of the 0° image defines the azimuthal angle in the

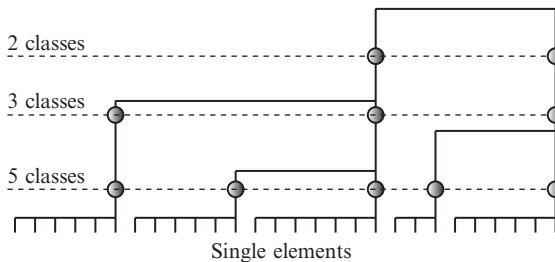


Figure 1.3 Dendrogram tree of a typical hierarchical ascendant classification (HAC). Classes are based on the Euclidean distances between elements or class centers. The lengths of the vertical lines represent these distances. Illustrated are three different cutting levels resulting in 5, 3, or 2 final classes.

conical tilt series. The fixed tilt angle is known from the fitting done during particle picking, which should be close to the readout of the microscope. 3-D reconstructions are calculated for each class separately.

2.5. 3-D reconstruction by Radon inversion

The 3-D Radon inversion algorithm described in [Radermacher \(1994, 1997\)](#) is a highly accurate linear algorithm and is one of the fastest available for the calculation of 3-D volumes from projections with random orientations ([Lanzavecchia et al., 1999](#)).

Radon transforms provide a number of advantages for image processing ([Deans, 1983; Radon, 1917](#)). The central section theorem applies to Radon transforms and to Fourier transforms: the 2-D Radon transform of a projection is a cross-section through the 3-D Radon transform of the object. Radon transforms are real valued, which eases the computational burden, because interpolations can be kept simpler than Fourier interpolations. Accurate interpolation of Fourier transforms requires kernels that cover large areas of the transform, for example, a moving window Shannon interpolation ([Bellon and Lanzavecchia, 1995](#)). Linear interpolations in Fourier transforms, in general, lead to substantial interpolation errors. When interpolating the (real valued) Radon transforms, linear interpolations are normally sufficient and in many cases even nearest neighbor interpolation suffices. The relation between Radon and Fourier transforms is simple. A 1-D Fourier transform along the lines of a multidimensional Radon transform produces a multidimensional Fourier transform in a polar coordinate system. Thus, whenever the use of Fourier transforms is advantageous, for example in cross-correlations, it is easy to switch between the two representations.

2.6. Refinement

The angles of the projections are refined after an initial 3-D reconstruction is obtained ([Radermacher, 1994, 1997](#)). Even when there are virtually no visible differences in the 0° projections within one class, experiments have shown that a wobbling of the particles by $\pm 15^\circ$ is not unusual (unpublished results). Therefore, the orientation of each projection is refined within a limited angular range. This alignment is achieved by cross-correlation of the 2-D Radon transforms of the projections with the 3-D Radon transform of the volumes ([Radermacher, 1997](#)). The correlations are carried out by Fourier multiplications. Mathematically, the technique is the same as correlating the 2-D Fourier transform of the projections with the 3-D Fourier transforms of the volume, the correlation parameters being the shifts in x and y in the projection plane and the three Euler angles.

Multiple rounds of translational/rotational alignment are carried out; after each round, a new volume is calculated. The search range is restricted

during the refinement process. Typically a starting range of $\pm 20^\circ$ around the original projection orientation is used with 5° angular search increments. After each round of refinement, the resolution of the reconstruction is observed. As the resolution improves, the angular range and angular increment are reduced. In each step, the 3-D reference Radon transform is low-pass filtered to a value below the last measured resolution to avoid overfitting. As the resolution increases, the high-pass filter is also increased to enable better fitting of finer substructures. This high-pass filter must be closely monitored. The strongest possible high-pass filter can be estimated by Crowther's formula (Crowther *et al.*, 1970) and depends on the maximum search range. The lowest resolution feature must be larger than the range spanned by the movement of a peripheral feature over the complete search range. An additional indication of correct refinement without overfitting is the shape of the Fourier shell correlation curve used for determining the resolution. This curve must not develop secondary maxima at very high resolution. There can be minima, however, but these minima should be only in locations where either there is limited information transfer because of the microscope transfer function, or, as can happen in rare cases, portions of the spatial frequencies are simply not present in the structure.

3. APPLICATION OF THE TECHNIQUES TO COMPLEX I FROM *YARROWIA LIPOLYTICA*

3.1. Sample preparation for electron microscopy

The reconstruction of Complex I from *Y. lipolytica* was carried out from stain-embedded samples (Radermacher *et al.*, 2006). Data collection from vitreous ice preparations is currently in progress.

The optimum staining conditions are sample and buffer dependent. For every new sample we test a large number of different stains to obtain the best results. A detailed description of these procedures can be found in Ruiz and Radermacher (2006). Complex I preparations were examined with 1% uranyl acetate (UA), 2% phosphotungstic acid, pH 7, with NaOH (PTA), 2% ammonium molybdate, pH 7, with NH_4 (AM), 2% methyl amine tungstate (MAT) and Nanovan (NAN) (Nanoprobes, Yaphank, NY), and NanoW (Nanoprobes, Yaphank, NY). Uranyl acetate was only used for screening new samples, because it is quite difficult to obtain thick stain embedding with this stain. The best results were obtained with phosphotungstic acid (PTA), air dried fast to achieve deep stain embedding (Radermacher *et al.*, 2001; Ruiz and Radermacher, 2006; Stoops *et al.*, 1992). Ammonium molybdate and NanoW also resulted in excellent grid preparations of Complex I.

3.2. Data collection

Data were collected at 100 kV and a nominal magnification of $52,000\times$ in an FEI Tecnai T12 microscope equipped with a Lab6 filament set up in point mode (Ruiz and Rademacher, 2006; Ruiz *et al.*, 2003). Under these conditions images typically show Thon rings visible to at least 6 Å.

A random conical data set of 110 tilt pairs, with tilt angles ranging between 55° and 58° was collected and resulted in approximately 15,000 image pairs of single particles (see Fig. 1.1). Images were digitized with a pixel size of $7\ \mu\text{m}$ with an Intergraph SCAI scanner (Z/I Imaging Corporation, Huntsville, AL). The images were converted to optical densities, then binned, and rescaled to a final pixel size of 3.6 Å on the sample scale.

3.3. 2-D and 3-D data analysis

We tested both self-organizing maps and correspondence analysis for classifying the 0° images of Complex I. Although in other applications self-organizing maps give good results, correspondence analysis generated the best separation of variable features for this dataset. We used a data reduction to 12 factors in correspondence analysis.

We obtained 13 major classes (Fig. 1.4) after classification of the complete *Y. lipolytica* Complex I dataset. Reconstructions were calculated from all 13 classes. Reconstructions from classes 2 to 7 resulted in very low resolution and rather undefined 3-D structures, which was expected, given the smoothness of the densities and lack of detail of the class averages. The reconstructions from classes 1 and 8 to 13 gave substantially better results. Therefore, we divided the dataset into two main subsets: subset 1, containing the images from classes 2 to 7 (approximately 4050 particles) and subset 2 containing the images from classes 1 and 8 to 13, corresponding to a total of 10,885 particles. Subset 2 underwent one additional round of multi

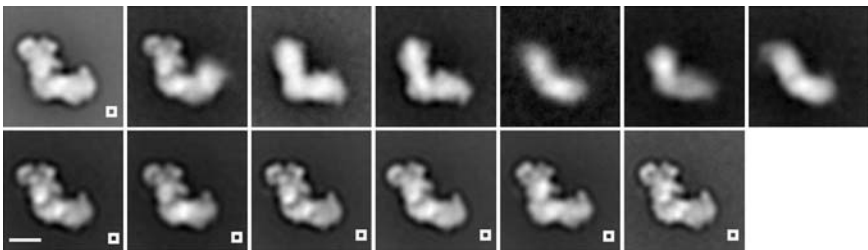


Figure 1.4 Classification of the complete data set of 14,961 particles. Thirteen classes were obtained. Classes 2 to 7 resulted in only low-resolution reconstructions. Classes 1 and 8 to 13 were used for further processing (from Rademacher *et al.* [2006], with permission).

reference alignment, correspondence analysis, and classification before further 3-D reconstruction. A reconstruction calculated from the complete subset 2 (Fig. 1.5) showed a resolution of 24 Å determined with the Fourier Shell Correlation criterion and a 0.3 fixed cutoff value. The reconstruction shows the main characteristic features that were also observed in the reconstructions calculated after finer classification. Clearly visible are the domains in the matrix arm, numbered 1 to 5, a central membrane protuberance (CMP) pointing from the membrane arm toward the mitochondrial matrix, and a distal membrane protuberance (DMP). It can be speculated that the two protuberances are in close neighborhood to the hydrophobic subunits ND4 and ND5, candidates for active proton pumping subunits.

The detailed analysis of the dataset led to a classification into 8 classes (Fig. 1.6A), with memberships of 507, 1921, 1960, 112, 1674, 2538, 172, and 2002 particles. 3-D structures were calculated only for classes 2, 3, 5, 6, and 8, which showed sufficiently high membership (Fig. 1.6B). The final resolutions of the five reconstructions were 16.5 Å, 22 Å, 20.5 Å, 18.5 Å, and 18.5 Å, respectively. It is noteworthy that the finer classification resulted in 3-D structures with higher resolution, even though the dataset size for each reconstruction was substantially smaller than for the combined reconstruction. Although all the major features are visible in all reconstructions, the finer classification reveals higher resolution variations in both the central membrane protuberance and in the matrix arm. Significantly, when Complex I is viewed from the “back” of the matrix arm, the lower

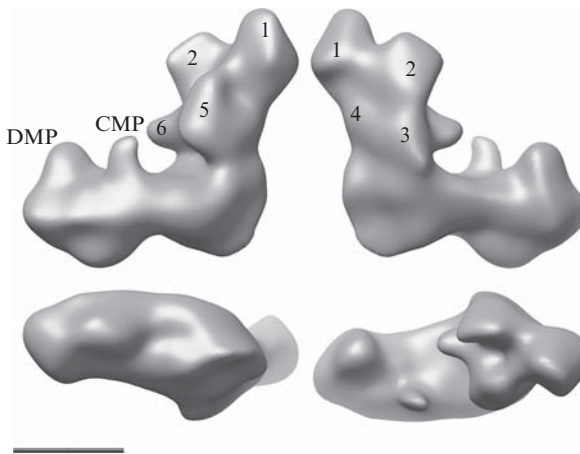


Figure 1.5 3-D reconstruction from combined classes 1 and 8 to 13. A clear domain structure is visible in the matrix arm. The domains are numbered 1 through 6. The membrane arm shows a central membrane protuberance (CMP) and a distal membrane protuberance (DMP). Scale bar 100 Å.

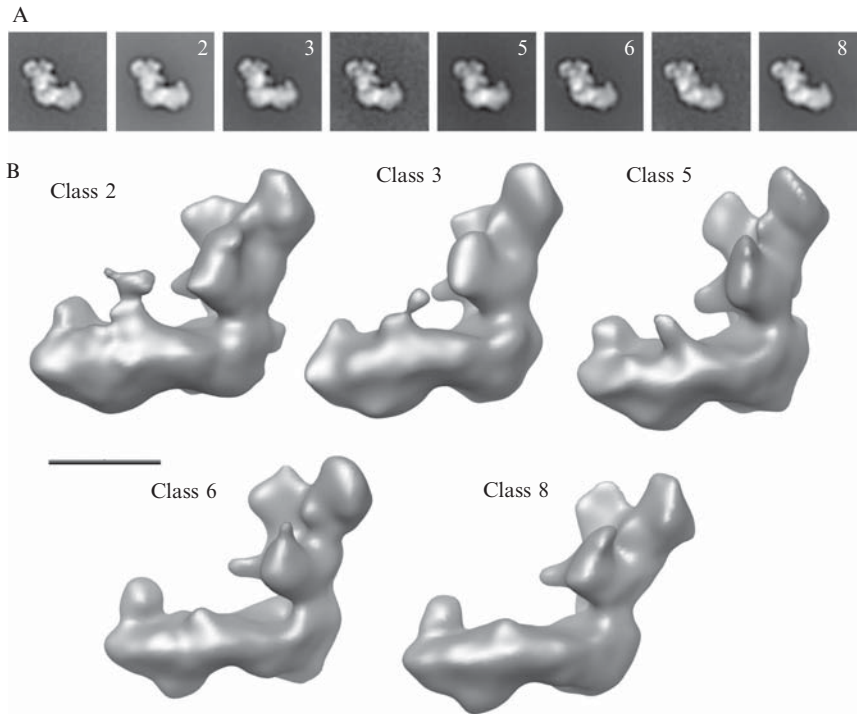


Figure 1.6 (A) Finer classification of the dataset used in the reconstruction shown in Fig. 1.4. Eight classes are shown. (B) Five reconstructions from the classes with the larger number of particles. Scale bar 100Å (from Radermacher *et al.* [2006], with permission).

resolution structure shows a single solid connection between the matrix and membrane arms, whereas the higher resolution structure clearly shows two separate connections visible in Fig. 1.9 upper left panel, one being the center part of the matrix arm, and the second connection between domain 2 and the matrix arm. This double connection has been observed in many of our reconstructions.

Our results suggest an active proton pumping mechanism of Complex I with the central and distal membrane protuberances playing a key role in the conformational changes occurring during catalysis. Occasionally, in 2-D averages, we have observed a thin connection reaching from domain five to CMP and from CMP to DMP. However, up to now we have been unable to clearly show this connection in 3-D. The potential role of CMP during catalysis led us to run a further classification using correspondence analysis with a round mask focused on the area surrounding CMP. We did not apply HAC but directly reconstructed the molecule from the first 35 classes obtained by the moving centers algorithm (Fig. 1.7). Strong variations in



Figure 1.7 Classification of subset 2 into 35 classes, focusing on changes near the central membrane protuberance (CMB). Scale bar 100Å (from [Radermacher *et al.* \[2006\]](#), with permission).

CMP are clearly visible. However, when we created a movie (not shown) from images sorted according to the movements of CMP, we could observe that the changes in the matrix arm accompanying the changes in CMP formed an irregular sequence. Although the series of reconstructions show the inherent flexibility of the enzyme, we believe that this specifically selected sequence of movements only demonstrates possible conformational changes of Complex I during a functional cycle. Further extensive studies are needed to be able to relate specific structural conformations to specific functional states.

We have reconstructed a subcomplex of Complex I from *Y. lipolytica* lacking the 24- and 51-kDa subunits by use of the same method as for the holoenzyme (Fig. 1.8) (Clason *et al.*, 2007; Zickermann *et al.*, 2007). The direct localization of these two subunits in domain 1 allowed us to fit the X-ray model of the matrix arm from *Thermus thermophilus* (Sazanov and Hinchliffe, 2006) into the structure of the holoenzyme (Fig. 1.9). Without the identification of domain 1 as the location of the 24- and 51-kDa subunits, there would have been 24 possible orientations for fitting the X-ray structure into the holoenzyme. The identification of domain 1 reduced this number to only 6. Only 5 of those were feasible and one additional fit (number 2) was recently excluded on the basis of structural studies of a bacterial enzyme (unpublished data). Thus, four major orientations remain. The closest distance between iron sulfur cluster N2, which represents the electron transfer site to ubiquinone, and the upper surface of the membrane arm is 40 Å (in fit 4). We favor fit 1, which is in agreement with a previous 2-D immunoelectron microscopic study (Zickermann *et al.*, 2003). In fit 1 the 49-kDa subunit and the iron sulfur cluster N2 are located in domain 2 and N2 is at a distance of 60 Å from the membrane. These distances render a direct coupling mechanism for electron transfer and proton translocation highly unlikely.

Mammalian and some of the yeast Complex Is undergo an active deactive transition, with presumed major conformational changes (Gavrikova and Vinogradov, 1999; Grivennikova *et al.*, 2003; Kotlyar and Vinogradov, 1990; Maklashina *et al.*, 2003). If fit 1 represents the true subunit arrangement, then a larger conformational change in the transition

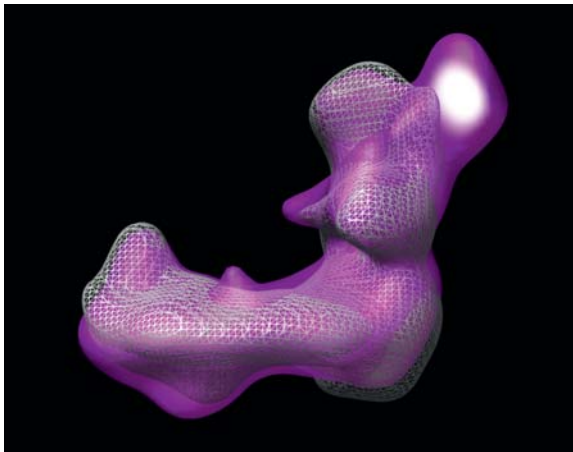


Figure 1.8 Overlay of the subcomplex reconstruction (mesh) and the holoenzyme (purple transparent surface). In white the maximum difference is shown (as density). Clearly visible domain 1 is missing in the subcomplex.

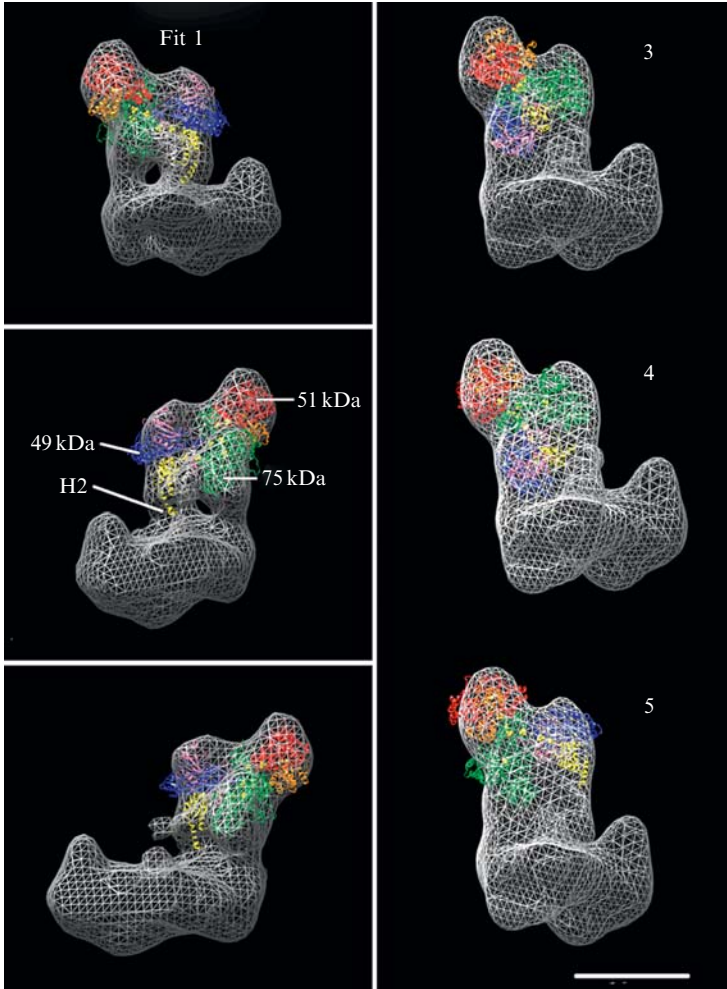


Figure 1.9 Fit of the X-ray model of the hydrophilic subunits from *T. thermophilus* into the structure of *Y. lipolytica* complex I. Shown are four fits. 1, and 3 to 5. Fit 1 is placed into the class 2 volume. The other fits are placed into the reconstruction from the complete subset 2. Note the two separate connections between the matrix and membrane arm in the top left panel (adapted from Clason *et al.* [2007], with permission).

from the inactive to the active state of the enzyme could bend domain 2 to make closer contact with the membrane arm than we observe now, for example, in the class 2 reconstruction (Fig. 1.6B, and Fig. 1.9 top left). A strong conformational change could bring the 49-kDa subunit and N2 substantially closer to the membrane arm. Such a bending may allow for an easier reconciliation of fit 1 with cross-linking studies (Kao *et al.*, 2004) and

may bring iron sulfur cluster N2 sufficiently close for a direct coupling mechanism to be possible. It may well be that Complex I exhibits both a direct coupling mechanism combined with an additional conformationally driven proton pump (Friedrich, 2001). Only higher resolution structural studies and the structural analysis of different conformations of the activated enzyme will be able to answer these questions.

4. CONCLUSION

Complex I is a highly dynamic enzyme and exhibits a range of conformations when prepared for electron microscopy. For obtaining correct structural results, methods must be used that reliably can separate the different conformations. By use of the random conical reconstruction technique in conjunction with extensive classification, it was possible to calculate the 3-D reconstruction of Complex I with a consistent domain structure. The separation of different conformations has resulted in a gallery of structures that give the first insights into the conformational spectrum of Complex I. Fitting of the X-ray model of the hydrophilic subunits in the 3-D structure of *Yarrowia* Complex I has restricted the possible positions of the electron transfer site to a distance of more than 35 Å away from the membrane, strongly suggesting a conformationally driven active proton pumping mechanism for Complex I.

ACKNOWLEDGMENTS

The work presented was supported by NIH grant NIH RO1 GM068650 (to M.R.) and Deutsche Forschungsgemeinschaft SFB 472 (to U. Brandt and V. Zickermann, University of Frankfurt). The work has benefited from grant NIH RO1 GM069551 (to T.Ruiz, University of Vermont). I thank Teresa Ruiz for critical reading of the manuscript.

REFERENCES

- Akey, C. W., and Radermacher, M. (1993). Architecture of the *Xenopus* nuclear pore complex revealed by three-dimensional cryo-electron microscopy. *J. Cell Biol.* **122**, 1–19.
- Bellon, P. L., and Lanzavecchia, S. (1995). A direct Fourier method (DFM) for X-ray tomographic reconstructions and the accurate simulation of sinograms. *Int. J. Biomed. Comput.* **38**, 55–69.
- Bostina, M. (2004). Determination of the structure of complex I of *Yarrowia lipolytica* by single particle analysis. PhD thesis MPI für Biophysik/Abteilung Strukturbioogie. Johann Wolfgang Goethe-Universität, Frankfurt.

- Böttcher, B., Scheide, D., Hesterberg, M., Nagel-Steger, L., and Friedrich, T. (2002). A novel, enzymatically active conformation of the *Escherichia coli* NADH: Ubiquinone oxidoreductase (complex I). *J. Biol. Chem.* **277**, 17970–17977.
- Bretaudiere, J. P., and Frank, J. (1986). Reconstitution of molecule images analysed by correspondence analysis: A tool for structural interpretation [published erratum appears in *J. Microsc.* 1987 May;146(Pt 2):222]. *J. Microsc.* **144**, 1–14.
- Clason, T., Zickermann, V., Ruiz, T., Brandt, U., and Radermacher, M. (2007). Direct localization of the 51 and 24kDa subunits of mitochondrial complex I by three-dimensional difference imaging. *J. Struct. Biol.* **159**, 433–442.
- Clason, T. A., Ruiz, T., Schaeffer, H., and Radermacher, M. (2006). Three-dimensional structure of Eukaryotic Complex I. *Microscopy Microanalysis* **12**, 380–381.
- Crowther, R. A., DeRosier, D. J., and Klug, A. (1970). The reconstruction of a three-dimensional structure from projections and its application to electron microscopy. *Proc. R. Soc London Ser. A* **317**, 319–340.
- Deans, S. R. (1983). “The Radon Transform and Some of Its Applications.” John Wiley & Sons, New York.
- Diday, E. (1971). La methode de nuees dynamiques. *Rev Statistique Appliquée* **19**, 19–34.
- Diday, E. (1973). The dynamic clusters method in nonhierarchical clustering. *Int. J. Comput. Info. Sci.* **2**, 61–88.
- Forster, F., Pruggnaller, S., Seybert, A., and Frangakis, A. S. (2008). Classification of cryo-electron sub-tomograms using constrained correlation. *J. Struct. Biol.* **161**, 276–286.
- Frank, J., Penczek, P., Grassucci, R., and Srivastava, S. (1991). Three-dimensional reconstruction of the 70S *Escherichia coli* ribosome in ice: The distribution of ribosomal RNA. *J. Cell Biol.* **115**, 597–605.
- Frank, J., Radermacher, M., Penczek, P., Zhu, J., Li, Y., Ladjadj, M., and Leith, A. (1996). SPIDER and WEB: Processing and visualization of images in 3D electron microscopy and related fields. *J. Struct. Biol.* **116**, 190–199.
- Frank, J., and van Heel, M. (1982). Correspondence analysis of aligned images of biological particles. *J. Mol. Biol.* **161**, 134–137.
- Friedrich, T. (2001). Complex I: A chimaera of a redox and conformation-driven proton pump. *J. Bioenerg. Biomembr.* **33**, 169–177.
- Fu, J., Gao, H., and Frank, J. (2007). Unsupervised classification of single particles by cluster tracking in multi-dimensional space. *J. Struct. Biol.* **157**, 226–239.
- Gavrikova, E. V., and Vinogradov, A. D. (1999). Active/de-active state transition of the mitochondrial complex I as revealed by specific sulfhydryl group labeling. *FEBS Lett.* **455**, 36–40.
- Grigorieff, N. (1998). Three-dimensional structure of bovine NADH: Ubiquinone oxidoreductase (complex I) at 22 Å in ice. *J. Mol. Biol.* **277**, 1033–1046.
- Grivennikova, V. G., Serebryanaya, D. V., Isakova, E. P., Belozerskaya, T. A., and Vinogradov, A. D. (2003). The transition between active and de-activated forms of NADH: Ubiquinone oxidoreductase (Complex I) in the mitochondrial membrane of *Neurospora crassa*. *Biochem. J.* **369**, 619–626.
- Guenebaut, V., Schlitt, A., Weiss, H., Leonard, K., and Friedrich, T. (1998). Consistent structure between bacterial and mitochondrial NADH: Ubiquinone oxidoreductase (complex I). *J. Mol. Biol.* **276**, 105–112.
- Guenebaut, V., Vincentelli, R., Mills, D., Weiss, H., and Leonard, K. R. (1997). Three-dimensional Structure of NADH-dehydrogenase from *Neurospora crassa* by electron microscopy and conical tilt reconstruction. *J. Mol. Biol.* **265**, 409–418.
- Hofhaus, G., Weiss, H., and Leonard, K. (1991). Electron microscopic analysis of the peripheral and membrane parts of mitochondrial NADH dehydrogenase (complex I). *J. Mol. Biol.* **221**, 1027–1043.

- Hoppe, W., Gassmann, J., Hunsmann, N., Schramm, H. J., and Sturm, M. (1974). Three-dimensional reconstruction of individual negatively stained yeast fatty-acid synthetase molecules from tilt series in the electron microscope. *Hoppe Seylers Z. Physiol. Chem.* **355**, 1483–1487.
- Hoppe, W., Langer, R., Knech, G., and Poppe, C. (1968). Proteinkristallstrukturanalyse mit Elektronenstrahlen. *Naturwissenschaften* **55**, 333.
- Hoppe, W., Schramm, H. J., Sturm, M., Hunsmann, N., and Gaßmann, J. (1976). Three-dimensional electron microscopy of individual biological objects. I. Methods. *Z. Naturforsch Section a-a* **31a**, 645–655.
- Kao, M. C., Matsuno-Yagi, A., and Yagi, T. (2004). Subunit proximity in the H⁺-translocating NADH-quinone oxidoreductase probed by zero-length cross-linking. *Biochemistry* **43**, 3750–3755.
- Knauer, V., Hegerl, R., and Hoppe, W. (1983). Three-dimensional reconstruction and averaging of 30 S ribosomal subunits of *Escherichia coli* from electron micrographs. *J. Mol. Biol.* **163**, 409–430.
- Kohonen, T. (1990). The selforganizing map. *Proc IEEE* **78**, 1464–1480.
- Kotlyar, A. B., and Vinogradov, A. D. (1990). Slow active/inactive transition of the mitochondrial NADH-ubiquinone reductase. *Biochim. Biophys. Acta* **1019**, 151–158.
- Lanzavecchia, S., Bellon, P. L., and Radermacher, M. (1999). Fast and accurate three-dimensional reconstruction from projections with random orientations via Radon transforms. *J. Struct. Biol.* **128**, 152–164.
- Lebart, L., Morineau, A., and Warwick, K. M. (1984). “Multivariate Descriptive Statistical Analysis: Correspondence Analysis and Related Techniques for Large Matrices.” Wiley, New York.
- Leonard, K., Haiker, H., and Weiss, H. (1987). Three-dimensional structure of NADH: Ubiquinone reductase (complex I) from *Neurospora* mitochondria determined by electron microscopy of membrane crystals. *J. Mol. Biol.* **194**, 277–286.
- Leschziner, A. E., and Nogales, E. (2006). The orthogonal tilt reconstruction method: an approach to generating single-class volumes with no missing cone for ab initio reconstruction of asymmetric particles. *J. Struct. Biol.* **153**, 284–299.
- Leschziner, A. E., Saha, A., Wittmeyer, J., Zhang, Y., Bustamante, C., Cairns, B. R., and Nogales, E. (2007). Conformational flexibility in the chromatin remodeler RSC observed by electron microscopy and the orthogonal tilt reconstruction method. *Proc. Natl. Acad. Sci. USA* **104**, 4913–4918.
- Maklashina, E., Kotlyar, A. B., and Cecchini, G. (2003). Active/de-active transition of respiratory complex I in bacteria, fungi, and animals. *Biochim Biophys. Acta* **1606**, 95–103.
- Marabini, R., and Carazo, J. M. (1994). Pattern-recognition and classification of Images of biological macromolecules using artificial neural networks. *Biophys. J.* **66**, 1804–1814.
- Marco, S., Chagoyen, M., de la Fraga, L. G., Carazo, J. M., and Carrascosa, J. L. (1996). A variant to the random approximation of the reference-free alignment algorithm. *Ultramicroscopy* **66**, 5–10.
- Morgan, D. G., Menetret, J. F., Radermacher, M., Neuhof, A., Akey, I. V., Rapoport, T. A., and Akey, C. W. (2000). A comparison of the yeast and rabbit 80 S ribosome reveals the topology of the nascent chain exit tunnel, inter-subunit bridges and mammalian rRNA expansion segments. *J. Mol. Biol.* **301**, 301–321.
- Radermacher, M. (1988). Three-dimensional reconstruction of single particles from random and nonrandom tilt series. *J. Electron Microsc. Techn.* **9**, 359–394.
- Radermacher, M. (1994). Three-dimensional reconstruction from random projections: Orientational alignment via Radon transforms. *Ultramicroscopy* **53**, 121–136.
- Radermacher, M. (1997). Radon transform techniques for alignment and 3D reconstruction from random projections. *Scan. Microsc.* **11**, 171–177.

- Radermacher, M., Rao, V., Grassucci, R., Frank, J., Timerman, A. P., Fleischer, S., and Wagenknecht, T. (1994). Cryo-electron microscopy and three-dimensional reconstruction of the calcium release channel/ryanodine receptor from skeletal muscle. *J. Cell Biol.* **127**, 411–423.
- Radermacher, M., Ruiz, T., Clason, T., Benjamin, S., Brandt, U., and Zickermann, V. (2006). The three-dimensional structure of complex I from *Yarrowia lipolytica*: A highly dynamic enzyme. *J. Struct. Biol.* **154**, 269–279.
- Radermacher, M., Ruiz, T., Wiczorek, H., and Grueber, G. (2001). The structure of the V1-ATPase determined by three-dimensional electron microscopy of single particles. *J. Struct. Biol.* **135**, 26–37.
- Radermacher, M., Srivastava, S., and Frank, J. (1992). The structure of the 50S ribosomal subunit from *E. coli* in frozen hydrated preparation reconstructed with SECRET. In “EUREM 92” (I. Megias-Megias, M. I. Rodriguez-Garcia, A. Rios, and J. M. Arias, Eds.), Vol. 3, pp. 19–20. Granada.
- Radermacher, M., Wagenknecht, T., Verschoor, A., and Frank, J. (1986). A new 3-dimensional reconstruction scheme applied to the 50s ribosomal subunit of *E. coli*. *J. Microsc.* **141**, Rp1–Rp2.
- Radermacher, M., Wagenknecht, T., Verschoor, A., and Frank, J. (1987). Three-dimensional reconstruction from a single-exposure, random conical tilt series applied to the 50S ribosomal subunit of *Escherichia coli*. *J. Microsc.* **146**, 113–136.
- Radon, J. (1917). Über die Bestimmung von Funktionen durch ihre Integralwerte längs gewisser Mannigfaltigkeiten. *Ber. Verh. König Sächs. Ges. Wiss. Leipzig, Math. Phys., Klasse* **69**, 262–277.
- Ruiz, T., Kopperschläger, G., and Radermacher, M. (2001). The first three-dimensional structure of phosphofructokinase from *Saccharomyces cerevisiae* determined by electron microscopy of single particles. *J. Struct. Biol.* **136**, 167–180.
- Ruiz, T., Mechin, I., Bar, J., Rypniewski, W., Kopperschläger, G., and Radermacher, M. (2003). The 10.8-Å structure of *Saccharomyces cerevisiae* phosphofructokinase determined by cryoelectron microscopy: Localization of the putative fructose 6-phosphate binding sites. *J. Struct. Biol.* **143**, 124–134.
- Ruiz, T., and Radermacher, M. (2006). Three-dimensional analysis of single particles by electron microscopy: Sample preparation and data acquisition. *Methods Mol. Biol.* **319**, 403–425.
- Sazanov, L. A., and Hinchliffe, P. (2006). Structure of the hydrophilic domain of respiratory complex I from *Thermus thermophilus*. *Science* **311**, 1430–1436.
- Scheres, S. H. W., Gao, H., Valle, M., Herman, G. T., Eggermont, P. P. B., Frank, J., and Carazo, J. M. (2007). Disentangling conformational states of macromolecules in 3D-EM through likelihood optimization. *Nature Methods* **4**, 20–21.
- Stoops, J. K., Kolodziej, S. J., Schroeter, J. P., Bretauiere, J. P., and Wakil, S. J. (1992). Structure-function relationships of the yeast fatty acid synthase: Negative-stain, cryo-electron microscopy, and image analysis studies of the end views of the structure. *Proc. Natl. Acad. Sci. USA* **89**, 6585–6589.
- Toyoshima, C., and Unwin, N. (1988). Contrast transfer for frozen-hydrated specimens: Determination from pairs of defocused images. *Ultramicroscopy* **25**, 279–291.
- Typke, D., and Radermacher, M. (1982). Determination of the phase of complex atomic scattering amplitudes from light optical diffractograms of electron microscope images. *Ultramicroscopy* **9**, 131.
- van Heel, M., and Frank, J. (1981). Use of multivariate statistics in analysing the images of biological macromolecules. *Ultramicroscopy* **6**, 187–194.
- Walz, J., Typke, D., Nitsch, M., Koster, A. J., Hegerl, R., and Baumeister, W. (1997). Electron tomography of single ice-embedded macromolecules: Three-dimensional alignment and classification. *J. Struct. Biol.* **120**, 387–395.

- Yoshioka, C., Pulokas, J., Fellmann, D., Potter, C. S., Milligan, R. A., and Carragher, B. (2007). Automation of random conical tilt and orthogonal tilt data collection using feature-based correlation. *J. Struct. Biol.* **159**, 335–346.
- Zickermann, V., Bostina, M., Hunte, C., Ruiz, T., Radermacher, M., and Brandt, U. (2003). Functional implications from an unexpected position of the 49-kDa subunit of NADH: Ubiquinone oxidoreductase. *J. Biol. Chem.* **278**, 29072–29078.
- Zickermann, V., Zwicker, K., Tocilescu, M. A., Kerscher, S., and Brandt, U. (2007). Characterization of a subcomplex of mitochondrial NADH: Ubiquinone oxidoreductase (complex I) lacking the flavoprotein part of the N-module. *Biochim. Biophys. Acta.* **1767**, 393–400.

CORRELATED LIGHT AND ELECTRON MICROSCOPY/ELECTRON TOMOGRAPHY OF MITOCHONDRIA *IN SITU*

Guy A. Perkins,^{*} Mei G. Sun,[†] and Terrence G. Frey[†]

Contents

1. Introduction	30
2. Light Microscopy	31
2.1. Cell culture	31
2.2. Confocal microscopy	33
2.3. Sample preparation for electron microscopy	34
2.4. Locating the identical cells	35
2.5. Conventional TEM	35
3. Electron Microscope Tomography	36
3.1. Introduction	36
3.2. Equipment and software requirements	36
3.3. Tomographic data collection	39
3.4. Tomographic image processing	45
3.5. Visualization and measurements of volumes	46
3.6. Movies, tele tomography, and databases	47
3.7. New developments for electron tomography of mitochondria <i>in situ</i>	48
3.8. Application to apoptotic HeLa cells	48
Acknowledgments	50
References	50

Abstract

Three-dimensional light microscopy and three-dimensional electron microscopy (electron tomography) separately provide very powerful tools to study cellular structure and physiology, including the structure and physiology of mitochondria. Fluorescence microscopy allows one to study processes in live cells with specific labels and stains that follow the movement of labeled proteins and

^{*} National Center for Microscopy and Imaging Research, Center for Research in Biological Systems, University of California, San Diego, La Jolla, California, USA

[†] Department of Biology, San Diego State University, San Diego, California, USA

changes within cellular compartments but does not have sufficient resolution to define the ultrastructure of intracellular organelles such as mitochondria. Electron microscopy and electron tomography provide the highest resolution currently available to study mitochondrial ultrastructure but cannot follow processes in living cells. We describe the combination of these two techniques in which fluorescence confocal microscopy is used to study structural and physiologic changes in mitochondria within apoptotic HeLa cells to define the apoptotic timeframe. Cells can then be selected at various stages of the apoptotic timeframe for examination at higher resolution by electron microscopy and electron tomography. This is a form of “virtual” 4-dimensional electron microscopy that has revealed interesting structural changes in the mitochondria of HeLa cells during apoptosis. The same techniques can be applied, with modification, to study other dynamic processes within cells in other experimental contexts.

1. INTRODUCTION

Light microscopy (LM) can be used to visualize live cells in both 2-D and 3-D and to study changes during various cellular processes. Furthermore, fluorescence light microscopy provides powerful tools to monitor the movement of particular cellular components labeled with fluorophores and physiologic changes by fluorescent indicators. However, even the highest resolution light microscopy modalities do not deliver resolution sufficient to study mitochondrial fine structure. Transmission electron microscopy (TEM) and 3-D electron tomography (ET) generate the highest resolution 2-D and 3-D images of mitochondria currently available, providing a bridge in the meso-resolution range between light microscopy and techniques such as X-ray and electron crystallography and multidimensional NMR spectroscopy that can yield atomic models of macromolecules (Fig. 2.1). However, TEM and ET suffer from the fact that they can only image “dead” specimens and cannot be used to follow dynamic processes in mitochondria such as those that occur during apoptosis. Combining LM with TEM and ET provides the best of both worlds if one can use LM to monitor a dynamic cellular process that can then be halted at defined states by fixation followed by preparation of the identical cells or organelles for observation of ultrastructure by TEM and ET. By sampling different stages of a process based on changes observed by LM, one can add in some form the time dimension to the three spatial dimensions provided by ET, yielding a form of virtual 4-D electron microscopy. This is the subject of the next sections using the example of release of cytochrome *c* and loss of membrane potential from mitochondria during apoptosis to illustrate the utility of this approach, which can be applied, with appropriate modification, to many different systems. The techniques of LM, TEM, and even ET that we describe are

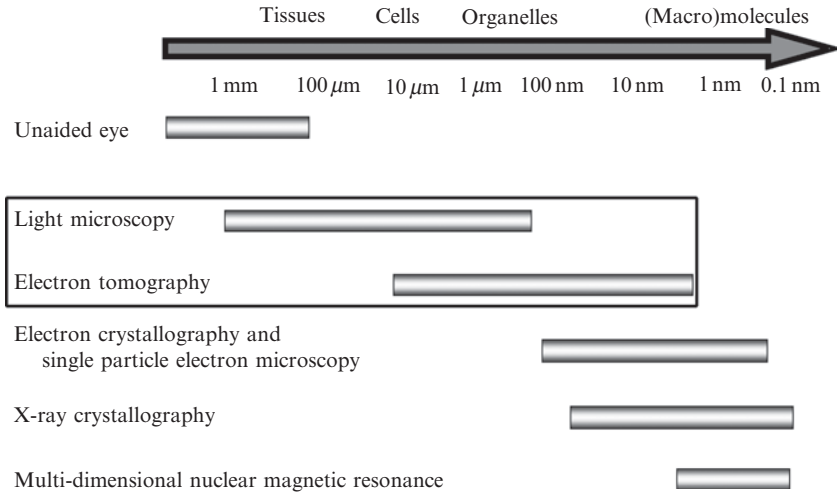


Figure 2.1 Resolution domains of common techniques used in structural biology research. Electron microscopy and tomography fills in the meso-resolution region between light microscopy and high-resolution techniques such as X-ray and electron crystallography and NMR spectroscopy.

quite conventional individually, but when combined to examine identical cells and subcellular organelles, they provide a very powerful multimode technique to characterize the dynamics of intracellular processes. We will illustrate the power of this approach by presenting our results on the structural changes in HeLa cell mitochondria during apoptosis as examples at each stage of the process.

2. LIGHT MICROSCOPY

2.1. Cell culture

In the following section we describe application of correlated light and electron microscopy and ET to characterize the ultrastructural changes in mitochondria during apoptosis in HeLa cells. However, the approach of this specific example can be applied to other cell culture models of other processes that can be characterized by LM, usually through the use of fluorescent labels and/or fluorescent indicators. We simultaneously monitored mitochondria within HeLa cells during apoptosis for cytochrome *c* release and inner mitochondrial membrane potential ($\Delta\Psi_m$) by use of confocal fluorescence microscopy of cells permanently transfected with fluorescent cytochrome *c* fusion proteins that were also labeled with TMRE, a membrane potential indicator (Goldstein *et al.*, 2000, 2005;

Sun *et al.*, 2007). In some studies we have also used calcein-AM to load mitochondria with calcein, while quenching cytoplasmic calcein with CoCl_2 to monitor the possible occurrence of a mitochondrial permeability transition (MPT) in which a large high-conductance channel opens in the mitochondrial inner membrane (Petronilli *et al.*, 1999; Sun, 2007). By growing the cells in petri dishes that contain a glass coverslip with an etched grid (MatTek Corp. Ashland, MA), we can not only easily find and image by LM identical cells over an extended period of time, but we can also subsequently fix and embed the identical cells for examination by TEM and ET (Fig. 2.2). Using the grid to identify by confocal microscopy a field of cells at defined stages of apoptosis, we prepare cells for TEM by conventional methods of chemical fixation and then locate the identical cells during sectioning for TEM and ET.

In the example described in the following we used HeLa cells permanently transfected with a 13.3-kD cytochrome *c* fusion protein containing a short tetracysteine motif (Cyt. *c*-4CYS); however, one could monitor the movement of many other mitochondrial proteins in cells as long as they can be labeled for observation by LM. Similarly, the conditions of cell growth can be modified for other cell types and experimental protocols.

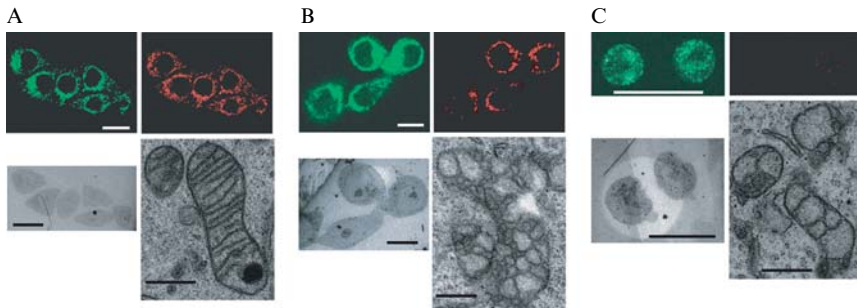


Figure 2.2 Correlated light and electron microscopy of HeLa cells at three stages of the apoptotic time frame after 16 h of exposure to $100 \mu\text{M}$ etoposide. Scale bars represent $25 \mu\text{m}$ in the fluorescent micrographs and low magnification TEMs and 500 nm in the high magnification TEMs. (A) Stage 1, Mitochondria retain cytochrome *c* as indicated by punctate FLAsH staining of Cyt. *c*-4CYS upper left and maintain a membrane potential indicated by punctate TMRE staining upper right. Lower left, Low magnification TEM of the same cells; lower right, high magnification TEM of normal mitochondria in one of the cells. (B) Stage 2, Mitochondria have released cytochrome *c* as indicated by diffuse FLAsH staining of Cyt. *c*-4CYS (upper left) but maintain a membrane potential indicated by punctate TMRE staining (upper right). Lower left, Low-magnification TEM of the same cells; lower right, high magnification TEM of a vesicular mitochondrion in one of the cells. (C) Stage 3, Mitochondria have released cytochrome *c* and have lost their membrane potential as indicated by diffuse FLAsH staining of Cyt. *c*-4CYS (upper left) and loss of TMRE staining (upper right). Lower left, Low-magnification TEM of the same cells; lower right, high magnification TEM of swollen/vesicular mitochondria in one of the cells.

The tetracysteine motif binds to the membrane permeable biarsenical fluorophores, FAsH and ReAsH (Gaietta *et al.*, 2002; Goldstein *et al.*, 2005). In this example the cells were grown and maintained at 37° in Dulbecco's modified Eagles' medium (DMEM, Gibco) supplemented with 10% FBS, 2 mM L-glutamine, 200 mg/ml penicillin, and 100 mg/ml streptomycin sulfate in a humidified atmosphere of 5% CO₂/95% air. Cells were sub-cultured 1:10 by incubating them in 0.25% trypsin (Gibco) while confluent and then resuspended in growth medium. Apoptosis was induced with 100 μ M etoposide (Sigma) for 12 to 18 h. Cells can be treated for specific effects. For example, in some experiments zVAD-fmk (100 μ M, Sigma) was added hours before the apoptotic stimulus to inhibit caspase activity or cyclosporine A was added to inhibit the MPT. FAsH (250 nM) staining reveals the distribution of Cyt. *c*-4CYS, while TMRE (50 nM, Sigma) that partitions into those mitochondria that maintain a membrane potential was added to monitor the $\Delta\Psi_m$ (Sun, 2007; Sun *et al.*, 2007).

2.2. Confocal microscopy

Cell images were acquired by fluorescence confocal light microscopy with a Leica TCS SP2 inverted confocal microscope that uses monochromators with adjustable slits rather than filters allowing greater control in the selection of the wavelengths of light detected. This is advantageous when fluorophores in multiply labeled samples have overlapping emission spectra but is not essential, and a microscope that uses filters could also be used. FAsH was excited with the 488 nm line from an argon laser attenuated to 35%, and TMRE was excited with a 543 nm line from a helium/neon laser attenuated to 34%. The detector slits of the confocal microscope were adjusted to detect FAsH emission between 497 and 553 nm and TMRE emission between 555 and 620 nm. Apoptosis was initiated by the addition of etoposide (100 μ M) that results in DNA fragmentation activating the p53 pathway. Western blot analysis of cytosolic and mitochondrial fractions indicated that half of cytochrome *c* had been released after 18 h, and previous studies have shown that cytochrome *c* release is asynchronous among cell populations. Once cytochrome *c* release begins within a HeLa cell, all mitochondria release all of their cytochrome *c* within a period of minutes (Goldstein *et al.*, 2000, 2005). Thus, when we observed HeLa cell cultures 16 h after addition of etoposide, we found populations of cells at different stages of the apoptotic pathway, including many whose mitochondria had not yet released cytochrome *c*. Images in Fig. 2.2A were recorded 16 h after addition of etoposide to initiate apoptosis but before release of cytochrome *c* as shown by the distribution of Cyt. *c*-4CYS stained with FAsH revealed in Fig. 2.2A (top left) that colocalized to mitochondria maintaining a membrane potential indicated by punctate TMRE staining in Fig. 2.2A (top right). In another field of cells recorded at a similar time point

we observed cells whose mitochondria had released cytochrome *c* as shown by diffuse FAsH staining but maintained a membrane potential indicated by punctate TMRE staining (Fig. 2.2B). Finally, the mitochondria in some cells had both released cytochrome *c* and had lost their membrane potential as indicated by diffuse FAsH staining and loss of TMRE staining in Fig. 2.2C.

On the basis of the changes in fluorescence observed in HeLa cells expressing Cyt. *c*-4CYS labeled with FAsH and TMRE, we identified three stages during apoptosis initiated by etoposide that define a new apoptotic time frame: *Stage 1*, Before release of cytochrome *c* and before loss of $\Delta\Psi_m$; *Stage 2*, After release of cytochrome *c*, but before loss of $\Delta\Psi_m$; and *Stage 3*, After both the release of cytochrome *c* and loss of $\Delta\Psi_m$.

We proceeded to study the ultrastructure of the mitochondria within the representative cells in these three stages by TEM and by ET of the identical cells that were characterized by fluorescence confocal microscopy.

2.3. Sample preparation for electron microscopy

2.3.1. Fixation

We found that the fixation, dehydration, and embedding protocol described below worked well with HeLa cells. Modifications or other protocols may be required in the case of other cell types. We generally use Durcupan as our embedding resin, because in our experience it has proven to provide the best results in ET of conventionally fixed and embedded samples; however, other resins may also be used.

After confocal imaging, the cells were fixed immediately by adding primary fixative at room temperature, followed by 1 h of incubation on ice. It is important to keep the samples cold at all times after primary fixation, until the 100% ethanol dehydration step, as described in the following. The fixative is composed of 2% paraformaldehyde and 2.5% glutaraldehyde in a 0.1 M sodium cacodylate, pH 7.4, buffer. After washing three times in an ice-cold 0.1 M sodium cacodylate buffer containing 3 μ M calcium chloride for 3 min, the primary fixed cells were then incubated with 1% osmium tetroxide, 0.8% potassium ferrocyanide, and 3 μ M calcium chloride in 0.1 M sodium cacodylate for 60 min on ice. After washing with distilled water three times for 3 min, the fixed cells were stained and stabilized in 2% uranyl acetate for 30 min on ice.

2.3.2. Dehydration, infiltration, and embedding

Cells were dehydrated in an ice-cold ethanol series of 20%, 50%, 70%, and 90% successively, on ice for 3 min each. The cells were then dehydrated at room temperature three times for 3 min each in 100% ethanol. Next, the cells were infiltrated in a mixture of 50% ethanol and 50% Durcupan ACM resin (Fluka) for 60 min with agitation at room temperature, followed by

100% Durcupan ACM twice for 1 h with agitation, after which the samples were placed in an oven to polymerize at 60 to 80° for at least 48 h.

2.4. Locating the identical cells

Once the samples were polymerized, the glass coverslip on the MatTek dish was peeled away from the bottom with a razor blade under the stereomicroscope. Careful insertion of the razor blade between the glass coverslip and the resin block allows air to go in and pop off the coverslip. The etched grid is reproduced on the sample block facilitating the identification of the appropriate grid location containing the same cells observed by confocal microscopy. The cell location is then circled according to the grid map with an indelible marker under a stereomicroscope, and the selected area is cut out and glued to a plain block for sectioning. Note that the surface of the block contains a single cell layer, so care must be taken when the block is trimmed and then sectioned.

2.4.1. Sectioning

The block surface was trimmed to as small an area of the sample as possible containing the cells of interest according to the grid map. Load the block into the holder of the microtome and bring the diamond knife close to the block. Because the sample thickness is only one cell layer, it is critical to make sure that the block surface is parallel to the diamond knife before sectioning. The gap between the sample surface and the knife-edge serves as a reference during adjustment, and once they are parallel to each other, the gap between the sample surface and the knife-edge will be identical in width all the way from left to right. When moving the block up and down, the gap will remain the same from the upper to lower edges of the surface. Sections were collected and post stained with 2% uranyl acetate and Sato lead (Perkins *et al.*, 1997) before examination in an FEI Tecnai 12 TEM. Sections of different thicknesses may be collected from the same block; for example, thinner sections (ca. 80 nm) for standard TEM thin section imaging and thicker sections (200 to 500 nm) for ET.

2.5. Conventional TEM

TEM of thin sections revealed an interesting structural transformation during apoptosis in this system. Figure 2.2A–C contains low and high magnification TEM images of the identical cells imaged by confocal microscopy at each of the three stages that define the apoptotic time frame. Stage 1 cells whether untreated or treated but observed before changes detected by confocal microscopy showed only normal mitochondria (Fig. 2.2A, bottom row). On the other hand, in cells at Stage 2, which follows release of cytochrome *c* but precedes loss of $\Delta\Psi_m$, many mitochondria exhibit a

markedly different ultrastructural morphology that we termed “vesicular” (Fig. 2.2B, bottom), although most mitochondria in Stage 2 cells appear normal. By Stage 3, cells have released cytochrome c , and lost $\Delta\Psi_m$ and normal mitochondria are in the minority. Many mitochondria in Stage 3 cells exhibit the vesicular morphology and/or appear swollen as indicated by a rounded or distended appearance and lighter staining of the mitochondrial matrix (Sun *et al.*, 2007). Characterization of these morphologic changes required the third spatial dimension provided by ET described next.

3. ELECTRON MICROSCOPE TOMOGRAPHY

3.1. Introduction

3.1.1. Electron tomography

ET is based on a series of tilted images usually collected from a comparatively thick section or from isolated mitochondria (Frey *et al.*, 2006). An ET reconstruction provides a 3-D density map that can be rotated and viewed from any angle and computationally “sliced” at voxel-thick intervals (a voxel or volume element is the 3-D analog of a pixel or picture element). The volume can be further segmented to model separately features of interest. These volumes can then be explored with sophisticated interactive 3-D rendering and visualization programs. The continual development of computational approaches for real-time interactive 3-D data processing and analyses aims at facilitating the generation of ET volumes by increasing automation of the processes. However, the volumes still need to be interpreted, and this requires substantial expert knowledge about mitochondrial structure and function. We will present a method that has worked well for our 3-D structural studies of mitochondria in conventionally fixed and embedded specimens. Other guides and resources can be found in these methods-oriented articles (Engelhardt, 2007; Frey *et al.*, 2006; Marco *et al.*, 2004; Marko and Hsieh, 2007; O’Toole *et al.*, 2007). Figure 2.3 presents an outline of data collection, processing, segmentation, and visualization for ET.

3.2. Equipment and software requirements

3.2.1. Electron microscope

The minimum microscope requirement is a 120-kV TEM with a goniometer specimen holder that can tilt from 0° to $\pm 60^\circ$. However, the ease of tilt series collection is governed by automation, and this requires computers that are now found on all modern TEMs. A eucentric goniometer that is computer controlled is advantageous because specimen movement and the focusing adjustment will be small during tilt series collection if the object is

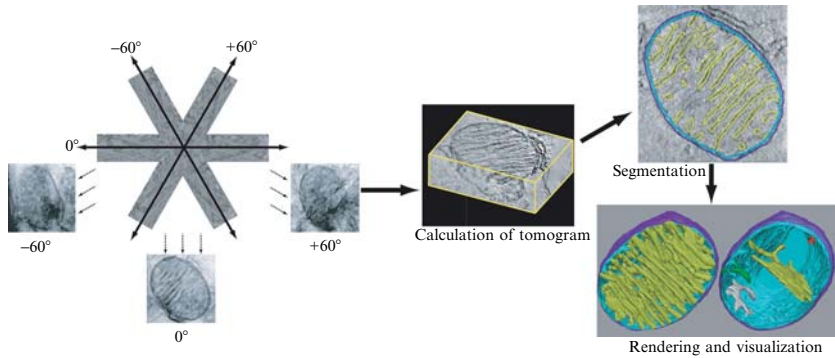


Figure 2.3 Schematic of the process required to generate a 3-D model by electron tomography. On the left collection of the tilt series from -60° to $+60^\circ$ at regular angular intervals is depicted with projection images of the -60° , 0° , and $+60^\circ$ tilts shown. In the center is a representation of the reconstructed volume containing part of a mitochondrion. Upper right shows segmentation of one slice of the tomogram by tracing the outer mitochondrial membrane in dark blue, the inner boundary membrane in turquoise, and the cristae membranes in yellow. Bottom right shows representations of two 3-D models based on segmentations of all of the sections of the tomogram. The model on the left shows the outer membrane in dark blue, the inner boundary membrane in turquoise, and all of the cristae in yellow. The model on the right is of the same mitochondrion but showing only four representative cristae in red, yellow, green, and grey from top to bottom.

made eucentric. With a 120-kV microscope, however, one is limited in section thickness to approximately 200 nm, depending on the electron density of the sample, because thicker sections produce more inelastically and multiply-scattered electrons that add noise to the image. The noise is seen as blurring of features that can reduce resolution or even render the image unusable. Even so, research questions can still be addressed if all that is needed is a portion of the mitochondrial volume (e.g., crista junction or contact site analyses). More commonly used for ET of mitochondria are intermediate-voltage TEMs (IVEM) operating at 200 to 400 kV including energy-filtered TEMs (EFTEM) or high-voltage TEMs (HVEM) operating at 750 to 3000 kV. With IVEMs a section thickness of 500 nm is commonly used, and with the 3000 kV HVEM section thicknesses up to 5000 nm have been used. The increased accelerating voltages of these microscopes reduce the scattering cross section of the electron beam, permitting greater penetration of the thicker specimens with less inelastic and multiple scattering, thus improving image quality. The use of an energy filter also improves image quality by removing the lower energy inelastically scattered electrons that blur the image by chromatic aberration, because they have longer wavelengths than elastically scattered electrons and, therefore, have different focal planes. One must also remember that the path of the electron beam

through slablike sections increases as the specimen is tilted. Decreased scattering cross section afforded at higher accelerating voltages becomes important when the specimen is tilted up to 60° or 70°, where path of the beam through the section doubles and triples, respectively.

3.2.2. Image recording

The use of a charge-coupled device (CCD) camera provides several advantages over the use of photographic film. (1) Direct digital recording eliminates the time spent for film development and subsequent digitization, thus increasing throughput. (2) Water contamination and vacuum pump-down in the TEM column are reduced because of the absence of photographic film. (3) CCD recording simplifies automated image collection. One advantage that photographic film still holds over CCD cameras is for large-area imaging needs (e.g., imaging long, clustered, or networked mitochondria). Film has a larger area than even the current high-end CCD cameras with 4k × 4k pixel detectors, such as the Gatan UltraScan™ 4000 and the Tietz TemCam F415. However, new generation CCD cameras have 8k × 8k pixel detectors, and this approaches the scan size of film that uses high-resolution film scanners (4000 dpi). Although scanning a tilt series recorded on film can take 3 to 6 h—longer than actually collecting the tilt series—an automatic scanning device was developed by Robert Glaeser (U. California, Berkeley) using a reasonably priced Nikon CoolScan (Typke *et al.*, 2005).

3.2.2. Computer and software

Modern TEMs are equipped by the manufacturer with computers and software to automatically or semiautomatically acquire tilt series. For older TEMs, software for automatic tilt series acquisition is available from a few sources: *TVIPS*, www.tvips.com; SerialEM, <http://bio3d.colorado.edu/>; TOM, <http://www.biochem.mpg.de/baumeister/>; and Utrecht suite, www.bio.uu.nl/mcb/3dem/Electron_tomography.html.

With an automated system, a tilt series can be recorded within an hour or two once the microscope is properly aligned and the specimen selected.

After the tilt series has been collected, extensive image processing is required. Previously, ET image processing required a large workstation or even a supercomputer, but modern desktop computers, including clusters of such machines, are adequate for routine ET image processing. For large volumes, however, generating a reconstruction in under a day still requires parallelized code run on clusters or a supercomputer. Several complete software packages are available to process, display, and analyze ET data. Currently, the most used is the freeware IMOD software package (<http://bio3d.colorado.edu/>), and there is an active IMOD listserv group (imod@lists.Colorado.EDU) that diligently troubleshoots installation and software problems as they arise. Similar software packages have been developed and made available, including SPIRE (SPIDER) (www.wadsworth.com).

[org/spider_doc/](http://spider_doc/)); SUPRIM (<http://ami.scripps.edu/software/suprim/>); TOM (http://www.biochem.mpg.de/baumeister/tom_e/index.html); EM3D (<http://em3d.stanford.edu/>), TxBR (<http://ncmir.ucsd.edu/>); EMAN (<http://blake.bcm.edu/EMAN/>); BSOFT (<http://lsbr.niams.nih.gov/bsoft/bsoft.html>); IMAGIC (<http://www.imagescience.de/>); and XMIPP (<http://xmipp.cnb.csic.es/>).

Certain of these packages emphasize molecular ET, whereas others specialize in cellular ET. The packages that we have used the most for mitochondrial ET are IMOD and TxBR (Lawrence *et al.*, 2006).

3.3. Tomographic data collection

Acquisition of high-quality images of mitochondria is the critical step to ensure a 3-D reconstruction at nanometer resolutions.

3.3.1. Considerations for tomography of mitochondria

The whole purpose of ET is to reconstruct volumes. It makes sense to aim for the thickest section that will provide the desired image quality and resolution. It is attractive to use sections thick enough (200 to 5000 nm) to contain a significant fraction of the organelle within the section volume. Threadlike mitochondria such as those found in axons can be as thin as 200 nm, but most mitochondria are thicker than this. Furthermore, even a thin mitochondrion may not be oriented parallel to and lie within a section. Yet, as pointed out previously, thicker sections produce more inelastically and multiply scattered electrons that degrade the image quality and resolution. It is also important to remember that the length of the beam path through a section increases twofold to threefold at tilt angles of 60° and 70°, respectively. Two strategies have been developed to perform ET on larger mitochondria without compromising resolution. One strategy is the use of energy-filtering TEMs and the other is to perform serial ET.

3.3.2. Energy-filtering and serial tomography

As the specimen thickness increases, the proportion of inelastically scattered electrons also increases (Bouwer *et al.*, 2007). Energy filtering applied to ET is a way to image thicker specimens (>500 nm) by reducing or eliminating altogether the blurring from chromatic aberration that results from inelastic scattering. Energy filters operating in either “zeroloss” mode or “most-probable-loss” mode select electrons within a narrow energy range, minimizing chromatic aberration from electrons of different energy (wavelength) and yielding images with significantly higher signal-to-noise ratio (Bouwer *et al.*, 2004, 2007). We have used the 300-kV EFTEM at the NCMIR to produce high-quality reconstructions of mitochondria in 1000-nm-thick sections.

The technique of serial sectioning can be combined with ET to derive a reconstruction of large volumes. Serial sections are cut through the sample block with a thickness determined by the desired resolution. Generally, for 120-kV TEMs the section thickness should be no greater than 200 nm, for 400-kV TEMs the section thickness should be no greater than 500 nm, and for 300-kV EFTEM no greater than 1000 nm. Tilt series are collected from the sliced mitochondrion found in each section, and ET reconstructions are computed for each tilt series, a single or double tilt series for each section. Afterward, the resulting series of volumes are aligned and combined to form a single, larger volume that contains the entire mitochondrion. The principal drawback to this approach is the loss of typically 25 to 40 nm of material at the edge of each section because of sectioning artifacts, which sometimes makes alignment, segmentation, and modeling across these gaps difficult. Extensive serial ET was recently used by Noske *et al.* to reconstruct two entire insulin-secreting beta cells including all of the mitochondria (Noske *et al.*, 2007).

3.3.3. Estimation of tomographic resolution

In planning an ET experiment, one must first determine whether sufficient resolution is possible for a specimen of given thickness, tilt geometry, and angular range and increment. The desired resolution determines the magnification of the images in the tilt series and the number of images and the angular interval with which the tilt series is recorded. One must also understand that the resolution is not isotropic, because the resolution along the z -axis (the axis perpendicular to the section plane) will be lower as it is not possible to tilt the specimen to 90° with conventional TEM holders because of occlusion by the specimen holder or the specimen grid bars. The resulting “missing wedge” of information, the shape of the volume above and below the specimen into which it cannot be tilted, lowers the resolution in z by an elongation factor. The missing wedge can be reduced in volume to a “missing pyramid” by recording a double-tilt series, two tilt series around orthogonal tilt axes of the same specimen. At the NCMIR, a newly designed 360° total tilt ET specimen holder has been used to reconstruct muscle mitochondria with isotropic resolution. This holder will support cantilevered samples of either the pyramidal geometry, ideal for cells and tissue, or epoxy thread geometry, useful for isolated mitochondria or cells in suspension.

Obtaining an accurate estimate of resolution in ET reconstructions of mitochondria is difficult because each mitochondrion is unique, so the concept of statistical reproducibility used in single-particle analysis of molecules to calculate resolution is not applicable. It is reasonable to postulate that the resolution in ET should be governed by: (1) the thickness of the section, or more accurately, the thickness of the portions of heavy-metal staining and other electron-dense material that affects electron scattering, (2) the collection

schema (e.g., single-tilt, double-tilt, or conical tilt), (3) the angular range and spacing of projection images in a tilt series, and (4) the signal-to-noise ratio in each image. Because the Crowther equation (Crowther *et al.*, 1970), even modified for slab (section) geometry, often underestimates the resolution in ET reconstructions of biologic material, other constructs for estimating sufficient sampling of Fourier space are currently in use (Frank, 2006). A number of tomographers today use some form of the Fourier shell correlation (FSC) (Frangakis and Hegerl, 2001) and/or spectral signal-to-noise ratio (SSNR) (Penczek, 2002) to estimate the resolution in an ET reconstruction. Despite criticism by Penczek and Frank (in (Frank, 2006; pp 307–330)), we have used the Bsoft program to estimate resolution in our reconstructions because it has been documented and is straightforward to use (Cardone *et al.*, 2005; Heymann *et al.*, 2008). A typical resolution range for our mitochondrial reconstructions is 5 to 10 nm.

3.3.4. Choice of pixel size and magnification

On the basis of the Shannon sampling theory, an image must be sampled at a frequency of at least twice the intended resolution. In practice, however, sampling at three or four times the desired resolution gives better image quality, especially when CCD cameras are used, in which case images are sometimes binned down by $2\times$ by averaging 2×2 arrays of adjacent pixels to improve the signal-to-noise ratio before ET processing. Thus, if the desired resolution for the image were 5 nm, a pixel size of 1.25 nm or even finer would be appropriate. When a CCD camera is used, the magnification must be chosen to match the desired resolution with the spacing of the elements of the CCD array taking into account whether the data from adjacent elements will be binned in producing the final images. When film is used, the choice of magnification is less critical, because current film scanners can digitize at various resolutions up to approximately 4000 dpi, depending on the film scanner, and so there is a range of magnifications that could be adequate.

3.3.5. Size and number of fiducial gold particles

The images of the tilt series must be carefully aligned to a common origin and spatially adjusted to correct for possible distortions during data collection to produce a high-quality tomogram (see Section 4.1). For the best image alignment, we found that it is advisable to use 30 to 80 colloidal gold particles spread more-or-less uniformly across the image as fiducial markers. Gold particles should be applied on both sides of the section, because both IMOD and TxBR perform better if the particles used for alignment are not all on one side. The number of particles on each side need not be equal, but there should be at least four particles on a side for good triangulation. We apply different size gold particles to each side (e.g., 15-nm particles on one side and 20-nm particles on the other side), so that we can visually gauge

whether there are enough particles on each side within the imaging area before collecting a tilt series. To correct for section bending or warping, one can use the “local” alignment option with IMOD (etomo). However, for proper correction, the number of fiducial markers needs to be greater—20 or more markers per side depending on the extent of the warping. A greater number of markers are required for the quadratic option (40 marker minimum) or the cubic option (60 marker minimum) in TxBR. These higher-order options provide a more accurate alignment and hence a higher quality reconstruction (Lawrence *et al.*, 2006).

Problems arise if the density or size of gold particles is too low or too high. Generally, larger size gold particles are used for thicker sections because the increased electron density in the projection image can obscure smaller particles. If the density of gold particles is low, sections can be made more hydrophilic by glow-discharging or UV irradiation before applying the colloidal gold solution. Just as one can have too few gold particles, one can also have too many gold particles or clusters of particles, which would cover and interfere with the structures under investigation and create streaks that “bleed” into the tomogram. Thus, it is advisable to use the smallest size gold particles that will not be obscured by the electron-dense (stained) material, remembering that the distance between particle and nearby stained material changes and can overlap on tilting the specimen. The utility “ccderaser” in IMOD can be used to remove gold particles, especially those in clusters, from images before computing the reconstruction and thus minimize the streaking.

3.3.6. Orientation of mitochondrion

For single-tilt reconstructions, it is advantageous to orient elongated mitochondria with their long axis parallel to the tilt axis to enhance outer and inner boundary membrane visualization. For double-tilt reconstructions, the orientation of the long axis should be 45° from the tilt axis for each tilt series. Similarly, when working with mitochondria having a predominance of lamellar cristae (e.g., brown fat or muscle), the lamellae should be oriented along the tilt axis.

3.3.7. Pre-irradiating (“cooking”) the area of interest

In ET of conventionally fixed and embedded specimens, “cooking” the area of interest and the surrounding area before a tilt series is collected is practiced so that the greatest shrinkage and mass loss occurs before data collection. We use an automatic cooking sequence that irradiates the specimen at each tilt angle for a user-defined amount of time, usually 10 to 20 sec. It is important to note that for a double-tilt series, the cooking should be done for each tilt axis before starting the tilt series. Because the beam-induced mass loss and warping should be minimized between first and last images of a tilt series to maximize reconstruction quality, it is important

to record a tilt series as quickly as feasible, paying attention to beam-induced specimen movement. Rapid image acquisition is facilitated by automated collection software. It is helpful to apply a thin film of carbon to both sides of the section, because the carbon film is conductive, adds stability, and reduces specimen charging. Once started, a tilt series should be completed with minimal interruptions because beam dynamics change with time and the effect is especially noticeable in images if the pause is overnight.

3.3.8. Single-tilt or double-tilt

With the double-tilt series protocol reconstructions are computed separately from separate tilt series taken about two orthogonal axes, and then the two reconstructions are aligned computationally to each other and combined to achieve a single reconstruction. This double-axis approach results in resolution that is more isotropic and is especially valuable in reconstructing membranes that are perpendicular to a tilt axis. Because of the advantages in reducing the missing data from a wedge to a pyramid with smaller volume, the double-tilt series collection schema is now the standard. With modern ET, there are only a few justifications for recording single-tilt series. They are: (1) if the specimen is fragile or cannot sustain the roughly double beam exposure required for double-tilt collection; (2) lack of time, this may be because the series is recorded on film with its inherently longer processing time, or because no automated collection is available; or (3) for the given specimen and research objectives a single-tilt series reconstruction will achieve the desired result. The last is justified when the membranes are heavily stained, which is how we commonly prepare mitochondrial samples, and the segmentation is done manually. Although fainter in specified orientations because of the missing wedge, the membranes are usually still visible and hence traceable. When automated segmentation is used, it makes sense to use double-tilt series to minimize “gaps” in the membrane opacity. Double-tilt ET, however, is not free from problems. The additional radiation used to collect the second tilt series induces further change (shrinkage and warping) in the specimen, so that the successive reconstructions are not from an identical specimen. Taking into account this change, pre- (TxBR) or post- (IMOD) reconstruction software is used to massage the two “halves” of the double-tilt data into a merged reconstruction.

3.3.9. Angular increment and tilt range

For ET of slablike sections, there is a limitation in the range of tilts that one can collect, generally $\pm 60^\circ$ to $\pm 70^\circ$. This is due to several factors such as the specimen support grid or rod occluding the image at high tilt, the physical stops in the microscope that prevent the specimen rod from hitting pole pieces and apertures, and increased inelastic and multiple scattering, hence image degradation, resulting from the increased path of the beam at high tilt angles. Only a few TEMs have 180° -tilt ET specimen holders, and these

require specimens with cylindrical or pyramidal geometry (Zhang *et al.*, 1998). Typical angular increments used in collecting tilt series are either 1° or 2° . A double-tilt series with 1° increment between $\pm 70^\circ$ amounts to 282 images. Even with automation software, this is a lot of beam exposure for biologic samples. Usually mitochondrial membranes are well delineated for a double-tilt series with 2° increment between $\pm 60^\circ$. It should be noted that the most commonly used reconstruction algorithm, weighted back-projection, requires a constant angular increment. Other schemas can sample Fourier space more evenly by use of a smaller increment for high tilts and a larger one for low tilts, following a formula. With these schemas, algorithms other than weighted back-projection are used to reconstruct the volume (e.g., ART or SIRT).

3.3.10. Microscope alignment, eucentricity, and focus

The TEM needs to be aligned well to acquire high-quality images. Smaller condenser apertures combined with larger spot sizes should be used to increase the spatial coherence of the electron beam while maintaining sufficient brightness. Condenser astigmatism should be corrected to minimize the ellipticity of the beam. Objective astigmatism should be corrected in the normal way and is facilitated with a CCD camera that allows calculation of the image Fourier transform whose noise spectrum is circularly symmetric when the objective lens astigmatism is corrected.

Before a tilt series is collected, the eucentric height for the object must be set in which the goniometer of the TEM is adjusted by moving the tilt axis up or down until it coincides with the plane of the object to allow eucentric tilting. This should be done at the magnification to be used for recording the tilt series. The most accurate way to set the eucentric height is to rotate the grid from $\pm 60^\circ$ and adjust the z -height so that the object at -60° is translated from the object at $+60^\circ$ only along the tilt axis. Computer control of the goniometer provides the greatest accuracy.

In acquiring a tilt series, an image is recorded, the goniometer is tilted by a defined increment, the object is recentered and refocused, and then another image is recorded. These steps are repeated until the full tilt range is covered. Recentering and refocusing are minimal when the eucentricity is accurate. It is important to recenter before refocusing, because recentering introduces slight beam-induced movement, and this movement along with residual stage movement usually dies down in the few seconds it takes to refocus. In this way, the next image is ready to be recorded immediately after focusing has been completed. All these steps can be done manually; however, the more automated these steps are the less operator time is required with less chance of error. With modern TEM's and CCD cameras, all of these steps can be accomplished automatically once the microscope is aligned.

3.4. Tomographic image processing

Image processing routines are constantly evolving, not only to add functionality but also to make procedures more user-transparent. This renders ET accessible to the nonexpert and as a result has led to the proliferation of publications reporting the use of ET, including those from scientists whose technical expertise is in areas other than electron microscopy and tomography.

3.4.1. Tilt series alignment

The alignment of the individual images of a tilt series is a critical step in obtaining high-quality reconstructions. The two most common alignment techniques are (1) cross-correlation alignment and (2) fiducial mark tracking, usually with colloidal gold particles applied to the section surfaces. The advantages of cross-correlation alignment are that it does not require application of gold particles and it is a fast procedure requiring little input from the user. Our experience, however, has shown that cross-correlation alignment is not capable of correcting image rotation or magnification changes between images of the tilt series to the same precision that fiducial tracking achieves. However, Engelhardt (Engelhardt, 2007) reports that second-generation “trifocal alignment” and third-generation “alignment without correspondence” methods, which are fully automatic alignment algorithms, perform well and are ready to replace fiducial tracking. To our knowledge, these have yet to be applied to mitochondrial ET.

The advantage of fiducial mark tracking is that in addition to alignment, the fiducial marks provide sufficient information to de-warp (correct image and specimen distortions) and to make higher order adjustments (e.g., quadratic or cubic alignments) in TxBR. Their success is based on tracking a large number of fiducial marks through the tilt series. Semiautomated fiducial placement has allowed the use of a relatively large number of markers (e.g., 40 markers tracked on 120 images amounts to the accurate placement of 4800 fiducials). We use IMOD to place 30 to 80 markers on the 0° untilted image. An automatic particle-tracking program is then used to track each marker through all of the images of the tilt series. The resulting dataset is then edited manually to correct any errors in the placement of the fiducials or to fill gaps in the dataset that occur when the tracking “loses” the particle, which can happen for high-tilts if the particle is obscured by an electron-dense region or if the area is warped. The positions of the fiducial markers are then used to refine tilt angles, image shifts and rotations, magnification changes, and beam and sample distortions. The resultant transforms are then applied to the tilt series stack of images to produce an aligned stack.

3.4.2. Tomographic reconstruction

The next step is to compute the ET reconstruction by use of the image densities in the aligned tilt series. This step is the most computationally intensive in the processing stream and can produce reconstruction files that are very large (>1 gigabyte). Even so, because of an increase in computer power, reconstructions are usually computed within a few hours. R*-weighted backprojection is the most popular method owing to its computational simplicity and predictable outcome. Both IMOD and TxBR use this method as default. Most alternative methods fall under “iterative techniques” (Frank, 2006) and maximum entropy methods (Engelhardt, 2007). The two most commonly used iterative techniques are the algebraic reconstruction technique (ART) and the simultaneous iterative reconstruction technique (SIRT), both of which rely on optimizing the reconstruction by iterative comparison between projections of the reconstruction and images of the aligned tilt series. Fourier and more general transform methods offer advantages of increased speed of reconstruction and corrections for multiple distortions arising from TEM imaging (Lawrence *et al.*, 2006; Sandberg *et al.*, 2003).

3.5. Visualization and measurements of volumes

Visualization from multiple vantage points is essential to resolve and interpret details in the 3-D configuration of mitochondria (Fig. 2.3). The first step in visualization is simply examining slices in arbitrary directions and making animations of slice fly-throughs. We use IMOD or Analyze (<http://www.mayo.edu/bir/Software/Analyze/Analyze.html>) for this. Another commonly used commercial visualization package is Amira (<http://www.tgs.com>), which is suitable for several steps in visualization, including the making of sophisticated movies. An advantage of ET is the capability to computationally section the reconstruction in slices as thin as 1 voxel in any orientation. This permits accurate measurements and analyses with the multipurpose freeware “ImageJ” (<http://rsb.info.nih.gov/nih-image>) or “homegrown” analysis software provided by several ET laboratories (e.g., Synuarea and Synuvolume [NCMIR]) that make surface area and volume measurements from segmented reconstructions.

3.5.1. Segmentation

The next step is usually manual segmentation of mitochondrial substructure (typically membranes) by use of traced contours, followed by surface rendering of the meshed stacked contours (Fig. 2.3). Once the contours of all the objects of interest are traced, the resulting model can then be viewed in several ways. The full model may be displayed to show all objects or

individual objects can be turned on or off or rendered translucent to explore the shapes of features and the spatial distribution of a class of objects (e.g., crista junctions) and their relation to other objects in the volume. This functionality has been useful when examining the elaborate membrane systems of mitochondria, which can change significantly over short distances. For example, the models in Fig. 2.3 at the lower right are of the same mitochondrion; the model on the left shows the outer membrane in blue, the inner boundary membrane in turquoise, and all of the cristae in yellow, whereas the model on the right displays only four representative cristae in different colors. Comprehension of cristae shape and crista junction and contact site size and distribution have been enhanced by assigning color and transparency level to the different structural components. We use either IMOD or Xvotrace (NCMIR) for segmentation, and this step is rate-limiting in ET throughput, because usually more than 100 slices are present in the reconstruction and often more than 30 objects are segmented. However, because oversampling exceeds the resolution present in the reconstruction, typically not every slice needs to be traced. For features that do not change much from slice-to-slice, tracing every other or even every fourth slice often suffices. Because of the segmentation bottleneck, researchers are developing autosegmentation tools (Bartesaghi *et al.*, 2005; Frank, 2006; Garduno *et al.*, 2008; Jiang *et al.*, 2004; Narasimha *et al.*, 2008; Nguyen and Ji, 2008). However, to date, manual segmentation has proven superior to the currently available autosegmentation tools, except perhaps for the topologically simple mitochondrial outer membrane.

3.6. Movies, tele tomography, and databases

3.6.1. Movies

Movies illustrate the rich quantity of ET information with more scope and detail than can be presented conveniently in images and are portable across different software and hardware environments (see <http://www.sci.sdsu.edu/TFrey/MitoMovie.htm>). Effective movies can be composites of separate movie clips. For example, the first clip may be a fly-through of the slices of the reconstruction. The fly-through can be done in different (often perpendicular) directions to highlight changes in features on a length scale. The second clip could be the surface-rendered view of the fully segmented reconstruction. The segmented volume is ideal for rotations and zoom-ins to focus the attention on the features of interest. Subsequent clips could involve turning on or off objects or making some partially transparent while rotating and zooming; this is a powerful way to emphasize shapes and spatial relationships. The rotation or zoom-in could be paused at any stage to display annotation (e.g., text and arrows) to demonstrate features.

3.6.2. Tele tomography

Because the higher-voltage TEMs most commonly used for ET are expensive, relatively few are available. To make ET more accessible, tele tomography (<https://telescience.ucsd.edu/>) was developed for the remote operation of TEMs and for online image processing. All that is required is a computer with Internet access. In practice, one sends the sample to the facility supporting tele tomography. At a preappointed time, someone at that facility places the sample in the TEM and informs the sender that ET data collection can now be performed. The sender not only collects a tilt series but also routes the images to computers at the facility for remote image processing or alternately those at the sender's institution. A 400-kV TEM and a 300-kV EFTEM at the NCMIR, a 3-MV TEM in Osaka, Japan, and a 1.2-MV TEM in Seoul, Korea, are tele tomography capable.

3.6.3. Databases

Because of the explosion of the amount of ET data that are now being generated, dedicated databases have been established. These databases not only aid the organization of these data but also provide the capability for data mining. A database containing mitochondrial ET data deposited is the cell-centered database (CCDB) (<http://ccdb.ucsd.edu/CCDBWebSite/index.html>). Through the CCDB, researchers can access mitochondrial volume reconstructions, the original tilt series, the aligned tilt series, the segmented objects, and measurements. Data mining is made available by means of keyword searches and enhanced by linkages to other archival databases.

3.7. New developments for electron tomography of mitochondria *in situ*

Image enhancement being developed for mitochondrial ET involves anisotropic nonlinear diffusion and bilateral filtering. These computational techniques suppress the noise in reconstructions while preserving high-resolution structural features. We anticipate that these techniques will not only enhance the visualization of features but also aid autosegmentation of mitochondria, because the tracking of membranes will be less easily derailed by the noise. Because of the effort involved with generating ET data, sampling size is often low. The recent combination of stereology and electron tomography (Vanhecke *et al.*, 2007) has opened the door for unbiased and precise quantitative analysis by use of the wealth of information in a few reconstructions. The parameters most easily measured with so-called quantitative ET are volumes, surfaces, lengths, and numbers.

3.8. Application to apoptotic HeLa cells

Our earlier work along with that of others using ET established the crista junction paradigm of mitochondrial structure in which the inner membrane has a more complicated conformation than that depicted in earlier models

and popularized in textbooks. The crista junction paradigm describes the conformation of the inner membrane with two principal components, the inner boundary membrane closely apposed to the outer membrane and the crista membrane projecting into the matrix compartment of the mitochondrion and joined to the inner boundary membrane by tubular crista junctions of variable length as shown in Fig. 2.3 (lower right) (Perkins *et al.*, 1997). This is believed to divide the inner membrane into two functional components with electron transport and energy transduction concentrated in the crista membrane and communication between the matrix and the cytosol through the inner boundary membrane at contact sites with the outer membrane (Frey and Mannella, 2000; Frey and Sun, 2008; Frey *et al.*, 2002). Likewise, the space between the inner and outer mitochondrial membranes is now thought to comprise two separate compartments, the intermembrane space between the outer membrane and the inner boundary membrane and the intracristal spaces within the cristae, that only communicate through crista junctions (Scorrano *et al.*, 2002; Yamaguchi *et al.*, 2008; Zick *et al.*, 2008).

The application of ET to the HeLa cells in Stages 1 to 3 of the apoptotic program determined by correlated LM proved invaluable in understanding the structural changes that had occurred and led to a topographical model for fission/fusion of the mitochondrial inner membrane. We were able to identify three mitochondrial ultrastructure classes: *Normal* mitochondria have lamellar cristae connected to the inner boundary membrane by means of crista junctions; *vesicular* mitochondria in which the inner membrane has fragmented into many separate vesicular matrix compartments, and *swollen* mitochondria containing swollen matrix compartments. Furthermore, we also observed hybrid structures that combined features of two of these classes: *Normal/vesicular* and *vesicular/swollen*. Three-dimensional models of fully segmented tomograms representing these five classes are shown in Fig. 2.4. These could be correlated to the stages of the apoptotic timeframe suggesting that the sequence of changes progressed from exclusively *normal* mitochondria in *Stage 1* cells to a significant number of *normal/vesicular* and *vesicular* mitochondria in *Stage 2* cells during and after release of cytochrome *c* to many *vesicular/swollen* and *swollen* mitochondria in *Stage 3* cells. Significantly, a bare majority of mitochondria in *Stage 2* cells maintained normal morphology, and even *Stage 3* cells contained a significant number of mitochondria that appeared normal. This suggests that this structural transformation is not required for release of cytochrome *c* from the intracristal spaces. Indeed, this was confirmed when inhibition of caspases by *z*-VAD-fmk effectively prevented the structural transformation but did not prevent release of cytochrome *c*. We speculate that the transformation to vesicular mitochondria represents the changes in inner mitochondrial membrane topology required for mitochondrial fission that in this case occurs throughout the mitochondrial volume rather than just at the sites of fission (Frey *et al.*, 2006; Sun *et al.*, 2007). This provides an example of the

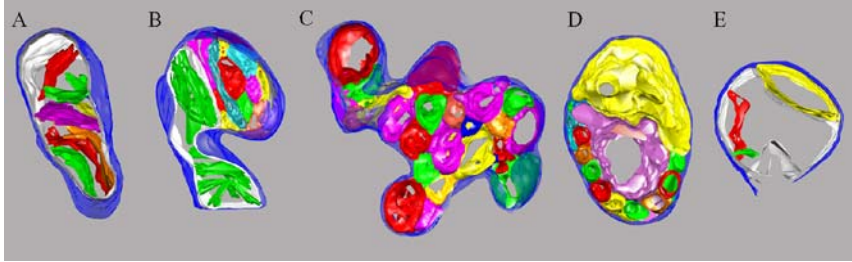


Figure 2.4 Three-dimensional models created from electron tomograms of mitochondria representing each of the structure classes observed in HeLa cells undergoing apoptosis induced by treatment with etoposide. The outer membrane is represented in dark blue and the inner boundary membrane, where present, in white. (A) Normal mitochondria contain only lamellar cristae represented in various colors connected to the inner boundary membrane by crista junctions. (B) Normal/vesicular mitochondria exhibit normal lamellar cristae connected to inner boundary membrane by means of crista junctions in one region (green cristae in the lower region) and separate vesicular matrix compartments (various colors in the upper region). (C) Vesicular mitochondria have only separate vesicular matrix compartments represented here in various colors in the absence of an inner boundary membrane. (D) Vesicular/swollen mitochondria have separate vesicular matrix compartments, and the large magenta and yellow compartments appear to be swollen. (E) Swollen mitochondria have normal and/or vesicular components that are swollen often to the point that the outer membrane is ruptured as seen at the bottom of this mitochondrion.

power of combining fluorescence confocal LM with TEM and ET of identical cells to characterize the changes in ultrastructure that accompany a dynamic cellular process.

ACKNOWLEDGMENTS

We acknowledge the help and support of our collaborators, Doug Green and Cristina Munoz-Pinedo at St. Jude Children's Research Hospital for providing HeLa cells transfected with cytochrome *c* fusion proteins and Mark Ellisman at the NCMIR/UCSD. We are grateful to Guido Gaietta (UCSD) for assistance with FAsH staining and to Roger Y. Tsien (UCSD) for providing the FAsH reagent. This work was supported by a Blasker Science and Technology Grant from the San Diego Foundation to TGF, NIH National Center for Research Resources Grant No. P41 RR004050 to Mark Ellisman, NIH Roadmap Grant GM72033 to Roger Y. Tsien and Mark Ellisman, and NIH grants ES010337 and DK54441.

REFERENCES

Bartasaghi, A., Sapiro, G., and Subramaniam, S. (2005). An energy-based three-dimensional segmentation approach for the quantitative interpretation of electron tomograms. *IEEE Trans. Image Process* **14**, 1314–1323.

- Bouwer, J. C., Mackey, M. R., Lawrence, A., Deerinck, T. J., Jones, Y. Z., Terada, M., Martone, M. E., Peltier, S., and Ellisman, M. H. (2004). Automated most-probable loss tomography of thick selectively stained biological specimens with quantitative measurement of resolution improvement. *J. Struct. Biol.* **148**, 297–306.
- Bouwer, J. C., Mackey, M. R., Lawrence, A., Deerinck, T. J., Jones, Y. Z., Terada, M., Martone, M. E., Peltier, S. T., and Ellisman, M. H. (2007). The application of energy-filtered electron microscopy to tomography of thick, selectively stained biological samples. *Methods Cell Biol.* **79**, 643–660.
- Cardone, G., Grunewald, K., and Steven, A. C. (2005). A resolution criterion for electron tomography based on cross-validation. *J. Struct. Biol.* **151**, 117–129.
- Crowther, R. A., Amos, L. A., Finch, J. T., De Rosier, D. J., and Klug, A. (1970). Three dimensional reconstructions of spherical viruses by fourier synthesis from electron micrographs. *Nature* **226**, 421–425.
- Engelhardt, P. (2007). Three-dimensional reconstruction of chromosomes using electron tomography. *Methods Mol. Biol.* **b**, 365–385.
- Frangakis, A. S., and Hegerl, R. (2001). Noise reduction in electron tomographic reconstructions using nonlinear anisotropic diffusion. *J. Struct. Biol.* **135**, 239–250.
- Frank, J. (2006). *Electron Tomography* Springer, New York.
- Frey, T., Renken, C., and Perkins, G. (2002). Insight into mitochondrial structure and function from electron tomography. *Biochim. Biophys. Acta* **1555**, 196–203.
- Frey, T. G., and Mannella, C. A. (2000). The internal structure of mitochondria. *Trends Biochem. Sci.* **25**, 319–324.
- Frey, T. G., Perkins, G. A., and Ellisman, M. H. (2006). Electron tomography of membrane-bound cellular organelles. *Annu. Rev. Biophys. Biomol. Struct.* **35**, 199–224.
- Frey, T. G., and Sun, M. G. (2008). Correlated light and electron microscopy illuminates the role of mitochondrial inner membrane remodeling during apoptosis. *Biochim. Biophys. Acta* **1777**, 847–852.
- Gaietta, G., Deerinck, T. J., Adams, S. R., Bouwer, J., Tour, O., Laird, D. W., Sosinsky, G. E., Tsien, R. Y., and Ellisman, M. H. (2002). Multicolor and electron microscopic imaging of connexin trafficking. *Science* **296**, 503–507.
- Garduno, E., Wong-Barnum, M., Volkmann, N., and Ellisman, M. H. (2008). Segmentation of electron tomographic data sets using fuzzy set theory principles. *J. Struct. Biol.* **162**, 368–379.
- Goldstein, J. C., Munoz-Pinedo, C., Ricci, J. E., Adams, S. R., Kelekar, A., Schuler, M., Tsien, R. Y., and Green, D. R. (2005). Cytochrome *c* is released in a single step during apoptosis. *Cell Death Differ.* **12**, 453–462.
- Goldstein, J. C., Waterhouse, N. J., Juin, P., Evan, G. I., and Green, D. R. (2000). The coordinate release of cytochrome *c* during apoptosis is rapid, complete and kinetically invariant. *Nat. Cell Biol.* **2**, 156–162.
- Heymann, J. B., Cardone, G., Winkler, D. C., and Steven, A. C. (2008). Computational resources for cryo-electron tomography in Bsoft. *J. Struct. Biol.* **161**, 232–242.
- Jiang, M., Ji, Q., and McEwen, B. (2004). Model-based automated segmentation of kinetochore microtubule from electron tomography. *Conf. Proc. IEEE Eng. Med. Biol. Soc.* **3**, 1656–1659.
- Lawrence, A., Bouwer, J. C., Perkins, G., and Ellisman, M. H. (2006). Transform-based backprojection for volume reconstruction of large format electron microscope tilt series. *J. Struct. Biol.* **154**, 144–167.
- Marco, S., Boudier, T., Messaoudi, C., and Rigaud, J. L. (2004). Electron tomography of biological samples. *Biochemistry (Mosc)*. **69**, 1219–1225.
- Marko, M., and Hsieh, C. E. (2007). Three-dimensional cryotransmission electron microscopy of cells and organelles. *Methods Mol. Biol.* **369**, 407–429.
- Narasimha, R., Aganj, I., Bennett, A. E., Borgnia, M. J., Zabransky, D., Sapiro, G., McLaughlin, S. W., Milne, J. L., and Subramaniam, S. (2008). Evaluation of denoising algorithms for biological electron tomography. *J. Struct. Biol.* **164**, 7–17.

- Nguyen, H., and Ji, Q. (2008). Shape-driven three-dimensional watersnake segmentation of biological membranes in electron tomography. *IEEE Trans. Med. Imaging* **27**, 616–628.
- Noske, A. B., Costin, A. J., Morgan, G. P., and Marsh, B. J. (2007). Expedited approaches to whole cell electron tomography and organelle mark-up *in situ* in high-pressure frozen pancreatic islets. *J. Struct. Biol.* **161**, 298–313.
- O'Toole, E. T., Giddings, T. H. Jr., and Dutcher, S. K. (2007). Understanding microtubule organizing centers by comparing mutant and wild-type structures with electron tomography. *Methods Cell Biol.* **79**, 125–143.
- Penczek, P. A. (2002). Three-dimensional spectral signal-to-noise ratio for a class of reconstruction algorithms. *J. Struct. Biol.* **138**, 34–46.
- Perkins, G., Renken, C., Martone, M. E., Young, S. J., Ellisman, M., and Frey, T. G. (1997). Electron tomography of neuronal mitochondria: Three-dimensional structure and organization of cristae and membrane contacts. *J. Struct. Biol.* **119**, 260–272.
- Petronilli, V., Miotto, G., Canton, M., Brini, M., Colonna, R., Bernardi, P., and Di Lisa, F. (1999). Transient and long-lasting openings of the mitochondrial permeability transition pore can be monitored directly in intact cells by changes in mitochondrial calcein fluorescence. *Biophys. J.* **76**, 725–734.
- Sandberg, K., Mastronarde, D. N., and Beylkin, G. (2003). A fast reconstruction algorithm for electron microscope tomography. *J. Struct. Biol.* **144**, 61–72.
- Scorrano, L., Ashiya, M., Buttle, K., Weiler, S., Oakes, S. A., Mannella, C. A., and Korsmeyer, S. J. (2002). A distinct pathway remodels mitochondrial cristae and mobilizes cytochrome *c* during apoptosis. *Dev. Cell* **2**, 55–67.
- Sun, M. G., Mitochondrial Structure During Apoptosis. Biology, Vol. Ph.D. San Diego State University, San Diego, 2007, pp. 140.
- Sun, M. G., Williams, J., Munoz-Pinedo, C., Perkins, G. A., Brown, J. M., Ellisman, M. H., Green, D. R., and Frey, T. G. (2007). Correlated three-dimensional light and electron microscopy reveals transformation of mitochondria during apoptosis. *Nat. Cell Biol.* **9**, 1057–1072.
- Typke, D., Nordmeyer, R. A., Jones, A., Lee, J., Avila-Sakar, A., Downing, K. H., and Glaeser, R. M. (2005). High-throughput film-densitometry: An efficient approach to generate large data sets. *J. Struct. Biol.* **149**, 17–29.
- Vanhecke, D., Studer, D., and Ochs, M. (2007). Stereology meets electron tomography: Towards quantitative 3D electron microscopy. *J. Struct. Biol.* **159**, 443–450.
- Yamaguchi, R., Lartigue, L., Perkins, G., Scott, R. T., Dixit, A., Kushnareva, Y., Kuwana, T., Ellisman, M. H., and Newmeyer, D. D. (2008). Opa1-mediated cristae opening is Bax/Bak and BH3 dependent, required for apoptosis, and independent of Bak oligomerization. *Mol. Cell* **31**, 557–569.
- Zhang, H., Takaoka, A., and Miyauchi, K. (1998). A 360°-tilt specimen holder for electron tomography in an ultrahigh-voltage electron microscope. *Rev. Sci. Instrum.* **69**, 4008–4009.
- Zick, M., Rabl, R., and Reichert, A. S. (2009). Cristae formation-linking ultrastructure and function of mitochondria. *Biochim. Biophys. Acta* **1793**, 5–19.

STUDIES OF COMPLEX I BY FOURIER TRANSFORM INFRARED SPECTROSCOPY

Douglas Marshall* and Peter R. Rich†

Contents

1. Spectroscopic Studies of Complex I	54
2. FTIR Difference Spectroscopy and Its Application to Complex I	56
2.1. General principles of IR absorbance and Fourier transform infrared spectroscopy	56
2.2. Analyses of complex I by FTIR difference spectroscopy	56
2.3. Transmission FTIR studies	57
2.4. ATR-FTIR studies	58
3. Preparation of Rehydrated Layers of Complex I for ATR-FTIR Spectroscopy	59
4. Analysis of Rehydrated Complex I Layers by Perfusion-Induced ATR-FTIR Difference Spectroscopy	62
5. Analysis of Rehydrated Complex I Layers by Electrochemically-Induced ATR-FTIR Difference Spectroscopy	64
6. Model Compounds and Strategies for Interpretation	64
7. Example IR Difference Spectra of Complex I	69
Acknowledgment	70
References	70

Abstract

Fourier transform vibrational infrared (FTIR) difference spectroscopy provides a novel spectroscopic tool to study atomic details of the structure and mechanism of respiratory NADH: ubiquinone oxidoreductase (complex I). Methods for the acquisition of difference spectra in both transmission and ATR modes in the mid-IR 4000 to 900 cm^{-1} region are reviewed. In both modes, redox transitions can be induced by electrochemistry, and ultraviolet (UV)/visible spectra can be recorded simultaneously. Use of the ATR method with complex I layers immobilized on an internal reflection element (IRE) additionally allows transitions to

* The Johnson Research Foundation and Department of Biochemistry and Biophysics, University of Pennsylvania, Philadelphia, Pennsylvania, USA

† Glynn Laboratory of Bioenergetics, Institute of Structural and Molecular Biology, University College London, London, United Kingdom

be induced by perfusion/buffer exchange, hence providing a versatile means of analyzing IR changes associated with, for example, ligand/substrate binding or specific catalytic intermediates at high signal-to-noise.

Absolute absorbance IR spectra can provide information on secondary structure, lipid/protein ratio, extent of isotope exchange, and sample quality and stability more generally. Such information is useful for quality control of samples during the acquisition of difference spectra in which specific atomic details of changes between two states may be probed. Examples of absolute and difference IR spectra of complex I are presented, and strategies for assignments of the spectral features are discussed.

1. SPECTROSCOPIC STUDIES OF COMPLEX I

Complex I functions as a proton-motive NADH: ubiquinone oxidoreductase in the respiratory chains of bacteria, plants, yeasts, and animals. Bovine complex I consists of at least 46 different subunits with a combined mass of ~ 980 kDa (Carroll *et al.*, 2003; Hirst *et al.*, 2003). Bacterial complex I (~ 500 kDa) typically consists of 14 subunits that are present throughout the superfamily and form a minimal catalytic core. Single particle image reconstruction has revealed that, under physiologically relevant conditions, complex I from all sources has an L-shaped structure, formed from a hydrophobic membrane arm and a hydrophilic arm (Sazanov and Hincliffe, 2006).

A recent X-ray crystal structure of a fragment corresponding to the hydrophilic arm of *Thermus thermophilus* complex I (Sazanov and Hincliffe, 2006) has established the positions of the known redox cofactors: a noncovalently bound flavin mononucleotide (FMN), two [2Fe-2S] type iron-sulfur (Fe-S) centers named N1a and N1b, and five [4Fe-4S] type Fe-S centers named N3, N4, N5, N6a, and N6b. An additional [4Fe-4S] Fe-S center named N7 is present only in certain bacteria (Nakamaru-Ogiso *et al.*, 2005). The structure supports the view that, with the exceptions of N1a and N7, they form a pathway for transferring electrons from the NADH binding site located at the end of the hydrophilic arm distal to the membrane to one or more Q-sites located at the interface of the hydrophilic and membrane arms. The order of centers N4, N5, and N6a in this pathway is currently under debate (Ohnishi and Nakamaru-Ogiso, 2008; Yakovlev *et al.*, 2007). Center N1a is close to FMN but separate from the main electron transfer pathway. Its position and very low potential ($E_{m7} = -380$ mV versus SHE (Ingledew and Ohnishi, 1980)) suggest that its role is additional to that of the main pathway.

The mechanism by which proton transfer across the membrane is coupled to internal electron transfers remains unknown. Such studies are hampered by the size and complexity of the enzyme and, in particular, because of the limited types of spectroscopies that can be used to resolve and

monitor the behavior of individual Fe-S centers and quinone(s) in such a large and complex system. To date, EPR has provided the most valuable spectroscopic tool, because the semiquinone forms of FMN and ubiquinone and the reduced forms of the Fe-S centers are paramagnetic and, therefore, amenable to EPR analyses.

A consensus assignment of EPR signals to Fe-S centers N1a, N1b, N2, N3, and N7 has been reached and, by combining EPR spectroscopy with redox potentiometry and pH titrations, their midpoint potentials and pH dependencies have been determined (Ingledew and Ohnishi, 1980; Nakamaru-Ogiso *et al.*, 2005, 2008; Ohnishi, 1998; Sled *et al.*, 1994; Yakovlev *et al.*, 2007; Yano *et al.*, 2003). However, assignments of the remaining EPR signals to Fe-S centers N4, N5, N6a, and N6b are still under debate (Ohnishi and Nakamaru-Ogiso, 2008; Yakovlev *et al.*, 2007). Euro *et al.* (Euro *et al.*, 2008) have recently reviewed these studies and extended them by potentiometric titration of EPR and optical signals of intact *Escherichia coli* complex I, with the analyses accommodating possible intrinsic electrostatic interactions between the Fe-S centers. EPR studies have also revealed three distinct ubisemiquinone species in complex I during steady-state NADH oxidation in tightly coupled bovine heart sub-mitochondrial particles whose significance and functions remain unclear (Magnitsky *et al.*, 2002; Vinogradov *et al.*, 1995; Yano *et al.*, 2005). SQ_{Nf} has a fast spin relaxation rate and is only observable in the presence of a membrane potential. SQ_{Ns} and SQ_{Nx} are both insensitive to membrane potential and have slow and very slow spin relaxation rates, respectively. The fast spin relaxation time of SQ_{Nf} has been proposed to arise from spin interaction with a tetranuclear Fe-S center. This was identified as center N2 on the basis of a close correlation between a lineshape alteration of center N2 and quenching of SQ_{Nf} (Magnitsky *et al.*, 2002), and a center-to-center distance between N2 and SQ_{Nf} of 12 Å was estimated (Yano *et al.*, 2005).

Deconvolution of UV/visible redox difference spectra of complex I is more difficult because of the broad and indistinct nature of the many overlapping Fe-S bands in the 300 to 600 nm range and the dominance of the stronger absorbance of oxidized FMN at 450 nm (Euro *et al.*, 2008; Hellwig *et al.*, 2000). Nevertheless, in combination with EPR, it can assist in resolving individual Fe-S centers during redox titration, as in the case of its recent application to *E. coli* complex I (Euro *et al.*, 2008). In an earlier UV/visible and EPR study of *E. coli* complex I, Fe-S centers N6a and N6b were resolved kinetically from the other Fe-S centers and their midpoint potentials determined (Friedrich *et al.*, 2000).

The sensitivity and stability of modern FTIR spectrometers have made possible the application of mid-IR vibrational spectroscopy to large protein complexes, and in recent years this has provided an additional spectroscopic tool with which to analyze complex I. This technology is briefly reviewed and its applications to date to complex I are summarized in the following sections.

2. FTIR DIFFERENCE SPECTROSCOPY AND ITS APPLICATION TO COMPLEX I

2.1. General principles of IR absorbance and Fourier transform infrared spectroscopy

IR absorption is caused by the coupling of the electric field vector of electromagnetic radiation with the dipole moment of a molecular vibration when the energy of the radiation and the vibrational transition are matched. It occurs only when the dipole moment of the molecule changes during the vibration and the absorption probability, and, therefore, the extinction coefficient, increases with increasing bond polarity. Many textbook accounts of the physical principles of IR absorption, for example, [Günzler and Gremlich \(2002\)](#) and [Stuart \(2004\)](#), and reviews of biological applications of IR spectroscopy, for example [Brittain *et al.* \(1997\)](#), [Burie *et al.* \(1993\)](#), [Goormaghtigh *et al.* \(1999\)](#), and [Mäntele \(1993, 1996\)](#), are available.

Modern infrared spectrometers generally operate in Fourier transform (FT) mode in which a broadband IR source is used in conjunction with a Michelson or other type of interferometer. In the Michelson interferometer, the beam is split and the pathlength of one half varied cyclically with time before being recombined with the fixed pathlength beam. Constructive and destructive interference produces an interferogram of intensity versus pathlength difference. The position of the moving mirror can be determined very precisely from the regularly spaced interferogram of a monochromatic laser beam that passes through the same optics. This allows accurate conversion of the interferogram into a plot of intensity versus frequency by Fourier transformation. Interferograms are typically recorded over tens of milliseconds (limited by the transit time of the moving element that controls the variable pathlength beam), and scans can be averaged before or after Fourier transformation. Major advantages of the FT method include the synchronous acquisition of a wide frequency range and the ability to use intense IR sources, because the intensity of the broadband beam is not restricted by the small apertures required by dispersive monochromators.

2.2. Analyses of complex I by FTIR difference spectroscopy

IR absolute absorbance spectra of even the smallest proteins consist of a large number of bands that make it difficult to deconvolute individual vibrational modes. Such spectra are nevertheless informative, particularly for characterization of secondary structural elements ([Arrondo *et al.*, 1993](#); [Goormaghtigh *et al.*, 1990](#)), and for assessments of, for example,

lipid/protein ratios (Goormaghtigh *et al.*, 1990), extents of isotope exchange (Rath *et al.*, 1998), and general quality control. However, by recording absolute absorbance spectra of the same sample before and after a localized change, difference spectra can be obtained that contain a manageable number of vibrational band changes that arise only from functional groups that were changed by the manipulation. If the alteration is reversible, the sample can be automatically cycled between two (or more) states many times so that signal averaging can be used to improve the signal-to-noise ratio of the resultant difference spectra. The technical challenge of this procedure is to be able to measure infrared absorption properties while simultaneously manipulating the protein sample in a precise and reversible manner.

2.3. Transmission FTIR studies

In transmission mode, the sample is typically placed between two windows made of an IR transmitting material, most commonly calcium fluoride, and the IR measuring beam is passed through this assembly. The sample thickness defines the pathlength and, for aqueous protein solutions, is limited to an effective maximum of approximately 15 μm because of the strong absorption of IR by water. Such thin samples require high protein concentrations to generate sufficiently large protein signals. In transmission FTIR studies, *E. coli* complex I solubilized in 0.15% *n*-dodecyl- β -D-maltoside has typically been used at 0.25 mM (Hellwig *et al.*, 2000). Manipulation of samples in transmission mode can in principle be made by light when suitable photochemistry is available (Braiman *et al.*, 1991; Fahmy *et al.*, 1993; Gerwert *et al.*, 1989; Hienerwadel *et al.*, 1997; Lemon *et al.*, 1993; Mäntele, 1996; Nabadryk *et al.*, 1995; Noguchi and Sugiura, 2002; Rich and Breton, 2001), by stop-flow mixing (George *et al.*, 1997), or by electrochemistry (Hellwig *et al.*, 1996, 1998, 2000, 2002; Moss *et al.*, 1990; Ritter *et al.*, 2003). To date, it has only been possible to apply the electrochemical method in transmission mode to complex I, where it has been used to measure redox difference spectra of both the intact complex and a soluble NADH dehydrogenase fragment of *E. coli* (Flemming *et al.*, 2003; Friedrich *et al.*, 2000; Hellwig *et al.*, 2000, 2004). This was accomplished with an ultrathin spectroelectrochemical cell consisting of two CaF_2 windows that sandwiched a 6 to 7 μl sample with a 6 to 8 μm pathlength and a 70% transparent 6 μm -thick gold grid working electrode in electrical contact with auxiliary and reference electrodes (Moss *et al.*, 1990). These studies and their interpretations are reviewed in detail in Marshall *et al.* (2006). Large redox-induced signals in the amide I region were interpreted initially in terms of extensive conformational reorganization of the polypeptide backbone linked to redox changes of both FMN and Fe-S centers (Hellwig *et al.*, 2000). Bands that appeared at 1710 cm^{-1} and 1548 cm^{-1} in

a -300 to -500 mV potential step were tentatively assigned to $\nu(\text{C}=\text{O})$ modes of the isoalloxazine ring of FMN on the basis of comparisons with redox difference spectra of pure FMN and FAD in solution, although their intensities were smaller than expected (Hellwig *et al.*, 2000).

Redox difference spectra of intact complex I were compared with those of an NADH dehydrogenase fragment. The double difference spectrum for a -100 to -300 mV potential step contained bands around 1715 cm^{-1} , which were tentatively assigned to deprotonation of, or perturbations in the environment of, an aspartic/glutamic acid on reduction of Fe-S center N2 because, at that time, the NADH dehydrogenase fragment was thought to contain all redox centers except N2. Double difference spectra for a 0 to -500 mV potential step contained bands around 1500 cm^{-1} , a region characteristic for protonation state change of tyrosine, and these bands were assigned to tyrosine 114 and 139 of subunit NuoB by comparisons of such bands in a range of site directed mutants (Flemming *et al.*, 2003).

Hellwig *et al.* also measured oxidized *minus* reduced difference spectra for the 150 mV to -450 mV potential step at pH 5.5, 6.5, and 7.5. At pH 5.5, a peak at 1732 cm^{-1} , together with troughs at 1585 cm^{-1} and 1408 cm^{-1} , was tentatively assigned to oxidation-induced protonation of an aspartic or glutamic acid (Hellwig *et al.*, 2004). In the same spectra, bands at 1264 cm^{-1} and 1610 cm^{-1} were tentatively assigned to redox changes of bound ubiquinone on the basis of model compound data, and a relation between extent of ubiquinone binding and protonation state of the carboxyl groups was suggested.

2.4. ATR-FTIR studies

ATR-FTIR spectroscopy (Goormaghtigh *et al.*, 1999; Heberle and Zscherp, 1996; Tatulian, 2003) provides an alternate method for IR analyses of protein changes. In this approach the IR measuring beam is passed through an internal reflective element (IRE), commonly a diamond or silicon crystal, with geometry such that the beam is reflected (usually several times) internally at a surface on which the sample is deposited. On each internal reflection, an evanescent wave penetrates into the sample to a distance governed by the ratio of refractive indices of the sample and IRE and the frequency of the IR radiation; roughly, the wave diminishes to $1/e$ intensity at a depth of one wavelength. A detailed account of evanescent wave properties may be found in Goormaghtigh *et al.* (1999). The increased sample accessibility in ATR mode allows buffer exchange by perfusion or dialysis (Rich and Iwaki, 2005), extending IR analyses to include changes caused by, for example, ligand, inhibitor or substrate binding, catalytic intermediates or pH, and other changes. Proteins in soluble form can be studied by use of a flow cell incorporating a dialysis

membrane or, for hydrophobic proteins such as complex I, an alternate and particularly versatile method involves deposition of a thin (several micron) layer of the protein in its active hydrated state onto the hydrophobic IRE surface and induction of changes by electrochemistry or by buffer perfusion (see later).

Because the optical pathlength in ATR measurements is not defined by the sample thickness and is frequency dependent, the quantitation of bands from their intensities relative to known extinction coefficients is less straightforward. Nevertheless, effective pathlength at a specific frequency can be determined by inclusion of a suitable IR marker of known extinction coefficient. From this, pathlength at any frequency can be calculated and, when available, conventional extinction coefficients used to quantitate concentrations of specific components.

3. PREPARATION OF REHYDRATED LAYERS OF COMPLEX I FOR ATR-FTIR SPECTROSCOPY

Promotion of protein–protein and protein–IRE hydrophobic interactions during layer deposition is critical if the layer is, after rehydration, to remain attached to the IRE and have sufficient stability for data acquisition. This can be accomplished by removing detergent and excess salt from detergent-solubilized preparations by washing with detergent-free weak buffer (Rich and Iwaki, 2005). If the protein is solubilized with a detergent of low critical micelle concentration (CMC) or poor exchange kinetics, it may be necessary to first exchange it with a more suitable detergent by prewashing with another detergent of higher CMC/faster unbinding that can subsequently be removed. Ideal procedures for deposition of thin layers of hydrophobic proteins onto the IRE that have suitable stability and reactivity (i.e., respond rapidly to *in situ* manipulation) vary with different proteins and preparation methods. However, for complex I prepared both from *Yarrowia lipolytica* (supplied by Ulrich Brandt [Ahlers *et al.*, 2000]) and from *Bos taurus* (supplied by Judy Hirst [Sharpley *et al.*, 2005]), the following method was found to be effective.

0.1 mg complex I (5– to 10- μ l volume) was diluted with 200 μ l of 20 mM potassium phosphate, pH 7.0, in a 2.5-ml ultracentrifuge tube; 1.5 μ l 10% (w/v) sodium cholate and 1.5 μ l 10% (w/v) octylglucoside were added, and the sample was gradually diluted to a volume of 2 ml with 20 mM potassium phosphate, pH 7.0, to give a final concentration of 0.0075% (w/v) of each detergent. The sample was then pelleted by centrifugation at 390,000 g_{av} for 30 min at 4°. The pellet, which had a cloudy appearance, was resuspended in 200 μ l of 20 mM potassium phosphate, pH 7.0, with a glass rod, diluted to 2 ml with the same buffer and

centrifuged at $300,000 g_{av}$ for 20 min at 4° . The resulting pellet was resuspended as before in 2 ml 1 mM potassium phosphate, pH 7.0, and centrifuged at $300,000 g_{av}$ for 20 min at 4° . After removing as much supernatant as possible, the final pellet, which had a translucent glasslike appearance, was resuspended with a glass rod in $10 \mu\text{l}$ of ultrapure water and split into $2\text{-}\mu\text{l}$ aliquots, which were either diluted to $8 \mu\text{l}$ with distilled water and applied directly to the IRE (3-mm diameter, 3 reflection silicon ATR microprism (SensIR Europe)) or stored at -80° for future use. At all stages after detergent removal, care was taken to work as rapidly as possible, because the hydrophobic surfaces critical for layer adhesion to the IRE decrease with time, probably by self-aggregation. Samples are placed uniformly over the IRE and dried onto it under a gentle stream of dry nitrogen or argon over approximately 5 min. Such dried layers can then be rehydrated with a suitable buffer while remaining firmly adhered to the prism surface.

Figure 3.1 shows typical ATR-FTIR absolute absorbance spectra recorded during the preparation of complex I layers. Such spectra are useful for optimizing and quality-controlling the resultant protein film. Absorption spectra of samples before drying are dominated by the water O-H scissoring and stretching modes at 1638 cm^{-1} and close to 3400 cm^{-1} , respectively (trace A). As the layer is dried onto the prism, the amplitudes of these bands decrease and amide I and II bands of protein appear at 1650 cm^{-1} and approximately 1540 cm^{-1} , respectively (trace B). This spectrum of the dried material will also contain bands arising from residual buffer or detergent; if present at high levels, these can result in poor layer stability, which could be easily rectified, for example, by additional wash steps. The dried layer can be rehydrated with an aqueous drop containing a desired buffer. This results in a partial diminution of protein bands (best monitored by the amplitude of the amide II band) and a gain in water bands caused by protein layer swelling on rehydration (trace C). Typically, a suitable protein layer will have an amide II band absorbance of approximately 0.5 when dried, which will diminish to 0.15 to 0.2 on rehydration and will become sufficiently stable for data acquisition within 1 h. Diminution of the amide II band beyond this level is indicative of insufficient bonding between protein and the IRE surface.

The amount of complex I applied to the prism is crucial; ideally, the rehydrated layer should be marginally thicker than the maximum depth of penetration of the evanescent wave at the lowest frequency of interest. Any additional protein will not be detected by the IR beam and will result in longer required times of equilibration with the surrounding medium, resulting in the acquisition of less data in a given time period. Conversely, a layer that is thinner than the depth of penetration will equilibrate rapidly but will yield smaller IR signals and, if swelling or contraction of the layer occurs, will result in changes in the absolute IR spectra that can grossly

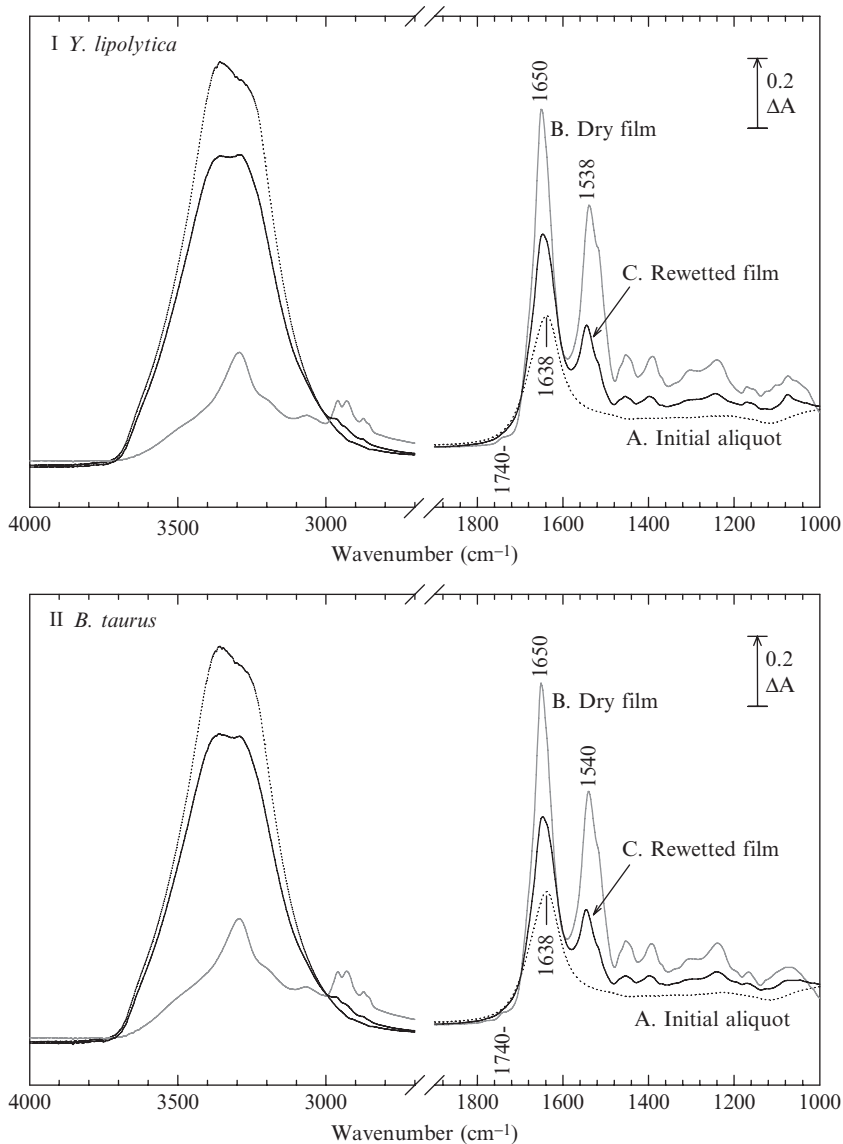


Figure 3.1 ATR-FTIR absolute absorbance spectra recorded during the preparation of rehydrated films of complex I from *Y. lipolytica* (I.) and *B. taurus* (II.). An 8- μ l diluted aliquot was applied to a 3-mm silicon IRE (trace A) and dried under a gentle stream of dry nitrogen or argon (trace B) before rehydration with 10 μ l of 20 mM potassium phosphate, 200 mM potassium chloride at pH 6.0 (trace C). The amide I (peak at 1650 cm^{-1}) and amide II (peak close to 1540 cm^{-1}) protein bands are specified on the figure, together with the O-H scissoring and stretching modes of water at 1638 cm^{-1} and close to 3400 cm^{-1} , respectively.

distort the difference spectra. The amplitude of the amide II band in the absolute spectra obtained during drying/rehydration (as described previously) provides a useful indication of thickness.

For any protein, it is essential that tests are conducted to confirm the integrity of the protein in the layer after drying/rehydration—although to date we have found no indications that any protein that we have studied in rehydrated layer form differs substantially from its native form. ATR-FTIR spectra of dried protein layers have shown that, regardless of the drying time, some structural water remains in the dried layer (see Fig. 3.1, trace b, 3400 cm^{-1} region); this is likely to be a key contributing factor to the protein retaining its active conformation. In the case of *Y. lipolytica* complex I, the NADH-hexaammineruthenium chloride oxidoreductase activity of protein that had been dried onto the IRE, rehydrated, and then removed from the IRE with gentle abrasion was only marginally reduced compared with untreated material. The integrity of the protein layer is further supported by the similarity of ATR-FTIR redox difference spectra of *Y. lipolytica* and *B. taurus* complex I layers to equivalent spectra of detergent-solubilized *E. coli* complex I acquired in soluble form in transmission mode (Hellwig *et al.*, 2000; Marshall *et al.*, 2006). Comparison of the amplitudes of signatures indicative of Fe-S redox change in redox difference spectra induced by electrochemistry and induced by buffer exchange with NADH as the reductant confirms that the NADH site is active and is consistent with the Fe-S centers retaining their native midpoint potentials and electron transfer partners (see later and Fig. 3.5).

4. ANALYSIS OF REHYDRATED COMPLEX I LAYERS BY PERFUSION-INDUCED ATR-FTIR DIFFERENCE SPECTROSCOPY

The construction of apparatus suitable for the perfusion of varying buffers over the IRE has been described previously (Iwaki *et al.*, 2003; Rich and Iwaki, 2005). Typical perfusion cells used in our laboratory (see Fig. 3.2, A and C) for anaerobic work are constructed from stainless steel and provide a chamber of approximately 75 μl internal volume above the protein layer in which varying buffers can be perfused. An optional 2-mm diameter glass window in the ceiling of the chamber allows the synchronous acquisition of UV/visible data by means of a fiberoptic reflection probe that is interfaced to a dispersive monochromator and photomultiplier detector. A watertight seal between the cell and the stainless steel surround of the IRE is made with a gasket formed from two layers of parafilm coated with a thin layer of vacuum grease. The gasket is assembled and pressed onto the cell, and the whole unit is clamped from above in a manner that provides

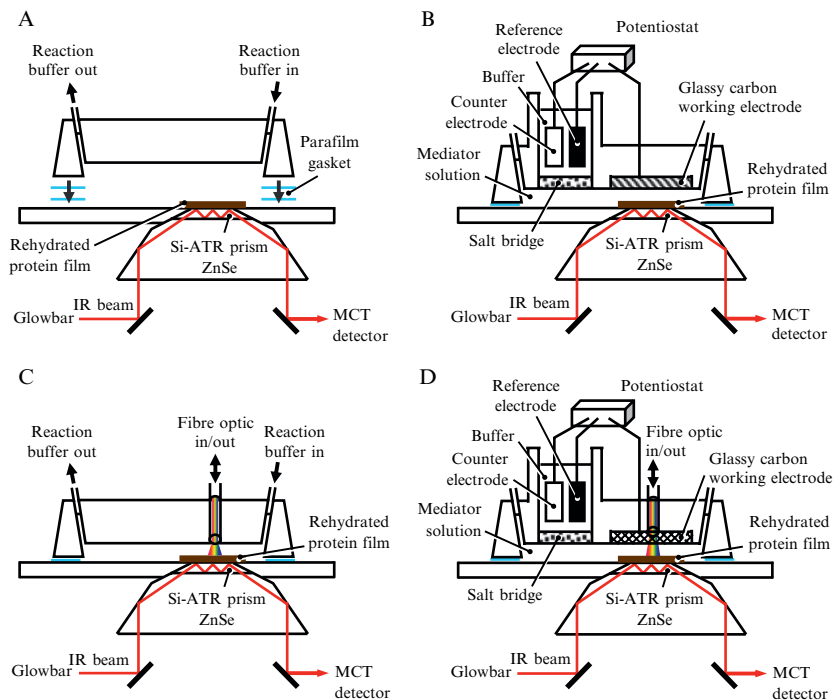


Figure 3.2 Schematic representation of perfusion and electrochemical ATR-FTIR cells. The perfusion cell (A) forms a sealed chamber over the rehydrated protein film and IRE. In/outlets and computer-controlled valves allow buffers to be continuously and sequentially perfused through the chamber. The electrochemical cell (B) forms a similar chamber, the ceiling of which is composed of a circular glassy carbon or platinum mesh working electrode, over the sample and IRE. A porous glass frit connects the sample chamber to a platinum auxiliary electrode and a Ag/AgCl reference electrode. Use of appropriate electrochemical mediators allows redox equilibration between the working electrode and the protein sample, the potential of the solution being controlled by a potentiostat. Versions incorporating fiberoptic light guides for simultaneous acquisition of UV/visible spectra are also represented (C and D); note that the electrochemical version (D) uses a platinum mini-grid working electrode.

uniform moderate pressure to prevent leaks. An optimally prepared rehydrated layer of complex I can be expected to remain stable for 5 to 10 h with a perfusion buffer flowing over its surface at approximately 1 ml/min. An electronically controlled two-way valve and peristaltic pump allows switching of alternating buffers over the rehydrated protein film. Computer control of buffer delivery and data acquisition allows automated system control and overnight accumulation of data from many cycles. To avoid bubbles forming during perfusion it is critical that buffers are degassed.

Where possible, care should be taken to ensure that the buffers are matched in pH and ionic strength to avoid introduction of artefacts from expansion/contraction of the layer or from the buffer itself.

5. ANALYSIS OF REHYDRATED COMPLEX I LAYERS BY ELECTROCHEMICALLY-INDUCED ATR-FTIR DIFFERENCE SPECTROSCOPY

A further ATR-compliant device has been developed (see Fig. 3.2, B and D) for manipulation of the oxidation/reduction state of the rehydrated layer by conventional three-electrode electrochemistry. The electrochemical cells are assembled over the IRE surround in the same manner as the perfusion cells described previously and form a chamber of approximately 25- μ l volume. The chamber ceiling, several hundred microns above the sample, is formed by a working electrode of glassy carbon or fine platinum mesh. A buffer containing appropriate mediators allows equilibration between the protein layer and electrode, and a salt bridge allows connection to a reservoir containing a platinum auxiliary electrode and an Ag/AgCl reference electrode. The glassy carbon working electrode can be used over a particularly broad potential range—at least -500 to $+500$ mV at pH 7 in typical media—without electrolysis of water. The platinum mesh electrode has a more limited range because of its greater reactivity with water. However, this is offset by its generally faster equilibration times, caused in part by its greater surface area and by the ability to pass a UV/visible measuring beam through the electrode itself, allowing simultaneous acquisition of UV/visible spectra without creating a redox-inactive area for probe access.

6. MODEL COMPOUNDS AND STRATEGIES FOR INTERPRETATION

Functional regions of specific amino acids or cofactors have a set of normal vibrational modes, and those that are IR-active produce their characteristic IR absorption spectra. Some modes are dominated by vibrations at a single bond, for example, the carbonyl group stretch that appears in the 1700 – to 1800 - cm^{-1} range. More generally, however, the normal modes involve coupled movements of several linked atoms so that it is not possible to assign a vibrational band to just one specific bond. The ways in which the normal modes change when the functional group is perturbed result in the IR difference spectra that can provide detailed structural, mechanistic, and dynamic information at the atomic level.

Frequencies and extinction coefficients of normal modes can be changed not just by chemical changes of the bonds concerned but also by minute changes in environment such as distances to other atoms, steric hindrances, hydrogen bonding strengths, and local dielectric strength and polarity changes.

Initial tentative assignments of bands to specific types of residues can often be made by comparisons of frequencies, bandwidths, and intensities of protein spectra with model compound spectra. Compendia of vibrational characteristics of amino acids are available (Barth, 2000; Barth and Zscherp, 2002; Rahmelow *et al.*, 1998; Rich and Iwaki, 2005; Venyaminov and Kalnin, 1990; Wolpert and Hellwig, 2006), and diverse data on model compounds related to prosthetic groups and amino acids can be found throughout the literature. Figure 3.3 summarizes IR redox difference spectra of FMN, ubiquinone, and a small [2Fe-2S] ferredoxin isolated from parsley, all of which are directly relevant to IR analyses of complex I. IR data on substrate NADH can be found in Iwaki *et al.* (2006). The origins of most principal bands in these spectra are relatively well understood. In the case of FMN, particularly useful redox-sensitive bands are seen at approximately 1710 cm^{-1} (redox-sensitive $\nu[\text{C}_4 = \text{O}]$) and at 1547 (ring $\nu[\text{C} = \text{N}]$ in oxidized form) and 1407 ($\nu[\text{N}_5\text{-H}]$ in reduced form) cm^{-1} (Wille *et al.*, 2003). In the case of Fe-S centers, the frequencies of the iron-ligand stretches occur only at low frequencies that are outside the standard mid-IR spectral window in the “far-IR” range. To date, this range has been little exploited with biological materials and presents significant technical hurdles, although some resonance Raman studies of small Fe-S centers at low frequencies have been reported (Xiao *et al.*, 2006). However, redox changes of Fe-S centers within proteins cause significant and characteristic perturbations of the surrounding polypeptide, dominated by amide I and II band changes, which are readily detectable in the mid-IR range (Marshall *et al.* [2006] and Fig. 3.3). The redox spectrum of ubiquinone (Fig. 3.3) is also well understood; for example, distinctive bands of ubiquinone occur at $1664/1648$ ($\nu[\text{C} = \text{O}]$), 1610 (ring $\text{C} = \text{C}$), and $1288/1262$ (methoxy/ring) cm^{-1} and of ubiquinol ring and OH modes in the 1492 to 1387 and 1112 to 1054 cm^{-1} ranges. Such spectra have been used to assign similar bands in redox spectra of complex I (Figs. 3.4 and 3.5; see Marshall *et al.* [2006] for details).

Although assignments can often be made with some confidence from such model compound comparisons, further confirmation and specification is generally needed. Analyses of alterations induced by isotopic labeling are particularly informative. Exchange of H_2O for D_2O provides a relatively simple method to replace exchangeable protons with deuterons. Figure 3.3 illustrates the effects of such H/D exchange on model compound spectra, and the characteristic shifts can be used to further test assignments of bands to specific groups within proteins. For large, tightly packed proteins, care must be taken because the rate of H/D exchange of occluded regions can be

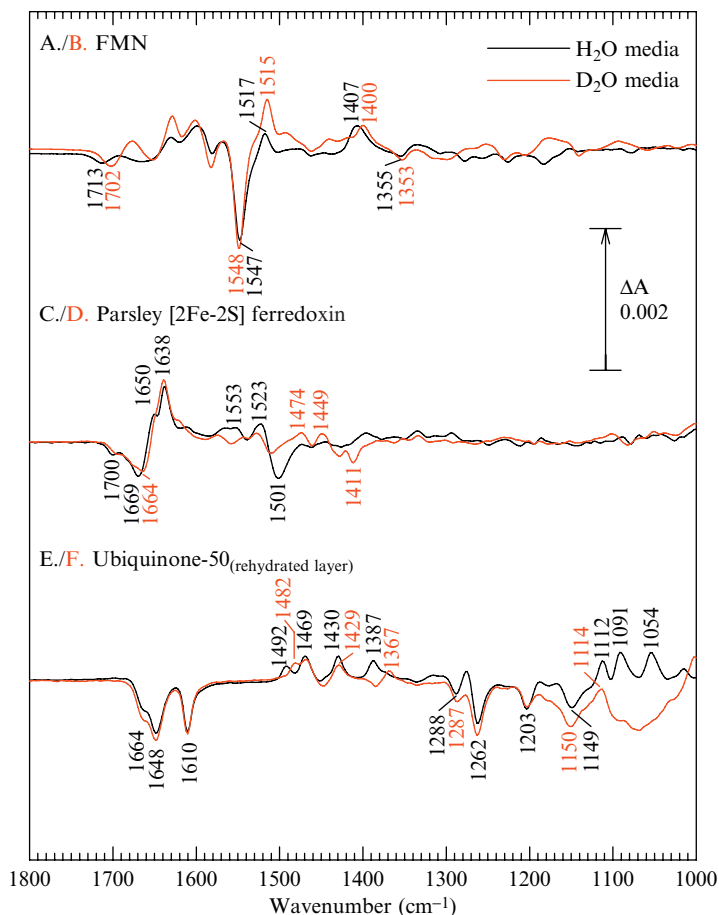


Figure 3.3 Electrochemically-induced reduced *minus* oxidized difference spectra of FMN, parsley [2Fe-2S] ferredoxin and ubiquinone-50 in H₂O and D₂O media. Redox difference spectra of a solution of 2 mM FMN in 20 mM potassium phosphate and 200 mM potassium chloride are shown at pH 6.0 (trace A) and pD 6.0 (trace B). Reducing and oxidizing conditions were -550 mV and 200 mV, respectively, and equilibration occurred within 6 min (Marshall *et al.*, 2006). Redox difference spectra of a solution of 2 mM parsley [2Fe-2S] ferredoxin in 50 μ M methyl viologen, 100 mM potassium phosphate, and 100 mM potassium chloride are shown at pH 8.0 (trace C) and pD 8.0 (trace D). Reducing and oxidizing conditions were -500 mV and 200 mV, respectively, and equilibration occurred within 8 min (Marshall *et al.*, 2006). Redox difference spectra of a rehydrated layer of ubiquinone-50 in 500 mM anthraquinone-2,6-disulfonate, 100 mM potassium phosphate, and 100 mM potassium chloride are shown at pH 8.0 (trace E) and pD 8.0 (trace F) (see Iwaki *et al.* [2004] for conditions.)

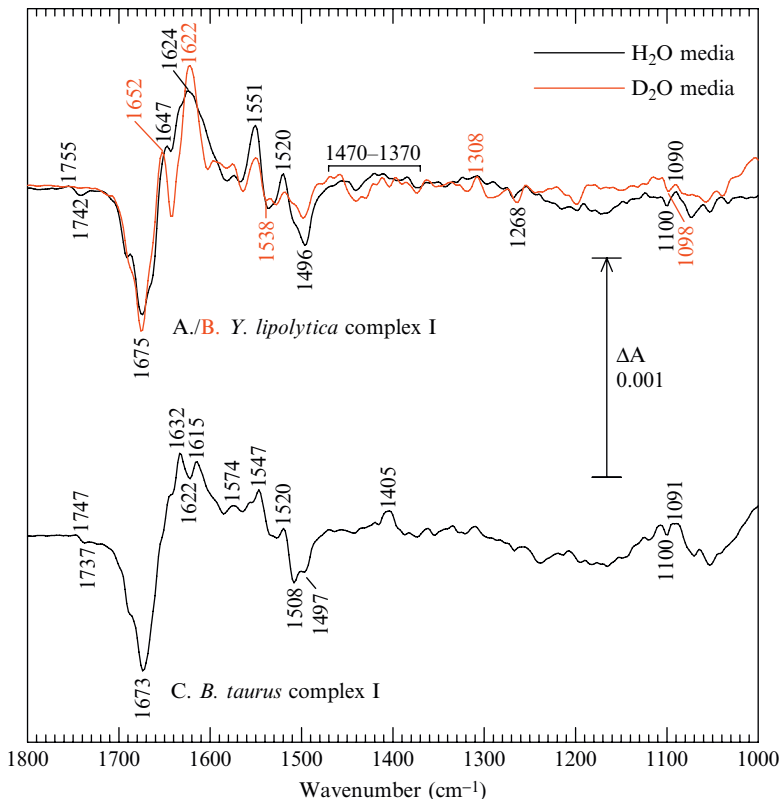


Figure 3.4 Electrochemically-induced reduced minus oxidized difference spectra of rehydrated layers of *Y. lipolytica* (traces A and B) and *B. taurus* (trace C) complex I. Layers were rehydrated with 20 mM potassium phosphate, 200 mM potassium chloride, 1 mM potassium ferricyanide, 100 μ M methyl viologen at pH 6.0 (traces A and C) and pD 6.0 (trace B). Reducing and oxidizing conditions were -425 mV and 425 mV, respectively; equilibration occurred within 8 min. Traces A, B, and C are the average of 140, 92, and 100 spectra, respectively, each individual spectrum being the average of 1000 interferograms.

extremely slow, in some cases being resistant to exchanges even after several days of exposure (Goormaghtigh *et al.*, 1999). For complex I we have routinely incubated the enzyme in D_2O media for 24 h at 4° before preparation of rehydrated layers, a procedure that results in $>90\%$ H/D exchange (Marshall *et al.*, 2006). Further informative, but costly, techniques include global labeling with ^{13}C or ^{15}N , labeling one just specific type of amino acid or cofactor or, in its most elegant form, labeling of just one specific amino acid (Sonar *et al.*, 1994, 1995). Site-directed mutagenesis of specific residues provides an additional powerful technique that can allow definitive assignment of IR bands. Information from these methods can be

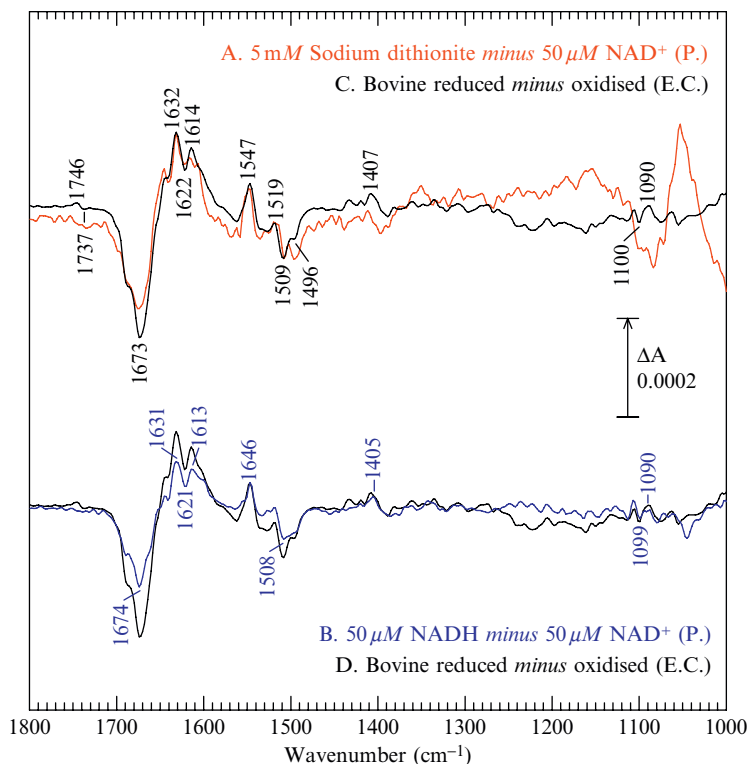


Figure 3.5 Perfusion-induced ATR-FTIR redox difference spectra of rehydrated layers of bovine complex I. Traces A and B are perfusion-induced reduced *minus* oxidized difference spectra by use of 5 mM sodium dithionite and 50 μM NADH as reductants, respectively; for both spectra the oxidant was 50 μM NAD^+ . Trace A is the average of three spectra each consisting of 2000 interferograms. Trace B is the average of data obtained from six separate layers and is equivalent to the average of 110 difference spectra each consisting of 1000 interferograms. Trace C (reproduced as D) is an electrochemistry-induced redox difference spectrum recorded at pH 8.0 under otherwise equivalent conditions of Fig. 3.4. All traces have been scaled by use of the amplitudes of their associated absolute absorption spectra. Buffer was 50 mM potassium phosphate, 150 mM potassium chloride at pH 8.0 and perfused at 1 ml/min. For each trace redox equilibration was complete in less than 10 min.

combined with static X-ray or NMR atomic structural models to extend structural and mechanistic understanding. Computational methods for *ab initio* calculations of normal mode frequencies, amplitudes, and isotope exchange shifts are also providing complementary information to such empirical data and can potentially provide a full atomic assignment of the normal mode spectra. At present these methods are sufficiently accurate only with relatively small molecules in simple environments, but with the availability of more powerful supercomputers, it is likely that this approach will be increasingly applicable to larger biological systems.

7. EXAMPLE IR DIFFERENCE SPECTRA OF COMPLEX I

Electrochemically-induced redox difference spectra of all components of *Y. lipolytica* complex I at pH and pD 6.0 and of *B. taurus* complex I at pH 6.0 are shown in Fig. 3.4. Rehydrated protein layers were prepared on the IRE, and the electrochemical cell was assembled as described previously. Preliminary reduction/oxidation cycles were run to establish optimal electrode/protein equilibration times, which were approximately 8 min for both reductive and oxidative directions. Spectra obtained during reductive cycles were mirror images of spectra data obtained during oxidative cycles, hence confirming the reversibility of the redox transition and the absence of irreversible processes. The spectra shown are the average of approximately 50 reductive and (the inverse of) 50 oxidative spectra, each consisting of 1000 interferograms. Minor contributions from redox mediators, phosphate buffer, and layer swelling have been subtracted interactively. Numerous assignments of features of these spectra are discussed in Marshall *et al.* (2006). The redox difference spectra are dominated by signals in the 1700 to 1590 cm^{-1} and 1570 to 1490 cm^{-1} ranges. On the basis of the effects of H-D exchange and global ^{15}N labeling (data not shown), these signals are assigned to reorganizations of the protein peptide backbone. Comparison of their shape and amplitude with those seen in the redox difference spectra of several small ferredoxins (for example, see traces C and D of Fig. 3.3) suggests that the reorganizations are local to the Fe-S centers and should not be interpreted as being indicative of large-scale conformational change as they have been in the past (Hellwig *et al.*, 2000). The peak at 1405 cm^{-1} in the bovine difference spectrum is tentatively assigned to reduced FMNH₂ on the basis of comparison with model compounds. We interpret the lack of a clear equivalent peak in the *Y. lipolytica* spectra as being caused by the presence of additional flanking contributions from redox changes of bound ubiquinone substrate, the concentration of which is greater in the *Y. lipolytica* material than the bovine material. This interpretation is strongly supported by the position and amplitude of ubiquinone signals in difference spectra arising from redox changes of Fe-S center N2 and ubiquinone that were separated from the other *Y. lipolytica* complex I components by selective redox poisoning. Possible assignments of additional features to changes of individual amino acids, including histidine, tyrosine, lysine, arginine, glutamine, and asparagine, are discussed in Marshall *et al.* (2006).

Perfusion-induced redox difference spectra of bovine complex I with either NADH or sodium dithionite as reductant are shown in Fig. 3.5. Rehydrated layers of complex I were prepared on the IRE, and the perfusion cell was assembled as described previously. For each reductive cycle requiring sodium dithionite, a fresh anaerobic solution was prepared

to minimize interference from dithionite decomposition products. Such products cause an interference that can be seen in the 1000 to 1100 cm^{-1} range in trace A of Fig. 3.5. Reduction with NADH was more straightforward, allowing acquisition of spectra over many cycles to be automated as described previously. The perfusion-induced difference spectrum with sodium dithionite as reductant (trace A) is broadly similar, particularly in shape and amplitude of amide I and II region, to the electrochemically-induced difference spectrum (trace C). Reduction with NADH resulted in decreased amplitude of signals in the amide I and II region. On the basis of comparison with redox difference spectra of small ferredoxins (Marshall *et al.*, 2006), we conclude that 1-3 dithionite-reducible Fe-S centers are not reduced by perfusion with NADH. This extent is consistent with the midpoint potentials of the Fe-S centers, supporting the retention of their native characteristics in the rehydrated layer and also demonstrating that the NADH substrate site retains its NADH dehydrogenase catalytic activity. Notably absent from the NADH-induced redox difference spectrum are signals supporting the existence of a large scale and functionally relevant conformational changes that have been suggested to occur only when complex I is reduced by NADH (Mamedova *et al.*, 2004; Pohl *et al.*, 2008). However, if such a conformational change involved relative movements of static globular domains around a hinge region, only a small number of residues would change their IR characteristics, and this could be difficult to detect by these FTIR methods. Most importantly, these spectra represent the establishment of a versatile procedure to measure perfusion-induced difference spectra of complex I. In combination with the electrochemistry cell described previously, almost any transition can now be probed by FTIR. Given the strengths of FTIR spectroscopy as a technique for the detection of protonation state changes, it seems likely that these approaches will make a valuable contribution, alongside X-ray crystallography, EPR, UV/visible and transmission mode FTIR spectroscopy, to defining the mechanism by which electron transfer is linked to proton translocation.

ACKNOWLEDGMENT

We acknowledge Mr. Santiago Garcia and Mrs. Vasanti Amin for invaluable technical support, Professor Ulrich Brandt and Dr. Judy Hirst for supplying complex I purified from *Y. lipolytica* and *B. taurus*, respectively, and Dr. Amandine Maréchal and Dr. Masayo Iwaki for valuable discussions. FTIR work of the PRR laboratory is currently funded by the BBSRC (grant BB/C51715X/1).

REFERENCES

- Ahlers, P. M., Zwicker, K., Kerscher, S., and Brandt, U. (2000). Function of conserved acidic residues in the PSST homologue of complex I (NADH: Ubiquinone oxidoreductase) from *Yarrowia lipolytica*. *J. Biol. Chem.* **275**, 23577–23582.

- Arrondo, J. L. R., Muga, A., Castresana, J., and Goñi, F. M. (1993). Quantitative studies of the structure of proteins in solution by Fourier-transform infrared spectroscopy. *Prog. Biophys. Molec. Biol.* **59**, 23–56.
- Barth, A. (2000). The infrared absorption of amino acid side chains. *Prog. Biophys. Mol. Biol.* **74**, 141–173.
- Barth, A., and Zscherp, C. (2002). What vibrations tell us about proteins. *Q. Rev. Biophys.* **35**, 369–430.
- Braiman, M. S., Bousché, O., and Rothschild, K. J. (1991). Protein dynamics in the bacteriorhodopsin photocycle: Submillisecond Fourier transform infrared spectra of the L, M, and N photointermediates. *Proc. Natl. Acad. Sci. USA* **88**, 2388–2392.
- Brittain, T., Baker, A. R., Butler, C. S., Little, R. H., Lowe, D. J., Greenwood, C., and Watmough, N. J. (1997). Reaction of variant sperm-whale myoglobins with hydrogen peroxide: The effects of mutating a histidine residue in the haem distal pocket. *Biochem. J.* **326**, 109–115.
- Burie, J.-R., Leibl, W., Navedryk, E., and Breton, J. (1993). Step-scan FT-IR spectroscopy of electron transfer in the photosynthetic bacterial reaction center. *Appl. Spectrosc.* **47**, 1401–1404.
- Carroll, J., Fearnley, I. M., Shannon, R. J., Hirst, J., and Walker, J. E. (2003). Analysis of the subunit composition of complex I from bovine heart mitochondria. *Mol. Cell. Proteomics.* **2**, 117–126.
- Euro, L., Bloch, D. A., Wikström, M., Verkhovskiy, M. I., and Verkhovskaya, M. (2008). Electrostatic interactions between FeS clusters in NADH: Ubiquinone oxidoreductase (complex I) from *Escherichia coli*. *Biochemistry* **47**, 3185–3193.
- Fahmy, K., Jäger, F., Beck, M., Zvyaga, T. A., Sakmar, T. P., and Siebert, F. (1993). Protonation states of membrane-embedded carboxylic acid groups in rhodopsin and metarhodopsin II. A Fourier-transform infrared spectroscopic study of site-directed mutants. *Proc. Natl. Acad. Sci. USA* **90**, 10206–10210.
- Flemming, D., Hellwig, P., and Friedrich, T. (2003). Involvement of tyrosines 114 and 139 of subunit NuoB in the proton pathway around cluster N2 in *Escherichia coli* NADH: Ubiquinone oxidoreductase. *J. Biol. Chem.* **278**, 3055–3062.
- Friedrich, T., Brors, B., Hellwig, P., Kintscher, L., Rasmussen, T., Scheide, D., Schulte, U., Mäntele, W., and Weiss, H. (2000). Characterization of two novel redox groups in the respiratory NADH: Ubiquinone oxidoreductase (complex I). *Biochim. Biophys. Acta* **1459**, 305–309.
- George, S. J., Ashby, G. A., Wharton, C. W., and Thorneley, R. N. F. (1997). Time-resolved binding of carbon monoxide to nitrogenase monitored by stopped-flow infrared spectroscopy. *J. Am. Chem. Soc.* **119**, 6450–6451.
- Gerwert, K., Hess, B., Soppa, J., and Oesterhelt, D. (1989). Role of aspartate-96 in proton translocation by bacteriorhodopsin. *Proc. Natl. Acad. Sci. USA* **86**, 4943–4947.
- Goormaghtigh, E., Cabiaux, V., and Ruyschaert, J.-M. (1990). Secondary structure and dosage of soluble and membrane proteins by attenuated total reflection Fourier-transform infrared spectroscopy on hydrated films. *Eur. J. Biochem.* **193**, 409–420.
- Goormaghtigh, E., Raussens, V., and Ruyschaert, J.-M. (1999). Attenuated total reflection infrared spectroscopy of proteins and lipids in biological membranes. *Biochim. Biophys. Acta* **1422**, 105–185.
- Günzler, H., and Gremlich, H.-U. (2002). IR Spectroscopy: An Introduction. Wiley-VCH, Weinheim, Germany.
- Heberle, J., and Zscherp, C. (1996). ATR/FT-IR difference spectroscopy of biological matter with microsecond time resolution. *Appl. Spectrosc.* **50**, 588–596.
- Hellwig, P., Behr, J., Ostermeier, C., Richter, O. M. H., Pfitzner, U., Odenwald, A., Ludwig, B., Michel, H., and Mäntele, W. (1998). Involvement of glutamic acid 278 in the redox reaction of the cytochrome *c* oxidase from *Paracoccus denitrificans* investigated by FTIR spectroscopy. *Biochemistry* **37**, 7390–7399.

- Hellwig, P., Pfitzner, U., Behr, J., Rost, B., Pesavento, P., Donk, W. v., Gennis, R. B., Michel, H., Ludwig, B., and Mäntele, W. (2002). Vibrational modes of tyrosine in cytochrome *c* oxidase from *Paracoccus denitrificans*: FTIR and electrochemical studies on Tyr-D4-labeled and on Tyr280His and Tyr35Phe mutant enzymes. *Biochemistry* **41**, 9116–9125.
- Hellwig, P., Rost, B., Kaiser, U., Ostermeier, C., Michel, H., and Mäntele, W. (1996). Carboxyl group protonation upon reduction of the *Paracoccus denitrificans* cytochrome *c* oxidase: Direct evidence by FTIR spectroscopy. *FEBS Lett.* **385**, 53–57.
- Hellwig, P., Scheide, D., Bungert, S., Mäntele, W., and Friedrich, T. (2000). FT-IR spectroscopic characterization of NADH: Ubiquinone oxidoreductase (complex I) from *Escherichia coli*: Oxidation of FeS cluster N2 is coupled with the protonation of an aspartate or glutamate side chain. *Biochemistry* **39**, 10884–10891.
- Hellwig, P., Stolpe, S., and Friedrich, T. (2004). Fourier transform infrared spectroscopic study on the conformational reorganization in *Escherichia coli* complex I due to redox-driven proton translocation. *Biopolymers* **74**, 69–72.
- Hiennerwadel, R., Boussac, A., Breton, J., and Berthomieu, C. (1997). Fourier transform infrared difference spectroscopy of photosystem II tyrosine D using site-directed mutagenesis and specific isotope labeling. *Biochemistry* **36**, 14712–14723.
- Hirst, J., Carroll, J., Fearnley, I. M., Shannon, R. J., and Walker, J. E. (2003). The nuclear encoded subunits of complex I from bovine heart mitochondria. *Biochim. Biophys. Acta* **1604**, 135–150.
- Ingledeu, W. J., and Ohnishi, T. (1980). An analysis of some thermodynamic properties of iron-sulphur centres in site I of mitochondria. *Biochem. J.* **186**, 111–117.
- Iwaki, M., Cotton, N. P. J., Quirk, P. G., Rich, P. R., and Jackson, J. B. (2006). Molecular recognition between protein and nicotinamide dinucleotide in intact, proton-translocating transhydrogenase studied by ATR-FTIR. *J. Am. Chem. Soc.* **128**, 2621–2629.
- Iwaki, M., Giotta, L., Akinsiku, A. O., Schägger, H., Fisher, N., Breton, J., and Rich, P. R. (2003). Redox-induced transitions in bovine cytochrome *bc*₁ complex studied by perfusion-induced ATR-FTIR spectroscopy. *Biochemistry* **42**, 11109–11119.
- Iwaki, M., Osyczka, A., Moser, C. C., Dutton, P. L., and Rich, P. R. (2004). ATR-FTIR spectroscopy studies of iron-sulfur protein and cytochrome *c*₁ in the *Rhodobacter capsulatus* cytochrome *bc*₁ complex. *Biochemistry* **43**, 9477–9486.
- Lemon, D. D., Calhoun, M. W., Gennis, R. B., and Woodruff, W. H. (1993). The gateway to the active site of heme-copper oxidases. *Biochemistry* **32**, 11953–11956.
- Magnitsky, S., Touloukhonova, L., Yano, T., Sled, V. D., Hagerhall, C., Grivennikova, V. G., Burbaev, D. S., Vinogradov, A. D., and Ohnishi, T. (2002). EPR characterization of ubisemiquinone and iron-sulfur cluster N2, central components of the energy coupling in the NADH-ubiquinone oxidoreductase (complex I) *in situ*. *J. Bioenerg. Biomemb.* **34**, 193–208.
- Mamedova, A. A., Holt, P. J., Carroll, J., and Sazanov, L. A. (2004). Substrate-induced conformational change in bacterial complex I. *J. Biol. Chem.* **279**, 23830–23836.
- Mäntele, W. (1993). Reaction-induced infrared difference spectroscopy for the study of protein function and reaction mechanisms. *Trends Biochem. Sci.* **18**, 197–202.
- Mäntele, W. (1996). Infrared and Fourier-transform infrared spectroscopy. In "Biophysical Techniques in Photosynthesis." (J. Amesz and A. J. Hoff, eds.), pp. 137–160. Kluwer Academic Publishers, Dordrecht.
- Marshall, D., Fisher, N., Grigic, L., Zickermann, V., Brandt, U., Shannon, R. J., Hirst, J., Lawrence, R., and Rich, P. R. (2006). ATR-FTIR redox difference spectroscopy of *Yarrowia lipolytica* and bovine complex I. *Biochemistry* **45**, 5458–5467.
- Moss, D., Nabedyk, E., Breton, J., and Mäntele, W. (1990). Redox-linked conformational changes in proteins detected by a combination of IR spectroscopy and protein electrochemistry. Evaluation of the technique with cytochrome *c*. *Eur. J. Biochem.* **187**, 565–572.

- Nabedryk, E., Breton, J., Hienerwadel, R., Fogel, C., Mäntele, W., Paddock, M. L., and Okamura, M. Y. (1995). Fourier transform infrared difference spectroscopy of secondary quinone acceptor photoreduction in proton transfer mutants of *Rhodobacter sphaeroides*. *Biochemistry* **34**, 14722–14732.
- Nakamaru-Ogiso, E., Matsuno-Yagi, A., Yoshikawa, S., Yagi, T., and Ohnishi, T. (2008). Iron-sulfur cluster N5 is coordinated by an HXXXXCXXCXXXXXC motif in the NuoG subunit of *Escherichia coli* NADH: Ubiquinone oxidoreductase (complex I). *J. Biol. Chem.* **283**, 25979–25987.
- Nakamaru-Ogiso, E., Yano, T., Yagi, T., and Ohnishi, T. (2005). Characterization of the iron-sulfur cluster N7 (N1c) in the subunit NuoG of the proton-translocating NADH-ubiquinone oxidoreductase from *Escherichia coli*. *J. Biol. Chem.* **280**, 301–307.
- Noguchi, T., and Sugiura, M. (2002). FTIR detection of water reactions during the flash-induced S-state cycle of the photosynthetic water-oxidizing complex. *Biochemistry* **41**, 15706–15712.
- Ohnishi, T. (1998). Iron-sulfur clusters/semiquinones in complex I. *Biochim. Biophys. Acta* **1364**, 186–206.
- Ohnishi, T., and Nakamaru-Ogiso, E. (2008). Were there any "misassignments" among iron-sulfur clusters N4, N5 and N6b in NADH-quinone oxidoreductase (complex I)? *Biochim. Biophys. Acta* **1777**, 703–710.
- Pohl, T., Schneider, D., Hielscher, R., Stolpe, S., Dörner, K., Kohlstädt, M., Böttcher, B., Hellwig, P., and Friedrich, T. (2008). Nucleotide-induced conformational changes in the *Escherichia coli* NADH: Ubiquinone oxidoreductase (complex I). *Biochem. Soc. Trans.* **36**, 971–975.
- Rahmelow, K., Hübner, W., and Ackermann, Th. (1998). Infrared absorbances of protein side chains. *Anal. Biochem.* **257**, 1–11.
- Rath, P., DeGrip, W. J., and Rothschild, K. J. (1998). Photoactivation of rhodopsin causes an increased hydrogen-deuterium exchange of buried peptide groups. *Biophys. J* **74**, 192–198.
- Rich, P. R., and Breton, J. (2001). FTIR studies of the CO and cyanide compounds of fully reduced bovine cytochrome *c* oxidase. *Biochemistry* **40**, 6441–6449.
- Rich, P. R., and Iwaki, M. (2005). Infrared protein spectroscopy as a tool to study protonation reactions within proteins. In "Biophysical and Structural Aspects of Bioenergetics." (M. Wikström, ed.), pp. 314–333. The Royal Society of Chemistry, Cambridge, U.K.
- Ritter, M., Anderka, O., Ludwig, B., Mäntele, W., and Hellwig, P. (2003). Electrochemical and FTIR spectroscopic characterization of the cytochrome *bc₁* complex from *Paracoccus denitrificans*: Evidence for protonation reactions coupled to quinone binding. *Biochemistry* **42**, 12391–12399.
- Sazanov, L. A., and Hinchliffe, P. (2006). Structure of the hydrophilic domain of respiratory complex I from *Thermus thermophilus*. *Science* **311**, 1430–1436.
- Sharpley, M. S., Shannon, R. J., Draghi, F., and Hirst, J. (2005). Interactions between phospholipids and NADH: Ubiquinone oxidoreductase (complex I) from bovine mitochondria. *Biochemistry* **45**, 241–248.
- Sled, V. D., Rudnitsky, N. I., Hatefi, Y., and Ohnishi, T. (1994). Thermodynamic analysis of flavin in mitochondrial NADH: Ubiquinone oxidoreductase (complex I). *Biochemistry* **33**, 10069–10075.
- Sonar, S., Lee, C.-P., Coleman, M., Patel, N., Liu, X., Marti, T., Gobind Khorana, H., RajBhandry, U. L., and Rothschild, K. J. (1994). Site-directed isotope labelling and FTIR spectroscopy of bacteriorhodopsin. *Nature Struct. Biol.* **1**, 512–517.
- Sonar, S., Liu, X.-M., Lee, C. -P., Coleman, M., He, Y. -W., Pelletier, S., Herzfeld, J., RajBhandry, U. L., and Rothschild, K. J. (1995). Site-directed isotope labelling and FT-IR spectroscopy: The Tyr 185/Pro 186 peptide bond of bacteriorhodopsin is perturbed during the primary photoreaction. *J. Am. Chem. Soc.* **117**, 11614–11615.

- Stuart, B. (2004). *Infrared spectroscopy: Fundamentals and applications*. John Wiley & Sons, Chichester.
- Tatullian, S. A. (2003). Attenuated total reflection Fourier transform infrared spectroscopy: A method of choice for studying membrane proteins and lipids. *Biochemistry* **42**, 11898–11907.
- Venyaminov, S. Y., and Kalnin, N. N. (1990). Quantitative IR spectrophotometry of peptide compounds in water (H₂O) solutions I Spectral parameters of amino acid residue absorption bands. *Biopolymers* **30**, 1243–1257.
- Vinogradov, A. D., Sled, V. D., Burbaev, D. S., Grivennikova, V. G., Moroz, I. A., and Ohnishi, T. (1995). Energy-dependent complex I-associated ubisemiquinones in submitochondrial particles. *FEBS Lett.* **370**, 83–87.
- Wille, G., Ritter, M., Friedemann, R., Mäntele, W., and Hübner, G. (2003). Redox-triggered FTIR difference spectra of FAD in aqueous solution and bound to flavoproteins. *Biochemistry* **42**, 14814–14821.
- Wolpert, M., and Hellwig, P. (2006). Infrared spectra and molar absorption coefficients of the 20 alpha amino acids in aqueous solutions in the spectral range from 1800 to 500 cm⁻¹. *Spectrochim. Acta A* **64**, 987–1001.
- Xiao, Y., Koutmos, M., Case, D. A., Couvouvannis, D., Wang, H., and Cramer, S. P. (2006). Dynamics of an [Fe₄S₄(SPh)₄]²⁻ cluster explored via IR, Raman, and nuclear resonance vibrational spectroscopy (NRVS)-analysis using ³⁶S substitution, DFT calculations, and empirical force fields. *Dalton. Trans.* **18**, 2192–2201.
- Yakovlev, G., Reda, T., and Hirst, J. (2007). Reevaluating the relationship between EPR spectra and enzyme structure for the iron-sulfur clusters in NADH: Quinone oxidoreductase. *Proc. Natl. Acad. Sci. USA* **104**, 12720–12725.
- Yano, T., Dunham, W. R., and Ohnishi, T. (2005). Characterization of the ΔμH + -sensitive ubisemiquinone species (SQNf) and the interaction with cluster N2: New insight into the energy-coupled electron transfer in complex I. *Biochemistry* **44**, 1744–1754.
- Yano, T., Sklar, J., Nakamaru-Ogiso, E., Takahashi, Y., Yagi, T., and Ohnishi, T. (2003). Characterization of cluster N5 as a fast-relaxing [4Fe-4S] cluster in the Nqo3 subunit of the proton-translocating NADH-ubiquinone oxidoreductase from *Paracoccus denitrificans*. *J. Biol. Chem.* **278**, 15514–15522.

ELECTRON TRANSFER IN RESPIRATORY COMPLEXES RESOLVED BY AN ULTRA-FAST FREEZE-QUENCH APPROACH

Nikolai P. Belevich, Marina L. Verkhovskaya, and
Michael I. Verkhovsky

Contents

1. Introduction	76
1.1. Transient kinetics as the main tool for enzyme catalytic cycle investigation	76
1.2. Comparison of the different flow techniques	76
2. Ultra-Fast Freeze-Quench Setup	79
2.1. Mixer design	80
2.2. Fast freezing	81
3. Sample Preparation	82
4. Calibration of the Freeze-Quench Setup	85
5. Application of Freeze-Quench Approach for the Monitoring of Complex I Reduction by NADH	85
References	92

Abstract

The investigation of the molecular mechanism of the respiratory chain complexes requires determination of the time-dependent evolution of the catalytic cycle intermediates. The ultra-fast freeze-quench approach makes possible trapping such intermediates with consequent analysis of their chemical structure by means of different physical spectroscopic methods (e.g., EPR, optic, and Mössbauer spectroscopies). This chapter presents the description of a setup that allows stopping the enzymatic reaction in the time range from 100 μ sec to tens of msec. The construction and production technology of the mixer head, ultra-fast freezing device, and accessories required for collecting a sample are described. Ways of solving a number of problems emerging on freezing of the reaction mixture and preparing the samples for EPR spectroscopy are proposed. The kinetics of electron transfer reaction in the first enzyme of the respiratory

chain, Complex I (NADH: ubiquinone oxidoreductase), is presented as an illustration of the freeze-quench approach. Time-resolved EPR spectra indicating the redox state of FeS clusters of the wild-type and mutant (R274A in subunit NuoCD) Complex I from *Escherichia coli* are shown.

1. INTRODUCTION

1.1. Transient kinetics as the main tool for enzyme catalytic cycle investigation

The investigation of the mechanism of any complex reaction requires determination of the time-dependent evolution of the molecular species involved. The typical turnover rate of the respiratory chain complexes under steady-state conditions is approximately 100 to 200 enzyme revolutions per second. Each turnover consists of a number of distinct intermediates, which are formed in a time range from microseconds to several milliseconds after the reaction initiation. The large number of catalytic intermediates, complicated by a hierarchy of transition rate constants between them because the transition rates may differ by several orders of magnitude, makes it practically impossible to study the molecular mechanism by means of conventional steady-state techniques. Under steady-state conditions only the slowest intermediate is populated, leaving all other intermediates completely invisible. The transient kinetics approach allows one to overcome the stated difficulties; this is why it is one of the most fruitful ways to investigate the reaction mechanism of enzymes that are considered as molecular machines. At the same time, such an approach requires certain conditions that must be fulfilled, such as

1. The initial state of all the enzyme molecules in the sample should be identical before the reaction initiation.
2. The start of the reaction (addition of substrate, inhibitor removal, etc.) has to be carried out faster than the fastest transition under the investigation. This is a real challenge, because the fastest mixing time of a conventional stopped-flow apparatus is in the range of milliseconds, which is much slower than most of the intermediate transitions in the catalytic cycle. During the last few years ultra-fast mixing devices based on very low volumes of the mixing chambers (~ 1 nl) have been developed (Cherepanov and de Vries, 2004, Lin *et al.*, 2003, Tanaka *et al.*, 2003, Verkhovskaya *et al.*, 2008).

1.2. Comparison of the different flow techniques

Historically, the earliest rapid kinetic measurements used a continuous-flow (CF) arrangement combined with absorbance measurements of the reaction progress at different points downstream. The drawback of this method is

significant reagent consumption. This has been replaced by the more commonly used stopped-flow (SF) method because of sample economy and the possibility to measure the kinetics over a relatively long time period (up to several minutes). However, the kinetics resolution time accessible to SF is generally limited to 1 msec or longer, because the measurements are made only after the flow comes to a complete stop, which is inherently slow and can result in vibration and pressure artifacts (Roder *et al.*, 2004). CF techniques have undergone a renaissance in recent years because of advances in mixer design and detection methods, which made it possible to push the time resolution into the microsecond time range (Bilsel *et al.*, 2005, Shastry *et al.*, 1998). For the reaction, which could not be investigated by optical spectroscopy, freeze-quench protocols can be used in combination with slower analytical techniques such as NMR, EPR, or mass spectrometry (Johnson, 1995).

In general, the freeze-quench mixing-and-sampling technique can be viewed as a three-stage process. At the first stage, the reaction is initiated by rapid mixing of the reaction components. At the second stage, the sample is transported from the mixer to the freeze-quenching device. And at the third stage, the sample undergoes fast freezing. Thus, the characteristic reaction time, τ_r , can be described as

$$\tau_r = \tau_m + \tau_t + \tau_f \quad (4.1)$$

where τ_m is the mixing time, τ_t is the sample-transport time, and τ_f is the freezing time.

An ideal freeze-quenching instrument should have a $\tau_m + \tau_f$ value close to zero, and in this case a reaction occurs mostly during the second stage. The sample-transport time τ_t is determined by the sample flow rate and the distance between the mixer and freeze-quenching device and could be varied during the experiment to follow the progress of a reaction. The conventional freeze-quenching devices have minimal $\tau_m + \tau_f$ (often defined as the dead time of a setup) approximately 5 msec (Ballou, 1978), which is not sufficient for studying most enzymatic reactions; therefore, attempts to achieve better kinetic resolution for this method concentrated on the mixer design, and improvements were made to the freezing technique.

The mixing time is determined by the sample flow rate, the effective volume of the mixer and the mixer geometry. Reduction in the mixing time can be achieved by decreasing the dimensions of the mixing chamber. However, this advantage is compromised by a concurrent decrease in the Reynolds number (Re), which characterizes the dynamics of a liquid flow inside a tube with a circular cross section. The Reynolds number is defined as $Re = \rho v d / \eta$, where v is the average flow speed, d represents the smallest cross section in the flow channel, and ρ and η are the density and the viscosity of the liquid. When the Reynolds number is low, a laminar flow results.

A Reynolds number greater than 2000 is characteristic of the turbulent flow required for efficient mixing. To reach this condition and prevent a laminar flow in the miniaturized mixers an increase in flow speed is typically required. Shastry *et al.* (1998) described a device with small mixing volume and high flow rate. It is based on the design by Regenfuss *et al.* (1985) and uses a principle of coaxial reagents flow combined with ball mixing (Berger, 1978). In this device they obtained full reagents mixing within 15 μsec . The mixer was built of quartz and consists of several fine inner parts. The complicated design of this mixer makes it fragile for use with freeze-quenching techniques and also it cannot easily be replicated.

Lin *et al.* (2003) described an ultra-fast micro fluidic mixer made of silicon with the use of photolithographic techniques. Its mixing chamber has the dimensions of $50 \times 100 \times 100 \mu\text{m}$ and contains seven vertical pillars with a diameter of $10 \mu\text{m}$ arranged perpendicularly to the flow direction in a staggered fashion. With this design, the flow velocity is modulated by the alternating passages as the mixed fluid travels down the mixing chamber. The associated changes in the Reynolds number fall within the 200 to 2000 range along the flow direction. Lin *et al.* (2003) claim that the mixing time for the silicon mixer is approximately 20 μsec . For the sample freezing they used a new freeze-quench device, which consisted of two rotating copper wheels maintained at 77 K. A free-flowing jet exits from the mixer and instantly freezes on the wheels' surface. The frozen sample is subsequently ground into an ultra fine powder. The use of a silicone mixer in combination with a new freeze-quench device enabled them to reach a time resolution of 50 μsec , although for calibration they used an uncorrected rate constant (Cherepanov and de Vries, 2004) for azide binding to metmyoglobin, and real-time resolution is not so high.

Cherepanov and de Vries (2004) reported a freeze-quench instrument with a dead time of approximately 120 μsec . They designed a tangential micro-mixer, which had a mixing time of up to 20 μsec . The mixer is composed of four channels arranged in an X-form geometry. The opposite channels have an offset with respect to each other by the half-width of the channel, so that the liquid streams are premixed in the middle of "X" with a resulting angular momentum at relatively low Reynolds numbers ($\text{Re} < 1000$). After premixing, the four-stream solution is forced through a narrow orifice and forms a free jet in a direction perpendicular to the plane of the channels. The flow through the orifice is accelerated to a high linear velocity, and the mixing of the reaction components takes place at Reynolds numbers of approximately 4000. For the freeze-quenching the sample jet was sprayed into the vial containing cold isopentane at 125 K.

Each of these two instruments has advantages and limitations. The sample freezing device designed by Lin *et al.* (2003) is evidently more efficient, because the metals have very high thermal conductivity, and the jet directed at the cold metal surface should freeze very fast. The fast rotation

of the wheels guarantees that the jet will have contact with an ice-free metal surface. On the contrary, freezing the jet by spraying it into cold isopentane should not be so fast, because the thermal conductivity of the isopentane at room temperature is approximately 4000 times worse than that of copper (0.11 and 401 W m⁻¹ K⁻¹, respectively).

The four jets tangential mixer designed by [Cherepanov and de Vries \(2004\)](#) seems to be efficient in a wider flow rate range than that presented by [Lin *et al.* \(2003\)](#). This conclusion is based on the general criteria for the mixer design ([Smith, 1973](#)); in particular, the efficiency of mixing depends on the ability of the mixer to break up the streams of the two reactants into elementary blocks of the smallest size.

In our freeze-quench system we used a mixer based on the design by [Cherepanov and de Vries \(2004\)](#) and combined it with the freeze-quench device described by [Lin *et al.* \(2003\)](#). The mixing chamber has a volume of 1 nl (dimensions of 0.15 mm × 0.15 mm × 0.05 mm), which allows us to approach the τ_m time of ~ 20 μ sec at the typical flux rate of the experiment of 3 ml/min. The freezing time t_f was minimized by an application of liquid nitrogen cooled silver—material with the highest possible thermal conductivity.

2. ULTRA-FAST FREEZE-QUENCH SETUP

The freeze-quench system was built in our laboratory based on the principles described by [Cherepanov and de Vries \(2004\)](#) and [Lin *et al.* \(2003\)](#). A block diagram of the system is depicted in [Fig. 4.1](#). It has a symmetric flow design and consists of two LKB 2150 high-performance liquid chromatography (HPLC) pumps (2a,b), two mechanically coupled Rheodyne 7125 sample injectors (4a,b) equipped with 100- μ l sample loops (5a,b), and a tangential four-jet mixer (8). To increase pressure stability, pulse suppressors were included into the flow path (3a,b). A pulse suppressor consists of a sequentially connected pressure damper (LP-21 LO-Pulse, Scientific System) and a short HPLC reverse-phase column. The use of a column allowed us to get an optimal loading for the HPLC pump to improve pressure stability. To protect the mixer orifice from clogging, filters were inserted into the flow path (6a,b). The filters consisted of two sequential in-line solvent filters 2 μ m and 0.5 μ m. All fluid transport lines were equipped with HPLC-grade 1/16" PEEK tubing (inner diameter 0.01") and standard high-pressure HPLC connections. Sample loops were made of PEEK tubes with inner diameter 0.05". To decrease sample dilution, the flow path after the sample injectors was designed to be as short as possible.

The mixing device works in continuous-flow mode. In the purging mode, the buffer (1, [Fig. 4.1](#)), which bypasses the sample loops, comes

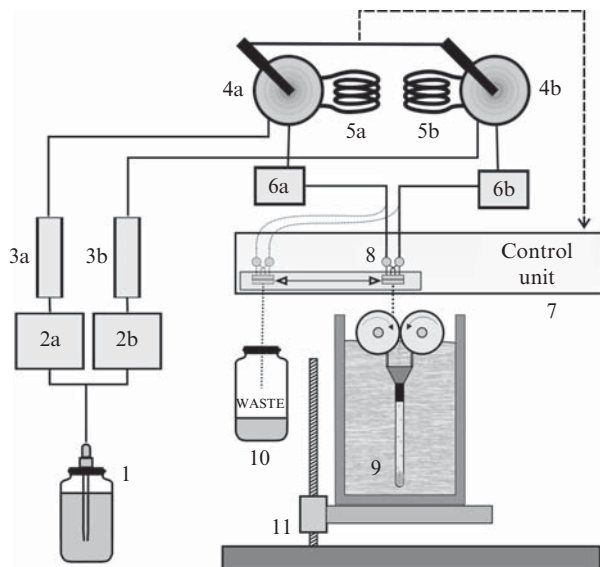


Figure 4.1 Schematic representation of the freeze-quench setup. 1, The vessel with the argon saturated carrier solvent; 2a,b, HPLC pumps; 3a,b, pressure pulsation dampers; 4a,b, Rheodyne-type sample injection valves; 5a,b, sample loops; 6a,b, solvent filters; 7, microcontroller-based timing control system; 8, tangential four-jet mixer; 9, low temperature quenching system; 10, waste container; 11, table with vertically adjustable position.

through the mixer, and a free-flowing jet is directed at the waste container (10, Fig. 4.1). Switching mechanically coupled sample injectors triggers the operational mode. At this moment, the sample loops filled with assay solutions are inserted into the flow path, and a microcontroller-based timing system (7, Fig. 4.1) generates the time delay necessary for assay solutions to reach the mixer head. Then, the mixer head moves into the “work” position, where the jet of the mixed solutions is directed at the freeze-quench device (FQD). At this point, the system delivers a volume equal to the volume of both sample loops and then returns the mixing head back to the “waste” position. Timing delays depending on tubing length and solvent flow rate can be adjusted with millisecond precision.

2.1. Mixer design

The tangential four-jet mixer is shown in Fig. 4.2 (see also Cherepanov and de Vries [2004]). The mixer body is made of a stainless-steel cylinder with a 6-mm outer diameter. Four holes (diameter, 1.5 mm) were drilled along the cylinder axis. Then stainless-steel tubes with 1/16'' outer and 0.005'' inner diameters were pressed into the cylinder to create flow channels. The top

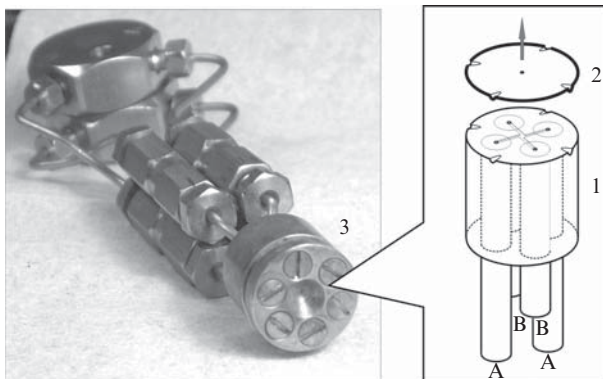


Figure 4.2 Picture and schematic drawing of the tangential four-jet mixer. 1, Stainless-steel body of the mixer with stainless steel HPLC tubing pressed in. 2, 50- μm -thick stainless-steel cover with the orifice. A and B are the entry for corresponding reaction components. 3, Brass holder of the mixer fastened by screws. Y-connectors distributing two reactants through the four channels arranged in cross geometry are seen in the picture. The channels etched on the surface are offset with respect to the opposite one for half-width of the channel.

surface of the cylinder was ground and polished. In addition, the tubes on the opposite side of the cylinder were caulked by soldering. On the top of the cylinder, crosslike channels were made by electrochemical etching. The width of the channel was $\sim 100\ \mu\text{m}$ and the depth $\sim 50\ \mu\text{m}$. On the top edge of the cylinder four asymmetric guiding grooves were made. These grooves serve as guides for the exact positioning of the stainless-steel cover on the mixer body. This cover with an orifice is placed on the top of the mixer body to form a mixing chamber. The cover was stamped out of a 50- μm stainless-steel sheet, and the mixer body serves as a punch head. After stamping, the cover has a shape that exactly fits the mixer body surface. On the inner surface of the cover an imprint of the cross-like channels can be obtained. This imprint lets us locate an orifice position in the center of the crosslike channels. The orifice hole was drilled by electrochemical micromachining technology (Schuster *et al.*, 2000). A number of covers were manufactured with an orifice diameter in the range 20 to 30 μm . The mixer body and cover were placed into a brass holder and fastened by screws (Fig. 4.2).

2.2. Fast freezing

The freeze-quench device (9, Fig. 4.1) was built based on the principles described by Lin *et al.* (2003) and Tanaka *et al.* (2003). It consists of a stainless-steel Dewar, drum unit, and a sample collecting funnel attached to an EPR tube.

The drum unit consists of two wheels and a driving motor (Fig. 4.3). The wheels are made of pure (99.99%) silver and have a cylindrical shape with a 4-cm diameter. They are arranged in a side-by-side fashion. The driving

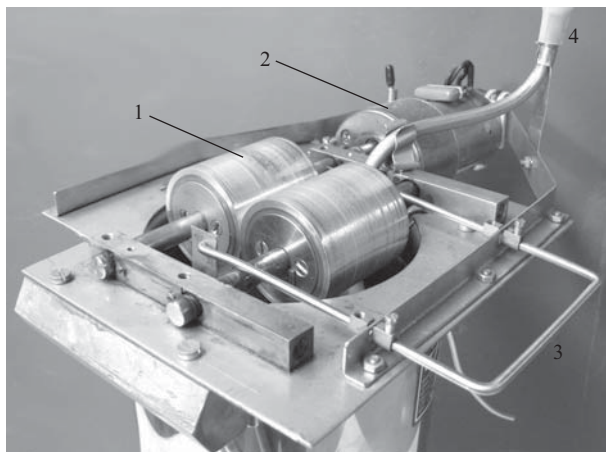


Figure 4.3 Drum unit of the freeze-quench device. 1, Silver cylinders; 2, motor driver; 3, lever for lifting the collecting funnel with the scrapers onto the cylinders' surface during collection of the samples; 4, liquid nitrogen refilling tube.

wheel, attached to a motor, drives the slave wheel through frictional contact. As a result, two wheels rotate in opposite directions at the same speed. During the experiment the drum unit is placed on top of the Dewar filled with liquid nitrogen in such a way that the bottom halves of both rotating wheels are immersed in liquid nitrogen to maintain low temperature. For sufficient cooling down of the wheels, a 10-min rotation is required before the experiment together with constant refilling of the Dewar with liquid nitrogen. For sample cryofixation, the mixed-solution jet is directed at the cold surface of the rotating cylinder, where it freezes instantly. To improve freezing efficiency, the mixer head executes a penduliform motion along the cylinder axis and directs the jet at the ice-free zone of the cylinder. The rotating cylinders grind the ice into a fine powder as it is carried down through the cylinder interface. The powder is collected into an EPR tube through a collecting funnel placed in liquid nitrogen directly below the cylinders. The top of the rectangular funnel is equipped with two scrapers. In the operational mode, the scrapers make contact with the cylinder's surface and improve the efficiency of the powder collection. An EPR tube (5-mm diameter) is attached to the funnel by a heat-shrinkable connection.

3. SAMPLE PREPARATION

Reaction species evolution could be monitored by changing the transportation time τ_t (Eq. 4.1). This parameter is the function of the distance between the mixer and the cooled wheel surface of the FQD.

Therefore, to obtain kinetics of the reaction, a number of samples with different distances between the mixer and FQD have to be collected. The fastest time points in the kinetics were collected with a jet speed of ~ 80 m/sec for a $28\text{-}\mu\text{m}$ orifice (flow speed 1.5 ml/min for each HPLC pump) and the distance varied from 8 to 32 mm. For all other samples the jet speed was decreased to 26 m/sec (flow speed 0.5 ml/min per HPLC pump). All reagent solutions and buffers were degassed on a vacuum/gas line before the experiment. The two sample loops were filled with $100\text{-}\mu\text{l}$ solutions of the reactants under investigation by a syringe equipped with Millex-HV $0.45\text{-}\mu\text{m}$ filter. The sample collection procedure consisted of the following. A rectangle funnel with attached EPR tube was placed inside a Dewar filled with liquid nitrogen. A dried-out drum unit was placed on top of the Dewar. The FQD was placed on a vertically adjustable table (11, Fig. 4.1), and the distance between the mixer head and the drum unit was set to a desirable value. Then rotation of the wheels was initiated, and they were allowed to cool down for approximately 10 min. During cooling, the level of liquid nitrogen in the Dewar was kept constant by continuous refilling. After cooling, injection of the sample and the cryofixation procedure were initiated. When the desired volume of the frozen sample was ground into a powder and the mixer head had returned to the waste position (Fig. 4.1), the drum unit was removed from the top of the Dewar. The funnel connected to the EPR tube filled with the powdered, frozen sample and immersed in liquid nitrogen was slowly lifted to allow evaporation of the liquid nitrogen and to let the powder settle inside the EPR tube. This procedure has to be performed with great care to prevent sample blowout caused by nitrogen boiling inside the EPR tube. A stick made of copper was used to accelerate the evaporation of liquid nitrogen from the EPR tube. During this procedure, the low end of the copper stick was manually placed at the nitrogen gas/liquid interface to intensify nitrogen evaporation. After the powder settled in the EPR tube, the funnel was removed.

Two possible complications exist with the liquefied gases in the sample. The first complication arises if all the liquid nitrogen is not completely removed from the sample powder. The powder, acting as a sponge, absorbs liquid very well. A small temperature rise during the transfer of the EPR tube to the cavity of the EPR spectrometer will blow the sample because of the immediate liquid to gas transition of the nitrogen in the sample. The second complication comes from oxygen. The boiling temperature of oxygen (90 K) is higher than that of nitrogen (77 K). Therefore, during the preparation of the sample, oxygen in the air could condense in liquid form inside the EPR tube. Oxygen as a biradical has a broad EPR spectrum that could overlap the studied signals. To avoid these two complications the sample was subjected to an annealing procedure to remove all traces of liquid gases. For annealing, the EPR tube was placed in a low-temperature chamber (Fig. 4.4), where it was incubated for 15 min at 100 K to evaporate

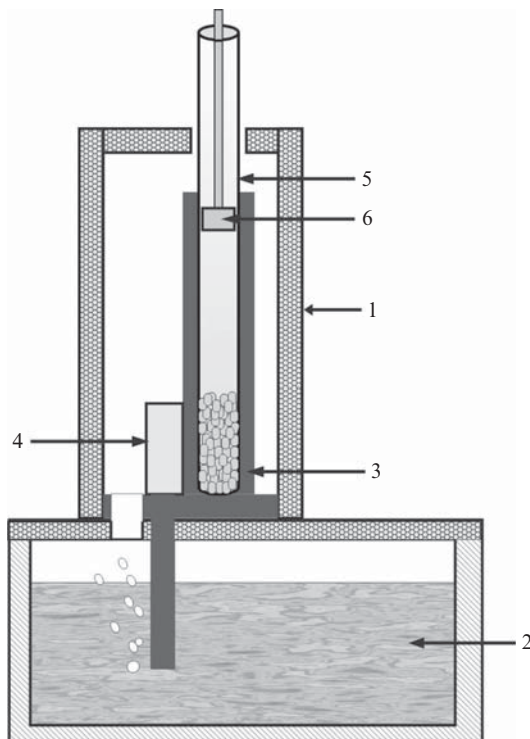


Figure 4.4 The annealing device consists of a thermal insulated Styrofoam chamber (1) designed as a lid, which is placed on top of the stainless-steel Dewar with liquid nitrogen (2). The passive “cold” exchanger made of copper (3) maintains the temperature inside the annealing chamber at approximately 100 K. An additional heating element (4) placed inside the annealing chamber coupled with a heat controller lets us use this device as a low temperature thermostat with a temperature range of 100 to 240 K. A safety plunger (6) placed inside the EPR tube (5) protects the sample against blowout during annealing.

any traces of liquid nitrogen and oxygen. After incubation, the sample was tamped down by a polycarbonate stick cooled with liquid nitrogen to completely pack it in the EPR tube with a packing factor of 0.5 to 0.6. The packing factor was calculated as a ratio between the volumes of the sample in the liquid and frozen powder states. As a final step in the sample preparation a plug made of cotton wool was inserted into the EPR tube above the sample powder to ensure that traces of liquefied gases would not destroy the sample. Then the EPR tube, which was tightly closed with a plastic lid, was transferred into an EPR spectrometer cavity. This is a very important point. If the EPR tubes were to remain open, oxygen from the atmosphere would liquefy inside the tube located in the helium cryostat at temperatures far below 100 K, and the problems described previously would occur.

4. CALIBRATION OF THE FREEZE-QUENCH SETUP

The mixing and freezing time of an ideal freeze-quench instrument can be assumed to be zero, and the sample-aging time can be calculated by use of the distance between the mixer and freeze-quench device and the jet speed. However, the following complications should be considered. First, the speed of the free-flowing jet could slow down because of air resistance that results in an increase in sample transportation time. The braking effect of air becomes significant with acceleration of the jet speed. For example, to minimize air-braking [Cherepanov and de Vries \(2004\)](#) used a low-pressure chamber. Therefore, all freeze-quench instruments require direct calibration to obtain a reliable sample-aging time.

To calibrate a freeze-quench system, a well-known chemical reaction is used as a molecular timer. For example, the binding of azide (N_3^-) with the metmyoglobin from horse heart often is used for this purpose. ([Ballou, 1978](#), [Cherepanov and de Vries, 2004](#), [Lin *et al.*, 2003](#)). It is important to note that azide binding is not a simple second-order reaction, because the rate constant decreases at high azide concentrations ($>1 \text{ mM}$). These peculiar properties of azide binding should be taken into account. A detailed analysis of this reaction can be found in [Cherepanov and de Vries \(2004\)](#). We also used the binding of azide to metmyoglobin to calibrate the time scale of our instrument. The rate constants for this reaction obtained on the basis of timing by jet length were found to be very close to those calculated from the known parameters of the reaction. The obtained kinetics of metmyoglobin ligand binding ([Fig. 4.5](#)) allowed estimation of the dead time, which represents the sum of mixing and freezing times. The zero time point (100% of the signal) was obtained by mixing metmyoglobin with the buffer without azide. The experimental points indicating the content of low- and high-spin heme in the sample were plotted against the time intervals calculated from the jet speed and the distance between the mixer head and cold silver surface ([Fig. 4.5](#)). The theoretical curve, which fits these experimental data, represents the reaction with a rate constant of $19\,500 \text{ M}^{-1} \text{ s}^{-1}$ ([Cherepanov and de Vries, 2004](#)) and a dead time of $57 \mu\text{sec}$.

5. APPLICATION OF FREEZE-QUENCH APPROACH FOR THE MONITORING OF COMPLEX I REDUCTION BY NADH

NADH:ubiquinone oxidoreductase (Complex I) is one of the key enzymes of the respiratory chain of mitochondria and many bacteria. Complex I couples electron transfer from NADH to ubiquinone with

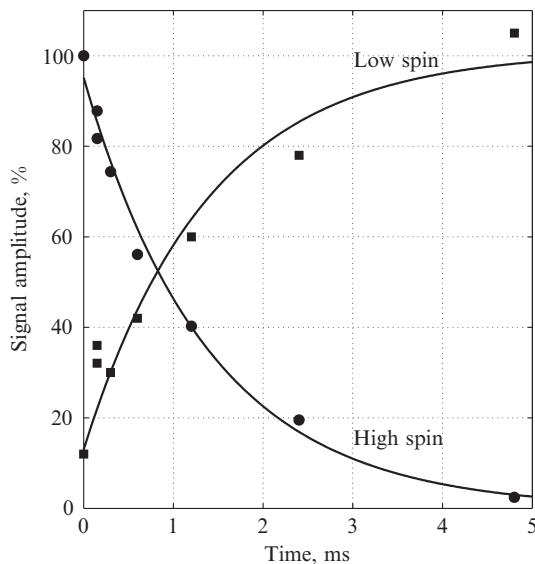


Figure 4.5 Kinetics of the NaN_3 binding to the metmyoglobin. Metmyoglobin from horse heart, 1 mM, was mixed 1:1 with 80 mM sodium azide (pH 5.0). The reaction was stopped in the time range from 0.09 to 5 msec, and the kinetics of the metmyoglobin ligand binding was followed by X-band (9.4 GHz) EPR measurements (10 K, microwave power 2 mW). The appearance of low-spin heme and decay of high-spin heme spectra were monitored.

translocation of $2 \text{ H}^+/\text{e}^-$ across the membrane (Galkin *et al.*, 1999, Wikström, 1984). Although the enzyme has been under investigation for more than 40 years, its molecular mechanism is not yet known. Complex I consists of water soluble and membrane domains; the former contains FMN followed by a chain of 8 to 9 FeS clusters, and no redox centers are found in the latter. So far, Complex I has not been accessible to time-resolved methods, because its catalytic reaction (k_{cat} ca. 500 sec^{-1}) is too fast to be captured by conventional techniques. Because multiple FeS clusters of Complex I have broad overlapped and unresolved spectra with low extinction coefficient, it was impossible to follow the redox states of particular clusters in the catalytic cycle of Complex I by means of optical spectroscopy. EPR spectroscopy reveals the individual signals of FeS clusters (see Ohnishi [1998] for a review), therefore, we investigated electron transfer in Complex I from *Escherichia coli* by use of an ultra-fast freeze-quench approach, which allowed us to follow electron distribution in the chain of FeS clusters during the catalytic cycle.

Complex I was purified from aerobically grown bacterial cells, as described in (Sinegina *et al.*, 2005). Because purified Complex I falls apart above pH 6.0, measurements at higher pH values require treating the

enzyme with phospholipids to secure protein stability and activity during the experiment (Sinegina *et al.*, 2005). Finally, the 1.1-ml volume sample containing Complex I at 20 to 24 mg/ml in a buffer consisting of 50 mM MES-NaOH, pH 6.0, 100 mM NaCl, 0.1% *n*-dodecyl β -D-maltoside, 7% sucrose, and 1.7% glycerol (nonactivated Complex I) or 20 mg/ml azolectin, 30 mM MES/NaOH, 70 mM HEPES/KOH, pH 7.5, 70 mM NaCl, 0.19% sodium cholate, 0.1% *n*-dodecyl β -D-maltoside, 7% sucrose, and 1.7% glycerol (activated Complex I) was degassed and saturated with argon in a vacuum/gas line and loaded into the sample syringe. The other syringe was filled with 1.1 ml of a solution containing 200 mM disodium NADH also saturated with argon. A high NADH concentration was required to avoid possible diffusion limitations of the substrate binding. The buffer, which was degassed and saturated with argon, consisted of 50 mM HEPES-Bis tris propane, pH 7.0, 100 mM NaCl, and 0.05% DM. After mixing and obtaining frozen samples by stopping the reaction within a desirable time range, X-band (9.4 GHz) EPR measurements were performed with a Bruker EMX EPR spectrometer, equipped with an Oxford Instruments ESR900 helium flow cryostat with an ITC4 temperature controller. The field modulation frequency was 100 kHz; the modulation amplitude was 1.27 mT. The obtained EPR spectra were normalized for temperature, gain, microwave power, and corrected for baseline.

Mechanical grinding of the frozen protein sample at cryogenic temperatures by silver wheels results in a rise in the artificial radical signal that appears regardless of the redox state of Complex I and can also be observed with other proteins (e.g., when Complex I was replaced with albumin) (Fig. 4.6). It is probable that the signal originates from amino acid radicals formed during cryogenic braking of protein molecules in the presence of oxygen. This proposal is supported by the observation that degassing of all the solutions used for freeze-quench experiments and saturating them with argon strongly decrease this artificial radical signal. When radicals are generated in frozen samples and most probably are not well divided spatially, their dismutation occurs on moderate warming of the sample. Therefore, the other way to diminish artificial signals is annealing the samples by use of the annealing device described previously. A shift from the liquid nitrogen temperature to -80 to 90° resulted in a strong decrease in artificial radical signals (Fig. 4.7). The radicals dismutation was practically accomplished at -60° ; however, at -40 to 50° , the frozen reaction of Complex I reduction started to proceed in a time scale of the order of minutes, indicating that the correct annealing temperature should be optimized for a particular reaction.

An example of the data obtained by freeze-quench on fast reduction of Complex I by NADH is shown in Fig. 4.8. Wild-type and mutated Complex I, R274A, where arginine 274 in NuoCD subunit was substituted for alanine (Belevich *et al.*, 2007), were used for the experiments. Six spectra

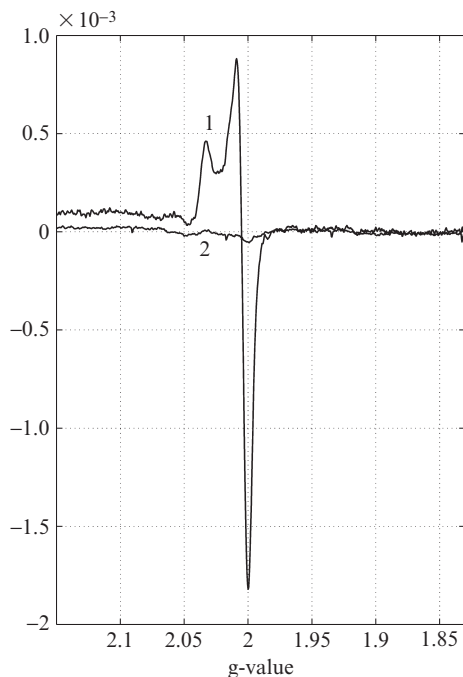


Figure 4.6 The radical spectrum appearing in a frozen albumin sample after cryogenic grinding with silver wheels. 45 K, 2 mW, albumin concentration 20 mg/ml. 1, EPR spectrum of the albumin frozen on the silver wheel and ground; 2, EPR spectrum of the albumin frozen in liquid N_2 .

from the top to the bottom present the redox state of FeS clusters in distinct samples where the reaction was stopped in the time range from 90 μsec to 3 to 8 msec. The last (seventh) spectrum, which is designated by infinite time, was obtained from one of the previous samples that was first melted and then immediately frozen again. On melting, Complex I was fully reduced with NADH. Therefore, the extent of the reduction in the FeS centers in this sample was taken as 100%. Analysis of the obtained spectra allowed the determination of the kinetics of the reduction of the particular centers, which are shown in the bottom row of Fig. 4.8 below the corresponding experimental spectra. Complex I contains two binuclear FeS clusters, N1a and N1b; the reduction of both of these was followed at 45 °K, a temperature at which the tetranuclear clusters do not contribute to the EPR spectra. In Fig. 4.8 only the g_x and g_y components of N1a ($g_{xy} = 1.95, 1.92$) and N1b ($g_{xy} = 1.938, 1.930$) spectra are presented. Similar kinetics of [2Fe-2S] clusters reduction was observed in wild-type and mutated complex I; the N1a cluster was rapidly reduced with a characteristic time close to 100 μsec in wild-type and 200 μsec in R274, meanwhile

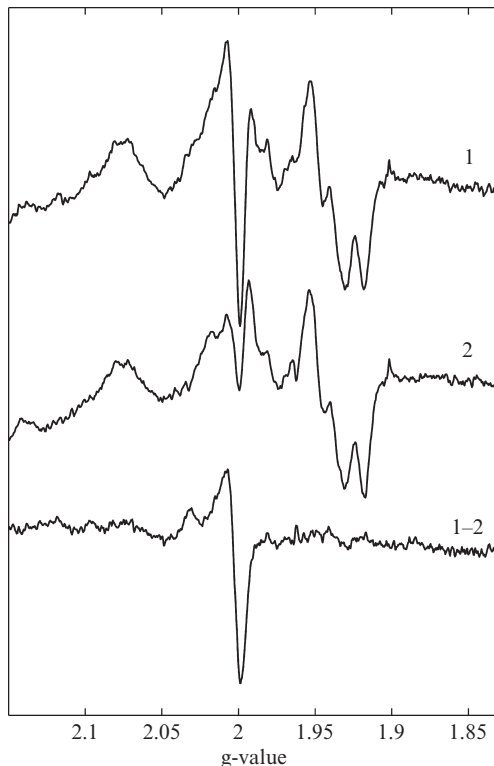


Figure 4.7 Disappearance of the artificial radical on annealing. The reaction of Complex I reduction was stopped at 160 μ sec. The EPR spectra (45 K, 2 mW) of the sample were obtained immediately after the sample preparation at liquid nitrogen temperature (curve 1) and after 20 min incubation at -90° (curve 2). The curve 1-2 showing the difference between two spectra above indicates the decrease in the artificial radical signal; meanwhile the redox state of Complex I (troughs at $g = 1.92$ and 1.93) did not change.

N1b in both cases was reduced much more slowly with a characteristic time slightly over 1 msec. The substitution of basic arginine 274 located in the NuoCD subunit at a distance of 5 Å from the tetranuclear N2 cluster for neutral alanine results in disappearance of the N2 EPR signal caused by either loss of this center (Grgic *et al.*, 2004) or such strong decrease of its midpoint redox potential that it cannot be reduced by NADH (Belevich *et al.*, 2007). The signal of N2 ($g_{xyz} = 1.895, 1.904, 2.045$) is the most prominent signal from all [4Fe-4S] clusters in *E. coli* Complex I; it overlaps these other signals and makes spectra analysis difficult. It is clearly seen from Fig. 4.8, where EPR spectra taken at 10 K and 10 mW are shown (it is mainly fast relaxing tetranuclear clusters that contribute EPR spectrum under these conditions). Again only g_{xy} components are presented. The strong signal of N2 ($g = 1.9$) in wild-type Complex I appearing with a short

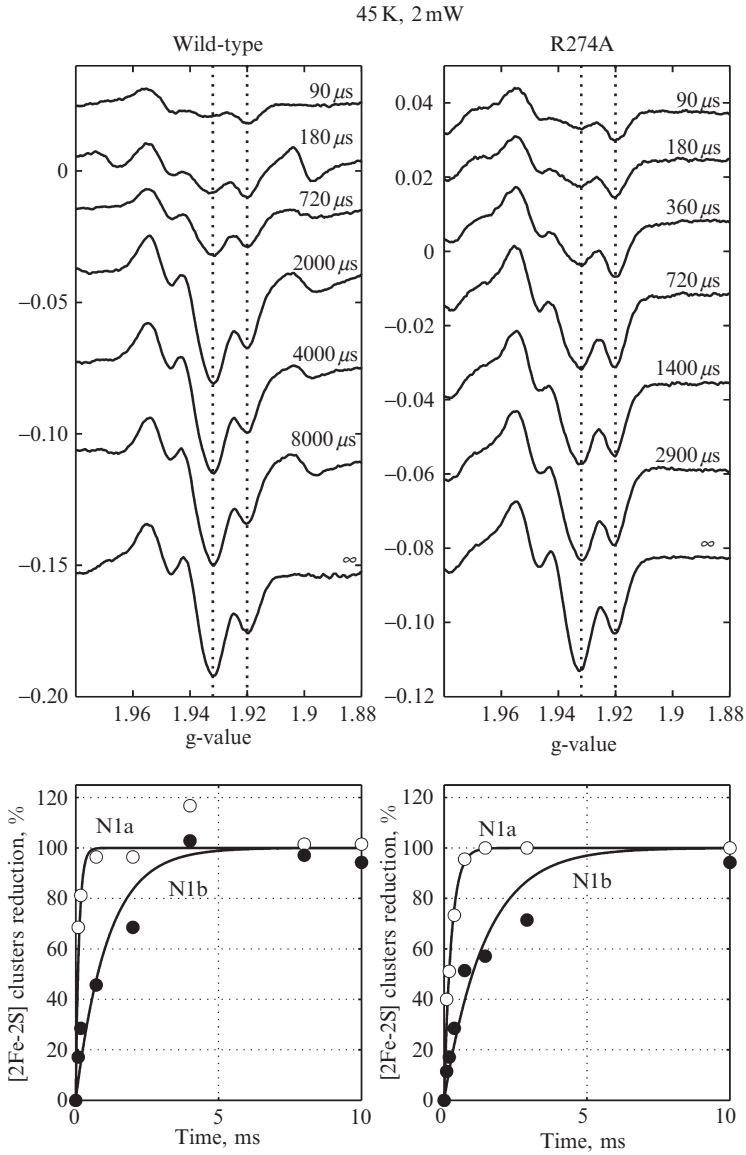


Figure 4.8 (Continued)

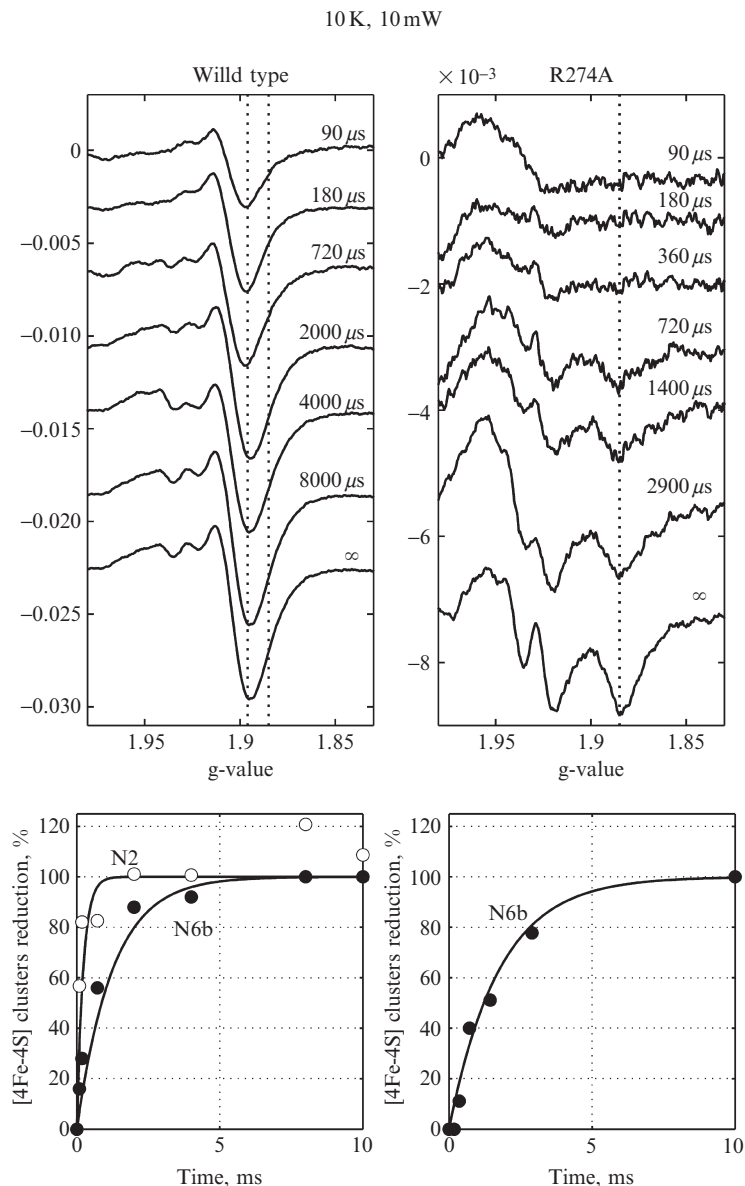


Figure 4.8 The results of freeze-quench experiments on fast reduction of Complex I with NADH. Purified nonactivated wild-type and mutated NuoCD R274A enzymes were used. The EPR spectra from the top to the bottom present the redox state of FeS clusters in distinct samples where the reaction was stopped at the time interval indicated above the curves. The spectrum designated by infinite time was obtained from one of the previous samples melted and immediately frozen again (100% reduction). The EPR spectra at 45 K show the changes in the redox state of only [2Fe-2S] clusters: N1a (trough at $g = 1.932$) and N1b (trough at $g = 1.932$). The EPR spectra at 10 K and 10 mW mainly show the redox state of fast-relaxing [4Fe-4S] clusters: N2 (trough at $g = 1.896$) and N6b (trough at $g = 1.887$). The obtained spectra allow determination of the individual reduction kinetics, which are shown below the corresponding set of spectra.

characteristic time of approximately 100 μ sec covers the relatively broad signal of N6b ($g = 1.887$), the appearance of which could be noticed by only a slight broadening of the entire band and an insignificant shift in the trough, which makes determination of the characteristic time for N6b reduction (2 msec) not fully reliable. In contrast, the spectra of R274 samples lacking an N2 signal clearly show the N6b band, which appears with a trustworthy characteristic time of 2 msec. Determination of the sequence of the redox events in FeS clusters of Complex I allows us to draw important conclusions on the molecular mechanism of this enzyme (Verkhovskaya *et al.*, 2008).

REFERENCES

- Ballou, D. P. (1978). Freeze-quench and chemical-quench techniques. *Methods Enzymol.* **54**, 85–93.
- Belevich, G., Euro, L., Wikström, M., and Verkhovskaya, M. (2007). Role of the conserved arginine 274 and histidine 224 and 228 residues in the NuoCD subunit of complex I from *Escherichia coli*. *Biochemistry* **46**, 526–533.
- Berger, R. L. (1978). Some problems concerning mixers and detectors for stopped flow kinetic studies. *Biophys. J.* **24**, 2–20.
- Bilsel, O., Kayatekin, C., Wallace, L. A., and Matthews, C. R. (2005). A microchannel solution mixer for studying microsecond protein folding reactions. *Rev. Sci. Instrum.* **76**, 014302 (1–7).
- Cherepanov, A. V., and de Vries, S. (2004). Microsecond freeze-hyperquenching: Development of a new ultrafast micro-mixing and sampling technology and application to enzyme catalysis. *Biochim. Biophys. Acta* **1656**, 1–31.
- Galkin, A. S., Grivennikova, V. G., and Vinogradov, A. D. (1999). \rightarrow H⁺/2e⁻ stoichiometry in NADH-quinone reductase reactions catalyzed by bovine heart submitochondrial particles. *FEBS Lett.* **451**, 157–161.
- Grgic, L., Zwicker, K., Kashani-Poor, N., Kerscher, S., and Brandt, U. (2004). Functional significance of conserved histidines and arginines in the 49-kDa subunit of mitochondrial complex I. *J. Biol. Chem.* **279**, 21193–21199.
- Johnson, K. A. (1995). Rapid quench kinetic analysis of polymerases, adenosinetriphosphatases, and enzyme intermediates. *Methods Enzymol.* **249**, 38–61.
- Lin, Y., Gerfen, G. J., Rousseau, D. L., and Yeh, S. R. (2003). Ultrafast microfluidic mixer and freeze-quenching device. *Anal. Chem.* **75**, 5381–5386.
- Ohnishi, T. (1998). Iron-sulfur clusters/semiquinones in complex I. *Biochim. Biophys. Acta* **1364**, 186–206.
- Regenfuss, P., Clegg, R. M., Fulwyler, M. J., Barrantes, F. J., and Jovin, T. M. (1985). Mixing liquids in microseconds. *Rev. Sci. Instrum.* **56**, 283–290.
- Roder, H., Maki, K., Cheng, H., and Shastry, M. C. (2004). Rapid mixing methods for exploring the kinetics of protein folding. *Methods* **34**, 15–27.
- Schuster, R., Kirchner, V. V., Allongue, P., and Ertl, G. (2000). Electrochemical micro-machining. *Science* **289**, 98–101.
- Shastry, M. C., Luck, S. D., and Roder, H. (1998). A continuous-flow capillary mixing method to monitor reactions on the microsecond time scale. *Biophys. J.* **74**, 2714–2721.

- Sinegina, L., Wikström, M., Verkhovsky, M. I., and Verkhovskaya, M. L. (2005). Activation of isolated NADH:ubiquinone reductase I (complex I) from *Escherichia coli* by detergent and phospholipids. Recovery of ubiquinone reductase activity and changes in EPR signals of iron-sulfur clusters. *Biochemistry* **44**, 8500–8506.
- Smith, M. H. (1973). Observations relating to the efficiency of mixing in rapid reaction flow devices. *Biophys. J.* **13**, 817–821.
- Tanaka, M., Matsuura, K., Yoshioka, S., Takahashi, S., Ishimori, K., Hori, H., and Morishima, I. (2003). Activation of hydrogen peroxide in horseradish peroxidase occurs within approximately 200 micros observed by a new freeze-quench device. *Biophys. J.* **84**, 1998–2004.
- Verkhovskaya, M. L., Belevich, N., Euro, L., Wikström, M., and Verkhovsky, M. I. (2008). Real-time electron transfer in respiratory complex I. *Proc. Natl. Acad. Sci. USA* **105**, 3763–3767.
- Wikström, M. (1984). Two protons are pumped from the mitochondrial matrix per electron transferred between NADH and ubiquinone. *FEBS Lett.* **169**, 300–304.

USE OF RUTHENIUM PHOTOOXIDATION TECHNIQUES TO STUDY ELECTRON TRANSFER IN THE CYTOCHROME bc_1 COMPLEX

Francis Millett *and* Bill Durham

Contents

1. Introduction	96
2. Design and Synthesis of Ruthenium-Labeled Proteins	98
2.1. Method for the synthesis of ruthenium-labeled cytochrome <i>c</i>	99
3. Measurement of Interprotein Electron Transfer in a Ruthenium-Labeled Protein	100
4. Measurement of Electron Transfer between Ru ₂ -39-Cc and Cytochrome bc_1	102
5. Measurement of Electron Transfer within the Cytochrome bc_1 Complex	105
Acknowledgments	107
References	107

Abstract

Ruthenium photooxidation methods are presented to study electron transfer between the cytochrome bc_1 complex and cytochrome *c* and within the cytochrome bc_1 complex. Methods are described to prepare a ruthenium cytochrome *c* derivative, Ru₂-39-Cc, by labeling the single sulfhydryl on yeast H39C;C102T iso-1-Cc with the reagent Ru(bpz)₂(4-bromomethyl-4'-methylbipyridine). The ruthenium complex attached to Cys-39 on the opposite side of Cc from the heme crevice does not affect the interaction with cyt bc_1 . Laser excitation of reduced Ru₂-39-Cc results in photooxidation of heme *c* within 1 μ sec with a yield of 20%. Flash photolysis of a 1:1 complex between reduced yeast cytochrome bc_1 and Ru₂-39-Cc leads to electron transfer from heme c_1 to heme *c* with a rate constant of $1.4 \times 10^4 \text{ s}^{-1}$. Methods are described for the use of the ruthenium dimer, Ru₂D, to photooxidize cyt c_1 in the cytochrome bc_1 complex within 1 μ sec with a yield of 20%. Electron transfer from the Rieske iron-sulfur center [2Fe2S] to cyt c_1 was

Department of Chemistry and Biochemistry, University of Arkansas, Fayetteville, Arkansas, USA

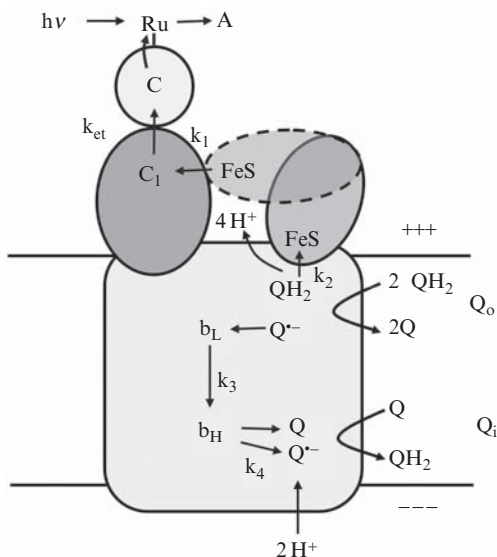
Methods in Enzymology, Volume 456
ISSN 0076-6879, DOI: 10.1016/S0076-6879(08)04405-4

© 2009 Elsevier Inc.
All rights reserved.

detected with a rate constant of $6 \times 10^4 \text{ s}^{-1}$ in *R. sphaeroides* *cyt bc₁* with this method. This electron transfer step is rate-limited by the rotation of the Rieske iron-sulfur protein in a conformational gating mechanism. This method provides critical information on the dynamics of rotation of the iron-sulfur protein (ISP) as it transfers electrons from QH_2 in the Q_o site to *cyt c₁*. These ruthenium photooxidation methods can be used to measure many of the electron transfer reactions in cytochrome *bc₁* complexes from any source.

1. INTRODUCTION

Cytochrome *bc₁* (*cyt bc₁*), an integral membrane protein in the energy-conserving electron transport chains of mitochondria and many prokaryotes, contains two b-type hemes (*b_L* and *b_H*) in the *cyt b* subunit, the Rieske iron-sulfur protein and *cyt c₁* (Trumpower and Gennis, 1994). The complex translocates four protons to the positive side of the membrane per two electrons transferred from ubiquinol to Cc in a widely accepted Q-cycle mechanism (Scheme 5.1) (Trumpower, 1990). A bifurcated electron transfer reaction occurs at the Q_o -site, where the first electron is transferred from ubiquinol to the Rieske iron-sulfur center [2Fe2S] and then to *cyt c₁* and Cc. The second electron is transferred from semiquinone in the Q_o site to *cyt b_L* and then to *cyt b_H* and ubiquinone in the Q_i site. X-ray crystallographic studies have shown that the conformation of the

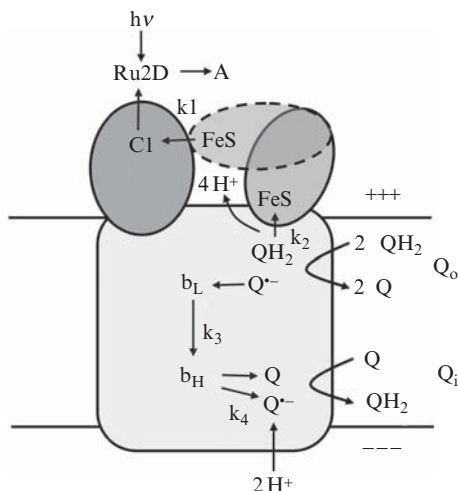


Scheme 5.1

Rieske iron-sulfur protein (ISP) depends on the crystal form and the presence of Q_o site inhibitors (Iwata *et al.*, 1998; Kim *et al.*, 1998; Xia *et al.*, 1997; Zhang *et al.*, 1998). The ISP is in a conformation with [2Fe2S] close to cyt c_1 , called the c_1 state, in native chicken or beef P6522 crystals (Iwata *et al.*, 1998; Zhang *et al.*, 1998). However, the ISP is in a conformation with [2Fe2S] proximal to the cyt b_L heme, called the b state, in beef, chicken, and yeast cyt bc_1 crystals grown in the presence of stigmatellin (Hunte *et al.*, 2000; Iwata *et al.*, 1998; Zhang *et al.*, 1998). A rotational shuttle mechanism has been proposed for the ISP during electron transfer on the basis of these structural studies (Scheme 5.1). QH_2 in the Q_o site transfers an electron to the oxidized [2Fe2S] center when the ISP is initially in the b state. The ISP then rotates by 57° to the c_1 state, and reduced [2Fe2S] transfers an electron to cyt c_1 (Iwata *et al.*, 1998; Zhang *et al.*, 1998). This mobile shuttle mechanism has received support from cross-linking and mutational studies that immobilize the ISP or alter the conformation of the neck region (Darrouzet and Daldal, 2002; Xiao *et al.*, 2000).

Detection of the rapid electron transfer reactions in cytochrome bc_1 has been challenging, and a number of different kinetics techniques have been used. Stopped-flow spectroscopy and rapid-mix/freeze-quench EPR spectroscopy have been used to study the kinetics of reduction of cytochrome bc_1 by QH_2 (Zhu *et al.*, 2007). Extensive kinetic studies have also been carried out in chromatophores of photosynthetic bacteria including *Rhodobacter sphaeroides* and *Rb. capsulatus* (Darrouzet and Daldal, 2002; Hong *et al.*, 1999). Photoexcitation of the photosynthetic reaction center in these systems leads to oxidation of cyt c_2 and reduction of Q to QH_2 .

Our laboratory has developed a new ruthenium photooxidation technique to study electron transfer in cytochrome bc_1 with greater time resolution than previously possible (Millett and Durham, 2002). In one method, a polypyridyl ruthenium complex [Ru(II)] is covalently attached to cytochrome c to form Ru-Cc (Engstrom *et al.*, 2003). Photoexcitation of Ru (II) to the metal-to-ligand charge-transfer state, Ru(II*), a strong oxidant, leads to rapid oxidation of the ferrous heme group in Cc. Subsequent electron transfer from cytochrome c_1 to the Ru-Cc heme can be measured on a time scale as fast as 50 nsec (Scheme 5.1). This new technique has been used to measure intracomplex electron transfer between cytochrome bc_1 and Cc for the first time (Engstrom *et al.*, 2003). In a second method, a new ruthenium dimer has been developed that binds with high affinity to cytochrome bc_1 and can photooxidize cyt c_1 within 1 μ sec (Sadoski *et al.*, 2000). This new technique has been used to measure the rate constant for electron transfer from the iron-sulfur center to cyt c_1 for the first time and provides critical information on the dynamics of rotation of the iron-sulfur protein (ISP) as it transfers electrons from QH_2 in the Q_o site to cyt c_1 (Scheme 5.2).



Scheme 5.2

2. DESIGN AND SYNTHESIS OF RUTHENIUM-LABELED PROTEINS

Several different methods have been developed for covalently attaching a polypyridyl ruthenium complex to a protein. One method involving the attachment of a $\text{Ru}(\text{bpy})_2(\text{dicarboxybipyridine})$ complex to a lysine amino group by an amide linkage has been used to prepare more than 10 different singly labeled Ru-Cc derivatives (Durham *et al.*, 1989). This ruthenium complex is useful for photoreduction of the heme in Ru-Cc, followed by electron transfer from Ru-Cc heme to $\text{cyt } c_1$, which is the reverse direction of physiologic electron transfer. Another method involves the formation of a thioether link between a protein cysteine residue and a ruthenium complex containing a bromomethyl group (Geren *et al.*, 1995). The location of the cysteine residue on the protein can be genetically engineered to address specific questions. All three chelating ligands can be altered to tune the redox potentials over a wide range, allowing measurement of the reorganization energy and optimization of the rate and yield of photo-induced electron transfer (Table 5.1). The $\text{Ru}(\text{bpz})_2(\text{dmb})$ complex can be used to photooxidize the heme in Ru-Cc, allowing the measurement of electron transfer from $\text{cyt } c_1$ to Ru-Cc in the physiologic direction.

Table 5.1 Standard reduction potentials of ruthenium complexes

Complex	(II)/(III)	(II [*])/(III)	(II)/(I)	(II [*])/(I)
Ru(bpy) ₃	1.27	-0.87	-1.31	0.83
Ru(bpy) ₂ (dmb)	1.27	-0.83	-1.36	0.79
Ru(bpz) ₂ (dmb)	1.76	-0.25	-0.79	1.22
Ru(bpd) ₂ (dmb)	1.49	-0.49	-1.00	0.98

The image shows four chemical structures of ligands used in ruthenium complexes. Top left: bpy (2,2'-bipyridine), consisting of two pyridine rings connected at the 2-positions. Top right: dmb (4,4'-dimethyl-2,2'-bipyridine), similar to bpy but with methyl groups at the 4-positions of both rings. Bottom left: bpd (2,2'-bipyridine-5,5'-diimine), where the nitrogen atoms at the 5-positions of the bipyridine core are double-bonded to each other. Bottom right: bpz (2,2'-bipyridine-5,5'-diazole), where the nitrogen atoms at the 5-positions are connected by a double bond and each has a nitrogen atom bonded to it, forming a diazole ring.

2.1. Method for the synthesis of ruthenium-labeled cytochrome *c*

The new brominated Ru(bpz)₂(dmb) reagent can be used to covalently attach a ruthenium complex to a protein containing a single cysteine sulfhydryl group on its surface (Engstrom *et al.*, 2003). To label yeast Cc, the single Cys-102 in wild-type yeast iso-1-Cc is first mutated to Thr, and then His-39 is mutated to Cys to form H39C;C102T yeast iso-1-Cc. The H39C;C102T yeast iso-1-Cc is first treated with a twofold excess of dithiothreitol for 15 min under anaerobic conditions to reduce any disulfide dimers that may have formed; 1.8 mM Ru(bpz)₂(4-bromomethyl-4'-methylbipyridine) is then added to the solution containing 530 μM H39C;C102T yeast iso-1-Cc and 260 μM dithiothreitol in 50 mM sodium borate, pH 9.0, under anaerobic conditions and allowed to react for 3 h at 37°. Amicon concentrators are used to exchange the reaction mixture into 5 mM sodium phosphate, pH 7.0, and remove excess reagent. The Ru_z-39-Cc derivative is purified by use of a high-resolution Waters 1 × 10 cm Sp 8HR cation exchange column in a Waters 625 HPLC (30). Usually there is a single major band containing Ru_z-39-Cc, a smaller band of unlabeled Cc, and several small bands of derivatives labeled at lysines. It is important to determine that the derivative is singly labeled with ruthenium. The UV/visible spectrum of the Ru_z-39-Cc band should be the sum of the spectra of one equivalent of Ru(bpz)₂(dmb) and one equivalent of native yeast iso-1-Cc. The yield of Ru_z-39-Cc is typically 70%, provided that fresh reagent is used under anaerobic conditions. Another important

step in the characterization of the derivative is to confirm the location of the ruthenium complex at Cys-39 by tryptic digestion, HPLC separation of the resulting peptides, and sequencing the ruthenium-labeled peptide (Engstrom *et al.*, 2003). Finally, steady-state kinetics is used to determine that yeast Ru₂-39-Cc has the same steady-state activity with yeast cytochrome *bc*₁ as wild-type yeast Cc. This important characterization provides evidence that the ruthenium complex has no effect on the interaction with cyt *bc*₁.

3. MEASUREMENT OF INTERPROTEIN ELECTRON TRANSFER IN A RUTHENIUM-LABELED PROTEIN

Flash photolysis methods are used to measure internal electron transfer between the ruthenium complex and the heme in a ruthenium-labeled protein (Engstrom *et al.*, 2003). The third harmonic of a Nd:YAG laser, with a pulse width of 20 nsec and wavelength of 356 nm is used for the excitation pulse, the probe source is a pulsed 75-W xenon arc lamp, and the photomultiplier detector has a response time of 10 nsec. Photoexcitation of Ru(II) in 5 μ M reduced yeast Ru₂-39-Cc under anaerobic conditions leads to electron transfer from Fe(II) to Ru(II*) to form Ru(I) and Fe(III) (Fig. 5.1A). The oxidation of Fe(II) is detected at 550 nm and the reduction of Ru(II*) is detected at 434 nm, an isobestic for the Cc heme. The back reaction from Ru(I) to Fe(III) is observed with a rate constant of $k_4 = 7000 \pm 1000 \text{ s}^{-1}$ (Fig. 5.1B). The kinetics are fit to Scheme 5.3 with $k_3 = (1.5 \pm 0.2) \times 10^6 \text{ s}^{-1}$, $k_4 = 7000 \pm 1000 \text{ s}^{-1}$, and $k_d = (3.5 \pm 0.6) \times 10^6 \text{ s}^{-1}$ (Engstrom *et al.*, 2003). The back electron transfer reaction from Ru(I) to Fe(III) is prevented by aerating the solution (Fig. 5.1B), indicating that Ru(I) was oxidized by oxygen in the solution. $[\text{Co}(\text{NH}_3)_5\text{Cl}]^{2+}$ can also be used to irreversibly oxidize Ru(I), preventing the back reaction under anaerobic conditions.

The yeast Ru₂-39-Cc derivative is optimized to study electron transfer with the cyt *bc*₁ complex in the physiologic direction. The ruthenium complex attached to Cys-39 on the opposite side of Cc from the heme crevice does not affect the interaction with cyt *bc*₁. The distance between the heme and the ruthenium complex is 12.6 Å, and there is an electron transfer pathway consisting of 13 covalent bonds and one hydrogen bond. The Ru(bpz)₂(dmb) complex has a reduction potential of 1.22 V for the Ru(II*)/Ru(I) transition (Table I), providing a driving force $\Delta G^{o'}$ of -1.0 V for the Ru(II*)-Fe(II)→Ru(I)-Fe(III) reaction. The value of $\Delta G^{o'}$ is thus nearly the same as the reorganization energy λ of 0.8 V providing an optimal electron transfer rate. The rate constant for the forward reaction k_3 is very large, $k_3 = 1.5 \times 10^6 \text{ s}^{-1}$, whereas the back electron transfer reaction from

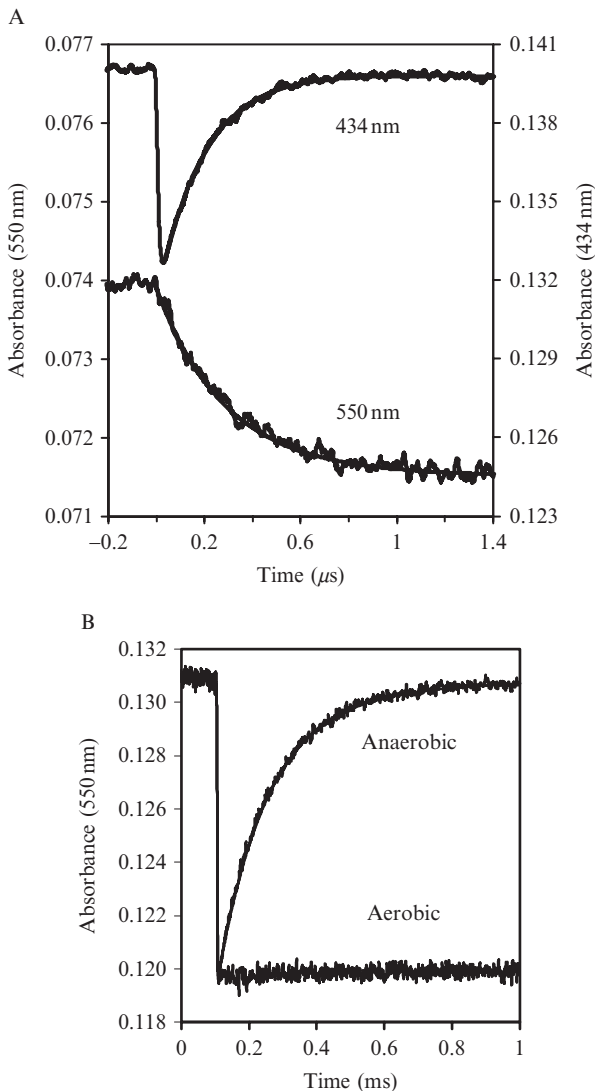
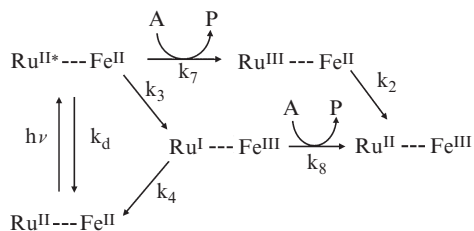


Figure 5.1 Photoinduced electron transfer within yeast $\text{Ru}_z\text{-39-Cc}$. (A) A solution of reduced $5 \mu\text{M}$ $\text{Ru}_z\text{-39-Cc}$ in 5 mM sodium phosphate, pH 7.0, was photoexcited with a 356 nm Nd:YAG laser flash, and the absorbance at 434 nm and 550 nm was monitored. (B) The same sample as in A at a longer time scale in the presence and absence of atmospheric oxygen.

Ru(I) to Fe(III) is quite slow, with a rate constant of $k_4 = 7000 \text{ s}^{-1}$. The yield of photooxidized heme c is quite large, 20% in a single flash, which is important for the electron transfer studies with $\text{cyt } bc_1$.



Scheme 5.3

4. MEASUREMENT OF ELECTRON TRANSFER BETWEEN $\text{Ru}_z\text{-39-Cc}$ AND CYTOCHROME bc_1

Flash photolysis is used to study electron transfer from cyt c_1 in the yeast cyt bc_1 complex to $\text{Ru}_z\text{-39-Cc}$ in the forward, physiological direction (Engstrom *et al.*, 2003). A Phase R model DL1400 flash lamp-pumped dye laser emitting a 480 nm light flash of $<0.5 \mu\text{sec}$ duration is used as the excitation source. The reactions are studied in 300- μl samples containing 3 to 6 μM cyt bc_1 , 3-10 μM $\text{Ru}_z\text{-39-Cc}$, 0.01% lauryl maltoside in 5 mM sodium phosphate, pH 7.0, and 0 to 800 mM NaCl. Cyt c_1 and $\text{Ru}_z\text{-39-Cc}$ are reduced with 10 μM sodium ascorbate and 2 μM TMPD. The reaction is first studied at high ionic strength where there is no stable complex between $\text{Ru}_z\text{-39-Cc}$ and cyt bc_1 . Flash photolysis of 5.2 μM reduced yeast cyt bc_1 and yeast $\text{Ru}_z\text{-39-Cc}$ in 260 mM ionic strength buffer leads to a decrease in the 550 nm absorbance, indicating rapid photooxidation of heme c Fe(II) by Ru(II*) in $\text{Ru}_z\text{-39-Cc}$ (Fig. 5.2). This is followed by an exponential increase in the 550 nm absorbance and decrease in the 557 nm absorbance with a rate constant of $3900 \pm 600 \text{ s}^{-1}$, indicating electron transfer from cyt c_1 Fe(II) to heme Fe(III) in $\text{Ru}_z\text{-39-Cc}$ (Fig. 5.2). 557 nm is an isobestic point for Cc, allowing observation of the oxidation of cyt c_1 . The very small difference between the absorbance spectra of cyt c_1 and Cc makes detection of the reaction between them difficult. The rate constant increased linearly with the concentration of cyt bc_1 , indicating a bimolecular reaction between solution $\text{Ru}_z\text{-39-Cc}$ and solution cyt bc_1 with a second order rate constant of $8.9 \times 10^8 \text{ M}^{-1}\text{s}^{-1}$. Therefore, at the high ionic strength of 260 mM, there is no tight complex between $\text{Ru}_z\text{-39-Cc}$ and cyt bc_1 .

To study intracomplex electron transfer, flash photolysis is carried out on a stable 1:1 complex of 5.2 μM yeast $\text{Ru}_z\text{-39-Cc}$ and 5.2 μM yeast cyt bc_1 in low 5-mM ionic strength buffer. The rate constant for electron transfer from cyt c_1 to $\text{Ru}_z\text{-39-Cc}$, $14,000 \pm 3000 \text{ s}^{-1}$, is independent of protein

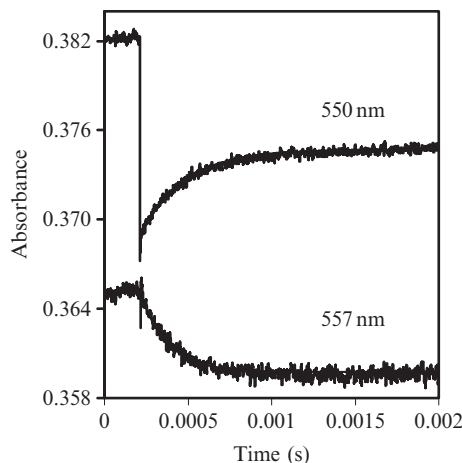
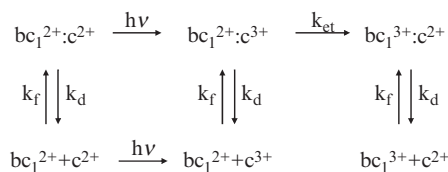


Figure 5.2 Photoinduced electron transfer between yeast Ru-39-Cc and yeast $cyt\ bc_1$. A solution containing reduced $5.2\ \mu M$ yeast Ru_z-39-Cc and yeast $cyt\ bc_1$ in $5\ mM$ sodium phosphate, pH 7.0, $250\ mM$ NaCl, and 0.1% lauryl maltoside was photoexcited with a 480-nm laser flash. The 550-nm transient shows Cc photooxidation and reduction, whereas the 557-nm transient shows $cyt\ c_1$ oxidation.



Scheme 5.4

concentration, indicating intracomplex electron transfer according to the top line of [Scheme 5.4](#). The rate constant of this fast, intracomplex phase of electron transfer does not change as the ionic strength is increased to $110\ mM$ ([Fig. 5.3](#)). However, the amplitude of the intracomplex phase decreases to 60%, and a new slow phase appears with an amplitude of 40% and a rate constant of $2500\ s^{-1}$. These results indicate that the complex begins to dissociate at $110\ mM$ ionic strength, and the slow phase is due to bimolecular reaction between solution Ru_z-39-Cc and $cyt\ bc_1$. An equilibrium constant of $K_d = 0.85\ \mu M$ can be calculated from the relative amplitudes of the intracomplex and bimolecular phases. Because both intracomplex and bimolecular phases are present at $110\ mM$ ionic strength, the bimolecular reaction involves formation of a 1:1 complex followed

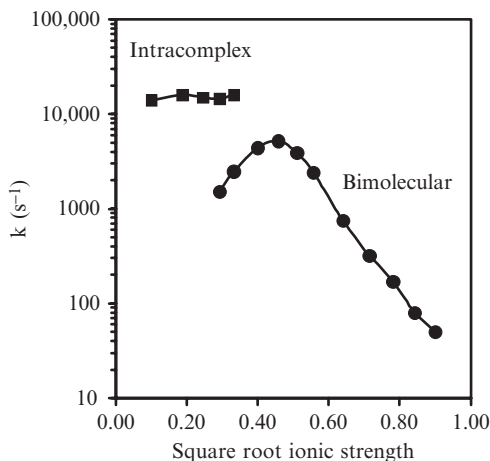


Figure 5.3 Ionic strength dependence of photoinduced electron transfer between yeast Ru_z-39-Cc and yeast cyt *bc*₁. The reaction was measured under the same conditions as in Fig. 5.3 with 0 to 800 mM NaCl.

by intracomplex electron transfer according to Scheme 5.4 with $k_d \ll k_{et}$. The observed bimolecular phase rate constant is given by Eq. 5.1:

$$k_{\text{obs}} = k_f \left(E_o - \frac{1}{2} \left(k_d/k_f + E_o + C_o - \left((k_d/k_f + E_o + C_o)^2 - 4E_o C_o \right)^{1/2} \right) \right) \quad (5.1)$$

where E_o is the concentration of cyt *bc*₁ and C_o is the concentration of Ru_z-39-Cc (Engstrom *et al.*, 2003). The formation and dissociation rate constants from this equation are $k_f = 2.0 \times 10^9 \text{ s}^{-1}$ and $k_d = 1.7 \times 10^3 \text{ s}^{-1}$, by use of the relation $K_d = k_d/k_f$. The rate constant k_{obs} increases to a maximum of 5200 s^{-1} as the ionic strength is increased to 200 mM, and the fast intracomplex phase disappears, indicating complex dissociation (Fig. 5.3). Assuming rapid equilibrium conditions apply to Scheme 5.4, the second-order rate constant is given by Eq. 5.2:

$$k_{2\text{nd}} = k_f k_{et} / (k_d + k_{et}) \quad (5.2)$$

The second-order rate constant decreases with increasing ionic strength above 250 mM, indicating a reaction between oppositely charged proteins (Fig. 5.3). Because k_{et} remained unchanged from 5 to 100 mM ionic strength, it is likely that it also remains constant at higher ionic strength. The decrease in $k_{2\text{nd}}$ with increasing ionic strength is, therefore, most likely due to a decrease in k_f and an increase in k_d . The results indicate that the

mechanism occurs according to [Scheme 5.4](#) at all ionic strengths. At low ionic strength electron transfer takes place within a preformed complex according to the top line of [Scheme 5.4](#), whereas at high ionic strength uncomplexed Ru_z -39-Cc must first bind to $cyt\ bc_1$ before intracomplex electron transfer can take place.

5. MEASUREMENT OF ELECTRON TRANSFER WITHIN THE CYTOCHROME bc_1 COMPLEX

To understand the mechanism of bifurcated electron transfer in $cyt\ bc_1$, it is important to determine the kinetics of each step in the reaction, as well as structural linkages between the conformation of the Q_o site and the conformation and dynamics of the Rieske iron-sulfur protein (ISP). We have developed a new ruthenium technique to measure electron transfer between the ISP and $cyt\ c_1$ for the first time ([Engstrom et al., 2002](#); [Sadoski et al., 2000](#); [Xiao et al., 2003](#)). The binuclear ruthenium complex Ru_2D has a charge of 4+, which allows it to bind with high affinity to the negatively charged binding domain on the surface of $cyt\ c_1$ as a surrogate for Cc ([Scheme 5.2](#)). To study electron transfer in the forward direction, the ruthenium dimer Ru_2D is used to rapidly photooxidize $cyt\ c_1$ in a solution containing 5 μM *Rsp. cyt bc₁* with $cyt\ c_1$ and [2Fe2S] initially reduced with QH_2 , and $cyt\ b_L$ and $cyt\ b_H$ oxidized ([Fig. 5.4](#)). The metal-to-ligand charge-transfer excited state of Ru_2D is a strong oxidant, and oxidizes $cyt\ c_1$ within 1 μsec as indicated by the decrease in absorbance at 552 nm. A sacrificial electron acceptor A must be present in the solution to oxidize Ru^{II*} and/or Ru^I according to the mechanism shown in [Scheme 5.3](#). The photooxidation of $cyt\ c_1$ Fe(II) may involve either the top or bottom pathway of [Scheme 5.3](#). The sacrificial electron acceptor $[Co(NH_3)_5Cl]^{2-}$ rapidly decomposes after reduction, providing an irreversible reaction that is advantageous. The sacrificial electron acceptor paraquat is used in aerobic buffer, because photoreduced paraquat is rapidly oxidized by oxygen. Concentration dependence studies have indicated that Ru_2D binds to $cyt\ bc_1$ with a dissociation constant of approximately 10 μM , so Ru_2D concentrations of 20 μM are adequate for efficient photooxidation of $cyt\ c_1$ with a yield of 20% in a single flash.

After rapid photooxidation by Ru_2D , $cyt\ c_1$ in *Rsp. cyt bc₁* is subsequently reduced in a biphasic reaction with rate constants of $k_1 = 60,000\ s^{-1}$ and $k_2 = 2300\ s^{-1}$, as indicated by the increase in absorbance at 552 nm ([Fig. 5.4](#), top trace). The fast phase k_1 is assigned to direct electron transfer from [2Fe2S] to $cyt\ c_1$, because it is inhibited by stigmatellin, which locks the ISP in the b position near the Q_o site ([Sadoski et al., 2000](#)). The slow phase of reduction of $cyt\ c_1$ has the same rate constant as the reduction of $cyt\ b_H$

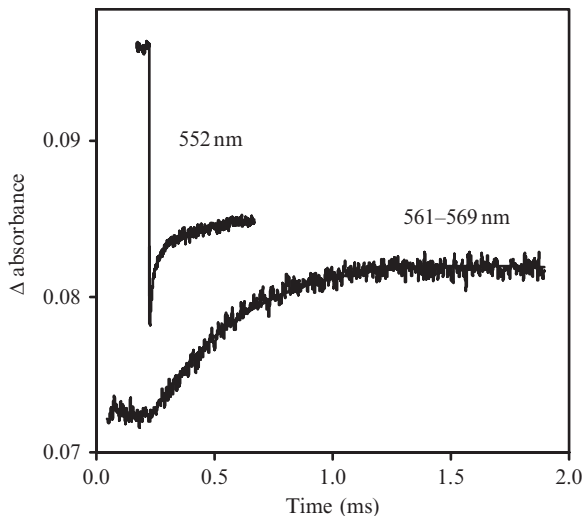


Figure 5.4 Photoinduced electron transfer within wild-type *R. sphaeroides* *cyt bc*₁. A sample containing 5 μM *cyt bc*₁, 20 μM Ru_2D , 5 mM $[\text{Co}(\text{NH}_3)_5\text{Cl}]^{2+}$, in 20 mM sodium borate, pH 9.0, with 0.01% dodecylmaltoside was treated with 10 μM $\text{Q}_\circ\text{C}_{10}\text{BrH}_2$, 1 mM succinate, and 50 nM SCR to reduce $[\text{2Fe2S}]$ and *cyt c*₁, and reduce *cyt b*_H by approximately 30%. Excitation of Ru_2D with 480-nm laser flash led to photo-oxidation of *cyt c*₁ within 1 μs , followed by reduction in a biphasic reaction with rate constants of 60,000 s^{-1} and 2000 s^{-1} as shown in the 552-nm transient. The 561 to 569 nm transient shows reduction of *cyt b*_H with a rate constant of 2300 s^{-1} .

observed in the 561 to 569 nm difference transient (Fig. 5.4, bottom trace). These results indicate rate-limiting electron transfer from QH_2 to $[\text{2Fe2S}]$ with rate constant k_2 followed by rapid electron transfer from $[\text{2Fe2S}]$ to *cyt c*₁, and from the semiquinone to *cyt b*_L and *cyt b*_H (Scheme 5.2). Electron transfer from the semiquinone to *cyt b*_L is very fast and has never been detected, whereas the rate constant for electron transfer from *cyt b*_L to *cyt b*_H is approximately $1 \times 10^4 \text{ s}^{-1}$ (Shinkarev *et al.*, 2001). One of the advantages of the ruthenium method is that it can be applied to *cyt bc*₁ from any organism. The rate constants for electron transfer in bovine *cyt bc*₁ have been found to be $k_1 = 16,000 \text{ s}^{-1}$ and $k_2 = 250 \text{ s}^{-1}$ (Sakoski *et al.*, 2000).

An important question about the mechanism of *cyt bc*₁ is whether the fast phase of electron transfer from $[\text{2Fe2S}]$ to *cyt c*₁ is rate-limited by pure electron transfer or instead by the rate of rotation of the ISP from the *b* position to the *c*₁ position in a conformational gating process. The best way to test this is to vary the driving force of the reaction, which depends on the difference in redox potentials of $[\text{2Fe2S}]$ and *cyt c*₁. If k_1 is rate-limited by true electron transfer from $[\text{2Fe2S}]$ to *cyt c*₁, then Marcus theory would predict a large dependence on the driving force of the reaction. As an example, it was found that the rate constant was not affected by the ISP

mutations Y156W, S154A, or Y156F/S154A that decrease the redox potential of [2Fe2S] by 62 mV, 109 mV, and 159 mV, respectively (Engstrom *et al.*, 2002). This experiment provides evidence that the reaction is not rate-limited by electron transfer, because Marcus theory predicts that the increase in the driving force of the reaction for these mutants would increase the rate constant by up to 15-fold. It, therefore, seems that the rate constant k_1 for electron transfer from [2Fe2S] to cyt c_1 is rate limited by the rotation of the ISP from the b state to the c_1 state (Scheme 5.2).

Ruthenium kinetics studies of the effects of Q_o site inhibitors on electron transfer in cyt bc_1 have revealed a crucial linkage between the conformations of the Q_o site and the ISP (Xiao *et al.*, 2003). The Q_o site inhibitors stigmatellin and famoxadone have many similarities to the natural ubiquinol substrate and lead to conformational changes in the Q_o pocket that stabilize the ISP in the b state. X-ray crystallographic studies have shown that both inhibitors displace the cd1 helix and the PEWY sequence in the ef helix outward to expand the Q_o pocket (Esser *et al.*, 2006). These changes in the Q_o pocket are relayed to the surface of cyt b to form a docking crater that captures the ISP in the b -state conformation. Stigmatellin forms a hydrogen bond with the His-161 ligand of the reduced [2Fe2S] center, thereby increasing its redox potential by 250 mV and immobilizing the ISP in the b conformation (Iwata *et al.*, 1998; Zhang *et al.*, 1998). Famoxadone binds somewhat deeper in the Q_o pocket than stigmatellin, does not contact the ISP or form a hydrogen bond with His-161, and only increases the redox potential of [2Fe2S] by 30 mV (Gao *et al.*, 2002). Famoxadone binding to *Rsp.* cyt bc_1 decreases the rate of forward electron transfer from [2Fe2S] to cyt c_1 from 60,000 s^{-1} to 4800 s^{-1} (Xiao *et al.*, 2003). This indicates that famoxadone does not completely lock the ISP in the b state, but instead decreases the rate of release of the ISP from the b state to the c_1 state to 4800 s^{-1} . The linkage between the conformation of the Q_o site and the conformation and dynamics of the ISP could be a key to how the enzyme promotes bifurcated electron transfer from QH_2 to [2Fe2S] and cyt b_L and minimizes short-circuit reactions such as delivery of both electrons to the ISP.

ACKNOWLEDGMENTS

This work was supported in part by NIH grants GM20488 and NCCR COBRE 1 P20 RR15569.

REFERENCES

- Darrouzet, E., and Daldal, F. (2002). Movement of the iron-sulfur subunit beyond the *ef* loop of cytochrome *b* is required for multiple turnovers of the bc_1 complex but not for a single turnover Q_o site catalysis. *J. Biol. Chem.* **277**, 3471–3476.

- Durham, B., Pan, L. P., Long, J., and Millett, F. (1989). Photoinduced electron-transfer kinetics of singly labeled ruthenium bis-(bipyridine) dicarboxybipyridine cytochrome *c* derivatives. *Biochemistry* **28**, 8659–8665.
- Engstrom, G., Xiao, K., Yu, C.-A., Yu, L., Durham, B., and Millett, F. (2002). Photoinduced electron transfer between the Rieske iron-sulfur protein and cytochrome *c*(1) in the *Rhodobacter sphaeroides* cytochrome *bc*(1) complex. Effects of pH, temperature, and driving force. *J. Biol. Chem.* **277**, 31072–31078.
- Engstrom, G., Rajagukguk, R., Saunders, A. J., Patel, C. N., Rajagukguk, S., Merbitz-Zahradnik, T., Xiao, K., Pielak, G. J., Trumpower, B., Yu, C. A., Yu, L., Durham, B., et al. (2003). Design of a ruthenium-labeled cytochrome *c* derivative to study electron transfer with the cytochrome *bc*₁ complex. *Biochemistry* **42**, 2816–2824.
- Esser, L., Gong, X., Yang, S., Yu, L., Yu, C.-A., and Xia, D. (2006). Surface-modulated motion switch: Capture and release of iron-sulfur protein in the cytochrome *bc*₁ complex. *Proc. Nat. Acad. Sci. USA* **103**, 13045–13050.
- Gao, X., Wen, X., Yu, C.-A., Esser, L., Tsao, S., Quinn, B., Zhang, L., Yu, L., and Xia, D. (2002). The crystal structure of mitochondrial cytochrome *bc*₁ in complex with famoxadone: The role of aromatic-aromatic interaction in inhibition. *Biochemistry* **41**, 11692–11702.
- Geren, L. M., Beasley, J. R., Fines, B. R., Saunders, A. J., Hibdon, S., Pielak, G. J., Durham, B., and Millett, F. (1995). Design of a ruthenium-cytochrome *c* derivative to measure the electron transfer to the initial acceptor in cytochrome *c* oxidase. *J. Biol. Chem.* **270**, 2466.
- Hong, S., Ugulava, N., Guergova-Kuras, M., and Crofts, A. R. (1999). The energy landscape for ubiquinone oxidation at the Q_o site of the *bc*₁ complex in *R. sphaeroides*. *J. Biol. Chem.* **274**, 33931–33944.
- Hunte, C., Koepke, J., Lange, C., Rossmann, T., and Michel, H. (2000). Structure at 2.3 Å resolution of the cytochrome *bc*(1) complex from the yeast *Saccharomyces cerevisiae* co-crystallized with an antibody Fv fragment. *Struct. Fold Des.* **8**, 669–684.
- Iwata, S., Lee, J. W., Okada, K., Lee, J. K., Wata, M., Rasmussen, B., Link, T. A., Ramaswamy, S., and Jap, B. K. (1998). Complete structure of the 11-subunit bovine mitochondrial cytochrome *bc*₁ complex. *Science* **281**, 64–71.
- Kim, H., Xia, D., Yu, C.-A., Xia, J.-Z., Kachurin, A. M., Zhang, L., Yu, L., and Deisenhofer, J. (1998). Inhibitor binding changes domain mobility in the iron-sulfur protein of the mitochondrial *bc*₁ complex from bovine heart. *Proc. Natl. Acad. Sci. USA* **95**, 8026–8033.
- Lange, C., and Hunte, C. (2002). Crystal structure of the yeast cytochrome *bc*₁ complex with its bound substrate cytochrome *c*. *Proc. Nat. Acad. Sci. USA* **99**, 2800–2805.
- Millett, F., and Durham, B. (2002). Design of photoactive ruthenium complexes to study interprotein electron transfer. *Biochemistry* **41**, 11315–11324.
- Sadoski, R. C., Engstrom, G., Tian, H., Zhang, L., Yu, C.-A., Yu, L., Durham, B., and Millett, F. (2000). Use of a photoactivated ruthenium dimer complex to measure electron transfer between the Rieske iron-sulfur protein and cytochrome *c*1 in the cytochrome *bc*₁ complex. *Biochemistry* **39**, 4231–4236.
- Shinkarev, V. P., Crofts, A. R., and Wraight, C. A. (2001). The electric field generated by photosynthetic reaction center induces rapid reversed electron transfer in the *bc*₁ complex. *Biochemistry* **40**, 12584–12590.
- Trumpower, B. L. (1990). The protonmotive Q cycle. Energy transduction by coupling of proton translocation to electron transfer by the cytochrome *bc*₁ complex. *J. Biol. Chem.* **265**, 11409–11412.
- Trumpower, B. L., and Gennis, R. B. (1994). Energy transduction by cytochrome complexes in mitochondrial and bacterial respiration: The enzymology of coupling electron

- transfer reactions to transmembrane proton translocation. *Annu. Rev. Biochem.* **63**, 675–716.
- Xia, D., Yu, C.-A., Kim, H., Xia, J.-Z., Kachurin, A. M., Zhang, L., Yu, L., and Deisenhofer, J. (1997). Crystal structure of the cytochrome bc_1 complex from bovine heart mitochondria. *Science* **277**, 60–66.
- Xiao, K., Yu, L., and Yu, C.-A. (2000). Confirmation of the involvement of protein domain movement during the catalytic cycle of the cytochrome bc_1 complex by the formation of an intersubunit disulfide bond between cytochrome b and the iron-sulfur protein. *J. Biol. Chem.* **275**, 38597–38604.
- Xiao, K., Engstrom, G., Rajagukguk, S., Yu, C.-A., Yu, L., Durham, B., and Millett, F. (2003). Effect of famoxadone on photoinduced electron transfer between the iron-sulfur center and cytochrome c_1 in the cytochrome bc_1 complex. *J. Biol. Chem.* **278**, 11419–11426.
- Zhang, Z., Huang, L., Shulmeister, V. M., Chi, Y.-I., Kim, K. K., Hung, L.-W., Crofts, A. R., Berry, E. A., and Kim, S.-H. (1998). Electron transfer by domain movement in cytochrome bc_1 . *Nature* **392**, 677–684.
- Zhu, J., Egawa, T., Yeh, S.-R., Yu, L., and Yu, C.-A. (2007). Simultaneous reduction of iron-sulfur protein and cytochrome b_l during ubiquinol oxidation in cytochrome bc_1 complex. *Proc. Nat. Acad. Sci. USA* **104**, 4864–4869.

MASS SPECTROMETRIC CHARACTERIZATION OF THE THIRTEEN SUBUNITS OF BOVINE RESPIRATORY COMPLEXES THAT ARE ENCODED IN MITOCHONDRIAL DNA

John E. Walker, Joe Carroll, Matthew C. Altman,
and Ian M. Fearnley

Contents

1. Introduction	112
2. Analysis of Mitochondrial Membranes for mt-Proteins	115
2.1. Extraction of proteins from mitochondria	115
3. Analysis of Respiratory Complexes for mt-Proteins	117
3.1. Isolation of respiratory complexes	117
3.2. CMW extraction of respiratory complexes	118
3.3. Fractionation of the CMW extracts of respiratory complexes	119
3.4. HILIC fractionation of the PAHW extract of complex I	119
4. Mass Spectrometric Analysis of mt-Proteins	120
4.1. Protein molecular mass measurements	120
4.2. Tandem MS of protein ions	123
5. Conclusions and Perspectives	125
References	128

Abstract

The genomes of mammalian mitochondria encode 13 hydrophobic membrane proteins. All of them are subunits of the respiratory complexes found in the inner membranes of the organelle. Although the sequences of human and bovine mitochondrial DNA were described in 1981 and 1982, respectively, and the encoded proteins were identified at the same time or soon after, because of their hydrophobic properties, the chemical compositions of some of these proteins have never been characterized. Therefore, we have developed procedures to extract them with organic solvents from the inner membranes of bovine mitochondria and from purified respiratory complexes and to fractionate the

The Medical Research Council Mitochondrial Biology Unit, Cambridge, United Kingdom

Methods in Enzymology, Volume 456
ISSN 0076-6879, DOI: 10.1016/S0076-6879(08)04406-6

© 2009 Elsevier Inc.
All rights reserved.

extracts, allowing the precise molecular masses of all 13 proteins to be measured by electrospray ionization mass spectrometry. It was found that, with one exception, the proteins retain their translational initiator formyl-methionine residues, and the only posttranslational modification detected was the removal of the formyl group or the formyl-methionine from the Cox III protein. These procedures can be adapted for analyzing the proteins encoded in mitochondrial DNAs in other species, for analyzing the subunit compositions of their respiratory complexes, and for establishing accurate and comprehensive proteomes of other cellular membranes. Because many membrane proteins have few proteolytic enzyme cleavage sites, identifying them by mass spectrometric sequencing of proteolytic peptides can be difficult. Therefore, we have studied the tandem mass spectra of fragment ions from a range of membrane proteins from mitochondria, including 10 of the 13 proteins encoded in mitochondrial DNA. In contrast to the highly complex spectra produced in this way by globular proteins, the spectra of membrane proteins are simple and easy to interpret, and so they provide sequence tags for the identification of membrane proteins.

1. INTRODUCTION

The respiratory complexes found in the inner membranes of mammalian mitochondria are multi-subunit assemblies of proteins originating from two sources. Most of the proteins are encoded in nuclear DNA, synthesized on cytoplasmic ribosomes, and imported into the organelle. Here, together with the 13 proteins that are encoded in mitochondrial DNA (Anderson *et al.*, 1981, 1982) and synthesized inside the organelle, they are assembled into the respiratory complexes. These 13 mitochondrially encoded proteins (referred to in the following as the mt-proteins) are all hydrophobic (see Table 6.1), and they are embedded in the inner membrane. Seven of them, subunits ND1-ND6 and ND4L, contribute approximately 60 transmembrane α -helices (TMH; Table 6.1) to the membrane arm of complex I (NADH: ubiquinone oxidoreductase), an L-shaped complex of 45 proteins in bovine mitochondria (Carroll *et al.*, 2006a). Three of them, subunits Cox I, Cox II, and Cox III, provide the catalytic core of complex IV (cytochrome *c* oxidoreductase), a complex of 13 subunits in mammals (Tsukihara *et al.*, 1996). Cytochrome *b*, the only one of the 11 subunits of complex III (cytochrome *c* ubiquinol oxidoreductase) encoded in mitochondrial DNA, is an essential component of the enzyme (Iwata *et al.*, 1998). Subunits a (ATPase-6) and A6L (ATPase-8), two of the 16 or 18 different proteins of the ATP synthase complex (the precise composition depends on the method of purification; Chen *et al.* [2006]) are encoded in the mitochondrial genome, and they form part of the F_0 proton-translocating domain of the enzyme (Fearnley and Walker, 1986).

Table 6.1 Properties of bovine mt-proteins

Protein ^a	Mass (Da) ^b	pI ^c	GRAVY ^c	TMH ^d	Tryptic peptides ^e	
					No. Peptides	Coverage (%)
CI ND1	35670.2	7.8	0.798	8	7	34.3
CI ND2	39254.4	10.0	0.785	10	7	36.0
CI ND3	13054.7	4.5	0.863	3	1	13.0
CI ND4L	10797.3	5.3	1.259	2	1	23.5
CI ND4	52099.4	9.4	0.826	13	7	20.9
CI ND5	68286.8	9.2	0.637	18	14	35.5
CI ND6	19077.7	4.2	1.031	5	1	12.6
CIII Cyt b	42590.8	7.8	0.680	8	4	16.6
Cox I	57032.5	6.1	0.685	12	4	12.5
Cox II	26021.6	4.8	0.247	2	4	23.3
Cox III	29932.8	6.5	0.413	7	1	5.4
F-ATPase a	24788.0	10.0	0.924	6	2	10.2
F-ATPase A6L	7936.6	9.5	0.083	1	3	45.5

^a CI, complex I or NADH: ubiquinone oxidoreductase; CIII, complex III or ubiquinol: cytochrome *c* oxidoreductase; Cox, cytochrome *c* oxidase; F-ATPase, ATP synthase.

^b Calculated from sequences.

^c GRAVY (grand average of hydropathicity) and pI values calculated with ProtParam (<http://www.expasy.ch/tools/protparam.html>).

^d TMH, the number of transmembrane α -helices in the molecular structures of cytochrome *c* oxidase (Tsukihara *et al.*, 1996) and complex III (Iwata *et al.*, 1998), or predicted with HMMTOP (<http://www.enzim.hu/hmmtop/>) for complex I and ATP synthase.

^e Tryptic peptides, number of peptides in an *in silico* digest in the *m/z* range 800 to 3000, and the theoretical coverage of the sequence by those peptides.

The compositions of mitochondrial proteomes have been investigated by a variety of mass spectrometric approaches, and the compositions of isolated respiratory complexes have been investigated in similar ways. Some experiments have analyzed mitochondrial proteins by first fractionating them by either 1-D or 2-D polyacrylamide gels, or RP-HPLC, followed by trypsin digestion of each protein band or spot or chromatographic peak and mass-mapping and sequence analysis of the tryptic peptides (Carroll *et al.*, 2003; Forner *et al.*, 2006; McDonald *et al.*, 2006; Murray *et al.*, 2003; Pagliarini *et al.*, 2008; Schilling *et al.*, 2006; Taylor *et al.*, 2003). Other attempts have used “shotgun” analysis of tryptic digests of unfractionated mitochondrial proteins (Da Cruz *et al.*, 2003; Forner *et al.*, 2006; Gaucher *et al.*, 2004; Mootha *et al.*, 2003; Pocsfalvi *et al.*, 2006). These approaches depend on the generation of peptides from the proteins by digestion with trypsin. However, as the mt-proteins have few tryptic cleavage sites, trypsin digestion produces predominantly large hydrophobic peptides that are recovered poorly both by in-gel digestion and chromatographic fractionation. Consequently, only

a small proportion of the tryptic peptides fall within the effective mass range (m/z 800 to 3000) for mass spectrometric analysis, and they represent only 5 to 45% of the total sequences of the mt-proteins (Table 6.1). Therefore, the identification of the mt-protein can become difficult or even unreliable, and in no proteomic analysis of mitochondria carried out so far were all the mt-proteins identified (Forner *et al.*, 2006; Gaucher *et al.*, 2004; McDonald *et al.*, 2005; Mootha *et al.*, 2003; Pagliarini *et al.*, 2008; Taylor *et al.*, 2003). Other practical difficulties associated with some of these approaches (although not with “shotgun” approaches) are that like many other hydrophobic proteins, bands of mt-proteins in gels stain poorly with Coomassie blue and related dyes, and so they may escape detection in 1-D gels and often they become lost irretrievably in 2-D gel analyses. Similarly, mt-proteins become bound irreversibly and are not recovered from standard reverse-phase columns eluted with aqueous trifluoroacetic acid and acetonitrile. For example, in a recent analysis of bovine complex I where reverse-phase high-performance liquid chromatography (RP-HPLC) was used to fractionate the subunits, all of the mt-protein subunits and two other subunits were not recovered (Lemma-Gray *et al.*, 2008).

Because of the low coverage of the sequences of the 13 mt-proteins achieved by the analysis of tryptic (and other) peptides, it has not been known whether they are modified posttranslationally, and it remained possible, for example, that an undefined redox cofactor was covalently attached to one of the mt-proteins in the membrane arm of complex I (Friedrich *et al.*, 2000). Moreover, the identification of the precise locations of site-specific covalent adducts introduced by chemical modification (see, for example, Nakamura-Ogiso *et al.* [2003]) and biochemical modifications (Galkin *et al.*, 2008; Gibson, 2005) has been difficult or even impossible. To address these methodological gaps, as described in this chapter, we have developed methods that permit the precise intact molecular masses of the 13 mt-proteins to be measured by electrospray ionization mass spectrometry (ESI-MS), allowing the presence of any posttranslational or chemical modifications to be detected (Carroll *et al.*, 2006b, 2007). We have shown also that partial sequences can be generated by tandem mass spectrometric analysis of 10 of the 13 mt-proteins providing sequence tags for their identification (Carroll *et al.*, 2007). With minor adjustments, these procedures can be applied to the analysis of orthologs from other species, including those found in bacteria, and to the analysis of hydrophobic membrane proteins in general. The procedures are based on the extraction of the 13 mt-proteins in organic solvents from the membranes of mitochondria, from purified respiratory complexes, and on the fractionation and purification of the proteins in similar solvents. These methods have been developed from earlier procedures involving extraction from mitochondria of subunits ND2, ND4, cytochrome *b*, ATPase-6 and A6L in chloroform-methanol mixtures (Fearnley and Walker, 1986, 1987).

2. ANALYSIS OF MITOCHONDRIAL MEMBRANES FOR MT-PROTEINS

2.1. Extraction of proteins from mitochondria

Mitochondria and mitochondrial membranes were prepared from bovine hearts (Walker *et al.*, 1995). As described in sections 2.1.1 and 2.1.2, they were extracted with either chloroform/methanol/1 M HCOONH₄, pH 3.7 (66.7:31.3:2.0, by vol; known as CMW), producing the CMW extract, or with propan-2-ol/acetonitrile/hexafluoro-propan-2-ol/1 M HCOONH₄, pH 3.7/water (70:25:0.56:2.0:2.44, by vol; known as PAHW), producing the PAHW extract. The parameters influencing the extraction of the mt-proteins by CMW especially were studied systematically. The ND6 subunit was particularly difficult to extract, and the key factor that led to it being solubilized efficiently in the solvent was the use of an acidic aqueous component (M. C. Altman, J. Carroll, I. M. Fearnley and J. E. Walker, unpublished results).

2.1.1. The CMW extract of mitochondria

Samples of mitochondrial membranes (~ 100 μ l; 4.25 mg protein) were vortexed at intervals for 5 min at 4° in 9 vol of CMW. The phases were separated by centrifugation (16,000g, 10 min, room temperature), and precipitated protein at the interface was discarded. The proteins in the lower phase (the CMW extract) were precipitated twice at -20° for 30 min with 4 vol of diethyl ether and centrifuged (16,000g, 10 min, 4°).

The protein content of the CMW extract was investigated extensively by SDS-PAGE (Fig. 6.1A) coupled with tandem mass spectrometric (MS) sequencing of tryptic peptides of gel slices of Coomassie-stained bands, and, in a second experiment of gel slices from the entire gel track. The presence of ND4L and ND6 was demonstrated by Western blotting. Ether precipitated samples of the extract were redissolved in formic acid/trifluoroethanol/hexafluoro-propan-2-ol/water (60:20:5:15, by vol; 50 μ l), centrifuged (16,000g, 5 min, room temperature), and the supernatant was injected into the flow (100 μ l/min) of solvent A consisting of trifluoroacetic acid/trifluoroethanol/hexafluoro-propan-2-ol/water (0.1:20:5:74.9, by vol), and fractionated by RP-HPLC at 60° on an mRP column (75 \times 2.1 mm internal diameter [id]; Agilent, Cheshire U. K.). When the ultraviolet (UV) absorbance at 225 nm of the column eluate had returned to baseline, the proteins were eluted at 60° with a linear gradient of solvent A with solvent B (trifluoroacetic acid/trifluoroethanol/hexafluoro-propan-2-ol/propan-2-ol/water, 0.08:20:1.0:70:8.92, by vol) at a flow rate of 100 μ l/min. Fractions corresponding to peaks in the absorbance trace (not shown)

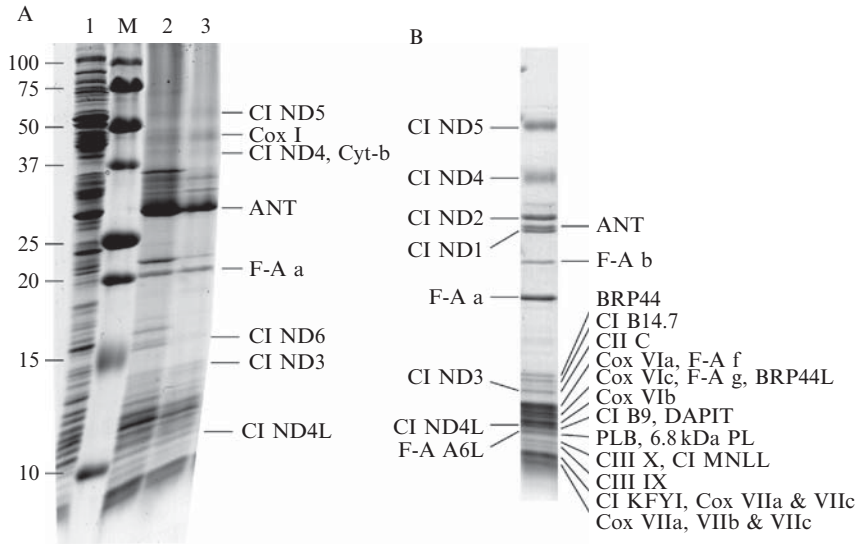


Figure 6.1 Protein contents of the organic solvent extracts of bovine heart mitochondria. Portions of the extracts were dried *in vacuo* in the presence of 0.01 vol of 20% SDS and 1 mM dithiothreitol (final concentration). They were resolubilized in SDS-PAGE sample buffer, and the pH values of any samples with residual acidity were adjusted to neutrality. Samples were analyzed by SDS-PAGE on 12 to 22% gradient gels and stained with Coomassie Blue R250 (Fearnley *et al.*, 2001). Proteins were identified by tandem MS sequencing of tryptic digests of the bands. (A) the CMW extract, lanes 1 and M are mitochondrial membranes and molecular weight markers (kDa; shown on the left), respectively; lanes 2 and 3 contain the CMW extract after one or two ether precipitations, respectively. On the right are shown the positions of 8 of the 13 mt-proteins that were detected in the extract, plus the adenine nucleotide carrier, ANT. (B) The PAHW extract. The positions of the 8 mt-proteins in the extract are shown on the left, and the positions of various nuclear encoded components of mitochondria on the right. They include components of respiratory complexes I, II, and III, cytochrome *c* oxidase and F-ATPase, plus brain protein 44 (BRP44), brain protein 44-like (BRP44L), diabetes-associated protein in insulin-sensitive tissue (DAPIT), phospholamban (PLB), and a 6.8-kDa proteolipid (PL). ND4L and ND6 were detected by Western blotting.

were collected manually. Samples were analyzed by SDS-PAGE and mass spectrometry (not shown).

These experiments demonstrated collectively the presence in the CMW extract of all of the 13 mt-proteins (together with approximately 70 nuclear encoded proteins); 9 of the mt-proteins (ND1, ND2, ND4, ND5, cytochrome *b*, Cox I, Cox III, and subunits a and A6L of the F-ATPase) were recovered from the RP-HPLC fractionation of the extract under conditions similar to those described in Section 3.3 (not shown).

2.1.2. The PAHW extract of mitochondria

Bovine mitochondria (~2.4 mg protein) were washed at 4° with 5 to 10 vol of buffer containing 2 mM TRIS-HCl, pH 7.4, 250 mM sucrose, and 1 mM EDTA and collected by centrifugation (16,000g, 6 min, 4°). Subsequent steps were performed at room temperature. The pellet of mitochondria was vortexed at intervals for 5 min in 9 vol of PAHW. Insoluble material was removed by centrifugation (16,000g, 10 min). Eight of the mt-proteins (F-ATPase subunits a and A6L, and subunits ND1, ND2, ND3, ND4, ND4L, and ND5 of complex I) were detected in the extract (Fig. 6.1B).

The PAHW extract was fractionated by hydrophilic interaction chromatography (HILIC) on a column of polyhydroxyethyl-aspartamide (100 mm × 2.1 mm id; 300 Å pore size; 5 μm particle size; PolyLC, Columbia, MD 21045, U. S. A.) protected with a guard column (10 mm × 2.1 id) and a precolumn filter (Hichrom; catalog number HI-685). The extract (~500 μl) was injected in ~100-μl portions into 100% buffer A consisting of propan-2-ol/acetonitrile/hexafluoro-propan-2-ol/1 M HCOONH₄, pH 3.7/water (63:22.5:0.5:2.0:12, by vol), pumped at a flow rate of 100 μl/min. When the UV absorbance at 225 nm of the eluate had returned to baseline, the column was eluted with a linear gradient of decreasing organic solvent of buffer A with buffer B (propan-2-ol/hexafluoro-propan-2-ol/1M HCOONH₄, pH 3.7/water (30:0.5:2.0:67.5, by vol). Fractions corresponding to UV absorbance peaks were collected manually and analyzed as shown in Fig. 6.2.

3. ANALYSIS OF RESPIRATORY COMPLEXES FOR MT-PROTEINS

3.1. Isolation of respiratory complexes

Mitochondrial membranes were solubilized in a buffer containing 20 mM TRIS-HCl, pH 7.4, 10% glycerol (v/v) and 1% (w/v) *n*-dodecyl-β-D-maltoside (DDM; Anatrace, Maumee, OH). Partially pure samples of respiratory complexes were obtained by fractionation of the mitochondrial extract by ion-exchange chromatography (Figs. 6.3 and 6.4; Buchanan and Walker [1996]; Sazanov *et al.* [2000]), but only the samples of complex III and cytochrome *c* oxidase were used in the experiments described here. They were precipitated with ammonium sulfate, and the precipitates were resuspended in buffer consisting of 10 mM TRIS-HCl, pH 7.4, 100 mM NaCl, and 0.04% DDM. The complexes were dialyzed against the same buffer and then the protein solutions were stored at -20°.

Complex I was purified from extracts of mitochondrial membranes by a combination of anion-exchange chromatography and gel filtration

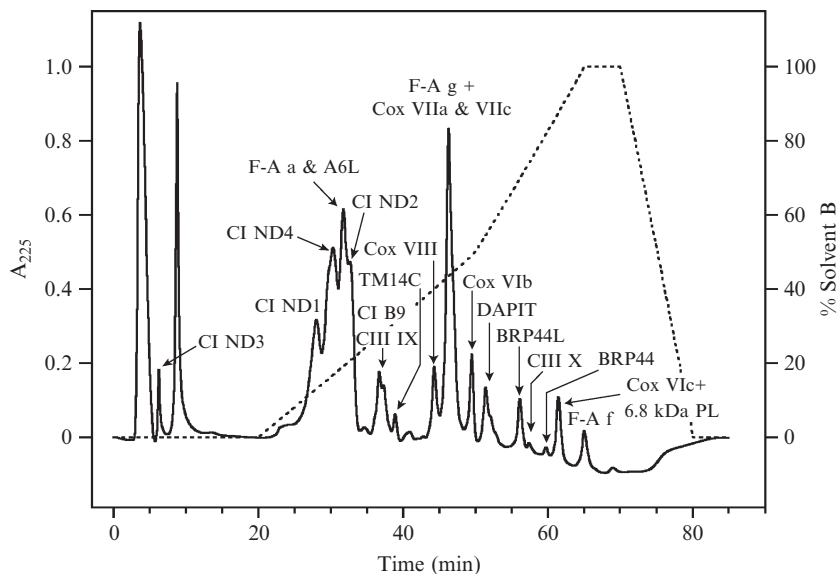


Figure 6.2 Fractionation of the PAHW extract of bovine heart mitochondrial membranes by HILIC. The elution profile (solid line) was monitored by UV absorbance at 225 nm. The column was eluted at 0.1 ml/min with a decreasing organic solvent gradient (dotted line). Proteins in fractions were identified by ESI-MS of intact proteins and tandem MS of tryptic peptides. The positions of various components of mitochondrial membranes are shown. For the definition of the abbreviated names see the legend to Fig. 6.1. TM14C is transmembrane protein 14C.

chromatography (Carroll *et al.*, 2003; Sazanov *et al.*, 2000). Purified complex I (see Fig. 6.4), recovered in a buffer containing 20 mM TRIS-HCl, pH 7.4, 50 mM NaCl, 0.04% DDM, and 10% glycerol, was concentrated to 5 to 7 mg/ml with a Vivaspin-4 membrane (Sartorius, Goettingen, Germany) with a 100-kDa cutoff. Samples were stored either in liquid nitrogen or at -20° . The ATP synthase complex (Fig. 6.4) was purified by affinity chromatography by use of an inhibitor protein (known as I1-60-GFPHis) consisting of residues 1 to 60 of the bovine F_1 -ATPase inhibitor protein, IF_1 , with the green fluorescent protein and six histidine residues attached to its C-terminus (M. J. Runswick, M. G. Montgomery, J. V. Bason, G. Robinson and J. E. Walker, unpublished work).

3.2. CMW extraction of respiratory complexes

Samples of the respiratory complexes (~ 50 to $100 \mu\text{l}$; 700 to $850 \mu\text{g}$) were extracted with 12 vol of CMW, similar to the procedure described in Section 2.1.1 for the CMW extraction of mitochondria. The twice ether precipitated pellet of the sample of complex I was dissolved in a minimal volume of chloroform/methanol/ 1 M HCOONH_4 , pH 3.7 (66.7:31.3:2.0, by vol)

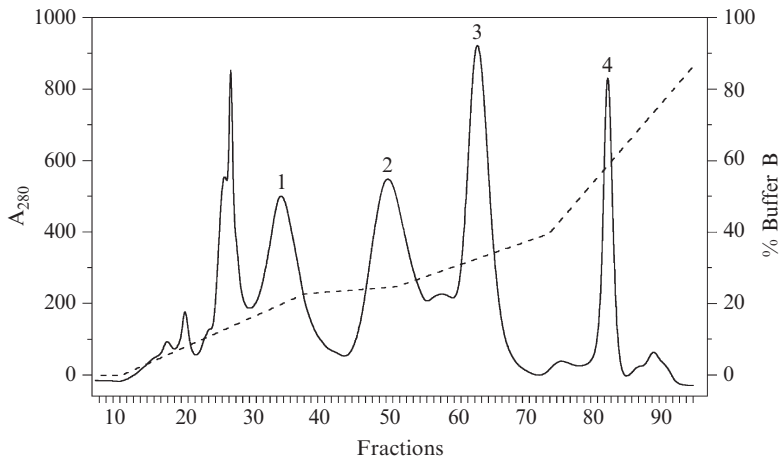


Figure 6.3 Fractionation of respiratory complexes from bovine heart mitochondria. An extract of mitochondrial membranes (~425 mg) in 20 mM TRIS-HCl (pH 7.4), 10% glycerol (v/v), and 1% DDM was applied to an HP column of HiTrap Q-Sepharose (50 ml) at 4° in buffer A containing 20 mM TRIS-HCl, pH 8.0, 1 mM EDTA, 1 mM dithiothreitol, 10% glycerol, and 0.1% DDM. The proteins were eluted with a gradient of buffer B (buffer A plus 1.0 M sodium chloride) as follows: 0 to 23% B for 3 column vols (60 min); 23 to 25% B for 1.5 column vols (30 min); 25 to 40% B for 2.5 column vols (50 min); and 40 to 100% B for 3 column vols (60 min). The absorbance of the eluate was monitored at 280 nm. Peaks 1 to 4 correspond to ATP synthase, and complexes IV, I, and III, respectively.

and diluted in the same solvent to a protein concentration appropriate for ESI-MS analysis.

3.3. Fractionation of the CMW extracts of respiratory complexes

Twice ether precipitated samples of the CMW extracts of respiratory complexes were fractionated by RP-HPLC on an mRP column as described in [Section 2.1.1](#) for the fractionation of CMW extracts of mitochondrial membranes ([Fig. 6.5A to D](#)). The CMW extraction of purified (or partially purified) mitochondrial respiratory complexes provided a route to all of the mt-proteins. However, although ND1, ND3, ND4L, and ND6 were present in the CMW extract of complex I, they were not recovered by RP-HPLC.

3.4. HILIC fractionation of the PAHW extract of complex I

Bovine complex I (60 μ l; 300 μ g) was extracted with 9 vol of PAHW as described for mitochondrial membranes in [Section 2.1.2](#). The extract contained subunits ND1, ND2, ND3, ND4, ND4L, and ND5. When it

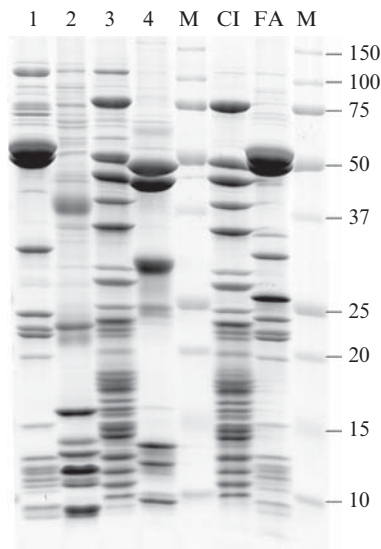


Figure 6.4 The subunit compositions of bovine respiratory complexes. The samples were analyzed by SDS-PAGE (see the legend to Fig. 6.1). Samples 1 to 4 correspond to the peaks in Fig. 6.3, precipitated with ammonium sulfate and dialyzed into 10 mM TRIS-HCl, pH 7.4, 100 mM NaCl, and 0.04% DDM. Lanes M contain molecular weight markers (kDa; shown on the right); lane CI, complex I; lane FA, F-ATPase.

was fractionated by HILIC (see Section 2.1.2; column size 100 mm \times 1 mm id; flow rate 50 μ l/min), subunits ND3 and ND4L were recovered in peak FT1 and ND1, ND2, ND4, and ND5 in peak FT2 (see Fig. 6.6). Both peaks were retarded slightly by the column, allowing the proteins to be freed from unretarded contaminating salts and detergents.

4. MASS SPECTROMETRIC ANALYSIS OF MT-PROTEINS

4.1. Protein molecular mass measurements

The CMW extract of complex I and column fractions from both HILIC and RP-HPLC experiments were analyzed by ESI-MS with a Q-TOF1 (quadrupole time-of-flight) mass spectrometer (Waters-Micromass, Manchester, U. K.) equipped with a nanoflow electrospray interface. The mass spectrometer was tuned and calibrated in positive ion mode over the m/z range 600 to 2500 with multiply charged ions from horse heart myoglobin (1 μ M) and bovine trypsinogen (1 μ M) dissolved in 50% aqueous acetonitrile containing 1% formic acid. Samples (1 to 10 μ l; protein concentration of 0.5 to 5 μ M) were injected by means of a Rheodyne injector valve into a

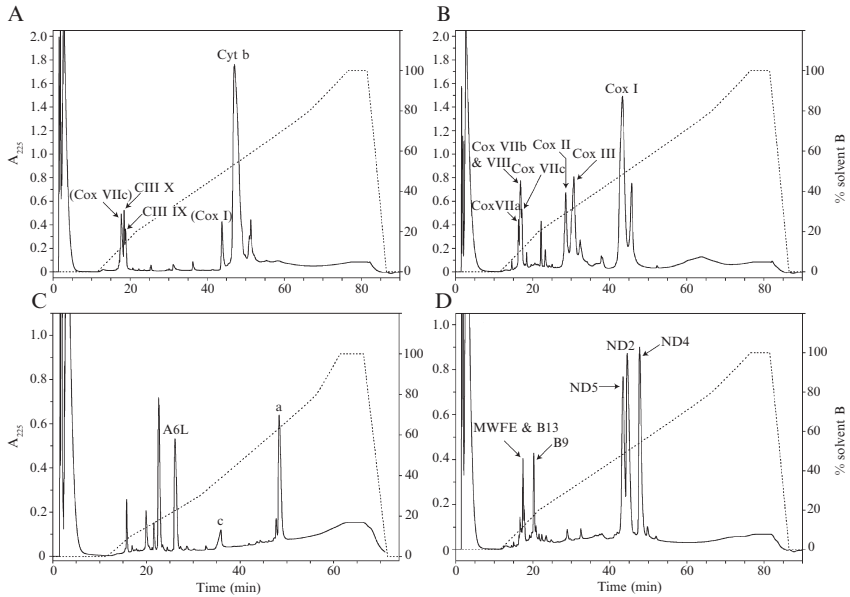


Figure 6.5 RP-HPLC of proteins extracted from respiratory complexes from bovine heart mitochondria. (A to D) Extracts of complexes III and IV, ATP synthase and complex I, respectively. —, absorbance of the eluate at 225 nm; ----, the solvent gradient. For the identification of proteins, see the legend to Fig. 6.2. In (D) MWFE, B13, and B9 are nuclear encoded subunits of complex I (Carroll *et al.*, 2003).

stream of 50% aqueous acetonitrile (flow rate 1 to 2 $\mu\text{l}/\text{min}$) except with the CMW extract of complex I (see Section 3.2), where the carrier solvent was chloroform/methanol/1 M HCOONH_4 , pH 3.7 (66.7:31.3:2.0, by vol). Sometimes, formic acid (final concentration 1 to 5%, by vol) was added to samples to improve the quality of the spectra. The positive ion spectra were recorded in single MS mode. They were interpreted with the aid of MassLynx software (Waters–Micromass, Manchester, U. K.), and in some instances they were transformed onto a molecular mass scale.

The molecular masses of all 13 mt-proteins were measured by mass spectrometry (Table 6.2). They demonstrate that, with the exception of the Cox III subunit of cytochrome oxidase, the proteins have retained their N-terminal translational initiator formyl-methionine residues and that their polypeptide chains are unmodified, in confirmation of previous data for the ATPase-6 and A6L (Fearnley and Walker, 1996) and supported by tandem MS data for ND1, ND2, ND3, ND6, ATPase-6, and A6L (see Section 4.2). Most of the Cox III subunit of cytochrome oxidase has lost the N-terminal formyl-methionine residue, as observed before (Buse and Steffens, 1978; Musatov *et al.*, 2002), and a smaller amount of the same subunit has lost the formyl group but retained methionine-1.

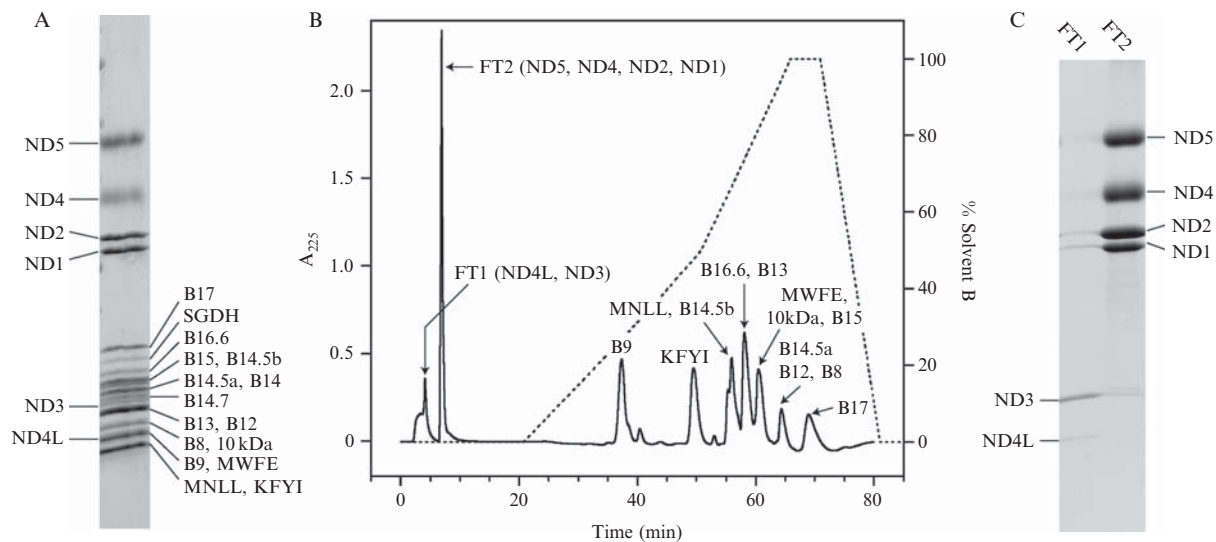


Figure 6.6 Extraction of complex I from bovine heart mitochondria with PAHW and fractionation of the extract by HILIC. (A) PAHW extract of complex I. (B) HILIC elution profile (solid line) monitored by UV absorbance at 225 nm. The column was eluted with a gradient of decreasing organic solvent (dotted line). (C) Analysis of peaks FT1 and FT2 in (B). For identification of proteins in (A to C), see the legends to Figs. 6.1 and 6.2. In (A) and (C), CI-ND4L was detected by Western blotting. For names of subunits of complex I see legend to Fig. 6.1 and Carroll *et al.* (2003).

Table 6.2 Molecular masses of mt-proteins (They were measured by ESI-MS and calculated from protein sequences.)

Protein	Source ^a	Mass (Da)		Mass difference	PTM ^b
		Observed	Calculated		
CI ND1	1, 2	35699.1	35670.2	+28.9	None
CI ND2	1, 2, 3	39283.5	39254.4	+29.1	None
CI ND3	1, 2	13082.4	13054.7	+27.7	None
CI ND4L	1, 2	10825.4	10797.3	+28.1	None
CI ND4	1, 2, 3	52130.0	52099.4	+30.6	None
CI ND5	1, 2, 3	68319.8	68286.8	+33.0	None
CI ND6	2	19106.7	19077.7	+29.0	None
CIII Cyt b	4	42619.7	42590.8	+28.9	None
Cox I ^c	5	57061.4	57032.5	+28.9	None
Cox II	5	26049.9	26021.6	+28.3	None
Cox III	5	29933.5	29932.8	None	- α -N-formyl
Cox III	5	29802.4	29932.8	-130.4	- Met-1
F-ATPase a	6, 7	24816.8	24788.0	+28.8	None
F-ATPase A6L	6, 7	7964.7	7936.6	+28.1	None

^a Sources of proteins for mass measurement; 1, HILIC fractionation of PAHW extracts of complex I; 2, CMW extract of complex I; 3, RP-HPLC fractionation of CMW extract of complex I; 4, RP-HPLC fractionation of CMW extract of complex III; 5, RP-HPLC fractionation of cytochrome *c* oxidase; 6, HILIC fractionation of PAHW extracts of mitochondrial membranes; 7, RP-HPLC of F-ATPase.

^b PTM, posttranslational modification; mt-proteins are synthesized with formyl-methionine as the translational initiator residue. It is retained in all of the mt-proteins except for Cox III.

^c Cox I contains a covalent crosslink between the side chains of tyrosine-240 and histidine-244 (Yoshikawa *et al.*, 1998). This modification reduces the calculated mass of the protein by 2 Da. The intact protein mass measured on this subunit was insufficiently accurate to detect its presence. The data were taken from Carroll *et al.* (2006b, 2007).

The ND6 subunit of complex I was the only protein encoded in the bovine mitochondrial genome not recovered by either RP-HPLC or HILIC. Its molecular mass was measured by analysis of the CMW extract of complex I by ESI-MS along with subunits ND1, ND2, ND3, ND4 and ND4L (Fig. 6.7).

4.2. Tandem MS of protein ions

Tandem mass spectrometry of protein ions, or “top-down” sequencing, has been applied to globular proteins especially (Ginter *et al.*, 2004; Kelleher *et al.*, 1999; Loo *et al.*, 1990). Partial sequences have been deduced from the fragment ions arising from collision-induced dissociation (CID) with argon or by electron capture dissociation (McLafferty *et al.*, 2008). However, the spectra are complex, and their successful interpretation depends on the use

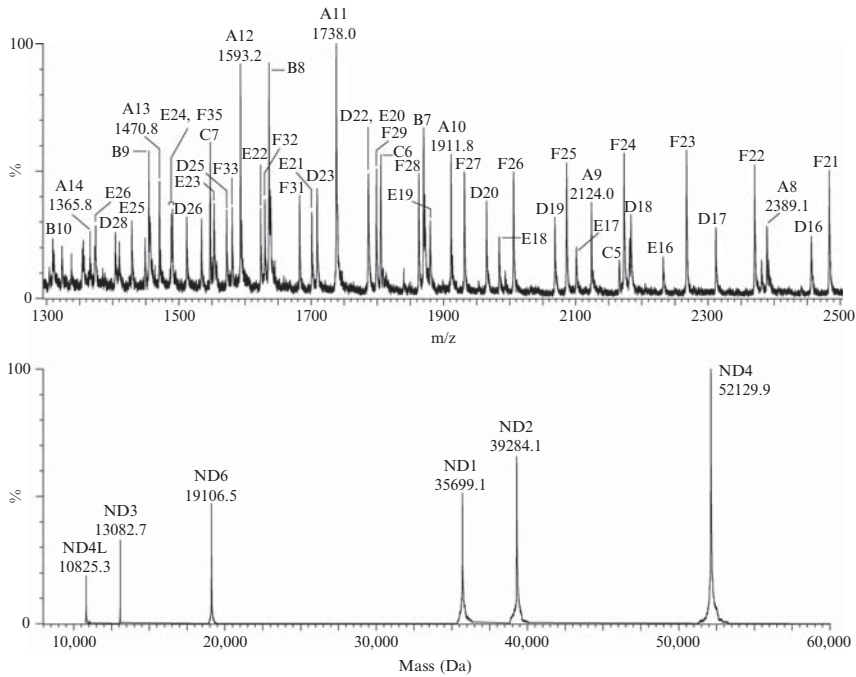


Figure 6.7 Analysis of the CMW extract of complex I by ESI-MS. The envelopes of multiply charged molecular ions of A to F correspond to subunits ND6, ND3, ND4L, ND2, ND1, and ND4, respectively. In the lower panel, the data have been transformed onto a molecular mass scale with Transform from MassLynx. The extract also contains some small subunits of complex I and cytochrome *c* oxidase that were retarded by the walls of the capillary tubing between the injection valve and the mass spectrometer and eluted after the hydrophobic proteins.

of high-resolution instruments, such as ion cyclotron resonance and Makarov ion trap (Makarov, 2000) mass spectrometers with Fourier transformation to separate the fragment ion isotopes and to determine the number of associated charges from the isotope spacings. The expense of this instrumentation has tended to limit access to these techniques.

A number of experiments have indicated that the fragment ion spectra, produced in instruments with triple quadrupole or time-of-flight analyzers by CID of small membrane proteins (3 to 8 kDa), are much simpler than those of globular proteins and that they can be interpreted easily by manual inspection to generate partial protein sequences (Buzy *et al.*, 1996; Fearnley and Walker, 1996; Whitelegge, 2005; Whitelegge *et al.*, 2002). With the availability of a range of membrane proteins from mitochondria provided by the fractionation methods described previously, we have carried out a

systematic study of their tandem mass spectra generated by CID in a quadrupole-time-of-flight (Q-TOF) instrument (Carroll *et al.*, 2007).

ESI-MS spectra were recorded in positive ion single MS mode to obtain a series of multiply charged protein ions from which the intact mass was calculated. From this series, an individual multiply charged ion, usually the most intense signal, was selected with the quadrupole of the Q-TOF1 instrument. This ion was dissociated by CID with argon at collision voltages of 30 to 50 V, and the masses of the fragments were determined by TOF analysis. The resulting spectra were interpreted manually. On the basis of the interpretation of the spectra, the membrane proteins fell into two overlapping categories. One category is made of “small” membrane proteins (up to ~12 kDa) with 1 to 4 TMH, where spectra were dominated by multiply charged series of fragment ions arising from internal regions of the protein, often with other singly charged series arising from one or both terminal regions, as observed before (Fearnley and Walker, 1996; Whitelegge *et al.*, 2002). The second category consists of membrane proteins with masses greater than 15 kDa with 4 to 18 TMH, where the spectra usually consisted of singly charged series arising from the N- and/or C-terminal regions of the intact protein. Examples of spectra from each class are shown in Fig. 6.8, and sequence data obtained on 10 of the 13 mt-proteins are summarized in Table 6.3. These partial sequences provided the means of identifying some mt-proteins unequivocally, allowing their functions (i.e., their names) to be associated with their measured molecular masses. Only the Cox I and Cox III subunits of cytochrome oxidase and the ND4 subunit of complex I gave no interpretable spectra.

5. CONCLUSIONS AND PERSPECTIVES

The methods described previously have at least three uses. First, they allow the precise masses of the 13 mt-proteins to be measured with sufficient accuracy to allow the presence of posttranslational modifications to be detected and possibly to allow the nature of the modification to be deduced. Such measurements are essential for establishing a comprehensive bovine mitochondrial proteome. Also, the methods have allowed many hydrophobic proteins in bovine mitochondrial membranes to be characterized, some of them for the first time, and for novel proteins to be discovered (Carroll *et al.*, 2007). Similar experiments have yet to be carried out on the products of other mitochondrial genomes and on the protein compositions of mitochondrial membranes of other species, but the methods described here can be adapted readily for that purpose. The methods are equally applicable to other nuclear encoded hydrophobic proteins or to bacterial

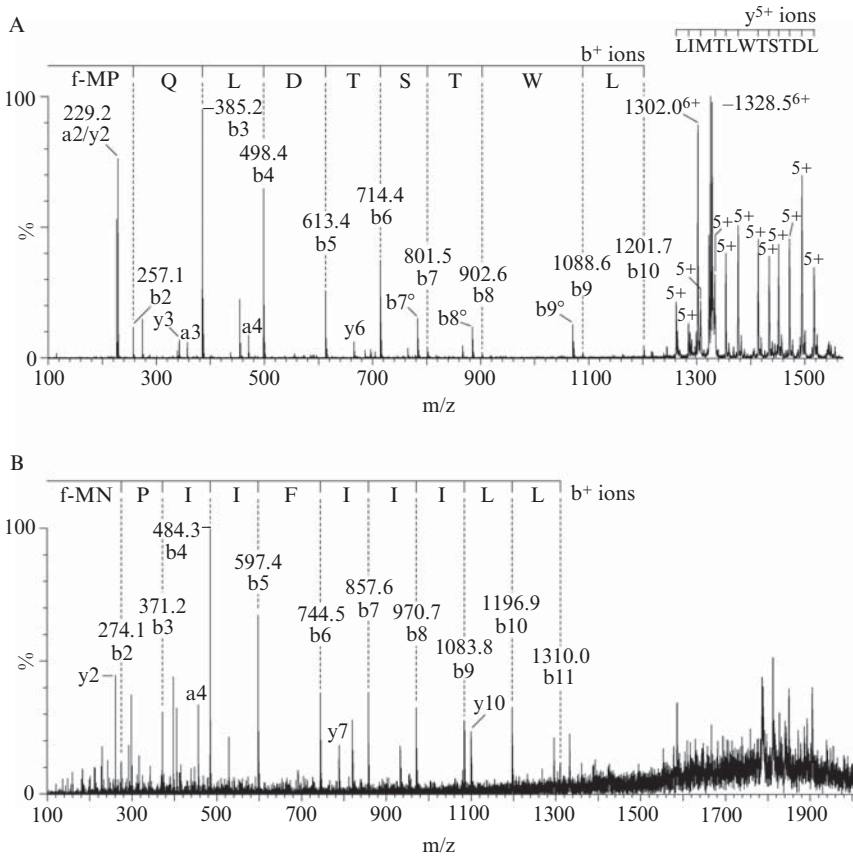


Figure 6.8 Tandem MS analyses of protein ions. (A) A fragment ion spectrum of the A6L subunit of the F-ATPase. The sequence LDTSTWLTML is defined by the quintuply charged ions, y_2 to y_6 , in the fragment ion spectra of a protein ion with m/z 1328.4 and six associated protons. Leucine and isoleucine residues were discriminated by reference to the known sequences of the proteins. The spectral interpretation is supported by an overlapping series of singly charged b -ions from the N-terminal region of the protein (f-MP)QLDTSTWL. Ions denoted b° correspond to the loss of water. (B) Fragment ion spectrum of a protein ion with m/z 1786.5 and 22 associated protons from subunit ND2 of bovine complex I. The N-terminal sequence (f-MN)PIIFIILL is defined by the singly charged ions, b_2 to b_{11} .

membrane proteins, where the same considerations apply if accurate and comprehensive proteomes are to be established.

Second, the methods have utility in verifying the subunit compositions and state of covalent modification of the subunits of isolated integral membrane multiprotein complexes, as exemplified by the bovine mitochondrial respiratory complexes. A related application not explored yet is in the study of

Table 6.3 Amino acid sequences determined by tandem MS of protein ions of mt-proteins

Protein	TMH	Residues	Ions		Fragment (z)	Sequence (residues)
			z	m/z		
F-ATPase A6L	1	66	6 ⁺	1328.4	b2-b10 (1 ⁺) y52-y63 (5 ⁺)	(f-MP)QLDTSTWL (1-10) LDTSTWLTMIL (4-14)
CI ND4L	2	98	6 ⁺	1805.3	y2-y8 (1 ⁺)	QNLNLL(QC) (91-98)
CI ND3	3	115	8 ⁺	1636.5	b2-b9 (1 ⁺) y2-y9 (1 ⁺)	(f-MN)LMLALLT (1-9) TQK(GL)EW(TE) (107-115)
CI ND6	5	175	11 ⁺	1738.5	b2-b9 (1 ⁺) y2-y7 (1 ⁺)	(f-MM)LYIVFIL (1-9) MEITR(NG) (169-175)
F-ATPase a	6	226	13 ⁺	1910.0	b2-b11 (1 ⁺) y3-y11 (1 ⁺)	(f-MN)ENLFTSFIT (1-11) LLVSLYLH(DNT) (216-226)
Cox II	2	227	15 ⁺	1737.6	b2-b4 (1 ⁺)	YP (3-4)
Cox II		69-227	15 ⁺	1737.6	b2-b9 (1 ⁺)	(PA)IILILIA (69-77)
CI ND1	8	318	21 ⁺	1701.1	b2-b8 (1 ⁺)	(f-MF)MINILM (1-8)
CI ND2	10	347	22 ⁺	1786.5	b2-b11 (1 ⁺)	(f-MN)PIIFIILL (1-11)
CIII Cyt b	8	379	21 ⁺	2030.6	b18-b23 (3 ⁺)	IDLPA (19-23)
CI ND5	18	606	40 ⁺	1709.0	y3-y7 (1 ⁺)	ILFN (600-603)

The data were taken from [Carroll *et al.* \(2007\)](#).

in vitro site-specific covalent modification of the membrane components of such complexes, as, for example, in mapping specific binding sites with chemical probes. Recently, the analysis of all of the subunits of ATP synthase complexes isolated from several species have been facilitated by connecting the output of the RP-HPLC column directly to a mass spectrometer (M. J. Runswick, I. M. Fearnley J. Carroll and J. E. Walker, unpublished results). Similar developments can be envisaged, for example, for analyzing complex I from a variety of species, although improvements to the chromatographic fractionation and recovery of subunits will probably be needed also. Recently, an alternate method for characterizing the subunit composition of complex I from *Yarrowia lipolytica* by mass spectrometry has been outlined by use of laser-induced liquid bead ion desorption mass spectrometry to measure the mass of the complex and its constituent subunits (Morgner *et al.*, 2008). Although this method has the obvious advantage of avoiding the extraction and chromatographic steps of our procedures, at present, the accuracies of the protein mass measurements are insufficient to allow proteins and any posttranslational modifications to be identified unambiguously.

Third, the demonstration that the tandem mass spectra of ions of membrane proteins are readily interpretable opens up a new way for generating protein sequence tags for use in the identification of membrane proteins. This method as applied to membrane proteins is in its infancy, but it is possible that the application of new methods for the dissociation of the protein ions, such as electron transfer dissociation, may lead to improved spectra and to more extensive coverage of the protein sequence. The use of proteolytic enzymes other than trypsin and/or chemical cleavage methods is an alternate possibility for generating peptides for MS analysis. However, most of the currently available specific proteases target cleavage sites in hydrophilic regions of the target protein, and so, as with trypsin, these approaches will leave much of the membrane protein inaccessible to MS analysis by standard procedures, and usually specific chemical cleavages of proteins are accompanied by extensive covalent modification of amino acid side chains. Thus, obtaining extensive or complete coverage of the sequence of membrane proteins by MS analysis, as may be required, for example, in pinpointing the site of any side-chain modifications, remains an unresolved challenge.

REFERENCES

- Anderson, S., Bankier, A. T., Barrell, B. G., de Bruijn, M. H., Coulson, A. R., Drouin, J., Eperon, I. C., Nierlich, D. P., Roe, B. A., Sanger, F., Schreier, P. H., Smith, A. J., *et al.* (1981). Sequence and organization of the human mitochondrial genome. *Nature* **290**, 457–465.

- Anderson, S., de Bruijn, M. H., Coulson, A. R., Eperon, I. C., Sanger, F., and Young, I. G. (1982). Complete sequence of bovine mitochondrial DNA. Conserved features of the mammalian mitochondrial genome. *J. Mol. Biol.* **156**, 683–717.
- Buchanan, S. K., and Walker, J. E. (1996). Large-scale chromatographic purification of F₁F₀-ATPase and complex I from bovine heart mitochondria. *Biochem. J.* **318**, 343–349.
- Buse, G., and Steffens, G. J. (1978). Studies on cytochrome *c* oxidase, II. The chemical constitution of a short polypeptide from the beef heart enzyme. *Hoppe-Seyler's Z. Physiol. Chem.* **359**, 1005–1009.
- Buzy, A., Ryan, E. M., Jennings, K. R., Palmer, D. N., and Griffiths, D. E. (1996). Use of electrospray ionization mass spectrometry and tandem mass spectrometry to study binding of F₀ inhibitors to ceroid lipofuscinosis protein, a model system for subunit *c* of mitochondrial ATP synthase. *Rapid Commun. Mass Spectrom.* **10**, 790–796.
- Carroll, J., Altman, M. C., Fearnley, I. M., and Walker, J. E. (2007). Identification of membrane proteins by tandem mass spectrometry of protein ions. *Proc. Natl. Acad. Sci. USA* **104**, 14330–14335.
- Carroll, J., Fearnley, I. M., Shannon, R. J., Hirst, J., and Walker, J. E. (2003). Analysis of the subunit composition of complex I from bovine heart mitochondria. *Mol. Cell. Proteomics* **2**, 117–126.
- Carroll, J., Fearnley, I. M., Skehel, J. M., Shannon, R. J., Hirst, J., and Walker, J. E. (2006a). Bovine complex I is a complex of 45 different subunits. *J. Biol. Chem.* **281**, 32724–32727.
- Carroll, J., Fearnley, I. M., and Walker, J. E. (2006b). Definition of the mitochondrial proteome by measurement of molecular masses of membrane proteins. *Proc. Natl. Acad. Sci. USA* **103**, 16170–16175.
- Chen, R., Runswick, M. J., Carroll, J., Fearnley, I. M., and Walker, J. E. (2006). Association of two proteolipids of unknown function with ATP synthase from bovine heart mitochondria. *FEBS Lett.* **581**, 3145–3148.
- Da Cruz, S., Xenarios, I., Langridge, J., Vilbois, F., Parone, P. A., and Martinou, J. C. (2003). Proteomic analysis of the mouse liver mitochondrial inner membrane. *J. Biol. Chem.* **278**, 41566–41571.
- Fearnley, I. M., and Walker, J. E. (1986). Two overlapping genes in bovine mitochondrial DNA encode membrane components of ATP synthase. *EMBO J.* **5**, 2003–2008.
- Fearnley, I. M., and Walker, J. E. (1987). Initiation codons in mammalian mitochondria: Differences in genetic code in the organelle. *Biochemistry* **26**, 8247–8251.
- Fearnley, I. M., and Walker, J. E. (1996). Analysis of hydrophobic proteins and peptides by electrospray ionization MS. *Biochem. Soc. Trans.* **24**, 912–917.
- Fearnley, I. M., Carroll, J., Shannon, R. J., Runswick, M. J., Walker, J. E., and Hirst, J. (2001). GRIM-19, a cell death regulatory gene product, is a subunit of bovine mitochondrial NADH: Ubiquinone oxidoreductase (complex I). *J. Biol. Chem.* **276**, 38345–38348.
- Forner, F., Foster, L. J., Campanaro, S., Valle, G., and Mann, M. (2006). Quantitative proteomic comparison of rat mitochondria from muscle, heart, and liver. *Mol. Cell. Proteomics* **5**, 608–619.
- Friedrich, T., Brors, B., Hellwig, P., Kintscher, L., Rasmussen, T., Scheide, D., Schulte, U., Mäntele, W., and Weiss, H. (2000). Characterization of two novel redox groups in the respiratory NADH: Ubiquinone oxidoreductase (complex I). *Biochim. Biophys. Acta.* **1459**, 305–309.
- Galkin, A., Meyer, B., Wittig, I., Karas, M., Schägger, H., Vinogradov, A., and Brandt, U. (2008). Identification of the mitochondrial ND3 subunit as a structural component involved in the active/deactive enzyme transition of respiratory complex I. *J. Biol. Chem.* **283**, 20907–20913.
- Gaucher, S. P., Taylor, S. W., Fahy, E., Zhang, B., Warnock, D. E., Ghosh, S. S., and Gibson, B. W. (2004). Expanded coverage of the human heart mitochondrial proteome using multidimensional liquid chromatography coupled with tandem mass spectrometry. *J. Proteome Res.* **3**, 495–505.

- Gibson, B. W. (2005). The human mitochondrial proteome: Oxidative stress, protein modifications and oxidative phosphorylation. *Int. J. Biochem. Cell Biol.* **37**, 927–934.
- Ginter, J. M., Zhou, F., and Johnston, M. V. (2004). Generating protein sequence tags by combining cone and conventional collision induced dissociation in a quadrupole time-of-flight mass spectrometer. *J. Am. Soc. Mass Spectrom.* **15**, 1478–1486.
- Iwata, S., Lee, J. W., Okada, K., Lee, J. K., Iwata, M., Rasmussen, B., Link, T. A., Ramaswamy, S., and Jap, B. K. (1998). Complete structure of the 11-subunit bovine mitochondrial cytochrome *b_c1* complex. *Science* **281**, 64–71.
- Kelleher, N. L., Lin, H. Y., Valaskovic, G. A., Aaserud, D. J., Fridriksson, E. K., and McLafferty, F. W. (1999). Top down versus bottom up protein characterization by tandem high-resolution mass spectrometry. *J. Am. Chem. Soc.* **121**, 806–812.
- Lemma-Gray, P., Valušová, E., Carroll, C. A., Weintraub, S. T., Musatov, A., and Robinson, N. C. (2008). Subunit analysis of bovine heart complex I by reversed-phase high-performance liquid chromatography, electrospray ionization-tandem mass spectrometry, and matrix-assisted laser desorption/ionization-time-of-flight mass spectrometry. *Anal. Biochem.* **382**, 116–121.
- Loo, J. A., Edmonds, C. G., and Smith, R. D. (1990). Primary sequence information from intact proteins by electrospray ionization tandem mass spectrometry. *Science* **248**, 201–204.
- Makarov, A. (2000). Electrostatic axially harmonic orbital trapping: A high-performance technique of mass analysis. *Anal. Chem.* **72**, 1156–1162.
- McDonald, T., Sheng, S., Stanley, B., Chen, D., Ko, Y., Cole, R. N., Pedersen, P., and Van Eyk, J. E. (2006). Expanding the subproteome of the inner mitochondria with protein separation technologies: One- and two-dimensional liquid chromatography and two-dimensional gel electrophoresis. *Mol. Cell. Proteomics* **5**, 2392–2411.
- McLafferty, F. W., Breuker, K., Jin, M., Han, X., Infusini, G., Jiang, H., Kong, X., and Begley, T. P. (2008). Top-down MS, a powerful complement to the high capabilities of proteolysis proteomics. *FEBS J.* **274**, 6256–6268.
- Mootha, V. K., Bunkenborg, J., Olsen, J. V., Hjerrild, M., Wisniewski, J. R., Stahl, E., Bolouri, M. S., Ray, H. N., Sihag, S., Kamal, M., Patterson, N., Lander, E. S., *et al.* (2003). Integrated analysis of protein composition, tissue diversity, and gene regulation in mouse mitochondria. *Cell* **115**, 629–640.
- Morgner, N., Zickermann, V., Kerscher, S., Wittig, I., Abdrakhmanova, A., Barth, H. D., Brutschy, B., and Brandt, U. (2008). Subunit mass fingerprinting of mitochondrial complex I. *Biochim. Biophys. Acta* **1777**, 1384–1391.
- Murray, J., Zhang, B., Taylor, S. W., Oglesbee, D., Fahy, E., Marusich, M. F., Ghosh, S. S., and Capaldi, R. A. (2003). The subunit composition of the human NADH dehydrogenase obtained by rapid one-step immunopurification. *J. Biol. Chem.* **278**, 13619–13622.
- Musatov, A., Carroll, C. A., Liu, Y. C., Henderson, G. I., Weintraub, S. T., and Robinson, N. C. (2002). Identification of bovine heart cytochrome *c* oxidase subunits modified by the lipid peroxidation product 4-hydroxy-2-nonenal. *Biochemistry* **41**, 8212–8220.
- Nakamura-Ogiso, E., Sakamoto, K., Matsuno-Yagi, A., Miyoshi, H., and Yagi, T. (2003). The ND5 subunit was labeled by a photoaffinity analogue of fenpyroximate in bovine mitochondrial complex I. *Biochemistry* **42**, 746–754.
- Pagliarini, D. J., Calvo, S. E., Chang, B., Sheth, S. A., Vafai, S. B., Ong, S. E., Walford, G. A., Sugiana, C., Boneh, A., Chen, W. K., Hill, D. E., Vidal, M., *et al.* (2008). A mitochondrial protein compendium elucidates complex I disease biology. *Cell* **134**, 112–123.
- Pocsfalvi, G., Cuccurullo, M., Schlosser, G., Cacace, G., Siciliano, R. A., Mazzeo, M. F., Scacco, S., Cocco, T., Gnoni, A., Malorni, A., and Papa, S. (2006). Shotgun proteomics for the characterization of subunit composition of mitochondrial complex I. *Biochim. Biophys. Acta* **1757**, 1438–1450.

- Sazanov, L. A., Peak-Chew, S. Y., Fearnley, I. M., and Walker, J. E. (2000). Resolution of the membrane domain of bovine complex I into subcomplexes: Implications for the structural organization of the enzyme. *Biochemistry* **39**, 7229–7235.
- Schilling, B., Murray, J., Yoo, C. B., Row, R. H., Cusack, M. P., Capaldi, R. A., and Gibson, B. W. (2006). Proteomic analysis of succinate dehydrogenase and ubiquinol-cytochrome *c* reductase (Complex II and III) isolated by immunoprecipitation from bovine and mouse heart mitochondria. *Biochim. Biophys. Acta* **1762**, 213–222.
- Taylor, S. W., Fahy, E., Zhang, B., Glenn, G. M., Warnock, D. E., Wiley, S., Murphy, A. N., Gaucher, S. P., Capaldi, R. A., Gibson, B. W., and Ghosh, S. S. (2003). Characterization of the human heart mitochondrial proteome. *Nat. Biotechnol.* **21**, 281–286.
- Tsukihara, T., Aoyama, H., Yamashita, E., Tomizaki, T., Yamaguchi, H., Shinzawa-Itoh, K., Nakashima, R., Yaono, R., and Yoshikawa, S. (1996). The whole structure of the 13-subunit oxidized cytochrome *c* oxidase at 2.8 Å. *Science* **272**, 1136–1144.
- Walker, J. E., Skehel, J. M., and Buchanan, S. K. (1995). Structural analysis of NADH: Ubiquinone oxidoreductase from bovine heart mitochondria. *Methods Enzymol.* **260**, 14–34.
- Whitelegge, J. P. (2005). Tandem mass spectrometry of integral membrane proteins for top-down proteomics. *Trends Anal. Chem.* **24**, 576–582.
- Whitelegge, J. P., Zhang, H., Aguilera, R., Taylor, R. M., and Cramer, W. A. (2002). Full subunit coverage liquid chromatography electrospray ionization mass spectrometry (LCMS+) of an oligomeric membrane protein: cytochrome b(6)f complex from spinach and the cyanobacterium *Mastigocladus laminosus*. *Mol. Cell. Proteomics* **1**, 816–827.
- Yoshikawa, S., Shinzawa-Itoh, K., Nakashima, R., Yaono, R., Yamashita, E., Inoue, N., Yao, M., Fei, M. J., Libeu, C. P., Mizushima, T., Yamaguchi, H., Tomizaki, T., *et al.* (1998). Redox-coupled crystal structural changes in bovine heart cytochrome *c* oxidase. *Science* **280**, 1723–1729.

TRACING HUMAN MITOCHONDRIAL COMPLEX I ASSEMBLY BY USE OF GFP-TAGGED SUBUNITS

Cindy E. J. Dieteren,^{*,†} Werner J. H. Koopman,^{†,*}
and Leo G. J. Nijtmans^{*}

Contents

1. Introduction	134
2. Selection of Complex I Subunit for GFP Labeling	136
2.1. Prediction of steric hindrance by GFP	136
3. Creation of Inducible Cell Line Expressing AcGFP ₁ -tagged NDUFS3	137
3.1. Creation of the AcGFP ₁ -destination vector	138
3.2. Creation of the entry clone containing complex I subunit NDUFS3	138
3.3. Creation of expression vector containing AcGFP ₁ -tagged NDUFS3	140
3.4. Stable transfection of expression vector containing AcGFP ₁ -tagged NDUFS3	141
3.5. Analysis of inducibility of stable cell line expressing AcGFP ₁ -tagged NDUFS3	142
4. Tracing AcGFP ₁ -Labeled NDUFS3 on BN-PAGE	143
4.1. Native gel analysis of complex I under leakage and induced condition	144
4.2. Pulse-chase labeling of complex I and its assembly intermediates	146
4.3. Accumulation of complex I assembly intermediates after chloramphenicol treatment	148
Acknowledgment	149
References	149

* Department of Paediatrics, Nijmegen Centre for Mitochondrial Disorders, Radboud University Nijmegen Medical Centre, Nijmegen, The Netherlands

† Department of Biochemistry, Nijmegen Centre for Molecular Life Sciences, Radboud University Nijmegen Medical Centre, Nijmegen, The Netherlands

‡ Microscopical Imaging Centre, Nijmegen Centre for Molecular Life Sciences, Radboud University Nijmegen Medical Centre, Nijmegen, The Netherlands

Abstract

Disturbances in the assembly of mitochondrial complex I (CI) are a frequent cause of mitochondrial disorders. Several lines of evidence hint at a semi-sequential assembly pathway, in which the 45 individual subunits that form the holoenzyme are pieced together by means of smaller intermediates. To understand this process, it is necessary to explain the exact order, the rate-limiting steps, and the dynamics of subunit incorporation. In this chapter, we describe an approach to regulate the expression levels of an AcGFP₁-tagged subunit (NDUFS3) in mammalian cells by means of a tetracycline-inducible promoter. This strategy allows the study of the dynamics of CI assembly intermediates in living cells on native gels. After establishing that the AcGFP₁ tag does not interfere with the activity and assembly of the enzyme, we show how this system can be used to trace the labeled subunit in an induction pulse-chase experiment or to study its accumulation in specific assembly intermediates after inhibition of mitochondrial translation.

1. INTRODUCTION

In the last decade, mitochondrial complex I (CI; NADH: ubiquinone oxidoreductase; EC 1.6.5.3) has emerged as a key player in the pathogenesis of a large variety of disorders, including neuromyopathies, but also Alzheimer's disease, Parkinson's disease, and cancer (Brandon *et al.*, 2006; Janssen *et al.*, 2006; Srivastava *et al.*, 2007). CI is the largest enzyme of the oxidative phosphorylation (OXPHOS) system and consists of a membrane part and a peripheral arm that is protruding into the matrix. Human CI contains 45 different proteins, encoded by both the nuclear and the mitochondrial genome, a noncovalently bound FMN-group, and eight iron-sulphur clusters (Carroll *et al.*, 2006). To get more insight into the role of CI in disease, it is necessary to understand how the biogenesis of this large enzyme takes place and how this process is regulated.

The functional "core" of the enzyme comprises 14 evolutionary conserved subunits that have coevolved and are arranged in three functional modules (Friedrich and Weiss, 1997): the dehydrogenase module (containing NDUFV1, NDUFV2, and NDUFS1), the hydrogenase module (containing NDUFS2, NDUFS3, NDUFS7, NDUFS8, ND1, and ND5), and the proton translocation module (containing ND2, ND3, ND4, ND4L, and ND6). The role of the other 31 subunits, called "accessory," is not explained yet. Our CI assembly model (Fig. 7.1) proposes that assembly in part reflects this evolutionary conservation of subunits (for details, see Vogel *et al.*, 2007c). Subunits of the hydrogenase module are first assembled into a subcomplex that is subsequently bound to an independently assembled membrane module. Then, more subunits are added in various stages of

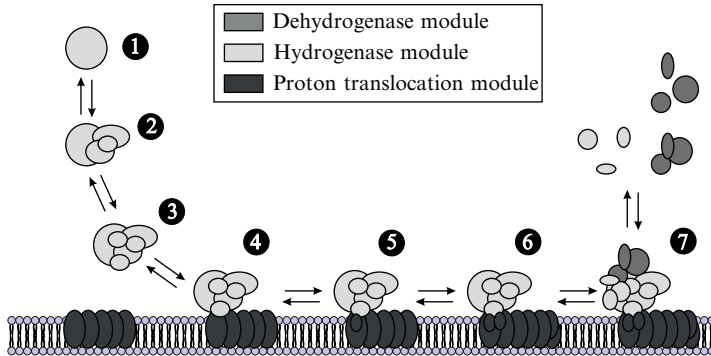


Figure 7.1 Assembly model for human complex I. The holoenzyme is assembled in distinct steps via the formation of smaller modules that are combined at different stages.

the process. The dehydrogenase module that forms the top of the peripheral arm is thought to be added in a late stage of assembly (Lazarou *et al.*, 2007). In addition to this mechanism, an “exchange” route was proposed, in which several subunits can be assembled directly into CI by replacing previously incorporated ones. Such a pathway may serve as a repair mechanism for damaged subunits. It has also become clear that the assembly of CI is assisted by specific assembly chaperones. Recently, a number of these chaperones have been identified, and several candidate assembly chaperones have been proposed. (Dunning *et al.*, 2007; Ogilvie *et al.*, 2005; Pagliarini *et al.*, 2008; Saada *et al.*, 2008; Vogel *et al.*, 2005, 2007b,d). At this moment neither their exact molecular function nor where in the CI assembly process they play a role have been clarified.

In this chapter we present a novel approach that will be of help to address questions regarding CI assembly, such as the exact composition of assembly intermediates, their dynamics in time and space, and the role of assembly chaperones in this process. Our method comprises the inducible expression of GFP-tagged CI subunits, which allows investigating the dynamic incorporation of subunits into CI or CI subassemblies by native electrophoresis in combination with fluorescent scanning or western blotting. This method makes it possible to trace the incorporation of a single-labeled protein (subunit) into CI and CI subassemblies without the use of a radioactive label, provided that such a tag does not interfere with its biologic function. As an example of this method, we will explain how we exploited a tetracycline-inducible cell line, conditionally expressing NDUFS3 fused to a monomeric GFP (AcGFP₁), to study the dynamics of CI assembly. In this chapter we initially describe some considerations before selecting a subunit for tagging. Next, we illustrate our cloning strategy for the required construct, explicate how stable cell lines were obtained, and describe how

we tested its inducible capacity. Finally, we show how assembly can be traced on native gels by intervening with the induction of the tagged subunit and by inhibiting mitochondrial translation.

2. SELECTION OF COMPLEX I SUBUNIT FOR GFP LABELING

Because subunits are incorporated at different stages in the assembly process and because they are in different positions in the structure, it is likely that GFP tagging of some of the subunits will interfere with proper assembly and/or function of CI. Therefore, it is necessary to select the right subunits for GFP tagging. Although it should be experimentally tested whether a subunit is amiable for GFP tagging without interfering with the assembly, stability, or function of the complex, some criteria can be given that will improve the chances of success. First, the GFP should be added to the C-terminus to prevent interference with the N-terminal mitochondrial presequence and to avoid that the GFP would be cleaved off (together with this presequence) on import into the mitochondria. Second, the GFP-tagged C-terminus should be free. It should not be buried inside the complex (see [section 2.1](#)). Third, to trace the different stages of the assembly process, the tagged subunits should be acquired at an early point in the assembly process.

In our example we planned to label a subunit that is incorporated in an early stage of assembly (at subcomplex 1; [Fig. 7.1](#)), so that tagging would provide more insight into onset and subsequent assembly steps. Possible candidates that meet this criterion were NDUFS2, NDUFS3, NDUFS7, and NDUFS8. To have an educated guess that C-terminal GFP-tagged subunit would not interfere with assembly, it would be useful to study the mammalian crystal structure of CI. Unfortunately, this has not been elucidated yet, in contrast to the other OXPHOS complexes ([Abrahams *et al.*, 1994](#); [Iwata *et al.*, 1998](#); [Sun *et al.*, 2005](#); [Tsukihara *et al.*, 1996](#); [Xia *et al.*, 1997](#)). To date, only the crystal structure of the peripheral arm of CI in *Thermus thermophilus* is solved ([Sazanov and Hinchliffe, 2006](#)). Although this complex solely contains the orthologs of the human core subunits NDUFV1, NDUFV2, NDUFS1, NDUFS2, NDUFS3, NDUFS7, and NDUFS8, it might be fruitful to study whether a GFP molecule fits at the c-termini of these subunits in this “minimal” form of CI.

2.1. Prediction of steric hindrance by GFP

To analyze whether GFP would hinder incorporation of the four “early” subunits, we opened the Protein Databank Bank (PDB) files of GFP (“2hfc”) and the *T. thermophilus* CI structure (“2FUG”) in YASARA. We marked the first residue of the c-terminus of different CI subunits

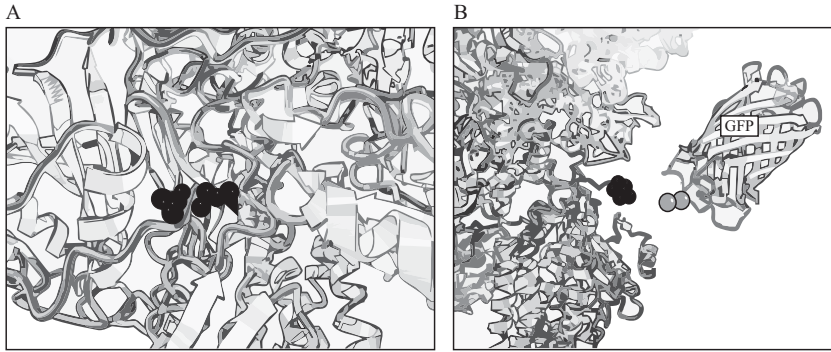


Figure 7.2 Prediction of incorporation of AcGFP₁-tagged subunits by use of the crystal structure of the peripheral arm of *Thermus thermophilus* complex I. The structure of the bacterial peripheral arm consists of eight subunits (Sazanov and Hinchliffe, 2006). These subunits are analogous with the human nuclear encoded core subunits. The first residues of the c-termini in the (A) NDUFS2 and (B) NDUFS3 orthologs in the *T. thermophilus* peripheral arm structure are indicated with black balls. The n-terminus of AcGFP₁ is marked with grey balls.

with black balls. The n-terminus of GFP was similarly characterized in grey. Molecular figures were drawn with the POV-Ray module in YASARA and were optimized for grey scale display in CorelDRAW. Two examples of the obtained pictures for NDUFS2 and NDUFS3 are shown in Fig. 7.2. At the c-terminus of NDUFS2 (Fig 7.2A) there is hardly space for GFP, whereas the c-terminus of NDUFS3 (Fig. 7.2B) is relatively free. Brandt and colleagues showed that this seemed to be the case in the yeast *Yarrowia lipolytica*, in which the eYFP-HIS-tagged NDUFS3 homolog could be used to isolate CI (Kashani-Poor *et al.*, 2001). We also analyzed the NDUFS7 and NDUFS8 c-termini and concluded that although they are relatively free in *T. thermophilus*, they are close to the membrane, which might hinder their incorporation when fused to GFP (data not shown). For these reasons we selected NDUFS3 to trace in assembly. Obviously, this approach may also be helpful to predict the success of adding a GFP tag to proteins of other larger protein complexes.

3. CREATION OF INDUCIBLE CELL LINE EXPRESSING ACGFP₁-TAGGED NDUFS3

A first requirement for our approach is the creation of a vector that allows inducible expression of our GFP-tagged subunit of interest. For our approach we chose the most widely used tetracycline-inducible system, but, in principle, every inducible system can be applied (i.e., sensitive to alcohol,

steroids, metal). The principle of this inducible system is based on constitutive expression of an inhibitor that blocks transcription by binding to the promoter, which can be released by doxycycline (a tetracycline derivate), allowing transcription to start. Numerous fluorescent tags are presently available. However, some of them, like wild-type GFP from *Aequorea victoria*, have the tendency to dimerize, which will lead to nonphysiologic binding interactions. We, therefore, selected a monomeric form of GFP (AcGFP₁; isolated from *A. ceruleus*). The creation of such a construct can be obtained by conventional restriction-ligation cloning; however, we chose a more efficient and flexible strategy, namely the use of cloning through recombination. Hence we first created a vector containing recombination sites in front of an AcGFP₁ tag. This construct allows a one-step insertion of any subunit of which the stop codon was removed to yield an in-frame subunit–AcGFP fusion protein. This strategy proved to be very efficient and allows high flexibility in cloning different subunits or different tags.

3.1. Creation of the AcGFP₁-destination vector

For our recombination strategy, first an AcGFP₁-destination construct was created as depicted in Fig. 7.3 (indicated with “A”). This was done as follows: an AcGFP₁ fragment was cut out of pAcGFP₁-N1 (Clontech) by *Bam*HI and *Not*I digestion. This AcGFP₁-containing fragment was agarose gel-purified and ligated into pcDNA4/TO/myc-HISA (Invitrogen) that was linearized with *Bam*HI and *Not*I, dephosphorylated, and gel purified. After amplification in DH5 α *E. coli* (Invitrogen) on ampicillin LB-agar plates, the construct was digested with *Bam*HI and the overhanging ends were filled in by a Klenow reaction. Subsequently, the Gateway reading frame cassette B (rfB; Invitrogen) was ligated in the blunt *Bam*HI site and transformed into DB3.1 *E. coli* cells (Invitrogen) for amplification in presence of ampicillin. After confirming the right orientation of rfB, the construct was cut out by *Pme*I and the obtained rfB–AcGFP containing fragment was gel purified. This fragment was ligated into vector pcDNA5/FRT/TO (Invitrogen) that was linearized with *Pme*I, dephosphorylated, and gel purified. Finally, the ligation reaction was transformed in DB3.1 *E. coli* cells for amplification on ampicillin LB-agar plates.

3.2. Creation of the entry clone containing complex I subunit NDUFS3

To clone the gene of interest into the destination vector previously described, first an entry vector containing this gene had to be generated. This is exemplified by use of the CI subunit NDUFS3. A schematic representation of the construct is shown in Fig. 7.3 (indicated with B). We used a two-step PCR protocol to clone the NDUFS3 sequence

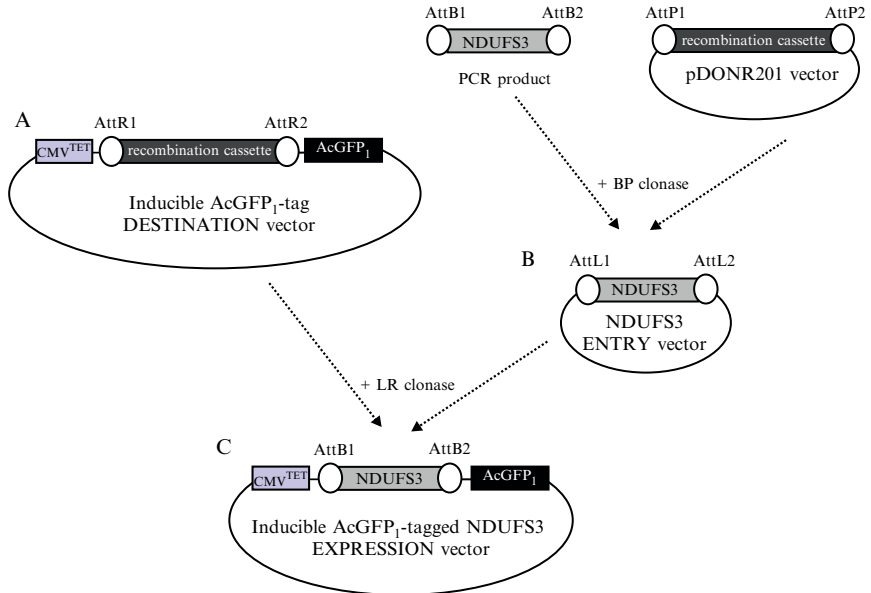


Figure 7.3 Schematic representation of cloning strategy for inducible vector containing AcGFP₁-tagged NDUFS3. The DESTINATION vector (A) contains a Gateway recombination cassette in frame with the AcGFP₁ sequence behind a tetracycline-inducible CMV promoter. In the BP-reaction, the ENTRY vector (B) is constructed by recombination of a PCR product (containing the NDUFS3 sequence, flanked by AttB-sites) and pDONR201. Eventually, the EXPRESSION vector (C) is constructed after recombination of the DESTINATION and ENTRY clone by LR-clonase. This inducible construct contains the NDUFS3 sequence (without stop codon) in frame with a c-terminal AcGFP₁-tag and is ready to be stably transfected in T-Rex293 flp-in cells.

(NM_004551) from a human heart cDNA bank (reverse transcribed from human heart polyA⁺ mRNA; Clontech) with in frame 5' and 3' Gateway AttB-sites. In the first step we used the following primers containing partial AttB-sites and 18 to 21 gene-specific nucleotides: forward 5'-AA AAA GCA GGC TTC GCC ACC *atg gcg gcg gcg gcg gta gcc*-3' and reverse 5'-A GAA AGC TGG GTG ctt ggc atc agg ctt ctt-3'. The capitalized sequences represent the partial AttB1 and AttB2 sequences, respectively. In the forward primer, we also added a Kozak sequence (*italic capitals*). Importantly, in the reverse primer, the gene-specific sequence has to exclude the stop codon to allow c-terminal tagging by AcGFP₁ later on. The PCR1 reaction mix contained ~10 ng human heart cDNA, 10 μ M forward primer, 10 μ M reverse primer, 2.5 μ l PfuUltra HF buffer (Stratagene), 10 μ M dNTPs, and 1.25 units PfuUltra HF DNA Polymerase (Stratagene) in a total volume of 25 μ l MQ. A PCR cyclor was programmed as follows: (1) 98° for 2 min; (2) 96° for 20 sec; (3) 54° for 40 sec; (4) 72° for

1 min and 20 sec (Pfu activity \sim 600bp/min); (5) repeat steps 2 to 4 35 times; (6) 72° for 10 min; and (7) 15° for ever.

After verification of the amplification product on an agarose gel, 5 μ l of the PCR1 product was used for a second PCR2 amplification to complete the AttB-sites. For this, the following AttB-adaptor primers were used: forward 5'- G GGG ACA AGT TTG TAC AAA AAA GCA GGC T-3' and reverse 5'- GGG GAC CAC TTT GTA CAA GAA AGC TGG GT-3'. The PCR2 reaction mix contained 5 μ l PCR1 product, 10 μ M forward primer, 10 μ M reverse primer, 2.5 μ l PfuUltra HF buffer (Stratagene), 10 μ M dNTPs, and 1.25 units PfuUltra HF DNA Polymerase (Stratagene) in a total volume of 25 μ l MQ. A PCR cycler was programmed as follows: (1) 98° for 1 min; (2) 96° for 20 sec; (3) 45° for 40 sec; (4) 72° for 1 min and 20 sec (Pfu activity \sim 600 bp/min); (5) repeat steps 2 to 45 times; (6) 95° for 20 sec; (7) 55° for 40 sec; (8) 72° for 1 min and 20 sec; (9) repeat steps 6 to 8 20 times; (10) 72° for 10 min; and (11) 15° for ever. The PCR2 product was verified on an agarose gel and purified. Finally, \sim 50 to 150 ng of the PCR product was recombined with \sim 150 ng of pDONR201 (Invitrogen) by use of Gateway BP Clonase II Enzyme Mix (Invitrogen) according to the manufacturer's instructions. After adding Proteinase K to inactivate the BP Clonase enzyme, 5 μ l of the reaction mix was transformed in DH5 α cells that were plated on kanamycin LB-agar plates. The construct was amplified in the surviving clones, purified, and sequenced to make sure that there were no mutations in the cloned ORF. Obviously, other proteins can be cloned in the same manner; however, for the PCR protocol optimization may be required.

3.3. Creation of expression vector containing AcGFP₁-tagged NDUFS3

To obtain an expression vector that can be transfected into mammalian cells, \sim 150 ng of the AcGFP₁-destination vector (created in 3.1) was recombined with \sim 50 to 150 ng of the NDUFS3 entry clone (created in 3.2) with LR Clonase II enzyme mix (Invitrogen) according to the manufacturer's instructions. After adding Proteinase K to inactivate the LR Clonase enzyme, 5 μ l of the reaction mix was transformed in DH5 α cells that were subsequently plated on ampicillin LB-agar plates. In principle, only the cells containing the NDUFS3-AcGFP₁ expression construct are able to survive. Finally, the construct was amplified, purified, checked by restriction analysis, and sequenced. With this cloning method, a linker between the NDUFS3 and AcGFP₁ was formed with the sequence CAC CCA GCT TTC TTG TAC AAA GTG GTT GAT GAT CCA CCG GTC. A schematic representation of the obtained expression construct is shown in Fig. 7.3 (indicated with C).

3.4. Stable transfection of expression vector containing AcGFP₁-tagged NDUFS3

We used Flp-in T-Rex293 cells (derived from human embryonic kidney cells; Invitrogen) for stable transfection of our inducible NDUFS3-AcGFP₁ vector. These cells are designed for targeted integration of our construct in the genome for optimal expression and have constitutive expression of the inhibitor that blocks transcription of the tetracycline-inducible promoter. Cells were cultured in DMEM supplemented with 10% fetal calf serum (PAA laboratories) (v/v), 1% penicillin/streptomycin (Gibco), 5 $\mu\text{g}/\text{ml}$ blasticidin (Invitrogen), and 300 $\mu\text{g}/\text{ml}$ zeocin (Invitrogen) at 37° and 5% CO₂. Forty-eight hours before transfection, 4.0×10^5 cells were seeded in a 6-well plates and cultured in 2 ml DMEM in the absence of blasticidin and zeocin. On the day of transfection, cells were ~70% confluent. For the stable cell line of one construct, two wells were used. Two Eppendorf tubes were prepared each containing 0.5 μg of the NDUFS3-AcGFP₁ expression construct and 4.5 μg POG44 vector (Invitrogen) in a total volume of 100 μl unmodified DMEM (POG44 encodes a Flp recombinase that incorporates the expression vector into the genome by means of Flp Recombination Target (FRT) sites). Importantly, the minimal amount of DMEM should be 90%. Ten microliters of Superfect reagent (Qiagen) was added to both tubes and mixed with the DNA and DMEM by pipetting up and down five times. The transfection mixes were incubated 5 to 10 min at room temperature. In the meantime, the medium was aspirated from the 6-well plate, and cells are washed once with 2 ml of pre-warmed phosphate-buffered saline (PBS). After the formation of transfection complexes, 600 μl of DMEM, supplemented with fetal calf serum and penicillin/streptomycin was added to the transfection mixes. After pipetting up and down twice, the complete content of each transfection mix was carefully added dropwise to two individual wells. After incubating the cells 2 to 3 h at 37° and 5% CO₂, the transfection mix was removed, cells were washed once with 2 ml pre-warmed PBS and allowed to grow one day in 2 ml DMEM supplemented with fetal calf serum and penicillin/streptomycin. We also included a mock transfection as negative control. Obviously, other transfection protocols may possibly be effective as well.

The next day, 24 h after transfection, the cells from the duplo wells were trypsinized and pooled in a 10-cm culture dish containing DMEM supplemented with fetal calf serum and penicillin/streptomycin. When the cells had attached to the culture dish, 5 $\mu\text{g}/\text{ml}$ blasticidin and 200 $\mu\text{g}/\text{ml}$ hygromycin (Calbiochem) were added to the medium. Every 3 days DMEM and all antibiotics were refreshed. The selective antibiotics were confirmed to have worked by the dish with mock transfected cells; this was completely devoid of cells. After ~1.5 weeks of selection clones were ready to be picked. To do so, after the medium in the culture dish was replaced by pre-warmed PBS, several clones were selected from the dish by a glass Pasteur's pipet and resuspended in individual 25-cm² culture flasks

containing DMEM supplemented with fetal calf serum and penicillin/streptomycin. When cells had attached to the bottom, selective antibiotics (blasticidin and hygromycin B) were included in the culture medium. Cells were allowed to grow until the required amount of stable cells was obtained.

3.5. Analysis of inducibility of stable cell line expressing AcGFP₁-tagged NDUFS3

To test the sensitivity of the promoter to doxycycline, a dose-response experiment was performed. Therefore, NDUFS3-AcGFP₁ cells were transferred to five 75-cm² culture flasks and cultured in DMEM supplemented with FCS, penicillin/streptomycin, blasticidin, and hygromycin at 37° and 5% CO₂ to 70% confluence. On the day of induction, doxycycline was dissolved in absolute ethanol to a concentration of 2 mg/ml. This stock was diluted to achieve different end-concentrations in the culture flasks (i.e., 1 to 50 ng doxycycline per ml of medium). Importantly, the amount of ethanol should not exceed 0.1% of the end volume of the culture medium. After adding doxycycline, cells were cultured for another 24 h at 37° and 5% CO₂. After harvesting, cell pellets (containing ~15 × 10⁶ cells) were washed twice with cold PBS, resuspended in 100 μl PBS and thoroughly mixed with 100 μl digitonin (4 mg/ml PBS) to isolate mitoplasts (mitochondria without outer membrane). After 10 min incubation on ice, 1 ml of PBS was added to dilute the digitonin, and the suspension was centrifuged at 10,000g at 4° for 10 min. The pellet, containing the mitoplasts, was washed twice with 1 ml of PBS and was subsequently resuspended in 50 μl of PBS plus 5.5 μl of 20% (w/v) β-lauryl maltoside (DDM) to solubilize the inner membranes (end percentage DDM 2%). The mix was incubated on ice for 10 min and centrifuged at 10,000g for 10 min. The supernatant was transferred to a new Eppendorf tube and its protein concentration was determined. Proteins were denatured by 1:1 dilution in SDS-sample buffer (Tricine sample buffer [Biorad] containing 2% β-mercaptoethanol) and were subsequently incubated at room temperature for 60 min (without boiling). Finally, 20 μg of each sample was loaded on 10% TRIS-tricine SDS-PAGE gel. After electrophoresis, induced protein expression could be analyzed in two ways. The barrel structure of AcGFP₁ remains intact after SDS-PAGE, which makes it possible to study its expression by in-gel fluorescence with an imaging analyzer FLA5000 (Fuji film) (473 nm excitation laser, FITC filter >510 nm; Fig. 7.4A). Otherwise, the induced protein can be visualized after Western blotting by immunodetection with a homemade polyclonal primary anti-EGFP antibody and secondary peroxidase-conjugated anti-rabbit antibody (Fig. 7.4B). The anti-EGFP antibody was directed against the complete EFGP protein (commercially available [e.g., Novus Biologicals]). Both detection methods showed a band of the expected molecular weight of AcGFP₁-tagged NDUFS3 (~50 kDa; filled arrowhead). However, on the fluorogram a

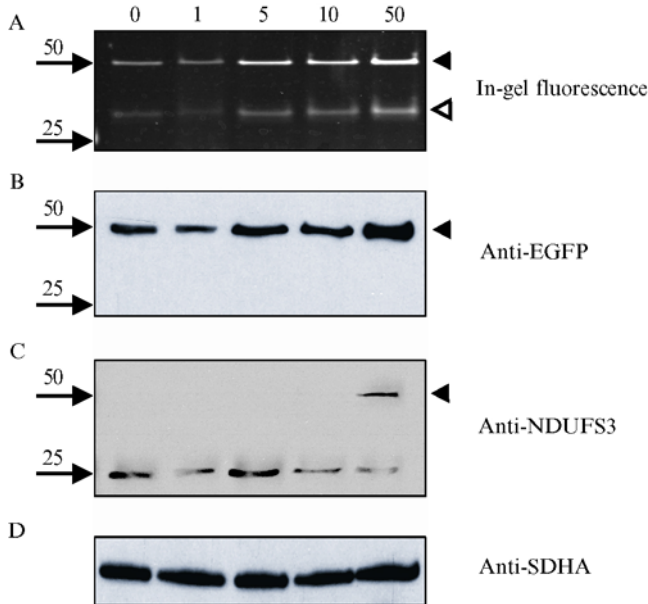


Figure 7.4 Induction test of stable Flp-in T-Rex293 clone, transfected with an inducible vector containing NDUFS3-AcGFP₁. Cells were induced with 0, 1, 5, 10, and 50 ng of doxycycline per ml medium for 30 min and 24 h later harvested. (A) Mitochondrial lysates were loaded on an SDS-PAGE gel and analyzed for in-gel fluorescence. Filled arrowhead indicates intact fusion proteins. Open arrowhead indicates smaller fluorescent products. (B) Immunodetection of a Western blot of the same gel as shown in (A) against EGFP. (C) Immunodetection of duplo Western blot shown in (B) against NDUFS3. On the height of 25 kDa, the endogenous NDUFS3 signal is visualized. (D) Immunodetection against a subunit of complex II (SDHA) serves as a loading control.

smaller fluorescent product was also visible (open arrowhead), which was absent after immunodetection with anti-EGFP. Immunodetection with an anti-NDUFS3 antibody confirmed that the band approximately 50 kDa indeed contained NDUFS3 (Fig. 7.4C; filled arrowhead). Importantly, also without adding doxycycline to the medium, a faint band of expression was visible. This leakage expression is possibly caused by tetracycline in the fetal calf serum used for cell culture and can be reduced with tetracycline approved medium (Clontech).

4. TRACING AC₁GFP₁-LABELED NDUFS3 ON BN-PAGE

To study dynamics of CI assembly intermediates, metabolic pulse labeling is often used. After creating an inducible NDUFS3-AcGFP₁ cell line, principally similar fluorescence pulse labeling experiments can

be performed. This approach brings specific advantages: instead of labeling all newly synthesized protein by radioactivity, a single subunit can be chased without the use of radioactivity. In this chapter, we describe two examples of how the inducible cell line can be combined with Blue Native PAGE (BN-PAGE), a technique originally developed by Schagger and von Jagow (1991) to trace the synthesis of subassemblies.

4.1. Native gel analysis of complex I under leakage and induced condition

Before we started to investigate CI assembly dynamics, we first wanted to exclude the fact that the AcGFP₁-tag interferes with the activity and assembly of the holoenzyme. Therefore, CI expression and activity were analyzed for noninduced (steady-state) and induced (overexpression) conditions on BN-PAGE gels. NDUFS3-AcGFP₁ cells were transferred to two 75-cm² culture flasks and cultured in 20 ml DMEM supplemented with FCS, penicillin/streptomycin, blasticin, and hygromycin at 37° and 5% CO₂ to 70% confluence. For induction, doxycycline was dissolved in absolute ethanol to a concentration of 2 mg/ml; 10 μl of this stock was added to the culture medium of one flask (to obtain a doxycycline concentration of 1 μg/ml in the medium) and cells were cultured for another 18 h at 37° and 5% CO₂. Subsequently, cells (~15 × 10⁶) were harvested and washed twice with cold PBS, resuspended in 100 μl PBS, and thoroughly mixed with 100 μl digitonin (4 mg/ml PBS) to isolate mitoplasts (mitochondria without outer membrane). After 10 min incubation on ice, 1 ml of PBS was added to dilute the digitonin, and the suspension was centrifuged at 10,000g at 4° for 10 min. The pellet, containing the mitoplasts was washed twice with 1 ml of PBS and then resuspended in 100 μl of ACBT solution (1.5 M aminocaproic acid, 75 mM BIS-TRIS) plus 11 μl of 20% (w/v) DDM to solubilize the inner membranes (end percentage DDM is 2%). The mix was incubated on ice for 10 min and centrifuged at 10,000g for 30 min. The supernatant, containing the isolated proteins, was transferred to a new Eppendorf tube and its protein concentration was determined. Blue Native sample buffer (100 mM BIS-TRIS (pH 7.0), 500 mM aminocaproic acid, 5% Serva blue G 250) was added 1:10 to the samples of which 80 μg was loaded in triple on a 5 to 15% BN-PAGE gradient gel (Calvaruso *et al.*, 2008). Alternatively, precast 4 to 16% gradient Native-PAGE gels are commercially available (Invitrogen).

After electrophoresis, two lanes were used for protein expression analysis by either in-gel fluorescence scanning with an imaging analyzer FLA5000 (Fujifilm) (473 nm excitation laser, FITC filter >510 nm; Fig. 7.5A) or immunodetection with a polyclonal anti-EGFP antibody after Western blotting (Fig. 7.5B). Both detection methods showed incorporation of AcGFP₁-tagged subunit into CI and 6 smaller labeled subcomplexes

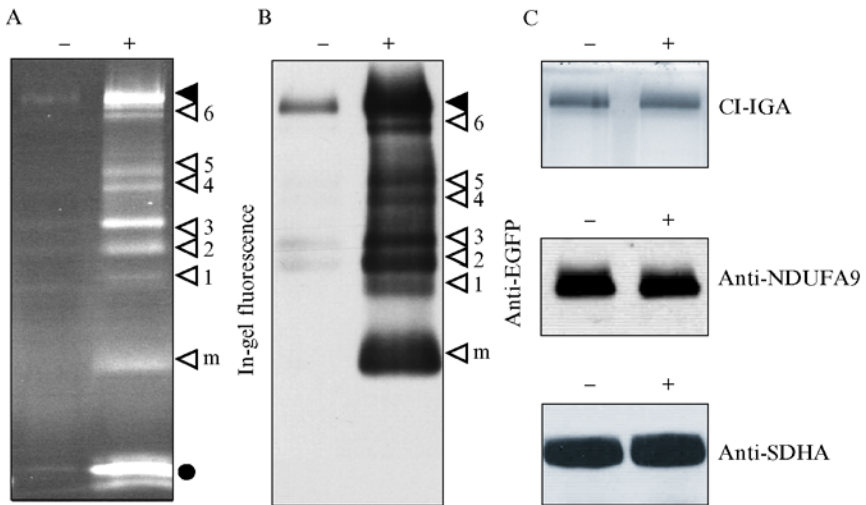


Figure 7.5 Incorporation of AcGFP₁-tagged NDUFS3 does not disturb CI activity and assembly. Mitochondrial enriched fractions of non-induced (-) and 18-h induced (+) NDUFS3-AcGFP₁ cells were loaded on a BN-PAGE gel. Holo-CI is indicated with filled arrowheads, subcomplexes with open arrowheads. (A) Fluorescence scan. (B) Immunodetection against EGFP. (C) CI in-gel activity (IGA) and immunodetection against NDUFA9 (a measure of the total amount of CI) and SDHA (loading control).

(indicated with open arrowheads 1 to 6) in addition to monomeric NDUFS3-AcGFP₁ (indicated with open arrow head “m”). This assembly pattern matches with previously identified endogenous NDUFS3 subcomplexes (Ugalde *et al.*, 2004b; Vogel *et al.*, 2007a). Although the two methods gave similar subassemblies, the ratios between the individual bands differed for each method. On the fluorogram a smaller fluorescent product was also visible (closed circle), which was absent after immunodetection with the antibody against EGFP. This was most probably due to the excess of Serva Blue G in the front of the gel, which prevented the EGFP-antibody to bind to its epitopes.

Both detection methods are appropriate for studying assembly intermediates. The anti-EGFP antibody is more sensitive than the fluorscan, because it can detect the leakage expression in the noninduced cells more strongly. However, if extrapolation of gel data to live-imaging records is required, the fluorescence scan is probably more appropriate than the anti-EGFP immunodetection. Fluorescence in the gel might reflect the fluorescence in the cell better than an antibody, which might have different affinities for NDUFS3-AcGFP₁ in different subassemblies. In addition, the relatively high contribution of the smaller product (closed circle) to the total amount of fluorescence would be overlooked by use of the EGFP-antibody

but might have a great influence on the outcome of live-imaging experiments.

After establishing that tagged NDUFS3 can be assembled into CI, the activity and stability of the holocomplex was analyzed. Therefore, two other lanes of the BN-PAGE gel were incubated in 20 ml 2mM TRIS-HCl (pH 7.4) containing 2 mg NADH and 50 mg nitrotetrazolium blue (Sigma) for 1 h at room temperature to stain the gel for in-gel activity (IGA; Fig. 7.5C) of CI. An additional lane-pair was blotted and subjected to immunodetection with an NDUFA9 antibody (NDUFA9; Fig. 7.5C). These analyses revealed an unaltered activity and amount of CI after induction, indicating that the tag did not introduce catalytic or assembly defects of the holoenzyme. Immunodetection against a subunit of complex II (SDHA; Fig. 7.5C) served as a loading control.

4.2. Pulse-chase labeling of complex I and its assembly intermediates

To investigate whether there is a certain order of appearance of NDUFS3 assembly intermediates and whether there are particular bottlenecks in the assembly process, a pulse-chase-induction experiment was performed. Therefore, NDUFS3-AcGFP₁ cells were transferred to eight 75-cm² culture flasks and cultured in 20 ml DMEM supplemented with FCS, penicillin/streptomycin, blasticin, and hygromycin at 37° and 5% CO₂ to 70% confluence. To give an induction pulse, doxycycline was dissolved in absolute ethanol to a concentration of 1 mg/ml, 1 μ l of this stock was added to the culture medium of one flask (to obtain a doxycycline concentration of 50 ng/ml in the medium), and cells were placed at 37° and 5% CO₂. After 30 min of induction, the medium was completely aspirated from the cells and carefully replaced by 20 ml of fresh prewarmed DMEM supplemented with FCS, penicillin/streptomycin, blasticin, and hygromycin. Because HEK293 cells easily detach from the bottom, we decided not to wash with PBS.

Cells were harvested 0, 2, 4, 6, 8, 10, 15, and 18 h after the induction pulse and pellets were further processed for BN-PAGE analysis as described previously (see section 4.1). To detect low expression levels better, we blotted the gel and probed it with anti-EGFP instead of scanning it for fluorescence. Results are shown in Fig. 7.6A. Less monomeric fusion protein (indicated “m”) was accumulating after 18 h of chase than after continuous induction (see Fig. 7.5B, “plus” condition and Vogel *et al.*, 2007a). With this pulse-induction method we mimicked a more physiologic condition, because monomeric endogenous NDUFS3 is hardly present in HEK293 cells under normal conditions (Vogel *et al.*, 2007a).

Quantification of Fig. 7.6A may help the interpretation of the results. Therefore, we determined the integrated optical density (IOD) per

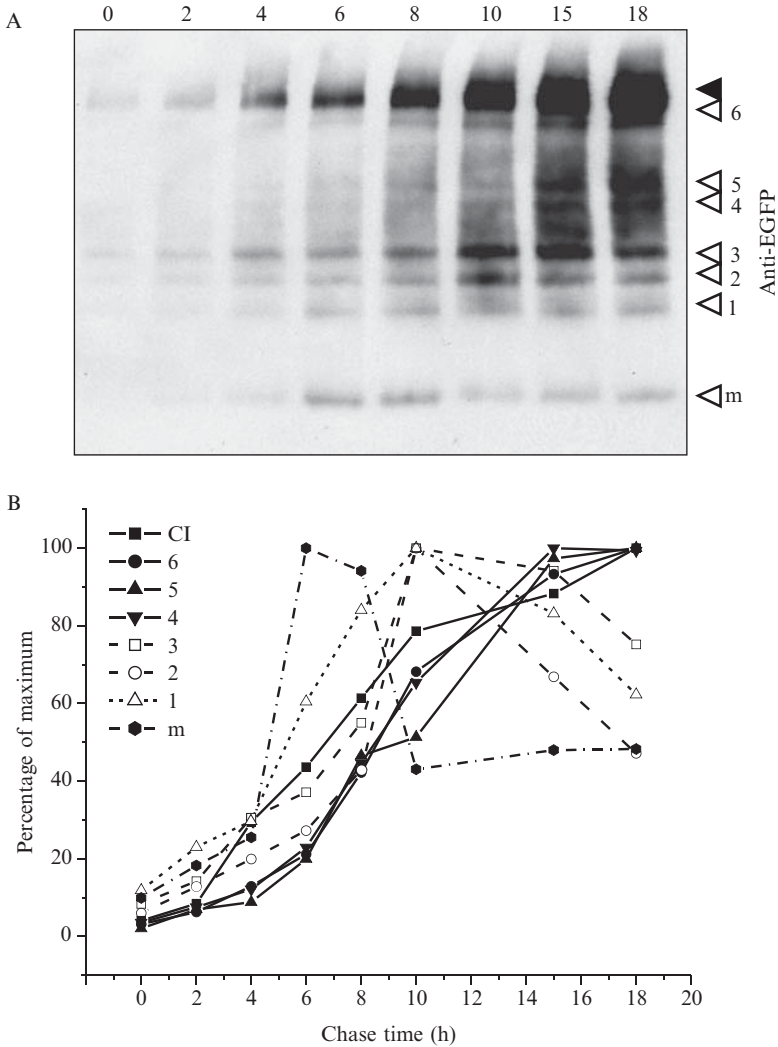


Figure 7.6 Induction pulse-chase experiment of NDUFS3-AcGFP₁ cells. Cells were pulse-induced for 30 min and chased for several durations. The time points after the pulse are indicated above the lanes. (A) Mitochondrial-enriched fractions were loaded on a BN-PAGE gel and blotted for immunodetection against EGFP. Holo-CI is indicated with filled arrowheads, subcomplexes with open arrowheads. (B) Quantitative analysis of the AcGFP₁-labeled subcomplexes shown in (A). IOD values were background corrected and expressed as percentage of the maximum.

subcomplex for each time point by use of ImagePro Plus 5.1 (Media Cybernetics) and corrected it for background. The resulting numeric values were displayed as a percentage of the maximum value per subcomplex

(Fig. 7.6B). During the first 10-h chase, all (sub)complexes showed an increase of NDUFS3–AcGFP₁ incorporation. Surprisingly, the fully assembled holo–CI showed a relatively fast increase at an early stage (between 2 and 4 h). This suggests that either incorporation of newly synthesized subunits through subassemblies 1 to 6 is relatively fast or that it occurs through an alternate and more direct exchange route as postulated by Lazarou *et al.* (2007). Monomeric NDUFS3–AcGFP₁ showed the steepest slope between 4 and 6 h, followed by subcomplex 1 between 6 to 8 h and subcomplexes 2 to 3 between 8 and 10 h. Interestingly, there seemed to be a correlation between the molecular weight on gel and the time of reaching the maximum. First monomeric NDUFS3–AcGFP₁ reached its maximum (6 h), followed by subassemblies 1 to 3 (10 h), subassemblies 4 to 5 (15 h), and subassembly 6 and holo–CI (18 h). These data strongly suggest that CI is, indeed, assembled sequentially by means of steps 1 to 6.

4.3. Accumulation of complex I assembly intermediates after chloramphenicol treatment

Chloramphenicol (CAP) can specifically inhibit the translation machinery of the mitochondrion without affecting translation in the cytosol. Because all mitochondrial DNA–encoded CI subunits (ND subunits) are embedded in the inner membrane, we reasoned that CAP treatment might reveal important clues for the role of these subunits in the appearance of the NDUFS3 subcomplexes 1 to 6. In absence of ND-subunits, it can be expected that CI assembly will seize at the point at which incorporation of these subunits is essential for formation of the next assembly intermediate. Because induction may well interfere with accumulation, we preferred steady-state labeling conditions. Therefore, we specifically selected a clone with very low expression under noninduced conditions (see Fig. 7.5A–B, “minus” signs).

We seeded NDUFS3–AcGFP₁ cells in two 75-cm² culture flasks and cultured them in 20 ml DMEM supplemented with FCS, penicillin/streptomycin, blasticin, and hygromycin at 37° and 5% CO₂ to 40% confluence. First, a CAP stock solution was freshly prepared by dissolving 40 mg CAP (Sigma) in 1 ml absolute EtOH. Subsequently, the medium of one flask was replaced by 30 ml fresh medium containing 30 µl of the stock solution (to obtain an end concentration of 40 µg CAP per ml medium). The other flask was only refreshed with 30 ml medium. After 3 days of incubation at 37° and 5% CO₂, cells were harvested and analyzed on BN-PAGE gel as described in section 4.1. The results are shown in Fig. 7.7.

CAP incubation induced the specific accumulation of subassemblies 2 and 3 and the disappearance of subcomplexes 4 to 6 and holo–CI (Fig. 7.7A). This was paralleled by a reduced in-gel NADH–NTB activity (IGA; Fig. 7.7B) and a decrease in the total amount of CI (NDUFA9;

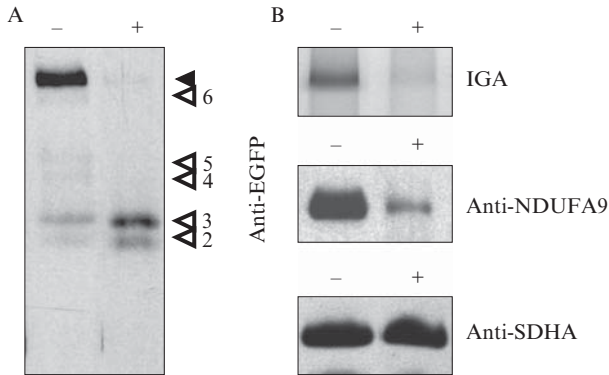


Figure 7.7 Subcomplexes 2 and 3 accumulate on mitochondrial translation. NDUFS3-AcGFP₁ “leakage” cells were 0 or 3 days treated with CAP (– and + respectively). (A) Mitochondrial enriched fractions were loaded on a BN-PAGE gel and blotted for immunodetection against EGFP. Holo-CI is indicated with filled arrowheads, subcomplexes with open arrowheads. (B) CI in-gel activity (IGA) and immunodetection against NDUFA9 (a measure of the total amount of CI) and SDHA (loading control).

Fig. 7.7B). Expression of complex II was unaltered (SDHA; Fig. 7.7B). These results suggest that CI assembly cannot proceed beyond subcomplex 2 and 3 in the absence of ND-subunits. For a more comprehensive CAP experiment we refer to our previous study (Vogel *et al.*, 2007a), in which we similarly accumulated assembly intermediates 2 and 3 by inhibiting mitochondrial translation and subsequently chased them after CAP removal.

ACKNOWLEDGMENT

We thank Flanka Venselaar (Centre for Molecular and Biomolecular Informatics, Nijmegen Centre for Molecular Life Sciences, Nijmegen, The Netherlands) for providing Figure 7.2.

REFERENCES

- Abrahams, J. P., Leslie, A. G., Lutter, R., and Walker, J. E. (1994). Structure at 2.8 Å resolution of F₁-ATPase from bovine heart mitochondria. *Nature* **370**, 621–628.
- Brandon, M., Baldi, P., and Wallace, D. C. (2006). Mitochondrial mutations in cancer. *Oncogene* **25**, 4647–4662.
- Calvaruso, M. A., Smeitink, J., and Nijtmans, L. (2008). Electrophoresis techniques to investigate defects in oxidative phosphorylation. *Methods* **46**, 281–287.
- Carroll, J., Fearnley, I. M., Skehel, J. M., Shannon, R. J., Hirst, J., and Walker, J. E. (2006). Bovine complex I is a complex of 45 different subunits. *J. Biol. Chem.* **281**, 32724–32727.
- Dunning, C. J., McKenzie, M., Sugiana, C., Lazarou, M., Silke, J., Connelly, A., Fletcher, J. M., Kirby, D. M., Thorburn, D. R., and Ryan, M. T. (2007). Human CIA30 is involved in the early assembly of mitochondrial complex I and mutations in its gene cause disease. *EMBO J.* **26**, 3227–3237.

- Friedrich, T., and Weiss, H. (1997). Modular evolution of the respiratory NADH: Ubiquinone oxidoreductase and the origin of its modules. *J. Theor. Biol.* **187**, 529–540.
- Iwata, S., Lee, J. W., Okada, K., Lee, J. K., Iwata, M., Rasmussen, B., Link, T. A., Ramaswamy, S., and Jap, B. K. (1998). Complete structure of the 11-subunit bovine mitochondrial cytochrome *bc₁* complex. *Science* **281**, 64–71.
- Janssen, R. J., Nijtmans, L. G., van den Heuvel, L. P., and Smeitink, J. A. (2006). Mitochondrial complex I: Structure, function and pathology. *J. Inherit. Metab. Dis.* **29**, 499–515.
- Kashani-Poor, N., Zwicker, K., Kerscher, S., and Brandt, U. (2001). A central functional role for the 49-kDa subunit within the catalytic core of mitochondrial complex I. *J. Biol. Chem.* **276**, 24082–24087.
- Lazarou, M., McKenzie, M., Ohtake, A., Thorburn, D. R., and Ryan, M. T. (2007). Analysis of the assembly profiles for mitochondrial- and nuclear-DNA-encoded subunits into complex I. *Mol. Cell Biol.* **27**, 4228–4237.
- Ogilvie, I., Kennaway, N. G., and Shoubridge, E. A. (2005). A molecular chaperone for mitochondrial complex I assembly is mutated in a progressive encephalopathy. *J. Clin. Invest.* **115**, 2784–2792.
- Pagliarini, D. J., Calvo, S. E., Chang, B., Sheth, S. A., Vafai, S. B., Ong, S. E., Walford, G. A., Sugiana, C., Boneh, A., Chen, W. K., Hill, D. E., Vidal, M., *et al.* (2008). A mitochondrial protein compendium elucidates complex I disease biology. *Cell* **134**, 112–123.
- Saada, A., Edvardson, S., Rapoport, M., Shaag, A., Amry, K., Miller, C., Lorberboum-Galski, H., and Elpeleg, O. (2008). C6ORF66 is an assembly factor of mitochondrial complex I. *Am. J. Hum. Genet.* **82**, 32–38.
- Sazanov, L. A., and Hinchliffe, P. (2006). Structure of the hydrophilic domain of respiratory complex I from *Thermus thermophilus*. *Science* **311**, 1430–1436.
- Schagger, H., and von Jagow, J. G. (1991). Blue native electrophoresis for isolation of membrane protein complexes in enzymatically active form. *Anal. Biochem.* **199**, 223–231.
- Srivastava, S., Barrett, J. N., and Moraes, C. T. (2007). PGC-1 α /beta upregulation is associated with improved oxidative phosphorylation in cells harboring nonsense mtDNA mutations. *Hum. Mol. Genet.* **16**, 993–1005.
- Sun, F., Huo, X., Zhai, Y., Wang, A., Xu, J., Su, D., Bartlam, M., and Rao, Z. (2005). Crystal structure of mitochondrial respiratory membrane protein complex II. *Cell* **121**, 1043–1057.
- Tsukihara, T., Aoyama, H., Yamashita, E., Tomizaki, T., Yamaguchi, H., Shinzawa-Itoh, K., Nakashima, R., Yaono, R., and Yoshikawa, S. (1996). The whole structure of the 13-subunit oxidized cytochrome *c* oxidase at 2.8 Å. *Science* **272**, 1136–1144.
- Ugalde, C., Vogel, R., Huijbens, R., Van Den, H. B., Smeitink, J., and Nijtmans, L. (2004b). Human mitochondrial complex I assembles through the combination of evolutionary conserved modules: A framework to interpret complex I deficiencies. *Hum. Mol. Genet.* **13**, 2461–2472.
- Vogel, R. O., Dieteren, C. E., van den Heuvel, L. P., Willems, P. H., Smeitink, J. A., Koopman, W. J., and Nijtmans, L. G. (2007a). Identification of mitochondrial complex I assembly intermediates by tracing tagged NDUFS3 demonstrates the entry point of mitochondrial subunits. *J. Biol. Chem.* **282**, 7582–7590.
- Vogel, R. O., Janssen, R. J., Ugalde, C., Grovenstein, M., Huijbens, R. J., Visch, H. J., van den Heuvel, L. P., Willems, P. H., Zeviani, M., Smeitink, J. A., and Nijtmans, L. G. (2005). Human mitochondrial complex I assembly is mediated by NDUFAF1. *FEBS J.* **272**, 5317–5326.
- Vogel, R. O., Janssen, R. J., van den Brand, M. A., Dieteren, C. E., Verkaart, S., Koopman, W. J., Willems, P. H., Pluk, W., van den Heuvel, L. P., Smeitink, J. A.,

- and Nijtmans, L. G. (2007b). Cytosolic signaling protein Ecsit also localizes to mitochondria where it interacts with chaperone NDUFAB1 and functions in complex I assembly. *Genes Dev.* **21**, 615–624.
- Vogel, R. O., Smeitink, J. A., and Nijtmans, L. G. (2007c). Human mitochondrial complex I assembly: A dynamic and versatile process. *Biochim. Biophys. Acta.* **1767**, 1215–1227.
- Vogel, R. O., van den Brand, M. A., Rodenburg, R. J., van den Heuvel, L. P., Tsuneoka, M., Smeitink, J. A., and Nijtmans, L. G. (2007d). Investigation of the complex I assembly chaperones B17.2L and NDUFAB1 in a cohort of CI deficient patients. *Mol. Genet. Metab.* **91**, 176–182.
- Xia, D., Yu, C. A., Kim, H., Xia, J. Z., Kachurin, A. M., Zhang, L., Yu, L., and Deisenhofer, J. (1997). Crystal structure of the cytochrome *bc*₁ complex from bovine heart mitochondria. *Science* **277**, 60–66.

TWO-DIMENSIONAL NATIVE ELECTROPHORESIS FOR FLUORESCENT AND FUNCTIONAL ASSAYS OF MITOCHONDRIAL COMPLEXES

Zibiernisha Wumaier, Esther Nübel, Ilka Wittig, *and* Hermann Schägger

Contents

1. Introduction	154
2. Materials and Methods	155
2.1. Materials	155
2.2. Summary of electrophoretic and accessory protocols	155
2.3. Short protocols for nonconventional 2-D and multidimensional gels	156
3. Analysis of Mitochondrial Supercomplexes	161
3.1. 2-D BN/SDS-PAGE	161
3.2. 2-D BN/hrCN electrophoresis	164
3.3. Final 3-D SDS-PAGE or dSDS-PAGE	166
References	167

Abstract

Supramolecular assemblies of native membrane protein complexes were solubilized from biological membranes by very mild detergents and isolated by native electrophoresis. The complexity of these higher order structures can be reduced for proteomic investigations by applying less mild native electrophoresis variants in the second dimension. Supercomplexes thereby dissociate into the individual complexes. Clear-native and blue-native electrophoresis variants are useful alternatives for the second native dimension, but clear-native electrophoresis is advantageous for the identification of fluorescence-labeled proteins and for in-gel activity assays that are hampered by Coomassie dye. The 2-D native gels comprising two orthogonal native dimensions are useful to determine the stoichiometry of complexes in supercomplexes. Strips from

Cluster of Excellence “Macromolecular Complexes,” Zentrum der Biologischen Chemie, Molekulare Bioenergetik, Goethe-Universität Frankfurt, Frankfurt, Germany

Methods in Enzymology, Volume 456
ISSN 0076-6879, DOI: 10.1016/S0076-6879(08)04408-X

© 2009 Elsevier Inc.
All rights reserved.

2-D native gels can also be used for 3-D SDS-PAGE to identify loosely bound accessory subunits of supercomplexes. The subunit composition of supercomplexes and individual complexes is investigated by 4-D gels. The 4-D protocol starts with isolation of highly pure membrane protein complexes by 2-D native electrophoresis, followed by doubled SDS-PAGE to resolve the subunits.

1. INTRODUCTION

Mild neutral detergents like dodecylmaltoside (DDM) and Triton X-100 are often used to solubilize mitochondrial complexes I to V from the inner mitochondrial membrane. The individual complexes are then separated according to their masses by use of acrylamide gradient gels for blue-native electrophoresis (BNE or BN-PAGE; Schagger and von Jagow, 1991; Schagger *et al.*, 1994; Wittig *et al.*, 2006). Digitonin, which is one of the mildest detergents, can preserve some labile physiological interactions between individual complexes. For example, respiratory supercomplexes I₁III₂IV₀₋₄ containing monomeric complex I, dimeric complex III, and a variable copy number of complex IV (0 to 4) can be isolated from mammalian mitochondria (Schagger and Pfeiffer, 2000). The molar ratio of complexes within supercomplexes can be determined by use of the apparent masses of supercomplexes in BNE (Schagger *et al.*, 1994) and by densitometric quantification of the constituent complexes in 2-D BN/BN gels. Modified BNE with the detergent DDM added to the cathode buffer is thereby used for the second-dimensional resolution (Schagger and Pfeiffer, 2000), because addition of detergent makes BNE less mild and dissociates supramolecular structures into the constituent complexes.

Noncolored variants of BNE like clear-native electrophoresis (CNE; Schagger *et al.*, 1994; Wittig and Schagger, 2005) and high-resolution clear-native electrophoresis (hrCNE; Wittig *et al.*, 2007a,b) have been shown to be advantageous for the identification and quantification of fluorescence-labeled proteins in the native gels and for in-gel catalytic activity assays. For a review of features and applications of BNE, CNE, and hrCNE, see Wittig and Schagger (2008). hrCNE seems especially interesting for 2-D native separations, because it offers high resolution comparable to BNE and has the potential to release individual complexes from supercomplexes similar to modified BNE with detergent added to the cathode buffer.

In this chapter we suggest to use two different native electrophoresis variants sequentially according to their special advantages for the first or second dimensional native separations. Solubilization by digitonin and separation by BNE should be used first to preserve supramolecular

structures. CNE is even milder; however, it suffers from streaking of many membrane proteins. Ideally, hrCNE is used next for the second-dimensional resolution, because less mild conditions are desired to achieve smooth disintegration of supercomplexes into the constituent complexes without significant further dissociation. Second-dimensional hrCNE allows for immediate identification and quantification of fluorescence-labeled proteins in the 2-D native gel. No background Coomassie stain, as observed with modified BNE (with DDM), can hamper the visualization of in-gel activities.

2. MATERIALS AND METHODS

2.1. Materials

Coomassie Blue G-250 (Serva Blue G) abbreviated here as Coomassie dye, acrylamide, and bisacrylamide (the twice crystallized products) were purchased from Serva. Dodecyl- β -D-maltoside (DDM) was from Glycon (Luckenwalde, Germany), and digitonin (catalog number 37006, >50% purity, used without recrystallization) from Fluka. Sodium deoxycholate (DOC) was obtained from Merck. Fluorescent monoreactive *N*-hydroxy-succinimide (NHS) ester dyes (Cy5 and Cy5.5) were purchased from GE Healthcare. All other chemicals were from Sigma. Bovine heart mitochondria were prepared according to [Smith \(1967\)](#) and finally washed twice with 10 mM sodium phosphate buffer to remove primary amines that would hamper fluorescence labeling of lysines by use of NHS ester CyDyes.

2.2. Summary of electrophoretic and accessory protocols

Buffers and protocols for BNE and SDS-PAGE originally described by [Schägger and von Jagow \(1991\)](#) and [Schägger *et al.* \(1994\)](#) were recently updated by [Wittig *et al.* \(2006\)](#) and [Schägger \(2006\)](#). Protocols for CNE and hrCNE and for final SDS-PAGE were published by [Schägger *et al.* \(1994\)](#), [Wittig and Schägger \(2005\)](#), and [Wittig *et al.* \(2007a,b\)](#).

The 2-D BN/BN electrophoretic system comprising BNE for the first electrophoresis and modified BNE (0.02% DDM added to the cathode buffer) for second-dimensional resolution has been described by [Schägger and Pfeiffer \(2000\)](#). Strips from such 2-D native gels were processed by 3-D SDS-PAGE as described by [Schägger and Pfeiffer \(2000\)](#). Gel pieces from 2-D native gels containing multiprotein complexes can be further resolved by doubled SDS-PAGE ([Rais *et al.*, 2004](#)). This 4-D system comprises two orthogonal native electrophoreses followed by two orthogonal SDS-PAGEs ([Meyer *et al.*, 2007](#)).

Fluorescence labeling that uses NHS ester CyDyes (Wittig *et al.*, 2007a), Coomassie staining (Wittig *et al.*, 2007b), silver staining (Rais *et al.*, 2004), and in-gel catalytic activity assays (Wittig *et al.*, 2007a,b) have been described recently. The novel combination of BNE and hrCNE to generate a 2-D native BN/hrCN system is described in the following.

2.3. Short protocols for nonconventional 2-D and multidimensional gels

2.3.1. Gel and sample preparation

Acrylamide gradient gels for BNE were cast according to Wittig *et al.* (2006). Here we used 3 to 13% acrylamide gradient gels to cover the 10-kDa to 10-MDa protein mass range. Buffers and stock solutions for specific electrophoresis variants are summarized in Tables 8.1 and 8.2.

Fluorescence labeling of membrane proteins can be performed with biological membranes before detergent is added or after solubilization by detergent. Here we used bovine heart mitochondria that had been labeled by the monoreactive fluorescent NHS esters dyes Cy5 or Cy5.5. Note, however, that these cheaper dyes are not suitable for DIGE experiments in

Table 8.1 Buffers and stock solutions for native gels

Solution	Composition
Gel buffer 3× (triple concentrated)	1.5 M 6-aminohexanoic acid, 75 mM imidazole/HCl (pH 7.0)
AB mix (49.5%T, 3%C - acrylamide-bisacrylamide mixture)	48 g acrylamide and 1.5 g bisacrylamide per 100 ml
^a Solubilization buffer A	50 mM NaCl, 2 mM 6-aminohexanoic acid, 1 mM EDTA, 50 mM imidazole/HCl, pH 7.0 (4°).
^b Solubilization buffer B	500 mM 6-aminohexanoic acid, 1 mM EDTA, 50 mM imidazole/HCl, pH 7.0 (at 4°).
5% Coomassie dye stock	5 g Coomassie dye suspended in 100 ml 500 mM 6-aminohexanoic acid
Glycerol/Ponceau S stock	50% glycerol (wt/vol), 0.1% Ponceau S
Anode buffer for BNE, CNE, and hrCNE	25 mM imidazole/HCl, pH 7.0

^a Solubilization buffer A is commonly used.

^b Solubilization buffer B is used when protein aggregation during protein entry into the native gel (because of high ionic strength) is observed and to dilute samples containing high salt concentration.

Table 8.2 Cathode buffers for native gels

	CNE	BNE		Modified BNE (+DDM)	^b hrCNE
		B	B/10		
Tricine (mM)	50	50	50	50	50
Imidazole (mM)	7.5	7.5	7.5	7.5	7.5
Coomassie dye (%)	—	0.02	0.002	0.02	—
DOC (%)	—	—	—	—	0.05
DDM (%)	—	—	—	0.02	0.02
^a pH	~7.0	~7.0	~7.0	~7.0	~7.0

^a Do not adjust the pH, which is approximately 7.0, except potentially with Tricine or imidazole.

^b The cathode buffer for the hrCNE-1 variant, as described by Wittig *et al.*, (2007a) was used for this work.

contrast to CyDIGE Fluor dyes Cy2, Cy3, and Cy5. The dye was dissolved in dimethylformamide (10 $\mu\text{g}/\mu\text{l}$), and aliquots were stored in liquid nitrogen for several weeks before use; 10- μl aliquots were added to 10 mg of mitochondria in 1 ml 250 mM sucrose, 20 mM sodium phosphate, pH 7.5, and gently shaken in the dark for 1 h at approximately 20°. Labeled mitochondria were sedimented by centrifugation (10 min, 20,000g) and stored at -80°.

Here we solubilized fluorescent-labeled bovine heart mitochondrial membranes by the mild neutral detergent digitonin to preserve supramolecular structures of mitochondrial respiratory chain complexes with masses larger than 2 MDa. Supercomplexes of respiratory complexes I, III, and IV ($I_1III_2IV_n$) contain monomeric complex I (approximately 1 MDa), dimeric complex III (approximately 500 kDa), and a varying copy number ($n = 0$ to 4) of complex IV (approximately 200 kDa for the monomer). Solubilization of small aliquots of sedimented membranes for application to 1-cm gel wells is described in the following: 14 times larger amounts were often handled to load preparative 14-cm-wide gels.

Aliquots of mitochondrial membrane pellets (400 μg protein) were suspended with 40 μl solubilization buffer A (Table 8.1) by vortexing; 8 μl 20% digitonin was then added to set a digitonin/protein ratio of 4 g/g for solubilization. After 5 to 10 min incubation at 20° or on ice, the sample was centrifuged for 10 min at 100,000g to remove undissolved material. After centrifugation, approximately 50% of the total protein was found in the supernatant. Glycerol/Ponceau S stock (5 μl) was then added to facilitate sample application to the gel, and finally 4 μl Coomassie stock was added to set a Coomassie dye/digitonin ratio of 1:8 g/g. The total supernatant containing approximately 200 μg protein in a 50 μl volume was applied to a 10 mm \times 1.5 mm gel well for BNE.

2.3.2. 2-D BN/SDS-PAGE

2-D BN/SDS-PAGE is a commonly used technique to analyze the subunit composition of native complexes. It is briefly described here for comparison with 2-, 3- and 4-D techniques that use two native separations for the initial purification of native protein complexes.

The native gel for BNE was mounted into the electrophoresis chamber, and anode buffer (Table 8.1) was added to the lower compartment. Dark blue cathode buffer B (Table 8.2) was added to the upper compartment before protein samples were underlaid the cathode buffer. By use of gels with dimensions 1.5 mm × 14 cm × 14 cm and an electrophoresis apparatus without special cooling device we typically set the limits to 500 V and 15 mA per gel. The actual running conditions at the start of electrophoresis were approximately 200 V and 15 mA. Voltage was gradually raised to 500 V during electrophoresis. When Coomassie dye reached approximately one third of the total running distance, cathode buffer B was removed by suction and replaced by cathode buffer B/10 (Table 8.2) containing 1/10th of the previous dye concentration. Electrophoresis was performed at a temperature of 4 to 7° and required 2 to 4 h. Gel strips from BNE (Fig. 8.1A) were then prepared for SDS-PAGE in the second dimension as described (Schägger, 2006; Wittig *et al.*, 2006). After 2-D SDS-PAGE that removed Coomassie dye from the proteins, the fluorescence-labeled protein subunits were visualized with a Typhoon laser scanner (Fig. 8.1B) and then reused for silver staining (Fig. 8.1C).

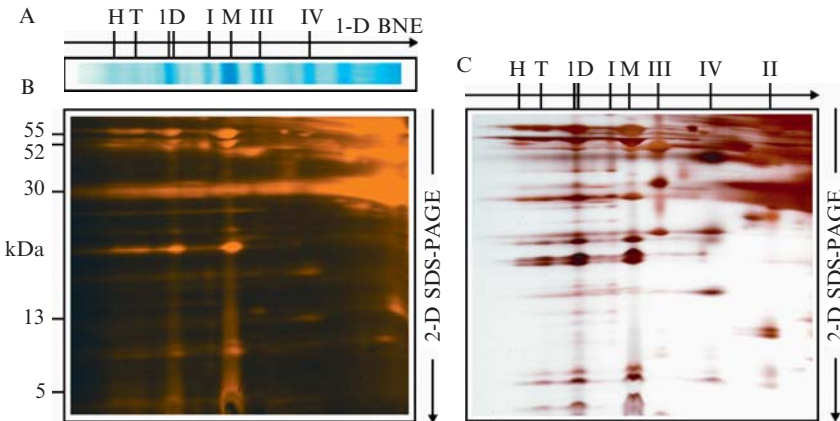


Figure 8.1 2-D BN/SDS-PAGE of mitochondrial complexes. 1, respiratory supercomplex I₁III₂IV₁. M, D, T, H, monomeric, dimeric, tetrameric, and hexameric ATP synthase. I, II, III, IV, respiratory complexes I, III, and IV. (A) Bovine heart mitochondria were solubilized by digitonin, and the solubilized complexes were separated by BNE in the first dimension. (B) Detection of Cy5.5-labeled protein subunits after SDS-PAGE in the second dimension. (C) Gel B was reused for silver staining.

2.3.3. 2-D BN/hrCN electrophoresis

2-D BN/hrCN electrophoresis is a novel combination of two published native electrophoresis systems with some similarities and differences compared with 2-D BN/BN electrophoresis (Schägger and Pfeiffer, 2000; Wittig *et al.*, 2006). The initial steps of the 2-D BN/BN and 2-D BN/hrCN variants are identical:

Gel strips from BNE (0.15 mm × 10 mm; see Fig. 8.2A) were incubated for seconds in water, and the strips were placed on glass plates at the common sample gel position. Spacers that ideally are thinner than the BN gels (1.5 mm) to avoid gliding of the gel strip were mounted. The second glass plate was put on top, the assembly was fixed with clamps, excess water was removed from the native gel strip with papers, and after a few minutes (for a better adherence of the gel strips to the glass plates) the gel was carefully brought to the upright position.

An acrylamide gradient gel (5 to 16%) was cast below the BN gel strip with the same buffers and stock solutions as described for casting BN gels (Wittig *et al.*, 2006; see also Table 8.1) and overlaid with some drops of water before polymerization. The overlaid water should not reach the gel strip at that time point. After polymerization, more water was added to surround the BN gel strip. The strip was then gently pushed down to the freshly polymerized separating gel with appropriate plastic cards. After removal of water, the gaps between the BN gel strip and side spacers were filled with a 4% acrylamide native gel to guarantee homogeneous field strength during the following hrCNE.

The gel was mounted into a vertical electrophoresis chamber, anode buffer was added to the lower compartment (Table 8.1, the same as used for BNE), and the cathode buffer for the hrCNE-1 variant (Table 8.2) was added that contains mixed micelles from 0.05% sodium deoxycholate (DOC) and 0.02% dodecylmaltoside (DDM), as described by Wittig *et al.* (2007a). The hrCNE-1 variant is the only variant used for the present work and is, therefore, abbreviated here as hrCNE for simplicity. Mixing DOC and DDM seems to alter considerably the critical micelle concentration of DOC (CMC approximately 1%) that is also the minimum concentration to keep membrane proteins in solution. Here it was possible to use considerably lower DOC concentrations (0.05% mixed with 0.02% DDM) to keep membrane proteins soluble during electrophoresis. This reduced DOC concentration was harsh enough to dissociate most supramolecular structures into the constituent complexes but was sufficiently mild to avoid dissociation and denaturation of the released individual respiratory complexes.

Electrophoresis conditions were then set according to the specific gel dimensions and the electrophoresis apparatus (the same as used in 2.3.2. for BNE) to avoid significant warming of the glass plates when the gel is run at an ambient temperature of 4°. Electrophoresis was stopped before the Coomassie dye front left the gel.

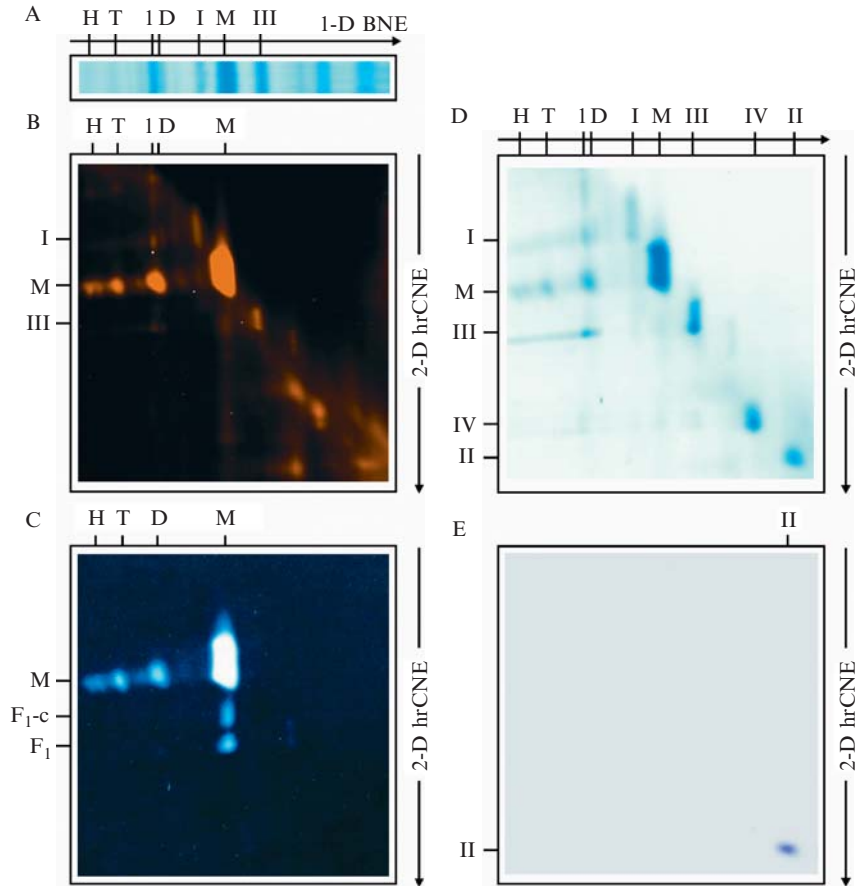


Figure 8.2 2-D BN/hrCN separation of oligomeric ATP synthase and monomeric respiratory complex II. Assignment of respiratory complexes and ATP synthase forms as in Fig. 8.1. (A) Supercomplex I₁III₂IV₁ (marked 1) comigrated with dimeric ATP synthase (marked D) in the 1-D BN gel. (B) The BN gel strip was then processed by hrCNE in the second dimension to generate a 2-D system that is native in both dimensions. The second native electrophoresis (hrCNE) is less mild than the first one (BNE) and dissociated supercomplexes into the individual complexes. Various oligomeric forms of complex V (M, D, T, H) were converted to the monomeric form by hrCNE. (C) Gel B was reused for an ATP hydrolysis assay to identify the different ATP synthase forms, the catalytically active F₁ subcomplex, and the F₁ subcomplex associated with a ring of c-subunits (F₁-c). (D) Gel C was reused for Coomassie staining to obtain a survey of the individual mitochondrial complexes that were released from the larger supercomplexes by hrCNE in the second dimension. (E) In-gel succinate/NTB reductase assay to identify complex II.

2-D BN/hrCN gels, still shielded by the glass plates, were then inspected for fluorescence-labeled proteins and complexes (Figs. 8.2B and 8.3B). Complete lanes from 2-D BN/hrCN gels containing, for example, respiratory complexes I, III, and IV as the major components released from respiratory supercomplexes can be marked on both glass plates (vertically boxed strip in Fig. 8.3B) and cut out for separation of the protein subunits by 3-D SDS-PAGE (see Fig. 8.4BC). Similarly, gel pieces containing complexes or supercomplexes can be excised for dSDS-PAGE (see Fig. 8.4DE).

2.3.4. Processing of 2-D BN/hrCN gels for SDS-PAGE

Gel strips from 2-D BN/hrCN gels were commonly wetted for 10 to 30 min with 1% SDS for final 3-D SDS-PAGE. Alternately, 1% SDS, 1% mercaptoethanol can be used for 30 min (at 37° in a sealed Falcon tube) in the rare cases when breaking of disulfide bonds is important (Wittig *et al.*, 2006). Tricine-SDS-PAGE (Schägger, 2006) is preferred to Laemmli SDS-PAGE whenever SDS-PAGE follows a native electrophoretic separation, because broad protein bands from broad native gel strips are well focussed to sharp protein spots because of the relatively high ionic strength of the separating gel.

Gel pieces from 2-D BN/hrCN gels containing, for example, highly purified multiprotein complexes were incubated for 30 min with 1% SDS, 0.05% Coomassie dye before they were used for dSDS-PAGE (Rais *et al.*, 2004). Optimal overall resolution for 10- to 100-kDa proteins is achieved with 10% or 12% acrylamide gels with 6 M urea for 3-D Tricine-SDS-PAGE, followed by 16% acrylamide gels (without urea) for the next orthogonal 4-D SDS-PAGE.

3. ANALYSIS OF MITOCHONDRIAL SUPERCOMPLEXES

A straightforward approach to analyze the subunit composition of complexes (e.g., for mass spectrometric or immunological analyses) is separation of native complexes by BNE followed by resolution of the subunits by SDS-PAGE. This reference system is briefly discussed in section 3.1. Higher order structures like respiratory chain supercomplexes or oligomeric ATP synthase, however, are often too complex for this two-step approach. Alternative protocols to reduce the complexity seem highly welcome (see sections 3.2. and 3.3).

3.1. 2-D BN/SDS-PAGE

Here, we separated digitonin-solubilized fluorescence-labeled bovine heart mitochondria by BNE. Fixation and Coomassie staining were required to detect the bands of separated complexes I, III, IV; and the monomeric (M);

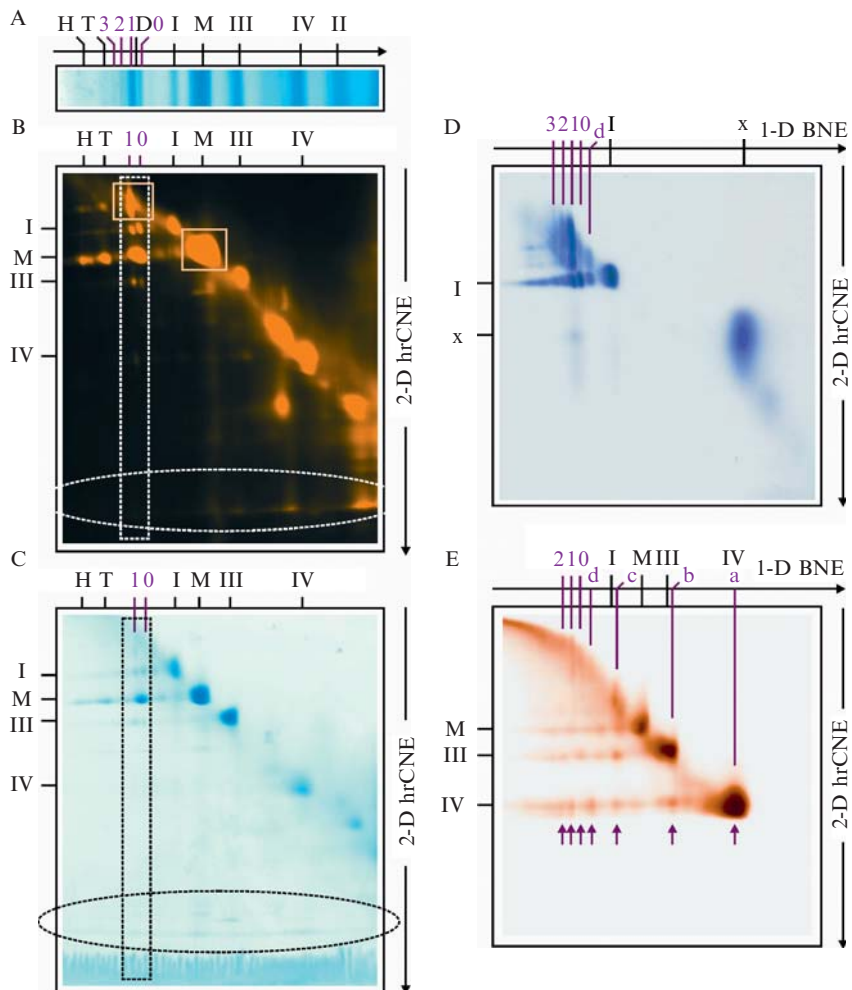


Figure 8.3 2-D BN/hrCN separation of mitochondrial supercomplexes. Respiratory complexes and ATP synthase forms were assigned as in Fig. 8.1. (A) Supercomplexes $I_1III_2IV_{0-3}$ (marked 0 to 3) containing monomeric complex I, dimeric complex III, and zero to three copies of complex IV were resolved by 1-D BNE. (B) Detection of fluorescence-labeled complexes after 2-D BN/hrCNE separation. Vertical gel strip (boxed) containing all fragments that were released from supercomplexes by hrCNE (as used for the final 3-D SDS-PAGE; see Fig. 8.4B,C). Labile subunits and potentially novel accessory proteins of supercomplexes can be expected in the marked gel area (ellipsoid). Two spots comprising a respiratory supercomplex and monomeric ATP synthase (boxed gel pieces) were used for dSDS-PAGE (see Fig. 8.4D,E). (C) A gel comparable to Fig. 8.3B was Coomassie stained. (D) Another similar gel was used for the NADH/NBT reductase assay to identify respiratory complex I (marked I), a presumed I_1IV_1 supercomplex (marked d) containing complexes I and IV, supercomplexes $I_1III_2IV_{0-3}$ (marked 0 to 3), and a presumed flavoprotein subcomplex of complex I (marked x). (E) A native heme stain assay identified horizontally aligned spots of complex IV (arrows) that were derived from bands a, b, c, d, and supercomplexes 0 to 2. The assay identified also complex III and for unknown reasons monomeric complex V as well. Tentative assignments of further complexes: band a, monomeric complex IV; band b, dimeric complex IV; band c, supercomplex III_2IV_2 , and band d, supercomplex I_1IV_1 .

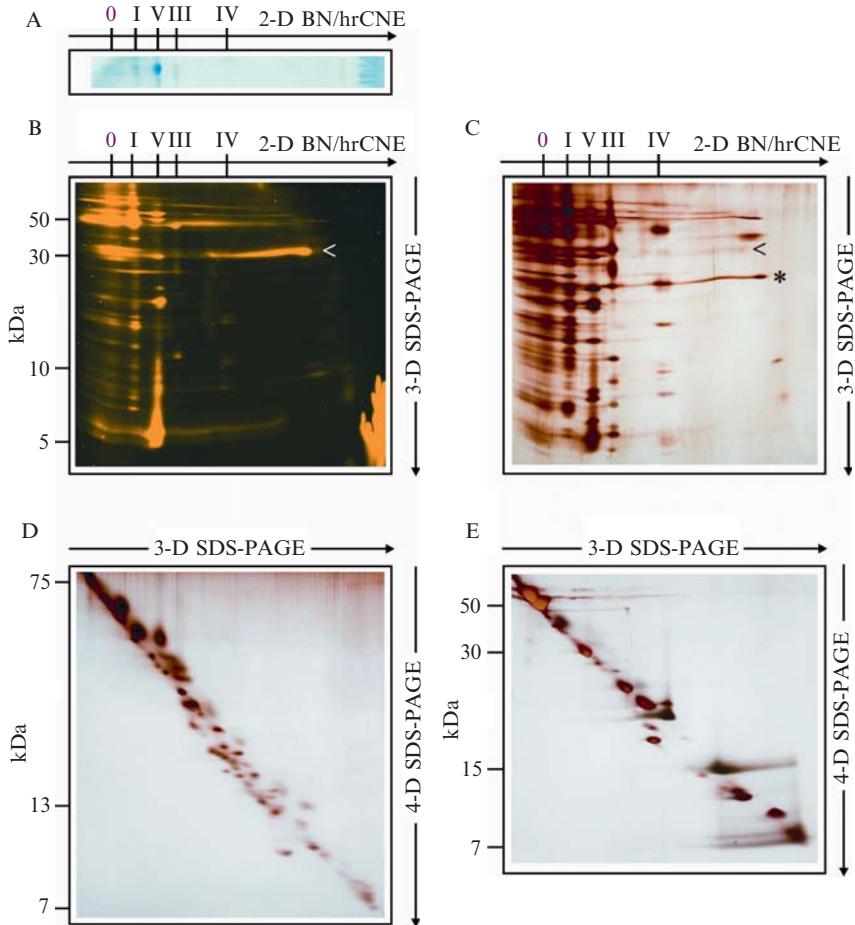


Figure 8.4 Separation of subunits of complexes by 3-D and 4-D SDS-PAGE. 0, I, III, IV, and V, residual supercomplex 0, and mitochondrial complexes I, III, IV, and V that were released from supercomplexes and oligomeric ATP synthase by second dimensional hrCNE. (A) Coomassie-stained gel strip from the 2-D BN/hrCNE gel (boxed vertically in Fig. 8.3B). (B) Detection of fluorescence-labeled protein subunits after 3-D Tricine-SDS-PAGE with a 16% acrylamide gel. (C) Gel B was reused for silver staining. Note the strongly differing fluorescence- and silver-stain intensities of two selected proteins (< and *). Labile subunits and novel accessory proteins generally are located on the right half of 3-D gels. (E) Spots containing residual supercomplex and monomeric complex V (boxed gel pieces in Fig. 8.3 B) were resolved by dSDS-PAGE (i.e., by 3-D Tricine-SDS-PAGE with 12% acrylamide, 6 M urea gels followed by 4-D Tricine-SDS-PAGE with 16% acrylamide gels).

dimeric (D); tetrameric (T); and hexameric (H) forms of complex V, the mitochondrial F_1F_0 ATP synthase (Fig. 8.1A). Dimeric complex V comigrated with supercomplex $I_1III_2IV_1$ (marked 1). Inspecting the native gel

before fixation (not shown), some blue-stained protein bands might be detectable but no fluorescent band, because Coomassie dye quenches approximately 95% of the fluorescence (Wittig *et al.*, 2007a). After Tricine-SDS-PAGE in the second dimension that removed protein-bound Coomassie dye, some fluorescence-labeled protein subunits were visualized with a Typhoon laser scanner (Fig. 8.1B). More proteins and characteristic subunit patterns of complexes were revealed after silver staining (Fig. 8.1C). For example, subunits of complexes I and III were identified in the column of subunits of dimeric complex V, suggesting that a respiratory supercomplex (marked 1) comigrated with dimeric complex V (D). The relatively low number of clearly fluorescence-labeled protein subunits can be explained by selective fluorescence labeling of the readily accessible protein surfaces. Occluded protein areas seem to remain unlabeled. Major differences between Fig. 8.1B and Fig. 8.1C can, thus, give first hints on the topology of proteins in multiprotein complexes.

3.2. 2-D BN/hrCN electrophoresis

BNE has been combined previously with modified BNE (with DDM added to the cathode buffer) to build a 2-D BN/BN system. This 2-D native system has been used to investigate the constituents of supercomplexes and to determine the ratio of these components in the supercomplexes (Schägger and Pfeiffer, 2000, 2001). Here, we combined BNE with hrCNE to build a 2-D BN/hrCN system offering advantages for fluorescent and functional analyses (e.g., to analyze oligomeric complex V, complex II (Fig. 8.2), and the respiratory supercomplexes [Fig. 8.3]). The 2-D BN/hrCN system seems especially advantageous for catalytic activity assays, because no Coomassie dye can interfere with the color of the activity stain, and no Coomassie dye can bind to substrates like cytochrome *c* in catalytic activity assays (e.g., of cytochrome *c* oxidase [complex IV]).

BNE was performed under the same conditions as used for Fig. 8.1A, and comparable resolution and band patterns were obtained (Fig. 8.2A). The strongest band in the high mass region contained respiratory supercomplex $I_1III_2IV_1$ (marked 1) overlaid with some comigrating dimeric complex V.

After 2-D BN/hrCNE, the gel was inspected for fluorescence-labeled proteins by a Typhoon laser scanner (Fig. 8.2B). The most prominent spots could be assigned to the monomeric (M) and oligomeric forms (D, T, H) of complex V. Faint spots could be attributed to individual complexes I and III. This 2-D gel was then reused to measure the ATP hydrolysis activity of complex V by the intensity of the white lead phosphate precipitates that appeared on release of phosphate from ATP during the catalytic cycle (Fig. 8.2C). In addition to the oligomeric forms of ATP synthase that were already identified by their fluorescent labels (Fig. 8.2B), two further

protein complexes with ATP hydrolysis activity were detected below monomeric complex V (M). This position in the 2-D gel indicated that both additional complexes were smaller than monomeric complex V and that they dissociated from monomeric complex V during 2-D hrCNE. Most likely these spots represent F_1 and F_1 -c subcomplexes that had been identified as stable subcomplexes in a different context with human mitochondrial biosynthesis disorders (Carrozzo *et al.*, 2006). After documentation of the 2-D gels, the white lead phosphate precipitates were dissolved by 10% acetic acid, and the same gel was reused for Coomassie staining (Fig. 8.2D). All complexes that had not been part of supramolecular structures during 1-D BNE (i.e., the individual complexes I, II, III, IV, and M) were found on a diagonal of spots in the 2-D gel. These bands of individual complexes, especially those with high mass like complexes I and V, appear as fairly broad bands, because the complexes were almost immobilized in the first-dimension BNE when they approached their mass-specific pore-size limits in the acrylamide gradient gel. Therefore, they were not easily transferred to the following hrCN gel. Individual complexes that are released from supramolecular structures, however, are significantly smaller than the original assemblies. Therefore, they gain higher electrophoretic mobility on dissociation from the supercomplexes and appear as much sharper spots in the 2-D BN/hrCN gel. For example, all oligomeric forms of complex V (D, T, and H, assigned on top of Fig. 8.2D) gave rise to comparably sharp spots after dissociation into the monomeric form (assigned M on the left side of Fig. 8.2D). Similarly, supercomplex $I_1III_2IV_1$ (marked 1) dissociated into sharp spots of the individual complexes (assigned I, III, and IV on the left side of Fig. 8.2D).

Complex II was identified by the succinate/NTB reductase activity assay. Its position on the initial BN gel indicated that complex II was clearly smaller than complex IV (200 kDa) and presumably was present in a monomeric state (calculated mass 130 kDa). Mass calibration (not shown) can be obtained from the migration distance of complexes assigned in Fig. 8.2AD and the masses given in Wittig *et al.* (2006).

The analysis of respiratory supercomplexes started with BNE similar to Fig. 8.2A, except that Cy5-labeled (instead of Cy5.5-labeled) mitochondria were used. Unintended minor experimental variations led to improved resolution in the high mass range in this experiment so that additional minor bands of further supercomplexes $I_1III_2IV_{0-3}$ (marked 0 to 3 in Fig. 8.3A) close to dimeric complex V could be detected and assigned. After 2-D BN/hrCNE, a laser scanner was used to inspect the 2-D gel for fluorescence-labeled proteins (Fig. 8.3B). Both major supercomplexes (marked 1 and 0 in Fig. 8.3A) dissociated partially, as visualized by the characteristic pairs of spots of complexes I and III within the boxed vertical strip (marked I and III on the left side of Fig. 8.3B). A similar protein pattern was also observed after Coomassie staining (Fig. 8.3C). The Coomassie-stained gel revealed that some protein subunits

dissociated from the complexes and migrated close to the dark blue electrophoretic front (ragged blue bottom area). The area above (ellipsoid) is expected to contain detergent-labile proteins or potentially novel accessory proteins of supercomplexes. A mass spectrometric survey of the dissociated proteins and complexes can be obtained with gel strips from unfixed fluorescence-labeled gels (vertically boxed area in Fig. 8.3B) and separation of the proteins by 3-D SDS-PAGE (see Fig. 8.4BC).

The in-gel NADH/NTB reductase assay (Fig. 8.3D) identified complex I (marked I), a number of respiratory supercomplexes (marked 0 to 3), a supercomplex containing complexes I and IV but no complex III (marked d), and a much smaller compound (marked x) that presumably represented the flavoprotein part of complex I with a mass approximately 200 kDa. The preceding assignment was also deduced from comparison with the in-gel heme stain according to Zerbetto *et al.* (1997) that identified complexes IV and III with comparable signal intensities (Fig. 8.3E), and for unknown reasons also marked complex V (M), which does not possess a heme group of its own. Complexes and supercomplexes resolved by 1-D BNE could be aligned with the columns of dissociated complexes (marked by arrows). Band a with lowest mass in BNE was assigned to monomeric complex IV. The complex remained essentially unchanged after 2-D BN/hrCNE. Complex b migrating close to complex III (480 kDa) in the BN gel most likely was dimeric complex IV (2×200 kDa). It was dissociated into the monomers by hrCNE in the second dimension. Complex c comigrating with complex I (1 MDa) was dissociated into the individual complexes III and IV and presumably represented a III₂IV₂ supercomplex (calculated mass 980 kDa). Band d was interpreted as a I₁IV₁-supercomplex, because released complexes I and IV were identified but no released complex III (Fig. 8.3DE). Complex 0 was interpreted as the core supercomplex I₁III₂ not containing complex IV, because hrCNE did not release any complex IV (i.e., the corresponding arrow pointed to a gap in the horizontally aligned spots of complex IV). Band 1 (supercomplex I₁III₂IV₁) was dissociated by hrCNE into complex I (Fig. 8.3D), complex IV (Fig. 8.3E), and complex III (optimally detected in Fig. 8.3BC).

3.3. Final 3-D SDS-PAGE or dSDS-PAGE

Fluorescence-labeled spots of complexes in the 2-D native gels were identified with a laser scanner, and the positions were marked on both covering glass plates. After removal of one glass plate, 1-cm-wide gel strips (e.g., containing all proteins and complexes that were released from supercomplexes [marked 1 and 0; boxed vertically in Fig. 8.3B]) were excised for 3-D SDS-PAGE. A typical Coomassie-stained gel strip from the 2-D BN/hrCN gel is shown in Fig. 8.4A. After resolution by 3-D SDS-PAGE, fluorescence-labeled subunits of supercomplex 0, of complexes I, V, III, and IV, and

dissociated individual proteins (located on the right half of the 3-D gel) were detected by their fluorescence (Fig. 8.4B) or after silver staining (Fig. 8.4C). Conditions and detergents used for fluorescence labeling seemed critical. We observed highly specific labeling under the conditions used here. For example, a 30-kDa protein (marked by arrowhead) showed intense fluorescence labeling but was hardly identified in silver stain. Another protein (marked \star) was detected only in silver stain. The dissociated individual proteins mostly are detergent-labile subunits of the supercomplexes and constituent complexes but also comprise novel proteins associated with supercomplexes that previously escaped detection. Supercomplex-associated proteins can be identified by mass spectrometric analyses, because these proteins are well separated from most of the protein subunits comprised in the residual individual complexes (Schägger *et al.*, manuscript in preparation).

Thorough protein analysis of multiprotein complexes requires highly pure complexes that can be isolated by the 2-D BN/hrCN system and processed by final dSDS-PAGE for mass spectrometric identification of the protein subunits. Gel pieces containing residual supercomplex or monomeric ATP synthase (boxed in Fig. 8.3B) were excised here and resolved by dSDS-PAGE as exemplified with Fig. 8.4DE. A similar 4-D electrophoretic approach that uses the 2-D BN/BN system for the isolation of highly pure native ATP synthase has been described recently for the identification of two novel accessory proteins of mammalian ATP synthase (Meyer *et al.*, 2007).

REFERENCES

- Carrozzo, R., Wittig, I., Santorelli, F. M., Bertini, E., Hofmann, S., Brandt, U., and Schägger, H. (2006). Subcomplexes of human ATP synthase mark mitochondrial biosynthesis disorders. *Ann. Neurol.* **59**, 265–275.
- Meyer, B., Wittig, I., Trifilieff, E., Karas, M., and Schägger, H. (2007). Identification of two proteins associated with mammalian ATP synthase. *Mol. Cell. Proteomics* **6**, 1690–1699.
- Rais, I., Karas, M., and Schägger, H. (2004). Two-dimensional electrophoresis for the isolation of integral membrane proteins and mass spectrometric identification. *Proteomics* **4**, 2567–2571.
- Schägger, H., and von Jagow, G. (1991). Blue native electrophoresis for isolation of membrane protein complexes in enzymatically active form. *Anal. Biochem.* **199**, 223–231.
- Schägger, H., Cramer, W. A., and von Jagow, G. (1994). Analysis of molecular masses and oligomeric states of protein complexes by blue native electrophoresis and isolation of membrane protein complexes by two-dimensional native electrophoresis. *Anal. Biochem.* **217**, 220–230.
- Schägger, H., and Pfeiffer, K. (2000). Supercomplexes in the respiratory chains of yeast and mammalian mitochondria. *EMBO J.* **19**, 1777–1783.
- Schägger, H., and Pfeiffer, K. (2001). The ratio of oxidative phosphorylation complexes I-V in bovine heart mitochondria and the composition of respiratory chain supercomplexes. *J. Biol. Chem.* **276**, 37861–37867.
- Schägger, H. (2006). Tricine-SDS-PAGE. *Nature Protocols* **1**, 16–22.

- Smith, A. L. (1967). Preparation, properties, and conditions for assay of mitochondria: Slaughterhouse material, small-scale. *Methods Enzymol.* **10**, 81–86.
- Wittig, I., and Schägger, H. (2005). Advantages and limitations of clear native polyacrylamide gel electrophoresis. *Proteomics* **5**, 4338–4346.
- Wittig, I., Braun, H. P., and Schägger, H. (2006). Blue-native PAGE. *Nature Protocols* **1**, 416–428.
- Wittig, I., Karas, M., and Schägger, H. (2007a). High resolution clear-native electrophoresis for in-gel functional assays and fluorescence studies of membrane protein complexes. *Mol. Cell. Proteomics* **6**, 1215–1225.
- Wittig, I., Carrozzo, R., Santorelli, F. M., and Schägger, H. (2007b). Functional assays in high resolution clear native gels to quantify mitochondrial complexes in human biopsies and cell-lines. *Electrophoresis* **28**, 3811–3820.
- Wittig, I., and Schägger, H. (2008). Features and applications of blue-native and clear-native electrophoresis. *Proteomics* **8**, 3974–3990.
- Zerbetto, E., Vergani, L., and Dabbeni-Sala, F. (1997). Quantification of muscle mitochondrial oxidative phosphorylation enzymes via histochemical staining of blue native polyacrylamide gels. *Electrophoresis* **18**, 2059–2064.

RELIABLE ASSAY FOR MEASURING COMPLEX I ACTIVITY IN HUMAN BLOOD LYMPHOCYTES AND SKIN FIBROBLASTS

L. Elly. A. de Wit *and* Wim Sluiter

Contents

1. Introduction	170
2. Complex I Activity Measurement	171
2.1. Background	171
2.2. Materials	172
2.3. Equipment	173
2.4. Methods	173
3. Characteristics of the Complex I Assay	175
References	179

Abstract

Complex I deficiency is probably the most common enzyme defect among the group of OXPHOS disorders. To evaluate a deficiency of complex I activity, biochemical measurements based on estimation of the mitochondrial rotenone-sensitive NADH: ubiquinone oxidoreductase activity are an important tool. Skeletal muscle is the most widely used tissue to examine complex I deficiency. However, obtaining a muscle biopsy requires an invasive surgical operation. It is much easier to obtain blood lymphocytes or skin fibroblasts, and, moreover, these cells can be expanded in number by standard techniques for extensive research on complex I. On the other hand, each of these cell types has disadvantages that hinder its measurement, such as the apparent low enzyme activity of lymphocytes and the highly contaminating nonmitochondrial NADH-quinone oxidoreductase activity of fibroblasts. This chapter describes a method to assay complex I activity reliably in a minute amount of either cell type.

Department of Biochemistry, Mitochondrial Research Unit, Erasmus MC, Dr. Molewaterplein 50-60, Rotterdam, The Netherlands

Methods in Enzymology, Volume 456
ISSN 0076-6879, DOI: 10.1016/S0076-6879(08)04409-1

© 2009 Elsevier Inc.
All rights reserved.

1. INTRODUCTION

The oxidative phosphorylation (OXPHOS) system is located in the inner mitochondrial membrane and is composed of five individual functional enzyme complexes. Complexes I, III, and IV are arranged as super-complexes (Schagger and Pfeiffer, 2000) containing two additional electron carriers, coenzyme Q₁₀ (ubiquinone), and cytochrome *c*.

The NADH: ubiquinone oxidoreductase, or complex I, with a total molecular mass of about 900 kDa, is the largest of these five enzyme complexes and is composed of seven subunits encoded by mitochondrial DNA (mtDNA) and 38 nuclear-encoded subunits (Carroll *et al.*, 2006). Although all of its subunits have been identified, how complex I assembles, which proteins aid this process (Lazarou *et al.*, 2008), and how complex I assembles further into higher ordered respirasomes with complex III and IV (Schafer *et al.*, 2006) is only partly understood. Its L-shape configuration contains a water-soluble peripheral arm protruding into the mitochondrial matrix and a water-insoluble hydrophobic arm embedded in the inner mitochondrial membrane (Brandt, 2006; Carroll *et al.*, 2003). The peripheral arm contains the FMN cofactor and several iron-sulfur clusters that provide a bifurcated electron transfer pathway (Verkhovskaya *et al.*, 2008) from NADH to ubiquinone, facilitating a state that might be required for conformational change of the membrane arm of the complex to translocate protons from the mitochondrial matrix to the intermembrane space. The subsequent proton motive force will drive the synthesis of ATP by complex V (Brandt, 2006; Ohnishi and Salerno, 2005).

Isolated complex I deficiency is probably the most common enzymatic defect of the oxidative phosphorylation disorders (Loeffen *et al.*, 2000). Clinical presentation of complex I deficiency starts mostly at birth or early childhood and includes a great variety of clinical presentations, ranging from lethal neonatal disease to adult-onset neurodegenerative disorders that complicate the diagnostic process in individual patients. Mutations or deletions in mitochondrial and nuclear genes appear to account for approximately 50% of the cases of complex I deficiency (Thorburn *et al.*, 2004). At present, it is becoming clear that mutations in assembly factor genes lead to impaired assembly and subsequent dysfunction of complex I as well (Dunning *et al.*, 2007; Ogilvie *et al.*, 2005; Pagliarini *et al.*, 2008; Saada *et al.*, 2008).

Skeletal muscle is the tissue most widely used for respiratory chain enzyme studies. Unfortunately, a biopsy that is large enough for extensive research requires a surgical operation. It would be more convenient to use tissue that can be obtained in a minimally invasive manner and expanded *in vitro*, such as blood cells or skin fibroblasts. However, determination of complex I in fibroblasts is difficult because of the high activity of

contaminating rotenone-insensitive NADH dehydrogenases (Chretien *et al.*, 1994), and in blood cells the apparent low enzyme activity hampers its proper assay.

This chapter describes a method to measure complex I activity spectrophotometrically in blood lymphocytes and in cultured skin fibroblasts in a limited amount of sample with minimal interference of contaminating rotenone-insensitive NADH dehydrogenases, providing a reliable tool in diagnosing respiratory chain disorders and in studying the relationship between the structure of complex I and its enzyme activity.

2. COMPLEX I ACTIVITY MEASUREMENT

2.1. Background

Mitochondrial NADH oxidation may proceed by means of two pathways. In one, NADH is oxidized by means of a rotenone-sensitive route by the NADH: ubiquinone oxidoreductase, which is located at the inner side of the mitochondrial inner membrane. In the other, NADH is oxidized in a rotenone-insensitive manner by NADH: cytochrome b_5 oxidoreductase (EC 1.6.2.2), which is located in the mitochondrial outer membrane (Sottocasa *et al.*, 1967). The most characteristic enzyme activity of complex I is its rotenone-sensitive NADH: ubiquinone reductase (EC 1.6.99.3). Hence biochemical measurement of complex I is based on estimation of that specific rotenone-sensitive enzyme activity (Fischer *et al.*, 1986). The NADH binding site of the enzyme is located in the peripheral arm of the complex; the ubiquinone-binding site resides in its hydrophobic membrane arm (Brandt, 2006; Carroll *et al.*, 2003; Degli Esposti and Ghelli, 1994; Friedrich *et al.*, 1993; Walker, 1992). The complex I inhibitor rotenone binds to that latter site and its inhibitory effect on the enzyme reaction is generally accepted as a standard for the integrity of complex I.

For the initial steady-state analysis of complex I, artificial electron acceptors such as ferricyanide (Galante and Hatefi, 1978) and 2,6-dichloroindophenol (Dooijewaard and Slater, 1976; Galante and Hatefi, 1978; Janssen *et al.*, 2007; Jewess and Devonshire, 1999; Majander *et al.*, 1991; Saada *et al.*, 2004) have been used. However, because these artificial electron acceptors react with the NADH binding site of those enzymes only, the assay is not rotenone sensitive, and, therefore, discrimination between complex I and other NADH dehydrogenases is not possible. Consequently, the use of such electron acceptors in the assay of complex I will not reveal any defects further down the electron pathway leading to the ubiquinone binding site in the enzyme complex (Ragan *et al.*, 1987; Verkhovskaya *et al.*, 2008). Only by addition of extra ubiquinone will such an assay acquire some rotenone sensitivity, but because fibroblasts contain high activities of rotenone-insensitive

NADH oxidases, complex I is still difficult to detect (De Wit *et al.*, 2008; Janssen *et al.*, 2007). A similar reasoning holds for the recently developed Dipstick Assay (Mitosciences, Eugene, Oregon). In this assay complex I is immunoprecipitated on a dipstick and its activity measured in gel as NADH dehydrogenase activity, which is, of course, not rotenone sensitive. Although this method is easy to carry out and could be of value in obtaining preliminary indication for a deficiency of complex I, to obtain abnormal values, a more specific biochemical measurement should be performed, which is focused on the function of the entire enzyme. To study the biochemical function of complex I, an assay that uses ubiquinone as electron acceptor would be ideal. However, a water-soluble ubiquinone analog would be a more appropriate electron acceptor.

It is important to note that the accumulation of rotenone at its binding site in complex I is not instantaneous (Burgos and Redfeam, 1965; De Vries *et al.*, 1996; De Wit *et al.*, 2007). Therefore, the rotenone-insensitive NADH oxidoreductase should be determined separately from the total NADH oxidase activities to discriminate complex I activity from the total NADH oxidase activities. Because this discrimination requires a substantial amount of material using standard methods, a reliable, miniaturized method is needed.

2.2. Materials

2.2.1. Buffers

Phosphate-buffered saline (PBS-EDTA): 140 mM NaCl, 1.5 mM KH₂PO₄, 8.1 mM Na₂HPO₄, 2.7 mM KCl, 2 mM EDTA, pH 7.4, store at 4 °C
Ammonium chloride solution (NH₄Cl): 155 mM NH₄Cl, 10 mM NaHCO₃, 0.1 mM EDTA, pH 7.4, store at 4 °C
SHE: 250 mM sucrose, 10 mM HEPES, 1 mM EDTA, pH 7.4, store at -20 °C

2.2.2. Other solutions

Lymphoprep™ (Axis-Shield PoC)
Complete protease inhibitors cocktail tablets (Roche Diagnostics)
4-(2-aminoethyl)-benzene sulfonyl-fluoride hydrochloride (AEBSF): 100 mM, store at -20 °C (Pefabloc SC, Roche Diagnostics)
Diisopropyl fluorophosphate (DFP): 0.2 M in dry isopropanol, store at -80 °C (Fluka Chemica)
SHE-PIM: SHE supplemented with two Complete tablets per 50 ml, 1 mM AEBSF and 2 mM DFP
DMEM (BioWhitaker)
Uridine (Sigma)

Digitonin, high purity (Calbiochem): 10 mg/ml heat for 5 min at 95 °C then cool down to room temperature, store at -20 °C
1 M K₂HPO₄, pH 7.4, store at 4 °C
2 M MgCl₂, store at 4 °C
5% fatty acid-free bovine serum albumin (BSA-FFA), store at -20 °C (Sigma)
5.7 mM NADH, make fresh daily
0.2 M KCN, make fresh daily
7.3 mM antimycin in dimethyl sulfoxide (DMSO), store at -20 °C (Sigma)
2.8 mM coenzyme Q₁ (CoQ₁) in ethanol, store at -20 °C (Sigma)
0.36 mM rotenone in DMSO, store at -20 °C (Sigma)

2.3. Equipment

Cary 300 Bio Spectrophotometer (Varian Inc., Middelburg, The Netherlands)
Cary WinUV software package, version 3.00 (Varian)
Sub-microcell quartz cuvettes, 80 µl, 4 mm × 10 mm (Hellma GmbH, Rijswijk, The Netherlands)

2.4. Methods

2.4.1. Isolation of blood lymphocytes

Lymphocytes are isolated from blood anticoagulated with 0.18% EDTA. Dilute the EDTA-blood by addition of an equal volume of PBS-EDTA at room temperature (RT). Layer two volumes of diluted blood carefully over one volume of LymphoprepTM in a centrifuge tube and centrifuge at 800g for 20 min at RT in a swing-out rotor. The mononuclear cells form a distinct band at the sample/medium interface. First, remove the upper layer, and then collect the cells from the interface. Dilute the cell fraction with ice-cold PBS-EDTA to reduce the density of the suspension and pellet the cells by centrifugation for 15 min at 140g and 4 °C. Next, lyse the erythrocytes with ice-cold NH₄Cl. Pellet the remaining mononuclear leukocytes by centrifugation for 15 min at 140g and 4 °C, wash once with ice-cold PBS-EDTA and resuspend the cells in ice-cold SHE-PIM. Count the number of lymphocytes and rapidly freeze 50-µl aliquots at a concentration of 100 × 10⁶ cells per ml SHE-PIM in liquid nitrogen and store at -80 °C.

Remarks: the addition of diisofluorophosphate to the buffer is important to effectively inhibit the active serine proteases that may come from any contaminating blood neutrophils (Maiani *et al.*, 2004). By reducing the centrifugal force from the usual 250g to 140g by use of this isolation method, the lymphocyte to platelet ratio increases from 9:15 to 9:1.

2.4.2. Preparation of a mitochondria-enriched fraction from fibroblasts

Human skin fibroblasts are cultured in DMEM supplemented with 10% (vol/vol) fetal calf serum (FCS), 100 units/ml penicillin, 100 $\mu\text{g}/\text{ml}$ streptomycin, and 0.2 mM uridine (fibroblasts suffering from a respiratory defect depend on uridine for their growth). Harvest approximately 7×10^6 cells, equivalent to about 2 mg protein, from a 175-cm² culture flask by trypsinization, wash with PBS at RT, resuspend in ice-cold SHE, rapidly freeze in liquid nitrogen, and keep at -80°C until use.

The mitochondrial fraction is isolated according to [Tiranti *et al.* \(1995\)](#) with some small modifications. Thaw the cell suspension and dilute 1:1 with ice-cold 0.2 mg/ml digitonin in SHE. Incubate on ice for 10 min and centrifuge at 750g for 10 min at 4°C . Save the supernatant and resuspend the pellet in the same volume of ice-cold SHE supplemented with 0.1 mg/ml digitonin. Incubate on ice for another 10 min, and centrifuge again at 750g for 10 min at 4°C . Combine the supernatants and centrifuge at 8000g for 10 min at 4°C . Resuspend the pellet in ice-cold 10 mM KPi buffer, pH 7.4, determine the protein concentration, and freeze in liquid nitrogen. If the mitochondrial fraction is not used immediately, store it at -80°C .

Protein concentration can be determined by the Bio-Rad Protein assay, which only requires 1 to 20 μg protein.

2.4.3. Spectrophotometric assay

The complex I activity is determined by measuring the oxidation of NADH to NAD^+ at 340 nm with 380 nm as the reference wavelength at 37° in an assay mixture of 20 mM K_2HPO_4 , pH 7.4, 4 mM MgCl_2 , 0.2% BSA, 200 μM NADH, 1.7 mM KCN, 3 μM antimycin, and 100 μM CoQ₁. The difference in activity with and without rotenone at a fully saturating level of 5 μM ([Majander *et al.*, 1996](#); [Nakashima *et al.*, 2002](#)) is calculated to differentiate complex I activity from that of the rotenone-insensitive NADH: ubiquinone oxidoreductase (RINQ).

Thaw the frozen lymphocytes; prepare two cell concentrations by dilution with ice-cold SHE-PIM buffer. After two additional cycles of freeze thawing, the permeabilized cells can be used directly in the complex I activity assay.

Dilute the mitochondria-enriched fraction from fibroblasts to 0.2 to 0.6 mg/ml protein with ice-cold 10 mM KPi-buffer, pH 7.4, and freeze-thaw by two additional cycles directly before determination of complex I. Use at least two protein concentrations to determine complex I enzyme activity.

The assay mixture contains 25 mM K_2HPO_4 , pH 7.4, 5 mM MgCl_2 , 0.25% BSA, 3.7 μM antimycin, and 2 mM KCN.

1. Transfer 120 μl of the assay mixture to a test cuvette and a blanc cuvette.
2. Add 2 μl DMSO plus 5 μl of 5.7 mM NADH to the test cuvette and 2 μl of 0.36 mM rotenone plus 5 μl of 5.7 mM NADH to the blanc cuvette.

3. Add 10 μl of the lymphocytes suspension or of the mitochondria-enriched fibroblasts fraction to each cuvette. Mix with a plastic rod and incubate for 1 min at 37 $^{\circ}\text{C}$.
4. Start the reaction by adding 5 μl of 2.8 mM CoQ₁. Measure the decrease in absorbance for 1.5 min at 340 nm with 380 nm as the reference wavelength.
5. By use of the velocity of the reaction (Δ absorbance/min) and the molar extinction coefficient of NADH (4.8 mM⁻¹ cm⁻¹; at 340 nm with reference wavelength 380 nm (Sherwood and Hirst, 2006), calculate the complex I activity by subtraction of the reaction rates in the presence (RINQ activity only) and absence of rotenone (RINQ and complex I activity).

Important: Clean the cuvettes thoroughly with ethanol after each measurement, because rotenone binds to the quartz surface.

3. CHARACTERISTICS OF THE COMPLEX I ASSAY

The duration of the first-order kinetics decreases in a few minutes even at low protein concentrations for both the blood lymphocytes (Fig. 9.1) and the mitochondrial fraction of the fibroblasts (Fig. 9.2).

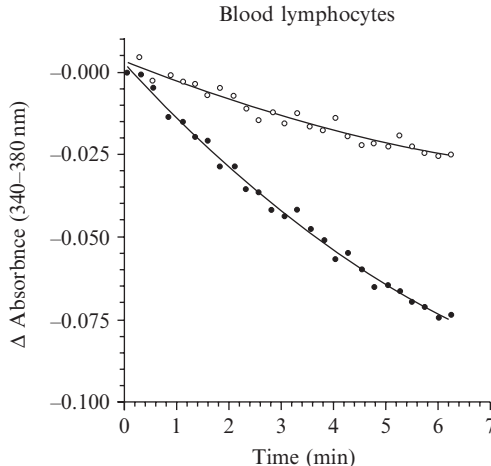


Figure 9.1 Course of the complex I activity reflected by the decrease in absorbance at 340 nm with 380 nm as the reference wavelength caused by the oxidation of NADH by 0.118 (○) and 0.234 (●) mg cell protein of blood lymphocytes/ml reaction mixture. The reaction mixture consisted of 20 mM KH₂PO₄, pH 7.4, 4 mM MgCl₂, 0.2% fatty acid free BSA, 1.7 mM KCN, 3 μM antimycin, 200 μM NADH, and 100 μM CoQ₁, with or without 5 μM rotenone. Complex I activity was calculated by subtraction of the reaction rates in the presence (RINQ activity only) and absence of rotenone (RINQ and complex I activity). The duration of the first-order kinetics decreased in a few minutes.

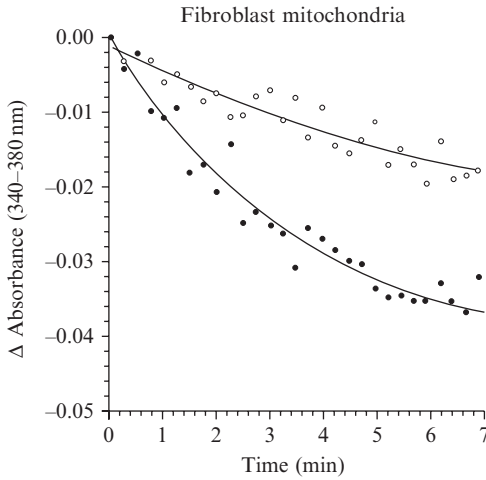


Figure 9.2 Course of the complex I activity reflected by the decrease in absorbance at 340 nm with 380 nm as the reference wavelength caused by the oxidation of NADH by 0.018 (-○-) and 0.035 mg (-●-) fibroblast mitochondrial protein/ml reaction mixture. The reaction mixture and the calculation of complex I activity was as described in the legend of Fig. 9.1. Again, the duration of the first-order kinetics decreased in a few minutes.

Therefore, it is impossible to determine complex I by adding rotenone to the same cuvette several minutes after the start of the reaction to save material. However, by use of sub-microcell cuvettes only minute amounts of material are required, for example, for the determination of the complex I activity in two cell protein concentrations of lymphocytes only 1 to 2 ml of anti-coagulated blood is needed. The relationship between protein concentration and complex I activity of the lymphocytes is linear up to at least 0.234 mg/ml reaction mixture ($y = -0.439 + 13.7x$; $R^2 = 0.797$, $P < 0.0001$; where y represents the initial rate expressed as $\text{nmol NADH min}^{-1} \text{ml}^{-1}$, and x , the cell protein concentration in mg/ml reaction mixture).

The amount of fibroblasts needed to determine the complex I activity in two mitochondrial protein concentrations by this assay is 250,000 to 750,000 cells. The activity is linearly related to the mitochondrial protein concentration up to at least 0.060 mg/ml reaction mixture ($y = 0.554 + 76.9x$; $R^2 = 0.978$, $P < 0.0001$; where y represents the initial rate expressed as $\text{nmol NADH min}^{-1} \text{ml}^{-1}$, and x the protein concentration of the mitochondrial fraction in mg/ml reaction mixture).

With both cell types, the intraassay imprecision (CV) has been determined at three protein concentrations in triplicate on the same day and varied between 8 and 15% (mean: 11.3%). The interassay imprecision was between 5 and 27% (mean: 15.9%) and was determined at three protein concentrations on three different days (Table 9.1). The normal donor

Table 9.1 Assay imprecisions for complex I in PBMC's and mitochondrial fractions of cultured fibroblasts

PBMC ^d	Complex I (U/mg protein)					
<i>Intraassay imprecision</i> ^b	Experiment 1	Experiment 2	Experiment 3	Mean	SD	CV %
4 times diluted	11.19	14.75	11.73	12.56	1.92	15
3 times diluted	11.73	12.39	9.73	11.28	1.39	12
2 times diluted	9.86	12.26	12.79	11.64	1.56	13
<i>Interassay imprecision</i> ^c	Day 1	Day 2	Day 3			
4 times diluted	14.15	8.05	12.56	11.59	3.16	27
3 times diluted	11.42	13.46	11.28	12.05	1.22	10
2 times diluted	11.87	12.82	11.64	12.11	0.63	5
Fibroblast mitochondria ^d	Complex I (U/mg protein)					
<i>Intraassay imprecision</i> ^b	Experiment 1	Experiment 2	Experiment 3	Mean	SD	CV %
4 times diluted	0.049	0.058	0.048	0.052	0.006	11
3 times diluted	0.053	0.062	0.053	0.056	0.005	9
2 times diluted	0.040	0.038	0.044	0.041	0.003	8
<i>Interassay imprecision</i> ^c	Day 1	Day 2	Day 3			
4 times diluted	0.048	0.052	0.043	0.048	0.004	9
3 times diluted	0.053	0.077	0.050	0.060	0.015	25
2 times diluted	0.039	0.057	0.049	0.048	0.009	19

(continued)

Table 9.1 (continued)

Fibroblast mitochondria ^d	Complex I (U/mg protein)					
	Isolation 1	Isolation 2	Isolation 3	Mean	SD	CV %
Imprecision due to isolation procedure and interassay variation ^f	0.052	0.059	0.075	0.062	0.012	19

^a The protein concentration of the undiluted blood cells (100×10^6 cells/ml) was 6.66 mg/ml.

^b Determined on the same day.

^c Determined by thawing a portion of one batch of isolated blood cells each day.

^d The protein concentration of the undiluted fibroblasts mitochondrial fraction was 0.995 mg/ml.

^e Determined by thawing a portion of one batch of mitochondrial protein each day.

^f The mitochondrial fractions were isolated on three different days from one batch of cultured skin fibroblasts, and complex I activity was measured on the day of isolation.

variation in the determination of complex I of blood lymphocytes amounted to 41.1% (De Wit *et al.*, 2007), which was there mistakenly held for the interassay imprecision.

To determine the effect of the isolation procedure of the mitochondrial fraction of fibroblasts on the complex I assay, mitochondrial fractions were isolated on three different days from the same batch of cultured fibroblasts. Complex I activities were measured in three cell concentrations on the day of isolation. The imprecision of 19% in the measured complex activities lay in the range of the interassay imprecision (Table 9.1).

REFERENCES

- Brandt, U. (2006). Energy converting NADH: Quinone oxidoreductase (complex I). *Annu. Rev. Biochem.* **75**, 69–92.
- Burgos, J., and Redfean, E. (1965). The inhibition of mitochondrial reduced nicotinamide-adenine dinucleotide oxidation by rotenoids. *Biochim. Biophys. Acta* **110**, 475–483.
- Carroll, J., Fearnley, I. M., Shannon, R. J., Hirst, J., and Walker, J. E. (2003). Analysis of the subunit composition of complex I from bovine heart mitochondria. *Mol. Cell Proteomics* **2**, 117–126.
- Carroll, J., Fearnley, I. M., Skehel, J. M., Shannon, R. J., Hirst, J., and Walker, J. E. (2006). Bovine complex I is a complex of 45 different subunits. *J. Biol. Chem.* **281**, 32724–32727.
- Chretien, D., Rustin, P., Bourgeron, T., Rotig, A., Saudubray, J. M., and Munnich, A. (1994). Reference charts for respiratory chain activities in human tissues. *Clin. Chim. Acta* **228**, 53–70.
- De Vries, D. D., Went, L. N., Bruyn, G. W., Scholte, H. R., Hofstra, R. M. W., Bolhuis, P. A., and Van Oost, B. A. (1996). Genetic and biochemical impairment of mitochondrial complex I activity in a family with Leber hereditary optic neuropathy and hereditary spastic dystonia. *Am. J. Hum. Genet.* **58**, 703–711.
- De Wit, L. E. A., Scholte, H. R., and Sluiter, W. (2008). Correct assay of complex I activity in human skin fibroblasts by timely addition of rotenone. *Clin. Chem.* **54**, 1921–1922.
- De Wit, L. E. A., Spruijt, L., Schoonderwoerd, G. C., De Coo, I. F. M., Smeets, H. J. M., Scholte, H. R., and Sluiter, W. (2007). A simplified and reliable assay for complex I in human blood lymphocytes. *J. Immunol. Methods* **326**, 76–82.
- Degli Esposti, M., and Ghelli, A. (1994). The mechanism of proton and electron transport in mitochondrial complex I. *Biochim. Biophys. Acta* **1187**, 116–120.
- Dooijewaard, G., and Slater, E. C. (1976). Steady-state kinetics of high molecular weight (type-I) NADH dehydrogenase. *Biochim. Biophys. Acta* **440**, 1–15.
- Dunning, C. J., McKenzie, M., Sugiana, C., Lazarou, M., Silke, J., Connelly, A., Fletcher, J. M., Kirby, D. M., Thorburn, D. R., and Ryan, M. T. (2007). Human CIA30 is involved in the early assembly of mitochondrial complex I and mutations in its gene cause disease. *EMBO J.* **26**, 3227–3237.
- Fischer, J. C., Ruitenbeek, W., Trijbels, J. M., Veerkamp, J. H., Stadhouders, A. M., Sengers, R. C., and Janssen, A. J. (1986). Estimation of NADH oxidation in human skeletal muscle mitochondria. *Clin. Chim. Acta* **155**, 263–273.
- Friedrich, T., Weidner, U., Nehls, U., Fecke, W., Schneider, R., and Weiss, H. (1993). Attempts to define distinct parts of NADH: Ubiquinone oxidoreductase (complex I). *J. Bioenerg. Biomembr.* **25**, 331–337.
- Galante, Y. M., and Hatefi, Y. (1978). Resolution of complex I and isolation of NADH dehydrogenase and an iron-sulfur protein. *Methods Enzymol.* **53**, 15–21.

- Janssen, A. J. M., Trijbels, F. J. M., Sengers, R. C. A., Smeitink, J. A. M., Van Den Heuvel, L. P., Wintjes, L. T. M., Stoltenborg-Hogenkamp, B. J. M., and Rodenburg, R. J. T. (2007). Spectrophotometric assay for complex I of the respiratory chain in tissue samples and cultured fibroblasts. *Clin. Chem.* **53**, 729–734.
- Jewess, P. J., and Devonshire, A. L. (1999). Kinetic microplate-based assays for inhibitors of mitochondrial NADH: Ubiquinone oxidoreductase (complex I) and succinate: Cytochrome *c* oxidoreductase. *Anal. Biochem.* **272**, 56–63.
- Lazarou, M., Thorburn, D. R., Ryan, M. T., and McKenzie, M. (2009). Assembly of mitochondrial complex I and defects in disease. *Biochim. Biophys. Acta* **1793**, 78–88.
- Loeffen, J. L., Smeitink, J. A., Trijbels, J. M., Janssen, A. J., Triepels, R. H., Sengers, R. C., and Van Den Heuvel, L. P. (2000). Isolated complex I deficiency in children: Clinical, biochemical and genetic aspects. *Hum. Mutat.* **15**, 123–134.
- Maianski, N. A., Geissler, J., Srinivasula, S. M., Alnemri, E. S., Roos, D., and Kuijpers, T. W. (2004). Functional characterization of mitochondria in neutrophils: A role restricted to apoptosis. *Cell Death Differ* **11**, 143–153.
- Majander, A., Finel, M., Savontaus, M. L., Nikoskelainen, E., and Wikstrom, M. (1996). Catalytic activity of complex I in cell lines that possess replacement mutations in the ND genes in Leber's hereditary optic neuropathy. *Eur. J. Biochem.* **239**, 201–207.
- Majander, A., Huoponen, K., Savontaus, M. L., Nikoskelainen, E., and Wikstrom, M. (1991). Electron transfer properties of NADH: Ubiquinone reductase in the ND1/3460 and the ND4/11778 mutations of the Leber hereditary optic neuroretinopathy (LHON). *FEBS Lett.* **292**, 289–292.
- Nakashima, Y., Shinzawa-Itoh, K., Watanabe, K., Naoki, K., Hano, N., and Yoshikawa, S. (2002). Steady-state kinetics of NADH: Coenzyme Q oxidoreductase isolated from bovine heart mitochondria. *J. Bioenerg. Biomembr.* **34**, 11–19.
- Ogilvie, I., Kennaway, N. G., and Shoubridge, E. A. (2005). A molecular chaperone for mitochondrial complex I assembly is mutated in a progressive encephalopathy. *J. Clin. Invest.* **115**, 2784–2792.
- Ohnishi, T., and Salerno, J. C. (2005). Conformation-driven and semiquinone-gated proton-pump mechanism in the NADH-ubiquinone oxidoreductase (complex I). *FEBS Lett.* **579**, 4555–4561.
- Pagliarini, D. J., Calvo, S. E., Chang, B., Sheth, S. A., Vafai, S. B., Ong, S. E., Walford, G. A., Sugiana, C., Boneh, A., Chen, W. K., Hill, D. E., Vidal, M., et al. (2008). A mitochondrial protein compendium elucidates complex I disease biology. *Cell* **134**, 112–123.
- Ragan, C. I., Wilson, M. T., Darley-USmar, V. M., and Lowe, P. N. (1987). Sub-fractionation of mitochondria and isolation of the proteins of oxidative phosphorylation. In "Mitochondria: A Practical Approach." (V. M. Darley-USmar, D. Rickwood, and M. T. Wilson, eds.) pp. 79–112. IRL Press, Oxford.
- Saada, A., Bar-Meir, M., Belaiche, C., Miller, C., and Elpeleg, O. (2004). Evaluation of enzymatic assays and compounds affecting ATP production in mitochondrial respiratory chain complex I deficiency. *Anal. Biochem.* **335**, 66–72.
- Saada, A., Edvardson, S., Rapoport, M., Shaag, A., Amry, K., Miller, C., Lorberboum-Galski, H., and Elpeleg, O. (2008). C6ORF66 is an assembly factor of mitochondrial complex I. *Am. J. Hum. Genet.* **82**, 32–38.
- Schafer, E., Seelert, H., Reifschneider, N. H., Krause, F., Dencher, N. A., and Vonck, J. (2006). Architecture of active mammalian respiratory chain supercomplexes. *J. Biol. Chem.* **281**, 15370–15375.
- Schagger, H., and Pfeiffer, K. (2000). Supercomplexes in the respiratory chains of yeast and mammalian mitochondria. *EMBO J.* **19**, 1777–1783.

- Sherwood, S., and Hirst, J. (2006). Investigation of the mechanism of proton translocation by NADH: Ubiquinone oxidoreductase (complex I) from bovine heart mitochondria: does the enzyme operate by a Q-cycle mechanism? *Biochem. J.* **400**, 541–550.
- Sottocasa, G. L., Kuylenstierna, B., Ernster, L., and Bergstrand, A. (1967). An electron-transport system associated with the outer membrane of liver mitochondria. *A biochemical and morphological study. J. Cell Biol.* **32**, 415–438.
- Thorburn, D. R., Sugiana, C., Salemi, R., Kirby, D. M., Worgan, L., Ohtake, A., and Ryan, M. T. (2004). Biochemical and molecular diagnosis of mitochondrial respiratory chain disorders. *Biochim. Biophys. Acta* **1659**, 121–128.
- Tiranti, V., Munaro, M., Sandona, D., Lamantea, E., Rimoldi, M., Didonato, S., Bisson, R., and Zeviani, M. (1995). Nuclear DNA origin of cytochrome *c* oxidase deficiency in Leigh's syndrome: Genetic evidence based on patient's-derived rho degrees transformants. *Hum. Mol. Genet.* **4**, 2017–2023.
- Verkhovskaya, M. L., Belevich, N., Euro, L., Wikstrom, M., and Verkhovsky, M. I. (2008). Real-time electron transfer in respiratory complex I. *Proc. Natl. Acad. Sci. USA* **105**, 3763–3767.
- Walker, J. E. (1992). The NADH: Ubiquinone oxidoreductase (complex I) of respiratory chains. *Q. Rev. Biophys.* **25**, 253–324.

PURIFICATION OF THE CYTOCHROME *C* REDUCTASE/CYTOCHROME *C* OXIDASE SUPER COMPLEX OF YEAST MITOCHONDRIA

Hans-Peter Braun,^{*} Stephanie Sunderhaus,^{*} Egbert J. Boekema,[†] and Roman Kouřil[†]

Contents

1. Introduction	184
2. Isolation of the III + IV Supercomplex	184
2.1. Cultivation of yeast cells in lactate medium	184
2.2. Isolation of mitochondria	185
2.3. Solubilization of the mitochondrial membranes	185
2.4. Separation of mitochondrial protein complexes by sucrose gradient ultracentrifugation	185
2.5. Blue-native PAGE	186
3. Characterization of the III + IV Supercomplex by EM	187
4. Perspectives	187
Acknowledgments	189
References	189

Abstract

The protein complexes of the respiratory chain interact by forming large protein particles called respiratory supercomplexes or “respirasomes”. Biochemical characterization of these particles proved to be difficult because of their instability. Here we describe a strategy to isolate and characterize the cytochrome *c* reductase/cytochrome *c* oxidase supercomplex of yeast, also termed the III + IV supercomplex, which is based on lactate cultivation of yeast, gentle isolation of mitochondria, membrane solubilization by digitonin, sucrose gradient ultracentrifugation, and native gel electrophoresis. The procedure yields pure forms of two varieties of the III + IV supercomplex composed of dimeric complex III and one or two copies of monomeric complex IV. Supercomplex preparations can be used for physiological or structural investigations.

^{*} Institute for Plant Genetics, Faculty of Natural Sciences, Universität Hannover, Hannover, Germany

[†] Department of Biophysical Chemistry, Groningen Biomolecular Sciences and Biotechnology Institute, University of Groningen, Groningen, The Netherlands

1. INTRODUCTION

The cytochrome *c* reductase and cytochrome *c* oxidase complexes can be separately purified from mitochondrial fractions of many organisms. This led to the view that the two complexes should be considered as independent structures (reviewed in Hackenbrock *et al.*, 1986). However, early investigations already indicated the occurrence of ordered supramolecular structures that consist of defined interactions of respiratory proteins complexes (Hatefi *et al.*, 1962). These findings were considerably supported by recent investigations on the basis of gentle biochemical preparations, native gel electrophoresis procedures, and electron microscopy (EM) (reviewed in Boekema and Braun, 2007). As a result, several so-called respiratory supercomplexes could be defined. One of the best-described respiratory supercomplexes is the cytochrome *c* reductase/cytochrome *c* oxidase supercomplex, which also is termed the III + IV supercomplex. It initially was described for the bacteria *Paracoccus denitrificans*, PS3, and *Sulfolobus sp.* (Berry and Trumpower, 1985; Iwasaki *et al.*, 1985; Sone *et al.*, 1987). In yeast mitochondria, its existence first was described physiologically by inhibitor titrations (Boumans *et al.*, 1998) and later by biochemical procedures (Cruciat *et al.*, 2000; Schägger and Pfeiffer, 2000). Its stability was found to depend on the cardiolipin concentration of the inner mitochondrial membrane (Pfeiffer *et al.*, 2003; Zhang *et al.*, 2002; 2005). Recently, a pseudo-atomic structure was presented for the III + IV supercomplex of yeast by comparison of medium-resolution 2-D maps from EM and the crystal structures of the two individual respiratory complexes, which are available for higher eukaryotes (Heinemeyer *et al.*, 2007; Nelson and Cox, 2008). According to the proposed structure, the cytochrome *c* binding pockets of cytochrome *c* reductase and cytochrome *c* oxidase are in close proximity, allowing cytochrome *c* to efficiently transfer electrons from one complex to the other by a simple ping-pong mechanism. Here we describe procedures to gently purify the III + IV supercomplex of yeast for its physiological and structural characterization.

2. ISOLATION OF THE III + IV SUPERCOMPLEX

2.1. Cultivation of yeast cells in lactate medium

Biosynthesis and assembly of respiratory complexes in yeast depends on growth conditions during cultivation (Heinemeyer *et al.*, 2007; Schägger and Pfeiffer, 2000). Lactate media lead to induced biosynthesis of complex IV and also induce formation of the III + IV supercomplex. For preparing

the III + IV supercomplex, yeast cells are cultivated in 2.5 L lactate medium (five 2-L Erlenmeyer vessels with 500 ml medium each composed of 0.3 % [w/v] yeast extract, 5 mM glucose, 7 mM KH_2PO_4 , 20 mM NH_4Cl , 4 mM CaCl_2 , 9 mM NaCl, 3 mM MgCl, 2.2 % [v/v] lactate, 0.2 M NaOH, pH 5.5) for 24 h at 30° and 120 rpm. Cells are harvested at an optical density (OD) of 1.2 to 1.3 and directly used for the preparation of mitochondria.

2.2. Isolation of mitochondria

Yeast mitochondria are prepared according to standard procedures. Preparations should be carried out as fast and gentle as possible. A very suitable protocol is outlined in Meisinger *et al.* (2006). For this procedure, the yeast cell wall is digested by zymolyase, cells are disrupted mechanically, and finally organelles are purified by differential centrifugations and a sucrose gradient ultracentrifugation. Purified mitochondria are resuspended in SEM buffer (250 mM sucrose, 1 mM EDTA, 10 mM MOPS-KOH, pH 7.2) at a protein concentration of 20 mg/ml and can be stored at -80°. For reproducibility of experiments, it is recommended to store stock solutions of mitochondria at one specific concentration.

2.3. Solubilization of the mitochondrial membranes

The solubilization step is most crucial for supercomplex characterization. Digitonin (1-8 g detergent/g protein) nicely allows stabilization of the III + IV supercomplex from yeast (Cruciat *et al.*, 2000; Heinemeyer *et al.*, 2007; Schägger and Pfeiffer, 2000). Routinely, 1 ml resuspended organelles (corresponding to 20 mg mitochondrial protein) are sedimented by centrifugation for 10 min at 14,000g. The pellet is directly resolved in 1 ml solubilization buffer (5% [w/v] digitonin, 30 mM HEPES, 150 mM potassium acetate, pH 7.4) and incubated for 20 min on ice. Insoluble material is removed by centrifugation for 10 min at 18,000g.

2.4. Separation of mitochondrial protein complexes by sucrose gradient ultracentrifugation

The solubilized mitochondrial protein complexes are directly transferred onto a linear sucrose gradient (volume: 12 ml; 0.3 to 1.5 M sucrose in 15 mM TRIS base, pH 7.0, 20 mM KCl, 0.2% digitonin) and centrifuged for 20 h at 150,000g and 4°. Afterwards, the gradient is fractionated into twenty-six 0.5-ml fractions from bottom to top, which most easily is achieved by use of a peristaltic pump linked to a needle, which gently is transferred into the tube.

2.5. Blue-native PAGE

Small aliquots of the sucrose gradient fractions ($\sim 50 \mu\text{l}$) can be used for analysis of the protein complex composition of the fractions by blue-native PAGE (Wittig *et al.*, 2006). Because 5% digitonin specifically destabilizes the dimeric ATP synthase supercomplex from yeast, the two largest bands visible on the gels represent III + IV supercomplexes (Fig. 10.1). As revealed by densitometric measurements, the largest band represents a supercomplex composed of dimeric complex III and two copies of monomeric complex IV, the second largest band a supercomplex of dimeric complex III and one copy of complex IV (Heinemeyer *et al.*, 2007; Schagger and Pfeiffer, 2000). Overall purity of the two supercomplexes is $>90\%$ in fraction 4 and $>80\%$ in fraction 5 of the gradient (Fig. 10.1) as estimated by silver staining of blue-native gels (not shown). These fractions can be directly taken for physiological measurements or structural

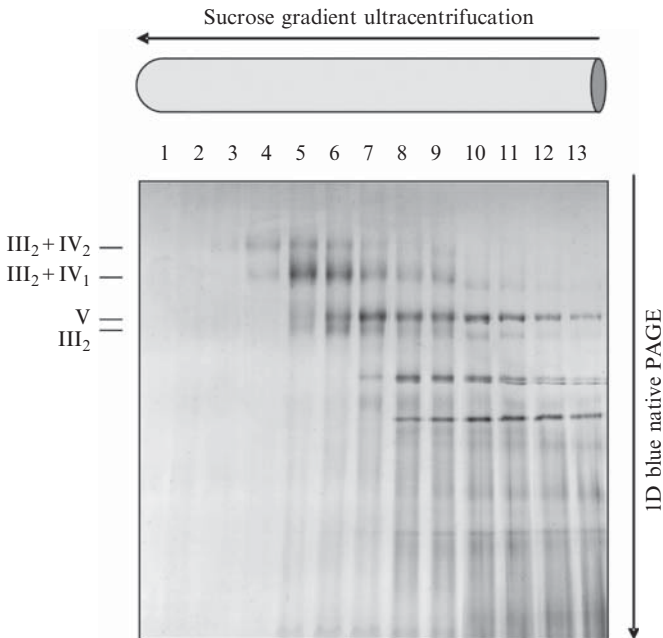


Figure 10.1 Purification of III + IV supercomplexes from yeast mitochondria. Mitochondrial membranes are solubilized by digitonin, and protein complexes are separated by sucrose gradient ultracentrifugation (horizontal separation dimension). Aliquots of 13 fractions of the gradient are subsequently separated by 1-D blue-native PAGE (vertical separation dimension). Identities of the four largest protein complexes are given to the left of the gel: $\text{III}_2 + \text{IV}_1$ and $\text{III}_2 + \text{IV}_2$, supercomplexes composed of dimeric complex III and one or two copies of monomeric complex IV; V, ATP synthase complex; III_2 , dimeric complex III.

analysis with EM (see below). Activity of the purified supercomplexes also can be directly monitored by *in-gel* activity assays for complex IV and complex III (Wittig *et al.*, 2007; Zerbetto *et al.*, 1997). For an even higher purification of the yeast III + IV supercomplexes, which might be necessary for cryo-EM or x-ray crystallography, the bands representing these supercomplexes can be directly electroeluted from a 1-D Blue-native gel according to standard procedures (Wittig *et al.*, 2006).

3. CHARACTERIZATION OF THE III + IV SUPERCOMPLEX BY EM

Purified supercomplex fractions can be used for structural analysis with negative stain single particle EM (Heinemeyer *et al.*, 2007). EM can record the signal of single molecules, and EM images can typically contain the projection maps of dozens to hundreds of proteins or other macromolecules. These images, however, are very noisy, and to retrieve the signal of molecules thousands of single particle projections need to be summed. Because molecules may have freedom to attach to the support film of the EM specimens, extensive image processing is necessary. Single particle image analysis is a well-developed method to analyze EM projections. In short, projections are compared by statistical methods and subsequently sorted into homogeneous groups (“classes”), which represent specific angular projections of studied proteins. Before they can be summed into final 2-D maps, the projections also need to be aligned, which means that rotational and translational shifts are calculated and imposed to bring them in optimal equivalent positions. The 2-D maps disclose many features of the studied macromolecules. In favorable cases, where the sample is homogeneous and randomly oriented molecules can be recorded, projections can become merged into 3-D structures. Recent reviews give an overview of the methods of single particle EM (Frank, 2002; van Heel *et al.*, 2000).

On single particle analysis, the obtained 2-D maps of the yeast III₂IV₂ supercomplex show that it has a symmetric shape with dimeric complex III in the center and two laterally attached complex IV monomers at opposite positions (Fig. 10.2).

4. PERSPECTIVES

With lactate medium for yeast cultivation, a gentle method for the preparation of yeast mitochondria, membrane solubilization by digitonin and sucrose gradient ultracentrifugation, supercomplexes composed of cytochrome *c* reductase and cytochrome *c* oxidase can be efficiently

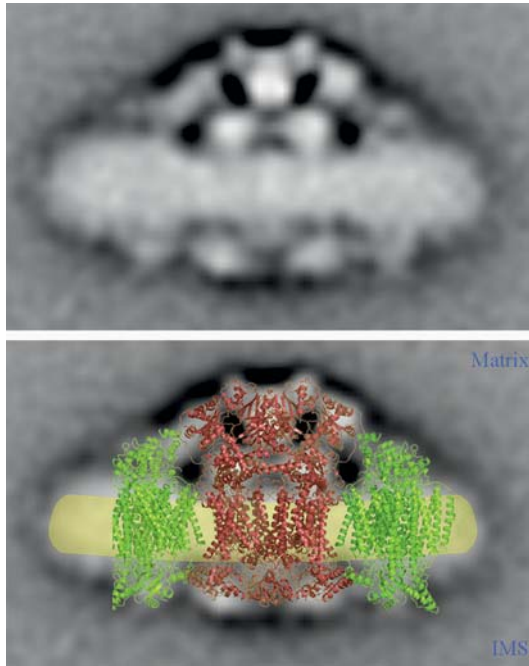


Figure 10.2 Structure of the III₂IV₂ supercomplex from yeast as obtained by single particle electron microscopy. Upper part, 2-D map of 832 aligned projections in a position vertical to the membrane plane. Lower part, pseudo-atomic structure of the III₂ + IV₂ supercomplex derived by fitting the crystal structures for the III₂ complex (in red) of yeast (Lange and Hunte, 2002) and complex IV (in green) of beef (Tsukihara *et al.*, 1996) into the projection map. Modified from Heinemeyer *et al.* (2007).

purified. Blue-native PAGE is a helpful tool to monitor the purification steps. Furthermore, blue-native PAGE can be used as the starting point for another purification step, which is based on electroelution and which leads to highly pure supercomplexes suitable for x-ray crystallography. However, despite considerable success in supercomplex purification, procedures still have to be further developed to characterize even larger protein structures, which are assumed to occur under *in vivo* conditions. Laboratory strains of *Saccharomyces cerevisiae* lack the NADH dehydrogenase complex (complex I), which in other organisms additionally is associated to complexes III and IV. Further protein complexes of the inner mitochondrial membrane possibly associated with III + IV supercomplexes are the ADP/ATP translocase or the preprotein translocase of the inner mitochondrial membrane, the so-called TIM complex (Dienhart and Stuart, 2008; Saddar *et al.*, 2008). Development of novel procedures might allow unraveling the megacomplex organization of the inner mitochondrial membrane.

ACKNOWLEDGMENTS

Research in our laboratories was supported by grants of the Deutsche Forschungsgemeinschaft (Br 1829-7/3 and Br 1829-8/1) and the Dutch Science Foundation NWO-CW.

REFERENCES

- Berry, E. A., and Trumppower, B. L. (1985). Isolation of ubiquinol oxidase from *Paracoccus denitrificans* and resolution into cytochrome bc_1 and cytochrome c -aa₃ complexes. *J. Biol. Chem.* **262**, 2458–2467.
- Boekema, E. J., and Braun, H. P. (2007). Supramolecular structure of the mitochondrial oxidative phosphorylation system. *J. Biol. Chem.* **282**, 1–4.
- Boumans, H., Grivell, L. A., and Berden, J. A. (1998). The respiratory chain in yeast behaves as a single functional unit. *J. Biol. Chem.* **273**, 4872–4877.
- Cruciat, C. M., Brunner, S., Baumann, F., Neupert, W., and Stuart, R. A. (2000). The cytochrome bc_1 and cytochrome c oxidase complexes associate to form a single supercomplex in yeast mitochondria. *J. Biol. Chem.* **275**, 18093–18098.
- Dienhart, M. K., and Stuart, R. A. (2008). The yeast Aac2 protein exists in physical association with the cytochrome bc_1 -COX supercomplex and the TIM23 machinery. *Mol. Biol. Cell* **19**, 3934–3943.
- Frank, J. (2002). Single-particle imaging of macromolecules by cryo-electron microscopy. *Annu. Rev. Biophys. Biomol. Struct.* **31**, 303–319.
- Hatefi, Y., Haavik, A. G., Fowler, L. R., and Griffiths, D. E. (1962). Studies on the electron transfer system. Reconstitution of the electron transfer system. *J. Biol. Chem.* **237**, 2661–2669.
- Hackenbrock, C. R., Chazotte, B., and Gupta, S. S. (1986). The random collision model and a critical assessment of the diffusion and collision in mitochondrial electron transport. *J. Bioenerg. Biomembr.* **18**, 331–368.
- Heinemeyer, J., Braun, H. P., Boekema, E. J., and Kouril, R. (2007). A structural model of the cytochrome c reductase/oxidase supercomplex from yeast mitochondria. *J. Biol. Chem.* **282**, 12240–12248.
- Iwasaki, T., Matsuura, K., and Oshima, T. (1995). Resolution of the aerobic respiratory system of the thermoacidophilic archaeon, *Sulfolobus* sp. Strain 7. I. The archaeal terminal oxidase supercomplex is a functional fusion of respiratory complexes III and IV with no c -type cytochromes. *J. Biol. Chem.* **270**, 30881–30892.
- Lange, C., and Hunte, C. (2002). Crystal structure of the yeast cytochrome bc_1 complex with its bound substrate cytochrome c . *Proc Natl. Acad. Sci. USA* **99**, 2800–2805.
- Meisinger, C., Pfanner, N., and Truscott, K. N. (2006). Isolation of yeast mitochondria. *Methods Mol. Biol.* **313**, 33–39.
- Nelson, D. L., and Cox, M. M. (2008). In “Lehninger—Principles of Biochemistry” 5th Ed., pp. 718–719. Freeman, New York.
- Pfeiffer, K., Gohil, V., Stuart, R. A., Hunte, C., Brandt, U., Greenberg, M. L., and Schagger, H. (2003). Cardiolipin stabilizes respiratory chain supercomplexes. *J. Biol. Chem.* **278**, 52873–52880.
- Saddar, S., Dienhart, M. K., and Stuart, R. A. (2008). The F₁F₀-ATP synthase complex influences the assembly state of the cytochrome bc_1 -cytochrome oxidase supercomplex and its association with the TIM23 machinery. *J. Biol. Chem.* **283**, 6677–6686.
- Schagger, H., and Pfeiffer, K. (2000). Supercomplexes in the respiratory chains of yeast and mammalian mitochondria. *EMBO J.* **19**, 1777–1783.

- Sone, N., Sekimachi, M., and Kutoh, E. (1987). Identification and properties of a quinol oxidase supercomplex composed of a bc_1 complex and cytochrome oxidase in the thermophilic bacterium PS3. *J. Biol. Chem.* **262**, 15386–15391.
- Tsukihara, T., Aoyama, H., Yamashita, E., Tomizaki, T., Yamaguchi, H., Shinzawa-Itoh, K., Nakashima, R., Yaono, R., and Yoshikawa, S. (1996). The whole structure of the 13-subunit oxidized cytochrome *c* oxidase at 2.8 Å. *Science* **272**, 1136–1144.
- van Heel, M., Gowen, B., Matadeen, R., Orlova, E. V., Finn, R., Pape, T., Cohen, D., Stark, H., Schmidt, R., Schatz, M., and Patwardhan, A. (2000). Single-particle electron cryo-microscopy: Towards atomic resolution. *Q. Rev. Biophys.* **33**, 307–369.
- Wittig, I., Braun, H. P., and Schagger, H. (2006). Blue-Native PAGE. *NATURE Protocols* **1**, 418–428.
- Wittig, I., Karas, M., and Schagger, H. (2007). High resolution clear native electrophoresis for in-gel functional assays and fluorescence studies of membrane protein complexes. *Mol. Cell. Proteomics* **6**, 1215–1225.
- Zerbetto, E., Vergani, L., and Dabbeni-Sala, F. (1997). Quantitation of muscle mitochondrial oxidative phosphorylation enzymes via histochemical staining of blue native polyacrylamide gels. *Electrophoresis* **18**, 2059–2064.
- Zhang, M., Mileykovskaya, E., and Dowhan, W. (2002). Gluing the respiratory chain together. *J. Biol. Chem.* **277**, 43553–43556.
- Zhang, M., Mileykovskaya, E., and Dowhan, W. (2005). Cardiolipin is essential for organization of complexes III and IV into a supercomplex in intact yeast mitochondria. *J. Biol. Chem.* **280**, 29403–29408.

SUPERCOMPLEX ORGANIZATION OF THE YEAST RESPIRATORY CHAIN COMPLEXES AND THE ADP/ATP CARRIER PROTEINS

Rosemary A. Stuart

Contents

1. Introduction	192
1.1. The OXPHOS complexes	192
1.2. Supercomplex organization state of the OXPHOS system	193
1.3. The AAC protein isoforms	195
1.4. The supercomplex organization of yeast AAC proteins—the presence of AAC-cytochrome <i>bc</i> ₁ -COX-TIM23 supercomplex	195
2. Choice of the Detergent—Digitonin	198
2.1. Comments on the choice and concentration of digitonin used in the mitochondrial solubilization step	198
2.2. Recrystallization of digitonin	198
2.3. Choice of the concentration of digitonin for the mitochondrial lysis step	199
3. Mitochondrial Solubilization and BN-PAGE/SDS-PAGE Analysis	199
3.1. Isolation and Storage of Mitochondria	199
3.2. Digitonin lysis step	200
3.3. BN-PAGE protein standard preparation	200
3.4. Electrophoresis of BN-PAGE and SDS-PAGE gels	201
3.5. Analysis after the SDS-PAGE and Western blotting steps	201
4. Expression and Affinity Purification of a His-Tagged Aac2 Protein (_{HIS} Aac2)	203
4.1. Cloning and expression of _{HIS} Aac2	203
4.2. Affinity purification of His-tagged Aac2 and coassociating proteins	205
4.3. Comments on the use of the His-tagged Aac2 derivative	206
Acknowledgments	206
References	206

Department of Biological Sciences, Marquette University, Milwaukee, Wisconsin, USA

Methods in Enzymology, Volume 456
ISSN 0076-6879, DOI: 10.1016/S0076-6879(08)04411-X

© 2009 Elsevier Inc.
All rights reserved.

Abstract

The enzymes involved in mitochondrial oxidative phosphorylation (OXPHOS) are coassembled into higher ordered supercomplexes within the mitochondrial inner membrane. The cytochrome bc_1 -cytochrome c oxidase (COX) supercomplex is formed by the coassociation of the two electron transport chain complexes, the cytochrome bc_1 (cytochrome c reductase) and the COX complex. Recent evidence indicates that a diversity in the populations of the cytochrome bc_1 -COX supercomplexes exists within the mitochondria, because different subpopulations of this supercomplex have been shown to further interact with distinct partner complexes (e.g., the TIM23 machinery and also the Shy1/Cox14 proteins). By use of native gel electrophoresis and affinity purification approaches, the abundant ADP/ATP carrier protein (AAC) isoform in the yeast *Saccharomyces cerevisiae*, the Aac2 isoform, has recently been found to also exist in physical association with the cytochrome bc_1 -COX supercomplex and its associated TIM23 machinery. The AAC proteins play a central role in cellular metabolism, because they facilitate the exchange of ADP and ATP across the mitochondrial inner membrane. The method used to analyze the cytochrome bc_1 -COX-AAC supercomplex and to affinity purify the Aac2 isoform and its associating proteins from *S. cerevisiae* mitochondria will be outlined in this chapter.

1. INTRODUCTION

Mitochondria are essential organelles in eukaryotic cells that house the enzymatic machinery, the oxidative phosphorylation (OXPHOS) system, responsible for the aerobic production of adenosine triphosphate (ATP)—the energy currency of the cell. Production of ATP within the mitochondria is a multistep process that requires intimate coordination of the electron transport chain component of the OXPHOS system and their H^+ pumping activities, with the ATP synthesizing enzyme (the F_1F_0 -ATP synthase complex) and its H^+ -transporting activity (Saraste, 1999). In addition, metabolite carrier proteins, the ADP/ATP carriers (AAC), and the phosphate (P_i) carrier form integral parts of the OXPHOS system, because they ensure both the replenishing of the mitochondrial matrix ADP and P_i levels and the export of the newly synthesized ATP across the inner membrane. ATP exported by the AAC proteins gains access to the cell's cytosol and becomes distributed to other locations within the cell that require the ATP to fuel their metabolic processes.

1.1. The OXPHOS complexes

The electron transport chain component of the OXPHOS machinery is composed of four multisubunit complexes embedded within the lipid bilayer of the inner mitochondrial membrane.

These complexes are termed the NADH: ubiquinone oxidoreductase (complex I), the succinate dehydrogenase (complex II), the ubiquinol cytochrome c reductase (also known as and referred to here as the cytochrome bc_1 complex, complex III), and the cytochrome c oxidase (complex IV). Electrons generated from NADH and $FADH_2$ are passed through complexes I to IV and ultimately become transferred to oxygen. The passage of electron through complexes I to IV is coupled to the pumping of H^+ from the matrix across the inner membrane to the intermembrane space by complexes I, III, and IV (Saraste, 1999). Electron transfer between complexes I to IV involves ubiquinone, a mobile electron carrier located within the inner membrane, and cytochrome c , a small nonmembrane anchored protein located on the intermembrane space-side of the inner membrane. The proton gradient established through the activity of the OXPHOS complexes energetically supports the synthesis of ATP by the F_1F_o -ATP synthase (also known as complex V of OXPHOS system) in the matrix and events such as metabolite and protein transport across the inner membrane.

For animal cells most ATP generated is through this process of OXPHOS or aerobic respiration in their mitochondria. Over the past years defects in the process of OXPHOS have been implicated in a variety of metabolic and degenerative diseases (Smeitink *et al.*, 2006 and references therein). A common feature of these disorders stems from a reduced capacity to generate energy, and hence muscle, brain, and cardiac tissues can be seriously affected because of their high-energy demands. In many cases, the molecular basis of the defect in these diseases remains unknown. Before the complexities of these defects and diseases can be fully explained, a complete understanding of the OXPHOS complexes at the level of their subunit composition, their assembly, and their molecular organization into the mitochondrial inner membrane structures is essential.

1.2. Supercomplex organization state of the OXPHOS system

The OXPHOS complexes I to V are large multisubunit enzymes formed by the coassembly of nuclear- and mitochondrially-encoded proteins. These enzymes are embedded in the lipid bilayer of the inner mitochondrial membrane and are largely composed of integral membrane proteins. The OXPHOS complexes can be purified in their enzymatically active forms after their detergent extraction from the mitochondria, a feature that has enabled their individual characterization. Extensive research into the subunit composition, enzymology, regulation, and, in many cases, the structure of these detergent-purified complexes has been documented over many years in the literature. Despite these significant advances in our understanding of the workings of the individually isolated OXPHOS complexes, how these complexes are organized within the mitochondrial inner

membrane remains the subject of some debate and novel research directions. Increasing evidence exists that the mitochondrial OXPHOS complexes are not randomly organized as individual complexes in the membrane, but rather exist as “supercomplexes” formed by physical association of one OXPHOS enzyme with another (Boekema and Braun, 2007; Genova *et al.*, 2008; Lenaz and Genova, 2007; Stuart, 2008).

The detergent solubilization procedures traditionally used to purify these individual enzymes for their further analysis often disturbed the physical associations that existed between the individual OXPHOS complexes in the membrane. Hence these detergent extraction approaches frequently resulted in the purification of the OXPHOS enzymes as individual entities rather than in their supercomplex assembly state they had existed in within the environment of the mitochondrial inner membrane. The recent use of milder detergents (e.g., digitonin) for the mitochondrial solubilization step, and in particular the use of native electrophoretic techniques to analyze the assembly states of the detergent-solubilized complexes (Schägger and von Jagow, 1991), has revolutionized our technical ability to isolate and study the supercomplex assemblies of the OXPHOS complexes. By use of these types of approaches, the organization of the mitochondrial OXPHOS complexes into supercomplexes has now been described for many organisms, including representatives from fungi, plants, and mammals (reviewed in Boekema and Braun, 2007; Devenish *et al.*, 2008; Schägger, 2002; Vonck and Schäfer, 2008). The predominant supercomplexes described to date involve complexes I-III-IV and the dimeric/oligomeric forms of the ATP synthase.

Formation of the OXPHOS supercomplexes has been proposed to concentrate these enzymes into localized areas within the mitochondrial inner membrane (i.e., to form “OXPHOS platforms” also termed “respirasomes”) (Schägger, 2002). Two supercomplex assemblies in yeast mitochondria, the dimeric ATP synthase and the cytochrome *bc*₁ cytochrome *c* oxidase (COX) supercomplex have been previously described (Stuart, 2008 and references therein). In addition, it has recently been established that a subpopulation of the cytochrome *bc*₁ COX complex has the capacity to interact with the TIM23 machinery and also to associate with the Shy1 and Cox14 proteins (Mick *et al.*, 2007; Saddar *et al.*, 2008; van der Laan *et al.*, 2006; Wiedemann *et al.*, 2007). The TIM23 machinery forms a voltage-sensitive channel in the mitochondrial inner membrane that facilitates the import of nuclearly encoded proteins into the mitochondria (Kutik *et al.*, 2007). The Shy1 and Cox14 proteins are assembly factors specific for the COX biogenesis pathway (Glerum *et al.*, 1995; Mashevich *et al.*, 1997). Finally, as will be outlined in more detail later, the AAC proteins also may exist in “respirasomes,” because their physical association with the cytochrome *bc*₁ COX supercomplex has recently been reported (Claypool *et al.*, 2008; Dienhart and Stuart, 2008).

1.3. The AAC protein isoforms

The ADP/ATP carrier (AAC) proteins are integral membrane proteins, which facilitate the equimolar exchange of ATP for ADP across the inner membrane (Pebey-Peyroula *et al.*, 2003). Previous research has shown that it is common for organisms to contain more than one isoform of AAC within their mitochondria. The expression profile of the genes encoding the different AAC isoforms can vary depending on growth conditions (e.g., for fungal organisms) or in a tissue-specific manner (e.g., for multicellular organisms). For example, in the yeast *S. cerevisiae*, the model organism of this study, there are three AAC isoforms, encoded by the AAC1, AAC2, and AAC3 genes, respectively (Drgon *et al.*, 1992). In aerobically grown cells, the Aac2 protein is the most abundant AAC isoform, and the Aac1 represents a minor isoform. The AAC3 gene is predominantly expressed under anaerobic growth conditions. The Sa11 protein represents a further member of the mitochondrial AAC family, which also catalyzes ADP/ATP exchange across the mitochondrial inner membrane, but it differs from other AAC family members in that it contains an extended N-terminal hydrophilic region of unknown function and proposed to be involved in Ca⁺⁺ binding (Chen, 2004). Although all three AAC isoforms and the Sa11 protein display the capacity to transport ADP in exchange for ATP, the physiological significance of having multiple isoforms of this metabolite carrier within an organism is not completely understood. In addition to their overlapping role in facilitating mitochondrial ADP/ATP exchange, current findings suggest that the AAC proteins may have acquired additional roles within the mitochondria, and the three AAC isoforms and the Sa11 protein may not be functionally equivalent in this respect. For example, deletion of the AAC2 and AAC3 genes in combination (but not the deletion of both AAC2 and AAC1 genes) results in a synthetic lethal phenotype under anaerobic conditions. Furthermore, deletion of the SAL1 gene together with the AAC2 gene (but not a SAL1 deletion in combination with the AAC1 or AAC3 genes) causes a synthetic lethal phenotype under aerobic conditions. Thus in addition to their role in ADP/ATP exchange, some of these AAC family members perform additional overlapping function(s) that are required for cell viability (Chen, 2004; Drgon *et al.*, 1992). It is currently unclear, however, what essential role(s) these AAC family members may have and if the AAC proteins exert this vital function alone or in a manner that involves other proteins/enzymes within the mitochondrial inner membrane.

1.4. The supercomplex organization of yeast AAC proteins—the presence of AAC-cytochrome *bc*₁-COX-TIM23 supercomplex

The oligomeric state of the AAC proteins within the mitochondrial membrane has been a topic of interest in the OXPHOS literature for many years. Evidence to support that the AAC proteins exist and function as monomers

or as dimers has been actively debated. Recent crystallographic and functional studies have favored that the operational unit of the AAC protein may, indeed, be the monomeric form of the protein (Bamber *et al.*, 2007a,b; Nury *et al.*, 2005; Pebay-Peyroula *et al.*, 2003). The ability to purify a functional ADP/ATP transporter as a monomeric protein, however, does not exclude the possibility that in the intact mitochondrial membrane system the AAC proteins could exist in physical association with other proteins and the detergent used for their solubilization may have dissociated such interactions. As outlined previously, the AAC family members, in addition to facilitating the exchange of ADP and ATP across the inner membrane, exert additional overlapping roles that are essential to cell viability. This observation suggests that the AAC proteins may cooperate with other proteins to fulfill this essential role in the cell. To further understand the additional function(s) of the AAC proteins, we have initiated an analysis of the molecular environment of the AAC proteins within the mitochondria, with the goal of identifying proteins that may physically and functionally interact with the AAC metabolite carriers. It had not been addressed until now whether the yeast AAC proteins may also form higher ordered assemblies or “supercomplexes” with other mitochondrial proteins or with the OXPHOS complexes. One report has indicated that some AAC protein may be associated with a population of the ATP synthase in bovine mitochondria (Ko *et al.*, 2003).

Analysis of the protein composition of the cytochrome bc_1 -COX supercomplex, solubilized from mitochondria with low digitonin concentrations, provided the initial observation that the yeast AAC proteins could be found in association with this OXPHOS supercomplex. The cytochrome bc_1 -COX supercomplex was initially resolved on a first-dimension blue-native polyacrylamide gel electrophoresis (BN-PAGE) and then individual polypeptides constituting this supercomplex were resolved in a second-dimensional separation on an SDS-PAGE. A novel and abundant polypeptide of approximately 30 kDa was observed to comigrate with the subunits of the cytochrome bc_1 -COX supercomplex. The use of increased digitonin levels (see later) during the lysis step resulted in the loss of this 30-kDa protein from the cytochrome bc_1 -COX supercomplex, suggesting its association with the OXPHOS supercomplex was sensitive to detergent levels. The identity of the 30-kDa comigrating protein was revealed as AAC by use of a specific antibody against this protein family (Dienhart and Stuart, 2008).

The association of Aac2 with the cytochrome bc_1 -COX and TIM23 complexes was independently verified by use of a His-tagged Aac2 derivative and Ni-NTA affinity purification approaches (Dienhart and Stuart, 2008). Ni-NTA purified His-Aac2 complexes were demonstrated to contain at least one other AAC protein (most likely another Aac2) and subunits of the cytochrome bc_1 (e.g., Core1, Core 2), COX (e.g., Cox2, Cox5), and TIM23 complexes (e.g., Tim17, Tim23). The association between the

AAC proteins and the cytochrome bc_1 -COX complex was observed to be highly sensitive to detergent concentration and was maintained by use of low concentrations of the mild detergent digitonin, which may explain why the association of AAC proteins with the cytochrome bc_1 -COX supercomplexes had not been described before (Dienhart and Stuart, 2008). It is currently unknown whether the Aac1, Aac3, or Sal1 proteins, like the Aac2 isoform, display the capacity to physically associate with the cytochrome bc_1 -COX and TIM23 complexes.

The functional relevance of an AAC-cytochrome bc_1 -COX-TIM23 association is currently under investigation. One possibility is that this association supports the ADP/ATP transport function of the AAC proteins. The import of ADP³⁻ in exchange for ATP⁴⁻ is not charge compensated and thus is supported energetically through the membrane potential generated by the activity of the OXPHOS complexes. Approximately 30% of the energy generated by the respiratory chain complexes has been estimated to be required to support the exchange of ADP for ATP (Duszyński *et al.*, 1981). The cytochrome bc_1 and COX complexes both play an active role in establishing the mitochondrial membrane potential through their H⁺-pumping activities, and thus their physical association with AAC may reflect a direct involvement in supporting the energetic demands of the ADP/ATP exchange process. On the other hand, it is also possible that the coassembly of Aac2 may be favorable for the assembly and/or activity of the cytochrome bc_1 -COX complex. In the absence of Aac2, a decrease in the levels of the COX complex and enzyme activity is detected (Dienhart and Stuart, 2008; Fontanesi *et al.*, 2004). In addition, an alteration in the assembly state of the cytochrome bc_1 -COX supercomplex was observed in the absence of the Aac2 isoform. In wild-type mitochondria, the cytochrome bc_1 -COX supercomplex is almost exclusively present in the III₂-IV₂ or larger forms (i.e., with a stoichiometry of two cytochrome bc_1 complexes [complex III] in association with two COX complexes [complex IV] [Schägger and Pfeiffer, 2000]). Only a minor population is observed to be present with a stoichiometry of III₂-IV. In the absence of Aac2, a significant change in the ratio of III₂-IV to III₂-IV₂ complexes and also the presence of some free cytochrome bc_1 (i.e., non-COX complex associated) subforms was observed (Dienhart and Stuart, 2008). The decreased levels of the COX enzyme complex observed in the $\Delta aac2$ mitochondria may be limiting to ensure the normal III₂-IV₂ assembly state of the cytochrome bc_1 -COX supercomplex. Enhanced proteolytic turnover of the COX complex in the absence of Aac2 or a perturbation in the assembly of the COX complex may underlie the observed reduction in the COX complex in the $\Delta aac2$ mitochondria. It is also conceivable that Aac2 may directly support the initial assembly of the COX complex through affecting the assembly state and possibly the function of COX assembly factors, Shy1 and Cox14, which have been shown to associate with the cytochrome bc_1 -COX supercomplex (Mick *et al.*, 2007).

In this chapter, the techniques used in our laboratory to identify and study the association of yeast Aac2 protein with the cytochrome bc_1 -COX-TIM23 supercomplex will be described.

2. CHOICE OF THE DETERGENT—DIGITONIN

2.1. Comments on the choice and concentration of digitonin used in the mitochondrial solubilization step

The association of the yeast AAC with the cytochrome bc_1 -COX-TIM23 supercomplex is observed after extraction of AAC from the mitochondrial membranes by use of low levels of the mild detergent, digitonin (see later). The concentration of digitonin used for the mitochondrial membrane solubilization step was observed to be critical to maintain the association of AAC with the cytochrome bc_1 -COX-TIM23 supercomplex, because increasing the concentration of this mild detergent (i.e., from 0.5 to 1.5% or higher under the lysis conditions described later) during the lysis step was observed with BN-PAGE analysis to result in the release of an AAC-containing subcomplex from the cytochrome bc_1 -COX subcomplex core. The digitonin used for this OXPHOS supercomplex analysis is of high quality and routinely recrystallized in ethanol before use.

2.2. Recrystallization of digitonin

Digitonin (5 g, Calbiochem) is placed in an Erlenmeyer flask and approximately 100 ml of ethanol p.a. is added under constant stirring conditions. The mixture is gently heated with a magnetic stirring heating block until the digitonin is fully dissolved. The solution is then divided between two 50-ml conical tubes and allowed to cool initially to room temperature before being placed at -20° overnight. The recrystallized digitonin is recovered through centrifugation (3000g at 4° , for 15 min), and the supernatant is decanted and discarded. The digitonin is then dried with a desiccator and then stored in sealed tubes in an airtight container. A digitonin stock solution (usually 10 or 20% [w/v]) is prepared just before use by dissolving a freshly weighed aliquot of digitonin in an appropriate volume of lysis buffer (see later). This digitonin stock solution is either used directly in the mitochondrial lysis step or can be used to prepare further dilutions of digitonin, as necessary. The digitonin stock solutions are routinely prepared fresh but may be stored for a limited period (order of weeks) at -20° . Frozen aliquots of digitonin solution are thawed once before use and then are discarded afterwards (i.e., are not subjected to cycles of refreezing).

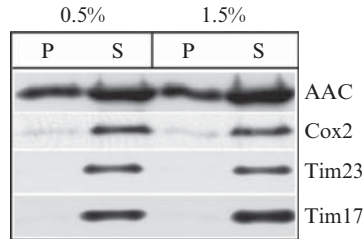


Figure 11.1 Efficiency of solubilization of AAC, the cytochrome bc_1 -COX supercomplex and TIM23 complexes. Wild-type mitochondria were treated with digitonin at concentrations indicated, and nonsolubilized material (P) was pelleted by centrifugation (30,000g, 30 min), and the solubilized proteins (S) were subjected to TCA precipitation. Protein samples were analyzed by SDS-PAGE, Western blotting, and immune decoration. The solubility profiles of AAC, Cox2, Tim23, and Tim17 were analyzed.

2.3. Choice of the concentration of digitonin for the mitochondrial lysis step

Lysis of mitochondria with low digitonin concentrations (0.5%), under the conditions described later results in the solubilization of approximately 60 to 70% of the total AAC protein and nearly all of the cytochrome bc_1 - and COX complexes. Similar solubilization efficiencies are obtained at 1.5% digitonin (Fig. 11.1). Comigration of the AAC proteins with the cytochrome bc_1 -COX supercomplex on BN-PAGE, however, is largely seen at the lower (0.5%) digitonin lysis conditions. When solubilization is performed at the higher concentrations (e.g., 1.5% digitonin), the association of the AAC protein with the OXPHOS supercomplex is largely disrupted, and the AAC proteins are observed to comigrate in a smaller complexes in the molecular mass range of 100 to 200 kDa, with a minor form in the 400-kDa range (Dienhart and Stuart, 2008).

3. MITOCHONDRIAL SOLUBILIZATION AND BN-PAGE/SDS-PAGE ANALYSIS

3.1. Isolation and Storage of Mitochondria

Mitochondria are routinely isolated from yeast (*S. cerevisiae*) culture grown to an OD_{578nm} of 1 to 2.0 in YP-media supplemented with 0.5% lactate and 2% galactose. Isolation of mitochondria is performed by use of previously published procedures (Herrmann *et al.*, 1994). The freshly isolated mitochondria are resuspended at a protein concentration of 10 mg protein/ml in SEM buffer (250 mM sucrose, 2 mM EDTA, 10 mM MOPS-KOH,

pH 7.2), aliquoted into 25- μ l aliquots and snap-frozen in liquid nitrogen. Frozen mitochondria are stored at -80° and are thawed briefly before use and are not subjected to refreezing.

3.2. Digitonin lysis step

To perform the BN-PAGE/SDS-PAGE analysis of the AAC and cytochrome bc_1 -COX supercomplexes, the OXPHOS complexes need initially to be detergent solubilized from the mitochondrial membranes. Mitochondria (20 μ l, i.e., equivalent to 200 μ g protein) are gently mixed together with 200 μ l of cold SEM buffer and subjected to centrifugation at 10,000g for 10 min at 4° . The supernatant is removed with a P200 pipette, and the resulting mitochondrial pellet is gently resuspended through pipetting in 38 μ l of ice-cold lysis buffer (50 mM potassium acetate, 50 mM HEPES-KOH, pH 7.4, 11.4% glycerol and 1 mM PMSF) and then supplemented with 2 μ l of freshly prepared 10% (w/v) digitonin (i.e., end concentration = 0.5% digitonin). The mixture is thoroughly mixed by gently pipetting up and down with a P200 pipette for a total of 12 times. The sample is left on ice for 30 min and then subjected to the pipetting ritual once again before performing a clarifying spin of 30,000g for 30 min at 4° . The supernatant is removed from the resulting pellet and transferred to a new tube. The sample is supplemented with 4 μ l of BN-PAGE dye buffer (5% Coomassie Blue [Serva blue G], in 500 mM aminocaproic acid) and immediately loaded on the BN-PAGE gel (3.5 to 10% gradient gel) (Schägger and von Jagow, 1991).

Duplicate samples of the same mitochondrial type are usually subjected to digitonin extraction and BN-PAGE analysis in parallel, where one sample will be used for the second-dimension SDS-PAGE separation step (see later) and the other sample together with the protein standards will be subjected to Western blotting after the BN-PAGE step. (To Western blot BN-PAGE gels, the gel should be soaked in SDS-containing Western blotting buffer for 30 min at room temperature before assembling the Western blot. Standard Western blot procedures are then used.)

3.3. BN-PAGE protein standard preparation

Protein standards are prepared in the digitonin-containing lysis buffer and run alongside the mitochondrial extract sample to standardize the separation profile of the BN-PAGE gel. Commonly used standards are thyroglobulin (667 kDa), apoferritin (443 kDa), β -amylase (200 kDa), alcohol dehydrogenase (150 kDa), and bovine serum albumin (BSA, 60 kDa). These standard proteins can be purchased together in one kit from Sigma-Aldrich. The protein standards are prepared in lysis buffer as 10 mg/ml stock solutions (these can be frozen in aliquots at -20°). To prepare the samples for BN-PAGE electrophoresis, 4 μ l of protein standard is supplemented with

34 μ l of lysis buffer, 2 μ l of 10% digitonin and 4 μ l of the BN-PAGE sample buffer. The protein standard samples should be prepared just before loading on the BN-PAGE gel.

3.4. Electrophoresis of BN-PAGE and SDS-PAGE gels

The BN-PAGE gels are initially run at 4° for 1 h at 100V followed by 30 to 45 min at 500 V, with the anode buffer (50 mM BISTRIS, pH 7.0) and a cathode buffer supplemented with Coomassie blue (50 mM Tricine, 15 mM BISTRIS, 0.02% Coomassie Blue [Serva blue G], pH 7.0) (Schägger and von Jagow, 1991). After this, the blue cathode buffer is discarded, the cathode buffer chamber washed briefly with water and replaced with clear cathode buffer (same cathode solution as before but Coomassie blue is omitted), and electrophoresis is continued at 500 V for approximately 2 to 2.5 h. After the first-dimension BN-PAGE separation, the gel strip containing the resolved protein complexes to be subjected to the second-dimension electrophoresis step is excised from the gel and allowed to soak in SDS-gel electrophoresis buffer for 30 min at room temperature. The strip is then carefully inserted between glass plates and on top of a preparative SDS-PAGE gel and sealed with a molten agarose solution (0.7% [w/v] low melting point agarose, 0.5% [w/v] SDS, and 15 mM β -mercaptoethanol). Molecular weight markers and an aliquot of SDS-solubilized mitochondrial proteins are loaded on the same gel in parallel lanes. Electrophoresis in the second dimension is then performed with standard SDS-PAGE electrophoresis conditions and is followed by Western blotting of the resulting gel onto nitrocellulose (Laemmli, 1970; Towbin *et al.*, 1979).

It is not uncommon to analyze the assembly states or protein subunit profiles of the AAC-cytochrome *bc*₁-TIM23 supercomplex in the mitochondria isolated from different yeast mutant strains. When this is the case, mitochondria isolated from the mutant and isogenic wild-type control are digitonin extracted in parallel and run side by side on the same BN-PAGE gel. The resulting parallel gel strips are both excised from the BN-PAGE and applied to two separate SDS-PAGE gels.

3.5. Analysis after the SDS-PAGE and Western blotting steps

After the SDS-PAGE and Western blotting steps, the resulting nitrocellulose membrane is washed in water and, before immune decoration with antibodies of interest, should be stained with Ponceau S to reveal the migration profiles of the resolved mitochondrial protein complexes and the applied molecular weight markers. To do so the blot is washed initially in water and then soaked in a Ponceau S solution (0.2% Ponceau S, 3% TCA) for 1 to 2 min and washed briefly in water again to remove excess stain. A digital scan of the Ponceau S-stained Western blot should be

prepared for documentation purposes before removing the stain (with thorough washing with water) and preparing the blot for immune decoration. This scanned image of the Ponceau S-stained blot can also be printed out onto transparency (or overhead) sheets, so that the protein migration pattern from the gel of one sample can be superimposed on and thereby compared with that of another that had been run in parallel (i.e., if the assembly states of the OXPHOS-containing supercomplexes are to be compared between wild-type and mutant mitochondrial samples analyzed in parallel on the same BN-PAGE gel).

The assembly states of the AAC, TIM23 complex, the cytochrome bc_1 -, and COX complexes can be determined through immune decoration of the Western blot resulting from the second dimension SDS-PAGE analysis with available subunit specific antibodies (e.g., α -AAC, α -Tim17, or α -Tim23 for the TIM23 complex, α -Core1 or α -Core2 for the cytochrome bc_1 complex, and α -Cox2 or α -Cox5 for the COX complex). Coassembly of AAC proteins with the cytochrome bc_1 -COX-TIM23 supercomplex can be indicated by the comigration of subunits of these complexes with the AAC proteins after the BN-PAGE resolution (Fig. 11.2).

Although the second-dimension SDS-PAGE step adds an extra step to the overall analysis, it confers the advantage that the assembly state of a series of individual proteins can be analyzed in parallel from one mitochondrial

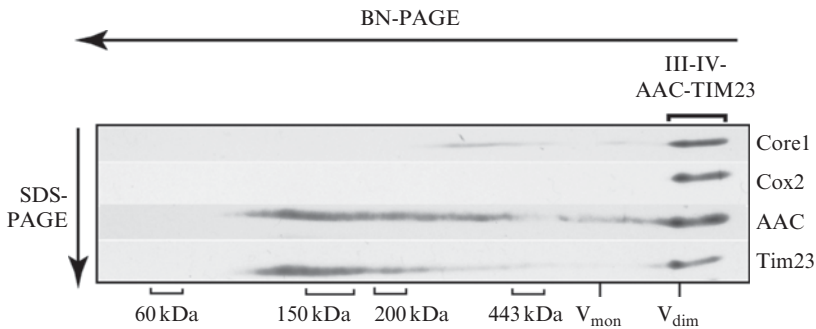


Figure 11.2 Assembly of the AAC protein and its comigration with the cytochrome bc_1 -COX complex with the TIM23 machinery. Mitochondria isolated from wild-type yeast were solubilized in digitonin (0.5 %), clarified by centrifugation, and directly analyzed by BN-PAGE. After the separation of the solubilized complexes by BN-PAGE, proteins were further resolved by a second-dimension SDS-PAGE step. After Western blotting, immune decoration with specific antisera against Core1, Cox2, AAC, and Tim23 was performed as indicated. The position of the cytochrome bc_1 -COX complex comigrating with the AAC and TIM23 complexes is indicated by III-IV-AAC-TIM23. Western blotting with Atp4 antisera (not shown) revealed the positions of the monomeric (approximately 550 kDa) and dimeric F_1F_0 -ATP synthase complexes, indicated here as V_{mon} and V_{dim} , respectively. The positions of molecular weight markers are indicated below.

sample through multiple immune decorations, given that the molecular masses of these proteins differs such that they can be resolved from each other in the SDS-PAGE step. On the other hand, if the goal of the experiment is to analyze the mass of the cytochrome bc_1 -COX supercomplex and in particular to analyze the stoichiometry of the III₂-IV₂ and III₂-IV forms or to ascertain the presence of bc_1 -COX complexes greater in mass than the III₂-IV₁₋₂ forms, then the first-dimension BN-PAGE resolution is usually sufficient and often preferable for resolution reasons. For this reason, as state previously, it is common practice to analyze duplicate samples from one mitochondrial type on the BN-PAGE gel, one of which can subsequently be subjected to the SDS-PAGE analysis to analyze the subunit composition of the supercomplexes and the partner sample can be directly Western blotted after the BN-PAGE analysis for direct immune decoration with cytochrome bc_1 -COX subunit specific antisera.

4. EXPRESSION AND AFFINITY PURIFICATION OF A HIS-TAGGED AAC2 PROTEIN ($_{\text{His}}\text{AAC2}$)

Comigration of two protein populations on a BN-PAGE gel is consistent with their coassembly into a common complex; however, it is not definitive proof of their physical association. To demonstrate that the similar migration profiles of AAC and the cytochrome bc_1 -COX supercomplex reflected their coassociation into a joint supercomplex, an affinity purification approach can be used. For this analysis we have chosen to create a Histidine-tagged Aac2 derivative and to use Ni-NTA chromatography for the affinity purification step. The Aac2 isoform can be tagged at its N-terminus with a histidine tag, a stretch of 12 histidine residues (a His-tag). The resulting His-tagged Aac2 ($_{\text{His}}\text{Aac2}$) and coassociating proteins can be affinity purified with Ni-NTA-agarose beads after their solubilization from the mitochondrial membranes with digitonin.

4.1. Cloning and expression of $_{\text{His}}\text{Aac2}$

To express the His-tagged Aac2 derivative in yeast, a polymerase chain reaction (PCR)-based approach was taken to generate an AAC2 open reading frame (ORF) containing an extension at the 5' end to include 12 additional codons encoding His, following the start ATG codon (Dienhart and Stuart, 2008). The 5'-forward primer used for the PCR reaction contained these additional His-encoding codons followed at the 3' end with a sequence that corresponded to codons 2 to 7 of the AAC2 ORF. The PCR-generated DNA fragment (purified yeast genomic DNA is used as template for PCR reaction) encoding the $_{\text{His}}\text{Aac2}$ protein was cloned as an *XbaI/PstI* fragment into a Yip351-LEU2-based vector and downstream

from the galactose-inducible GAL10 promoter. The forward and reverse primers used for the PCR reaction were designed to contain *Xba*I and *Pst*I restriction sites at their 5' and 3'-termini, respectively. The resulting recombinant plasmid was linearized with *Bst*EII and integrated into *leu2* locus of the yeast genome of the wild-type and $\Delta aac2$ strains to result in the expression of $_{\text{His}}\text{Aac2}$ in addition to the endogenous Aac2 protein, or the sole source of Aac2, respectively. Leucine-positive transformants (i.e., LEU2⁺) are selected, and mitochondria were isolated from cultures grown in the presence of galactose. The expression of the $_{\text{His}}\text{Aac2}$ protein in mitochondria isolated from the transformants, with both His-specific and AAC-specific antisera. The addition of the N-terminal His-tag adds 1 to 2 kDa to the size of the Aac2 protein and, therefore, it can be easily distinguished from the authentic Aac2 protein (Fig. 11.3). Expression of the $_{\text{His}}\text{Aac2}$ protein is achieved through supplementation of the growth media with galactose, together with the omission of glucose. Cells expressing $_{\text{His}}\text{Aac2}$ can, therefore, be propagated in glycerol (3%)-containing media (a nonfermentable carbon source) in the presence of 0.1% galactose or in media where galactose (2%) (a fermentable carbon source) is the sole carbon source. The functionality of the $_{\text{His}}\text{Aac2}$ derivative was confirmed through its ability to complement the respiratory-deficient phenotype of the $\Delta aac2$ null mutant when induced though the addition of 0.1% galactose to the glycerol-containing media (Dienhart and Stuart, 2008). The control $\Delta aac2$ strain (i.e., not expressing the $_{\text{His}}\text{Aac2}$ derivative) does not grow under these conditions.

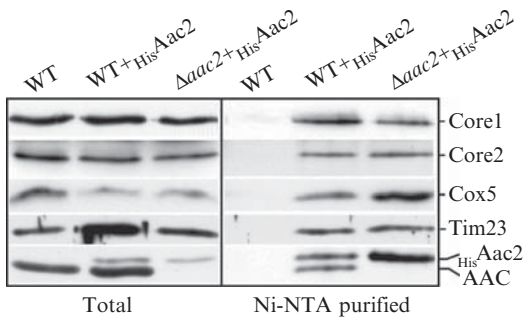


Figure 11.3 Affinity purification of the cytochrome bc_1 -COX-TIM23 complex with the $_{\text{His}}\text{Aac2}$ protein. Mitochondria (wild type and $\Delta aac2$ null) harboring the His-tagged Aac2 protein (WT+ $_{\text{His}}\text{Aac2}$ and $\Delta aac2+_{\text{His}}\text{Aac2}$, respectively), or control wild-type mitochondria (WT), were solubilized with digitonin (0.5 %) and subjected to Ni-NTA chromatography. An aliquot of the total material applied to the Ni-NTA beads (“Total”, corresponds to 5% of input) and the Ni-NTA beads purified material and were analyzed by SDS-PAGE, Western blotting. The resulting blots were immune decorated with antisera specific for the cytochrome bc_1 (Core1, Core2), COX (Cox5), AAC, and the TIM23 (Tim23) complexes, as indicated.

4.2. Affinity purification of His-tagged Aac2 and coassociating proteins

A freshly thawed aliquot of isolated mitochondria (200 μ g protein) harboring the HisAac2 derivative is mixed in SEM buffer and pelleted as described previously for BN-PAGE lysis. The resulting pellet was resuspended in 77 μ l of the lysis buffer used previously for the BN-PAGE lysis and supplemented with 3 μ l of digitonin (10%, w/v) (i.e., end concentration of digitonin is 0.375%). Solubilization was performed on ice before subjecting the sample to a clarifying spin of 30,000g for 30 min at 4°. After the clarifying spin, the sample (70 μ l) is supplemented with additional lysis buffer (150 μ l), digitonin (to final concentration 0.3%), imidazole, and bovine serum albumin (BSA) to final concentrations of 20 mM and 3 mg/ml, respectively. The imidazole and BSA are added to the binding reaction to reduce the level of nonspecific binding (as judged by binding of non-His-tagged AAC [i.e., authentic AAC to the Ni-NTA agarose beads]). The sample is applied to Ni-NTA beads (which had been preequilibrated in the lysis buffer) and incubated with constant turning at 4° for 1.5 h. The beads are washed twice with lysis buffer containing 20 mM imidazole and 0.2% digitonin and once with lysis buffer plus imidazole but without digitonin. The bound proteins can be eluted with SDS-sample buffer and analyzed by SDS-PAGE. Western blotting with subunit-specific antisera can be performed to assay for the recovery of the cytochrome *bc*₁-COX and TIM23 complexes with the affinity-purified HisAac2 protein (Fig. 11.3).

By use of this approach, it could be demonstrated that the Aac2 protein exists in physical association with the cytochrome *bc*₁-COX-TIM23 supercomplex (Dienhart and Stuart, 2008). Subunits of the cytochrome *bc*₁ (e.g., Core1, Core2), the COX complex (e.g., Cox5), and the TIM23 complex (Tim23) can be recovered on the Ni-NTA beads along with the HisAac2 protein (Fig. 11.3). It is important to analyze control mitochondria in parallel to test for the specificity of the Ni-NTA binding step. Wild-type mitochondria (i.e., containing the authentic [non-His-tagged] Aac2 protein) are lysed in parallel and subjected to the Ni-NTA purification step. The recovery of the AAC proteins and the cytochrome *bc*₁-COX-TIM23 subunits should be specific for the presence of the His-tagged Aac2 protein (Fig. 11.3).

When the HisAac2 purification is performed from wild-type mitochondria harboring the His-tagged Aac2 derivative in addition to the authentic Aac2 protein, recovery of both HisAac2 and the non-His-tagged AAC protein on the Ni-NTA beads is achieved, in addition to the previously described components of the cytochrome *bc*₁-COX-TIM23 supercomplex (Fig. 11.3). It may, therefore, be concluded that the HisAac2 protein exists in a complex that contains more than one subunit of AAC. We consider it most likely that the AAC protein copurified with the HisAac2 includes another Aac2 protein, because the same level of authentic AAC protein

was not recovered with the HisAac2 protein from the $\Delta aac2$ null mutant mitochondria (i.e., mitochondria containing Aac1, Aac3, but not Aac2 isoforms) (Fig. 11.3).

4.3. Comments on the use of the His-tagged Aac2 derivative

The presence of the His-tag at the N-terminus of Aac2 seems to partially compromise the stability of the Aac2 derivative, because the levels of $_{\text{His}}\text{Aac2}$ are routinely observed to be substoichiometric to the authentic Aac2 protein, despite that the expression of the $_{\text{His}}\text{AAC2}$ gene is under the control of the strong GAL10 promoter (Dienhart and Stuart, 2008). It should also be noted that during the course of our studies we observed that the addition of the His-tag to the N-terminus of Aac2 increased the stability of the association of Aac2 with the cytochrome bc_1 -COX supercomplex. When solubilized with digitonin levels high enough (e.g., 1.5%) to release most of the authentic AAC proteins from this OXPHOS supercomplex, the BN-PAGE analysis indicated that the $_{\text{His}}\text{Aac2}$ protein remained in tight association with the supercomplex. Thus, it is possible that the His-tag present at the N-terminus of Aac2 increased its affinity for specific components of either the cytochrome bc_1 or COX complexes (Dienhart and Stuart, 2008). We are currently further investigating this. Finally, the placement of the His-tag at the N-terminus (rather than the C-terminus) of Aac2 was found to be critical. We observed that cloning of a C-terminal Aac2 derivative into the Yip-based vector was problematic and expression of a functional C terminally tagged Aac2 derivative was not achieved. It is currently unclear what the underlying reason for this was, but it may reflect that expression of a C-terminally His-tagged derivative of Aac2 could have been toxic to the cell.

ACKNOWLEDGMENTS

Research in the author's laboratory on the assembly and supercomplex organizational state of OXPHOS complexes is supported by research grants from the NIH (RO1 GM 61573) and the NSF (MCB 0347025 and MCB 0744067).

REFERENCES

- Bamber, L., Slotboom, D. J., and Kunji, E. R. (2007a). Yeast mitochondrial ADP/ATP carriers are monomeric in detergents as demonstrated by differential affinity purification. *J. Mol. Biol.* **371**, 388–395.
- Bamber, L., Harding, M., Monné, M., Slotboom, D. J., and Kunji, E. R. (2007b). The yeast mitochondrial ADP/ATP carrier functions as a monomer in mitochondrial membranes. *Proc. Natl. Acad. Sci. USA* **104**, 10830–10834.

- Boekema, E. J., and Braun, H. P. (2007). Supramolecular structure of the mitochondrial oxidative phosphorylation system. *J. Biol. Chem.* **282**, 1–4.
- Chen, X. J. (2004). Sal1p, a calcium-dependent carrier protein that suppresses an essential cellular function associated with the Aac2 isoform of ADP/ATP translocase in *Saccharomyces cerevisiae*. *Genetics* **167**, 607–617.
- Claypool, S. M., Oktay, Y., Boontheung, P., Loo, J. A., and Koehler, C. M. (2008). Cardiolipin defines the interactome of the major ADP/ATP carrier protein of the mitochondrial inner membrane. *J. Cell. Biol.* **182**, 937–950.
- Devenish, R. J., Prescott, M., and Rodgers, A. J. (2008). The structure and function of mitochondrial F₁F_o-ATP synthases. *Int. Rev. Cell. Mol. Biol.* **267**, 1–58.
- Dienhart, M. K., and Stuart, R. A. (2008). The yeast Aac2 protein exists in physical association with the cytochrome *bc*₁-COX supercomplex and the TIM23 machinery. *Mol. Biol. Cell* **19**, 3934–3943.
- Drgon, T., Sabová, L., Gavurniková, G., and Kolarov, J. (1992). Yeast ADP/ATP carrier (AAC) proteins exhibit similar enzymatic properties but their deletion produces different phenotypes. *FEBS Lett.* **304**, 277–280.
- Duszyński, J., Bogucka, K., Letko, G., Küster, U., Kunz, W., and Wojtczak, L. (1981). Relationship between the energy cost of ATP transport and ATP synthesis in mitochondria. *Biochim. Biophys. Acta.* **637**, 217–223.
- Fontanesi, F., Palmieri, L., Scarzia, P., Lodi, T., Donnini, C., Limongelli, A., Tiranti, V., Zeviani, M., Ferrero, I., and Viola, A. M. (2004). Mutations in AAC2, equivalent to human adPEO-associated ANT1 mutations, lead to defective oxidative phosphorylation in *Saccharomyces cerevisiae* and affect mitochondrial DNA stability. *Hum. Mol. Genet.* **13**, 923–934.
- Genova, M. L., Baracca, A., Biondi, A., Casalena, G., Faccioli, M., Falasca, A. I., Formiggini, G., Sgarbi, G., Solaini, G., and Lenaz, G. (2008). Is supercomplex organization of the respiratory chain required for optimal electron transfer activity? *Biochim. Biophys. Acta.* **1777**, 740–746.
- Glerum, D. M., Koerner, T. J., and Tzagoloff, A. (1995). Cloning and characterization of COX14, whose product is required for assembly of yeast cytochrome oxidase. *J. Biol. Chem.* **270**, 15585–15590.
- Herrmann, J. M., Fölsch, H., Neupert, W., and Stuart, R. A. (1994). In “Cell Biology: A Laboratory Handbook, (J. E. Celis, ed.), pp. 538–544. Academic Press, San Diego.
- Ko, Y. H., Delannoy, M., Hullihen, J., Chiu, W., and Pedersen, P. L. (2003). Mitochondrial ATP synthasome. Cristae-enriched membranes and a multiwell detergent screening assay yield dispersed single complexes containing the ATP synthase and carriers for Pi and ADP/ATP. *Biol. Chem.* **278**, 12305–12309.
- Kutik, S., Guiard, B., Meyer, H. E., Wiedemann, N., and Pfanner, N. (2007). Cooperation of translocase complexes in mitochondrial protein import. *J. Cell Biol.* **179**, 585–591.
- Laemmli, U. K. (1970). Cleavage of structural proteins during the assembly of the head of bacteriophage T4. *Nature* **227**, 680–685.
- Lenaz, G., and Genova, M. L. (2007). Kinetics of integrated electron transfer in the mitochondrial respiratory chain: Random collisions vs. solid state electron channeling. *Am. J. Physiol. Cell. Physiol.* **292**, C1221–C1239.
- Mashkevich, G., Repetto, B., Glerum, D. M., Jin, C., and Tzagoloff, A. (1997). SHY1, the yeast homolog of the mammalian SURF-1 gene, encodes a mitochondrial protein required for respiration. *J. Biol. Chem.* **272**, 14356–14364.
- Mick, D. U., Wagner, K., van der Laan, M., Frazier, A. E., Perschil, I., Pawlas, M., Meyer, H. E., Warscheid, B., and Rehling, P. (2007). Shy1 couples Cox1 translational regulation to cytochrome *c* oxidase assembly. *EMBO J.* **26**, 4347–4358.
- Nury, H., Dahout-Gonzalez, C., Trézéguet, V., Lauquin, G., Brandolin, G., and Pebay-Peyroula, E. (2005). Structural basis for lipid-mediated interactions between mitochondrial ADP/ATP carrier monomers. *FEBS Lett.* **579**, 6031–6036.

- Pebay-Peyroula, E., Dahout-Gonzalez, C., Kahn, R., Trézéguet, V., Lauquin, G. J., and Brandolin, G. (2003). Structure of mitochondrial ADP/ATP carrier in complex with carboxyatractyloside. *Nature* **426**, 39–44.
- Saddar, S., Dienhart, M. K., and Stuart, R. A. (2008). The F_1F_0 -ATP synthase complex Influences the Assembly State of the cytochrome bc_1 -cytochrome oxidase supercomplex and its association with the TIM23 machinery. *J. Biol. Chem.* **283**, 6677–6686.
- Saraste, M. (1999). Oxidative phosphorylation at the fin de siècle. *Science* **283**, 1488–1493.
- Schägger, H. (2002). Respiratory chain supercomplexes of mitochondria and bacteria. *Biochim. Biophys. Acta* **1555**, 154–159.
- Schägger, H., and von Jagow, G. (1991). Blue native electrophoresis for isolation of membrane protein complexes in enzymatically active form. *Anal Biochem.* **199**, 223–231.
- Schägger, H., and Pfeiffer, K. (2000). Supercomplexes in the respiratory chains of yeast and mammalian mitochondria. *EMBO J.* **19**, 1777–1783.
- Smeitink, J. A., Zeviani, M., Turnbull, D. M., and Jacobs, H. T. (2006). Mitochondrial medicine: A metabolic perspective on the pathology of oxidative phosphorylation disorders. *Cell Metab.* **1**, 9–13.
- Stuart, R. A. (2008). Supercomplex organization of the oxidative phosphorylation enzymes in yeast mitochondria. *J. Bioenerg. Biomem.* **40**, 411–417.
- Towbin, H., Au, J., and Gordon, J. (1979). “Electrophoretic transfer of proteins from polyacrylamide gels to nitrocellulose sheets: Procedure and some applications” *Proc. Natl. Acad. Sci. USA* **76**, 4350–4354.
- van der Laan, M., Wiedemann, N., Mick, D. U., Guiard, B., Rehling, P., and Pfanner, N. (2006). A role for Tim21 in membrane-potential-dependent preprotein sorting in mitochondria. *Curr Biol.* **16**, 2271–2276.
- Vonck, J., and Schäfer, E. (2008). Supramolecular organization of protein complexes in the mitochondrial inner membrane. *Biochim. Biophys. Acta.* Jun 3. [Epub ahead of print].
- Wiedemann, N., van der Laan, M., Hutu, D. P., Rehling, P., and Pfanner, N. (2007). Sorting switch of mitochondrial presequence translocase involves coupling of motor module to respiratory chain. *J. Cell Biol.* **179**, 1115–1122.

CONTROLLED EXPRESSION OF IRON-SULFUR CLUSTER ASSEMBLY COMPONENTS FOR RESPIRATORY CHAIN COMPLEXES IN MAMMALIAN CELLS

Oliver Stehling, Alex D. Sheftel, *and* Roland Lill

Contents

1. Introduction	210
2. Depletion of Fe/S Cluster Assembly Components by RNA Interference	212
2.1. Vector-based RNAi	212
2.2. siRNA design	213
2.3. Electroporation-based transfections	213
2.4. Assessing the efficiency of the RNAi treatment	215
2.5. Assessing the specificity of the RNAi treatment	216
3. Analysis of Respiratory Complex Assembly	218
3.1. Assessing the incorporation of iron-containing cofactors into respiratory complexes	218
3.2. Assessing the subunit composition of respiratory complexes by two-dimensional BN-PAGE	221
4. Analysis of Respiratory Complex Function	222
4.1. Determination of lactate formation	222
4.2. Determination of complex I activity by in-gel activity staining	223
4.3. Determination of complex I activity by spectrophotometry	224
4.4. Analysis of enzyme activities in multiwell plates	224
5. Concluding Remarks	228
Acknowledgments	228
References	228

Abstract

Three of the respiratory chain complexes contain essential iron-sulfur (Fe/S) cluster prosthetic groups. Besides respiration, these ancient inorganic cofactors are also necessary for numerous other fundamental biochemical processes in

virtually every known organism. Both the synthesis of Fe/S clusters and their delivery to apoproteins depend on the concerted function of specialized, often dedicated, proteins located in the mitochondria and cytosol of eukaryotes. Impaired function of the mitochondria-located Fe/S cluster (ISC) assembly machinery affects all cellular Fe/S proteins, including enzymes of the respiratory chain, NADH: ubiquinone oxidoreductase (complex I; eight Fe/S clusters), succinate: ubiquinone oxidoreductase (complex II; three Fe/S clusters), and cytochrome *bc*₁ complex (complex III; one Fe/S cluster). Here, we describe strategies and techniques both to deprive respiratory chain proteins of their Fe/S cofactors and to study changes in activity and composition of these proteins. As examples, we present the results of the depletion of two types of Fe/S biogenesis proteins, huNfs1 and hulnd1, in a human tissue culture model. The ISC assembly component huNfs1 is required for biogenesis of all cellular Fe/S proteins, its loss exerting pleiotropic effects, whereas hulnd1 is specific for Fe/S cluster maturation of complex I. Disorders in Fe/S cluster assembly are candidate causes for defects in respiratory complex assembly of unknown etiology.

1. INTRODUCTION

The respiratory chain of mammalian mitochondria is a multienzyme system comprising more than 80 polypeptide chains, assembled into five individual complexes at the mitochondrial inner membrane (Scheffler, 2007). Together with two electron carriers, coenzyme Q and cytochrome *c*, complexes I to IV constitute an electron transport chain, transferring electrons from NADH and FADH₂ to molecular oxygen. This electron flow results in a concomitant translocation of protons across the inner membrane into the intermembrane space, thereby establishing a proton motive force that finally drives complex V to generate ATP.

Electron transfer within the electron transport chain is conducted by low-molecular mass, serially arranged redox components, including flavins, Fe/S clusters, quinones, heme species, and copper centers. Consequently, the formation of each of the multi subunit respiratory complexes not only requires the concerted action of numerous protein assembly factors (Coenen *et al.*, 2001) but also depends on the functionality of many systems involved in cofactor biosynthesis and insertion. The most abundant redox centers within the electron transport chain are Fe/S clusters located in respiratory complexes I, II, and III. So far, three different biogenesis systems required for the *de novo* synthesis of Fe/S clusters and their incorporation into apoproteins have been identified in nongreen eukaryotes: the iron-sulfur cluster (ISC) assembly and the ISC export machineries located within mitochondria, and the cytosolic Fe/S protein assembly (CIA) apparatus [for a recent comprehensive review see Lill and Mühlenhoff (2008)].

Among these systems, the mitochondrial ISC assembly machinery holds a central role in that it is required for the biogenesis of all cellular Fe/S proteins. One of the key events catalyzed by this machinery is the abstraction of sulfur from cysteine by a heteromultimeric complex consisting of the pyridoxal 5'-phosphate (PLP)-dependent cysteine desulfurase Nfs1 and the eukaryote-specific component Isd11 (Adam *et al.*, 2006; Lill and Mühlhoff, 2008; Wiedemann *et al.*, 2006). During catalysis, the cysteine substrate is transiently bound to the PLP cofactor of Nfs1, and the substrate cysteine sulfur is then attacked by an active-site cysteinyl residue to produce a "persulfidic sulfur" (Zheng *et al.*, 1993, 1994). The activated sulfur is subsequently available for the formation of a transient Fe/S cluster on the scaffold protein Isu1. This step involves the assistance of frataxin as an iron donor and of the electron transfer chain NADH—ferredoxin reductase—ferredoxin possibly required for reduction of the sulfur to sulfide (Lill and Mühlhoff, 2008). Finally, the Isu1-bound Fe/S cluster is delivered to recipient apoproteins, a process aided by a dedicated Hsp70 chaperone system and the monothiol glutaredoxin Grx5 (Craig *et al.*, 2006; Herrero and de la Torre-Ruiz, 2007).

Fe/S protein assembly within mitochondria is connected to the respective extramitochondrial process by the ISC export machinery. The central component of this latter system is an ABC transporter of the mitochondrial inner membrane, termed Atm1 in yeast and ABCB7 in mammals, which appears to export a still unknown compound to the cytosol, where it is used by the CIA components for maturation of extramitochondrial Fe/S proteins (Cavadini *et al.*, 2007; Kispal *et al.*, 1997; Pondarré *et al.*, 2006). According to a current model, the cytosolic P-loop NTPases Nbp35 and Cfd1 (in mammals also known as Nubp1 and Nubp2, respectively) form a heterotetrameric complex and serve as a scaffold to assemble a transient Fe/S cluster (Lill and Mühlhoff, 2008; Netz *et al.*, 2007; Stehling *et al.*, 2008). The labile metallocluster is then transferred to target apoproteins, a process that has been shown in yeast to require the function of the iron-only hydrogenase-like protein Nar1 (in mammals known as IOP1) and the WD40 repeat protein Cia1 (termed Ciao1 in mammals) (Lill and Mühlhoff, 2008; Song and Lee, 2008).

Because key components of the mitochondrial ISC assembly machinery participate in the maturation of respiratory complexes I, II, and III by means of formation of their respective Fe/S clusters (Biederbick *et al.*, 2006; Fosset *et al.*, 2006; Lill and Mühlhoff, 2008; Puccio *et al.*, 2001; Rötig *et al.*, 1997; Song and Lee, 2008; Stehling *et al.*, 2004), these components can be referred to as general assembly factors for these enzymes. In addition, a specific assembly component termed Ind1 (iron-sulfur protein required for NADH-dehydrogenase) has been identified that assists in the formation of respiratory complex I (NADH: ubiquinone oxidoreductase, NADH reductase), the largest enzyme of the mammalian respiratory chain

(Bych *et al.*, 2008; Sheftel *et al.*, manuscript in preparation). Complex I consists of 45 subunits arranged in an L-shaped manner with one arm embedded into the inner membrane and the other one protruding into the mitochondrial matrix (Brandt, 2006; Vogel *et al.*, 2007). The latter arm harbors a noncovalently bound FMN cofactor involved in NADH oxidation and eight Fe/S clusters (Hinchliffe and Sazanov, 2005). Seven of them form an “electrical wire” to bridge the distance between the catalytically active FMN center to the ubiquinone reduction site (Brandt, 2006). Until now, only a few assembly factors primarily required for the maturation of complex I have been identified. Three of them, NDUFAF1, B17.2L, and Ecsit, are aiding the assembly of complex I subcomplexes (Vogel *et al.*, 2007). The fourth, the aforementioned Ind1, was recently identified in both the yeast *Yarrowia lipolytica* and in human cells as a mitochondrial homolog of the cytosolic CIA components Nbp35 and Cfd1 that facilitates the assembly of Fe/S clusters and subunits of complex I (Bych *et al.*, 2008; Sheftel *et al.*, manuscript in preparation).

In this chapter, we describe approaches to analyze the role of human Nfs1 (huNfs1) as a general ISC assembly component and of human Ind1 (huInd1) as a specific assembly factor for respiratory complex I. As basic strategies, we first deplete the assembly proteins of interest by RNAi technology in tissue culture cells and then analyze the loss-of-function phenotypes by Fe/S enzyme activity measurements, 1-D and 2-D gel electrophoresis, and the incorporation of ^{55}Fe into Fe/S proteins. The experimental techniques described in the following are generally applicable to study the function of Fe/S protein assembly factors, and, in particular, may be useful in future analyses of Fe/S cluster assembly into respiratory complexes.



2. DEPLETION OF Fe/S CLUSTER ASSEMBLY COMPONENTS BY RNA INTERFERENCE

2.1. Vector-based RNAi

RNA interference (RNAi) is a mechanism by which small interfering RNAs (siRNAs) drive an endogenous machinery to degrade distinct RNA target molecules (Wu and Belasco, 2008). Although duplex siRNAs can be directly administered to cell culture cells, we have good experience with the vector-based endogenous production of siRNAs for inducing the degradation of a specific mRNA (Sandy *et al.*, 2005). Usually, we use the pSUPER vector developed by Brummelkamp *et al.* (2002) or one of its commercially available derivatives (OligoEngine, Seattle, WA, USA). The vector contains a polymerase-III H1-RNA gene promoter that drives the expression of so-called short hairpin RNAs (shRNA) that are intracellularly processed to siRNA duplicates of 19 nucleotides in length.

2.2. siRNA design

Because only guidelines but no unequivocal rules for the selection of appropriate siRNA sequences exist (Birmingham *et al.*, 2007), we usually test three different mRNA target sites and choose the ones with the strongest effect on the intended protein. Tools for the design of siRNAs are available at numerous websites (a repertory is provided by Pei and Tuschl, 2006). Alternately, the choice of useful siRNAs may be facilitated by testing commercially available sets of siRNAs that are selected by computational methods performed by the manufacturers. In the case of huNfs1 and huInd1, we finally opted for the 19mer gene-specific targeting sequences GCACCATTATCCCGGCTGT (positions 1041 to 1059 of the huNfs1 coding region) (Biederbick *et al.*, 2006) and GCAGAAACCGA-TAGAAGGT (positions 177 to 195 of the huInd1 coding region) (Sheftel *et al.*, manuscript in preparation). On the basis of these sequences, 64mer oligonucleotides were synthesized (Fig. 12.1A) consisting of a *Bgl*II restriction site-compatible nucleotide quadruplet, a cytosine triplet, the mRNA target sequence, a nonameric spacer encoding the shRNA hairpin (TTCAAGAGA), the mRNA target sequence in its antisense orientation, a thymidine quintuplet to terminate shRNA expression, and a terminal GGAAA sequence (Brummelkamp *et al.*, 2002). Corresponding complementary oligonucleotides are designed to carry a *Hind*III-compatible nucleotide quadruplet at their 5' end but to lack the *Bgl*II-compatible sequence at the 3' end. After annealing and phosphorylation, the resulting oligomeric DNA duplexes are cloned into the pSUPER vector by means of its *Bgl*II/*Hind*III restriction sites according to standard procedures, yielding the RNAi vectors huNFS1-R3 and siIND1, respectively.

2.3. Electroporation-based transfections

Because HeLa cells (human cervix carcinoma) are easy to handle and transfect, we routinely use this model system to study the maturation of respiratory chain complexes (Biederbick *et al.*, 2006; Sheftel *et al.*, manuscript in preparation; Stehling *et al.*, 2004). To introduce plasmids and/or siRNA duplexes, cells are transfected by electroporation. After harvesting by trypsinization and washing in transfection buffer (21 mM HEPES, 137 mM NaCl, 5 mM KCl, 0.7 mM Na₂HPO₄, and 6 mM dextrose, pH 7.2) (Chu *et al.*, 1987), typically approximately 4×10^6 cells are resuspended in 525 μ l transfection buffer and supplemented with 25 μ g of the required plasmids or with 15 μ g of the respective siRNA duplexes. The deployment of up to twice as many cells is possible but may affect transfection efficiency. Cells are transferred into a 4-mm-gap electroporation cuvette and immediately transfected to prevent sedimentation within the cuvette. Electroporation is carried out at room temperature with an EASYJect+ device

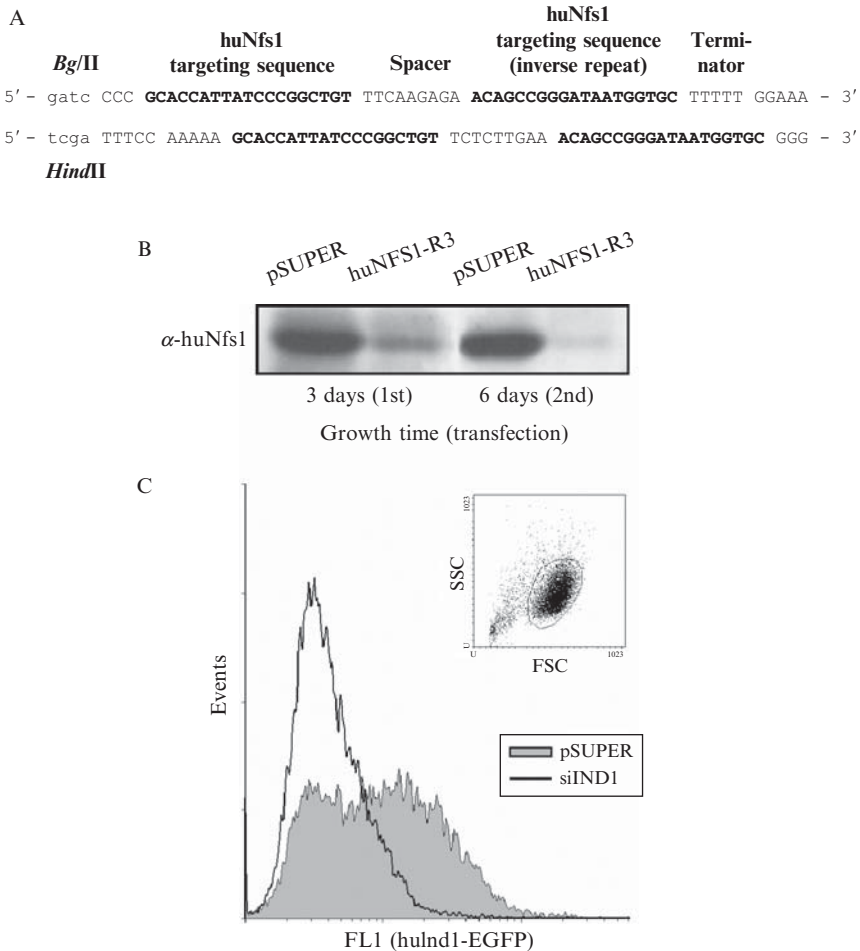


Figure 12.1 RNAi-mediated depletion of huNfs1 and huInd1. (A) Sequences of a 64mer oligonucleotide hairpin insert (top) and of its complementary strand (bottom) encoding a shRNA species that is directed against *huNFS1* mRNA. (B) HeLa cells were transfected twice by electroporation in 3-day intervals with either the empty pSUPER vector or the pSUPER-derived vector huNFS1-R3 containing the 64mer oligonucleotide hairpin insert of part (A). Cell lysates obtained 3 days after each round of transfection were immunoblotted and stained for huNfs1. (C) HeLa cells were transfected by electroporation with a vector encoding a huInd1-EGFP fusion protein either in combination with the empty pSUPER vector or with the huInd1 mRNA-directed siRNA vector, designated siIND1 (20 μ g and 15 μ g, respectively). Three days later, EGFP-fluorescence was determined by flow cytometry (fluorescence channel 1, FL1) and served as a measure for the efficiency of siIND1 to deplete the mRNA of the tagged huInd1 version. The insert shows the physical parameters of huInd1-EGFP-expressing cells and the region used for gating. FSC, Forward scatter; SSC, side scatter.

with settings of 250 V and 1500 μF , resulting in a pulse time of approximately 30 msec. Considerably longer pulse times should be avoided, because they will lead to massive cell damage, whereas shorter pulses will decrease the transfection efficiency. Immediately after electroporation (essentially within 30 sec, according to the manufacturer's recommendations), cells are transferred to culture medium supplemented with 20% conditioned HeLa medium (HeLa tissue culture supernatant) and grown on an area of 75 cm^2 . The addition of conditioned medium is strongly suggested, because it substantially improves recovery and yield of transfected cells (unpublished observations).

Transfection of the huNFS1-R3 or siIND1 RNAi vector will decrease the target protein levels nearly to the detection limit as early as 3 to 4 days after electroporation (Biederbick *et al.*, 2006; Sheftel *et al.*, manuscript in preparation). Only beginning at this point, can the maturation of Fe/S subunits of respiratory complexes be assumed to be affected. Hence, the occurrence of conspicuous cellular phenotypes requires at least another 3 or 4 days. However, because of the transient character of the transfection, vector-mediated RNAi effects will disappear over time (Stehling *et al.*, 2004). To prolong the time period of huNfs1 or huInd1 depletion, HeLa cells have to be retransfected, under conditions identical to the first electroporation. Principally, these retransfections can be carried out every third to fourth day as long as it is necessary. Time intervals shorter than 3 or longer than 4 days are not recommended. On the one hand, cells require time to recover from the electroporation procedure, and on the other hand, huNfs1 and huInd1 protein levels will start to recuperate (unpublished observations).

2.4. Assessing the efficiency of the RNAi treatment

Electroporation is an effective but invasive method to transfect cells (Meldrum *et al.*, 1999; Stehling *et al.*, 2004). One may expect the loss of one fourth to up to one half of the deployed cells. Transfection efficiency can be assessed by inclusion of 5 to 10 μg of an EGFP-encoding reporter vector in the electroporation mixture. Analysis of cell-associated fluorescence 3 to 4 days after the first transfection by flow cytometry usually results in more than 80% GFP-positive cells. Retransfection may increase the proportion of transfected cells to more than 90%, leading to the rapid development of a nearly homogeneous cell population without any need for selection or lineage generation. Consequently, changes in composition and activity of the respiratory chain can be monitored rather early after the depletion of assembly factors, as documented for huNfs1 or huInd1 (Biederbick *et al.*, 2006; Sheftel *et al.*, manuscript in preparation).

Successful and thorough depletion of target proteins is a prerequisite for analysis of RNAi-mediated loss-of-function phenotypes. Although the

determination of mRNA levels (e.g., by Northern blotting or quantitative PCR) encoding the intended target proteins is a useful indicator for the action of siRNAs, we prefer to directly assess the protein levels of the investigated assembly factors (Biederbick *et al.*, 2006; Sheftel *et al.*, manuscript in preparation). First, only the depletion of the proteins under study most reliably reflects the phenotypical consequences. Second, stability and turnover of the intended proteins are both independent of the RNAi efficiency. For example, huNfs1 and huInd1 levels are analyzed by reducing SDS-PAGE followed by immunoblotting and compared with the amounts of endogenous actin or tubulin. Although after the first round of transfection the levels of RNAi target proteins are usually still above the detection limit, they frequently drop below after retransfection (Fig. 12.1B). When no specific antibodies are available, the efficiency of siRNAs to deplete the intended proteins may be assessed by vector-based coexpression of an epitope-tagged version of the respective target protein. Depending on the expression levels, translation of the fusion proteins may not be completely abrogated by RNAi but will be lowest in case of the most efficient siRNA species (Fig. 12.1C).

2.5. Assessing the specificity of the RNAi treatment

Although siRNAs are designed to be directed solely to one distinct target, usually an mRNA, they may nonspecifically affect unintended targets, so-called off-targets, in an unpredictable manner (Birmingham *et al.*, 2006; Cullen, 2006; Jackson *et al.*, 2006b). Consequently, a strong cellular phenotype caused by an allegedly efficient siRNA is not necessarily a specific one related to the depletion of the intended target as found for an siRNA directed against the mRNA of the cytosolic huInd1 homolog huNbp35 (Stehling *et al.*, 2008). Because intrusion into the respiratory chain by RNAi will affect multiple cellular pathways, global gene expression studies are neither suitable nor feasible to discriminate between specific and nonspecific RNAi effects. Instead, two different strategies have been developed to minimize the risk of off-target effects (Chatterjee-Kishore and Miller, 2005; Cullen, 2006). One strategy suggests the application of a pool of multiple, often chemically modified, siRNA duplexes (Jackson *et al.*, 2006a) to minimize the contribution of one individual siRNA species to the overall RNAi-induced cellular phenotype. However, because the siRNA duplexes are frequently not individually tested, the specificity of the total pool can be estimated only by statistical considerations but evades unequivocal practical evaluation. Consequently, this strategy is only recommendable when the following second approach is difficult to apply.

Our preferred strategy is to verify the specificity of individual siRNA duplexes by complementation of the RNAi-mediated cellular phenotypes on the basis of the expression of RNAi-resistant versions of target proteins.

For instance, the consequences of huNFS1-R3-mediated huNfs1 deficiency can be specifically remedied by coexpression of murine Nfs1 (muNfs1) (Biederbick *et al.*, 2006). Both the mRNA and protein sequences of muNfs1 are nearly identical to huNfs1. However, at the siRNA target site, *muNFS1* mRNA differs in four nucleotide residues from the *huNFS1* mRNA (Fig. 12.2A). These four mismatches are sufficient to prevent *muNFS1* mRNA from RNAi-mediated degradation and to allow the heterologous, vector-based expression of muNfs1. Because cellular proteins, especially assembly factors, are part of a coordinated proteinaceous network, expression levels have to be empirically optimized to achieve best complementation. Usually, we titrate the amount of the complementing vector to modify cellular expression levels. As a rule, we apply 2.5, 7.5, and 22.5 μg of the complementing vector to the transfection mixture and choose the amount of DNA that complements best. On the basis of these results, a second round of titration with closer increments might sometimes be useful to further narrow down the optimal amount of DNA.

In an alternate approach, the RNAi-mediated huInd1 deficiency was complemented by vector-based expression of a mutated huInd1 version (smIND1) whose mRNA contained seven silent mutations within the siIND1 target site (Sheftel *et al.*, manuscript in preparation) (Fig. 12.2B). As few as four point mutations may suffice to confer resistance against RNAi as found for *muNFS1* mRNA. Although mismatches are able to prevent siRNA-mediated cleavage of mRNA, they may instead lead to translational stalling (Doench *et al.*, 2003; Saxena *et al.*, 2003; Zeng *et al.*, 2003). Thus, the more silent mutations are introduced into the siRNA target site, the less likely RNAi-mediated gene silencing becomes. A versatile PCR-based method to introduce a whole array of closeby

A					
muNFS1	:	GGGACCCGAA	GCAGCACTAC	CCTGGCTGTA	TCAACCTCTC
huNFS1	:	GGGACCCTAA	GCACCATTAT	CCC GGCTGTA	TCAACCTCTC
huNFS1-R3	:	-----	GCACCATTAT	CCC GGCTGT-	-----
			1041	1059	
B					
smIND1	:	GACTTCCAAA	ACA AAAGCCA	ATTGAGGGAG	TTAAACAAGT
huIND1	:	GACTTCCAAA	GCAGAAACCG	ATAGAAGGTG	TTAAACAAGT
siIND1	:	-----	GCAGAAACCG	ATAGAAGGT-	-----
			177	195	

Figure 12.2 Complementation of RNAi-mediated huNfs1 and huInd1 depletion. (A) Partial nucleotide sequence alignment of muNFS1, huNFS1, and the huNFS1-directed siRNA sequence that is part of RNAi vector huNFS1-R3 (cf. Fig. 12.1A and 12.1B). Mismatches in muNFS1 are underlined in bold. (B) Partial nucleotide sequence alignment of silently mutated huIND1 (smIND1), huIND1, and of the huIND1-directed siIND1. Mismatches in smIND1 are underlined in bold. The numbers indicate the nucleotide positions of the mRNA sequence starting at the AUG start codon.

mutations at the same time into a vector has been developed by [Zheng *et al.* \(2004\)](#). Once the mutations have been established, optimal complementation has to be determined by appropriate titration of smIND1 expression levels (see earlier).

3. ANALYSIS OF RESPIRATORY COMPLEX ASSEMBLY

Depletion of huNfs1 or huInd1 has profound effects on mitochondrial electron transport complexes ([Biederbick *et al.*, 2006](#); [Fosset *et al.*, 2006](#); [Sheffel *et al.*, manuscript in preparation](#)). A multitude of assays has been established to analyze the activity of the respiratory chain as a whole or of its individual complexes. In the following sections we will mainly focus on assays that we have adapted to directly assess the presence of iron-containing cofactors including Fe/S clusters in individual respiratory chain complexes or to determine changes in the function of respiratory complexes at high performance with a microtiter plate reader device.

3.1. Assessing the incorporation of iron-containing cofactors into respiratory complexes

Proper maturation of respiratory complexes I to IV includes the appropriate incorporation of the various cofactors. The presence of iron, in the form of heme or Fe/S cluster cofactors, within the individual respiratory complexes can be directly assessed on incorporation of radioactive iron (^{55}Fe) followed by blue-native polyacrylamide gel electrophoresis (BN-PAGE) ([Schägger, 2003](#)) and autoradiography. Because of their high Fe/S cluster content, respiratory complexes I and II will be radiolabeled at high specificity. Cells lacking a general ISC assembly factor like Nfs1 will contain less radioactive iron in both enzymes, whereas cells lacking the specific assembly factor Ind1 will incorporate less ^{55}Fe only in respiratory complex I.

The principal route by which mammalian cells take up iron is by receptor-mediated endocytosis of transferrin (Tf), a soluble protein containing two binding sites for ferric iron ([Richardson and Ponka, 1997](#)). To provide HeLa cells the radioactive isotope ^{55}Fe in a physiologic manner it has to be coupled to transferrin basically as described by [Ponka and Schulman \(1985\)](#).

3.1.1. Preparation and application of ^{55}Fe -loaded transferrin

Dilute $^{55}\text{FeCl}_3$ (approximately 250 nmol $^{55}\text{Fe}^{3+}$, equivalent to an activity of 1 mCi) in 1 ml of 0.1 N HCl and add a 50% (w/v) sodium citrate solution in a 100-fold molar excess. The color of the mixture will turn from clear to pale yellow. After an incubation of at least 3 h at room temperature add to approximately 60 μM apotransferrin dissolved in 0.6 M sodium hydrogen

carbonate (bicarbonate, NaHCO_3) to a final volume of 2 ml. The color of the mixture will now turn from yellow to salmon. The final molar ratio of transferrin to $^{55}\text{Fe}^{3+}$ should be 1:2. Ensure that carbonate is in high excess to hydrogen chloride, because transferrin loading requires bicarbonate anions (Richardson and Ponka, 1997). Incubate at room temperature overnight. ^{55}Fe -loaded transferrin is separated from nonbound iron by desalting with Hanks balanced salt solution (HBSS) on a PD-10 gel filtration column. The elution process can be nicely followed because of the light brownish color of iron-loaded transferrin. Dilute the eluate as desired, add 1% BSA, sterile filter and store at 4° until use.

For loading with ^{55}Fe , cells are seeded at low densities in complete growth medium [e. g., after electroporation (see earlier)] and cultured for 3 or 4 days in the presence of $1 \mu\text{M}$ ^{55}Fe -Tf. Because transferrin receptor (TfR) expression, and consequently iron uptake, is cell density-dependent (Ponka and Lok, 1999; Stehling *et al.*, 2008), the comparison of different samples requires identical growth conditions. The higher the degree of confluence, the lower is the relevance of density for TfR expression. Harvesting of cells by trypsinization removes surface-bound transferrin and allows the determination of total cellular ^{55}Fe uptake by scintillation counting as described for yeast model systems (Stehling *et al.*, 2007).

3.1.2. Preparation of membranes containing respiratory chain complexes

Membrane preparations of ^{55}Fe -loaded HeLa cells are used to visualize the incorporation of radioactive iron into respiratory chain complexes by BN-PAGE (Schägger, 2003). To prepare membrane samples, suspend pelleted HeLa cells at an amount of 10 mg wet weight per 100 μl in BN Mitobuffer (250 mM sucrose in 20 mM sodium phosphate, pH 7.0) and homogenize cells with a tight-fitting, motorized glass/Teflon homogenizer by 40 passes at a rotation of 2,000 rpm. Cell opening may be monitored by trypan blue exclusion. Rinse the pestle with up to 1 ml BN Mitobuffer and determine the total sample volume. Transfer the lysate in aliquots corresponding to 20 mg HeLa cell wet weight into 1.50-ml microfuge tubes and centrifuge at $13,000g$ for 10 min at 4° . After discarding the supernatant, pellets may be used immediately or quick-frozen in liquid nitrogen and stored at -80° until use.

For loading on a BN gel solubilize membrane preparations by suspending each aliquot in 35 μl of BN gel solubilization buffer (50 mM NaCl, 50 mM imidazole, 2 mM aminocaproic acid, 1 mM EDTA, pH 7.0). Suspending may require mechanical dispersion (e.g., by a spatula). Add 10 μl of a 20% (w/v) digitonin solution (dissolved in water at 95°) and mix immediately by vortexing or pipetting. Clear suspension by centrifuging at $100,000g$ for 15 min at 4° . Determine protein content of the clear supernatant to ensure equal loading of the gel, add 10 μl of a 5% (w/v) Coomassie blue G250 solution (weighed in

500 mM aminocaproic acid), vortex immediately, and finally add 5% (w/v) glycerol. Samples with equal protein content ($\sim 300 \mu\text{g}$) are loaded on a BN gel and electrophoresed. Inclusion of a respiratory complex-rich reference sample into the same gel allows monitoring of separation and migration of mammalian respiratory complexes (Fig. 12.3A) to verify the positions of the respective HeLa cell complexes. The reference sample may be prepared from bovine heart mitochondria (Schägger, 2003) and solubilized in digitonin/Coomassie as described previously for the HeLa cell lysates.

3.1.3. Blue-native PAGE and autoradiography

Cast a 1.5-mm-thick BN gradient gel from 4 to 13% with a gradient mixer and a peristaltic pump. The 4% BN gel mix (final volume approximately 35 ml) consists of 2.8 ml of a 49.5% acrylamide/3% bis-acrylamide solution

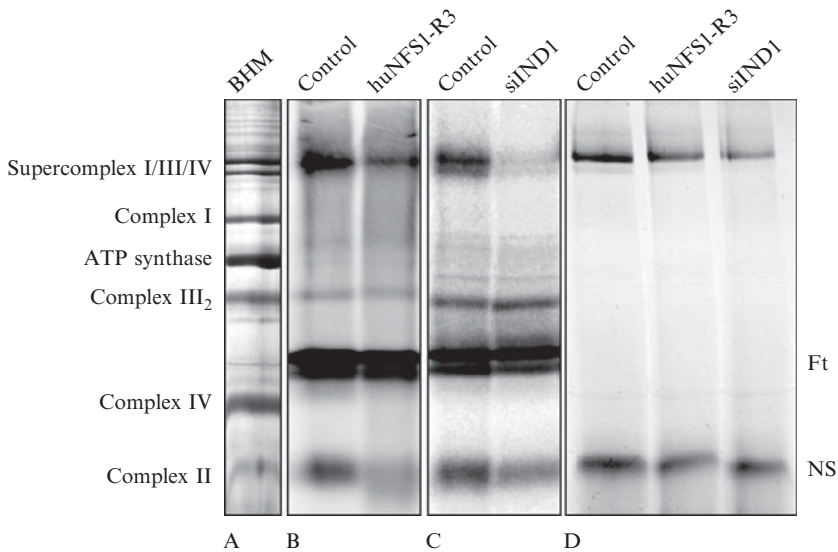


Figure 12.3 Effects of huNfs1 or huInd1 depletion on respiratory complexes. (A) Bovine heart mitochondria (BHM), solubilized in digitonin, resolved by BN-PAGE, and stained with Coomassie blue G250. Note that supercomplexes containing complex I, complex III dimer (III_2), and varying amounts of complex IV are present when digitonin is used. (B, C) HeLa cells were labeled with ^{55}Fe -transferrin, fractionated, and mitochondrial membrane-containing samples were prepared. On BN-PAGE, respiratory complex I is only detectable as part of a supercomplex and its iron content decreases on application of the RNAi vectors huNfs1-R3 (B) and siIND1 (C). Complex II associated iron is only barely detectable in the huNfs1-deficient cells (B). The most prominent band is that of ferritin [Ft], which partially fractionates into the crude mitochondrial preparation. (D) In-gel complex I activity assay. Complex I activity decreases on huNfs1 or huInd1 depletion by RNAi. Again, complex I is only apparent as part of a supercomplex. A nonspecific band (NS) is apparent in the lower part of the gel.

(AA solution), 11.7 ml of a 3× BN gel buffer (75 mM imidazole in 1.5 M aminocaproic acid), 20.5 ml water, 175 μ l of a 10% (w/v) ammoniumperoxodisulfate solution (APS), and 30 μ l N,N,N',N'-tetramethylethan-1,2-diamine (TEMED). The 13% BN gel mix (final volume approximately 35 ml) is made up by 9.2 ml AA solution, 11.7 ml 3× BN gel buffer, 5.6 ml glycerol, 8.5 ml water, 119 μ l APS, and 11.9 μ l TEMED. With the aid of a long needle inserted to the bottom of the cast, we pour our gels from the bottom up, the lower percentage acrylamide solution entering the cast first. Adding 1 ml of water to the cast, before pouring the gel, forms a level top edge to the separating gel. Adjust the flow rate to an intermediate speed (4 ml/min) to allow for good gradient formation and to avoid premature polymerization. An ambient temperature of 4° will facilitate casting. Polymerization is promoted by carefully transferring poured gels to room temperature. When the separating gel has congealed, add a stacking gel (final volume approximately 29 ml) consisting of 1.75 ml AA solution, 8.3 ml 3× BN gel buffer, 18.45 ml water, 200 μ l APS, and 20 μ l TEMED. Gel run is initially performed with Deep Blue Cathode Buffer (50 mM Tricine, 7.5 mM imidazole, 0.02% Coomassie G250, pH 7.0) in the top reservoir and 25 mM imidazole as anode buffer (bottom reservoir) at 100 V and 20 mA in the cold for 15 to 25 min to allow the protein to run into the gel. The voltage is then turned up to 500 V. Once the leading edge of the samples has migrated one-third the length of the gel, the Deep Blue Cathode Buffer is exchanged by B/10 Cathode Buffer (50 mM Tricine, 7.5 mM imidazole, 0.002% Coomassie G250, pH 7.0) to diminish the amount of Coomassie within the gel. After the run is completed, bovine heart mitochondrial complexes I to V of the reference sample are visible without further staining (Fig. 12.3A); however, Coomassie staining may be necessary to visualize all of the respiratory complexes. This can be achieved by shaking the respective gel strip for 1 to 2 h in 0.025% Coomassie blue G250 dissolved in 10% acetic acid and then washing the gel in 10% acetic acid for a few hours. The remaining gel containing the HeLa cell samples is dried either by use of a gel dryer or gel drying film. Iron-containing complexes are visualized by exposure to a phosphor storage screen and phosphorimaging (Fig. 12.3B,C), or by autoradiography. In the latter case, appropriate signal enhancing systems and a longer exposure time are required.

3.2. Assessing the subunit composition of respiratory complexes by two-dimensional BN-PAGE

Maturation of respiratory complexes occurs in multiple steps by which individual subunits or preformed subcomplexes are successively assembled to build the functional enzyme (Coenen *et al.*, 2001; Fernandez-Vizarra *et al.*, 2007; Pickova *et al.*, 2005; Vogel *et al.*, 2007). In the absence of general assembly factors like Nfs1 or specific assembly factors like Ind1,

Fe/S subunits are lacking their cofactors and frequently become unstable. As a consequence, assembly of the respective complexes is impaired, and protein levels of individual subunits may decrease by proteolysis (Bych *et al.*, 2008; Gerbeth *et al.*, manuscript in preparation; Sheftel *et al.*, manuscript in preparation). Subunit composition of respiratory complexes or preassembled subcomplexes can be assessed by 2-D BN-PAGE (Schägger, 2003). Respiratory complexes are first separated by BN-PAGE, and then individual complexes and subcomplexes are deconstructed into their individual subunits by SDS-PAGE in a second dimension.

To run the second dimension, soak 1.5-mm-thick BN gel strips containing mitochondrial membrane preparations resolved by BN-PAGE (see section 3.1.) for 15 to 30 min in 1% (w/v) sodium dodecylsulfate (SDS) at room temperature. Take care that the strips are completely covered. Place each strip horizontally on a gel plate containing the “ears” and squeeze it by assembly of the second plate with 0.7- to 1.0-mm spacers. Prepare a 10% 2D SDS-gel solution consisting of 13.3 ml 2-D SDS-gel buffer (0.3% w/v SDS in 3 M TRIS-HCl, pH 8.45), 8.13 ml AA solution (see section 3.1.3), 4 ml glycerol, 14.4 ml water, 200 μ l APS, and 10 μ l TEMED. Pour the 2-D SDS-gel solution nearly up to the gel strip and overlay with water. After polymerization, push down the gel strip to improve contact to the SDS-gel, remove the remaining water, and pour a 10% BN gel solution (1.04 ml AA solution, 1.67 ml 3 \times BN gel buffer, 2.26 ml water, 28 μ l APS, 2.8 μ l TEMED; c. f. section 3.1.3.) along sides but not on top of the gel strip. Run the gel at room temperature for 4 to 5 h at 200 V (or 50 V overnight, not exceeding 50 mA in each case) with 0.1 M TRIS, 0.1 M Tricine, and 0.1% w/v SDS as 2-D cathode buffer and 0.2 M TRIS-HCl (pH 8.9) as anode buffer. Resolved proteins can be detected within the gel by conventional silver staining (Sheftel *et al.*, manuscript in preparation). Alternately, individual proteins may be identified by immunoblotting subsequent to the gel run.

4. ANALYSIS OF RESPIRATORY COMPLEX FUNCTION

4.1. Determination of lactate formation

Respiratory chain deficiencies are often associated with excess lactate formation. NADH generated by glycolysis and the citric acid cycle cannot be oxidized by complex I, either because of a direct dysfunction of this enzyme (Triepeles *et al.*, 2001) or because of an impaired electron drain caused by dysfunctions downstream of the electron transport chain (Munnich and Rustin, 2001). Instead, NADH is used by lactate dehydrogenase to convert pyruvate to lactate. Increased lactate levels in the culture medium of HeLa cells are thus an indication for impaired respiratory complex activity on

huNfs1 and huInd1 deficiency. We use multiwell plates to facilitate the biochemical determination of lactate levels in the respective tissue culture supernatants. The assay is based on the reduction of NAD^+ because of the action of lactate dehydrogenase that converts lactate to pyruvate (Gawehn, 1988). To shift the equilibrium of the reaction toward the conversion of lactate, D-glutamate-pyruvate transaminase and D-glutamate are added to transfer the amino group to pyruvate yielding D-alanine and 2-oxoglutarate.

To determine lactate concentrations, dilute conditioned tissue culture supernatants 10-fold in water. Prepare aqueous lactate reference solutions containing 0.1 to 1.5 mM lactate and 10% nonconditioned culture medium. If the tissue culture cells produce large amounts of lactate, dilutions of the media have to be increased respectively. Load 11.2 μl of each sample as well as a solvent only blank of 10-fold diluted nonconditioned culture medium into wells of a 96-well UV/Vis plate. Immediately before use, make up the reaction buffer (pH 10.0) containing 250 mM glycylglycine, 500 mM glutamate, 4.8 mM NAD^+ , and 40 U/ml D-glutamate-pyruvate transaminase (GPT). Pipette 238 μl of this reaction buffer to each sample and begin measuring absorption at $\lambda = 340$ nm. Allow the reaction to proceed for approximately 5 min until the signal has stabilized. Add 3 μl L-lactate dehydrogenase solution (LDH, 16.5 U) to each well and resume data acquisition for approximately 40 min. When other sample sizes are used, volumes of buffers and reagents have to be adjusted accordingly. The increase in the optical density at $\lambda = 340$ nm is calculated by subtracting the absorbance before the addition of LDH from the absorbance plateau reached at the end of the assay. The absolute amount of lactate in each tissue culture sample can be deduced from the absorbance changes occurring in the lactate reference samples.

4.2. Determination of complex I activity by in-gel activity staining

Although increased lactate formation is a general indication for impaired respiratory chain activity upon huNfs1 and huInd1 depletion, the direct determination of the activities of individual respiratory complexes is providing more quantitative information about the functional deficits. We frequently apply 1-dimensional BN-PAGE to individually determine the activity of complex I (Zerbetto *et al.*, 1997). The assay is based on the NADH-dependent reduction of *p*-nitrotetrazolium blue chloride (NBT), which is leading to a discoloration and in-gel precipitation of the dye.

For activity staining, apply an adequate volume of 3 mM *p*-nitrotetrazolium blue chloride dissolved in 5 mM TRIS/HCl (pH 7.4) to sufficiently cover the gel. Next, add NADH to a final concentration of 120 μM and immediately immerse the gel in the reaction solution. Gently shake at room temperature for 1 to 30 min, monitoring the gel for the formation of violet

bands near the top of the gel (Fig. 12.3D; complex I monomer is approximately 1 MDa, whereas supercomplexes can be approximately twice this size). When an appropriate time has been reached, decant the liquid and fix the gel by adding 10% (v/v) acetic acid in 50% (v/v) methanol and shaking for 1 to 2 h. If necessary, exchange the fixing solution as desired to remove the residual blue dye from the gel, and then place the gel in water. Scan the gel for quantification before drying.

4.3. Determination of complex I activity by spectrophotometry

Despite that enzymatic in-gel activity can be densitometrically evaluated, spectrophotometry allows a more quantitative determination of complex I activity. Examining the oxidation of deaminodiphosphopyridine nucleotide (dNADH), a NADH derivative, provides a direct evaluation of the enzymatic activity of this respiratory complex (Grgic *et al.*, 2004). In reference samples, nonspecific dNADH oxidation can be monitored by inhibition of complex I by adding 2-decyl-4-quinazolinyl amine (DQA).

Prepare complex I reaction buffer (1.5 ml is required per sample) by adding 2 mM KCN, 60 μ M decylubiquinone (DBQ), and 100 μ M dNADH to an appropriate volume of complex I stock buffer consisting of 20 mM sodium MOPS (pH 7.4), 50 mM NaCl, and 2.5 mg/ml BSA, and gently invert several times to mix. After adding the DBQ to the reaction solution, it becomes sensitive to air and must not be vigorously shaken. We find that measurements are more stable when the reaction buffer is allowed to rest at room temperature for approximately 20 min subsequent to mixing. Split the reaction buffer in half, and to one half add the complex I inhibitor DQA to yield 27 μ M. Pipette each half of the reaction buffer (750 μ l; \pm DQA) into one of two UV/Vis cuvettes. To each cuvette, add 30 to 50 μ g protein from the mitochondrial membrane preparations (see section 3.1.2.) and mix samples with a plastic stirring spatula. Changes in absorbance are measured for several minutes. Complex I activity is determined by the rate of dNADH oxidation, which results from the difference in absorption at 340 nm between the two samples that lack or contain DQA. The molar extinction coefficient for dNADH at $\lambda = 340$ nm is similar to NADH and amounts to $\epsilon_{340 \text{ nm}} = 6200 \text{ M}^{-1} \times \text{cm}^{-1}$.

4.4. Analysis of enzyme activities in multiwell plates

The continuous spectrophotometric measurement of enzyme activities in individual cuvettes is time-consuming. Because the analysis of diverse enzyme activities in differentially treated cells by replicative samples results in an exponential increase in sample number, we perform parallel enzyme assays in multiwell plates with a Tecan infinite M200 device (Tecan,

Switzerland) in its kinetics mode. The plates are placed on a bottom-cooled dry surface and samples are loaded as required. The amount of protein deployed has to be adjusted so that low enzyme activities can be followed for at least 10 to 15 min. Sample volumes should not exceed 10% of the final reaction volumes in one well. Buffer stocks can be prepared in advance, but enzyme substrates should be added fresh. Right before analysis, the multiwell plate is placed at room temperature and equal volumes of pre-warmed reaction buffer are poured quickly into the wells with a repeat-volume pipettor. The final volume within a well does not require further adjustment, because the dilution of the reaction buffer by the protein sample is not influencing enzyme-related changes in total optical density. Although slightly increased final volume increases the light path, the simultaneously diminished concentration of the respective absorbing substance is compensating the effects on extinction. Care has to be taken not to produce air bubbles; otherwise, they have to be destroyed by tapping with a sharp needle. Immediately after addition of reaction buffer, the multiwell plate is placed into the reader device and orbitally shaken for 5 sec with an amplitude of 2.5 mm. Changes in optical densities are recorded at an ambient temperature of 37°.

4.4.1. Determination of complex II (SDH) activity

Mammalian respiratory complex II (succinate: ubiquinone oxidoreductase) is an interface between the citric acid cycle and the respiratory chain (Cecchini, 2003). It converts succinate to fumarate, thereby feeding electrons to the quinone pool of the electron transport chain. Complex II consists of four subunits, with two of them, SdhA and SdhB, exposed to the mitochondrial matrix, whereas subunits SdhC and SdhD serve as membrane anchors. Because of its enzymatic activity, complex II is also referred to as succinate dehydrogenase (SDH). Three Fe/S clusters are located in SdhB, channeling electrons from FAD in SdhA to redox centers in the membrane domain. The consequence especially of huNfs1 deficiency on SDH activity can easily be tested in total HeLa cell samples with a multiwell plate-based, enzymatic assay (Hatefi and Stiggall, 1978). The method is based on the oxidation of succinate to fumarate with concomitant reduction of the blue dye 2,6-dichloro-*N*-(4-hydroxyphenyl)-1,4-benzoquinoneimine (DCPIP), rendering it colorless, by use of decylubiquinone as the electron carrier.

To determine SDH activity, load equal amounts of HeLa cell samples corresponding to 4 to 12 μg of total protein in each of two wells of a 48-well plate. Prepare SDH reaction buffer by adding 1 mM KCN, 60 μM DBQ, and 7,5 mM disodium succinate solution to a SDH stock buffer consisting of 50 mM TRIS/SO₄ (pH 7.4), 0.1 mM EDTA, 70 μM DCPIP, and 0.1% Triton X-100. Subsequently, dispense 750 μl of this SDH reaction buffer in one of the two sample wells. Because DBQ may transfer electrons derived from other sources than SDH, nonspecific DCPIP reduction can be

determined by specific inhibition of SDH with malonate. Thus, immediately add 12 mM disodium malonate solution to the remaining SDH reaction buffer, dispense 750 μl of this reference buffer into the remaining second sample well, and start measurement. When multiwell plates of other sizes are used, protein amounts and buffer volumes have to be adjusted accordingly. DCPIP reduction will proceed for 20 to 30 min. The molar extinction coefficient of DCPIP is $\epsilon_{600\text{ nm}} = 21,000\text{ M}^{-1} \times \text{cm}^{-1}$. SDH activity is determined by calculating the difference between total and nonspecific DCPIP bleaching.

4.4.2. Determination of complex IV (COX) activity

Respiratory complex IV (cytochrome *c* oxidase, COX) is the final member of the electron transport chain, transferring electrons from cytochrome *c* to molecular oxygen (Ludwig *et al.*, 2001). It consists of 13 subunits and contains two heme and two copper centers in its functional core that is formed by three mitochondria-encoded polypeptide chains. Because Fe/S clusters are absent, the enzyme is often used as internal reference for the analysis of mitochondrial Fe/S proteins. However, COX activity is not inevitably invariable but regulated by various physiologic factors such as the intramitochondrial ATP/ADP-ratio, cAMP and calcium-dependent phosphorylation and dephosphorylation, and subunit expression (Fontanesi *et al.*, 2008; Ludwig *et al.*, 2001). In HeLa cells, we observed a cell-density dependent increase in COX activity (unpublished). Moreover, depletion of general assembly factors for respiratory complexes like Nfs1, as well as other members of the ISC assembly machinery, impairs cellular iron homeostasis (Biederbick *et al.*, 2006; Rouault and Tong, 2008) with a potential impact on heme formation and COX activity. Thus, use of COX for standardizing activities of other mitochondrial enzymes is not unequivocal. In any case, we suggest determination of COX activity in cultured cells grown at several cell densities to obtain reference values. Measurements can be done with total HeLa cell lysates by examining COX-mediated oxidation of cytochrome *c* with a multiwell plate-based enzymatic assay (Birch-Machin and Turnbull, 2001; Trounce *et al.*, 1996).

4.4.2.1. Preparing reduced cytochrome *c* Before its use as COX substrate, cytochrome *c* (cyt-*c*) has to be reduced. Dissolve the oxidized protein at a concentration of 100 mg/ml in 30 mM potassium phosphate buffer (pH 7.2) and add an equal volume of 20 mM sodium dithionite. The color of the solution will change from a dark brownish red to a light red. Desalt the reduced cyt-*c* anaerobically by passage through a PD-10 column with 15 mM potassium phosphate buffer (pH 7.2). Reduction and concentration of the eluted protein can be determined spectrophotometrically. The molar extinction coefficient is $\epsilon_{550\text{ nm}} = 19,500\text{ M}^{-1} \times \text{cm}^{-1}$. Quick-freeze appropriate aliquots in liquid nitrogen and store at -80° until use.

4.4.2.2. Measuring COX activity Load HeLa cell samples corresponding to 0.5 to 2 μg of total protein in a 96-well plate. Immediately before use, add 20 μM reduced cyt-c to the COX stock buffer (15 mM potassium phosphate, 0.1% BSA, 0.5 mM dodecylmaltoside, pH 7.2) and dispense 250 μl of this COX assay buffer to each protein sample. Because cyt-c is rapidly oxidized in air, we usually load another three wells with COX assay buffer alone as an internal standard to determine nonspecific changes in cyt-c absorbance. Alternately, COX assay buffer containing 1 mM KCN may be dispensed to replicate samples of HeLa cells as a reference, but in our hands cyt-c is oxidized as fast as in the standard wells mentioned previously. Immediately place the multiwell plate into the reader device, because cyt-c oxidation will proceed only for 10 to 15 min. COX activity is determined by calculating the difference between total and nonspecific cyt-c oxidation. The molar extinction coefficient of reduced cyt-c is $\lambda_{550\text{ nm}} = 19,500\text{ M}^{-1} \times \text{cm}^{-1}$.

4.4.3. Determination of citrate synthase activity

Because of the potential variability of COX activity, we instead prefer citrate synthase (CS) as an alternative mitochondrial reference enzyme to scrutinize mitochondrial function. Although CS is not a direct member of the respiratory chain, it is indirectly linked by means of its participation in the citric acid cycle to produce the substrates for respiratory complexes I and II. CS is a homodimer, expediently not containing any cofactor, resides within the mitochondrial matrix, and catalyzes the condensation of acetyl-coenzyme A with oxaloacetate to form citrate (Wiegand and Remington, 1986). In our experience, CS activity did not significantly change by any manipulation we performed on mitochondria of HeLa cells. Enzymatic activity can easily be measured in total HeLa cell samples with a sensitive multiwell plate-based enzymatic assay according to a published procedure (Srere *et al.*, 1963). The method builds on the hydrolytic cleavage of 5,5'-dithiobis[2-nitrobenzoic acid] (DTNB, Ellman's reagent) to form 5-mercapto-2-nitrobenzoate by free sulfhydryl groups of coenzyme A that is liberated on the condensation of acetyl-CoA with oxaloacetate.

To determine CS activity, load equal amounts of HeLa cell samples (2 to 5 μg of total protein) in each of two wells of a 48-well plate. Prepare CS reference buffer by adding 175 μM acetyl-CoA to the CS stock buffer (50 mM TRIS/HCl, 100 mM NaCl, 0.5 mM DTNB, 0.1% Triton X-100, pH 8.0) and dispense 750 μl in one of the two wells to monitor nonspecific DTNB hydrolysis. Quickly add 1 mM sodium oxaloacetate to the reference buffer to obtain complete CS assay buffer, dispense 750 μl to the second HeLa cell sample, and start measurement. When multiwell plates of other sizes are used, protein amounts and buffer volumes have to be adjusted accordingly. DTNB hydrolysis may proceed for more than 30 min, depending on the protein amount applied. Take care to not load too much protein to avoid depletion of the substrates. The molar extinction

coefficient of the DTNB hydrolysis product 5-mercapto-2-nitrobenzoate is $\epsilon_{412 \text{ nm}} = 13,300 \text{ M}^{-1} \times \text{cm}^{-1}$. CS activity is determined from the difference between total and nonspecific DTNB hydrolysis.

5. CONCLUDING REMARKS

Maturation of respiratory chain complexes requires the concerted interaction of multitudinous assembly factors that either directly assist complex formation or act indirectly by means of their involvement in cofactor synthesis and/or insertion. The intricate dependence of the respiratory chain on Fe/S clusters makes complexes I, II, and III excellent targets for the molecular and functional analysis of Fe/S protein biogenesis. Thus, examination of the catalytic activities and the Fe/S status of individual respiratory complexes considerably contributes to our understanding of how Fe/S clusters are synthesized and inserted into apoproteins. Vice versa, studying Fe/S protein formation may facilitate the identification of new assembly factors, such as huInd1 for respiratory complex I. The experimental strategies and techniques described herein may help in future investigations to deepen our insights into both general mechanisms of the assembly of cellular Fe/S proteins and the specific maturation pathways of respiratory chain complexes.

ACKNOWLEDGMENTS

We acknowledge the generous gift of DQA by Dr. Hermann Schägger as well as his invaluable advice and the technical assistance of Christian Bach. We also thank Carolin Gerbeth for providing the huNfs1 immunoblot. A. D. S. is supported by fellowships from the Fonds de la Recherche en Santé Québec and the Alexander-von-Humboldt Foundation. R. L. acknowledges support from Deutsche Forschungsgemeinschaft (SFB 593 and TR1, Gottfried-Wilhelm Leibniz program, and GRK 1216), the German-Israeli Foundation GIF, Rhön Klinikum AG, von Behring-Röntgen Stiftung, and Fonds der chemischen Industrie.

REFERENCES

- Adam, A. C., Bornhove, C., Prokisch, H., Neupert, W., and Hell, K. (2006). The Nfs1 interacting protein Isd11 has an essential role in Fe/S cluster biogenesis in mitochondria. *EMBO J.* **25**, 174–183.
- Biederick, A., Stehling, O., Rösser, R., Niggemeyer, B., Nakai, Y., Elsässer, H. P., and Lill, R. (2006). Role of human mitochondrial Nfs1 in cytosolic iron-sulfur protein biogenesis and iron regulation. *Mol. Cell. Biol.* **26**, 5675–5687.
- Birch-Machin, M. A., and Turnbull, D. M. (2001). Assaying mitochondrial respiratory complex activity in mitochondria isolated from human cells and tissues. *Methods Cell Biol.* **65**, 97–117.

- Birmingham, A., Anderson, E., Sullivan, K., Reynolds, A., Boese, Q., Leake, D., Karpilow, J., and Khvorova, A. (2007). A protocol for designing siRNAs with high functionality and specificity. *Nat. Protoc.* **2**, 2068–2078.
- Birmingham, A., Anderson, E. M., Reynolds, A., Ilsley-Tyree, D., Leake, D., Fedorov, Y., Baskerville, S., Maksimova, E., Robinson, K., Karpilow, J., Marshall, W. S., and Khvorova, A. (2006). 3' UTR seed matches, but not overall identity, are associated with RNAi off-targets. *Nat. Methods* **3**, 199–204.
- Brandt, U. (2006). Energy converting NADH: Quinone oxidoreductase (complex I). *Annu. Rev. Biochem.* **75**, 69–92.
- Brummelkamp, T. R., Bernards, R., and Agami, R. (2002). A system for stable expression of short interfering RNAs in mammalian cells. *Science* **296**, 550–553.
- Bych, K., Kerscher, S., Netz, D. J., Pierik, A. J., Zwicker, K., Huynen, M. A., Lill, R., Brandt, U., and Balk, J. (2008). The iron-sulphur protein Ind1 is required for effective complex I assembly. *EMBO J.* **27**, 1736–1746.
- Cavadini, P., Biasiotto, G., Poli, M., Levi, S., Verardi, R., Zanella, I., Derosas, M., Ingrassia, R., Corrado, M., and Arosio, P. (2007). RNA silencing of the mitochondrial ABCB7 transporter in HeLa cells causes an iron-deficient phenotype with mitochondrial iron overload. *Blood* **109**, 3552–3559.
- Cecchini, G. (2003). Function and structure of complex II of the respiratory chain. *Annu. Rev. Biochem.* **72**, 77–109.
- Chatterjee-Kishore, M., and Miller, C. P. (2005). Exploring the sounds of silence: RNAi-mediated gene silencing for target identification and validation. *Drug Discov. Today* **10**, 1559–1565.
- Chu, G., Hayakawa, H., and Berg, P. (1987). Electroporation for the efficient transfection of mammalian cells with DNA. *Nucleic Acids Res.* **15**, 1311–1326.
- Coenen, M. J., van den Heuvel, L. P., and Smeitink, J. A. (2001). Mitochondrial oxidative phosphorylation system assembly in man: Recent achievements. *Curr. Opin. Neurol.* **14**, 777–781.
- Craig, E. A., Huang, P., Aron, R., and Andrew, A. (2006). The diverse roles of J-proteins, the obligate Hsp70 co-chaperone. *Rev. Physiol. Biochem. Pharmacol.* **156**, 1–21.
- Cullen, B. R. (2006). Enhancing and confirming the specificity of RNAi experiments. *Nat. Methods* **3**, 677–681.
- Doench, J. G., Petersen, C. P., and Sharp, P. A. (2003). siRNAs can function as miRNAs. *Genes Dev.* **17**, 438–442.
- Fernandez-Vizarra, E., Bugiani, M., Goffrini, P., Carrara, F., Farina, L., Procopio, E., Donati, A., Uziel, G., Ferrero, I., and Zeviani, M. (2007). Impaired complex III assembly associated with BCS1L gene mutations in isolated mitochondrial encephalopathy. *Hum. Mol. Genet.* **16**, 1241–1252.
- Fontanesi, F., Soto, I. C., and Barrientos, A. (2008). Cytochrome *c* oxidase biogenesis: New levels of regulation. *IUBMB Life* **60**, 557–568.
- Fosset, C., Chauveau, M. J., Guillon, B., Canal, F., Drapier, J. C., and Bouton, C. (2006). RNA silencing of mitochondrial m-Nfs1 reduces Fe-S enzyme activity both in mitochondria and cytosol of mammalian cells. *J. Biol. Chem.* **281**, 25398–25406.
- Gawehn, K. (1988). D-(–)-Lactate. In “Methods of Enzymatic Analysis” (H. U. Bergmeyer, ed.), Vol. VI, pp. 588–592. VCH Publishers, Cambridge.
- Grgic, L., Zwicker, K., Kashani-Poor, N., Kerscher, S., and Brandt, U. (2004). Functional significance of conserved histidines and arginines in the 49-kDa subunit of mitochondrial complex I. *J. Biol. Chem.* **279**, 21193–21199.
- Hatefi, Y., and Stiggall, D. L. (1978). Preparation and properties of succinate: Ubiquinone oxidoreductase (complex II). *Methods Enzymol.* **53**, 21–27.
- Herrero, E., and de la Torre-Ruiz, M. A. (2007). Monothiol glutaredoxins: A common domain for multiple functions. *Cell Mol. Life Sci.* **64**, 1518–1530.

- Hinchliffe, P., and Sazanov, L. A. (2005). Organization of iron-sulfur clusters in respiratory complex I. *Science* **309**, 771–774.
- Jackson, A. L., Burchard, J., Leake, D., Reynolds, A., Schelter, J., Guo, J., Johnson, J. M., Lim, L., Karpilow, J., Nichols, K., Marshall, W., Khvorova, A., *et al.* (2006a). Position-specific chemical modification of siRNAs reduces “off-target” transcript silencing. *Rna* **12**, 1197–1205.
- Jackson, A. L., Burchard, J., Schelter, J., Chau, B. N., Cleary, M., Lim, L., and Linsley, P. S. (2006b). Widespread siRNA “off-target” transcript silencing mediated by seed region sequence complementarity. *Rna* **12**, 1179–1187.
- Kispal, G., Csere, P., Guiard, B., and Lill, R. (1997). The ABC transporter Atm1p is required for mitochondrial iron homeostasis. *FEBS Lett.* **418**, 346–350.
- Lill, R., and Mühlenhoff, U. (2008). Maturation of iron-sulfur proteins in eukaryotes: Mechanisms, connected processes, and diseases. *Annu. Rev. Biochem.* **77**, 669–700.
- Ludwig, B., Bender, E., Arnold, S., Huttemann, M., Lee, I., and Kadenbach, B. (2001). Cytochrome *c* oxidase and the regulation of oxidative phosphorylation. *ChemBiochem.* **2**, 392–403.
- Meldrum, R. A., Bowl, M., Ong, S. B., and Richardson, S. (1999). Optimisation of electroporation for biochemical experiments in live cells. *Biochem. Biophys. Res. Commun.* **256**, 235–239.
- Munnich, A., and Rustin, P. (2001). Clinical spectrum and diagnosis of mitochondrial disorders. *Am. J. Med. Genet.* **106**, 4–17.
- Netz, D. J., Pierik, A. J., Stümpfig, M., Mühlenhoff, U., and Lill, R. (2007). The Cfd1-Nbp35 complex acts as a scaffold for iron-sulfur protein assembly in the yeast cytosol. *Nat. Chem. Biol.* **3**, 278–286.
- Pei, Y., and Tuschl, T. (2006). On the art of identifying effective and specific siRNAs. *Nat. Methods* **3**, 670–676.
- Pickova, A., Potocky, M., and Houstek, J. (2005). Assembly factors of F1FO-ATP synthase across genomes. *Proteins* **59**, 393–402.
- Pondarre, C., Antiochos, B. B., Campagna, D. R., Clarke, S. L., Greer, E. L., Deck, K. M., McDonald, A., Han, A. P., Medlock, A., Kutok, J. L., Anderson, S. A., Eisenstein, R. S., *et al.* (2006). The mitochondrial ATP-binding cassette transporter Abcb7 is essential in mice and participates in cytosolic iron-sulfur cluster biogenesis. *Hum. Mol. Genet.* **15**, 953–964.
- Ponka, P., and Lok, C. N. (1999). The transferrin receptor: Role in health and disease. *Int. J. Biochem. Cell Biol.* **31**, 1111–1137.
- Ponka, P., and Schulman, H. M. (1985). Acquisition of iron from transferrin regulates reticulocyte heme synthesis. *J. Biol. Chem.* **260**, 14717–14721.
- Puccio, H., Simon, D., Cossee, M., Criqui-Filipe, P., Tiziano, F., Melki, J., Hindelang, C., Matyas, R., Rustin, P., and Koenig, M. (2001). Mouse models for Friedreich ataxia exhibit cardiomyopathy, sensory nerve defect and Fe-S enzyme deficiency followed by intramitochondrial iron deposits. *Nat. Genet.* **27**, 181–186.
- Richardson, D. R., and Ponka, P. (1997). The molecular mechanisms of the metabolism and transport of iron in normal and neoplastic cells. *Biochim. Biophys. Acta* **1331**, 1–40.
- Rötig, A., de Lonlay, P., Chretien, D., Foury, F., Koenig, M., Sidi, D., Munnich, A., and Rustin, P. (1997). Aconitase and mitochondrial iron-sulphur protein deficiency in Friedreich ataxia. *Nat. Genet.* **17**, 215–217.
- Rouault, T. A., and Tong, W. H. (2008). Iron-sulfur cluster biogenesis and human disease. *Trends Genet.* **24**, 398–407.
- Sandy, P., Ventura, A., and Jacks, T. (2005). Mammalian RNAi: A practical guide. *Biotechniques* **39**, 215–224.

- Saxena, S., Jonsson, Z. O., and Dutta, A. (2003). Small RNAs with imperfect match to endogenous mRNA repress translation. Implications for off-target activity of small inhibitory RNA in mammalian cells. *J. Biol. Chem.* **278**, 44312–44319.
- Schägger, H. (2003). Blue native electrophoresis. In “Membrane Protein Purification and Crystallization: A Practical Guide (Second Edition)” (C. Hunte, G. V. Jagow, and H. Schägger, eds.), pp. 105–130. Academic Press, San Diego.
- Scheffler, I. E. (2007). “Mitochondria.” New Jersey: John Wiley & Sons, Hoboken, New Jersey.
- Song, D., and Lee, F. S. (2008). A role for IOP1 in mammalian cytosolic iron–sulfur protein biogenesis. *J. Biol. Chem.* **283**, 9231–9238.
- Srere, P. A., Brazil, M., and Gonen, L. (1963). The citrate condensing enzyme of pigeon breast muscle and moth flight muscle. *Acta Chem. Scand.* **17**, 129–134.
- Stehling, O., Elsässer, H. P., Brückel, B., Mühlenhoff, U., and Lill, R. (2004). Iron-sulfur protein maturation in human cells: Evidence for a function of frataxin. *Hum. Mol. Genet.* **13**, 3007–3015.
- Stehling, O., Netz, D. J., Niggemeyer, B., Rösser, R., Eisenstein, R. S., Puccio, H., Pierik, A. J., and Lill, R. (2008). Human Nbp35 is essential for both cytosolic iron-sulfur protein assembly and iron homeostasis. *Mol. Cell Biol.* **28**, 5517–5528.
- Stehling, O., Smith, P. M., Biederbick, A., Balk, J., Lill, R., and Mühlenhoff, U. (2007). Investigation of iron-sulfur protein maturation in eukaryotes. *Methods Mol. Biol.* **372**, 325–342.
- Triepels, R. H., Van Den Heuvel, L. P., Trijbels, J. M., and Smeitink, J. A. (2001). Respiratory chain complex I deficiency. *Am. J. Med. Genet.* **106**, 37–45.
- Trounce, I. A., Kim, Y. L., Jun, A. S., and Wallace, D. C. (1996). Assessment of mitochondrial oxidative phosphorylation in patient muscle biopsies, lymphoblasts, and trans-mitochondrial cell lines. *Methods Enzymol.* **264**, 484–509.
- Vogel, R. O., Smeitink, J. A., and Nijtmans, L. G. (2007). Human mitochondrial complex I assembly: A dynamic and versatile process. *Biochim. Biophys. Acta* **1767**, 1215–1227.
- Wiedemann, N., Urzica, E., Guiard, B., Müller, H., Lohaus, C., Meyer, H. E., Ryan, M. T., Meisinger, C., Mühlenhoff, U., Lill, R., and Pfanner, N. (2006). Essential role of Isd11 in mitochondrial iron-sulfur cluster synthesis on Isu scaffold proteins. *EMBO J.* **25**, 184–195.
- Wiegand, G., and Remington, S. J. (1986). Citrate synthase: Structure, control, and mechanism. *Annu. Rev. Biophys. Chem.* **15**, 97–117.
- Wu, L., and Belasco, J. G. (2008). Let me count the ways: Mechanisms of gene regulation by miRNAs and siRNAs. *Mol. Cell* **29**, 1–7.
- Zeng, Y., Yi, R., and Cullen, B. R. (2003). MicroRNAs and small interfering RNAs can inhibit mRNA expression by similar mechanisms. *Proc. Natl. Acad. Sci. USA* **100**, 9779–9784.
- Zerbetto, E., Vergani, L., and Dabbeni-Sala, F. (1997). Quantification of muscle mitochondrial oxidative phosphorylation enzymes via histochemical staining of blue native polyacrylamide gels. *Electrophoresis* **18**, 2059–2064.
- Zheng, L., Baumann, U., and Reymond, J. L. (2004). An efficient one-step site-directed and site-saturation mutagenesis protocol. *Nucleic Acids Res.* **32**, e115.
- Zheng, L., White, R. H., Cash, V. L., and Dean, D. R. (1994). Mechanism for the desulfurization of L-cysteine catalyzed by the nifS gene product. *Biochemistry* **33**, 4714–4720.
- Zheng, L., White, R. H., Cash, V. L., Jack, R. F., and Dean, D. R. (1993). Cysteine desulfurase activity indicates a role for NIFS in metallocluster biosynthesis. *Proc. Natl. Acad. Sci. USA* **90**, 2754–2758.

LOCALIZATION AND FUNCTION OF THE 2Fe-2S OUTER MITOCHONDRIAL MEMBRANE PROTEIN MITONEET

Sandra E. Wiley,^{*} Matthew J. Rardin,[‡] and Jack E. Dixon^{*,†}

Contents

1. Introduction	234
2. Purification of Highly Enriched Mitochondria from Rat Liver	235
2.1. Differential centrifugation to isolate crude mitochondria	236
2.2. Histodenz gradient purification of mitochondria	237
2.3. Fractionation of highly purified mitochondria	239
2.4. Analysis of mitochondrial fractions by Western blotting	240
3. Expression of Recombinant mitoNEET	240
3.1. Generation of expression plasmids and mutagenesis	241
3.2. Expression and purification of His-tagged mitoNEET	242
3.3. Expression and purification of untagged mitoNEET	242
4. <i>In Vitro</i> Analysis of Purified mitoNEET	243
4.1. Optical spectra of mitoNEET to assess redox status	243
4.2. Assessing pH lability of cluster	244
References	245

Abstract

MitoNEET is an integral protein of the outer mitochondrial membrane and is the flagship of a small family of proteins whose hallmark is the presence of a CDGSH domain. Initially annotated as a zinc finger, the CDGSH domain actually binds a redox-active 2Fe-2S cluster, giving mitoNEET the distinction of being the first 2Fe-2S protein identified in the outer membrane of mitochondria. This chapter describes methods for isolating mitochondrial membrane fractions that are enriched in mitoNEET, generating constructs for the expression of recombinant mitoNEET protein and analyzing the 2Fe-2S cluster of mitoNEET *in vitro*.

^{*} Departments of Pharmacology, Cellular and Molecular Medicine, Chemistry and Biochemistry, University of California, San Diego, La Jolla, California, USA

[†] The Howard Hughes Medical Institute, University of California, San Diego, La Jolla, California, USA

[‡] Gibson Lab, The Buck Institute for Age Research, Novato, California, USA

1. INTRODUCTION

Type 2 diabetes, which is often associated with obesity, is characterized by an initial period of insulin resistance and altered lipid metabolism that is followed by decreased insulin secretion (Wiederkehr and Wollheim, 2006). It is well established that mitochondria play an important role in insulin secretion and that mitochondrial dysfunction is prevalent in patients with type 2 diabetes (Asmann *et al.*, 2006; Lowell and Shulman, 2005; Maechler *et al.*, 2006; Mootha *et al.*, 2004; Petersen and Shulman, 2006; Ritov *et al.*, 2005). Two of the major drugs on the market to treat type 2 diabetes, namely rosiglitazone and pioglitazone, both belong to the thiazolidinedione class of insulin-sensitizers (Colca, 2006; Hofmann *et al.*, 1992). MitoNEET was initially identified as a protein that cross-linked to pioglitazone in tissue lysates (Colca *et al.*, 2004).

MitoNEET is a small dimeric protein that consists of little more than an amino-terminal mitochondrial targeting sequence, a transmembrane domain, and a CDGSH domain at its carboxy-terminus (Fig. 13.1) (Paddock *et al.*, 2007; Wiley *et al.*, 2007a). The CDGSH domain represents a novel class of 2Fe-2S cluster binding domains. It is unique in its fold (the NEET fold) and in its use of 3 cysteines and 1 histidine to coordinate the binding of a redox active 2Fe-2S cluster (Hou *et al.*, 2007; Lin *et al.*, 2007; Paddock *et al.*, 2007; Wiley *et al.*, 2007b). These domains are of ancient origin and are found throughout evolution, from archaea to humans. There are three CDGSH domain-containing proteins expressed in humans (Fig. 13.1) (Wiley *et al.*, 2007a).

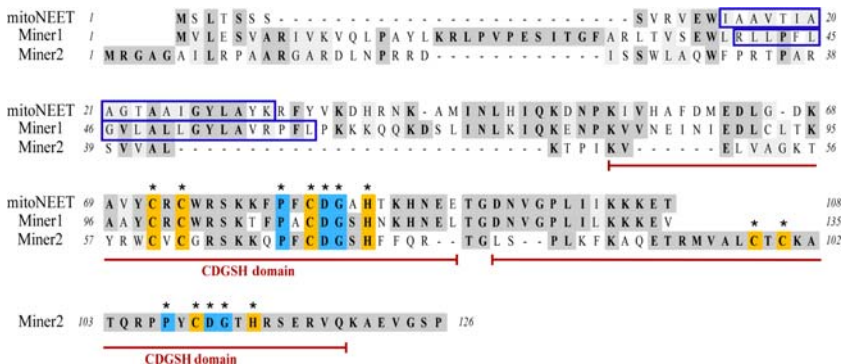


Figure 13.1 The mitoNEET family of proteins. Aligned amino acid sequences of human mitoNEET, Miner1, and Miner2 with conserved amino acids indicated in grey. Amino acids marked with an asterisk are invariant across multiple species. The CDGSH domains, which coordinate the 2Fe-2S clusters, are underlined. Transmembrane domains are marked by boxes. Reprinted with permission from PNAS (Wiley *et al.*, 2007a).

Collectively, they are known as the mitoNEET family and are encoded by the C1SD1, C1SD2, and C1SD3 genes. These proteins are generally referred to as mitoNEET, Miner1 (or ERIS), and Miner2 (or mel-13), respectively (Amr *et al.*, 2007; Tetsu *et al.*, 1996; Wiley *et al.*, 2007a). Although all family members bind redox active Fe-S clusters, they differ in subcellular localization, with mitoNEET and Miner2 localizing to the mitochondria and Miner1 localizing to the endoplasmic reticulum (Amr *et al.*, 2007; Colca *et al.*, 2004; Wiley *et al.*, 2007a).

The exact function of the mitoNEET family of proteins has not been determined; however, several intriguing observations have been made in knockout mice and in human patients. Mitochondria isolated from cardiac tissue of mitoNEET null mice demonstrate reduced oxidative capacity (Wiley *et al.*, 2007a). It has also been shown that mitoNEET mRNA is downregulated in cells from patients with cystic fibrosis (Taminelli *et al.*, 2008). In addition, a mutation in the C1SD2 gene (resulting in a loss of the CDGSH domain in Miner1/ERIS protein) has been reported to cause Wolfram syndrome, which is characterized by childhood presentation of diabetes insipidus and diabetes mellitus, followed by optic atrophy, deafness, psychiatric disorders, and increased bleeding (Amr *et al.*, 2007). Although not a mitochondrial protein, the breadth and severity of problems associated with lack of Miner1 function underscores the importance of this family of CDGSH 2Fe-2S proteins in metabolism and physiology.

The initial studies performed by Colca and colleagues suggested that pioglitazone interacted with crude mitochondrial membranes and the mitochondrial protein mitoNEET (Colca *et al.*, 2004). However, the different compartments of mitochondria can have vastly different implications for the role a protein may play in mitochondrial function. We examined the exact location of mitoNEET within mitochondria and determined it to be an integral protein of the outer membrane with the uniquely pH-sensitive CDGSH domain oriented toward the cytoplasm (Wiley *et al.*, 2007a). This chapter describes methods for isolating mitochondrial membrane fractions that are enriched in mitoNEET, generating constructs for the expression of recombinant mitoNEET protein, and analyzing the 2Fe-2S cluster of mitoNEET *in vitro*.

2. PURIFICATION OF HIGHLY ENRICHED MITOCHONDRIA FROM RAT LIVER

Most of the methods described here can be used to study other mitochondrial proteins. To isolate large quantities of highly purified mitochondria, we extract tissue from rats because of accessibility and availability. The liver is the preferred source for mitochondria because of the size of the

organ, the ease of homogenization, and the large amounts of mitochondria and mitoNEET expressed within this tissue. It should be noted here that mitochondria from different tissues might vary significantly in their method of isolation caused in part by their protein content and the subcellular makeup of different tissues. Although sufficient quantities of mitochondria for many applications may be obtained from the liver of a single adult rat, the scale described here is larger to allow for purification of sufficient material for subsequent submitochondrial fractionation. It is possible to generate enough material for methods 2.1 and 2.2 with tissue culture cells expressing recombinant epitope-tagged mitoNEET. This will require at least 6 to 10 15-cm dishes of cells.

2.1. Differential centrifugation to isolate crude mitochondria

Liver tissue is excised from 2 to 3 adult male Sprague–Dawley rats and immediately placed into ice-cold MSHE/BSA buffer (210 mM mannitol, 70 mM sucrose, 5 mM HEPES (pH 7.4 with KOH), 2 mM EGTA, 0.5% ultra fatty acid free BSA, and Complete protease inhibitor cocktail [Roche]) (Lapidus and Sokolove, 1993; Pagliarini *et al.*, 2005; Wiley *et al.*, 2007a). To minimize contaminating blood in the purified mitochondrial fractions, the aorta should be cut or the rat decapitated and allowed to bleed out briefly before the liver is excised. The liver tissue is rinsed twice in MSHE/BSA buffer to remove excess blood and hair and should remain on ice for the duration of the procedure. The tissue is finely minced with scissors and washed three times in MSHE/BSA buffer. (More rinses may be necessary if there is blood visible in the wash solution.) After the tissue is sufficiently minced, it is homogenized in MSHE/BSA buffer with a tight-fitting Potter–Elvehjem tissue homogenizer (8 to 10 g tissue/5 volumes buffer, 4 passes at rheostat setting of 70%). This will likely require several rounds of homogenization because of volume constraints. Remove a small aliquot (0.1 to 0.5 ml) of the homogenate to be used for later analysis. Dilute the homogenate with 2 to 3 volumes of buffer. To remove unbroken cells and large organelles, the homogenate is centrifuged at 600g for 10 min at 4 °C (all spins are done in a Sorvall SS-34 rotor or equivalent). The postnuclear supernatant is poured through two layers of cheesecloth, and the pellet is resuspended in MSHE/BSA buffer, homogenized, and spun again at 600g for 10 min at 4 °C. Once again, filter the supernatant through the cheesecloth and discard the final pellet. Remove a small aliquot of postnuclear supernatant to be analyzed later. The postnuclear supernatants are combined and centrifuged at 12,000g for 10 min at 4 °C to pellet crude mitochondria. Save a small aliquot of the postmitochondrial supernatant and discard the rest. It is imperative to work as quickly as possible from the time the tissue is homogenized to the point that the crude mitochondrial pellet is obtained to prevent damage to the mitochondria by other cellular proteins including proteases.

The crude mitochondrial pellet (dark brown in color) is washed by gentle dispersal into a minimal amount of MSHE/BSA buffer with a glass rod or fine-tipped paintbrush. Care must be taken to gently resuspend the mitochondrial pellet or the mitochondria will become damaged and leak soluble proteins from interior compartments. After resuspension of the pellet, additional MSHE/BSA buffer is added (approximately 25 ml/pellet), and the mixture is spun at 12,000g for 10 min at 4 °C. The supernatant is removed and, with a fine-tipped aspirator, the white layer containing microsomes and endoplasmic reticulum contaminants is removed. The aggressive removal of contaminating vesicles is preferred over the recovery of total mitochondrial protein. Wash the pellet once more as previously in MSHE/BSA buffer, followed by a wash with BSA-free MSHE (all subsequent steps will use MSHE buffer without BSA). Resuspend the final crude mitochondrial pellet in a minimal amount of MSHE.

2.2. Histodenz gradient purification of mitochondria

To remove any remaining contaminants, it is advisable to gradient purify the crude mitochondria. Both Histodenz (Sigma) and Optiprep (Sigma) work well for obtaining ultrapure mitochondria; however, only the protocol for the Histodenz gradient purification will be presented here (Pagliarini *et al.*, 2005; Rardin *et al.*, 2008; Taylor *et al.*, 2003; Wiley *et al.*, 2007a). Gradients are prepared in ultraclear tubes (14 × 95 mm for an SW40 Ti swinging bucket rotor [Beckman]) by layering 3 ml of 17% Histodenz on top of 2 ml of 35% Histodenz prepared from a 70% wt/vol stock of Histodenz in MSHE buffer (prepare at least 1 day in advance and allow for considerable swelling of the Histodenz; store at 4 °C); 5 to 6 ml of Percoll (Sigma) diluted to 6% in MSHE is then layered on top of the 17% Histodenz layer (Fig 13.2A). Prepare 4 to 6 gradients to purify enough mitochondria for later fractionation. Layer differential centrifugation mitochondria (from section 2.1, ≤ 30 mg/gradient) on top of the Percoll gradient. The mitochondria may fall through the top layer. Fill the tube with additional MSHE as needed. Histodenz gradients are then centrifuged at 45,500g for 45 min at 4 °C in an ultracentrifuge. After centrifugation, collect the light mitochondrial layer between the 6% Percoll and 17% Histodenz layers. Remove intervening material and collect the heavy mitochondrial layer at the interface of the 35% and 17% Histodenz layers. Wash the heavy and light fractions two times with 20 to 30 ml of MSHE buffer by centrifugation at 12,000g for 10 min at 4 °C. Resuspend the light membrane and heavy mitochondrial fraction in a minimal amount of MSHE. The light mitochondrial fraction will be heavily contaminated with ER membranes, whereas the heavy mitochondrial fraction should be relatively free of ER contaminants. See section 2.4 for analysis of fractions by Western blotting.

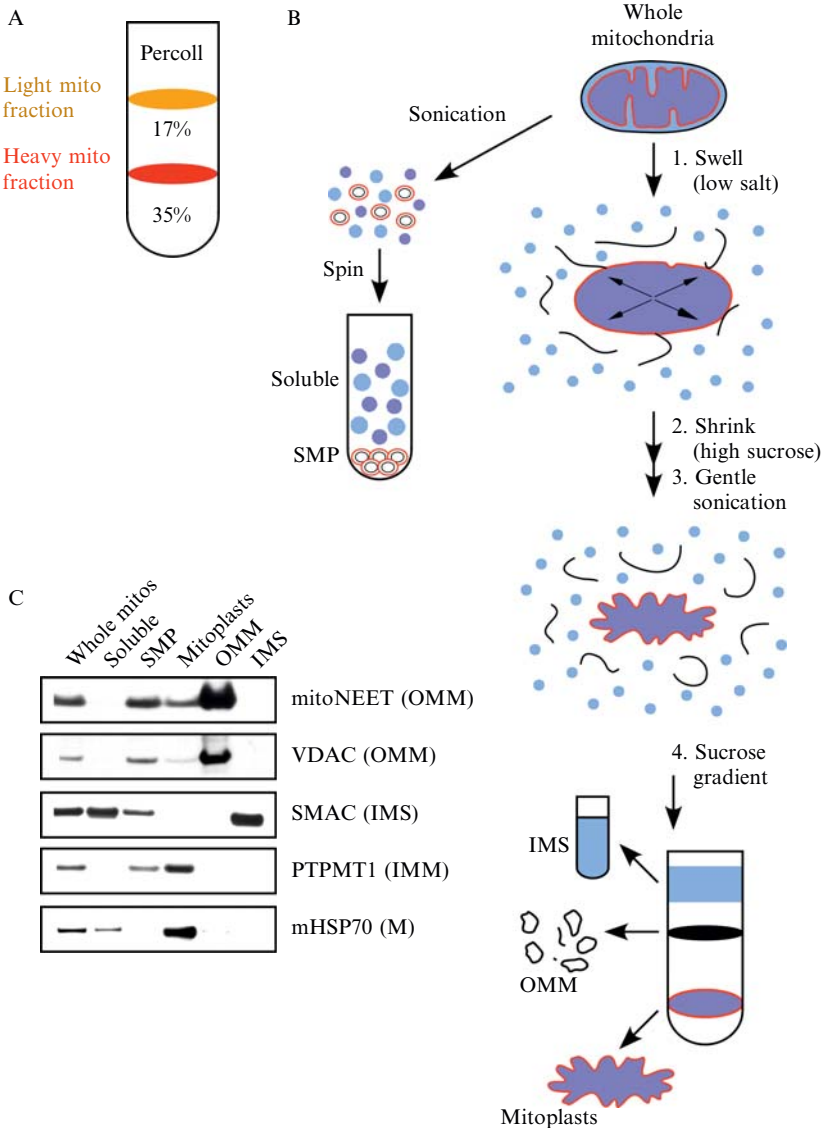


Figure 13.2 Gradient purification and fractionation of rat liver mitochondria. (A) The highly purified “heavy” mitochondria will band at the interface of the 35% and 17% Histodenz layers. The more contaminated “light” mitochondria will band at the interface of the 17% Histodenz and the Percoll layers. (B) Schematic of mitochondrial fractionation. OMM, outer mitochondrial membrane; IMS, intermembrane space; IMM, inner mitochondrial membrane; SMP, submitochondrial particles; IMM and OMM; soluble, IMS and matrix. (C) Western blot of mitochondrial subfractions with antibodies that recognize various mitochondrial marker proteins. Reprinted with permission from PNAS (Wiley *et al.*, 2007a).

2.3. Fractionation of highly purified mitochondria

To determine in which compartment or membrane of the mitochondria mitoNEET is localized, we separated mitochondria into different fractions (Fig. 13.2B) (Felgner *et al.*, 1979; Pagliarini *et al.*, 2005; Rardin *et al.*, 2008; Sottocasa *et al.*, 1967; Wiley *et al.*, 2007a). This method complements other methods of submitochondrial localization, such as immuno-gold electron microscopy, which has resolution limitations because of the combined lengths of the primary and secondary antibodies plus the gold particle, making it extremely difficult to unambiguously determine whether a protein is localized to one of the membranes or soluble compartments of the mitochondria. To subfractionate mitochondria, gradient purified mitochondria (≥ 50 mg) were placed in a hypotonic solution (10 mM KCl, 2 mM HEPES, pH 7.2) at a concentration of 2 mg/ml for 20 min on ice with gentle agitation. This causes the mitochondria to swell, rupturing the outer mitochondrial membrane (OMM) because of the greater surface area of the inner mitochondrial membrane (IMM). Addition of a one third volume of hypertonic solution (1.8 mM sucrose, 2 mM ATP, 2 mM MgSO₄, 2 mM HEPES, pH 7.2) shrinks the matrix and IMM back down. Gently sonicating the mitochondria for 15 sec at 3 amps then largely disrupts the OMM/IMM contact sites, freeing ruptured OMM vesicles. This can also be accomplished with a few gentle passes in a DOUNCE homogenizer. The swollen/shrunk mitochondrial solution is then layered on top of a stepwise sucrose gradient (7 ml each) containing 0.76 M, 1 M, 1.32 M, and 1.8 M sucrose in ultraclear tubes (for an SW28 swinging bucket rotor [Beckman]). Gradients are spun at 75,000g for 3 h at 4 °C. This allows for isolation of the intermembrane space (IMS) soluble fraction collected from the uppermost portion of the gradient. The IMS fraction collected is usually rather dilute and the proteins should be concentrated in a Centricon YM-3000 MWCO (Qiagen) following the manufacturer's directions. The white outer mitochondrial membrane (OMM) fraction is isolated from the 0.76 M and 1 M sucrose interface, washed with MSHE, and pelleted by centrifugation at 120,000g. Mitoplasts (intact IMM and matrix) are collected from the interface of the 1.32 M and 1.8 M sucrose layers, washed with MSHE, and pelleted by centrifugation at 12,000g (Fig. 13.2B).

Purified heavy mitochondria can also be used to generate submitochondrial particles (SMP), which are membrane vesicles lacking soluble proteins (Lesnefsky *et al.*, 2001; Pagliarini *et al.*, 2005; Rardin *et al.*, 2008; Wiley *et al.*, 2007a). SMPs consist of both outer and inner mitochondrial membrane components oriented in an "inside out" fashion with the OMM on the inside and IMM on the outside. Resuspend mitochondria at a concentration of ~ 10 mg/ml in MSHE in a small beaker on ice. Mitochondria are sonicated with a large probe 3×1 min at 50% power on ice with 1-min intervals in between sonication steps. The solution should transition to a darker color and become quite translucent. This sonicated solution is spun at 12,000g for

10 min at 4 °C to remove intact mitochondria. The supernatant is then spun at 120,000g for 45 min at 4 °C to pellet SMP. The supernatant now contains the combined soluble fractions from the IMS and soluble matrix. Wash the SMP pellet with MSHE, then resuspend with a homogenizer. This collection of fractions: IMS, OMM, mitoplasts, SMP, IMS/matrix will allow us to determine where in the mitochondria proteins such as mitoNEET are localized.

2.4. Analysis of mitochondrial fractions by Western blotting

The purity of the mitochondria and fractions generated previously can be evaluated by Western blotting with standard protocols. MitoNEET is a small protein requiring either a 12% or 4 to 12% gel for separation from other proteins without running the mitoNEET protein off of the gel. The tissue homogenate, PNS, PMS, light and heavy mitochondrial samples generated in sections 2.1 and 2.2 should be analyzed by loading equal amounts of protein from each fraction (e.g., 20 µg) and, after SDS-PAGE, blotting for both ER markers (e.g., Calreticulin or KDEL) and mitochondrial proteins (e.g., VDAC, mitoNEET). As the mitochondria become more pure (going from crude homogenate to differential centrifugation purified mitochondria to light, then heavy gradient purified mitochondria), the relative amount of mitoNEET and other mitochondrial proteins should increase relative to the amount of ER proteins on a per microgram protein basis.

The purity of mitoNEET-containing mitochondrial subfractions (OMM and SMP) generated in section 2.3 should also be evaluated by SDS-PAGE and Western blotting. Again, it is important to load equal amounts of protein. We commonly blot with antibodies that recognize the following marker proteins: OMM (VDAC, EMD Biosciences), IMS (SMAC, EMD Biosciences, or cyto-c, BD Pharmingen), IMM (many available from MitoSciences that recognize electron transport chain components), matrix (mito Hsp70, Stressgen Bioreagents). There is currently no commercial antibody available to mitoNEET; however, one can easily be made with recombinant mitoNEET-His protein (see section 3.2) as the antigen (Wiley *et al.*, 2007a). MitoNEET protein should be enriched in the OMM vesicles along with VDAC (Fig. 13.2C) (Wiley *et al.*, 2007a). Note that it is common with this swell/shrink protocol for mitochondrial subfractionation to have a small amount of OMM proteins, such as VDAC, also present in the mitoplast fraction because of retention of OMM and IMM contact site proteins.

3. EXPRESSION OF RECOMBINANT MITONEET

Because of the difficulty of obtaining large amounts of pure mitoNEET-containing OMM vesicles and the necessity to obtain pure mitoNEET for *in vitro* studies, it is advantageous to express and purify mitoNEET as a

recombinant protein. MitoNEET contains an N-terminal mitochondrial targeting sequence and transmembrane domain. When mitoNEET was expressed in bacteria as a full-length recombinant protein, the yield was low, so we routinely express only amino acids 33 to 108 (lacking the N-terminal hydrophobic portion of the molecule but containing the entire CDGSH domain, amino acids 55 to 93, Fig. 13.1) (Wiley *et al.*, 2007a,b). Recombinant mitoNEET is red (Wiley *et al.*, 2007a). It exists as a dimer with each protomer binding a single 2Fe-2S cluster that is coordinated by 3 Cys and 1 His amino acids (Lin *et al.*, 2007; Paddock *et al.*, 2007; Wiley *et al.*, 2007b). His-tagged mitoNEET is suitable for most *in vitro* studies; however, it was necessary to produce untagged mitoNEET for the generation of protein crystals for structural studies (Paddock *et al.*, 2007).

3.1. Generation of expression plasmids and mutagenesis

To generate recombinant protein to test the biophysical properties of mitoNEET (accession # GI:37590611), the portion of the human mitoNEET cDNA encoding amino acids 33 to 108 was cloned into the *Nde*I and *Hind* III restriction sites of the pET21a⁺ vector (Novagen/EMD Biosciences), which contains a carboxy-terminal His₆ tag (Wiley *et al.*, 2007b). The natural stop codon for the mitoNEET cDNA was not included in the reverse primer.

To generate an expression construct for the production of untagged mitoNEET (pET21a⁺-mitoNEET³³⁻¹⁰⁸), the strategy described previously was used, except that the natural stop codon of the mitoNEET cDNA was included in the reverse primer (Wiley *et al.*, 2007b). This results in termination of translation upstream of the His tag.

The His87Cys mutant of recombinant mitoNEET was generated with the Quickchange site-directed mutagenesis kit (Stratagene). His 87 is one of the four amino acids that coordinate binding of the 2Fe-2S cluster of mitoNEET and is responsible for the pH sensitivity of the protein (see section 4.2) (Wiley *et al.*, 2007b).

Primers for PCR amplification of mitoNEET³³⁻¹⁰⁸ and site directed mutagenesis:

Forward: 5'GGGCCCCATATGAGATTTTATGTTAAAGATCATCGA
AAT

Rev. (His tag): 5'GGGCCCAAGCTTAGTTTCTTTTTTCTTGATGA
TCAGAGG

Rev. (no tag): 5'GGGCCCAAGCTTTTAAGTTTCTTTTTTCTTGAT
GATCAGAGG

His87Cys for: 5'CCCATTCTGTGATGGGGCTTGACAAAACAT
AACGAAG

His87Cys rev: 5'CTTCGTTATGTTTTGTGCAAGCCCCATCACAGA
ATGGG

3.2. Expression and purification of His-tagged mitoNEET

BL21(DE3)-CodonPlus-RIL *E. coli* bacteria (Stratagene) were transformed with the pet21a⁺ plasmids encoding wild-type and His87Cys mitoNEET^{33–108} for protein expression (Wiley *et al.*, 2007b). Cultures are grown in 2× YT with antibiotics (100 μg/ml ampicillin and 34 μg/ml chloramphenicol) at 37 °C with shaking until an OD₆₀₀ = 0.4 is reached. The cultures are then supplemented with 1 μM FeCl₃ (final conc.) and growth continued until the OD₆₀₀ = 0.6 to 0.8. Fresh ampicillin is then added, and protein expression is induced by the addition of 0.4 mM isopropyl-β-thiogalactopyranoside (IPTG) (Denville) for 18 h at room temperature with shaking.

Purification of His-tagged mitoNEET can easily be accomplished either by use of an IMAC His-purification column on a Profinia protein purification machine (Biorad) or with Ni-NTA agarose beads and standard protocols (described later) (Rardin *et al.*, 2008; Wiley *et al.*, 2007b). The bacteria are harvested by centrifugation at 5000g for 10 min at 4 °C, and the supernatant is discarded. The bacterial pellet from a 1 L culture is resuspended in 30 ml of lysis buffer (50 mM TRIS-HCl, pH 8.0, 0.3 M NaCl, 10 mM imidazole, fresh 14 μM β-mercaptoethanol (BME), and fresh EDTA-free complete protease inhibitors [Roche]) and lysed by two passes through a Microfluidizer (Avestin) at 12 to 15 kpsi. Triton-X 100 is added to 1% and lysate is spun at 18,000g for 30 min at 4 °C to pellet insoluble cellular debris, which is discarded. The cleared lysate supernatant is then incubated with 1 ml Ni-NTA agarose slurry (Qiagen) at 4 °C for 2 h to bind the His-tagged protein.

The agarose beads with bound mitoNEET-His₆ protein are washed five times with 25 ml of wash buffer (50 mM TRIS-HCl, pH 8.0, 0.3 M NaCl, 20 mM imidazole) for 5 min at 4 °C. If desired, recombinant mitoNEET-His₆ can be eluted from the Ni-NTA agarose by washing with elution buffer (50 mM TRIS-HCl, pH 8.0, 0.3 M NaCl, 250 mM imidazole). The protein is eluted with 2 × 10 min washes (1 ml each) followed by 4 × 30 min washes (1 ml each). The purified protein is combined and dialyzed against 50 mM TRIS-HCl, pH 8.0, with 50 mM NaCl. It is very important to keep the pH of the buffers at 8.0 or above to maintain fidelity of the 2Fe-2S cluster.

3.3. Expression and purification of untagged mitoNEET

The untagged protein can be purified with a combination of ammonium sulfate precipitation and cation exchange chromatography. The growth and expression of untagged mitoNEET protein in BL21(DE3)-CodonPlus-RIL *E. coli* bacteria is performed exactly as described previously for the His-tagged mitoNEET. However, the purification steps are different (Paddock *et al.*, 2007; Wiley *et al.*, 2007b). The bacteria are harvested by

centrifugation and lysed in a buffer consisting of 50 mM TRIS-HCl, pH 8.0, 50 mM NaCl, and 14 μ M BME. The lysate is then clarified by centrifugation at 18,000g for 30 min at 4 °C. The mitoNEET^{33–108} protein is purified with ammonium sulfate precipitations. To the initial lysate, (NH₄)₂SO₄ is added to 25% saturation while stirring, and the solution is then centrifuged at 31,000g for 20 min. At this point, the recombinant mitoNEET protein will be in the supernatant. Next, mitoNEET is precipitated by the addition of (NH₄)₂SO₄ to 75%. The protein is pelleted by centrifuging as earlier. Resuspend the pellet containing mitoNEET in lysis buffer containing 25% (saturating) (NH₄)₂SO₄ and centrifuge as previously to clear the solution of insoluble material. The mitoNEET protein will remain in the supernatant; however, the pellet will also be red, largely because of the precipitation of another protein with an absorbance peak at 420 nm. Dialyze the mitoNEET protein overnight against 100 mM TRIS-HCl, pH 8.0, 1 M NaCl, followed by dialysis against 100 mM TRIS-HCl, pH 8.0, 300 mM NaCl, and ultimately against 50 mM TRIS-HCl, pH 8.0, 50 mM NaCl, making sure to allow for approximately a 30 to 50% expansion of the volume of the solution during dialysis. The next step in the purification takes advantage of the basic nature of the mitoNEET protein. The protein can be run over a cation exchange column on an HPLC or FPLC or passed over an SP-Toyopearl 650 (Tosoh Corporation, Tokyo) cation exchange column, equilibrated with 20 mM TRIS-HCl, pH 8.0, 10 mM NaCl. Immediately before loading the mitoNEET protein onto the column, dilute 1:3 with water and filter through a 0.45- μ m filter. Wash the column with 50 mM TRIS-HCl, pH 8.0, 10 mM NaCl until no protein elutes. The mitoNEET protein can be eluted with 50 mM TRIS-HCl, pH 8.0, 200 mM NaCl. Finally, the protein is dialyzed against a buffer containing 100 mM TRIS-HCl, pH 8.0, 50 mM NaCl. Purity can be evaluated by SDS-PAGE and silver staining.

4. IN VITRO ANALYSIS OF PURIFIED MITONEET

Purified recombinant mitoNEET protein should be red in color with the major absorbance peak at 458 nm (Paddock *et al.*, 2007; Wiley *et al.*, 2007b). The integrity of the mitoNEET protein with respect to binding the 2Fe-2S cluster can be assessed by calculating the ratio of protein to cluster (A_{280}/A_{458}). This value of “optical purity” should be ≥ 2.3 .

4.1. Optical spectra of mitoNEET to assess redox status

The 2Fe-2S cluster of mitoNEET can undergo oxidation and reduction reactions, possibly reflecting its *in vivo* function (Paddock *et al.*, 2007; Wiley *et al.*, 2007b). When the cluster is fully oxidized, the absorbance at 458 nm is

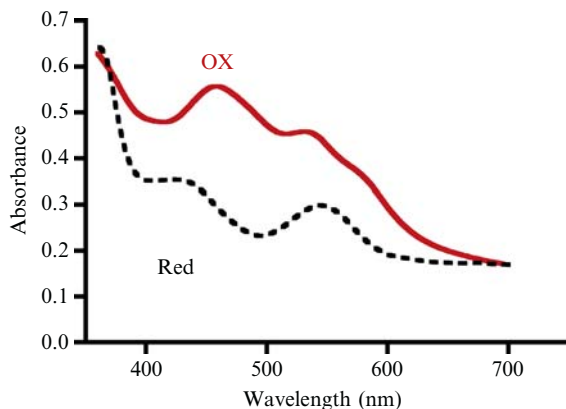


Figure 13.3 Optical spectra of mitoNEET. The recombinant protein is isolated in the oxidized state (solid) and has an absorbance peak at 458 nm. Chemical reduction with dithionite (dashed) results in a decrease in absorbance.

at its maximum and at a minimum when the cluster is reduced (Fig. 13.3). The absorbance can easily be measured on a spectrophotometer, such as the Cary 4000. The absorbance peak at 458 nm will be obvious on a wavelength scan from 350 to 700 nm. For a blank sample, use a buffer of 50 mM TRIS, pH 8.0, 50 mM NaCl. Use this same buffer to dilute the recombinant mitoNEET protein to 10 to 20 μM (final concentration) in a 500- μl sample volume and perform a wavelength scan. To chemically reduce the 2Fe-2S cluster of mitoNEET, add sodium dithionite (Sigma) to a final concentration of 2 to 4 mM. On reduction of the 2Fe-2S cluster, the solution should lose its reddish color. Repeat the wavelength scan. The peak at 458 nm should have decreased in amplitude. Dithionite readily oxidizes with time, and you may find that it takes higher concentrations to reduce the mitoNEET protein. If your stock bottle does not have an intensely pungent odor when opened, it is best to order new material.

The absorbance at 458 nm, which reflects the redox status of mitoNEET, can be used to monitor the effects of various proteins or chemical entities with respect to their ability to donate or accept electrons from mitoNEET. If testing hydrophobic compounds, it is best to use a carrier, such as 0.1% BSA, to prevent nonspecific interactions between the compound and the mitoNEET protein.

4.2. Assessing pH lability of cluster

The 2Fe-2S cluster of mitoNEET is coordinated by an unusual combination of three cysteines and one histidine. This histidine (amino acid 87 in human mitoNEET, Fig. 13.1) is sensitive to protonation, resulting in an

extrusion of the 2Fe-2S cluster from the protein when the pH is lowered below neutral (Paddock *et al.*, 2007; Wiley *et al.*, 2007b). This cluster decay can be followed over time by monitoring the decrease in the amplitude of the A₄₅₈ peak. In separate tubes/cuvettes, dilute mitoNEET protein to 10 to 20 μM in either 200 mM phosphate-HCl (pH 7.5) buffer or 200 mM citrate (pH 6.0) buffer. Perform an absorbance scan from 350 to 600 nm. Continue to scan the same samples periodically over the next 1000 min. At pH 6.0, the A₄₅₈ peak should be half decayed after approximately 200 min, with maximum decay after 1000 min. Samples with the addition of drugs (such as pioglitazone) can be run in parallel to monitor the affects of these chemical entities on the stability of the 2Fe-2S cluster of mitoNEET. Data can be plotted as A₄₅₈ versus time (on a log scale) or entire scans (350 to 600 nm) can be overlaid to show the decrease in the 458 nm peak. The His87Cys mutant mitoNEET protein will not liberate its 2Fe-2S cluster under low pH.

REFERENCES

- Amr, S., Heisey, C., Zhang, M., Xia, X. J., Shows, K. H., Ajlouni, K., Pandya, A., Satin, L. S., El-Shanti, H., and Shiang, R. (2007). A homozygous mutation in a novel zinc-finger protein, ERIS, is responsible for Wolfram syndrome 2. *Am. J. Hum. Genet.* **81**, 673–683.
- Asmann, Y. W., Stump, C. S., Short, K. R., Coenen-Schimke, J. M., Guo, Z., Bigelow, M. L., and Nair, K. S. (2006). Skeletal muscle mitochondrial functions, mitochondrial DNA copy numbers, and gene transcript profiles in type 2 diabetic and nondiabetic subjects at equal levels of low or high insulin and euglycemia. *Diabetes* **55**, 3309–3319.
- Colca, J. R. (2006). Insulin sensitizers may prevent metabolic inflammation. *Biochem. Pharmacol.* **72**, 125–131.
- Colca, J. R., McDonald, W. G., Waldon, D. J., Leone, J. W., Lull, J. M., Bannow, C. A., Lund, E. T., and Mathews, W. R. (2004). Identification of a novel mitochondrial protein ("mitoNEET") cross-linked specifically by a thiazolidinedione photoprobe. *Am. J. Physiol. Endocrinol. Metab.* **286**, E252–260.
- Felgner, P. L., Messer, J. L., and Wilson, J. E. (1979). Purification of a hexokinase-binding protein from the outer mitochondrial membrane. *J. Biol. Chem.* **254**, 4946–4949.
- Hofmann, C. A., Edwards, C. W., 3rd, Hillman, R. M., and Colca, J. R. (1992). Treatment of insulin-resistant mice with the oral antidiabetic agent pioglitazone: Evaluation of liver GLUT2 and phosphoenolpyruvate carboxykinase expression. *Endocrinology* **130**, 735–740.
- Hou, X., Liu, R., Ross, S., Smart, E. J., Zhu, H., and Gong, W. (2007). Crystallographic studies of human MitoNEET. *J. Biol. Chem.* **282**, 33242–33246.
- Lapidus, R. G., and Sokolove, P. M. (1993). Spermine inhibition of the permeability transition of isolated rat liver mitochondria: An investigation of mechanism. *Arch. Biochem. Biophys.* **306**, 246–253.
- Lesnefsky, E. J., Guduz, T. I., Migita, C. T., Ikeda-Saito, M., Hassan, M. O., Turkaly, P. J., and Hoppel, C. L. (2001). Ischemic injury to mitochondrial electron transport in the aging heart: Damage to the iron-sulfur protein subunit of electron transport complex III. *Arch. Biochem. Biophys.* **385**, 117–128.

- Lin, J., Zhou, T., Ye, K., and Wang, J. (2007). Crystal structure of human mitoNEET reveals distinct groups of iron sulfur proteins. *Proc. Natl. Acad. Sci. USA* **104**, 14640–14645.
- Lowell, B. B., and Shulman, G. I. (2005). Mitochondrial dysfunction and type 2 diabetes. *Science* **307**, 384–387.
- Maechler, P., Carobbio, S., and Rubi, B. (2006). In beta-cells, mitochondria integrate and generate metabolic signals controlling insulin secretion. *Int. J. Biochem. Cell Biol.* **38**, 696–709.
- Mootha, V. K., Handschin, C., Arlow, D., Xie, X., St Pierre, J., Sihag, S., Yang, W., Altshuler, D., Puigserver, P., Patterson, N., Willy, P. J., Schulman, I. G., Heyman, R. A., Lander, E. S., and Spiegelman, B. M. (2004). Erralpha and Gabpa/b specify PGC-1alpha-dependent oxidative phosphorylation gene expression that is altered in diabetic muscle. *Proc. Natl. Acad. Sci. USA* **101**, 6570–6575.
- Paddock, M. L., Wiley, S. E., Axelrod, H. L., Cohen, A. E., Roy, M., Abresch, E. C., Capraro, D., Murphy, A. N., Nechushtai, R., Dixon, J. E., and Jennings, P. A. (2007). MitoNEET is a uniquely folded 2Fe 2S outer mitochondrial membrane protein stabilized by pioglitazone. *Proc. Natl. Acad. Sci. USA* **104**, 14342–14347.
- Pagliarini, D. J., Wiley, S. E., Kimple, M. E., Dixon, J. R., Kelly, P., Worby, C. A., Casey, P. J., and Dixon, J. E. (2005). Involvement of a mitochondrial phosphatase in the regulation of ATP production and insulin secretion in pancreatic beta cells. *Mol. Cell* **19**, 197–207.
- Petersen, K. F., and Shulman, G. I. (2006). Etiology of insulin resistance. *Am. J. Med.* **119**, S10–16.
- Rardin, M. J., Wiley, S. E., Murphy, A. N., Pagliarini, D. J., and Dixon, J. E. (2008). Dual specificity phosphatases 18 and 21 target to opposing sides of the mitochondrial inner membrane. *J. Biol. Chem.* **283**, 15440–15450.
- Ritov, V. B., Menshikova, E. V., He, J., Ferrell, R. E., Goodpaster, B. H., and Kelley, D. E. (2005). Deficiency of subsarcolemmal mitochondria in obesity and type 2 diabetes. *Diabetes* **54**, 8–14.
- Sottocasa, G. L., Kuylenstierna, B., Ernster, L., and Bergstrand, A. (1967). An electron-transport system associated with the outer membrane of liver mitochondria. A biochemical and morphological study. *J. Cell. Biol.* **32**, 415–438.
- Taminelli, G. L., Sotomayor, V., Valdivieso, A. G., Teiber, M. L., Marin, M. C., and Santa-Coloma, T. A. (2008). CISD1 codifies a mitochondrial protein upregulated by the CFTR channel. *Biochem. Biophys. Res. Commun.* **365**, 856–862.
- Taylor, S. W., Fahy, E., Zhang, B., Glenn, G. M., Warnock, D. E., Wiley, S., Murphy, A. N., Gaucher, S. P., Capaldi, R. A., Gibson, B. W., and Ghosh, S. S. (2003). Characterization of the human heart mitochondrial proteome. *Nat. Biotechnol.* **21**, 281–286.
- Tetsu, O., Kanno, R., Isono, K., Taniguchi, M., and Kanno, M. (1996). Cloning and characterization of two transcripts generated from the mel-13 gene positioned adjacent to the mammalian Polycomb group-related gene mel-18. *Biochim. Biophys. Acta* **1305**, 109–112.
- Wiederkehr, A., and Wollheim, C. B. (2006). Minireview: Implication of mitochondria in insulin secretion and action. *Endocrinology* **147**, 2643–2649.
- Wiley, S. E., Murphy, A. N., Ross, S. A., van der Geer, P., and Dixon, J. E. (2007a). MitoNEET is an iron-containing outer mitochondrial membrane protein that regulates oxidative capacity. *Proc. Natl. Acad. Sci. USA* **104**, 5318–5323.
- Wiley, S. E., Paddock, M. L., Abresch, E. C., Gross, L., van der Geer, P., Nechushtai, R., Murphy, A. N., Jennings, P. A., and Dixon, J. E. (2007b). The outer mitochondrial membrane protein mitoNEET contains a novel redox-active 2Fe-2S cluster. *J. Biol. Chem.* **282**, 23745–23749.

NUCLEOTIDE-DEPENDENT IRON-SULFUR CLUSTER BIOGENESIS OF ENDOGENOUS AND IMPORTED APOPROTEINS IN ISOLATED INTACT MITOCHONDRIA

Boominathan Amutha,^{*} Donna M. Gordon,[‡] Andrew Dancis,[†]
and Debkumar Pain^{*}

Contents

1. Introduction	248
2. Stock Solutions and Storage	250
3. Isolation and Purification of Mitochondria	251
4. Depletion of Endogenous Nucleotides in Isolated Mitochondria	252
5. Nucleotide-Dependent [Fe-S] Cluster Biogenesis of Endogenous Aconitase in Purified Mitochondria	253
5.1. Insertion of newly formed [Fe- ³⁵ S] clusters into endogenous apoaconitase and nucleotide (GTP and ATP) dependence	253
5.2. Requirement for nucleotide hydrolysis	255
5.3. Effects of matrix GTP levels	257
6. [Fe-S] Cluster Biogenesis of Imported Apoferredoxin	258
6.1. Bacterial expression and purification of unlabeled apoferredoxin precursor protein	259
6.2. Synthesis of ³⁵ S-methionine-labeled apoferredoxin precursor protein in reticulocyte lysate cell-free translation system	260
6.3. Insertion of newly formed [Fe-S] clusters into imported apoferredoxin—A single step coupled assay	260
6.4. GTP-dependent [Fe-S] cluster biogenesis of imported apoferredoxin—A two-step assay	261
7. Concluding Remarks and Perspectives	263
Acknowledgments	265
References	266

^{*} Department of Pharmacology and Physiology, UMDNJ, New Jersey Medical School, Newark, New Jersey, USA

[†] Department of Medicine, Division of Hematology-Oncology, University of Pennsylvania, Philadelphia, Pennsylvania, USA

[‡] Department of Biological Sciences, Mississippi State University, Mississippi State, Mississippi, USA

Abstract

Iron-sulfur [Fe-S] clusters are cofactors of proteins involved in electron transfer, enzyme catalysis, radical generation, sulfur donation, and signal transduction. Biogenesis of [Fe-S] clusters is mediated by numerous conserved proteins present in *E. coli* and in mitochondria of eukaryotic cells such as yeast and humans. Although a completely reconstituted system for study of this process does not yet exist, isolated intact mitochondria are capable of synthesizing new [Fe-S] clusters when supplied with a few ingredients. Here we describe methods for studying the biogenesis of [Fe-S] clusters in intact mitochondria. In these assays, metabolically active mitochondria isolated from a wild-type *Saccharomyces cerevisiae* strain are incubated with ^{35}S -cysteine. The ^{35}S is rapidly (~ 15 min) and efficiently incorporated by physiologic pathways into newly formed [Fe-S] clusters and inserted into target proteins. Proteins labeled with [Fe- ^{35}S] clusters are then separated by native polyacrylamide gel electrophoresis followed by autoradiography, thereby allowing direct visualization and quantitation. Both endogenous (Aco1p aconitase) and newly imported (Yah1p ferredoxin) apoproteins can be used as substrates. [Fe-S] cluster biogenesis in isolated intact mitochondria is greatly enhanced by the addition of nucleotides (GTP and ATP) and requires hydrolysis of both. A major advantage of the methods described here is that neither *in vivo* overexpression of target substrates nor enrichment by immunoprecipitation is necessary to detect radiolabeled proteins. It is also not necessary to perform these assays under anaerobic conditions, because intact mitochondria are capable of protecting newly formed [Fe-S] clusters from oxidative damage.

1. INTRODUCTION

Iron-sulfur [Fe-S] clusters are modular cofactors consisting of iron and sulfur liganded to cysteine sulfurs of proteins. They are present throughout evolution and are found in archaea, protists, prokaryotes, and eukaryotes. [Fe-S] clusters function in essential processes such as enzyme catalysis, electron transfer, regulation of gene expression, structural stabilization of protein domains, and in sensing of environmental signals such as oxygen, superoxide, and iron (Kiley and Beinert, 2003; Lill and Mühlenhoff, 2008; Rouault and Tong, 2005). The most common types of [Fe-S] clusters are [2Fe-2S] and [4Fe-4S] clusters. In mitochondria, [Fe-S] proteins of the respiratory electron transport chain are found associated with the inner membrane. [Fe-S] proteins are also found in the mitochondrial matrix. In *Saccharomyces cerevisiae* mitochondria, ferredoxin (Yah1p) and aconitase (Aco1p) contain [2Fe-2S] and [4Fe-4S] clusters, respectively, and both of these proteins are found in the matrix.

[Fe-S] cluster biogenesis is a complex process involving more than 12 genes/proteins (Fontecave and Ollagnier-de-Choudens, 2008; Johnson *et al.*, 2005; Lill and Mühlenhoff, 2008). Lethal phenotypes are associated with disruption of many of these genes, consistent with the essential nature of the process. Our current knowledge of [Fe-S] cluster biogenesis in mitochondria is derived mostly from studies of proteins in *S. cerevisiae* and their homologs in *E. coli*. Mitochondrial [Fe-S] cluster biogenesis can be divided into early, intermediate, and late stages (Fig. 14.1). The early stage involves generation of the sulfur precursor for [Fe-S] cluster formation. In this step, the mitochondrial cysteine desulfurase (Nfs1p) activates and abstracts sulfur from the substrate cysteine, generating a persulfide on a conserved cysteine residue of the enzyme's active site (Nfs1p-S-SH). In the intermediate stage, an [Fe-S] cluster intermediate is assembled on a scaffold protein (Isu1p or Isu2p in yeast). At this stage, the persulfide sulfur is transferred from Nfs1p to the scaffold, and iron must also be supplied. In the late stage, [Fe-S] cluster intermediates are transferred from scaffold proteins to recipient apoproteins, with the formation of the corresponding holo and active proteins. Chaperones, including ATP-requiring Hsp70 (Ssq1p) and accessory J protein (Jac1p), are likely required for the transfer process. Other components such as reductases, ferredoxins, and glutaredoxins are

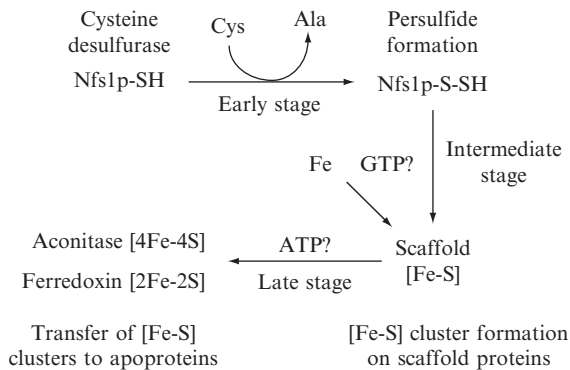


Figure 14.1 A model for [Fe-S] cluster biogenesis in mitochondria. Several proteins with [Fe-S] cluster cofactors reside in mitochondria, including aconitase [4Fe-4S] and ferredoxin [2Fe-2S]. Mitochondria contain complete machinery for [Fe-S] cluster biogenesis of these proteins. The process requires iron import into mitochondria and generation of sulfur from the amino acid cysteine within the organelle. During an early stage, a persulfide is formed on the Nfs1p cysteine desulfurase. The intermediate stage involves transfer of the persulfide sulfur from Nfs1p to the scaffold protein. At this stage, iron is also acquired by the scaffold protein, and [Fe-S] cluster intermediates are formed. At a subsequent late stage, [Fe-S] cluster intermediates are transferred to apoproteins, generating the corresponding holo proteins.

also required as noted in a recent review (Lill and Mühlenhoff, 2008). Nucleotides (GTP and ATP) are required for [Fe-S] cluster biogenesis, serving as substrates for GTPases and chaperones (Amutha *et al.*, 2008), although the roles of nucleotides in distinct stages of mitochondrial [Fe-S] cluster biogenesis have not been established.

Here we describe an experimental system for evaluating [Fe-S] cluster biogenesis in intact and metabolically active mitochondria isolated from a wild-type yeast strain. The approach is unique because nucleotide levels in isolated mitochondria can be effectively and reversibly manipulated without any significant effects on mitochondrial integrity and metabolic functions, and thus effects of nucleotides on [Fe-S] cluster synthesis can be tested. By contrast, in intact cells, it has been difficult to manipulate nucleotide levels without compromising critical metabolic processes, and, therefore, specific and nonspecific effects of nucleotides have not previously been ascertained. In assays with isolated mitochondria, nucleotides (GTP and ATP) are depleted and added back in controlled amounts. Radioactive sulfur is generated from ^{35}S -cysteine by the Nfs1p cysteine desulfurase activity in mitochondria and used for [Fe-S] cluster synthesis. Newly formed [Fe- ^{35}S] clusters are subsequently incorporated into proteins such as aconitase [4Fe-4S] and ferredoxin [2Fe-2S] (Amutha *et al.*, 2008; Zhang *et al.*, 2006). The polypeptide backbone of the substrate protein is unlabeled. The clusters are destroyed by denaturants such as SDS, and, thus, radiolabeled proteins can only be analyzed by native polyacrylamide gel electrophoresis (PAGE).

2. STOCK SOLUTIONS AND STORAGE

Stocks of ATP (100 mM) and GTP (100 mM) are made in water, and pH is adjusted to 7.5 with 1 N KOH. Aliquots are kept frozen at -80° . Stocks (50 to 100 mM) of nucleotide analogs, such as 5'-adenylyl imidodiphosphate (AMP-PNP) and guanosine 5'-3-O-(thio)triphosphate (GTP γ S), are made in 20 mM HEPES/KOH, pH 7.5, and stored at -80° . NADH (250 mM) is made fresh in water just before use. Dithiothreitol (DTT, 1 M in water) is kept frozen at -20° . ^{35}S -cysteine (1075 Ci/mmol) and ^{35}S -methionine (1175 Ci/mmol) are stored at -80° . A mixture of ferrous ammonium sulfate (100 μM) and sodium ascorbate (1 mM) is made fresh in water just before use. A protease inhibitor mixture (PIM) of E-64, leupeptin, pepstatin A, bestatin A, and AEBSF (4-(2-aminoethyl)-benzene sulfonyl fluoride hydrochloride) is used at final concentrations of 1 μM , 2 μM , 1.4 μM , 1.2 μM , and 75 μM , respectively. The PIM stock (1000 \times) is made in dimethyl sulfoxide (DMSO) and stored in aliquots at -80° .

Phenylmethylsulfonyl fluoride (PMSF) stock (200 mM) is made fresh in ethanol. Other stock solutions are stored either at room temperature or at 4° as needed.

3. ISOLATION AND PURIFICATION OF MITOCHONDRIA

Mitochondria are isolated from *Saccharomyces cerevisiae* strain D273-10B (ATCC 24657) as described (Murakami *et al.*, 1988) with some modifications. The following protocol is designed for 4 to 12 L of culture corresponding to ~16 to 48 g of cells, respectively. Cells are grown in rich media supplemented with iron (0.3% yeast extract, 0.1% glucose, 2% lactate, 7.4 mM KH₂PO₄, 18.7 mM NH₄Cl, 8.6 mM NaCl, 4 mM CaCl₂, 4 mM MgSO₄, 19 μM FeCl₃) to OD₆₀₀ of 1.4 and harvested by centrifugation (4500g, 7 min, 20°). Cells are suspended in 0.1 M TRIS-SO₄, pH 9.4, containing 10 mM DTT (~5 to 6 ml/g of cells) and incubated at 30° for 10 min. After centrifugation, cell pellets are resuspended in spheroplast buffer (20 mM potassium phosphate, pH 7.4, 1.2 M sorbitol; ~6 to 7 ml/g of cells), and incubated with Zymolyase 100T (0.8 to 1 mg/g of cells) at 30°. At 15- to 20-min intervals, an aliquot (10 μl) of the reaction mixture is diluted with water, and OD₆₀₀ is measured. A decrease in OD₆₀₀ because of cell lysis is a measure of conversion to spheroplasts. In approximately 50 to 60 min, ~80 to 90% of cells are converted to spheroplasts. At this stage, spheroplast suspension is diluted with an equal volume of spheroplast buffer and centrifuged (4000g, 5 min, 20°). The spheroplast pellet is washed twice with spheroplast buffer and then suspended at a concentration of 1 g of starting cells per ml of ice-cold buffer A (20 mM HEPES/KOH, pH 7.5, 0.6 M sorbitol, 0.1% bovine serum albumin [BSA], 1 mM EDTA, 1 mM PMSF, 10 U/ml Trasylol) containing PIM (1:1000). Spheroplasts are homogenized with ~15 strokes with a tight-fitting piston in a Dounce homogenizer kept on ice. The homogenate is diluted with an equal volume of ice-cold buffer A and centrifuged at 1500g for 5 min at 4°. The supernatant is saved, and the pellet is again homogenized, diluted and centrifuged as previously. Supernatants are combined and centrifuged (1500g, 5 min, 4°) to remove residual unbroken cells and cell debris. A "crude" mitochondrial fraction is obtained by centrifugation (10,000g, 10 min, 4°) of the supernatant. This fraction can be stored (see later) and used for [Fe-S] cluster loading and import assays. However, we recommend mitochondria be further purified, particularly for experiments aimed at determining nucleotide dependence, because "crude" mitochondria may be contaminated with other organelles and their ATPases and GTPases.

To purify mitochondria, the crude mitochondrial pellet is resuspended in buffer A (~5 ml per pelleted material corresponding to 4 L starting

culture) and is loaded onto a step gradient consisting of 20% Percoll (24.5 ml) and 40% Percoll (6.5 ml), both in buffer A. Loading of excess crude mitochondria usually results in a smear in the gradient after centrifugation and, therefore, is not recommended. Samples are centrifuged in a Beckman SW28 rotor ($70,000g_{av}$, 28 min, 4°). Mitochondria are collected from the interface between 20 and 40% Percoll, diluted at least 10-fold with buffer A containing no EDTA, and centrifuged ($10,000g$, 10 min, 4°). The mitochondrial pellet obtained from each gradient is resuspended in a small volume (1 to 1.5 ml) of buffer A (no EDTA). Typically, the yield is ~ 40 to 48 mg of purified mitochondrial proteins per 4 L of starting culture. For storage, an equal volume of ice-cold 20% DMSO in 20 mM HEPES/KOH, pH 7.5, 0.6 M sorbitol, 2% BSA, 1 mM PMSF, 40 U/ml Trasylol, and 1:1000 PIM is added drop wise to the mitochondrial suspension while gently mixing. Aliquots corresponding to 0.5 to 1 mg are immediately frozen in liquid nitrogen and stored at -80° . These frozen mitochondria can be used without any significant loss of import or [Fe-S] cluster loading activity for at least 3 years. Just before the experiment, frozen mitochondria are thawed, diluted with 1 ml of ice-cold buffer (20 mM HEPES/KOH, pH 7.5, 0.6 M sorbitol, 0.1% BSA, 0.5 mM $Mg(OAc)_2$, 1 mM PMSF, 1:1000 PIM), and centrifuged at $15,000g$ for 2 min at 4° to remove DMSO. Mitochondrial pellets are gently resuspended in 20 mM HEPES/KOH, pH 7.5, 0.6 M sorbitol, 0.1 mg/ml BSA at 10 mg of proteins per ml and kept on ice. We recommend the use of these mitochondria within 30 min, even though they remain metabolically active for at least 4 h after thawing. These purified mitochondria contain ~ 3 nmol iron per mg of mitochondrial protein, and this endogenous iron can be used for [Fe-S] cluster synthesis (Amutha *et al.*, 2008).

4. DEPLETION OF ENDOGENOUS NUCLEOTIDES IN ISOLATED MITOCHONDRIA

Mitochondria as isolated often contain a pool of nucleotides, depending on growth and isolation conditions. To deplete these endogenous nucleotides, mitochondria are incubated at 25° for 5 to 10 min in buffer lacking respiratory substrates. Nucleotide-depleted mitochondria are then kept on ice for assembly of reaction mixtures. Depletion of nucleotides in this manner does not produce any significant changes in mitochondrial integrity and function. For example, when nucleotides are added back after depletion, import of proteins into mitochondria proceeds with the usual efficiency, and the normal localization of imported and endogenous proteins within the organelle is maintained. Furthermore, nucleotide depletion does not alter the levels of endogenous apoaconitase (our unpublished observations).

5. NUCLEOTIDE-DEPENDENT [Fe-S] CLUSTER BIOGENESIS OF ENDOGENOUS ACONITASE IN PURIFIED MITOCHONDRIA

Aconitase reversibly catalyzes the conversion of citrate to isocitrate in the tricarboxylic acid cycle and requires a [4Fe-4S] cluster for this activity. In *S. cerevisiae*, aconitase (Aco1p) is encoded by a single nuclear gene *ACO1*. It is an abundant protein and is primarily localized to mitochondria. Mitochondria isolated from a wild-type yeast strain contain a pool of apoaconitase (~8 to 10% of the total aconitase protein) (Amutha *et al.*, 2008), perhaps because of incomplete *in vivo* [Fe-S] cluster insertion. In the following sections, methods are described for assessing [Fe-S] cluster insertion into this endogenous pool of apoaconitase in isolated mitochondria.

5.1. Insertion of newly formed [Fe-³⁵S] clusters into endogenous apoaconitase and nucleotide (GTP and ATP) dependence

Reaction mixtures are assembled on ice. The assay mixture (50 μ l) contains nucleotide-depleted mitochondria (100 μ g of proteins) in HSB buffer (20 mM HEPES/KOH, pH 7.5, 0.6 M sorbitol, 0.1 mg/ml BSA, 10 mM Mg(OAc)₂, 40 mM KOAc) containing 5 mM NADH and 1 mM DTT. ATP (1 to 4 mM), and GTP (1 mM) are added individually or together. Samples with no added ATP and GTP serve as controls. After addition of 10 μ Ci ³⁵S-cysteine, samples are incubated at 30° for 15 min. Reaction mixtures are diluted with 20 mM HEPES/KOH, pH 7.5, 0.6 M sorbitol, 0.1 mg/ml BSA (1 ml) and mitochondria are reisolated by centrifugation at 15,000g for 5 min at 4°. The mitochondrial pellet is resuspended in 50 mM TRIS/HCl, pH 8.0, containing 0.5 mM PMSF (35 μ l). Mitochondrial membranes are ruptured by freezing the samples at -80° (15 to 20 min), followed by thawing and bath sonication for 30 sec at 4°. This procedure is repeated three times, and then the samples are centrifuged at 15,000g for 15 min at 4°. The supernatant containing soluble proteins is removed, mixed with 10 μ l of loading buffer (75% glycerol, 40 mM DTT, 0.04% bromophenol blue), and analyzed by electrophoresis on 12% native (non-denaturing) polyacrylamide gels at 4°C. The gel is washed three times with 20% methanol in 50 mM TRIS/HCl, pH 8.0, over a period of 60 to 90 min at 4°, dried at 60°, and exposed to film for autoradiography. Radiolabeled protein bands are quantitated with the software NIH Image.

An example of such an experiment is shown in Fig. 14.2. No significant radiolabeling was observed in the absence of added nucleotides (lane 1). A single predominant endogenous protein was radiolabeled after incubation



Figure 14.2 Nucleotide (GTP and ATP)-dependent $[\text{Fe-}^{35}\text{S}]$ labeling of endogenous aconitase. Isolated intact mitochondria were incubated at 25° for 5 min to promote turnover of endogenous nucleotides. As indicated, samples were then supplemented with ATP (4 mM) and/or GTP (1 mM). All reaction mixtures contained ^{35}S -cysteine (10 μCi). After 15 min incubation at 30° , samples were analyzed by native PAGE followed by autoradiography. The intensity of radiolabeled aconitase (Aco1p) in the presence of both ATP and GTP was arbitrarily defined as 100% (Amutha *et al.*, 2008).

of mitochondria with ^{35}S -cysteine in the presence of nucleotides. The signal was enhanced by addition of ATP (lane 2) or GTP (lane 3), and the process was most effective in the presence of both ATP and GTP (lane 4). The radiolabeled protein was identified as aconitase (Aco1p) by tagging and mutational experiments (Amutha *et al.*, 2008). These results suggest that both ATP and GTP together are required for optimal biogenesis of the $[\text{Fe-S}]$ cluster of aconitase.

Several important features of this assay are as follows. (1) Nfs1p is the only known cysteine desulfurase in mitochondria, and generation of $[\text{Fe-}^{35}\text{S}]$ -labeled Aco1p in isolated wild-type mitochondria is strictly dependent on Nfs1p activity. For example, Nfs1p-depleted (*nfs1*) mitochondria contain aconitase protein but exhibit very little aconitase activity. Most likely Aco1p exists primarily in apo form in *nfs1* mitochondria. When *nfs1* mutant mitochondria are incubated with ^{35}S -cysteine, endogenous apoAco1p is not radiolabeled even after addition of both ATP and GTP

(Amutha *et al.*, 2008). In the absence of sufficient levels of Nfs1p, cysteine cannot be used as a source of sulfur for [Fe-S] cluster synthesis. (2) Insertion of newly formed [Fe-³⁵S] clusters into endogenous apoAco1p is not affected by the presence of chloramphenicol, which blocks mitochondrial protein synthesis. Thus, mitochondrial protein synthesis is not required for biogenesis of the [Fe-S] cluster of aconitase (Amutha *et al.*, 2008). (3) Once endogenous aconitase is labeled with [Fe-³⁵S] clusters, a large excess of unlabeled cysteine cannot remove the radiolabel from the protein. Thus, the nucleotide-dependent radiolabeling of Aco1p in these assays is not due to exchange of ³⁵S into existing clusters of Aco1p, but rather is due to formation and insertion of new [Fe-³⁵S] clusters into apoAco1p (Amutha *et al.*, 2008). (4) Aconitase is susceptible to oxidative [Fe-S] cluster damage. Three different forms of aconitase have been described: holoAco1p [4Fe-4S], Aco1p with a damaged cluster [3Fe-4S], and apoAco1p with no [Fe-S] cluster. However, radiolabeling of aconitase probably does not reflect cluster repair, because repair of the damaged [3Fe-4S] form to the holo [4Fe-4S] form would involve insertion of iron alone, and thus sulfur labeling would not occur. (5) Formation of new [Fe-S] clusters requires both iron and sulfur. Assays described previously can use endogenous or imported iron for [Fe-S] cluster biogenesis. The experiment shown in Fig. 14.2 was performed in the absence of added iron. Most likely, a pool of stored iron in mitochondria was used for the formation of new [Fe-³⁵S] clusters. Iron added as ferrous ascorbate can enter the matrix of isolated intact mitochondria and further stimulate [Fe-S] cluster biogenesis (Amutha *et al.*, 2008). Further evidence for iron-dependent cluster biogenesis in these assays is that treatment of isolated mitochondria with a membrane-permeable chelator such as *o*-phenanthroline, but not with a membrane-impermeable chelator such as EDTA, strongly inhibits [Fe-³⁵S] labeling of Aco1p. More importantly, the inhibitory effects of iron chelation by *o*-phenanthroline can be completely reversed by the addition of ferrous ascorbate (Amutha *et al.*, 2008). In summary, [Fe-S] cluster biogenesis of endogenous apoaconitase in purified mitochondria requires iron, the Nfs1p cysteine desulfurase activity for the generation of sulfur from cysteine, and nucleotides (GTP and ATP). The process reflects biochemical activities of intact mitochondria that differ from chemical [Fe-S] cluster reconstitution, which occurs independently of nucleotides. Furthermore, unlike as observed for chemical reconstitution, anaerobic conditions are not needed, perhaps because intact mitochondria deploy mechanisms to protect newly formed [Fe-S] clusters from oxidative damage.

5.2. Requirement for nucleotide hydrolysis

When added to isolated intact yeast mitochondria, nucleotides (ATP and GTP) can freely diffuse across the outer membrane into the intermembrane space. However, nucleotide transport across the inner membrane into the

matrix requires specific carrier proteins in this membrane. ATP is transported by the ADP/ATP carriers (AAC), and GTP by the GTP/GDP carrier (Ggc1p). In the mitochondrial intermembrane space, ATP can be converted to GTP and vice versa by the nucleoside diphosphate kinase (NDPK) activity in this compartment (Amutha and Pain, 2003). Effects of added ATP or GTP on [Fe-S] cluster biogenesis in intact mitochondria must, therefore, be carefully evaluated to delineate the individual roles of these nucleotides. For example, a portion of added ATP may directly enter into the matrix by means of AAC. Another portion may be converted to GTP by the NDPK activity in the intermembrane space ($\text{ATP} + \text{GDP} \rightarrow \text{ADP} + \text{GTP}$), and GTP thus generated may enter into the matrix by means of Ggc1p to stimulate [Fe-S] cluster biogenesis (see Fig. 14.4, left panel). It is also important to determine whether [Fe-S] cluster biogenesis requires nucleotide hydrolysis or whether nucleotide binding is sufficient. These possibilities can be tested with poorly hydrolyzable nucleotide analogs as follows.

The reaction mixture (50 μl) contains nucleotide-depleted mitochondria (100 μg of proteins) in HSB buffer containing 5 mM NADH, 1 mM DTT, and increasing concentrations (0.5 to 2 mM) of AMP-PNP or GTP γ S. After addition of ^{35}S -cysteine (10 μCi) and ATP (1 mM), samples are incubated at 30° for 15 min and processed for analysis by native gels followed by autoradiography as described previously. In one such experiment (Fig. 14.3), the radiolabeling of endogenous apoAco1p in the presence of added ATP (lane 1) was found to be greatly inhibited by GTP γ S (lanes 2 and 3) or AMP-PNP (lanes 4 and 5) in a dose-dependent manner. These results suggest that hydrolysis of both GTP and ATP is necessary for efficient [Fe-S] cluster biogenesis of aconitase (Amutha *et al.*, 2008).

GTP and ATP may participate in one or more stages of [Fe-S] cluster biogenesis in mitochondria (Fig. 14.1, early, intermediate, and late stages). The cysteine desulfurase activity of the bacterial expressed and purified Nfs1p does not seem to require nucleotides ATP or GTP (Mühlenhoff *et al.*, 2004), although a regulatory role of these nucleotides in persulfide

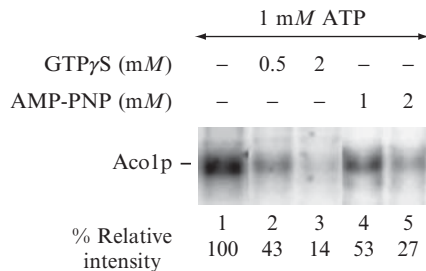


Figure 14.3 Hydrolysis of both GTP and ATP is required for [Fe-S] cluster biogenesis of endogenous aconitase. Nucleotide-depleted intact mitochondria were supplemented with different concentrations of GTP γ S or AMP-PNP as indicated. After addition of ^{35}S -cysteine (10 μCi) and ATP (1 mM), samples were incubated at 30° for 15 min and analyzed by native PAGE followed by autoradiography.

formation in mitochondria (“early stage”) cannot be ruled out. GTP hydrolysis may be needed at the “intermediate stage” of [Fe-S] cluster biogenesis for transfer of the persulfide sulfur from Nfs1p to the scaffold protein, acquisition of iron by the scaffold protein, and/or formation of [Fe-S] cluster intermediates on the scaffold protein (Amutha *et al.*, 2008). GTP hydrolysis required for [Fe-S] cluster biogenesis is likely mediated by a mitochondrial GTPase, which remains to be identified. ATP hydrolysis may be required at the “late stage” of [Fe-S] cluster biogenesis (i.e., transfer of [Fe-S] cluster intermediates from the scaffold protein to apoproteins). The Hsp70 chaperone (Ssq1p) may be involved in this process (Mühlenhoff *et al.*, 2003). With reversible manipulation of nucleotides in isolated, intact, and metabolically active mitochondria as described here, it may now be possible to dissect different stages of [Fe-S] cluster biogenesis and to ascertain the nucleotide requirements for each.

5.3. Effects of matrix GTP levels

In *S. cerevisiae*, GTP is not made in the mitochondrial matrix, and these mitochondria depend on cytosolic GTP supply. The GTP/GDP carrier (Ggc1p) in the mitochondrial inner membrane allows exchange of cytosolic GTP for matrix GDP across this membrane. The $\Delta ggc1$ mutant mitochondria lack this exchange activity, and the matrix contains greatly reduced levels of GTP and increased levels of GDP (Voza *et al.*, 2004). With this background, we undertook experiments with $\Delta ggc1$ mutant mitochondria, showing that they were severely compromised in [Fe-S] cluster forming activity (Amutha *et al.*, 2008). The block could be corrected by targeting Nm23-H4 to the mitochondrial matrix. This is a human enzyme capable of converting ATP (and GDP) to GTP, and its heterologous activity was capable of correcting both the GTP deficiency and the [Fe-S] cluster deficiency of $\Delta ggc1$ mitochondria (Amutha *et al.*, 2008; Gordon *et al.*, 2006). In isolated $\Delta ggc1$ mitochondria, [Fe-S] clusters were not inserted into endogenous apoAco1p even in the presence of added ATP and GTP (Fig. 14.4, middle panel). The greatly reduced level of matrix GTP in $\Delta ggc1$ mitochondria was inadequate for the process, and this defect was not corrected by the addition of GTP, because these mutant mitochondria cannot transport GTP across the inner membrane into the matrix. In contrast, isolated $\Delta ggc1 + Nm23-H4$ mitochondria were able to efficiently insert newly formed clusters into endogenous apoAco1p in the presence of added ATP and GTP or ATP alone (Fig. 14.4, right panel). As in the case of $\Delta ggc1$ mitochondria, added GTP cannot enter into the matrix of $\Delta ggc1 + Nm23-H4$ mitochondria. However, unlike $\Delta ggc1$ mitochondria, ATP that enters into the matrix by means of ADP/ATP carriers (AAC) is converted to GTP by matrix-localized Nm23-H4, thereby facilitating [Fe-S] cluster biogenesis of aconitase. Thus, GTP acts in the mitochondrial matrix to support [Fe-S]

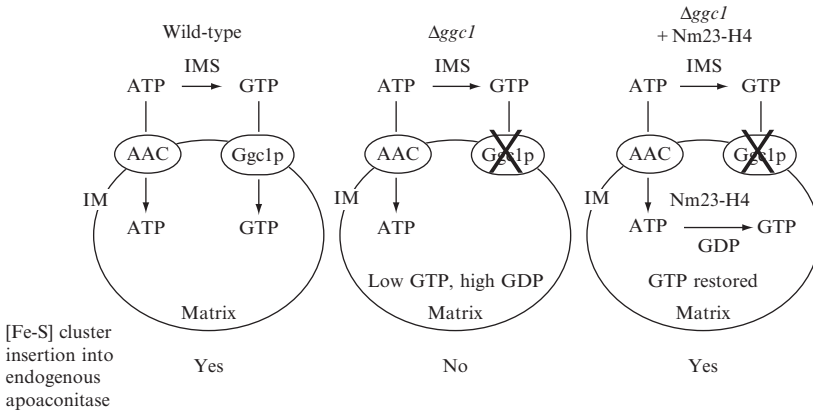


Figure 14.4 Schematic of GTP-dependent [Fe-S] cluster biogenesis in mitochondria. In *S. cerevisiae* mitochondria, the nucleoside diphosphate kinase (NDPK) activity is present in the intermembrane space (IMS), but not in the matrix (Amutha and Pain, 2003). The NDPK activity in the IMS of isolated mitochondria can convert added ATP to GTP, and vice versa. ATP and GTP are transported into the matrix by ADP/ATP carriers (AAC) and the GTP/GDP carrier (Ggc1p) in the inner membrane (IM), respectively (left panel). [Fe-S] cluster biogenesis in isolated intact mitochondria, therefore, occurs in the presence of added ATP or GTP, although the process is most efficient when both ATP and GTP are added (see Fig. 14.2). The $\Delta ggcl$ mutant exhibits decreased levels of matrix GTP and increased levels of matrix GDP (Vozza *et al.*, 2004). In isolated $\Delta ggcl$ mitochondria, radiolabeled [Fe-S] clusters are not inserted into endogenous apoAco1p even in the presence of added ATP and GTP (middle panel) (Amutha *et al.*, 2008). In contrast, isolated $\Delta ggcl$ mitochondria containing the human enzyme Nm23-H4 in the matrix can efficiently insert [Fe-³⁵S] clusters into endogenous apoAco1p in the presence of added ATP alone. Nm23-H4 is a NDPK and exhibits activity capable of converting GDP to GTP with ATP as the phosphate donor in the mitochondrial matrix, and it is this activity that is responsible for restoring [Fe-S] cluster biogenesis in $\Delta ggcl$ mitochondria (right panel) (Amutha *et al.*, 2008; Gordon *et al.*, 2006).

cluster biogenesis. These results also demonstrate that the main function of Ggc1p is to transport GTP/GDP across the mitochondrial inner membrane as suggested (Vozza *et al.*, 2004) and that the role of Ggc1p in the mitochondrial [Fe-S] cluster biogenesis is mediated by its effects on GTP/GDP levels in the matrix (Amutha *et al.*, 2008). These assays may be extended to other yeast mutants to determine the function of the corresponding proteins in nucleotide homeostasis or [Fe-S] cluster biogenesis in mitochondria.

6. [Fe-S] CLUSTER BIOGENESIS OF IMPORTED APOFERREDOXIN

In addition to aconitase, several other proteins with [Fe-S] cluster cofactors reside in mitochondria. For example, ferredoxin (Yah1p) contains a [2Fe-2S] cluster, and the protein itself is involved in [Fe-S] cluster

biogenesis in mitochondria (Lange *et al.*, 2000). Like in the case of Aco1p, the precursor form of Yah1p is also encoded by nuclear DNA, and the precursor protein with an N-terminal mitochondrial targeting signal is synthesized on cytoplasmic ribosomes. On import into the mitochondria, the targeting signals of aconitase and ferredoxin are proteolytically removed by matrix proteases. The mature proteins thus generated reside in the matrix and are used as substrates for addition of [Fe-S] clusters within mitochondria. Thus the overall biogenesis of aconitase and ferredoxin are very similar, with the exception that aconitase contains a [4Fe-4S] cluster, whereas ferredoxin contains a [2Fe-2S] cluster. In the method described previously, ³⁵S-labeling of endogenous Yah1p (analogous to endogenous Aco1p) was not observed (see Fig. 14.2), perhaps because of its lesser abundance. In the following sections, methods are described that can be used to study [Fe-S] cluster biogenesis of newly imported apoferradoxin. The procedure uses bacterial expressed and urea-denatured ferredoxin (Yah1p) or native (non-denatured) Yah1p synthesized in a reticulocyte lysate cell-free translation system. Bacterial expressed Yah1p is preferred because the apoprotein can be easily purified and obtained in large quantity.

6.1. Bacterial expression and purification of unlabeled apoferradoxin precursor protein

The open reading frame (ORF) of the Yah1p precursor protein is amplified from a yeast genomic library by the polymerase chain reaction. The NdeI-ORF-XhoI fragment of the product is cloned into the pET21b vector (Novagen), thereby introducing a His₆ tag in frame at the C-terminus of the protein (Zhang *et al.*, 2006). *Escherichia coli* BL21(DE3) cells carrying the plasmid pET21b/Yah1p are cultured in LB medium (50 ml) supplemented with ampicillin (0.1 mg/ml) at 37°. When cultures reach an OD₆₀₀ of 0.8, expression of Yah1p-His₆ is induced by the addition of isopropyl-1-thio-β-D-galactopyranoside (1 mM). After 15 min incubation at 37°, rifampicin (0.1 to 0.2 mg/ml) is added to inhibit transcription by the host RNA polymerase. Incubation at 37° is continued for another 3 h. Cells are harvested (10,000g, 15 min, 4°) and washed with ice-cold buffer B (50 mM TRIS/HCl, pH 8.0, 5 mM EDTA, 1 mM DTT, 1 mM PMSF). At this stage, cell pellets may be stored at -80° for future use. The pellet is resuspended in buffer B (3 ml) containing 1 mg lysozyme, transferred to a Corex tube (12 ml) and incubated on ice for 45 to 60 min. Cell suspension becomes viscous because of released DNA. Cells are ruptured with a probe sonicator (Branson Sonifier, 6 × 20 sec with 100% duty cycle and output control setting at 2) while keeping the tube on ice. Samples are diluted with ice-cold buffer B (9 ml), and centrifuged (6000g, 20 min, 4°). Yah1p is found in the pellet fraction sequestered in inclusion bodies. The pellet is resuspended in ice-cold 50 mM TRIS/HCl, pH 8.0, 1 mM PMSF (3 ml),

and sonication and centrifugation steps are repeated at least once, preferably twice. The final pellet is solubilized with 8 M urea in 50 mM TRIS/HCl, pH 8.0, 1 mM PMSF (0.5 ml), incubated at 25° for 5 to 10 min, and centrifuged (Beckman TLA 120.2 rotor, 355,000_g_{av}, 20 min, 20°). The supernatant fraction contains Yah1p with ~95% purity, as judged by SDS-PAGE and Coomassie Blue staining (Zhang *et al.*, 2006). The yield is ~0.4 to 0.5 mg of Yah1p per 50 ml of the starting culture. For the experiments described later, it is not necessary to further purify Yah1p-His₆ by Ni-NTA agarose chromatography. The urea-solubilized protein is stored in aliquots at -80° until further use.

6.2. Synthesis of ³⁵S-methionine-labeled apoferradoxin precursor protein in reticulocyte lysate cell-free translation system

The NdeI-ORF-XhoI fragment of *YAH1* (see earlier) is cloned into the pSP64T vector (Zhang *et al.*, 2006). The circular plasmid pSP64T/Yah1p is linearized with BamHI, and its transcription is carried out with the Ribo-max-SP6 kit (Promega). The protein (Yah1p, no His₆ tag) is translated from the *in vitro* transcribed mRNA with rabbit reticulocyte lysate (Promega) in the presence of ³⁵S-methionine following the manufacturer's protocol. The ribosomes are removed by centrifugation (Beckman TLA 100 rotor, 250,000_g_{av} 10 min, 4°), and the postribosomal supernatant containing radiolabeled Yah1p is stored at -80° until further use. The protein backbone is radiolabeled, and, therefore, it is analyzed by SDS-PAGE to confirm molecular mass and purity.

6.3. Insertion of newly formed [Fe-S] clusters into imported apoferradoxin—A single step coupled assay

Conditions for import and [Fe-S] cluster biogenesis (Amutha *et al.*, 2008; Zhang *et al.*, 2006) in isolated intact mitochondria are very similar, and, therefore, these two different reactions can be combined in a single step assay. Reactions are done without prior depletion of endogenous nucleotides in mitochondria. The assay mixture (50 μl) contains mitochondria (100 μg of proteins) in HSB buffer containing NADH (5 mM), DTT (1 mM), ATP (4 mM), GTP (1 mM), ferrous ascorbate (10 μM), and ³⁵S-cysteine (10 μCi). Reactions are started by the addition of bacterial expressed and unlabeled Yah1p precursor protein (200 ng) from a stock in 8 M urea. Immediate mixing is recommended; otherwise, the precursor protein in 8 M urea may settle to the bottom of the tube or may come out of solution. The final urea concentration is usually kept below 0.16 M, and this does not interfere with import (Sepuri *et al.*, 1998) or [Fe-S] cluster assembly (Amutha *et al.*, 2008; Zhang *et al.*, 2006). After incubation at 30° for 15 min, samples are diluted with 20 mM HEPES/KOH, pH 7.5, 0.6 M

sorbitol, 0.1 mg/ml BSA (1 ml), mitochondria are reisolated and processed for analysis by 12% native gels followed by autoradiography as described above to identify proteins labeled with [Fe-³⁵S] clusters. As necessary, samples may also be analyzed by 12% SDS gels, followed by immunoblotting with anti-Yah1p antibodies to detect imported Yah1p-His₆ molecules, which can be distinguished from the endogenous Yah1p by their retarded mobility because of the His₆ tag (Zhang *et al.*, 2006).

To use native (nondenatured) Yah1p as a substrate for [Fe-S] cluster biogenesis, the assay mixture (50 μ l) contains mitochondria (100 μ g of proteins) in HSB buffer containing NADH (5 mM), DTT (1 mM), ATP (4 mM), GTP (1 mM), ferrous ascorbate (10 μ M), unlabeled cysteine (1 μ M), and a postribosomal supernatant (2 μ l) containing ³⁵S-methionine-labeled Yah1p (no His₆ tag). The reaction mixture does not contain ³⁵S-cysteine. After incubation at 30° for 15 min, samples are analyzed by native-PAGE (for [Fe-S] cluster biogenesis) or SDS-PAGE (for import), followed by autoradiography. In this case, the protein backbone of imported Yah1p is radiolabeled, and newly inserted [Fe-S] clusters into imported Yah1p are not radiolabeled. On native gels, imported radiolabeled Yah1p migrates as holoprotein and slower apoprotein species (Duby *et al.*, 2002; Lutz *et al.*, 2001; Zhang *et al.*, 2006). On SDS-gels, clusters are destroyed and, therefore, imported radiolabeled Yah1p migrates as a single band.

Fig. 14.5 shows a representative experiment analyzed by native gel electrophoresis followed by autoradiography. Samples for lanes 1 and 2 were supplemented with ³⁵S-cysteine to generate [Fe-³⁵S] clusters, and, therefore, radiolabeling of endogenous aconitase served as an internal control. Unlabeled Yah1p-His₆ (bacterial expressed) was imported into mitochondria in the presence of ³⁵S-cysteine, and efficient labeling of imported Yah1p with [Fe-³⁵S] clusters was detected (lane 1). Unlike in the case for endogenous Aco1p, radiolabeling of endogenous Yah1p of mitochondria was not visible (lane 2). In a separate sample (lane 3), the Yah1p precursor protein with ³⁵S-methionine incorporated in the polypeptide backbone was imported into mitochondria. In this case, the reaction mixture was supplemented with unlabeled cysteine and not with ³⁵S-cysteine, and, therefore, newly formed Fe-S clusters were not radiolabeled. The Yah1p apoprotein migrated much more slowly than the imported Yah1p that was converted to holoprotein (lane 3). In conclusion, isolated intact mitochondria can use both endogenous apoaconitase and imported apoferrredoxin as substrates for [Fe-S] cluster biogenesis.

6.4. GTP-dependent [Fe-S] cluster biogenesis of imported apoferrredoxin—A two-step assay

Both mitochondrial protein import and [Fe-S] cluster biogenesis require nucleotides. The single step coupled assay described in the previous section for [Fe-S] cluster biogenesis of imported apoferrredoxin, therefore, cannot

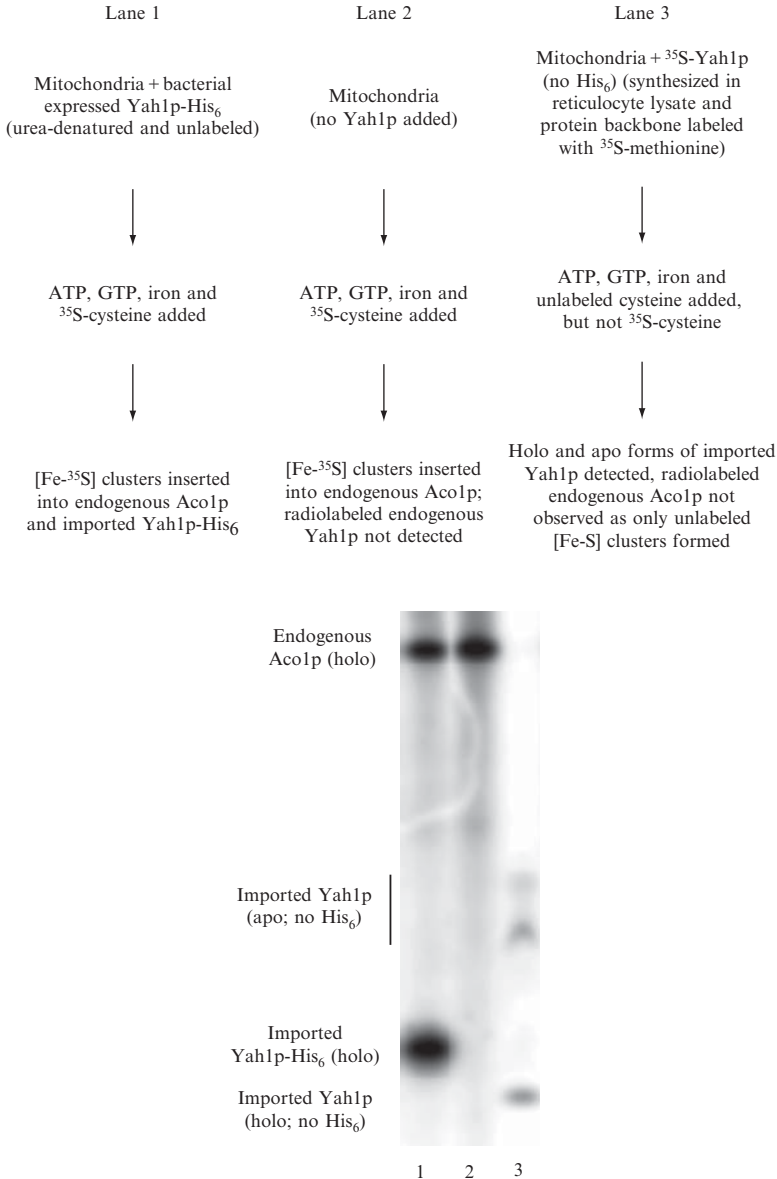


Figure 14.5 [Fe-S] cluster biogenesis of imported apoferrodoxin. The experimental procedure is outlined in the top panel, and the data are presented in the bottom panel. Isolated intact mitochondria were supplemented with ATP, GTP, ferrous ascorbate, and ³⁵S-cysteine and incubated without (lane 2) or with (lane 1) unlabeled apoferrodoxin precursor protein expressed in bacteria. For lane 3, mitochondria were supplemented with ATP, GTP, ferrous ascorbate, and unlabeled cysteine and incubated with ³⁵S-methionine-labeled apoferrodoxin precursor protein synthesized in reticulocyte lysate. Samples were analyzed by native PAGE, followed by autoradiography.

be used to specifically determine the requirement of nucleotides for formation of holoferritin. Protein import and [Fe-S] cluster biogenesis are two very different processes mediated by different proteins, and they can be uncoupled in isolated intact mitochondria. A two-step method is described here that separates the import and [Fe-S] cluster biogenesis, and, therefore, this procedure is ideal to determine the requirement of GTP hydrolysis for [Fe-S] cluster loading of newly imported apoferredoxin (Amutha *et al.*, 2008).

The reaction mixture (50 μ l) contains mitochondria (200 μ g of proteins) in HSB buffer containing NADH (5 mM), DTT (1 mM), and ATP (1 mM). Import is initiated by adding bacterial expressed and unlabeled Yah1p precursor protein (400 ng) from a stock in 8 M urea. After incubation at 30° for 15 min, samples are diluted 20-fold with 20 mM HEPES/KOH, pH 7.5, 0.6 M sorbitol, 0.1 mg/ml BSA, and mitochondria are reisolated by centrifugation at 15,000g for 2 min at 4°. The mitochondrial pellet is resuspended in HSB buffer (50 μ l) containing NADH (5 mM), DTT (1 mM), ³⁵S-cysteine (10 μ Ci), and ATP (1 mM), with or without GTP γ S (1 mM). Reaction mixtures are incubated at 30° for 15 min and processed for analysis by native PAGE followed by autoradiography as described previously. The ³⁵S-cysteine, with or without GTP γ S, is added after ferritin import and reisolation of mitochondria, and, therefore, the effects of GTP γ S on the insertion of [Fe-³⁵S] clusters into imported apoferredoxin are independent of import efficiency. Figure 14.6 shows the schematic outline (top panel) and the data (bottom panel) of a representative experiment. [Fe-³⁵S] clusters were found to be efficiently inserted into imported Yah1p (lane 2), and the process was strongly inhibited in the presence of GTP γ S (lane 3). Endogenous apoaconitase served as an internal control. Results suggest that as in the case of endogenous apoaconitase, [Fe-S] cluster biogenesis of imported apoferredoxin also requires GTP hydrolysis (Amutha *et al.*, 2008).

7. CONCLUDING REMARKS AND PERSPECTIVES

[Fe-S] cluster biogenesis in mitochondria is a complex process. Sulfur derived from cysteine must be combined with iron in the correct form to make [Fe-S] cluster intermediates (Fig. 14.1, early and intermediate stages). Intermediates assembled on the scaffold protein must then be inserted into apoproteins (Fig. 14.1, late stage). The iron and sulfur precursors, the intermediates, and the insertion process must be tightly regulated, because both components (iron and sulfur) are toxic when unassembled or present in excess. No reconstituted system yet exists for study of this essential process.

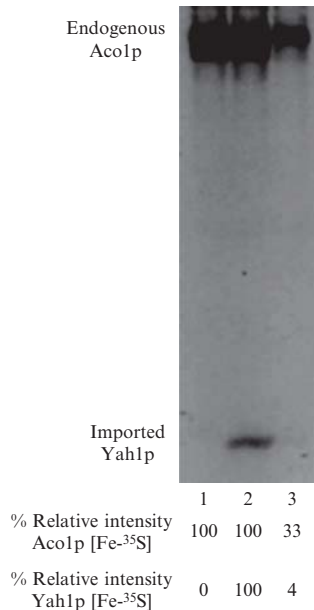
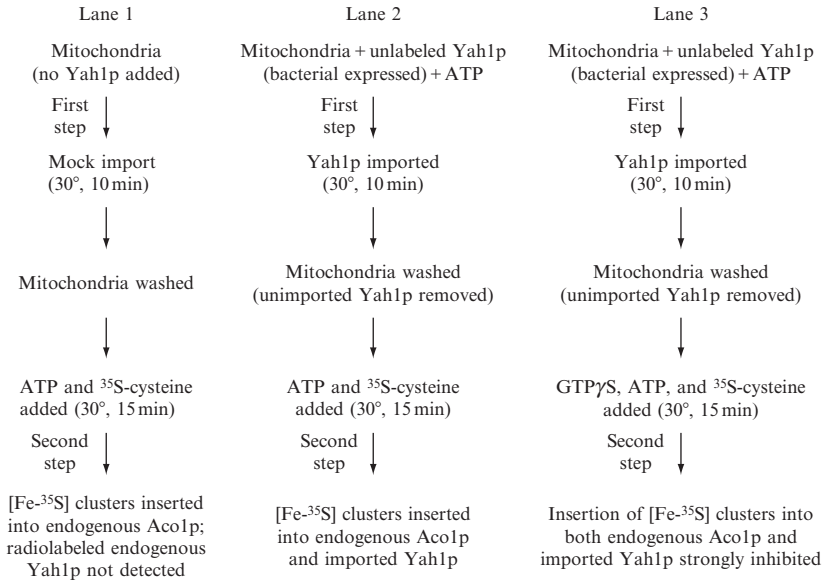


Figure 14.6 [Fe-S] cluster biogenesis of newly imported apoferrredoxin requires GTP hydrolysis. Mitochondria with (lanes 2 and 3) or without (lane 1) imported apoferrredoxin was incubated with ATP (1 mM) and ³⁵S-cysteine (10 μCi) in the absence (lane 2) or presence (lane 2) of GTPγS (1 mM) at 30° for 15 min. Samples were analyzed by native PAGE followed by autoradiography (Amutha *et al.*, 2008).

However, isolated intact mitochondria not only make [Fe-S] clusters but also retain key physiologic regulatory mechanisms and controls. Thus the methods described here for study of [Fe-S] cluster biogenesis in intact mitochondria may be timely and useful for defining regulatory controls of the process.

Interestingly, isolated intact mitochondria can use an endogenous pool of stored iron or imported iron for [Fe-S] cluster formation (Amutha *et al.*, 2008). Methods for study of [Fe-S] cluster biogenesis in intact mitochondria may help in addressing the nature of this iron pool and its regulation. This may be relevant to the pathogenesis of Friedreich ataxia. In this neurodegenerative disease caused by lack of frataxin, iron accumulates in mitochondria, and [Fe-S] proteins, including aconitase, are deficient, as in yeast mutants that do not contain the frataxin homolog. The basis for the connection between these phenotypes remains mysterious (Knight *et al.*, 1999).

Most [Fe-S] proteins in mitochondria contain the cubic [4Fe-4S] cluster as in aconitase or the rhombic [2Fe-2S] cluster as in ferredoxin. Biogenesis of the [Fe-S] clusters in these proteins requires GTP hydrolysis, likely mediated by a GTPase located on the matrix side of the inner membrane (Amutha *et al.*, 2008). A particular challenge will be to identify GTPase(s) involved in the mitochondrial [Fe-S] cluster biogenesis. Many GTPases/GTP-binding proteins appear to exist at this location, but most have not been characterized. Furthermore, the requirement of GTP hydrolysis for cluster biogenesis may or may not be universal for all mitochondrial [Fe-S] proteins, and this will need to be evaluated individually for each [Fe-S] protein. The ATP hydrolysis required for [Fe-S] cluster biogenesis may be mediated by Ssq1p, a chaperone of the Hsp70 class in the mitochondrial matrix. However, this has not been experimentally established. Other ATP-requiring proteins such as the mitochondrial Hsp60 may also be involved (Chaudhuri *et al.*, 2001). Future work will seek to establish the molecular mechanisms of [Fe-S] cluster biogenesis in mitochondria. This work will likely use well-established yeast genetic techniques to manipulate protein expression levels in mitochondria. Such techniques may be combined with biochemical assays as described here involving protein import and reversible nucleotide and iron manipulations in isolated intact mitochondria.

ACKNOWLEDGMENTS

Studies in the authors' laboratories are supported by grants from the National Institute on Aging (AG030504) and American Heart Association (0655946T) to D. P., and National Institutes of Health (DK 053953) to A. D.

REFERENCES

- Amutha, B., Gordon, D. M., Gu, Y., Lyver, E. R., Dancis, A., and Pain, D. (2008). GTP is required for iron-sulfur cluster biogenesis in mitochondria. *J. Biol. Chem.* **283**, 1362–1371.
- Amutha, B., and Pain, D. (2003). Nucleoside diphosphate kinase of *Saccharomyces cerevisiae*, Ynk1p: Localization to the mitochondrial intermembrane space. *Biochem. J.* **370**, 805–815.
- Chaudhuri, T. K., Farr, G. W., Fenton, W. A., Rospert, S., and Horwich, A. L. (2001). GroEL/GroES-mediated folding of a protein too large to be encapsulated. *Cell* **107**, 235–246.
- Duby, G., Foury, F., Ramazzotti, A., Herrmann, J., and Lutz, T. (2002). A non-essential function for yeast frataxin in iron-sulfur cluster assembly. *Hum. Mol. Genet.* **11**, 2635–2643.
- Fontecave, M., and Ollagnier-de-Choudens, S. (2008). Iron-sulfur cluster biosynthesis in bacteria: Mechanisms of cluster assembly and transfer. *Arch. Biochem. Biophys.* **474**, 226–237.
- Gordon, D. M., Lyver, E. R., Lesuisse, E., Dancis, A., and Pain, D. (2006). GTP in the mitochondrial matrix plays a crucial role in organellar iron homeostasis. *Biochem. J.* **400**, 163–168.
- Johnson, D. C., Dean, D. R., Smith, A. D., and Johnson, M. K. (2005). Structure, function, and formation of biological iron-sulfur clusters. *Ann. Rev. Biochem.* **74**, 247–281.
- Kiley, P. J., and Beinert, H. (2003). The role of Fe-S proteins in sensing and regulation in bacteria. *Curr. Opin. Microbiol.* **6**, 181–185.
- Knight, S. A. B., Kim, R., Pain, D., and Dancis, A. (1999). Insights from model systems: The yeast connection to Friedreich ataxia. *Am. J. Hum. Genet.* **64**, 365–371.
- Lange, H., Kaut, A., Kispal, G., and Lill, R. (2000). A mitochondrial ferredoxin is essential for biogenesis of cellular iron-sulfur proteins. *Proc. Natl. Acad. Sci. USA* **97**, 1050–1055.
- Lill, R., and Mühlenhoff, U. (2008). Maturation of iron-sulfur proteins in eukaryotes: Mechanisms, connected processes and diseases. *Annu. Rev. Biochem.* **77**, 669–700.
- Lutz, T., Westermann, B., Neupert, W., and Herrmann, J. H. (2001). The mitochondrial proteins Ssq1 and Jac1 are required for the assembly of iron sulfur clusters in mitochondria. *J. Mol. Biol.* **307**, 815–825.
- Mühlenhoff, U., Balk, J., Richhardt, N., Kaiser, J. T., Sipo, K., Kispal, G., and Lill, R. (2004). Functional characterization of the eukaryotic cysteine desulfurase Nfs1p from *Saccharomyces cerevisiae*. *J. Biol. Chem.* **279**, 36906–36915.
- Mühlenhoff, U., Gerber, J., Richhardt, N., and Lill, R. (2003). Components involved in assembly and dislocation of iron-sulfur clusters on the scaffold protein Isu1p. *EMBO J.* **22**, 4815–4825.
- Murakami, H., Pain, D., and Blobel, G. (1988). 70-kD heat shock-related protein is one of at least two distinct cytosolic factors stimulating protein import into mitochondria. *J. Cell Biol.* **107**, 2051–2057.
- Rouault, T. A., and Tong, W.-H. (2005). Iron-sulphur cluster biogenesis and mitochondrial iron homeostasis. *Nat. Rev. Mol. Cell Biol.* **6**, 345–351.
- Sepuri, N. B. V., Gordon, D. M., and Pain, D. (1998). A GTP-dependent “push” is generally required for efficient protein translocation across the mitochondrial inner membrane into the matrix. *J. Biol. Chem.* **273**, 20941–20950.
- Voza, A., Blanco, E., Palmieri, L., and Palmieri, F. (2004). Identification of the mitochondrial GTP/GDP transporter in *Saccharomyces cerevisiae*. *J. Biol. Chem.* **279**, 20850–20857.
- Zhang, Y., Lyver, E. R., Knight, S. A. B., Pain, D., Lesuisse, E., and Dancis, A. (2006). Mrs3p, Mrs4p, and frataxin provide iron for Fe-S cluster synthesis in mitochondria. *J. Biol. Chem.* **281**, 22493–22502.

ISOLATION OF *SACCHAROMYCES CEREVISIAE* MITOCHONDRIA FOR MÖSSBAUER, EPR, AND ELECTRONIC ABSORPTION SPECTROSCOPIC ANALYSES

Paul A. Lindahl,^{*,†} Jessica Garber Morales,^{*} Ren Miao,^{*} and Gregory Holmes-Hampton^{*}

Contents

1. Introduction	268
2. Large-Scale Growth of <i>S. Cerevisiae</i>	270
3. Anaerobic Isolation	272
4. Isolation Procedure	273
5. Characterization of Mitochondria	275
6. Determining The Absolute [Fe] and [Protein] in Mitochondria	275
7. Packing Samples into Spectroscopy Holders	277
8. Advances with This Approach	281
9. Summary	283
Acknowledgments	283
References	284

Abstract

Methods are presented to aid in the study of iron metabolism in isolated mitochondria. The “iron-ome” of mitochondria, including the type and concentration of all Fe-containing species in the organelle, is evaluated by integrating the results of four spectroscopic methods, including Mössbauer spectroscopy, electron paramagnetic resonance, electronic absorption spectroscopy, and inductively coupled plasma mass spectrometry. Although this systems biology approach only allows *groups* of Fe centers to be assessed, rather than individual species, it affords new and useful information. There are many considerations in executing this approach, and this chapter focuses on the practical methods that we have developed for this purpose. First, large quantities of mitochondria are required, and so published isolation methods must be

* Department of Chemistry, Texas A&M University, College Station, Texas, USA

† Department of Biochemistry and Biophysics, Texas A&M University, College Station, Texas, USA

scaled up. Second, mitochondria are isolated under strict anaerobic conditions to allow control of redox state and to protect O₂-sensitive Fe-containing proteins from degradation. Third, the importance of packing mitochondria for both spectroscopic and analytical characterizations is developed. By measuring the volume of packed samples and the percentage of mitochondria contained within that volume, absolute Fe and protein concentrations within the organelle can be obtained. Packing samples into spectroscopy holders also affords maximal signal intensities, which are critical for these studies. Custom inserts designed for this purpose are described. Also described are the designs of a 25-L glass bioreactor, a mechanical cell homogenizer, a device for inserting short EPR tubes into the standard Oxford Instruments EPR cryostat, and a device for transferring samples from Mössbauer holders to EPR tubes while maintaining samples at liquid N₂ temperatures. A brief summary of what we have learned by use of these methods is included.

1. INTRODUCTION

Starting in the mid 1950s, biophysical chemists isolated mitochondria, typically from bovine and rat livers, and studied them by use of bioenergetic and biophysical methods (Chance and Williams, 1955; Sands and Beinert, 1960). They probed the mechanism of respiration, determined O₂ consumption rates and coupling ratios, and began to characterize the metal centers contained in the respiratory complexes. By the 1970s, methods for purifying individual respiratory complexes had been developed (Beinert, 2002; Katan *et al.*, 1976; Hartzell and Beinert, 1976; Ragan, 1976; Trumpower and Edwards, 1979), allowing these complexes to be characterized in terms of structures, redox and spectroscopic properties, and the mechanisms of catalysis and proton pumping. Genetic methods, typically involving the design of mutants and the characterization of associated phenotypes, became widely available in the 1980s (Hartl *et al.*, 1989; Lill and Kispal, 2000; Tzagoloff and Myers, 1986). These studies provided additional details of mitochondrial function, including (but not limited to) previously unknown aspects of Fe trafficking, Fe/S cluster assembly, and heme biosynthesis. The turn of the century witnessed the development of “omics” technologies (genomics, transcriptomics, proteomics, metabolomics, etc.) that makes it possible (or at least conceivable) to study, at the molecular level of detail, entire organelles and, indeed, whole cells as biological molecular systems (Vo and Palsson, 2007).

Our interests in systems biology and “omics” methods piqued approximately 6 years ago as the details of iron metabolism in this organelle began to emerge. Besides heme biosynthesis and Fe/S cluster assembly, mitochondrial iron metabolism includes the import and trafficking of Fe, the incorporation of Fe-containing prosthetic groups into apoproteins within the

mitochondria, the export of Fe-containing species into the cytosol, and the regulation of all Fe-dependent processes. We wondered whether any combination of spectroscopic methods would suffice to describe the “iron-ome” of this organelle—which we define as the complete iron content within mitochondria, including the identity and concentration of each Fe center contained therein. In essence, we wanted to develop a method for iron analogous to those used in other “omic” studies, such as microarrays that are used to analyze the expression levels of the mRNA transcriptome. We now realize that this grand goal is unrealistic, at least with the technologies we use. However, we have discovered that these technologies, especially when combined, are quite effective, and that even a modicum of progress toward this goal can provide novel and important insights into the metabolism of iron in mitochondria.

The ideal spectroscopic method for iron-omic studies would be capable of resolving all Fe-containing species in the organelle, identifying each species, and determining its *in organello* concentration. If this could be realized, changes in the iron-ome caused by environmental growth conditions and/or genetic alterations could be interpreted at the molecular level of detail. This *systems-biological* approach has advantages over the classical reductionistic approach in that it allows Fe species to be studied within the cellular environments and compartments where they are naturally found. This allows trafficking issues (Fe species moving across membranes from one compartment to another) to be addressed, and it avoids nonphysiological reactions that might occur in cell extracts where Fe species from different compartments have mixed. This approach also allows relative amounts of broadly defined classes of Fe species within the organelle to be estimated. Such information is lost during the purification of individual proteins. On the other hand, there are also inherent disadvantages to the systems biology approach in that reactions are studied within complex and incompletely defined environments where unknown agents might alter the kinetics or mechanism of the process under investigation. Establishing the kinetics and mechanism of reactions (e.g., distinguishing *cause* from *effect*) under these circumstances is difficult and often confusing. In the end, both approaches afford complementary information, and both must be used to understand chemical processes occurring within cells.

As has been described elsewhere (Münck, 1978; Münck *et al.*, 1993), Mössbauer spectroscopy is an especially powerful tool for studying iron in biology. The reasons for this are as follows. First, *all* ^{57}Fe ions in a sample are observed by Mössbauer; there are no “Mössbauer silent” forms of ^{57}Fe . (The isotope ^{57}Fe is required because it has nuclear spin angular momentum $I = 1/2$, and Mössbauer spectroscopy involves transitions between this ground state and the next higher state with $I = 3/2$) Second, the spectral intensities of those ions are directly proportional to the relative amounts present. Thus, if 10% of the ^{57}Fe in a sample is due to $[\text{Fe}_4\text{S}_4]$ clusters, 10% of the spectral intensity will be due to such species. Third, Mössbauer

spectra of different Fe species often differ sufficiently such that spectral contributions of one species can be disentangled from those of another by changing sample temperature and applied magnetic field. The ability to deconvolute multiple species in a sample depends on differences in spin state, oxidation state, ligand environment, spin-coupling, etc. and the skill of the spectroscopist. These characteristics suggest that, in the right hands, Mössbauer could be an ideal tool for iron-omic studies. However, the ability to resolve spectral features declines as the complexity of the sample increases, and in this regard the number of different types of Fe species in mitochondria (there seem to be at least 24 different Fe-containing proteins in the organelle [Hudder *et al.*, 2007]) overwhelms the resolving ability of Mössbauer, such that only *groups* of Fe centers can be identified.

Our strategy to deconvolute the iron-ome better is to supplement the information gathered by Mössbauer spectroscopy with results from two other spectroscopic methods, namely electron paramagnetic resonance (EPR) and electronic absorption (UV-vis) spectroscopy. These methods probe complementary Fe-related properties that can help identify contributors to the iron-ome. EPR is useful for identifying Fe species that have odd numbers of unpaired electrons (e.g., heme and nonheme Fe³⁺ centers, [Fe₄S₄]¹⁺, [Fe₃S₄]¹⁺, and [Fe₂S₂]¹⁺ clusters), and the concentrations of these species can be determined by spin-integrating corresponding EPR signals. Electronic absorption spectroscopy has been widely used to characterize and quantify heme centers in mitochondria. When the results of these three spectroscopic methods are integrated with the determination of the absolute Fe concentration (see later), the iron-ome of mitochondria can be resolved at an unprecedented level of detail—although still far less than the grand goal described previously. This chapter describes various practical methods developed to work with these organelles and to coordinate various aspects of this integrated approach.

2. LARGE-SCALE GROWTH OF *S. CEREVISIAE*

One difficulty of our approach is that large quantities of mitochondria are required. We have begun our studies by isolating mitochondria from budding yeast, *S. cerevisiae*, because we can grow them in large quantities (at modest expense) and in suspension culture. This is the best-understood eukaryote with many genetic strains available. Also, yeast cells are homogeneous (ignoring stochastic and cell cycle processes) and can be grown under controlled growth conditions. In contrast, tissues from mammalian organs consist of many types of cells, which undoubtedly obscure analyses.

We grow cells in a custom-designed bioreactor (Fig 15.1). Pure O₂ rather than air is bubbled through the solution (because of the low

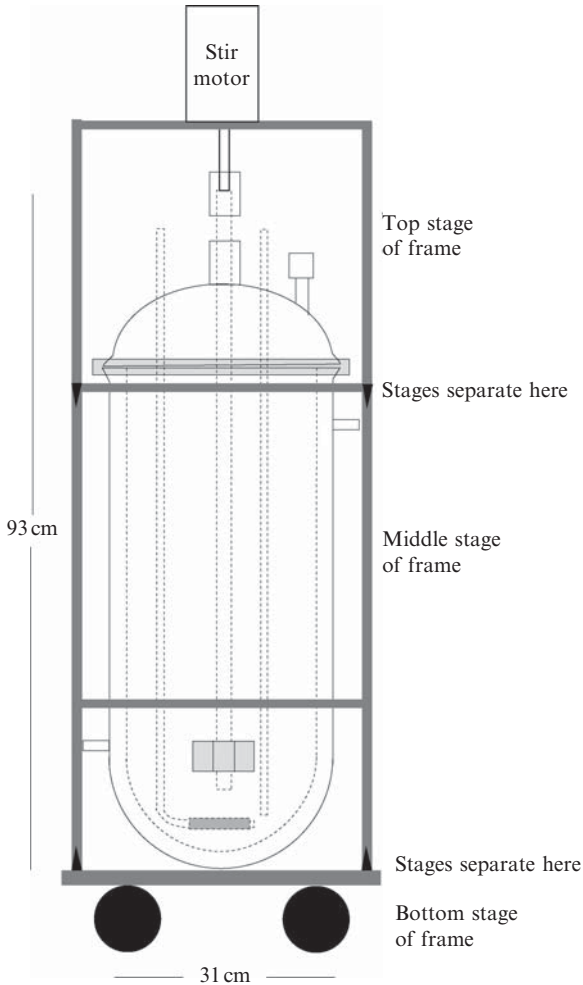


Figure 15.1 Bioreactor. This all-glass (except for a Teflon impeller) reactor was constructed starting from a 10-L water-jacketed cylindrical reaction vessel (Chemglass Inc) with a 200-mm ID and an Schott O-ring flange. A customized vertical extension was added to increase the volume to 25 L. A matching lid was customized to include a central coupling for a rotating impeller and three Chemthread™ inlets evenly distributed about the lid. A tube attached to a high-capacity glass-fitted filter disc (Chemglass, cat. CG-201-37, 60-mm diameter, fine grade) located at the bottom of the reactor directly below the impeller passes through one inlet. A glass tube, used for filling the bioreactor with media and for harvesting cells, passes through another inlet. The third inlet is used for inoculating the media and adding incidental solutions. The entire reactor is supported by a three-stage steel frame. Each stage reversibly interlocks with the adjacent stage by inserting pointy steel rods from the top and bottom stages into matching hollow rods of the middle stage. Stages can be separated by pulling the interlocking unions apart. The top stage supports a rotary motor for stirring the impeller, and the middle stage supports the bioreactor. The bottom stage consists of an aluminum platform base with

surface-to-volume ratio of the reactor), facilitating rapid growth and preventing the cell walls from becoming inordinately difficult for lyticase to hydrolyze. With either strain D237-10B or W303, 24 L of cells grown to an Abs_{600} of 1.4 ± 0.2 (1-cm pathlength) on lactate (SSLac), glucose (YPD), or synthetic minimal media typically yield 100 to 300 g of wet cell paste; the mass obtained depends on metabolic mode (fermenting or respiring), the absorbance at harvesting, and whether rich versus minimal media is used. Fermenting cells contain \sim threefold less mitochondria than respiring cells, such that one harvest of fermenting cells yields only enough mitochondria for a single Mössbauer sample (ca. 400 μ L of packed mitochondria). Compounding this situation, we do not thaw and reuse samples once they have been frozen in liquid N_2 because of concerns that doing so would damage membranes and allow species in different compartments to mix. Thus, we use large quantities of sample relative to most laboratories and have had to scale-up mitochondria isolation procedures accordingly.

3. ANAEROBIC ISOLATION

A novel feature of our mitochondrial isolation method is to do so in a refrigerated inert-atmosphere glovebox. We use an MBraun box (<http://www.mbraunusa.com/>) that maintains an argon atmosphere with ~ 1 ppm O_2 and a temperature of ~ 6 °C. Isolating these organelles anaerobically might seem odd initially, in that mitochondria are well-known consumers of O_2 during respiration. However, there is substantial evidence that the matrix region of the mitochondria is actually anaerobic (Muhlenhoff and Lill, 2000; Henze and Martin, 2003). Iron-sulfur cluster assembly occurs in this region, and Fe/S cluster assembly assays, involving matrix-localized Fe/S scaffold proteins, require anaerobic, reducing conditions (Agar *et al.*, 2000; Mühlenhoff *et al.*, 2002). A number of other matrix-localized Fe-containing proteins are O_2 -sensitive, including biotin synthase (Ollagnier-de-Choudens *et al.*, 2002), lipoic acid synthase (Ollagnier-de-Choudens *et al.*, 1999), and aconitase (Haile *et al.*, 1992). The anaerobicity of the matrix can be

wheels that allow the system to be rolled. For autoclaving, the middle stage (frame and bioreactor) is separated from the top and bottom stages and placed into a standard autoclave (with dimensions 18'' \times 18'' \times 36''). Once sterilized, the bioreactor should be handled, with gloves, by the framework rather than by the glass. Handlers should be extremely careful not to burn themselves while removing the hot bioreactor from the autoclave. The major advantage of this design is that it is far more economical to construct than commercially available alternatives with similar volumes. The all-glass construction allows isotopic enrichments in ^{57}Fe without the worry of cells leaching iron from any metal reactor components.

reconciled with the use of O_2 in respiration by assuming that the rate of respiration is fast relative to the rate of O_2 diffusion across the inner membrane. A vivid analogy is that of a closed room whose walls are set on fire; the room would become anaerobic if the rate of O_2 diffusion (perhaps through the crack at the bottom of the door) were less than that at which the O_2 in the room reacted at the walls.

Besides preventing the O_2 -dependent degradation of matrix proteins, we isolate mitochondria anaerobically to give us control of the redox state of Fe-containing species within the organelle. Being able to examine reduced, oxidized, and as-isolated samples spectroscopically allows us to assess the iron-ome better than we could by examining only the redox state obtained on exposure to air.

4. ISOLATION PROCEDURE

We use the isolation method of [Glick and Pon \(1995\)](#) as modified by Lill and coworkers ([Diekert *et al.*, 2001](#)); we refer readers to the original articles for details. We have made a few modifications, mainly to facilitate the scale-up required for our biophysical studies. During the cell homogenization step, suspended cells are disrupted with a Dounce homogenizer with a tight-fitting Teflon plunger that is repeatedly raised and lowered, causing a pressure differential that ruptures the cells' plasma membranes. For large volumes, the process becomes tedious, because only a small volume of suspended cells can be processed at once. Also the number of strokes required can vary with the pressure applied (which depends on the strength of the person who uses the homogenizer). We have addressed both problems by constructing a machine into which the homogenizer fits. This mechanical homogenizer ([Fig.15.2](#)) raises and lowers the plunger at a fixed rate (11 cycles/min), making the process independent of the user. With our system, approximately 25 strokes are optimal for processing 40 ml of suspended cells.

To accommodate the large quantities of cellular material used in our preparations, we use the high-capacity Beckman SW 32 Ti rotor (which holds six 38.5-ml tubes) for the density gradient step. The dominant contaminant in crude mitochondrial preparations has been described by [Glick and Pon \(1995\)](#) as a broad granular band of cell debris, having a density equivalent to $\sim 19\%$ NycodenzTM. This is only a slightly higher density than mitochondria exhibit, equivalent to $\sim 16\%$ Nycodenz. Other contaminating species have densities of $\sim 12\%$ Nycodenz. Lill and coworkers ([Diekert *et al.*, 2001](#)) recommend use of a discontinuous density gradient with a 14.5% Nycodenz solution on the top and 18.5% solution on the bottom. After trying various other percentages, we have found this to be

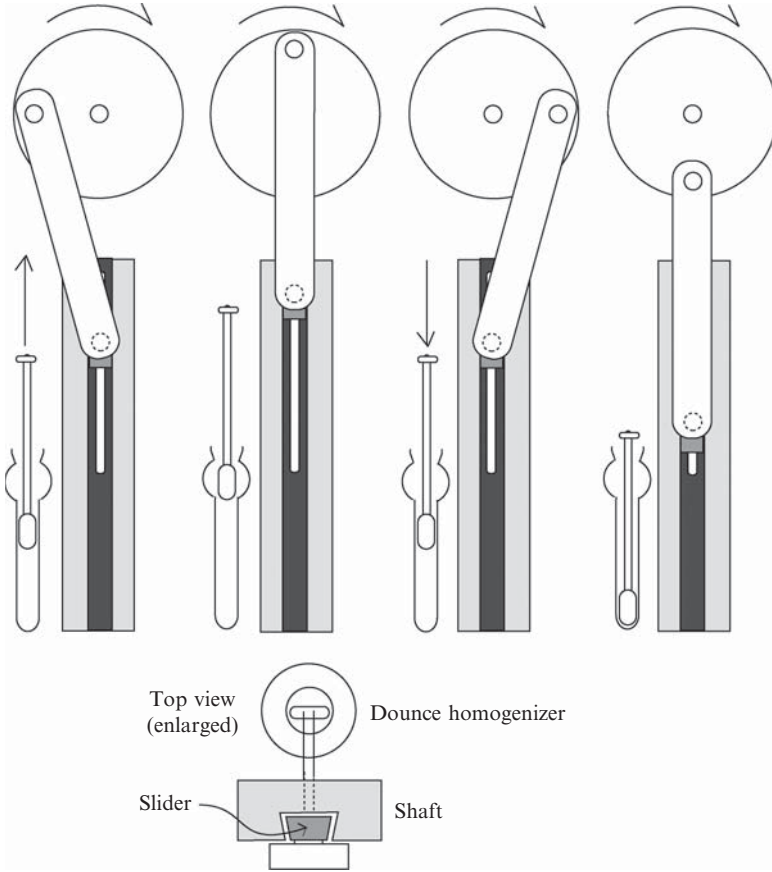


Figure 15.2 Mechanical cell homogenizer. The instrument is driven by an adjustable speed gear motor (Dayton Model 6K119A) that is attached to the center of a rotating disk. Attached near the edge of the disk is one end of a rod, the other end of which is attached to one face of a “slider” that moves vertically within a shaft. The other face of the slider is attached to the Teflon pestle of a tight-fitting 40-ml Dounce homogenizer (Fisher Scientific).

optimal, now with Nycodenz or equivalent densities of Optiprep™. We have also tried a continuous Optiprep density gradient, with a low of 10% and high of 20%, but the mitochondria-containing band was severely spread throughout the tube. Rather than collecting the mitochondrial band by manually piercing the side of these tubes with a syringe, as has been recommended, we fractionate the contents of the tubes with a commercially available apparatus that pierces tubes from the bottom (Isco model 69-3873-007). This allows a solution of the high-density Fluorinert™ FC40 (3M) liquid to be pumped into the bottom of the tubes, pushing the tube contents out to

a fraction collector. Especially within a glovebox, we have found this collection procedure to be more reliable and less user-dependent than manually puncturing the side of the tubes.

5. CHARACTERIZATION OF MITOCHONDRIA

The ability to correctly interpret spectra in biologic terms improves with the purity and functional integrity of samples. For a single metalloprotein, assessing these characteristics can be accomplished with SDS-PAGE, a functional assay (e.g., monitoring an enzyme activity) and protein and metal concentration determinations. In contrast, mitochondria contain ~800 proteins, each with a different molecular-level function (some of which are unknown), two aqueous compartments and two membranes, each with distinct composition, and a large number of metabolites and ions, only a portion of which have been identified. Given this, establishing the purity and function of an organelle at the same level of rigor vis-à-vis a metalloprotein is simply not possible. A useful, although limited, approach is to perform Western blots that use antibodies of a few sample proteins known to be present in the mitochondria and of a few proteins that are known to be present in common contaminants (e.g., endoplasmic reticulum) (Diekert *et al.*, 2001). By comparing the intensity of spots from these proteins in mitochondrial extracts to those found in crude cell extracts, it is possible to evaluate the relative purity of those proteins in the mitochondrial extract. MitotrackerTM (Molecular Probes) is a fluorescent dye that selectively accumulates in mitochondria, and it is commonly used to identify the organelle and assess membrane integrity. Electron microscopy can be used to qualitatively assess the purity of samples (e.g., the size and hue distributions of objects in a field). O₂ consumption ability and coupling ratio provide simple assays to assess an important mitochondrial function.

6. DETERMINING THE ABSOLUTE [Fe] AND [PROTEIN] IN MITOCHONDRIA

In contrast to working with protein solutions, isolated mitochondria in buffered aqueous solutions form turbid milky suspensions of variably sized clumps of mitochondrial particles. These properties render protein and iron concentration determinations difficult and less reliable than similar determinations of, for example, metalloprotein solutions. We have addressed these difficulties by packing mitochondria into a custom-designed graduated cylinder (an insert for an SW 32 Ti rotor tube) and measuring their volume (Hudder *et al.*, 2007). We have performed an experiment that

uses radiolabeled sucrose to determine the percentage of mitochondria in those volumes (see below). Packed material was quantitatively transferred into another tube (containing protein-determination reagent or acid), keeping track of the fold dilution. The protein or metal concentration of the final solution was measured, and the protein or metal concentration in isolated or “neat” mitochondria was calculated.

In the radiolabeled sucrose experiment, pelleted mitochondria from wild-type (WT) fermenting cells were suspended in a volume (V_{stock} , Table 15.1) of a stock solution of ^{14}C -labeled sucrose (American Radiolabeled Chemicals, 625 mCi/mol) with counts per min of radioactivity per ml given as C_{stock}^* in Table 15.1. The suspension was centrifuged (10,000g for 1 hr), the supernatant was removed, and its volume (V_{super}) and the amount of radioactivity contained therein (C_{super}^*) were quantified. The volume of the pellet (V_{pellet}), assumed to consist of mitochondria and excluded buffer, was also determined. Thus, $V_{pellet} = V_{mitos} + V_{buffer}$. Assuming that none of the radioactivity penetrated the mitochondria, the relationship $C_{stock}^* V_{stock} = C_{super}^* (V_{super} + V_{buffer})$ should hold. This equation was solved for V_{buffer} , allowing us to determine V_{mito}/V_{pellet} from the previous equation. We have published a similar experiment for mitochondria isolated from respiring yeast cells (Hudder *et al.*, 2007) and obtained $V_{mito}/V_{pellet} = 0.79$. Here we report that for mitochondria isolated from fermenting yeast, $V_{mito}/V_{pellet} = 0.84$ (average of five trials, with a standard deviation of ± 0.1). The relative error in the two sets of values is substantial such that there is no significant difference between them. In subsequent calculations, we assume that our pellets consist of 82% mitochondria (and 18% buffer). This number undoubtedly depends on the g-force and time used in packing, so it should be applied cautiously when other packing conditions are used. Taking the presence of excluded buffer into account, we estimated the concentrations of Fe and protein in respiring mitochondria to be $800 \pm 200 \mu\text{M}$ and $70 \pm 20 \text{ mg/ml}$, respectively (Hudder *et al.*, 2007).

Table 15.1 Volumes and radioactivity used to determine the percentage of mitochondria in packed samples

C_{stock}^* (cpm/ml)	V_{stock} (ml)	C^* (cpm/ml)	V_{super} (ml)	V_{buffer} (ml)	V_{pellet} (ml)	V_{mito}/V_{pellet}
1,574,600	0.6	857,500	0.96	0.14	0.819	0.83
111,420	0.5	109,750	0.45	0.058	0.613	0.90
10,975	0.4	10,848	0.37	0.035	0.405	0.91
10,975	0.5	8,849	0.45	0.17	0.521	0.67
4,448	0.5	4,390	0.47	0.037	0.405	0.91

7. PACKING SAMPLES INTO SPECTROSCOPY HOLDERS

To maximize the spectral intensity of isolated mitochondrial samples, we pack the organelle by centrifugation into spectroscopy sample holders. Mössbauer sample holders consist of hollowed Delrin cylinders with an external height of 10 mm and an external diameter of 12.5 mm (Fig. 15.3A). The wall thickness tapers from 0.8 mm at the top to 2.4 mm at the bottom to minimize the amount of sample required. Two opposing 0.5-mm diameter holes are drilled in the walls of the cylinder approximately 1 mm from the top. A Lexan insert for the SW 32 Ti rotor was designed such that the sample holders, with fishing line threaded through the holes, can be inserted and pushed to the bottom of the hollowed-out region in the insert. The ends of the line are affixed to the outer walls of the insert with tape. Once assembled into the tube, the insert is filled with a suspension of ^{57}Fe -enriched mitochondria, and the assembly is centrifuged (10,000g; RCF (avg) for 1 h). After spinning, the buffer is removed, and the Mössbauer holder, now packed with mitochondria, is removed by pulling the line. Finally, the line is removed and the sample is frozen in a liquid- N_2 -cooled aluminum block that is brought into the glovebox to ensure anaerobicity while freezing.

Samples are packed into modified EPR tubes in a similar manner. We constructed another insert (out of Teflon or Lexan) for the rotor that fits a short EPR tube (Fig. 15.3B). Thick-walled Supracil quartz tubes (5 mm OD \times 77-mm long; 0.8-mm wall thickness; cut from Wilmad 721-PQ7 0 EPR tubes) are loaded into the insert and filled with a mitochondrial suspension. The assembly is spun (10,000g) for 1 h, which is sufficient for the mitochondrial particles to pellet to the bottom of the tube. A thin metal rod is used to lift the EPR tube, with packed mitochondria at the bottom, out of the insert, and the supernatant is removed. Samples are then sealed with a rubber septum, removed from the anaerobic box, and slowly frozen in liquid N_2 from the bottom of the tube before removing the septum.

EPR spectra are obtained with an Oxford Instruments ESR910 cryostat. However, doing so requires a special device for inserting and removing short EPR tubes into/out of the cryostat. The spring on one end of the device that we designed (Fig. 15.4) is compressed by twisting and then inserted into the top of the shortened EPR tubes. Then the spring is allowed to relax, which causes its diameter to expand slightly. In this state, the sample, located at the end of the assembly, can be safely lowered into the cryostat. After spectra are obtained, the assembly can be removed, and the loading device can be detached by compressing the spring and sliding the tube out. The loader works well except that the spring is powerful and can easily crack EPR tubes if inadvertently wound in the wrong direction.

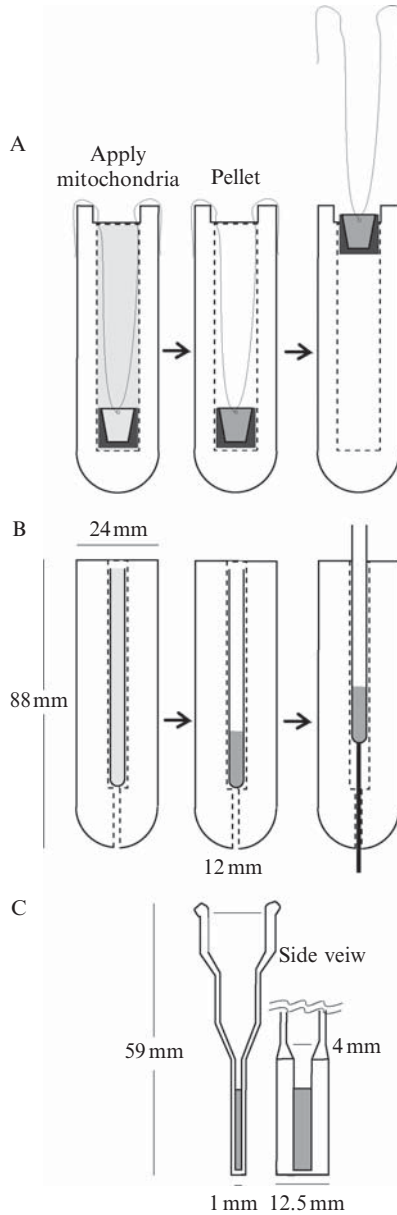


Figure 15.3 Inserts for packing samples for Mossbauer (A), EPR (B), and electronic absorption (C) spectroscopic analyses. See text for details.

In some applications, it is desirable to use the same sample for both Mössbauer and EPR studies. This requires the use of a Mössbauer “crusher” (Fig.15.5). Besides lessening the quantity of sample needed for biophysical

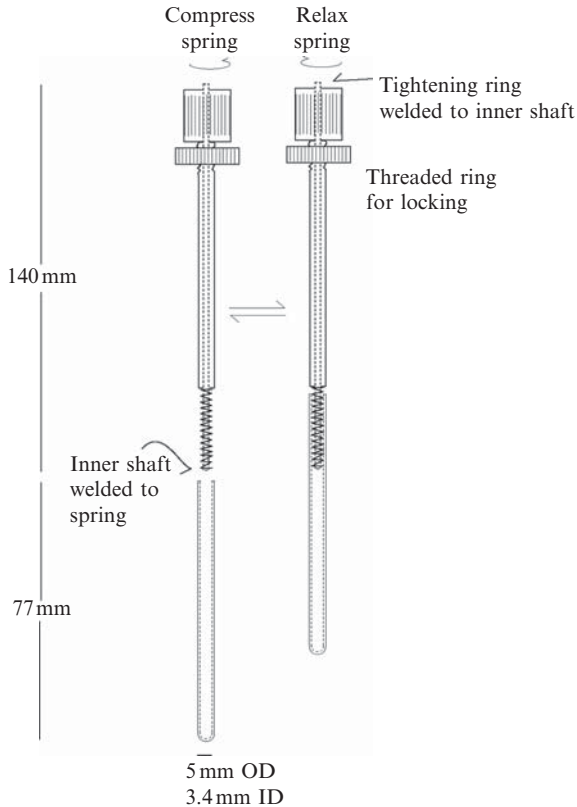


Figure 15.4 EPR tube loader. Short EPR tubes are attached to the loader so that they can be inserted into (and, more importantly, reliably removed from) a standard Oxford Instruments EPR helium cryostat (e.g., models ESR900 or ESR910). The mostly brass loader consists of a spring (Century Spring Corp, model BB-83) through which is passed an inner shaft. One end of the shaft is welded to the distal end of the spring, the other to the top of a knurled knob. The proximal end of the spring is welded to one end of an outer tube; the other end of that tube is attached to the bottom of the knurled knob. In this way, the spring can be compressed by twisting the knurled knob relative to the outer shaft. A threaded ring can be tightened against the knurled knob to lock the spring in the compressed state. This compression narrows the diameter of the spring slightly such that it can be inserted into the EPR tube. Once inserted, the spring is relaxed (by unlocking the threaded ring), resulting in an EPR tube that is securely attached to the loader.

analysis, this procedure allows EPR and Mössbauer spectra to be collected on exactly the same sample (which connects the analyses of both spectra more tightly together). The disadvantage is that the sample particles are not uniformly packed into the EPR tube such that spin concentrations cannot be quantified as accurately as when separate matching EPR and Mössbauer samples are prepared.

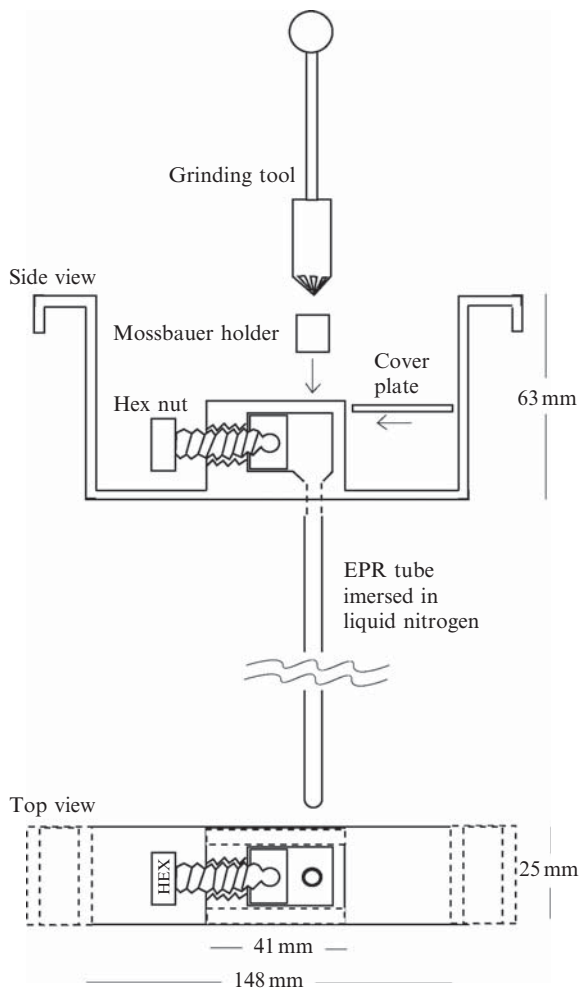


Figure 15.5 Mössbauer cup crusher. This stainless steel device is used to transfer material from a Mössbauer cup to an EPR tube while maintaining the sample at temperatures at or near that of liquid N_2 (77 K). A standard EPR tube is attached with a short piece of rubber tubing to the bottom opening, and the unit is placed into a liquid N_2 Dewar (preferably steel rather than glass, for reasons of safety) filled with LN_2 . The frozen Mössbauer cup is dropped into the chamber (see vertical arrow), and a cover plate is slid over the chamber (see horizontal arrow). The hex nut is tightened with a wrench until a sound indicates that the Delrin cup has cracked. The chamber is opened, the Delrin remnants are removed with forceps, and a precooled grinding tool is used to pulverize the sample. A stainless steel rod (not shown) is used to pack particles into the EPR tube. Finally, a small quantity of glass wool is stuffed into the EPR tube, such that the particles do not blow out of the tube once it is removed from the Liquid N_2 .

We do not pack mitochondria into quartz UV-vis cuvettes for analysis by electronic absorption spectroscopy (our one attempt broke an expensive cuvette). Rather, we pack samples in an EPR tube, mark the tube so that the volume of the packed material can be determined, then transfer the material into the UV-vis cuvette after resuspending it in a minimum of added buffer, keeping track of the fold dilution. The spectrometer used for these studies (Hitachi model U3310 with a Head-On photomultiplier tube) allows use of highly turbid samples such as mitochondrial suspensions. The 1-mm pathlength quartz cuvettes (custom made by NSG Precision Cells) are designed to minimize the volume required and to allow spectra to be obtained under anaerobic conditions (Fig. 15.3C). Samples are loaded in the glovebox and sealed with a rubber septum (Sigma-Aldrich cat. number Z554057) before removing it from the box. The optimal dimensions of the cuvette will depend on the size and position of the light beam in the instrument used. In our system, cuvettes are placed on a Delrin stand within the sample chamber of the instrument to raise the cuvette approximately 3 mm. This places the light beam near the bottom of the cuvette, allowing sample volumes of as little as $\sim 50 \mu\text{l}$ to be used.

There are advantages for use of the same packing technology for all three spectroscopic methods. First, packing mitochondria into sample holders maximizes the intensity of the signals obtained; this is critical, because mitochondria cannot be concentrated extensively as can solutes in solution. Second, packing provides a means of accurately determining analytical properties (protein or Fe concentration) for a suspension of particles that settle with time. Third, the concentration of mitochondria in packed samples should be constant, allowing results from one spectroscopy (and from one batch of mitochondria) to be easily compared with those from another spectroscopy and/or batch.

8. ADVANCES WITH THIS APPROACH

Our first study involved mitochondria from respiring wild-type yeast cells under as-isolated, dithionite-reduced, and O_2 -oxidized states (Hudder *et al.*, 2007). As mentioned previously, we determined that the concentration of Fe in mitochondria is $\sim 800 \mu\text{M}$. As shown in (Fig. 15.6) most of this Fe is found as Fe_4S_4 clusters, followed by nonheme high-spin (HS) mononuclear Fe^{2+} ions, Fe_2S_2 clusters, and heme groups. One surprise was the large portion of Fe present as nonheme mononuclear magnetically isolated Fe^{2+} ions, corresponding to $\sim 160 \mu\text{M}$, an order-of-magnitude higher than previous estimates on the basis of fluorescence (Rauen *et al.*, 2007). We are currently evaluating whether a significant portion of this Fe is adventitiously bound to the organelle during isolation or whether most is contained within the organelle and functions therein. Determining this may help reveal the

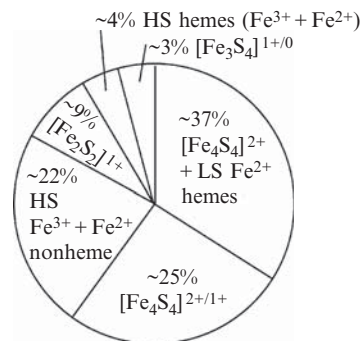


Figure 15.6 Iron-ome of mitochondria isolated from respiring yeast. Adapted from Hudder *et al.* (2007).

origin of the reactive oxygen species (ROS) generated by mitochondria. Substantial evidence points to the respiratory complexes as the generator of ROS (Balaban and Nemoto, 2005), but mononuclear Fe^{2+} complexes are established ROS generators (Gutteridge, 1984). If such species are present within the mitochondria at high concentration, the role they play in cellular ROS generation might be greater than previously assumed. We caution readers that the first step in investigating this hypothesis is to determine whether these HS Fe^{2+} ions are artifactual or not; this is one of our current research directions.

Our second study (Miao *et al.*, 2008) focused on the Fe that accumulates in the mitochondria of yeast cells that are depleted in Yah1p, a ferredoxin known to play a role in Fe/S cluster assembly. Before this study, neither the type of Fe that accumulates nor the mechanism of accumulation had been established. With the approach described earlier, we found that high concentrations (~ 6 mM) of 2- to 4-nm ferric nanoparticles accumulate in these mitochondria. These particles could be reduced by treatment with dithionite, forming HS Fe^{2+} ions, most of which are passed out of the organelle. Cells grown under an argon atmosphere did not accumulate Fe, suggesting that the O_2 present during normal cell growth oxidizes $\text{Fe}^{2+} \rightarrow \text{Fe}^{3+}$ ions that then precipitate.

The two studies may be related, in that the mononuclear HS Fe^{2+} ion observed as magnetically isolated species in wild-type (WT) mitochondria may be the feedstock used in Fe/S cluster assembly and heme biosynthesis. The corresponding high-spin mononuclear ferric ions in WT mitochondria do not accumulate as ferric nanoparticles, even on exposure to O_2 . In contrast, oxidized Fe^{3+} ions precipitate in yah1p-depleted cells. We are currently examining why oxidization leads to aggregation in one case but not in the other. One intriguing possibility is that the mononuclear Fe ions in WT cells are coordinated by a ligand that “protects” these ions from precipitation and that yah1p-depleted cells do not contain this ligand (or do not contain enough of it).



9. SUMMARY

We have developed methods for isolating large quantities of yeast mitochondria and analyzing such samples with Mössbauer, EPR, electronic absorption spectroscopy, and inductively coupled plasma emission mass spectrometry. Perhaps the most unique aspect of our method is to perform the isolation procedure under strict anaerobic conditions. We do this to: (1) avoid O_2 -dependent inactivation of certain Fe-containing mitochondrial enzymes; (2) prevent general oxidative damage to mitochondrial membranes and proteins; and (3) control the redox state of the Fe-containing components within the organelle. Large quantities of mitochondria are required by the spectroscopic tools that we use; we pack samples into the spectroscopy sample holders to maximize signal intensities. In scaling-up the isolation procedure, we have standardized the homogenization process by designing and using a mechanical homogenizer. We also fractionate samples obtained from the discontinuous density gradient step. We determine analytical parameters (protein and metal concentration) starting with the packed state, minimizing the problems of determining the concentration of turbid particulate species like mitochondria that are suspended but not dissolved in solutions.

These are relatively recent developments, and we are still exploring new ways of better resolving the iron-ome of mitochondria. It is clear that with our current integrated biophysical approach, we can never match the resolution achievable by true -omic methods. Nevertheless, it is also clear, even at this early stage in our investigations, that our ability to evaluate the iron-ome of mitochondria is dramatically improved by use of these methods. Although further studies are required to establish this, we may have discovered a metabolic pool of HS Fe^{2+} ions that plays important roles in Fe/S cluster assembly and heme biosynthesis, in the aggregation of Fe, and perhaps in generating ROS. Our ability to test these intriguing possibilities further will require improving and refining our approach (i.e., *ironing out* current difficulties and challenges).

ACKNOWLEDGMENTS

We thank the Robert A. Welch Foundation (A-1170) for supporting the studies reported here. We also thank our collaborators in this project, including Eckard Münck, Roland Lill, Michael P. Hendrich, E. Ann Ellis, Hansoo Kim, and the Texas A&M University Chemistry department machine shop for help in the design and construction of the equipment described here, including Tony Montalbano, Kenneth Greer, William Seward, and Carl Johnson.

REFERENCES

- Agar, J. N., Krebs, C., Frazzon, J., Huynh, B. H., Dean, D. R., and Johnson, M. K. (2000). IscU as a scaffold for iron-sulfur cluster biosynthesis: Sequential assembly of [2Fe-2S] and [4Fe-4S] clusters in IscU. *Biochemistry* **39**, 7856–7862.
- Balaban, R. S., and Nemoto, S. (2005). Mitochondria, oxidants, and aging review. *Cell* **120**, 483–495.
- Beinert, H. (2002). Spectroscopy of succinate dehydrogenase, a historical perspective. *Biochim. Biophys. Acta* **1553**, 7–22.
- Chance, B., and Willams, G. R. (1955). Simple and rapid assay of oxidative phosphorylation. *Nature* **175**, 1120–1121.
- Diekert, K., deKroon, A. I. P. M., Kispal, G., and Lill, R. (2001). Isolation and subfractionation of mitochondria from the yeast *Saccharomyces cerevisiae*. *Methods Cell Biol.* **65**, 37–51.
- Glick, B. S., and Pon, L. A. (1995). Isolation of highly purified mitochondria from *Saccharomyces cerevisiae*. *Methods Enzymol.* **260**, 213–223.
- Gutteridge, J. M. C. (1984). Ferrous ion-EDTA-stimulated phospholipid peroxidation. *Biochem. J* **224**, 697–701.
- Haile, D. J., Rouault, T. A., Harford, J. B., Kennedy, M. C., Blondin, G. A., Beinert, H., and Klausner, R. D. (1992). Cellular regulation of the iron responsive element binding protein—Disassembly of the cubane iron-sulfur cluster results in high-affinity RNA binding. *Proc. Natl. Acad. Sci. USA* **89**, 11735–11739.
- Hartl, F. U., Pfanner, N., Nicholson, D. W., and Neupert, W. (1989). Mitochondrial protein import. *Biochim. Biophys. Acta* **988**, 1–45.
- Hartzell, C. R., and Beinert, H. (1976). Oxido-reductive titrations of cytochrome c oxidase followed by EPR spectroscopy. *Biochim. Biophys. Acta* **423**, 323–338.
- Henze, K., and Martin, W (2003). Evolutionary biology: Essence of mitochondria. *Nature* **426**, 127–128.
- Hudder, N., Morales, J. G., Stubna, A., Münck, E., Hendrich, M. P., and Lindahl, P. A. (2007). Electron paramagnetic resonance and Mössbauer spectroscopy of intact mitochondria from respiring *Saccharomyces cerevisiae*. *J. Biol. Inorg. Chem.* **12**, 1029–1053.
- Katan, M. B., Pool, L., and Groot, G. S. P. (1976). Cytochrome bc₁ complex of yeast mitochondria—Isolation and partial characterization of cytochrome bc₁ complex and cytochrome b. *Eur. J. Biochem.* **65**, 95–105.
- Lill, R., and Kispal, G. (2000). Maturation of cellular Fe-S proteins: an essential function of mitochondria. *Trends Biochem. Sci.* **25**, 352–356.
- Miao, R., Martinho, M., Morales, J. G., Kim, H., Ellis, E. A., Lill, R., Hendrich, M. P., Münck, E., and Lindahl, P. A. (2008). EPR and Mössbauer Spectroscopy of intact mitochondria isolated from Yah1p-depleted *Saccharomyces cerevisiae*. *Biochemistry* **47**, 9888–9899.
- Mühlenhoff, U., and Lill, R. (2000). Biogenesis of iron-sulfur proteins in eukaryotes: A novel task of mitochondria that is inherited from bacteria. *Biochim. Biophys. Acta Bioenergetics* **1459**, 370–382.
- Mühlenhoff, U., Richhardt, N., Gerber, J., and Lill, R. (2002). Characterization of iron-sulfur protein assembly in isolated mitochondria—A requirement for ATP, NADH, and reduced iron. *J. Biol. Chem.* **277**, 29810–29816.
- Münck, E. (1978). Mössbauer spectroscopy of proteins: Electron carriers. *Methods Enzymol.* **54**, 346–379.
- Münck, E., Surerus, K. K., and Hendrich, M. P. (1993). Combining Mössbauer spectroscopy with integer spin electron paramagnetic resonance. *Methods Enzymol.* **227**, 463–479.

- Ollagnier-de-Choudens, S., Mulliez, E., and Fontecave, M. (2002). The PLP-dependent biotin synthase from *Escherichia coli*: Mechanistic studies. *FEBS Let.* **532**, 465–468.
- Ollagnier-de-Choudens, S., and Fontecave, M. (1999). The lipoate synthase from *Escherichia coli* is an iron-sulfur protein. *FEBS Let.* **453**, 25–28.
- Ragan, C. I. (1976). NADH-ubiquinone oxidoreductase. *Biochim. Biophys. Acta* **456**, 249–290.
- Rauen, U., Springer, A., Weisheit, D., Petrat, F., Korth, H.-G., deGroot, H., and Sustmann, R. (2007). Assessment of chelatable mitochondrial iron by using mitochondrion-selective fluorescent iron indicators with different iron-binding affinities. *Chem. Biochem.* **8**, 341–352.
- Sands, R. H., and Beinert, H. (1960). Studies on mitochondria and submitochondrial particles by paramagnetic resonance (EPR) spectroscopy. *Biochem. Biophys. Res. Comm.* **3**, 47–52.
- Trumppower, B. L., and Edwards, C. A. (1979). Purification of a reconstitutively active iron-sulfur protein (oxidation factor) from succinate cytochrome c reductase complex of bovine heart mitochondria. *J. Biol. Chem.* **254**, 8697–8706.
- Tzagoloff, A., and Myers, A. M. (1986). Genetics of mitochondrial biogenesis. *Ann. Rev. Biochem.* **55**, 249–285.
- Vo, T. D., and Palsson, B. O. (2007). Building the power house: Recent advances in mitochondrial studies through proteomics and systems biology. *Am. J. Physiol. Cell Physiol.* **292**, C164–C177.

THE USE OF FLUORESCENCE CORRELATION SPECTROSCOPY TO PROBE MITOCHONDRIAL MOBILITY AND INTRAMATRIX PROTEIN DIFFUSION

Peter H. G. M. Willems,^{*,†} Herman G. Swarts,^{*} Mark A. Hink,[‡]
and Werner J. H. Koopman^{*,†}

Contents

1. Introduction	288
2. Principle of Fluorescence Correlation Spectroscopy	289
3. Performing FCS Experiments with mitoEYFP In Human Skin Fibroblasts	292
3.1. Cell culture	292
3.2. Baculoviral transfection	292
3.3. Calibration of the FCS setup	292
3.4. Performing mitochondrial FCS recordings	294
3.5. Data analysis	294
3.6. Data interpretation	297
References	299

Abstract

Within cells, functional changes in mitochondrial metabolic state are associated with alterations in organelle mobility, shape, and configuration of the mitochondrial matrix. Fluorescence correlation spectroscopy (FCS) is a technique that measures intensity fluctuations caused by single fluorescent molecules moving through a small detection volume. By mathematically correlating these fluctuations, information can be obtained about the concentration and rate of diffusion of the fluorescent molecules. Here we present an FCS-based approach for determining the mobility of enhanced yellow fluorescent protein (mitoEYFP) in

* Department of Biochemistry, Nijmegen Centre for Molecular Life Sciences, Radboud University Nijmegen Medical Centre, Nijmegen, The Netherlands

† Microscopical Imaging Centre, Nijmegen Centre for Molecular Life Sciences, Radboud University Nijmegen Medical Centre, Nijmegen, The Netherlands

‡ Max Planck Institute for Molecular Physiology, Dortmund, Germany

the mitochondrial matrix of primary human skin fibroblasts. This protocol allows simultaneous quantification of intramatrix EYFP concentration and its diffusion constant, as well as the fraction of moving mitochondria and their velocity.

1. INTRODUCTION

In addition to their “classical” function as ATP generators, mitochondria play crucial roles in apoptosis, reactive nitrogen- and oxygen species-generation (RNS/ROS), transduction of electrical signals, and calcium homeostasis (Duchen *et al.*, 2008; Koopman *et al.*, 2007a; Willems *et al.*, 2008). Changes in the functional state of mitochondria are paralleled by alterations in the configuration of the mitochondrial matrix (Amchenkova *et al.*, 1988; Benard and Rossignol, 2008; Frey and Mannella, 2000; Gottlieb *et al.*, 2003; Hackenbrock, 1966; Halestrap, 1989; Koopman *et al.*, 2007a; Mannella, 2006; Scalettar, 1991). It has been suggested that, because of its high protein content, the mitochondrial matrix constitutes the most crowded aqueous compartment of the cell (Jakobs, 2006). However, evidence obtained by fluorescence recovery after photobleaching (FRAP) analysis of matrix-targeted GFP and GFP-tagged tricarboxylic acid cycle (TCA) enzymes revealed that endogenous mitochondrial proteins are bound to the mitochondrial inner membrane (MIM) and, therefore, matrix protein diffusion is as fast as in the cytosol (Haggie and Verkman, 2002; Partikian *et al.*, 1998; Verkman, 2002). Depending on metabolic state, the mitochondrial matrix can assume two extreme configurations in which it either has a large (orthodox state) or small (condensed state) volume. As a consequence, the rate of any biochemical process that is diffusion-limited will be altered, independent of whether this process involves large molecules, small molecules, or both (Ellis, 2001). Therefore, changes in matrix protein diffusion can have profound effects on the rate of metabolic reactions occurring in this compartment, and theoretical evidence suggests that mitochondria may regulate the dynamics of interior reaction pathways (e.g., the Krebs cycle) by shape and volume changes (Lizana *et al.*, 2008).

Given the intricate connections between mitochondrial and cellular functioning, it is important that physiological analysis of mitochondrial protein diffusion is carried out within living cells. This necessitates selective staining of the mitochondrial matrix with a fluorescent reporter molecule followed by subsequent monitoring of its mobility by a noninvasive technique. Proper quantification of intramatrix solute diffusion furthermore requires that the fluorescent reporter does not bind to mitochondrial membranes and/or matrix constituents. The latter requirement prevents use of well-known mitochondria-specific fluorescent cations like rhodamine 123 (Koopman *et al.*, 2006; Scaduto Jr. and Grottyohann, 1999). Therefore, the inert green fluorescent protein (GFP) and/or its spectral variants have been

widely applied (Haggie and Verkman, 2002; Koopman *et al.*, 2007b, 2008a; Partikian *et al.*, 1998; Verkman, 2002). An additional challenge is the small size of the mitochondrial compartment, which is close to the resolution limit of light microscopy (Partikian *et al.*, 1998). This means that high-resolution optical sectioning (confocal) microscopy is required to properly analyze intramatrix diffusion.

With human primary skin fibroblasts as a model, we recently developed an approach in which EYFP is specifically expressed in the mitochondrial matrix (mitoEYFP) using baculoviral transfection (Koopman *et al.*, 2007b, 2008a). Subsequently, the diffusion properties of mitoEYFP are assessed with fluorescence correlation spectroscopy (FCS). The latter is an optical technique with single-molecule sensitivity that extracts information from fluctuations in molecule concentrations within the confocal measuring volume (Elson *et al.*, 2001; Enderlein *et al.*, 2004; Haustein and Schwillie, 2007; Hink and Visser, 1999; Hink *et al.*, 2000; Visser and Hink, 1999). Importantly, in contrast to the photobleaching approach used previously (Haggie and Verkman, 2002; Partikian *et al.*, 1998; Verkman, 2002) FCS requires only minute amounts of fluorescent proteins, making it well suited to collect data under physiological conditions (Jakobs, 2006). In the following we provide an introduction to the FCS technique and a detailed description of its use to quantify intramatrix protein diffusion and concentration, as well as mitochondrial mobility.

2. PRINCIPLE OF FLUORESCENCE CORRELATION SPECTROSCOPY

Fluorescence correlation spectroscopy (FCS) is a technique that measures fluorescence fluctuations in an open volume element created by a focused laser beam. When a fluorescent molecule enters the confocal volume, it will be excited, and a burst of fluorescence photons will be generated. When the molecule diffuses out of the excitation cavity, the process can be repeated, either by back-diffusion of the same molecule or by another entering molecule (Hink and Visser, 1999). Fluorescence intensity fluctuations are measured with a fast and sensitive photodetector like an avalanche photodiode. The time that a single molecule resides inside the detection volume depends on the mobility of the molecule and on the dimensions of the detection volume. This means that reliable quantification of mobility requires a detection volume with a fixed size, which is determined by the choice of the magnifying objective. The shape of a 3-D Gaussian-shaped detection volume is essentially ellipsoid and its volume (V_{gauss}) is given by:

$$V_{gauss} = \pi^{3/2} \cdot r_{xy}^2 \cdot r_z \quad (16.1)$$

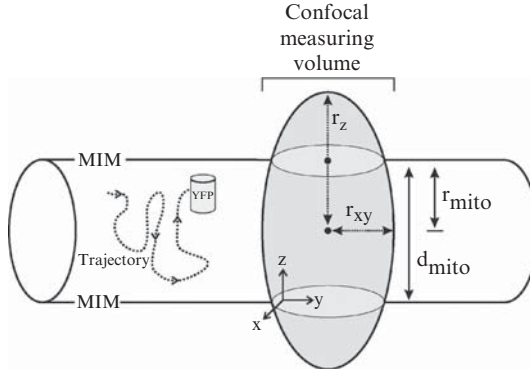


Figure 16.1 Principle of mitochondrial fluorescence correlation spectroscopy. FCS measures fluorescence intensity fluctuations caused by the entry and exit of fluorophores into a small confocal measuring volume (grey oval). This volume has constant radii in the axial (r_z) and radial direction (r_{xy}) and, therefore, a fixed volume. By auto-correlating the intensity fluctuations and fitting the obtained autocorrelation function (ACF) by a suited model, the diffusion constant(s) and concentration of the fluorophore can be determined. For quantifying lateral diffusion of mitoEYFP (dotted line), which diffuses within the boundaries of the mitochondrial inner membrane (MIM), it is important to consider the radius (r_{mito}) and diameter (d_{mito}) of the mitochondrion to select the proper model for fitting. This is because the confocal measuring volume might be confined by the MIM (grey oval).

With r_{xy}^2 and r_z^2 representing the size of the measuring volume in the radial and axial direction, respectively (Fig. 16.1). The intensity detection function from this ellipsoid volume is given by:

$$I(x, y, z) = I\sigma\phi_f\kappa \cdot \exp\left(\frac{-2(x^2 + y^2)}{r_{xy}^2} - \frac{2z^2}{r_z^2}\right) \quad (16.2)$$

With I as the maximal intensity of the laser beam, σ as the optical absorption cross section, ϕ_f as the quantum yield of the fluorophore, κ as the maximum value of the light-collecting efficiency, x and y represent the radial coordinates, and z is the axial coordinate (Vukojević *et al.*, 2005). Because the relative fluorescence fluctuations increase as the number of fluorescent particles $\langle N \rangle$ decreases, it is important to perform experiments with a minimum amount of fluorescent molecules. For live cell FCS, the optimal concentration range of fluorescent molecules lies between ~ 200 pM and ~ 1000 nM (Brock *et al.*, 1999; Enderlein, 2004; Haustein and Schwille, 2003; Hink and Visser, 1999; Levin and Carson, 2004; Lippincott-Schwartz *et al.*, 2001; Visser and Hink, 1999).

A key parameter describing protein mobility is its translational diffusion coefficient (D_{tran} ; Haggie and Verkman, 2002; Hink *et al.*, 2000; Lippincott-Schwartz *et al.*, 2001; Partikian *et al.*, 1998; Verkman, 2002). This parameter can be determined from the autocorrelation function $G(\tau)$, which is related to the fluctuations of the fluorescence intensity. In our experiments, intensity fluctuations were software correlated, and individual autocorrelations were displayed on-line. The autocorrelation function (ACF) describing j independent molecular species diffusing freely in a 3-D Gaussian-shaped observation volume is given by:

$$G(\tau) = 1 + \frac{1}{\langle N \rangle} \times \frac{1 - T + T e^{-\tau/\tau_{kin}}}{(1 - T)} \times \sum_j \frac{F_j}{\left(1 + \frac{\tau}{\tau_{dif,j}}\right) \sqrt{1 + \left(\frac{r_{xy}}{r_z}\right)^2 \frac{\tau}{\tau_{dif,j}}}} \quad (16.3)$$

with $j = 1, 2, 3, \dots$ and $\sum_j F_j = 1$ (Visser and Hink, 1999). The amplitude of the ACF, $G(0)$, represents the average number of molecules $\langle N \rangle$ found in the observation volume: $G(0) - 1 = 1/\langle N \rangle$. Autofluorescent proteins like EYFP show additional fluorescence fluctuations because of conformational changes between fluorescent and dark states (Schwille *et al.*, 2000). The probability and relaxation time of the dark state are given by T and τ_{kin} , respectively. The lateral diffusion time, $\tau_{dif,j}$, describes the residence time of a particle in the observation volume. This residence time is related to the translational diffusion coefficient (D_{tran}) as follows:

$$\tau_{dif} = r_{xy}^2 / (4 \cdot D_{tran}) \quad (16.4)$$

The relationship between D_{tran} and the hydrodynamic radius of an (spherical) object in solution is given by the Stokes–Einstein relationship (Haustein and Schwille, 2007):

$$D_{tran} = \frac{kT}{6\pi\eta R_{h,i}} \quad (16.5)$$

Where η is the viscosity of the medium (in Poise), T is the temperature (in Kelvin), and k is the Boltzmann constant ($1.3806503 \times 10^{-23} \text{ m}^2 \text{ kg s}^{-2} \text{ K}^{-1}$). Finally, the molecular mass (M) of globular molecules can also be estimated from FCS measurements (Vukojević *et al.*, 2005):

$$\frac{1}{D_{tran}} \propto \frac{6\pi\eta}{kT} \sqrt[3]{M} \quad (16.6)$$

3. PERFORMING FCS EXPERIMENTS WITH MITO EYFP IN HUMAN SKIN FIBROBLASTS

3.1. Cell culture

Fibroblasts were obtained from a healthy volunteer (cell line: #5120) according to the relevant institutional review boards. During culture, a fibroblast-optimized medium is used (medium 199 with Earle's salt) supplemented with 10% (v/v) fetal calf serum, 100 IU/ml penicillin, and 100 IU/ml streptomycin (Invitrogen, Breda, The Netherlands). For combined confocal and fluorescence correlation spectroscopy (FCS), an eight-well chamber mounted on a thin ($137 \pm 2 \mu\text{m}$) borosilicate glass coverslip was used (Lab-Tek[®], Nalgen Nunc International, IL). Each well had a dimension of $0.85 \times 0.85 \times 0.9 \text{ mm}$, a surface area of 0.722 mm^2 on the coverslip and an effective working volume of $650 \mu\text{l}$. Culture chambers were kept in a humidified atmosphere (95% air, 5% CO_2 , 37°C) until $\sim 70\%$ cell confluence is reached. Before microscopy experiments, culture medium was replaced by a colorless HEPES-TRIS (HT) solution (132 mM NaCl, 4.2 mM KCl, 1 mM CaCl_2 , 1 mM MgCl_2 , 5.5 mM D-glucose and 10 mM HEPES, pH 7.4; all from Sigma Aldrich, Zwijndrecht, The Netherlands).

3.2. Baculoviral transfection

Mitochondria-targeted enhanced yellow fluorescent protein (mitoEYFP) was transiently expressed with a modified baculovirus vector containing a mammalian active promoter driving the expression of a fusion between EYFP and the targeting sequence of subunit VIII of cytochrome *c* oxidase (COX8), as described in more detail previously (Visch *et al.*, 2004). FCS measurements were performed 3 days after the onset of baculovirus transduction, when virtually all cells expressed the construct. The virus remained present in the culture medium during the entire incubation period.

3.3. Calibration of the FCS setup

Combined confocal and FCS microscopy was performed with a commercially available system (ConfoCor II[®], Carl Zeiss, Sliedrecht, The Netherlands). MitoEYFP was excited with the 514-nm line of an Ar-ion laser focused on the sample by means of an HFT 458/514 dichroic mirror and a Zeiss C-Apochromat objective (40 \times , N.A. 1.2, water immersion). Fluorescence light was guided by means of the dichroic mirror, a mirror, and a 545DF35-bandpass filter onto an avalanche photodiode. An aqueous solution of EYFP in PBS ($\sim 100 \text{ nM}$) was used to optimize the positions of the confocal

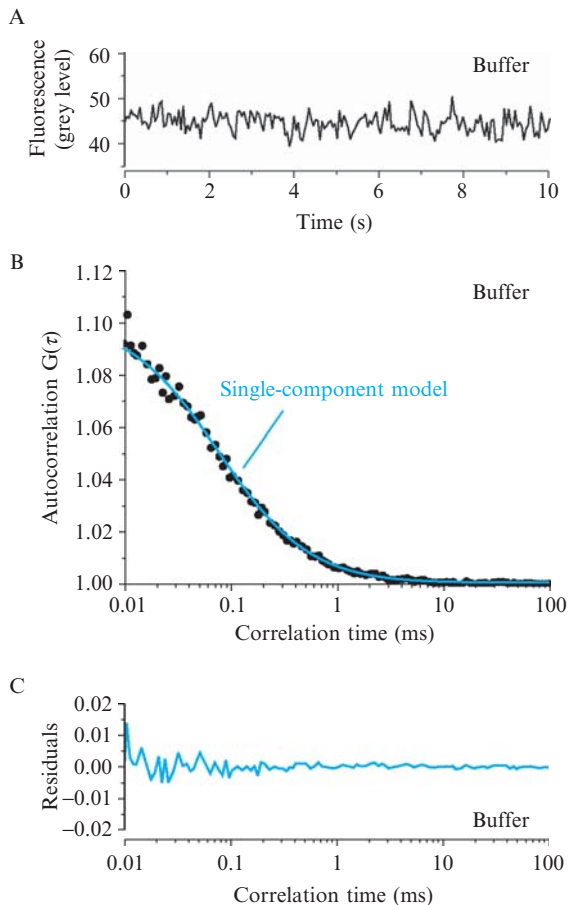


Figure 16.2 Diffusion of EYFP in PBS. To calibrate the FCS system, FCS is performed on a solution of EYFP in PBS (“Buffer”). (A) Fluorescence fluctuation recording. (B) Calculated autocorrelation curve for the fluctuations in (A) (dots) fitted with a single-component diffusion model (blue line). (C) Differences (residuals) between the calculated autocorrelation curve and the fitted model in panel B.

pinhole and the correction ring of the objective lens. Optimal settings were considered to be reached when the highest molecular brightness was observed. Next, the dimensions of the Gaussian detection volume V_{gauss} , essential for correct calculation of $\langle N \rangle$ and fluorophore concentration, were determined by recording the intensity fluctuations from an aqueous EYFP solution during 10 sec at 20 °C (Fig. 16.2A). The calculated ACF ($G(\tau)$; Fig. 16.2B; symbols) was fitted with a single-component model with equation 3 with $j = 1$ (Fig. 16.2B; blue curve). This revealed that in our experimental setup the FCS detection volume had radii of 0.253 μm and

1.37 μm in the radial (r_{xy}) and axial direction (r_z), respectively (Fig. 16.1). Substitution of these values in equation 1 yielded a V_{gauss} of 0.488 μm^3 . Because 1 μm^3 equals $1 \cdot 10^{-15}$ dm^3 , V is equivalent to $4.88 \cdot 10^{-16}$ dm^3 . The concentration (C) of the fluorophore in moles per liter is given by:

$$C = \frac{\langle N \rangle / N_A}{V_{gauss}} \quad (16.7)$$

With V_{gauss} in dm^3 and N_A being Avogadro's constant ($6.02214 \cdot 10^{23}$ mole $^{-1}$).

3.4. Performing mitochondrial FCS recordings

Before each FCS recording, mitoEYFP-expressing cells were visualized by confocal microscopy, and 3 to 6 regions of interest (ROIs) were randomly defined (Fig. 16.3A). Then, the system was switched to FCS mode, and fluorescence intensity fluctuations were acquired during 10 sec. Because each ROI was measured in succession, recordings were performed at 20 °C to minimize mitochondrial movement (Koopman *et al.*, 2006). Laser output power was limited to 20 kW/cm 2 , because the diffusion time of EGFP was distinctly shorter at higher laser intensities (Visser and Hink, 1999). For each ROI, the experimental ACF of the photodetector output was calculated on-line, allowing rapid visual inspection. Fluctuation recording from a nuclear ROI (Fig. 16.3B) followed by subsequent calculation of the ACF (Fig. 16.3C) revealed no autocorrelation. Given the single-molecule sensitivity of the FCS technique (Haustein and Schwille, 2003), this demonstrates that mitoEYFP was absent from this compartment in baculovirally transfected cells. FCS analysis of mitochondrial ROIs (Fig. 16.3D) yielded an ACFs (Fig. 16.3E) that were fitted with either a single- or two-component model according to criteria explained in the next paragraph.

3.5. Data analysis

Mitochondria moving into or out of the measuring ROI can cause progressive upward or downward changes in the fluorescence fluctuation trace that interfere with proper calculation of the ACF. In addition, reliable ACF analysis is not possible in the presence of photobleaching. Therefore, intensity recordings displaying progressive increases, decreases (>5% over the full duration of the recording) and/or high amplitude spikes in the fluorescence signal were omitted from analysis.

During fitting of the ACF, a single-component model ($j = 1$; Eq. 16.3) was evaluated first (Fig. 16.3E; blue curve). This model was considered appropriate when the residuals (Fig. 16.3F; blue curve), being the difference between the experimental and fitted ACF, did not exceed 0.05

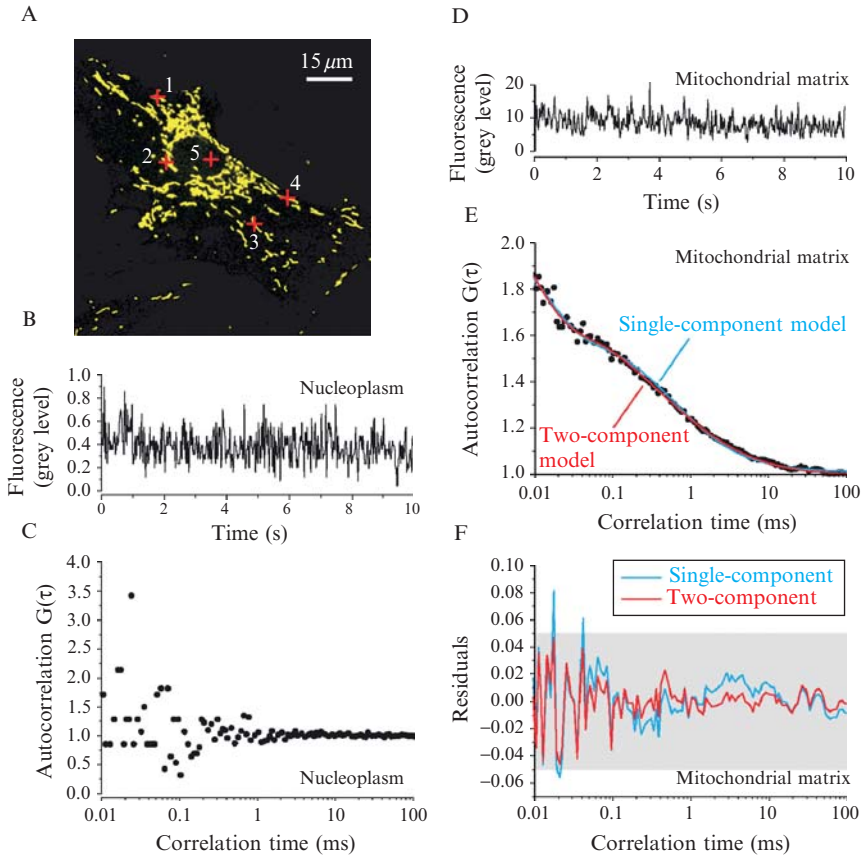


Figure 16.3 Quantification of mitoEYFP diffusion and mitochondrial movement in human skin fibroblasts. (A) Contrast optimized confocal image of a human skin fibroblast expressing mitochondria-targeted EYFP (mitoEYFP). Crosses indicate regions of interest (ROIs) used for FCS recording. ROIs were positioned on mitochondrial filaments (1 to 4) and in the nucleoplasm (5). (B) Fluorescence fluctuation recording for EYFP in the nucleoplasm. (C) Calculated autocorrelation curve for the fluctuations in (B). No autocorrelation was observed, indicating that no mitoEYFP is present in the nucleus. (D) Fluorescence fluctuation recording for mitoEYFP within the mitochondrial matrix (ROI3). (E) Calculated autocorrelation curve for the fluctuations in (D) (dots) fitted with a single-component diffusion model (blue line) and a two-component diffusion model (red line). (F) Differences (residuals) between the calculated autocorrelation curve and the fitted single-component (blue) and two-component (red) model in (E). The grey box denotes the maximal (0.05) and minimal (-0.05) residual values considered acceptable for fitting. The two-component model provides a better fit of the autocorrelation curve.

(Brock *et al.*, 1998; Hink and Visser, 1999; Hink *et al.*, 2000; Koopman *et al.*, 1999; Ruchira *et al.*, 2004; Sengupta *et al.*, 2003). When the latter was not the case, as in the example depicted in Fig. 16.3D-F, the

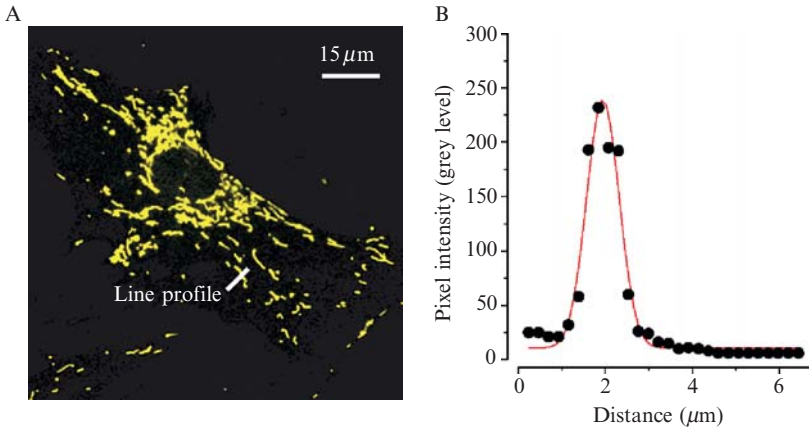


Figure 16.4 Quantification of mitochondrial diameter with a Gaussian fitting model. (A) Contrast optimized confocal image of a human skin fibroblast expressing of mitochondria-targeted EYFP (mitoEYFP). To determine mitochondrial diameter, a line was perpendicularly placed across the mitochondrion. (B) MitoEYFP fluorescence intensity of the line profile as a function of position. A Gaussian curve was fitted (line) to determine the diameter of the filament.

single-component model was rejected, and a two-component model with $j = 2$ (Fig. 16.3E; red line) was evaluated with similar criteria (Fig. 16.3F; red line). In our experiments, we observed that either a model with $j = 1$ or $j = 2$ was appropriate for fitting of the ACF curve and that both “types” of mitochondria were present within the same cell (Koopman *et al.*, 2007b, 2008a).

However, Eq. 16.3 describes the ACF of a fluorescent molecule displaying free 3-D diffusion. Within the mitochondrial matrix, diffusion of mitoEYFP occurs within the boundaries of the mitochondrial inner membrane (MIM), which confines the confocal measuring volume (Fig. 16.1). When free diffusion is confined, alternative equations can be used for proper fitting of the ACF (Gennerich and Schild, 2000). Which model to use depends on the diameter of the mitochondrion relative to the dimensions of the FCS measuring volume.

Mitochondrial diameter is assessed by measuring the intensity of a 1 pixel wide profile perpendicular to the long axis of the mitochondrial filament (Fig. 16.4A). The width (w) of this profile at its half-maximal height is determined by fitting a Gaussian curve (Fig. 16.4B; Gennerich and Schild, 2000 and supplement of Boxma *et al.*, 2005):

$$y = y_0 + \frac{A}{w\sqrt{\pi/2}} \exp\left(-2\frac{(x - x_c)^2}{w^2}\right) \quad (16.8)$$

The average mitochondrial diameter (w -value) obtained by this analysis ($0.85 \pm 0.05 \mu\text{m}$, $N = 35$; [Koopman *et al.*, 2007b](#)) was in good agreement with that determined in human dermal fibroblasts by electron microscopy ([Amchenkova *et al.*, 1988](#)). Calculating the ratio between the minimal radii of a mitochondrion oriented in the plane of focus ($0.85/2 \mu\text{m} = 0.38 \mu\text{m}$) and the FCS detection volume (see [section 3.3](#): $r_{xy} = 0.253 \mu\text{m}$; $r_z = 1.37 \mu\text{m}$), revealed values of 1.5 and 0.28 in the y - and z -direction, respectively. On the basis of these results, we evaluated the appropriate alternative ACF fitting model for confined diffusion along the y - and z -axis (Eq. 45 in [Gennerich and Schild, 2000](#)). However, this equation and [Eq. 16.3](#) fitted our experimental curves equally well, as judged from χ^2 statistics and visual inspection of the fit residuals ([Brock *et al.*, 1998](#); [Hink and Visser, 1999](#); [Hink *et al.*, 2000](#); [Koopman *et al.*, 1999](#), [Sengupta *et al.*, 2003](#)) and returned the same fit parameters ([Koopman *et al.*, 2007b, 2008a](#)). This result was confirmed by fitting simulated data that used the same parameters and noise contribution as encountered in our FCS measurements. Therefore, all ACFs were fitted with [Eq. 16.3](#). Of note, FCS was successfully used previously to determine the concentration of a GFP fusion protein in single immobilized *Escherichia coli* ([Cluzel *et al.*, 2000](#)). These bacteria have a diameter even smaller than mitochondria in control fibroblasts (0.4 to $0.7 \mu\text{m}$; [Trueba and Woldringh, 1980](#)). To determine diffusion times (τ_{dif}) ACF curves were fitted between $\tau = 0.01$ msec and $\tau = 100$ msec, a range associated with translational diffusion ([Enderlein *et al.*, 2004](#)). The fast autocorrelation decay observed at approximately $20 \mu\text{sec}$ was independent of the size of the detection volume, which could be altered by varying the pinhole diameter (data not shown) and is associated with YFP photophysics ([Schwille *et al.*, 2000](#)). However, the decay(s) present in the (sub-) millisecond region scaled with the size of the detection volume and can, therefore, be attributed to diffusion processes.

3.6. Data interpretation

In PBS (e.g., [Fig. 16.2](#)), EYFP displayed a single diffusion time (τ_{dif}) of 0.165 ± 0.04 ms ($N = 4$). Inserting this value into [Eq. 16.4](#) yielded a translational diffusion coefficient (D_{tran}) of $92.3 \pm 0.22 \mu\text{m}^2/\text{sec}$ ([Koopman *et al.*, 2007b, 2008a](#)). Inside the mitochondrial matrix, the ACF was shifted to the right ([Fig. 16.3E](#)), indicating an increased correlation time and consequent slower diffusion. In human skin fibroblasts, $\sim 20\%$ of the mitochondria showed a single mitoEYFP translational diffusion time (referred to as τ_{fast1} , equaling 0.73 ± 0.083 msec), whereas the remainder displayed two translational diffusion times (referred to as τ_{fast2} , equaling 0.89 ± 0.236 msec, and τ_{slow2} , equaling 262 ± 59.2 msec). Both “types” of mitochondria were present within one and the same cell. Calculation of D_{tran} yielded values of $22 \pm 2.1 \mu\text{m}^2/\text{sec}$ (D_{fast1} ; $N = 12$ mitochondria),

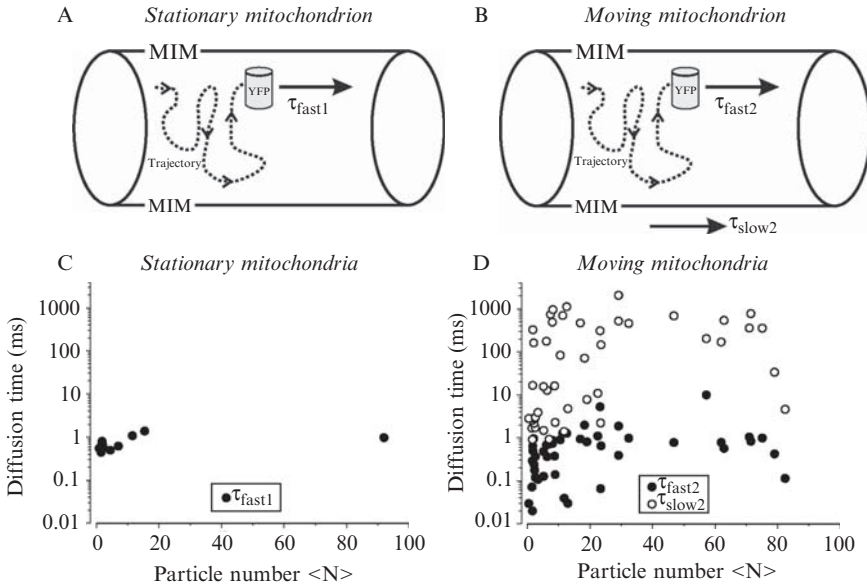


Figure 16.5 Meaning of τ_{fast1} , τ_{fast2} , and τ_{slow} and their relationship with the particle number $\langle N \rangle$. (A) A stationary mitochondrion displays a single fast diffusion time (τ_{fast1}), reflecting intramatrix EYFP diffusion. (B) Moving mitochondria display both a fast (τ_{fast2}) and slow (τ_{slow2}) diffusion time reflecting combined intramatrix EYFP diffusion and mitochondrial movement, respectively. (C) Lack of correlation between τ_{fast1} and the particle number $\langle N \rangle$ in stationary mitochondria ($N = 12$). (D) Lack of correlation between τ_{fast2} and τ_{slow2} and the particle number $\langle N \rangle$ in stationary mitochondria ($N = 46$).

$18 \pm 4.7 \mu\text{m}^2/\text{sec}$ (D_{fast2} ; $N = 46$), and $0.06 \pm 0.01 \mu\text{m}^2/\text{sec}$ (D_{slow2} ; $N = 46$). In many studies, multiple components with different diffusion times have been observed (Brock *et al.*, 1999; Haustein and Schwille, 2003; Koopman *et al.*, 1999; Nomura *et al.*, 2001; Saito *et al.*, 2003; Wachsmuth *et al.*, 2000). The fastest component usually corresponds to freely diffusing fluorophore and provides information about the diffusion constant of the protein. The slow component can arise from lateral mobility of membrane-bound proteins, translocation of proteins between subcellular compartments, directional transport along cytoskeletal components, and binding/unbinding to an immobile binding partner (Haustein and Schwille, 2003; Levin and Carson, 2004). The value of D_{slow2} equals the apparent diffusion coefficient for mitochondrial movement estimated from mitochondrial displacement plots (0.03 to 0.10 $\mu\text{m}^2/\text{sec}$; Müller *et al.*, 2005). When mitochondrial movement was abolished by nocodazole treatment (10 $\mu\text{g}/\text{ml}$; 2 h), subsequent FCS analysis demonstrated that all mitochondria displayed only a single fast mitoEYFP translational diffusion time. This means that D_{slow2} is a measure of mitochondrial velocity (Fig. 16.5B),

whereas D_{fast1} and D_{fast2} correspond to intramatrix mitoEYFP diffusion in stationary and moving mitochondria, respectively (Fig. 16.5B; Koopman *et al.*, 2007b, 2008a). For a population of mitochondria, determining the fraction of mitochondria displaying only a single fast diffusion time can be used to quantify the percentage of stationary organelles (Fig. 16.5A).

The average number of mitoEYFP molecules $\langle N \rangle$ detected in the observation volume after baculoviral transduction equaled 11.8 ± 7.41 and 21.7 ± 3.65 in stationary and moving mitochondria, respectively. Substituting these values in Eq. 16.7 yields values for [mitoEYFP] of 40.2 ± 25.2 nM (stationary mitochondria) and 73.8 ± 12.4 nM (moving mitochondria). However, Eq. 16.7 is intended to be used for a purely Gaussian detection volume. Given the fact that the mitochondrial diameter is smaller than the axial dimensions of the Gaussian volume (see Fig. 16.1), it is more appropriate to calculate the “real” confocal measuring volume (V_{cyl}) with a cylindrical approximation:

$$V_{cyl} = \pi \cdot r_{xy}^2 \cdot d \quad (16.9)$$

With d being the mitochondrial diameter. Calculation of V_{cyl} yields a value of $0.171 \mu\text{m}^2$ (equaling $1.71 \cdot 10^{-17} \text{ dm}^3$). This means that $V_{gauss}/V_{cyl} = 2.854$ and [mitoEYFP] is underestimated by a factor of 2.854 when V_{gauss} is used. With the cylindrical approximation [mitoEYFP] equaled 115 ± 72.1 nM for stationary mitochondria and 210 ± 35.3 nM for moving mitochondria. Importantly, the expression level of mitoEYFP was not related to the diffusion times for stationary (Fig. 16.5C) and moving mitochondria (Fig. 16.5D). This demonstrates that increased mitoEYFP expression does not hinder mitoEYFP diffusion.

In summary, the presented FCS approach gives life-cell quantitative information about the matrix EYFP concentration ($\langle N \rangle$), matrix protein diffusion in stationary mitochondria (D_{fast1}), matrix protein diffusion in moving mitochondria (D_{fast2}), the fraction of moving mitochondria (given by the ratio between the number of mitochondria displaying a both a D_{fast2} and D_{slow2} and the number of mitochondria displaying only a single D_{fast1}) and their velocity (D_{slow2}).

REFERENCES

- Amchenkova, A. A., Bakeeva, L. E., Chentsov, Y. S., Skulachev, V. P., and Zorov, D. B. (1988). Coupling membranes as energy-transmitting cables. I. Filamentous mitochondria in fibroblasts and mitochondrial clusters in cardiomyocytes. *J. Cell Biol.* **107**, 481–495.
- Benard, G., and Rossignol, R. (2008). Ultrastructure of the mitochondrion and its bearing on function and bioenergetics. *Antioxid. Redox Signal.* **10**, 1313–1342.

- Boxma, B., de Graaf, R. M., van der Staay, G. W., van Alen, T. A., Ricard, G., Gabaldon, T., van Hoek, A. H., Moon-van der Staay, S. Y., Koopman, W. J. H., van Hellemond, J. J., Tielens, A. G., Friedrich, T., *et al.* (2005). An anaerobic mitochondrion that produces hydrogen. *Nature* **434**, 74–79.
- Brock, R., Hink, M. A., and Jovin, T. M. (1998). Fluorescence correlation spectroscopy of cells in the presence of autofluorescence. *Biophys. J.* **75**, 2547–2557.
- Brock, R., Vamosi, G., Vereb, G., and Jovin, T. M. (1999). Rapid characterization of green fluorescent protein fusion proteins on the molecular and cellular level by fluorescence correlation microscopy. *Proc. Natl. Acad. Sci. USA* **96**, 10123–10128.
- Cluzel, P., Surette, M., and Leibler, S. (2000). An ultrasensitive bacterial motor revealed by monitoring signaling proteins in single cells. *Science* **287**, 1652–1655.
- Duchen, M. R., Verkhatsky, A., and Muallem, S. (2008). Mitochondria and calcium in health and disease. *Cell Calcium* **44**, 1–5.
- Enderlein, J., Gregor, I., Patra, D., and Fitter, J. (2004). Art and artifacts of fluorescence correlation spectroscopy. *Curr. Pharm. Biotech.* **5**, 155–161.
- Ellis, R. J. (2001). Macromolecular crowding: Obvious but underappreciated. *Trends Biochem. Sci.* **26**, 597–604.
- Elson, E. L. (2001). Fluorescence correlation spectroscopy measures molecular transport in cells. *Traffic* **2**, 789–796.
- Frey, T. G., and Mannella, C. A. (2000). The internal structure of mitochondria. *Trends Biochem. Sci.* **25**, 319–324.
- Gennerich, A., and Schild, D. (2000). Fluorescence correlation spectroscopy in small cytosolic compartments depends critically on the diffusion model used. *Biophys. J.* **79**, 3294–3306.
- Gottlieb, E., Armour, S. M., Harris, M. H., and Thompson, C. B. (2003). Mitochondrial membrane potential regulates matrix configuration and cytochrome *c* release during apoptosis. *Cell Death Differ.* **10**, 709–717.
- Hackenbrock, C. R. (1966). Ultrastructural bases for metabolically linked mechanical activity in mitochondria. I. Reversible ultrastructural changes with change in metabolic steady state in isolated liver mitochondria. *J. Cell Biol.* **30**, 269–297.
- Haggie, P. M., and Verkman, A. S. (2002). Diffusion of tricarboxylic acid cycle enzymes in the mitochondrial matrix *in vivo*. Evidence for restricted mobility of a multi enzyme complex. *J. Biol. Chem.* **277**, 40782–40788.
- Halestrap, A. P. (1989). The regulation of the matrix volume of mammalian mitochondria *in vivo* and *in vitro* and its role in the control of mitochondrial metabolism. *Biochim. Biophys. Acta* **973**, 355–382.
- Haustein, E., and Schwille, P. (2003). Ultrasensitive investigations of biological systems by fluorescence correlation spectroscopy. *Methods* **29**, 133–166.
- Haustein, E., and Schwille, P. (2007). Fluorescence correlation spectroscopy: Novel variations of an established technique. *Annu. Rev. Biophys. Biomol. Struct.* **36**, 151–169.
- Hink, M. A., and Visser, A. J. (1999). Characterization of membrane mimetic systems with fluorescence. In “Applied Fluorescence in Chemistry, Biology and Medicine” (W. Rettig, B. Strehmel, S. Schrader, and H. Seifert, eds), pp. 101–118. Springer Verlag, New York.
- Hink, M. A., Griep, R. A., Borst, J. W., van Hoek, A., Eppink, M. H., Schots, A., and Visser, A. J. (2000). Structural dynamics of green fluorescent protein alone and fused with a single chain Fv protein. *J. Biol. Chem.* **275**, 17556–17560.
- Jakobs, S. (2006). High resolution imaging of live mitochondria. *Biochim. Biophys. Acta* **1763**, 561–575.
- Koopman, W. J. H., Hink, M. A., Visser, A. J., Roubos, E. W., and Jenks, B. G. (1999). Evidence that Ca^{2+} -waves in *Xenopus* melanotropes depend on calcium-induced calcium

- release: A fluorescence correlation microscopy and line scanning study. *Cell Calcium* **26**, 59–67.
- Koopman, W. J. H., Visch, H. J., Smeitink, J. A. M., and Willems, P. H. G. M. (2006). Simultaneous, quantitative measurement and automated analysis of mitochondrial morphology, mass, potential and motility in living human skin fibroblasts. *Cytometry A* **69**, 1–12.
- Koopman, W. J. H., Verkaart, S., Visch, H. J., van Emst-de Vries, S. E., Nijtmans, L. G. J., Smeitink, J. A. M., and Willems, P. H. G. M. (2007a). Human NADH: Ubiquinone oxidoreductase deficiency: Radical changes in mitochondrial morphology? *Am. J. Physiol. Cell Physiol.* **293**, C22–C29.
- Koopman, W. J. H., Hink, M. A., Verkaart, S., Visch, H. J., Smeitink, J. A. M., and Willems, P. H. G. M. (2007b). Partial complex I inhibition decreases mitochondrial motility and increases matrix protein diffusion as revealed by fluorescence correlation spectroscopy. *Biochim. Biophys. Acta* **1767**, 940–947.
- Koopman, W. J. H., Distelmaier, F., Hink, M. A., Verkaart, S., Wijers, M., Fransen, J., Smeitink, J. A. M., and Willems, P. H. G. M. (2008a). Inherited complex I deficiency is associated with faster protein diffusion in the matrix of moving mitochondria. *Am. J. Physiol. Cell Physiol.* **294**, 1124–1132.
- Levin, M. K., and Carson, J. H. (2004). Fluorescence correlation spectroscopy and quantitative cell biology. *Differentiation* **72**, 1–10.
- Lippincott-Schwartz, J., Snapp, E., and Kenworthy, A. (2001). Studying protein dynamics in living cells. *Nat. Rev. Mol. Cell Biol.* **2**, 444–456.
- Lizana, L., Bauer, B., and Orwar, O. (2008). Controlling the rates of biochemical reactions and signaling networks by shape and volume changes. *Proc. Natl. Acad. Sci. USA* **105**, 4099–4104.
- Mannella, C. A. (2006). Structure and dynamics of the mitochondrial inner membrane cristae. *Biochim. Biophys. Acta* **1763**, 542–548.
- Müller, M., Mironov, S. L., Ivannikov, M. V., Schmidt, J., and Richter, D. W. (2005). Mitochondrial organization and motility probed by two-photon microscopy in cultured mouse brainstem neurons. *Exp. Cell Res.* **303**, 114–127.
- Nomura, Y., Tanaka, H., Poellinger, L., Higashino, F., and Kinjo, M. (2001). Monitoring of *in vitro* and *in vivo* translation of green fluorescent protein and its fusion proteins by fluorescence correlation spectroscopy. *Cytometry* **44**, 1–6.
- Partikian, A., Ölveczky, B., Swaminathan, R., Li, X., and Verkman, A. S. (1998). Rapid diffusion of green fluorescent protein in the mitochondrial matrix. *J. Cell Biol.* **140**, 821–829.
- Ruchira, Hink, M. A., Bosgraaf, L., van Haastert, P. J., and Visser, A. J. (2004). Pleckstrin homology domain diffusion in Dictyostelium cytoplasm studied using fluorescence correlation spectroscopy. *J. Biol. Chem.* **279**, 10013–10019.
- Saito, K., Ito, E., Takakuwa, Y., Tamura, M., and Kinjo, M. (2003). *In situ* observation of mobility and anchoring of PKC β in plasma membrane. *FEBS Lett.* **541**, 126–131.
- Scaduto, R. C. Jr., and Grotyohann, L. W. (1999). Measurement of mitochondrial membrane potential using fluorescent rhodamine derivatives. *Biophys. J.* **76**, 469–477.
- Scalettar, B. A., Abney, J. R., and Hackenbrock, C. R. (1991). Dynamics, structure, and function are coupled in the mitochondrial matrix. *Proc. Natl. Acad. Sci. USA* **88**, 8057–8061.
- Schwille, P., Kummer, S., Heikal, A. A., Moerner, W. E., and Webb, W. W. (2000). Fluorescence correlation spectroscopy reveals fast optical excitation-driven intramolecular dynamics of yellow fluorescent proteins. *Proc. Natl. Acad. Sci. USA* **97**, 151–156.
- Sengupta, P., Garai, K., Balaji, J., Periasamy, N., and Maiti, S. (2003). Measuring size distribution in highly heterogeneous systems with fluorescence correlation spectroscopy. *Biophys. J.* **84**, 1977–1984.

- Trueba, F. J., and Woldringh, C. L. (1980). Changes in cell diameter during the division cycle of *Escherichia coli*. *J. Bacteriology* **142**, 869–878.
- Verkman, A. S. (2002). Solute and macromolecular diffusion in cellular aqueous compartments. *Tr. Bioch. Sci.* **27**, 27–33.
- Visch, H. J., Rutter, G. A., Koopman, W. J. H., Koenderink, J. B., Verkaart, S., de Groot, T., Varadi, A., Mitchell, K. J., van den Heuvel, L. W., Smeitink, J. A. M., and Willems, P. H. G. M. (2004). Inhibition of mitochondrial Na^+ - Ca^{2+} exchange restores agonist-induced ATP production and Ca^{2+} handling in human complex I deficiency. *J. Biol. Chem.* **279**, 40328–40336.
- Visser, A. J. W.G, and Hink, M. A. (1999). New perspectives on fluorescence correlation spectroscopy. *J. Fluorescence* **9**, 81–87.
- Vukojević, V., Pramanik, A., Yakovleva, T., Rigler, R., Terenius, L., and Bakalkin, G. (2005). Study of molecular events in cells by fluorescence correlation spectroscopy. *Cell. Mol. Life. Sci.* **62**, 535–550.
- Wachsmuth, M., Waldeck, W., and Langowski, J. (2000). Anomalous diffusion of fluorescent probes inside living cell nuclei investigated by spatially-resolved fluorescence correlation spectroscopy. *J. Mol. Biol.* **298**, 677–689.
- Willems, P. H. G. M., Valsecchi, F., Distelmaier, F., Verkaart, S., Visch, H. J., Smeitink, J. A. M., and Koopman, W. J. H. (2008). Mitochondrial Ca^{2+} homeostasis in human NADH: Ubiquinone oxidoreductase deficiency. *Cell Calcium* **44**, 123–133.

TYPE II NADH: QUINONE OXIDOREDUCTASES OF *PLASMODIUM FALCIPARUM* AND *MYCOBACTERIUM TUBERCULOSIS*: KINETIC AND HIGH-THROUGHPUT ASSAYS

Nicholas Fisher, Ashley J. Warman, Stephen A. Ward, and
Giancarlo A. Biagini

Contents

1. Introduction	304
1.1. Structure and function	304
1.2. Functional role of <i>ndh</i> in the respiratory chain of <i>P. falciparum</i> and <i>M. tuberculosis</i>	305
2. Kinetic Assays	308
2.1. PfNDH2 native assay	308
2.2. PfNDH2 linked assay	309
2.3. Kinetic assays with an <i>E. coli</i> -based heterologous expression system	311
3. Endpoint Assay for HTS	315
4. Summary and Conclusions	318
Acknowledgments	318
References	319

Abstract

Type II NADH: quinone oxidoreductases (*ndh*) are flavoenzymes found in a broad range of organisms including plants, fungi, protozoa, and bacteria. The *ndh* enzymes catalyze the oxidation of NADH with concomitant reduction of quinone (Q). These membrane-bound respiratory enzymes differ from the canonical NADH: dehydrogenase (complex I), because they are not involved in the vectorial transfer of protons across membranes. In *Plasmodium falciparum* and *Mycobacterium tuberculosis*, causative agents of malaria and tuberculosis,

Liverpool School of Tropical Medicine, Pembroke Place, Liverpool, United Kingdom

Methods in Enzymology, Volume 456
ISSN 0076-6879, DOI: 10.1016/S0076-6879(08)04417-0

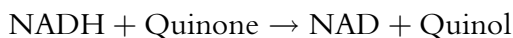
© 2009 Elsevier Inc.
All rights reserved.

respectively, ndhs have aroused interest because of the essential role played in maintaining a reduced Q-pool during infection. In this chapter, we present methods for the measurement of steady-state parameters for ndhs from both pathogens, highlighting best practices and caveats. In addition, owing to the interest in ndhs as potential chemotherapeutic targets, we describe a miniaturized endpoint assay that is validated for high-throughput screening (HTS) of chemical libraries.

1. INTRODUCTION

1.1. Structure and function

Type II NADH: quinone oxidoreductases (ndh) catalyze the following reaction:



This class of flavoenzyme is found in the respiratory chain of a broad range of organisms, including plants, fungi, protozoa, and bacteria, including important human pathogens such as *Plasmodium falciparum* (malaria), *Trypanosoma brucei* (sleeping sickness) and *Mycobacterium tuberculosis* (pulmonary tuberculosis) (Biagini *et al.*, 2006; Fang and Beattie, 2002; Fisher *et al.*, 2007; Kerscher, 2000; Melo *et al.*, 2004; Teh *et al.*, 2007). Some differences exist among type II NADH: quinone oxidoreductases from various organisms with respect to substrate specificity (e.g., NADH and/or NADPH, quinone or menaquinone [Kerscher, 2000; Melo *et al.*, 2004]), but what sets them functionally apart from the multimeric NADH dehydrogenase complex (complex I) is the absence of any transmembrane proton translocation.

There are, as yet, no high-resolution three-dimensional structures or biophysical data available for this class of enzyme, and structure–function information is restricted to modeling studies based on sequence similarity with other flavoenzymes such as the lipoamide dehydrogenases, for which the structures have been resolved by X-ray crystallography (Kerscher, 2000; Mattevi *et al.*, 1992). These comparative studies suggest that type II NADH: quinone oxidoreductases possess two regions with a dinucleotide $\beta\alpha\beta$ fold domain. The first domain is believed to be the region for the noncovalent attachment of the flavin cofactor (FAD or FMN), whereas the second domain is responsible for binding NAD(P)H (Fisher *et al.*, 2007; Kerscher, 2000; Melo *et al.*, 2004; Schmid and Gerloff, 2004).

In contrast with the nucleotide-binding domains, identification of the (mena)quinone-binding site (Q site) is more challenging. However, on the basis of broad physicochemical constraints of Q-sites from respiratory enzymes (Fisher and Rich, 2000), we have recently described a putative

quinone-binding region in a structural model of *Plasmodium* type II NADH: quinone oxidoreductase (Fisher *et al.*, 2007). This region is predicted to be formed from two short antiparallel sheets close to the surface of the membrane and satisfies distance constraints for rapid electron transfer from the NAD(P)H- and flavin-binding domains (Moser *et al.*, 1992). These predicted sheets are relatively well conserved among type II NADH: quinone oxidoreductase from all species.

Type II NADH: quinone oxidoreductases vary in the manner by which they are tethered to the membrane with some (e.g., from *Mycobacterium*) possessing a putative single transmembrane domain (Melo *et al.*, 2004) and others (e.g., *Plasmodium*) possessing an amphipathic α -helix, which is likely to anchor the enzyme into the lipid bilayer (Fisher *et al.*, 2007). Regardless of mechanism of membrane tethering, it can be further predicted that the Q-site of *ndh* enzymes is located at the membrane interface facilitating access to both the (mena)quinone pool from the lipid phase and to protons from the aqueous phase.

There is limited steady-state kinetic information regarding this class of enzyme, but one study indicates that the reaction kinetics of type II NADH: quinone oxidoreductases operate a ping-pong (double displacement) mechanism, whereby one product is released from the enzyme before all of the substrates have bound (Yano *et al.*, 2006).

1.2. Functional role of *ndh* in the respiratory chain of *P. falciparum* and *M. tuberculosis*

Despite malaria and tuberculosis (Tb) being two of the most devastating human pathogens, causing some 4 million deaths each year, the pathways and components of central energy metabolism are poorly defined.

The organization of the respiratory chains for *P. falciparum* and *M. tuberculosis* are largely based on genome data (Cole *et al.*, 1998; Gardner *et al.*, 2002); a schematic representation of these pathways is shown in Fig. 17.1. In the electron transport chain (ETC) of *Plasmodium*, the canonical multimeric complex I (NADH: dehydrogenase) found in mammalian mitochondria is absent, and, instead, the parasite possesses five quinone-dependent oxidoreductases, namely a type II NADH: quinone oxidoreductase (PfNDH2), a malate: quinone oxidoreductase (MQO), a dihydroorotate dehydrogenase (DHOD), a glycerol-3-phosphate dehydrogenase (G3PDH), and a succinate: quinone oxidoreductase (SDH). These enzymes link cytosolic metabolism to mitochondrial metabolism, generating reducing power (QH₂) for the *bc*₁ complex and an *aa*₃-type cytochrome oxidase, enabling proton pumping and energy conservation. There is doubt as to whether asexual intraerythrocytic-staged parasites use the ETC for ATP generation (Fry *et al.*, 1990), but thermodynamically, a proton leak

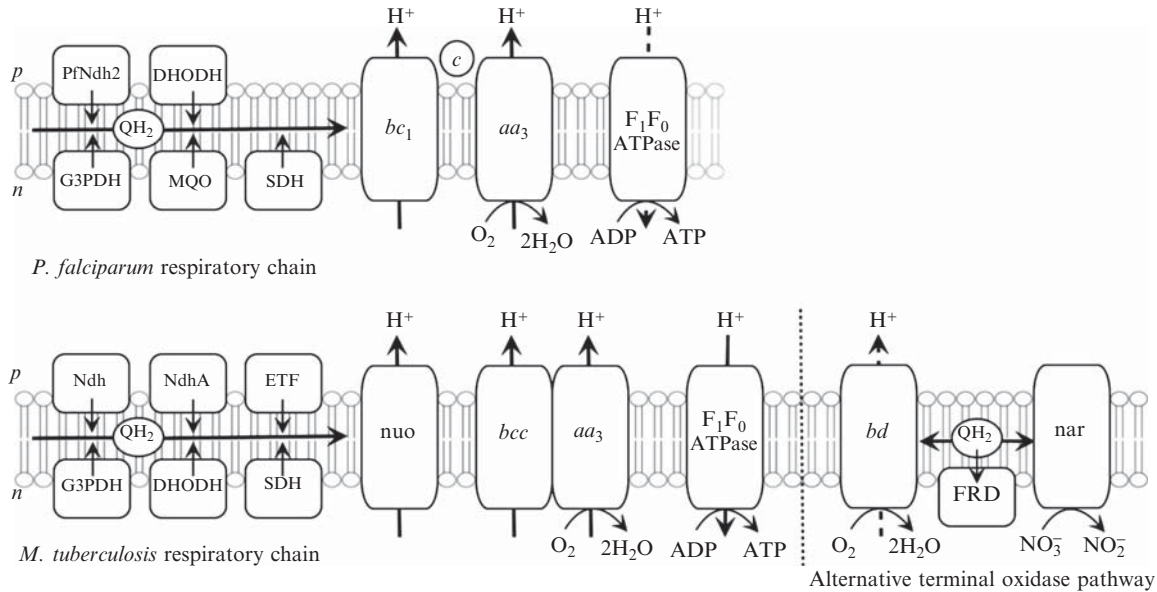


Figure 17.1 Schematic representation of the respiratory chains of *P. falciparum* and *M. tuberculosis*. The chain components are (1) *P. falciparum*: PfNdh2–type II NADH: quinone oxidoreductase, DHODH–dihydroorotate dehydrogenase, G3PDH–glycerol-3-phosphate dehydrogenase, MQO–malate: Quinone oxidoreductase, SDH–succinate dehydrogenase, bc_1 –cytochrome bc_1 complex, c –cytochrome c , aa_3 –cytochrome c oxidase, and the F_1F_0 –ATPase (complex V). Note that the “a” and “b” subunits of the F_0 subunit of complex V have yet to be identified in *P. falciparum*, and this enzyme shows little or no proton-linked ATP synthase activity (Fry *et al.*, 1990). (2) *M. tuberculosis*: Ndh/NdhA–type II NADH: (mena)quinone oxidoreductase (two isoforms), ETF–electron transferring flavoprotein (transfer of reducing equivalents from fatty acid β -oxidation into the Q-pool), nuo–protonmotive NADH dehydrogenase (complex I), bcc –cytochrome bcc complex (note that there is no evidence for soluble cytochrome c in this organism), aa_3 –cytochrome bcc oxidase, postulated to form a super complex with bcc . An alternative terminal oxidase pathway is used in *M. tuberculosis* under conditions of low oxygen tension, containing quinol oxidase (cytochrome bd), fumarate reductase (FRD), and nitrate reductase (nar) components. p and n correspond to the positive and negative sides of the respiratory membrane with respect to proton translocation. Proton movements are indicative only and do not represent H^+/e^- ratios for the respective complexes.

must exist to enable the maintenance of a high transmembrane proton potential (Ψ_m) (Fisher *et al.*, 2007).

Given that PfNDH2 does not pump protons, we can predict that the overall proton translocation stoichiometry for the transfer of $2e^-$ from NADH by means of ubiquinol to O_2 is $6H^+/2e^-$ compared with $10H^+/2e^-$ in typical mitochondria harboring complex I. We have hypothesized that this difference may be an evolutionary adaptation to a microaerophilic lifestyle enabling (proton) uncoupled oxidation of NADH. This adaptive feature has several advantages, including: (1) a reduction of proton “back-pressure” in the absence of extensive ATP synthesis; (2) a reduction of mitochondrial superoxide generation; and (3) a mechanism for the deregulated oxidation of cytosolic NADH (Fisher *et al.*, 2007).

In comparison, *M. tuberculosis* contains a branched respiratory chain terminating in a cytochrome *bd* (quinol) oxidase and an *aa3*-type cytochrome *c* oxidase (Fig 17.1). Both chains are fed by a menaquinol (MQH₂) pool that is generated by four dehydrogenases; one succinate menaquinone oxidoreductase (SQR), one multimeric type I NADH: dehydrogenase (complex I), and two type II NADH: menaquinone oxidoreductases (*ndh* and *ndhA*).

The direction of the respiratory flux (i.e., *aa3* cytochrome oxidase or cytochrome *bd* oxidase) seems to be dependent on the metabolic state and the surrounding milieu (e.g., O_2 and nutrient concentrations) during infection. Significantly, *ndh* and *ndhA* are believed to play a critical role in supplying MQH₂ during infection. During this period *M. tuberculosis* must survive attack from the host immune system, and it is hypothesized that part of the coping strategy may involve the downregulation of the *aa3* cytochrome oxidase-branch of the respiratory chain, and the upregulation of the cytochrome *bd* oxidase branch that, while yielding less energy, is able to function at the low dissolved O_2 tensions found inside granulomas and that may be more resistant to inhibition by macrophage-generated NO (Shi *et al.*, 2005; Teh *et al.*, 2007).

The *ndh* enzymes of both *P. falciparum* and *M. tuberculosis* have been highlighted as potential drug targets (Biagini *et al.*, 2006; Fisher *et al.*, 2007; 2008; Weinstein *et al.*, 2005; Yano *et al.*, 2006). Evidence of essentiality has been provided both genetically and chemically. In *P. falciparum*, single crossover recombination of PfNDH2 fails to generate viable parasites (e.g., no integration is observed after ~100 days, unpublished). Similarly for *M. tuberculosis*, experiments that use a transposon insertion knockout strategy reveal that disruption of the *ndh* gene is lethal or extremely deleterious (gene essentiality with this strategy is only indicative), whereas insertional knockout strains of complex I (*nuo*) and the second type II NADH: menaquinone oxidoreductase isoenzyme, *ndhA*, remain viable (Sasseti *et al.*, 2003). Chemical inhibition of PfNDH2 by the flavin antagonist DPI (diphenylene iodonium chloride) and the *ndh* inhibitor HDQ

(1-hydroxy-2-dodecyl-4(1H)quinolone) results in a loss of mitochondrial membrane potential leading to parasite death (Biagini *et al.*, 2006; Saleh *et al.*, 2007). In *M. tuberculosis*, inhibition of *ndh* enzymes by phenothiazine drugs tracks both *in vitro* and *in vivo* (murine models) growth inhibition (Weinstein *et al.*, 2005).

Furthermore, recent transcriptome analysis of important pathogens such as *Mycobacterium* and *Plasmodium* indicate that *ndh* enzymes are not only essential to parasite survival *in vivo* but may also contribute to the severity and outcome of disease (Daily *et al.*, 2007; Shi *et al.*, 2005).

In this chapter, assays will be described for the measurement of *ndh* activity and steady-state kinetics in both *P. falciparum* and *M. tuberculosis*, highlighting best practices and potential pitfalls. Assays are described for the measurement of *ndh* activity from both native and heterologously expressed enzyme. In addition, given the interest of these enzymes as potential chemotherapeutic targets, a miniaturized endpoint assay suitable for high-throughput screening is described together with calculated assay performance measures (APM).

2. KINETIC ASSAYS

2.1. PfNDH2 native assay

The activity of PfNDH2 can be measured directly from *P. falciparum* erythrocyte-freed cell-free extracts (Biagini *et al.*, 2006). In this method, cyanide and atovaquone are added to prevent downstream electron transfer; however the assay can work equally well by substituting atovaquone for other *bc*₁ complex inhibitors such as antimycin or stigmatellin (Biagini *et al.*, 2008). Note that owing to the Biosafety Level 3 (BSL3) status of *M. tuberculosis*, the culture, membrane preparation, and native enzyme assay procedure of this pathogen has been omitted from this section, because it would have limited applicability. Analysis of heterologously expressed *M. tuberculosis ndh* is provided in Section 2.3.1.

Plasmodium falciparum strains may be acquired free of charge (for research purposes only) at the Malaria Research and Reference Reagent Resource Centre (MR4, <http://www.mr4.org>). Parasites were maintained in continuous culture on the basis of established methods (Trager and Jensen, 1976). Cultures contained a 2% suspension of O+ human erythrocytes in RPMI 1640 medium (R8758, glutamine and NaHCO₃) supplemented with 10% pooled human AB+ serum, 25 mM HEPES (pH 7.4), and 20 μ M gentamicin sulfate. Cultures were grown under a gaseous head space of 4% O₂ and 3% CO₂ in N₂ at 37°. Parasite growth was synchronized by treatment with sorbitol (Lambros and Vanderberg, 1979).

Free parasites were prepared from aliquots of infected erythrocytes (typically 8×10^9 cells ml^{-1}) by adding 5 volumes of 0.15% (wt/vol) saponin in phosphate-buffered saline (137 mM NaCl, 2.7 mM KCl, 1.76 mM K_2HPO_4 , 8.0 mM Na_2HPO_4 , 5.5 mM D-glucose, pH 7.4) for 5 min, followed by three washes by centrifugation and resuspension in HEPES (25 mM)-buffered RPMI and a final resuspension in assay buffer containing a protease inhibitor cocktail (Complete Mini; Roche).

Cell extract was prepared by repeated freeze-thawing in liquid N_2 , followed by disruption with a sonicating probe. Care should be taken to prevent overheating of the cell-free extracts during the sonication procedure.

The native assay (final volume 0.7 ml) was performed in 50 mM potassium phosphate, 2 mM EDTA (pH 7.5). Potassium cyanide, NADH (both prepared in assay buffer), and atovaquone (2-[4-(4-chlorophenyl)cyclohexyl]-3-hydroxynaphthalene-1,4-dione dissolved in dimethyl sulfoxide, [DMSO]) were added to final concentrations of 1 mM, 200 μM , and 10 μM , respectively. Cell-free *P. falciparum* extract (~ 500 μg protein) was added to the cuvette, and the reaction initiated by the addition of 50 μM decylubiquinone (in ethanol). PfNDH2 activity was measured spectrophotometrically by monitoring the decrease in absorbance at 340 nm (NADH $\epsilon = 6.22 \text{ mM}^{-1} \text{ cm}^{-1}$).

The presence of parasite haemozoin (malaria pigment) results in a heterogenous and optically dense cell-free extract that does not lend itself to the detailed analysis of kinetic parameters. Nevertheless, quinone-dependent NADH oxidation can be measured, and approximate kinetic parameters indicate an apparent K_m for NADH of 5.1 μM with a V_{max} of 0.12 $\mu\text{mol min}^{-1} \text{ mg}^{-1}$ (cell-free extract protein, [Biagini *et al.*, 2006]). Comparable kinetic parameters are observed when decylubiquinone is replaced by Q_1 (apparent K_m for NADH of 16.7 μM with a V_{max} of 0.16 $\mu\text{mol min}^{-1} \text{ mg}^{-1}$ [Biagini *et al.*, 2006]).

Note that a molar solution of potassium cyanide (KCN) is strongly basic and requires pH adjustment to 7.5 with concentrated HCl before use. Great care must be taken during the pH titration, because toxic hydrogen cyanide (HCN) gas will be liberated if the pH drops below 7.0.

2.2. PfNDH2 linked assay

As a quinone reductase, PfNDH2 can also be used in Q-pool linked assays to drive the reduction of exogenous cytochrome *c* through bc_1 complex activity. This assay is not suitable for investigating *M. tuberculosis* bc_1 (bc_c) complex activity, because this enzyme is unreactive with soluble cytochrome *c*. Care must also be taken if Q-pool linked assays are used to investigate inhibition of bc_1 complex activity (through mutation or exogenous antagonists), because the supply of reduced quinone to the bc_1 complex

may be rate-determining, resulting in the erroneous interpretation of the kinetics of cytochrome *c* reduction.

P. falciparum bc_1 complex cytochrome *c* reductase activity was measured by monitoring NADH-linked cytochrome *c* reduction at 550 versus 542 nm in an assay buffer consisting of 50 mM potassium phosphate, 2 mM EDTA, 1 mM KCN (pH 7.5) at room temperature. The 542 nm parameter corresponds to an isosbestic point in the redox difference spectrum of equine cytochrome *c* and thus provides a convenient baseline for correction of drift in the 550 nm (α -band) data. The protein concentration of the *P. falciparum* cell-free extract was $15 \mu\text{g ml}^{-1}$ (total assay volume 0.7 ml). The cell-free extract was prepared immediately before use (as described in section 2.1). Horse heart cytochrome *c* was present at a concentration of $30 \mu\text{M}$. The concentration of the stock solution of cytochrome *c* was determined spectrophotometrically ($\epsilon_{550-542} = 18.5 \text{ mM}^{-1} \text{ cm}^{-1}$, dithionite-reduced *minus* ferricyanide-oxidized difference spectra) (Fisher *et al.*, 2004). The reaction was initiated by the addition of 0.2 mM NADH, and allowed to proceed for 3 min. Data were fitted as initial rate estimates (cytochrome *c* reduction) with $\epsilon_{550-542} = 18.5 \text{ mM}^{-1} \text{ cm}^{-1}$.

A typical trace of *P. falciparum* NADH: cytochrome *c* reductase activity is shown in Fig. 17.2. This method is less susceptible to interference by haemozoin offering an advantage over direct analysis of NADH oxidation. This method can also be used for studies attempting to measure the relative flux of the 5 quinone-dependent oxidoreductases (see Fig. 17.1); however,

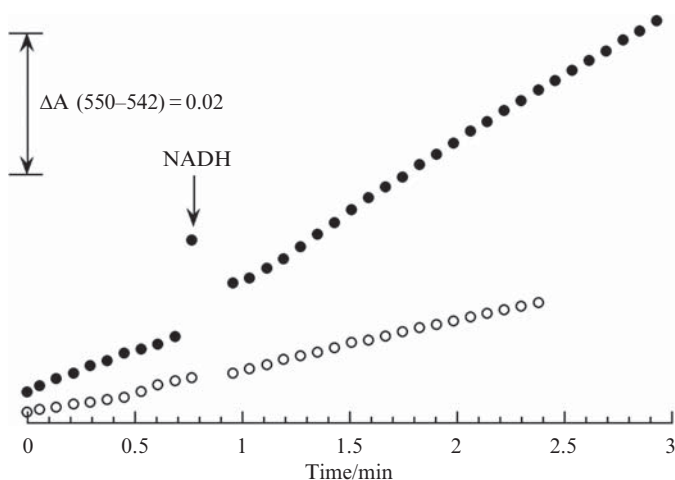


Figure 17.2 *P. falciparum* (cell-free extract) NADH: cytochrome *c* reductase steady-state kinetic data. Assay conditions as given in section 2.2. On addition of NADH, the observed rate of cytochrome *c* reduction was $55 \text{ nmol cyt } c \text{ reduced mg protein}^{-1} \text{ min}^{-1}$ (●). In comparison, the nonenzymatic rate of cytochrome *c* reduction (○) was $20 \text{ nmol cyt } c \text{ reduced mg protein}^{-1} \text{ min}^{-1}$.

as noted earlier, data resulting from experiments involving inhibitors should be analyzed with caution, because linked assays have the additional complication of potentially different maximum activity rates of oxidation and reduction of the Q-pool.

2.3. Kinetic assays with an *E. coli*-based heterologous expression system

Because of interference from haemozoin and the difficulty of obtaining sufficient PfNDH2 from native *P. falciparum* mitochondrial preparations for enzymatic analysis, we have developed a simple heterologous expression system in *E. coli* NADH dehydrogenase knockout strain ANN022 (*nuoB::nptI-sacRB, ndh::tet*). This method has also been used to successfully express *M. tuberculosis* *ndh*, circumventing complications arising from the preparation of this enzyme from a BSL 3 organism. ANN022 (derived from strain ANN387 [Wallace and Young, 1977]) has no associated NADH: quinone oxidoreductase activity and is unable to grow on minimal media containing mannitol as the sole carbon source unless NADH dehydrogenase activity is restored (Schneider *et al.*, 2008).

The gene encoding PfNDH2 (PlasmDB identifier PFI0735c) was amplified as a 1.5-kb fragment from *P. falciparum* 3D7 cDNA and subcloned as an *EcoRI/SphI* fragment into pUC19, creating construct pF571. A predicted 22-residue N-terminal mitochondrial leader sequence was omitted from the PFI0735c amplicon, and a stop codon was introduced immediately after the C-terminal residue, Lys-533. The *lac* promoter containing-pUC19 was chosen as the expression vector in preference to a more strongly expressing T7-based system such as provided by the pET series of plasmids to facilitate production of enzymologically active PfNDH2 without the need to solubilize and renature the recombinant protein from inclusion bodies. pF571 was transformed into *E. coli* strain ANN022 for expression of PfNDH2, which underwent initial enzymologic characterization in crude membrane preparations. The transformed *E. coli* strain was named F571. Yield of recombinant PfNDH2 from F571 was estimated to be 100 to 200 $\mu\text{g}\cdot\text{l}^{-1}$.

Note that the preceding expression vector and knockout strain was similarly used for the heterologous expression of *M. tuberculosis* *ndh* (gene identifier Rv1854c).

2.3.1. Production of crude membrane preparations from *E. coli* F571

PfNDH2 (or *ndh* for *M. tuberculosis* homolog) was expressed in *E. coli* strain F571 in 1-L cultures of Luria-Bertani medium (10 $\text{g}\cdot\text{l}^{-1}$ bactotryptone, 5 $\text{g}\cdot\text{l}^{-1}$ yeast extract, 10 $\text{g}\cdot\text{l}^{-1}$ NaCl, pH adjusted to 7.5) supplemented with 100 $\mu\text{g}\cdot\text{ml}^{-1}$ ampicillin, 50 $\mu\text{g}\cdot\text{ml}^{-1}$ kanamycin, and 10 $\mu\text{g}\cdot\text{ml}^{-1}$ tetracycline. To induce expression and maximize the yield of the recombinant PfNDH2,

1 mM IPTG was added to the culture at the point of inoculation. The cells were grown at 37° for 16 h, with shaking at 200 rpm. After growth, the cells were harvested by centrifugation at 4000g for 10 min and resuspended in 100 ml of buffer (50 mM potassium phosphate, 2 mM EDTA [pH 7.5]) per liter of culture volume. The centrifugation step was repeated, and the cells resuspended in 30 ml of buffer per liter of culture volume. DNase and hen egg-white lysozyme were added from 50 mg ml⁻¹ stock solutions to a final concentration of 0.2 mg.l⁻¹, and the mixture was incubated on ice for 20 min. The resuspended cells were disrupted by two passes through a standard laboratory French press operating at 20,000 psi, and the debris pelleted by centrifugation at 12,000g at 4° for 20 min. The supernatant was collected and centrifuged at 100,000g at 4° for 1 h, depositing the membranes as a highly viscous pellet. This was collected and resuspended with the aid of a Potter homogenizer in 2 ml of 50 mM potassium phosphate, 2 mM EDTA (pH 7.5) per liter of original culture volume. Glycerol was added to a final concentration of 10% (v/v) and the membrane suspension stored in 50- μ l aliquots at -80°. The total protein concentration of the membrane suspension should be in the order of 10 to 20 mg.ml⁻¹. To maintain enzyme activity, aliquots should not be repeatedly freeze-thawed, but are stable for at least 6 months when stored -80°.

2.3.2. NADH: Ubiquinone oxidoreductase assay

NADH oxidation and decylubiquinone (dQ) reduction were monitored spectrophotometrically at 340 and 283 nm, respectively in a 1-cm path length quartz cuvette in a reaction buffer consisting of 50 mM potassium phosphate, 2 mM EDTA (pH 7.5); 10 mM potassium cyanide (1 M stock solution, pH adjusted to 7.5) was added to the reaction buffer to inhibit the endogenous *E. coli* quinol oxidases cytochrome *bo* and *bd*. The NADH concentration was 0.2 mM, and the reaction initiated by the addition of 50 μ M decylubiquinone (15 mM stock solution in ethanol). Extinction coefficients of 6.22 mM⁻¹ cm⁻¹ (340 nm) and 8.1 mM⁻¹ cm⁻¹ (283 nm) were used to quantify NADH and dQ concentration, respectively (Barquera *et al.*, 2002; Dawson *et al.*, 1986). The concentration of F571 crude membrane preparation was 15 μ g ml⁻¹, and the total assay volume was 0.7 ml. It should be noted that the order in which the reagents are added to the cuvette is important and should be as follows: assay buffer, potassium cyanide, NADH, membranes. Inhibitors, if present, should be added after the addition of membranes. The assay is carried out at room temperature.

A typical trace of showing NADH oxidation with concomitant quinone reduction by heterologously expressed PfNDH2 is shown in Fig. 17.3. The observed reaction kinetics are biphasic, consisting of an initial linear fast phase with a rate of approximately 0.1 to 0.15 AU sec⁻¹ (1 to 1.5 μ mol NADH oxidized min⁻¹ mg protein⁻¹) in the first 30 sec, followed by a slower phase with a zero order rate constant of 0.01 to 0.02 AU sec⁻¹ (0.1 to

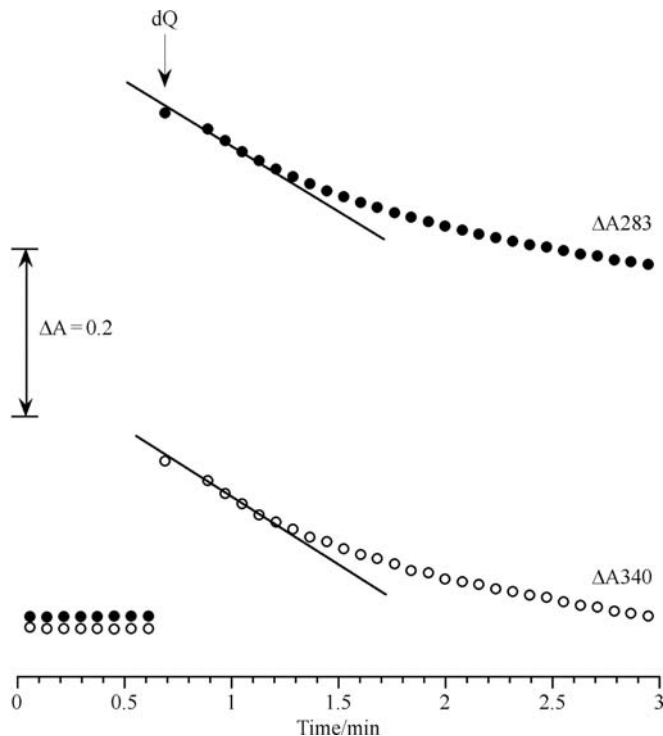


Figure 17.3 Recombinant PfNDH2 NADH: quinone oxidoreductase steady state kinetic data monitored at 283 nm (quinone reduction, ●) and 340 nm (NADH oxidation, ○). The reaction was initiated by the addition of 50 μM decylubiquinone (dQ), with other experimental conditions as given in section 2.3. The rates of quinone reduction and NADH oxidation were 1- and 1.4 $\mu\text{mol. mg protein}^{-1} \text{ min}^{-1}$, respectively. The 1.4:1 stoichiometry of NADH oxidation and quinone reduction is indicative of electron transfer to an additional alternate acceptor, which is most likely to be oxygen.

0.2 $\mu\text{mol NADH oxidized min}^{-1} \text{ mg protein}^{-1}$). The reaction is essentially complete within 3 min of addition of dQ. Initial reaction kinetics of *M. tuberculosis* give rise to similar traces (not shown).

Under the standard assay conditions detailed in section 2.3.2, nonenzymatic oxidation of NADH by decylubiquinone or coenzyme Q_1 is minimal and has essentially no influence on the observed enzymatic rate. Traditionally, detergents are included when assaying membrane-associated enzymes, because they often facilitate access of hydrophobic substrates to the active site and solubilize polydisperse preparations. We have noticed that inclusion of 0.025% (w/v) dodecyl maltoside (DDM), a widely used nonionic detergent, in the NADH: quinone oxidoreductase assay introduces a significant nonenzymatic NADH oxidation artefact (80 nmol NADH oxidized $\text{min}^{-1} \text{ mg}^{-1}$ DDM) that is not linked to quinone reduction (Fig. 17.4). The electron acceptor in this instance is presumably molecular oxygen. A similar

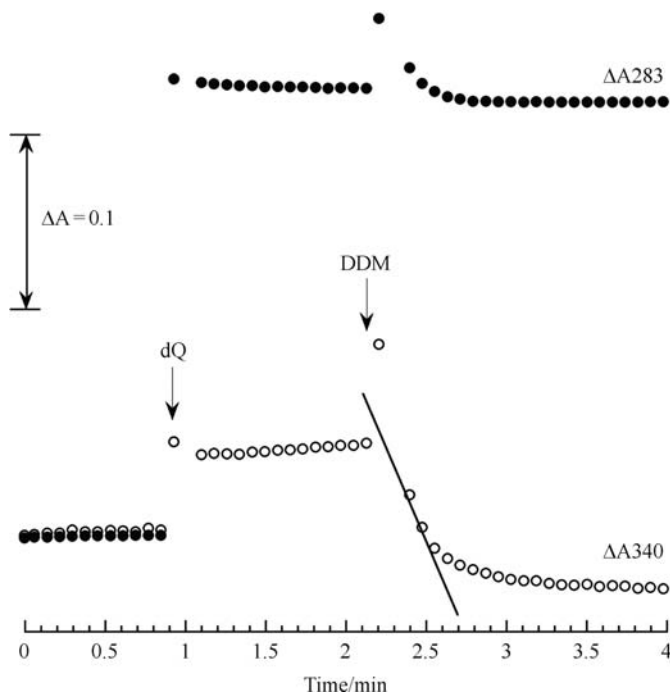


Figure 17.4 Nonenzymatic oxidation of NADH in the presence of dodecyl maltoside (DDM). Kinetic data were recorded at 283 nm (quinone reduction, ●) and 340 nm (NADH oxidation, ○). The reaction was initiated by the addition of 0.025% DDM (arrow), resulting in a NADH oxidation rate of $80 \text{ nmol min}^{-1} \text{ mg}^{-1}$ detergent.

phenomenon is observed for the Na^+ -translocating NADH: quinone oxidoreductase from *Vibrio cholerae* with the detergent LDAO (*n*-dodecyl-*N,N*-dimethylamine *N*-oxide) (Barquera *et al.*, 2002).

Interestingly, analysis of NADH: quinone oxidoreductase activity from *P. falciparum* and *M. tuberculosis* reveal differences in substrate specificity and inhibitor sensitivity. For example, PfNDH2 can use both NADH and NADPH as electron donor, whereas *M. tuberculosis* ndh is selective for only NADH (Fig. 17.5). The general flavin reagent DPI is also more selective for *M. tuberculosis* ndh than PfNDH2 (Fig. 17.6), whereas the Hydroxyquinone HOQ (1-hydroxy-2-oxyl-4(1H)quinolone) is more active against PfNDH2 than ndh (Fig. 17.7). Given that the natural substrate of *M. tuberculosis* ndh is menaquinone that contains the naphthoquinone head group, a reduced sensitivity to Hydroxyquinone-based analogs is perhaps not surprising.

Recently it has been reported (Dong *et al.*, 2008, Dong *et al.*, 2009) that PfNDH2 is not sensitive to DPI, contrary to data presented here (Fig. 17.6). We note that the Dong *et al.* (2008) study used detergent in the assay procedure. As noted previously, it is likely that the addition of detergent resulted in a nonenzymatic oxidation of NADH, which would explain the observed apparent insensitivity to PfNDH2 inhibitors such as DPI.

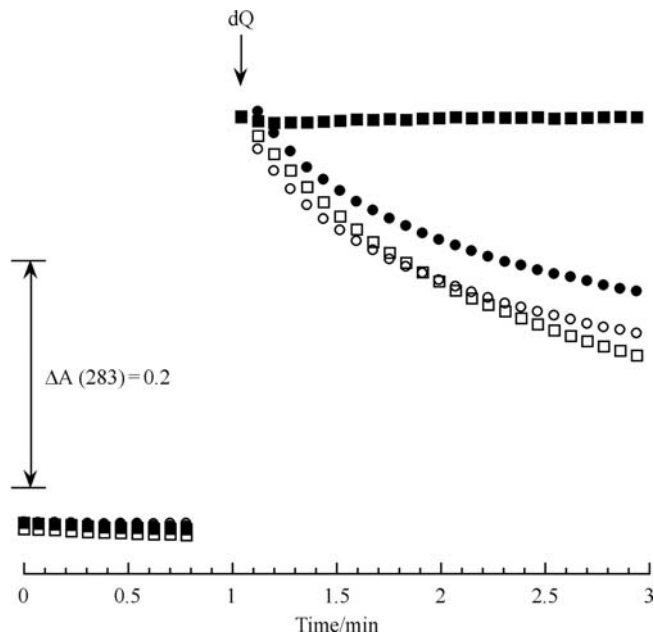


Figure 17.5 Recombinant *M. tuberculosis* ndh (■,●) and *P. falciparum* PfNDH2 (□,○) NADH/NADPH: quinone oxidoreductase steady-state kinetic data monitored at 283 nm. The data shown correspond to NADH oxidation (○,●) and NADPH oxidation (□, ■). NADH and NADPH were present at 200 μM . The reaction was initiated by the addition of 50 μM decylubiquinone (dQ), with other experimental conditions as given in section 2.3.2. The rates of quinone reduction by *M. tuberculosis* ndh and *P. falciparum* PfNDH2 with NADH as electron donor were 1.10- and 1.40 $\mu\text{mol} \cdot \text{min}^{-1} \text{mg}^{-1}$ protein, respectively. The rates of quinone reduction by *M. tuberculosis* ndh and *P. falciparum* PfNDH2 with NADPH as electron donor were 0- and 1.40 $\mu\text{mol} \cdot \text{min}^{-1} \text{mg}^{-1}$ protein, respectively.

3. ENDPOINT ASSAY FOR HTS

As described in section 1.2, the ndh enzymes of *P. falciparum* and *M. tuberculosis* have been highlighted as potential chemotherapeutic targets owing to their selectivity and essentiality. High-throughput screening (HTS) of focused chemical libraries is an effective strategy toward obtaining chemical hits to take onto further drug development through traditional medicinal chemistry approaches. Here, we describe a miniaturized endpoint assay we have developed that is amenable to a HTS format.

HTS assays were performed in 20 mM HEPES (pH 7.5) with a 96-well plate format with a final reaction volume of 0.2 ml. To ensure homogeneity an assay master mix of sufficient volume was prepared containing potassium cyanide (pH 7.5) and NADH (both freshly prepared in assay buffer) to final

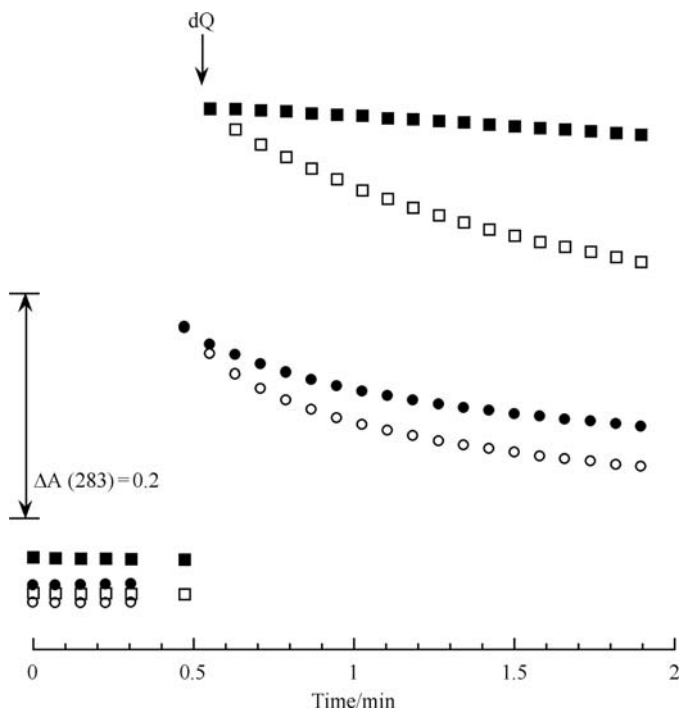


Figure 17.6 Inhibition of steady-state NADH: quinone reductase activity in *P. falciparum* PfNDH2 and *M. tuberculosis* ndh by diphenylene iodonium chloride (DPI). Assay conditions as given in section 2.4. *M. tuberculosis* ndh quinone reductase activity in the presence (■) and absence (□) of 28 μM DPI. Quinone reductase rates are 0.15 $\mu\text{mol} \cdot \text{min}^{-1} \cdot \text{mg}^{-1}$ protein (■) and 1.25 $\mu\text{mol} \cdot \text{min}^{-1} \cdot \text{mg}^{-1}$ protein (□). *P. falciparum* PfNDH2 quinone reductase activity in the presence (●) and absence (○) of 28 μM DPI. Quinone reductase rates are 1.40 $\mu\text{mol} \cdot \text{min}^{-1} \cdot \text{mg}^{-1}$ protein (○) and 1.10 $\mu\text{mol} \cdot \text{min}^{-1} \cdot \text{mg}^{-1}$ protein (●).

concentrations of 10 mM and 0.2 mM, respectively. *E. coli* membrane (ca. 4 μg) preparation (see section 2.3.1) per assay was added to the mixture and thoroughly incorporated before plating.

The reaction was initiated by addition of 4 μl Coenzyme Q_1 (1 mM stock in ethanol) of and the reaction followed at 340 nm and stopped with 20 μl of 10% (w/v) sodium dodecyl sulfate (SDS) after 20 min. Monitoring the reaction at 340 nm (instead of monitoring Q_1 reduction at 283 nm) reduces potential interference from inhibitors and generates more robust assay performance measures.

Note that the assay volume of 200 μl is suitable for use in a 96-well microtiter plate format; however, the assay can also be readily miniaturized further to suit other formats (e.g., 384 well).

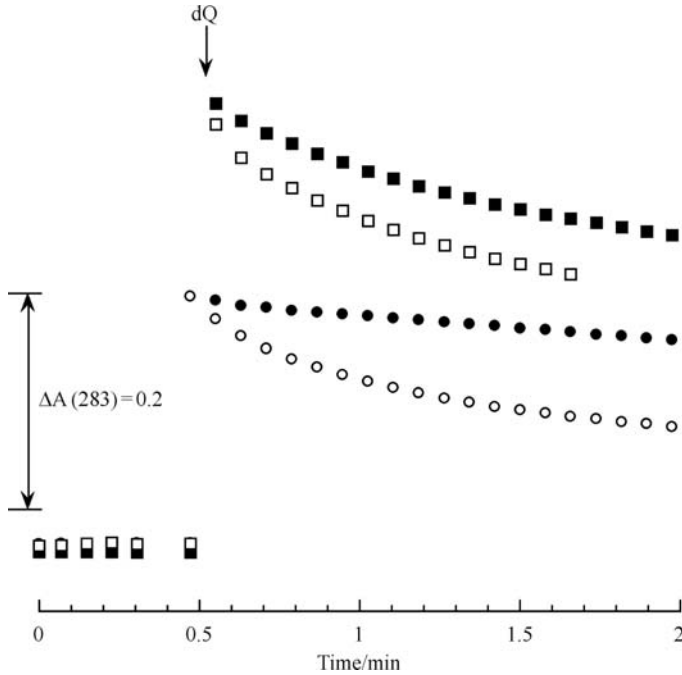


Figure 17.7 Inhibition of steady-state NADH: quinone reductase activity in *P. falciparum* PfNDH2 (●,○) and *M. tuberculosis* ndh (■,□) by 28 μM HOQ (1-hydroxy-2-ocyl-4 (1H)quinolone). The inhibited quinone reductase rates correspond to 1.4- and 1.5 $\mu\text{mol. min}^{-1} \text{mg}^{-1}$ protein for the *P. falciparum* and *M. tuberculosis* proteins, respectively. Addition of 28 μM HOQ (●,■) reduced these rates to 0.2 and 1.1 $\mu\text{mol. min}^{-1} \text{mg}^{-1}$ protein, respectively.

The following assay performance measures (APMs) were calculated from *E. coli* membrane preparations expressing PfNDH2 (section 2.3.1); however, comparable values were determined for *E. coli* membrane preparations expressing *M. tuberculosis* ndh (not shown).

Coefficient of variance

$$\%CV = \frac{\sigma}{\mu} \times 100 = 1.9\%$$

Signal/noise

$$S : N = \frac{\mu_{max} - \mu_{min}}{\sigma_{min}} = 13$$

Signal window

$$SW = \frac{\mu_{max} - \mu_{min} - 3(\sigma_{max} + \sigma_{min})}{\sigma_{max}} = 16$$

Z'

$$Z' = 1 - \frac{3\sigma_{max} + 3\sigma_{min}}{\mu_{max} - \mu_{min}} = 0.7$$

In all cases σ = standard deviation and μ = mean signal.

The calculated APMs reflect the robustness and reproducibility of the assay and comfortably fall within the values commonly used by industry (Frearson *et al.*, 2007; Inglese *et al.*, 2007; Iversen *et al.*, 2006). To increase the hit rate of screens, researchers may wish to alter the Q_1 assay concentration to equal that of the apparent K_m of the enzyme of interest.

4. SUMMARY AND CONCLUSIONS

Assay procedures have been described for the measurement of *ndh* activity and steady-state kinetics from both *P. falciparum* and *M. tuberculosis*. Measurement of native activity in *P. falciparum* is complicated by the presence of haemozoin in cell-free extracts, whereas the BSL3 classification of *M. tuberculosis* makes experimentation prohibitively restrictive for most laboratories. To solve these issues we have developed a simple heterologous expression system in *E. coli* NADH dehydrogenase knockout strain ANN0222 (*nuoB::nptI-sacRB*, *ndh::tet*) for the expression of both PfNDH2 and *M. tuberculosis ndh*. This expression system allows not only the measurement of steady-state kinetics but also the development of a miniaturized endpoint assay validated for use in HTS screening of small molecule inhibitors.

ACKNOWLEDGMENTS

We acknowledge the Leverhulme Trust, NHIR Biomedical Research Centre, and the Wellcome Trust for financial support. Prof. Thorsten Friedrich, Prof. Harvey Rubin, and Prof. Walter Oettmeier are gratefully acknowledged for their generous donations of biological and chemical reagents and for helpful discussions. We also thank the staff and patients of Ward 7Y and the Gastroenterology Unit, Royal Liverpool Hospital, for their donation of blood.

REFERENCES

- Barquera, B., Hellwig, P., Zhou, W., Morgan, J. E., Hase, C. C., Gosink, K. K., Nilges, M., Bruesehoff, P. J., Roth, A., Lancaster, C. R., and Gennis, R. B. (2002). Purification and characterization of the recombinant Na(+)-translocating NADH: Quinone oxidoreductase from *Vibrio cholerae*. *Biochemistry* **41**, 3781–3789.
- Biagini, G. A., Fisher, N., Berry, N., Stocks, P. A., Meunier, B., Williams, D. P., Bonar-Law, R., Bray, P. G., Owen, A., O'Neill, P. M., and Ward, S. A. (2008). Acridinediones: Selective and potent inhibitors of the malaria parasite mitochondrial bc1 complex. *Mol. Pharmacol.* **73**, 1347–1355.
- Biagini, G. A., Viriyavejakul, P., O'Neill, P. M., Bray, P. G., and Ward, S. A. (2006). Functional characterization and target validation of alternative complex I of *Plasmodium falciparum* mitochondria. *Antimicrob. Agents Chemother.* **50**, 1841–1851.
- Cole, S. T., Brosch, R., Parkhill, J., Garnier, T., Churcher, C., Harris, D., Gordon, S. V., Eiglmeier, K., Gas, S., Barry, C. E., 3rd, Tekaia, F., Badcock, K., et al. (1998). Deciphering the biology of *Mycobacterium tuberculosis* from the complete genome sequence. *Nature* **393**, 537–544.
- Daily, J. P., Scafield, D., Pochet, N., Le Roch, K., Plouffe, D., Kamal, M., Sarr, O., Mboup, S., Ndir, O., Wypij, D., Levasseur, K., Thomas, E., et al. (2007). Distinct physiological states of *Plasmodium falciparum* in malaria-infected patients. *Nature* **450**, 1091–1095.
- Dawson, R. M. C., Elliot, D. C., Elliot, W. H., and Jones, K. M. (1986). "Data for Biochemical Research." Oxford Science Publications, Clarendon Press, Oxford.
- Dong, C., Patel, V., Clardy, J., and Wirth, D. (2008). Type II NADH dehydrogenase of the respiratory chain of *Plasmodium falciparum*. In "2008 Molecular Parasitology Meeting" pp. 148C. The Marine Biological Laboratory at Woods Hole, Massachusetts.
- Dong, C. K., Patel, V., Yang, J. C., Dvorin, J. D., Duraisingh, M. T., Clardy, J., Wirth, D. F. (2009) Type II NADH dehydrogenase of the respiratory chain of *Plasmodium falciparum* and its inhibitors. *Bioorg. Med. Chem. Lett.* **19**, 972–975.
- Fang, J., and Beattie, D. S. (2002). Novel FMN-containing rotenone-insensitive NADH dehydrogenase from *Trypanosoma brucei* mitochondria: Isolation and characterization. *Biochemistry* **41**, 3065–3072.
- Fisher, N., Bray, P. G., Ward, S. A., and Biagini, G. A. (2007). The malaria parasite type II NADH: Quinone oxidoreductase: An alternative enzyme for an alternative lifestyle. *Trends Parasitol.* **23**, 305–310.
- Fisher, N., Bray, P. G., Ward, S. A., and Biagini, G. A. (2008). Malaria-parasite mitochondrial dehydrogenases as drug targets: Too early to write the obituary. *Trends Parasitol.* **24**, 9–10.
- Fisher, N., Castleden, C. K., Bourges, I., Brasseur, G., Dujardin, G., and Meunier, B. (2004). Human disease-related mutations in cytochrome b studied in yeast. *J. Biol. Chem.* **279**, 12951–12958.
- Fisher, N., and Rich, P. R. (2000). A motif for quinone binding sites in respiratory and photosynthetic systems. *J. Mol. Biol.* **296**, 1153–1162.
- Frearson, J. A., Wyatt, P. G., Gilbert, I. H., and Fairlamb, A. H. (2007). Target assessment for antiparasitic drug discovery. *Trends Parasitol.* **23**, 589–595.
- Fry, M., Webb, E., and Pudney, M. (1990). Effect of mitochondrial inhibitors on adenosine triphosphate levels in *Plasmodium falciparum*. *Comp. Biochem. Physiol. [B]* **96**, 775–782.
- Gardner, M. J., Shallom, S. J., Carlton, J. M., Salzberg, S. L., Nene, V., Shoaibi, A., Ciecko, A., Lynn, J., Rizzo, M., Weaver, B., Jarrahi, B., Brenner, M., et al. (2002). Sequence of *Plasmodium falciparum* chromosomes 2, 10, 11 and 14. *Nature* **419**, 531–534.

- Inglese, J., Johnson, R. L., Simeonov, A., Xia, M., Zheng, W., Austin, C. P., and Auld, D. S. (2007). High-throughput screening assays for the identification of chemical probes. *Nat. Chem. Biol.* **3**, 466–479.
- Iversen, P. W., Eastwood, B. J., Sittampalam, G. S., and Cox, K. L. (2006). A comparison of assay performance measures in screening assays: Signal window, Z' factor, and assay variability ratio. *J. Biomol. Screen* **11**, 247–252.
- Kerscher, S. J. (2000). Diversity and origin of alternative NADH: Ubiquinone oxidoreductases. *Biochim. Biophys. Acta* **1459**, 274–283.
- Lambros, C., and Vanderberg, J. P. (1979). Synchronization of *Plasmodium falciparum* erythrocytic stages in culture. *J. Parasitol.* **65**, 418–420.
- Mattevi, A., Obmolova, G., Sokatch, J. R., Betzel, C., and Hol, W. G. (1992). The refined crystal structure of *Pseudomonas putida* lipoamide dehydrogenase complexed with NAD⁺ at 2.45 Å resolution. *Proteins* **13**, 336–351.
- Melo, A. M., Bandejas, T. M., and Teixeira, M. (2004). New insights into type II NAD(P)H: Quinone oxidoreductases. *Microbiol. Mol. Biol. Rev.* **68**, 603–616.
- Moser, C. C., Keske, J. M., Warncke, K., Farid, R. S., and Dutton, P. L. (1992). Nature of biological electron transfer. *Nature* **355**, 796–802.
- Saleh, A., Friesen, J., Baumeister, S., Gross, U., and Bohne, W. (2007). Growth inhibition of *Toxoplasma gondii* and *Plasmodium falciparum* by nanomolar concentrations of 1-hydroxy-2-dodecyl-4(1H)quinolone, a high-affinity inhibitor of alternative (type II) NADH dehydrogenases. *Antimicrob. Agents Chemother.* **51**, 1217–1222.
- Sasseti, C. M., Boyd, D. H., and Rubin, E. J. (2003). Genes required for mycobacterial growth defined by high density mutagenesis. *Mol. Microbiol.* **48**, 77–84.
- Schmid, R., and Gerloff, D. L. (2004). Functional properties of the alternative NADH: Ubiquinone oxidoreductase from *E. coli* through comparative 3-D modelling. *FEBS Lett.* **578**, 163–168.
- Schneider, D., Pohl, T., Walter, J., Dorner, K., Kohlstadt, M., Berger, A., Spehr, V., and Friedrich, T. (2008). Assembly of the *Escherichia coli* NADH: Ubiquinone oxidoreductase (complex I). *Biochim. Biophys. Acta* **1777**, 735–739.
- Shi, L., Sohaskey, C. D., Kana, B. D., Dawes, S., North, R. J., Mizrahi, V., and Gennaro, M. L. (2005). Changes in energy metabolism of *Mycobacterium tuberculosis* in mouse lung and under *in vitro* conditions affecting aerobic respiration. *Proc. Natl. Acad. Sci. USA* **102**, 15629–15634.
- Teh, J. S., Yano, T., and Rubin, H. (2007). Type II NADH: Menaquinone oxidoreductase of *Mycobacterium tuberculosis*. *Infect. Disord. Drug Targets* **7**, 169–181.
- Trager, W., and Jensen, J. B. (1976). Human malaria parasites in continuous culture. *Science* **193**, 673–675.
- Wallace, B. J., and Young, I. G. (1977). Role of quinones in electron transport to oxygen and nitrate in *Escherichia coli*. Studies with a ubiA- menA- double quinone mutant. *Biochim. Biophys. Acta* **461**, 84–100.
- Weinstein, E. A., Yano, T., Li, L. S., Avarbock, D., Avarbock, A., Helm, D., McColm, A. A., Duncan, K., Lonsdale, J. T., and Rubin, H. (2005). Inhibitors of type II NADH: Menaquinone oxidoreductase represent a class of antitubercular drugs. *Proc. Natl. Acad. Sci. USA* **102**, 4548–4553.
- Yano, T., Li, L. S., Weinstein, E., Teh, J. S., and Rubin, H. (2006). Steady-state kinetics and inhibitory action of antitubercular phenothiazines on mycobacterium tuberculosis type-II NADH-menaquinone oxidoreductase (NDH-2). *J. Biol. Chem.* **281**, 11456–11463.

ANALYSIS OF RESPIRATORY CHAIN COMPLEX ASSEMBLY WITH RADIOLABELED NUCLEAR- AND MITOCHONDRIAL-ENCODED SUBUNITS

Matthew McKenzie, Michael Lazarou, *and* Michael T. Ryan

Contents

1. Introduction	322
2. Analysis of mtDNA-Encoded Subunit Assembly	324
2.1. Pulse-chase labeling of mtDNA-encoded translation products in cultured cells	324
2.2. Sample preparation	325
3. Isolation of Crude Mitochondria From Cultured Cells	326
4. Mitochondrial Import and Assembly of Nuclear DNA-Encoded Subunits	326
4.1. <i>In vitro</i> transcription and translation of radiolabeled precursor proteins	327
4.2. Mitochondrial <i>in vitro</i> import and assembly assay	329
4.3. Variations to the import assay for further characterization	330
5. Separation of Proteins with SDS-PAGE	331
6. Separation of Protein Complexes with Blue-Native PAGE	331
6.1. Sample preparation and electrophoresis conditions	332
7. Separation of Individual Subunits From Their Complexes with BN-PAGE and SDS-PAGE in the Second Dimension	333
8. Processing and Analysis of Gels After Electrophoresis	334
8.1. Processing of BN-PAGE and SDS-PAGE gels	334
8.2. Analysis	334
Acknowledgments	337
References	338

Abstract

The mitochondrial respiratory chain is composed of individual complexes that range widely in terms of size and subunit composition. For example, whereas

complex II is approximately 260 kDa and is composed of 4 subunits, complex I is almost 1 MDa and contains 45 different subunits. Furthermore, complexes I, III, IV, and V harbor additional complexity, because their subunits are encoded by both nuclear and mitochondrial DNA. Subunits that are encoded by nuclear genes must be imported into mitochondria before undergoing processing, folding, and assembly with other subunits that are synthesized within the organelle. This process requires the coordinated action of assembly factors with the integration of subunits into intermediate assembly complexes. Recent studies have used various techniques to analyze subunit assembly to gain information into the biogenesis of these respiratory chain complexes and to understand how defects in assembly lead to disease. Here we describe methods to monitor the assembly of newly synthesized subunits encoded by mitochondrial DNA from cultured mammalian cells, as well as the import and assembly of individual subunits encoded by nuclear DNA.

1. INTRODUCTION

In mammals (and most other eukaryotes), the mitochondrial respiratory chain is composed of complex I (NADH-ubiquinone oxidoreductase), complex II (succinate-ubiquinone oxidoreductase), complex III (ubiquinol-ferricytochrome *c* oxidoreductase), complex IV (cytochrome *c* oxidoreductase), and complex V (F₁F₀-ATPase). Complexes I, III, and IV pump protons out of the mitochondrial matrix to generate a potential ($\Delta\psi_m$) across the inner membrane, which is subsequently used by complex V to condense ADP and Pi to ATP.

Each of the respiratory holoenzymes are composed of multiple subunits and form large-sized complexes that can be readily observed with blue-native polyacrylamide gel electrophoresis (BN-PAGE) (Schagger and Pfeiffer, 2000). Complexes I, III, IV, and V contain a mixture of subunits encoded by mtDNA and nuclear genes. Thus, for these complexes to be assembled, the nuclear-encoded subunits must translocate across the TOM and TIM channels (Hoogenraad and Ryan, 2001) before assembling with mtDNA-encoded subunits. Adding extra complexity is that the respiratory complexes also associate with one another to form so-called supercomplexes (Schagger and Pfeiffer, 2000). It has been suggested that these supercomplexes are required for channeling of substrates for efficient oxidative phosphorylation, as well as for assembly/stability of some individual complexes (Acin-Perez *et al.*, 2004; Schagger *et al.*, 2004). A stable association between complexes I, III, and IV can be visualized by BN-PAGE after solubilization of mitochondria with the detergent digitonin, yet they

dissociate after Triton X-100 solubilization (McKenzie *et al.*, 2007). Solubilization of mitochondria in the detergent *n*-dodecyl- β -D-maltoside results in an intermediate dissociation, with the formation of a complex I/III₂ supercomplex, as well as monomeric complexes I, III, and IV (McKenzie *et al.*, 2007). It is important to note that these respiratory complex profiles can also alter, depending on the detergent/protein ratio (Schagger, 2002; Schagger and Pfeiffer, 2000). For example, a low ratio will result in supercomplexes being resolved in Triton X-100 (Lazarou *et al.*, 2007), whereas higher ratios in *n*-dodecyl- β -D-maltoside will result in increasing amounts of monomeric complex I being resolved with a corresponding decrease in supercomplex levels (McKenzie *et al.*, 2006).

Defects in the respiratory chain result in human mitochondrial disease that presents with a wide variety and combination of clinical symptoms but regularly involve neurologic and muscular disease (encephalomyopathy). The incidence of respiratory chain disorders is approximately 1 in 5000 live births (Skladal *et al.*, 2003). Onset can be at any age, although severe childhood disease is common and is most often lethal (Smeitink *et al.*, 2006; Wallace, 1999). Mutations in most of the 37-mtDNA protein-, tRNA- and rRNA-encoding genes have been identified, whereas some 46 nuclear gene defects have been found to affect the respiratory chain (MITOMAP: A Human Mitochondrial Genome Database. <http://www.mitomap.org>, 2008). Notably, most patients diagnosed so far do not have mutations in genes encoding respiratory chain subunits, but rather must have mutations in genes affecting processes such as protein import, subunit processing and assembly, mtDNA replication, and synthesis or transport of nucleotides or metals (Thorburn *et al.*, 2004). In many cases, the enzymatically deficient complex correlates with the steady-state levels of the complex in mitochondria, pointing to defects in assembly and/or turnover of the complex. Furthermore, analysis of patient cells containing a specific respiratory complex defect has led to the identification of a number of candidate assembly factors (Dunning *et al.*, 2007; Ogilvie *et al.*, 2005; Pagliarini *et al.*, 2008; Saada *et al.*, 2008). The functional characterization of these candidates requires an ability to identify at which point in the assembly pathway of the respiratory complex is affected. This, in turn, requires a general understanding of how subunits are assembled into respiratory complexes. In this chapter, a method is outlined for analyzing subunit assembly into respiratory complexes and the intermediates that can be detected. Although the method outlined to monitor the assembly of mtDNA-encoded subunits is restricted to respiratory chain complexes, the method to study the import and assembly of nuclear encoded subunits may be adapted to analyze the biogenesis of any imported mitochondrial protein that can assemble into a protein complex.

2. ANALYSIS OF MTDNA-ENCODED SUBUNIT ASSEMBLY

This section describes techniques to monitor the progression of newly translated mtDNA-encoded subunits into intermediate and fully assembled complexes. The technique is adapted from the original subunit labeling method described by Chomyn (1996). It involves the use of cultured cells that are treated with cycloheximide to block cytosolic protein synthesis and the specific labeling of mitochondrial translation products, which continue to be synthesized, with ^{35}S -methionine/cysteine. Both radiolabel and cycloheximide are removed to enable new protein synthesis to occur and to facilitate the chase of radiolabeled mtDNA-encoded subunits along their respective assembly pathway. For these pulse-chase experiments, cells are routinely subjected to a chloramphenicol pretreatment before the labeling. Chloramphenicol inhibits the translation of mtDNA-encoded proteins, thus allowing for the accumulation of cytosolically translated respiratory chain enzyme protein subunits within mitochondria. After removal of the chloramphenicol, these cytosolically translated proteins can help to stabilize the newly synthesized mtDNA-encoded subunits and aid in their assembly into intermediate and mature respiratory chain complexes.

The assembly of subunits into complexes I, III, IV, and V can be observed by separating detergent-solubilized protein complexes by BN-PAGE, whereas individual radiolabeled subunits can be visualized by separating the subunits from complexes with SDS-PAGE in the second dimension. The technique can be adapted for many cell types (e.g., patient cells harboring a specific mutation or cells depleted of a specific factor with RNA interference) or after treatment of cells to other insults (e.g., oxidants, uncouplers).

2.1. Pulse-chase labeling of mtDNA-encoded translation products in cultured cells

All types of cultured cells can be used for this assay. However, although 13 subunits are encoded by mtDNA in mammals, not all of these are readily labeled with this technique, and this may depend on the cell type used. The following protocol describes the labeling assay performed in 9-cm plates ($\sim 60\text{ cm}^2$); however, the procedure can be scaled up or down as required.

Cells seeded onto 9-cm plates are grown at $37^\circ/5\% \text{ CO}_2$ in Dulbecco's modified Eagle's Medium (DMEM) supplemented with 5% (v/v) fetal bovine serum (FBS) and antibiotics. However, if the cells harbor mitochondrial respiratory defects, they are cultured in DMEM supplemented with 10% FBS and $50\ \mu\text{g/ml}$ uridine. When the cells reach approximately 90% confluence (approximately $1\text{ to }2 \times 10^6$ fibroblasts), chloramphenicol

([Sigma] in a 50 mg/ml stock in ethanol) is added to a final concentration of 50 $\mu\text{g}/\text{ml}$, and cells are incubated a further 6 to 16 h. The media containing chloramphenicol is removed, and cells are rinsed in phosphate-buffered saline (PBS) prewarmed to 37°. Cells are then incubated in methionine-free DMEM for 10 min at 37°/5% CO₂. The media is removed and replaced with 5 ml methionine-free DMEM supplemented with 5% dialyzed FBS and 0.1 mg/ml cycloheximide (from a 100 mg/ml stock in ethanol). Cells are incubated for 15 min at 37°/5% CO₂ before addition of 55 μCi (1175 Ci/mmol) ³⁵S-methionine/³⁵S-cysteine (EXPRE³⁵S³⁵S Protein Labeling Mix; Perkin Elmer Life Sciences, Boston, MA, USA) to the culture media (1 μl of labeling mix per ml of media). Cells are incubated for 2 h at 37°/5% CO₂ to allow synthesis of radiolabeled mtDNA translation products (pulse). After this, cold methionine (from a sterile 10 mM stock in H₂O) is added to the media to a final concentration of 0.1 mM and incubated for a further 15 min at 37°/5% CO₂. The media is carefully removed and cells are washed in PBS. To perform a chase reaction, DMEM supplemented with 5% (v/v) FBS is added and the cells are incubated at 37°/5% CO₂. Cells are usually harvested at 0, 3, 6, and 24 h chase after pulse labeling; however, chase times up to 120 h can be performed. After this, cells are harvested by trypsin treatment, pelleted by centrifugation, and washed with ice-cold PBS.

2.2. Sample preparation

After pulse-chase labeling, the analysis of mtDNA-encoded subunits can be performed with either whole cells or by preparing isolated mitochondria. Mitochondria should be isolated immediately after harvesting cells (section 3), or whole cells may be snap-frozen as pellets in liquid nitrogen and stored at -80°. The use of whole cell protein has the benefit of simple preparation and is suitable for one-dimensional SDS-PAGE and BN-PAGE analysis (sections 5 and 6). We routinely use approximately 100 μg of whole cell protein per lane on a large (18 × 16 cm) format gel (SE600, Hoefer, Holliston, MA, USA) and have found that a sufficient amount of whole cells (e.g., fibroblasts) can be grown in one well (~9.5 cm²) of a 6-well plate to provide enough material to be analyzed on 2 to 3 lanes of a polyacrylamide gel (McKenzie *et al.*, 2007). In contrast to the simplicity of the use of whole cells, the isolation of mitochondria requires further preparation but generally results in superior resolution of translation products and their complexes on polyacrylamide gels. For large-format SDS- and BN-PAGE gels, 30 to 50 μg of mitochondrial protein is loaded per lane. Furthermore, although total cell extracts are suitable for 1-D gel analysis, we have found that the use of isolated mitochondria is essential for BN-PAGE followed by SDS-PAGE in the second dimension (2-D-PAGE, see section 7). For this analysis 70 to 100 μg of mitochondrial protein is used in the first dimension.

3. ISOLATION OF CRUDE MITOCHONDRIA FROM CULTURED CELLS

We use a simple technique involving mechanical homogenization and differential centrifugation to isolate mitochondria. All steps are performed on ice. Cells from each 9-cm plate are harvested, washed in PBS, and resuspended in 3 ml of solution A (20 mM HEPES, pH 7.6, 220 mM mannitol, 70 mM sucrose, 1 mM EDTA, 0.5 mM phenylmethylsulfonyl fluoride (PMSF; added fresh from a 100 mM stock in isopropanol), and 2 mg/ml bovine serum albumin [BSA]). Cells are left on ice for 15 min to facilitate cell swelling before being homogenized in a 5-ml glass homogenizer with 20 strokes of a drill-fitted Teflon pestle. If a drill-fitted pestle is not available, the homogenization can be done by hand with approximately 30 strokes. Homogenates are centrifuged at 800g for 15 min at 4° to pellet nonlysed cells, cell debris, and nuclei, and the supernatant is retained and centrifuged at 10,000g for 15 min at 4°. The supernatant is removed, and the pellet representing crude mitochondria is resuspended in 3 ml solution B (solution A without BSA). The mitochondria are pelleted again with centrifugation (10,000g for 10 min at 4°) and gently resuspended in 100 μ l of solution B for BN-PAGE analysis or 100 μ l import buffer (20 mM HEPES-KOH [pH 7.4], 250 mM sucrose, 80 mM KOAc, 5 mM MgOAc, 10 mM sodium succinate, 5 mM ATP, and 5 mM methionine) for *in vitro* import studies. The amount of mitochondrial protein can be calculated by adding 1 μ l of mitochondrial suspension to 600 μ l of 50 mM TRIS-Cl, pH 8.0, 0.1% (w/v) SDS, and measuring the absorbance at 280 nm and 310 nm. Mitochondrial protein concentration in mg/ml is given by $(A_{280\text{nm}} - A_{310\text{nm}}) / 1.05 \times 600$ (Clarke, 1976).

4. MITOCHONDRIAL IMPORT AND ASSEMBLY OF NUCLEAR DNA-ENCODED SUBUNITS

The import of proteins into mitochondria has been well characterized, in part because of a robust *in vitro* import assay. After the advent of BN-PAGE to resolve membrane protein complexes (Schagger and von Jagow, 1991), the *in vitro* import assay has been adapted to also analyze the assembly pathways of many mitochondrial proteins into their multisubunit complexes. Although most studies that use this technique have focused on the assembly of subunits into the translocation complexes of mitochondria, more recent reports have demonstrated its appropriateness in analyzing the assembly profiles of individual respiratory chain subunits (Brandner *et al.*, 2005; Lazarou *et al.*, 2007; Mick *et al.*, 2007). The technique involves

preparing ^{35}S -labeled precursor proteins *in vitro* from rabbit reticulocyte lysates and then adding them to freshly isolated mitochondria. After incubation, the mitochondria are isolated, and precursor import is verified by SDS-PAGE and assembly by BN-PAGE.

4.1. *In vitro* transcription and translation of radiolabeled precursor proteins

4.1.1. Preparation of template DNA for transcription reactions

Precursor proteins are synthesized from rabbit reticulocyte lysates in the presence of ^{35}S -methionine. A number of different kits are available and require either the addition of *in vitro* synthesized RNA to lysates or the addition of DNA templates for use in coupled transcription/translation. In either case template DNA is required. We commonly amplify open reading frames (ORFs) from a mix panel human cDNA library (Clontech), with the PCR Extender System (5Prime) according to manufacturer's instructions. Each PCR reaction consisted of $1\times$ High Fidelity Buffer (5Prime), 400 nM of both 5' and 3' oligonucleotide primers (Sigma), 200 μM dNTP's (Promega), 10 to 50 ng template DNA, and 3.75 U of PCR Extender Enzyme Mix in a final volume of 50 μl . Amplification parameters typically involve an initial denaturation step at 94° (2 min) followed by five cycles consisting of a denaturation step at 94° (30 sec), a primer annealing step at 50 to 55° (30 sec) and an elongation step at 72° with a time allocation of 1 min per 1000 bp DNA product. After the initial five cycles, an additional 30 cycles are carried out consisting of a higher annealing temperature, typically 55 to 60° (30 sec). All other steps remain unchanged. The reaction is completed with a final elongation step at 72° for 6 min.

In most cases, we clone subunit ORFs into the pGEM-4Z vector (Promega). This vector incorporates an SP6 RNA polymerase transcription initiation site upstream of the cloned ORF initiation codon. Circular or linearized plasmid DNA containing the ORF of interest can be used for transcription reactions. ORFs may also be amplified from any source with a forward primer that incorporates the SP6 RNA polymerase promoter region upstream of the initiation codon (shown in bold): 5' GGATT TAGGT GACAC TATAG AATAC **ATG** N₁₅₋₁₈ 3', (N refers to nucleotides that are complementary to the template DNA of a complex I subunit). Furthermore, it is important to design a reverse primer that includes a termination codon. Before use in transcription reactions all DNA templates must be purified with commercially available DNA purification kits.

4.1.2. *In vitro* transcription

Extra care must be taken when working with RNA to avoid the introduction of RNases in your sample. It is best to use sterile filter tips, tubes, and sterile reagents wherever possible. For *in vitro* transcription, purified

template DNA (1 μg circular/linearized plasmid DNA, or ~ 500 ng PCR product including an SP6 RNA polymerase promoter site) is incubated at 37° for 2 to 3 h with 120 μl transcription premix (filter sterilized 40 mM HEPES, pH 7.4, 6 mM $\text{Mg}(\text{OAc})_2$, 2 mM spermidine, 40 $\mu\text{g}/\text{ml}$ BSA, 6 mM DTT, 0.3 mM ATP, 0.3 mM CTP, 0.3 mM UTP, 0.3 mM GTP), 28 U of SP6 RNA polymerase (Promega), and 80 U of RNasin ribonuclease inhibitor (Promega) in a total volume of 200 μl . After transcription, the RNA is precipitated by the addition of 20 μl 10 M LiCl_2 and 600 μl ice-cold ethanol and incubated at -20° for at least 15 min. RNA is recovered by centrifugation in a table top centrifuge at 16,000g at 4° for 30 min followed by a wash step with 70% ice-cold ethanol. The RNA is then resuspended in 50 μl sterile MilliQ H_2O (Millipore) containing 80 U RNasin ribonuclease inhibitor (Promega). RNA can be stored in aliquots at -80° where it can remain stable for more than a year.

4.1.3. *In vitro* synthesis of radiolabeled precursor proteins from RNA

We typically undertake *in vitro* translation reactions with 32 μl rabbit reticulocyte lysate (Promega), 3 μl RNA (generated from *in vitro* transcription as described previously), 7 μl H_2O , 20 μCi of ^{35}S -methionine/cysteine (EXPRE $^{35}\text{S}^{35}\text{S}$ Protein Labeling Mix; Perkin Elmer Life Sciences, Boston, MA, USA), and 2 μl amino acids minus methionine (Promega). The reaction is incubated at 30° for 90 min. Cycloheximide may be added to stop the reaction. Optimization of RNA and/or salt concentrations may be necessary to obtain optimal amounts of translation product. Radiolabeled precursors may be used either immediately or frozen in liquid nitrogen and stored at -80° . The total reaction volume may be adjusted according to the volume of lysate required for the experiment.

4.1.4. Coupled *in vitro* transcription/translation

Commercial kits are available to perform coupled transcription/translation reactions (e.g., TNT Quick Coupled transcription/translation kit from Promega). In this case, a DNA template with the suitable promoter region upstream of the initiation codon is required. A standard reaction consists of 0.5 μg of plasmid DNA or PCR product, 28 μCi ^{35}S -methionine/cysteine (EXPRE $^{35}\text{S}^{35}\text{S}$ Protein Labeling Mix; Perkin Elmer Life Sciences, Boston, MA, USA) and 40 μl lysate premix (Promega), incubated at 30° for 90 min. To determine the success of translation reactions, 1 μl of lysate is analyzed on SDS-PAGE and subjected to phosphor image analysis (Amersham Biosciences).

4.2. Mitochondrial *in vitro* import and assembly assay

Mitochondria isolated from any cultured cell line appear to be suitable for *in vitro* import and assembly assays (section 3). We routinely use mitochondria isolated from human fibroblasts owing to the importance of patient fibroblast cell lines for investigations into subunit assembly into respiratory chain complexes (Lazarou *et al.*, 2008). Transformed cell lines such as 143B and HEK293T also work well. Typically, fibroblasts cultured to 100% confluence on 150 cm² plates yield ~300 μ g of mitochondrial protein when isolated.

The following protocol describes the approach to undertake a simple import and assembly analysis of a respiratory chain subunit. A typical *in vitro* import reaction consists of a radiolabeled precursor subunit incubated with freshly isolated, energized mitochondria at 37° for various times. The duration and number of time points for the import reaction vary depending on the subunit under investigation. Typically, three import time points are chosen, and an extra control sample is used where mitochondria lack a membrane potential to block import. One half of the sample is treated with external protease and subjected to BN-PAGE. Thus, any complexes observed to contain radiolabeled protein are likely to have formed after import. The other half is split in two and treated with or without external protease before SDS-PAGE analysis. This enables one to assess precursor binding to mitochondria and the degree of import, as well as potential cleavage of the mitochondrial presequence that is often (but not always) present.

Four 1.5-ml tubes are set up on ice with tubes 1 to 3 containing 100 μ g mitochondrial protein in 100 μ l import buffer (20 mM HEPES-KOH [pH 7.4], 250 mM sucrose, 80 mM KOAc, 5 mM MgOAc, 10 mM sodium succinate, 5 mM ATP, and 5 mM methionine). Tube 4 is set up in the same way but with import buffer lacking sodium succinate and containing 10 μ M of the potassium ionophore valinomycin (from a 1 mM stock in ethanol; Sigma) to dissipate the membrane potential ($\Delta\psi_m$). After the addition of 10 μ l of lysate containing the radiolabeled precursor, samples are incubated at 37° in reverse order of time points (i.e., a 45-min time point first, followed by a 15 min, and then a 5 min time point). Tubes 3 and 4 are incubated for the longest time point. This approach allows the removal of all tubes at the same time once the import is complete.

After import, mitochondria are pelleted at maximum speed in a tabletop centrifuge at 4° for 5 min. The supernatants are carefully discarded, and the mitochondrial pellets are resuspended in 100 μ l of ice-cold sucrose buffer (20 mM HEPES-KOH, pH 7.0, 500 mM sucrose). Three tubes (A, B, and C) are then set up for each sample and placed on ice; 50 μ l of the import

reaction is added to tube A and 25 μl to each of tubes B and C. Both A and B samples are subjected to protease treatment to degrade nonimported radiolabeled precursor by the addition of 50 $\mu\text{g}/\text{ml}$ proteinase K (from a freshly made 5 mg/ml stock in dH_2O). Samples are incubated on ice for 10 to 15 min before stopping the reaction with 1 mM PMSF (from a 100 mM stock in isopropanol) for 10 min. Mitochondrial pellets (25 μg protein) from tubes C (minus protease) and B (protease-treated) are first precipitated with trichloroacetic acid (TCA) before SDS-PAGE analysis. This treatment prevents any proteinase K reactivation from occurring. Samples are precipitated by the addition of one fifth volume of 72% (w/v) TCA and incubated on ice for 15 min followed by centrifugation for 20 min at 20,000g at 4°. Protein pellets are washed with 100% ice-cold acetone, air-dried, and resuspended in SDS-PAGE loading dye (50 mM TRIS-Cl, pH 6.8, 100 mM DTT, 2% [w/v] SDS, 10% [v/v] glycerol, 0.1% [w/v] bromophenol blue). A 1- μl sample of lysate in SDS-PAGE loading dye is also loaded onto the gel as a control to confirm the success of the translation reaction. SDS-PAGE is performed as described in [section 5](#). Mitochondrial pellets (50 μg protein), from the “A” tubes are solubilized in 50 μl 1% (w/v) *n*-dodecyl- β -D-maltoside (Sigma), in 50 mM NaCl, 10% (v/v) glycerol, 20 mM BIS-TRIS, pH 7.0, and subjected to 4 to 13% gradient BN-PAGE ([section 6](#)).

4.3. Variations to the import assay for further characterization

The import assay can be varied in a number of different ways to further characterize the biogenesis of a particular protein. For example, the incorporation of an imported protein into membranes can be studied with carbonate extraction techniques, and its submitochondrial location can be further assessed with mitochondrial swelling and protease treatments (e.g., [Humphries *et al.*, 2005](#)). In the following, we have listed two modifications to the technique that can be used to further assess the assembly pathway of a subunit of the respiratory chain.

4.3.1. Chase assays

An *in vitro* import and chase assay may be performed if a putative assembly intermediate of a respiratory chain subunit is identified. Import reactions are set up as described earlier, and the subunit under investigation is imported for 2 to 10 min at 37° (import time will depend on when the assembly intermediate forms). After this, mitochondria are reisolated at 16,000g for 5 min at 4°, and the supernatant containing excess precursor is removed. Mitochondria are gently resuspended in the original volume of import buffer and incubated at 37° for various times. Mitochondria are then reisolated and subjected to BN-PAGE analysis as described in [section 6](#).

4.3.2. Identifying other subunits within complexes with antibody-shift assays

To confirm whether an imported subunit has assembled into a specific complex that contains known subunits to which antibodies are available, antibody-shift assays can be performed (Humphries *et al.*, 2005; Johnston *et al.*, 2002). In this case, the mitochondrial extract is first resuspended in BN-solubilization buffer containing the appropriate detergent for BN-PAGE (as described in section 6.1). Polyclonal antibody sera are then added, and the sample is incubated on ice for 30 min. The amount of sera required may range from 1 to 5 μ l and should be determined empirically. As an example, 50 μ g of isolated mitochondria are resuspended in 50 μ l of BN-solubilization buffer (with detergent) followed by the addition of 1 μ l of sera. After 30 min, a clarifying spin is performed at 18000g for 5 min at 4°. The sample is then combined with BN-loading dye and applied to BN-PAGE as described in section 6.1. If the antibody binds to a subunit of the complex, then it will shift to a higher molecular weight and will run higher on the BN-PAGE gel.

5. SEPARATION OF PROTEINS WITH SDS-PAGE

The cell or mitochondrial pellets are resuspended in SDS-PAGE loading dye (50 mM TRIS-Cl, pH 6.8, 100 mM DTT, 2% [w/v] SDS, 10% [v/v] glycerol, 0.1% [w/v] bromophenol blue). For analysis of mtDNA translation products, the samples are not boiled as this can induce aggregation of these hydrophobic proteins (Chomyn, 1996). For SDS-PAGE, we typically use a TRIS-tricine buffering system on large format (18 cm \times 16 cm) plates as described (Schagger and von Jagow, 1987), but with minor modifications. Gel solutions of 4, 10, and 16% (w/v) are prepared from an acrylamide stock (48% [w/v] acrylamide/1.5% [w/v] bisacrylamide) in 1 M TRIS-Cl, pH 8.45, 0.1% SDS. A continuous 10 to 16% (w/v) acrylamide gradient is prepared for the separation phase with a 4% (w/v) stacking phase. Proteins are electrophoresed at 100 V/25 mA for 14 h at room temperature with cathode (100 mM TRIS-Cl, pH 8.25, 100 mM Tricine, 0.1% SDS) and anode (0.2 M TRIS-Cl, pH 8.9) buffers. The gels are subjected to further processing as described in section 8.

6. SEPARATION OF PROTEIN COMPLEXES WITH BLUE-NATIVE PAGE

Blue-native polyacrylamide gel electrophoresis (BN-PAGE) is a technique developed by Schagger and von Jagow (1991) for the separation of membrane protein complexes. “Blue” refers to Coomassie Brilliant Blue G

that is present in both the sample loading dye and in the cathode buffer that binds to proteins and (1) imparts a slight negative charge on the proteins enabling them to enter the native gel at neutral pH and (2) minimizes protein aggregation during electrophoresis because the dye binds to hydrophobic regions of proteins. It should be noted that not all membrane proteins/complexes resolve well on BN-PAGE. In fact, many proteins streak along a large molecular weight range, perhaps because of their dissociation during electrophoresis. However, the complexes of the respiratory chain resolve very well and served as models for the optimization of the technique (Schagger and von Jagow, 1991).

Our protocol is based on the original method, but with slight differences in the concentrations of some components. We use the Ruby SE 600 standard dual cooled vertical electrophoresis unit from GE Healthcare with 18×16 cm glass plates, 1-mm spacers, and 15-well combs. The cooling chamber enables the apparatus to be connected to a recirculating, refrigerated water bath (set at 4°) to maintain a constant temperature under conditions of high voltage. In general we use a 4 to 13% acrylamide gradient gel with a 4% acrylamide stacking gel. This resolves protein complexes from ~ 1000 kDa to ~ 50 kDa. The higher percentage acrylamide mix contains 10% (v/v) glycerol to aid in pouring the gradient.

6.1. Sample preparation and electrophoresis conditions

Cell pellets (100 μg protein) or isolated mitochondria (30 to 70 μg protein) are solubilized for 30 min on ice in 50 μl of 20 mM Bis-TRIS, pH 7.4, 50 mM NaCl, 10% (v/v) glycerol containing either 1% (w/v) digitonin (Merck), 1% (w/v) Triton X-100 (Sigma) or 0.2 to 1% (w/v) *n*-dodecyl- β -D-maltoside (Sigma). After solubilization, insoluble material is removed by centrifugation at 18 000g for 5 min at 4° . Five microliters of 10 \times BN-PAGE loading dye (5% [w/v] Coomassie Blue G, 500 mM ϵ -amino *n*-caproic acid (Sigma), 100 mM BIS-TRIS pH 7.0) is added to the sample and loaded onto the gel; 20 μg of thyroglobulin (669 kDa), ferritin (440 kDa), and bovine serum albumin (134 and 67 kDa) are used as molecular weight markers (all available from Sigma). The cathode buffer (15 mM BIS-TRIS, pH 7.0, 50 mM tricine) containing 0.02% (w/v) Coomassie Blue G is used until the dye front had reached approximately one third of the way through the gel before exchanging with cathode buffer lacking Coomassie Blue G. The anode buffer contains 50 mM BIS-TRIS, pH 7.0. Native complexes are separated at 100 V/5 mA for 13.5 h at 4° . After electrophoresis, gels are processed as described in [section 8](#).

7. SEPARATION OF INDIVIDUAL SUBUNITS FROM THEIR COMPLEXES WITH BN-PAGE AND SDS-PAGE IN THE SECOND DIMENSION

For more detailed analysis of protein assembly, in particular to analyze the assembly of individual mtDNA-encoded subunits, 2-D PAGE can be performed. This technique is useful for identifying the subunit composition of each intermediate or mature complex, and as a result an assembly pathway can be deduced.

After BN-PAGE, individual lanes are excised and sandwiched between two 18- to 16-cm glass plates (Fig. 18.1). The BN-PAGE strips are placed on an angle with the bottom of the strip (higher percentage acrylamide) slightly lower. This facilitates a more even entry of the proteins into the stacking gel from the BN-PAGE strip and to prevent air bubbles forming when pouring the stacking gel. A continuous 10 to 16% polyacrylamide TRIS-tricine gradient gel (section 5) is poured underneath the BN-PAGE

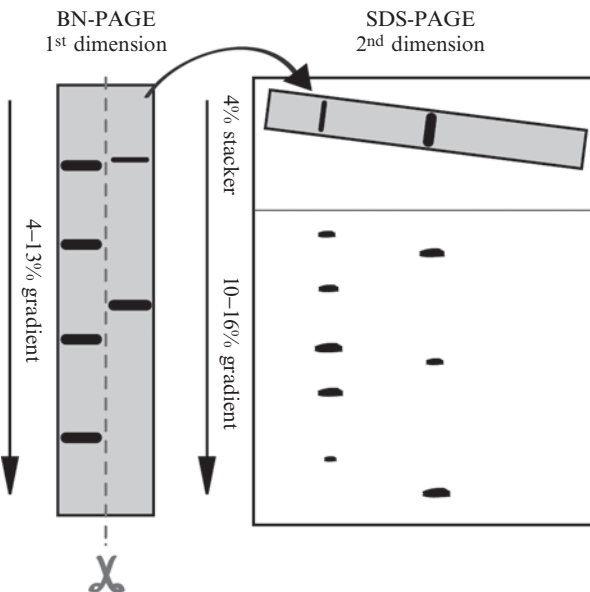


Figure 18.1 Schematic depicting the preparation of two-dimensional BN-PAGE. Isolated mitochondria (~50 to 70 μ g) are solubilized in the desired detergent and resolved on a 4 to 13% Blue-Native (BN)-PAGE gradient gel in the first dimension (left panel). A gel strip is removed and “sandwiched” on a slight angle between two glass plates. The higher percentage acrylamide end of the BN-strip is placed lower and near the edge of the gel (right panel). A 10 to 16% SDS-PAGE gradient gel is poured underneath the BN-strip, and a 4% stacking gel around the strip for separation in the second dimension.

strip and overlaid with isopropanol and allowed to set before a 4% (w/v) polyacrylamide stacking gel is poured around the strip. Approximately 1 to 2 cm of stacking gel should be between the BN-PAGE strip and the separating gel. Electrophoresis in the second dimension is performed at 100 V/25 mA for 14 h at room temperature. The gel is then processed as described below.

8. PROCESSING AND ANALYSIS OF GELS AFTER ELECTROPHORESIS

8.1. Processing of BN-PAGE and SDS-PAGE gels

After electrophoresis, gels are stained with Coomassie, dried, and exposed to a phosphor intensifying screen and developed by phosphor imaging. Alternately, after PAGE separation, proteins can be transferred to nitrocellulose filters (in the case of SDS-PAGE) or to polyvinylidene fluoride membranes (PVDF; in the case of BN-PAGE). The benefit of Western transfer is that after phosphor image analysis, the blot can be probed with various antibodies as loading controls and to ascertain the position of respiratory complexes and their levels. Many antibodies against mitochondrial proteins and, in particular, subunits of the respiratory chain are available from commercial sources.

8.2. Analysis

Figures 18.2 to 18.4 demonstrate the techniques described previously. In Fig. 18.2A, mtDNA-encoded translation products for complex I (ND1, ND2, ND3, ND4, ND4L, ND5), complex III (cytb), complex IV (COI, COII, COIII), and complex V (ATP6, ATP8) can be identified by SDS-PAGE and are stable at 0, 3, and 24 h chase. Separation of isolated mitochondria on BN-PAGE after pulse-chase labeling and solubilization in Triton X-100 reveals various assembly intermediates and mature respiratory complexes (Fig. 18.2B). At 0 h chase a complex IV intermediate (“IVa”, ~100 kDa) and two complex I intermediates (“CIa”, ~460 and “CIb”, ~830 kDa) along with mature complex V (“V”, ~650 kDa) are visible. At 3 h chase the mature complex III homo-dimer (“III2”, ~500 kDa), a larger complex IV intermediate (“CIVb”, ~180 kDa), and mature complex IV (“IV”, ~200 kDa) have assembled. By 24 h chase mature complex I (“I”, ~980 kDa) is also visible.

The assembly of individual mtDNA-encoded subunits can be monitored for complexes I, III, IV, and V at 0, 3, and 24 h chase with 2-D PAGE (Fig. 18.3). This technique has been used to identify a novel complex III assembly intermediate (McKenzie *et al.*, 2007) and to model the assembly of

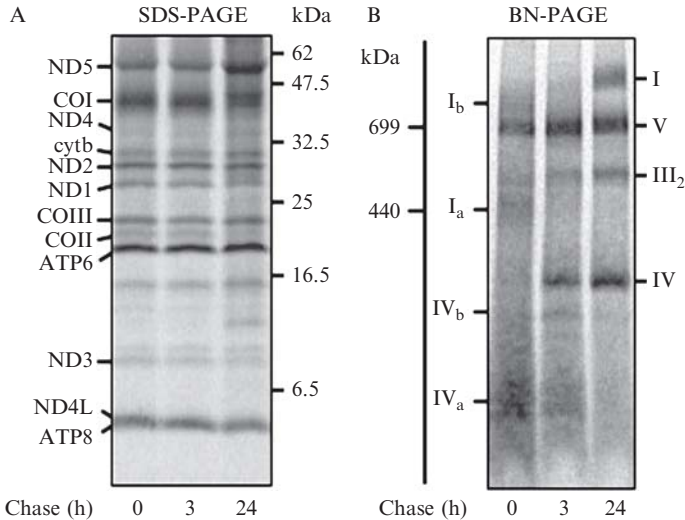


Figure 18.2 Analysis of labeled mtDNA-encoded translation products by SDS- and BN-PAGE. MtDNA-translation products were labeled in human fibroblasts for 2 h (pulse), followed by chases of 0, 3, and 24 h. After the pulse/chase, mitochondria were isolated and (A) proteins subjected to 10 to 16% SDS-PAGE gradient gel or (B) solubilized in Triton X-100 and protein complexes separated on a 4 to 13% BN-PAGE gradient gel. Radiolabeled proteins were detected by phosphor image analysis. (A) MtDNA-encoded translation products are indicated and are stable at 0, 3, and 24 h chase. (B) After separation by BN-PAGE, various respiratory complexes are visible: the complex IV intermediate (“IV_a”, ~100 kDa), two complex I intermediates (“CI_a”, ~460 and “CI_b”, ~830 kDa) and mature complex V (“V”, ~650 kDa) at 0 h chase, the mature complex III homo-dimer (“III₂”, ~500 kDa), a larger complex IV intermediate (“CIV_b”, ~180kDa) and mature complex IV (“IV”, ~200 kDa) at 3 h chase and the mature complexes I (“I”, ~980 kDa), V, III₂ and IV at 24 h chase.

complex IV (Nijtmans *et al.*, 1998). The COI subunit can be identified in the complex IV intermediate IV_a at 0 h chase, in the intermediates IV_a and IV_b and mature complex IV (“IV”) at 3 h chase, and primarily in mature complex IV (“IV”) at 24 h chase. COII and COIII subunits appear to assemble differently to COI, with these subunits already present in mature complex IV (“IV”) at 0 h chase. The assembly of cytb can be followed through a monomeric form (~30 kDa) and an assembly intermediate (~120 kDa) at 0 h chase, the complex III homodimer (“III₂”, ~500 kDa) at 3 h chase and the complex III₂/complex IV supercomplex (“III₂/IV”, ~700 kDa, near complex V) by 24 h chase. Subunits ND1 and ND2 can be detected in complex I assembly intermediates of ~460 kDa (“CI_a”) and ~830 kDa (“CI_b”) at 0 h and 3 h chase. ND3 is also weakly detected in the ~460 kDa intermediate at these chase times. After 3 h chase, ND6 is weakly detected in the ~460 kDa intermediate, whereas ND4 and ND5 are weakly detected in an intermediate of ~650 kDa. By 24 h chase all seven

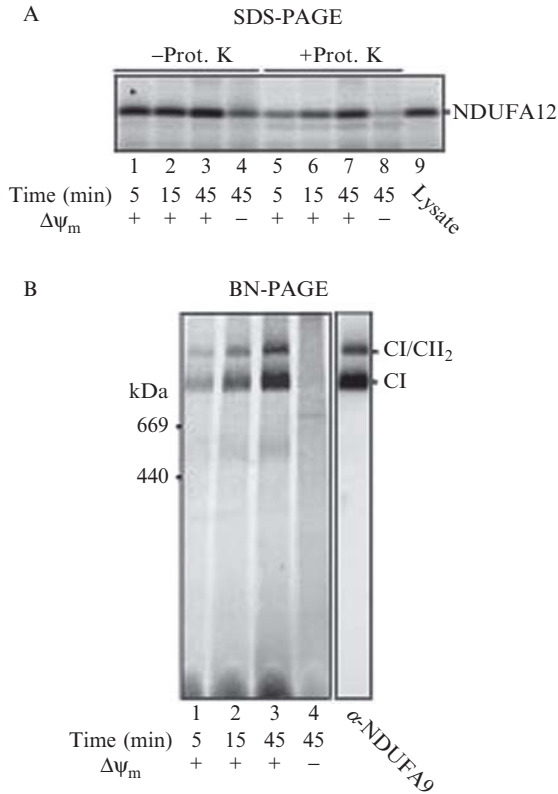


Figure 18.4 *In vitro* import and assembly of NDUFA12 into preexisting complex I. ^{35}S -NDUFA12 was incubated for different times with mitochondria isolated from fibroblasts in the presence or absence of a membrane potential ($\Delta\psi_m$). Samples were treated with or without proteinase K (Prot. K) and subjected to (A) SDS-PAGE or (B) solubilized in DDM-containing buffer and BN-PAGE (protease treated samples only). Radiolabeled proteins were detected by phosphor image analysis. CI, Complex I; CI/CIII₂, complex I/complex III₂ supercomplex. Right panel in (B), the migration of CI and the CI/CIII₂ supercomplex were identified by Western blot analysis with polyclonal antibodies to the complex I subunit NDUFA9.

analysis with antibodies against the complex I subunit NDUFA9 (right panel). Dissipation of the membrane potential abolished any assembly of ^{35}S -NDUFA12 (Fig. 18.4B, lane 4).

ACKNOWLEDGMENTS

This work was supported by grants from the Australian National Health and Medical Research Council and the Ramaciotti Foundation. M. McK. is supported by an NHMRC Peter Doherty Fellowship.

REFERENCES

- Acin-Perez, R., Bayona-Bafaluy, M. P., Fernandez-Silva, P., Moreno-Loshuertos, R., Perez-Martos, A., Bruno, C., Moraes, C. T., and Enriquez, J. A. (2004). Respiratory complex III is required to maintain complex I in mammalian mitochondria. *Mol. Cell* **13**, 805–815.
- Brandner, K., Mick, D. U., Frazier, A. E., Taylor, R. D., Meisinger, C., and Rehling, P. (2005). Taz1, an outer mitochondrial membrane protein, affects stability and assembly of inner membrane protein complexes: Implications for Barth Syndrome. *Mol. Biol. Cell* **16**, 5202–5214.
- Chomyn, A. (1996). *In vivo* labeling and analysis of human mitochondrial translation products. *Methods Enzymol.* **264**, 197–211.
- Clarke, S. (1976). A major polypeptide component of rat liver mitochondria: Carbamyl phosphate synthetase. *J. Biol. Chem.* **251**, 950–961.
- Dunning, C. J., McKenzie, M., Sugiana, C., Lazarou, M., Silke, J., Connelly, A., Fletcher, J. M., Kirby, D. M., Thorburn, D. R., and Ryan, M. T. (2007). Human CIA30 is involved in the early assembly of mitochondrial complex I and mutations in its gene cause disease. *EMBO J.* **26**, 3227–3237.
- Hoogenraad, N. J., and Ryan, M. T. (2001). Translocation of proteins into mitochondria. *IUBMB Life* **51**, 345–350.
- Humphries, A. D., Streimann, I. C., Stojanovski, D., Johnston, A. J., Yano, M., Hoogenraad, N. J., and Ryan, M. T. (2005). Dissection of the mitochondrial import and assembly pathway for human Tom40. *J. Biol. Chem.* **280**, 11535–11543.
- Johnston, A. J., Hoogenraad, J., Dougan, D. A., Truscott, K. N., Yano, M., Mori, M., Hoogenraad, N. J., and Ryan, M. T. (2002). Insertion and assembly of human tom7 into the preprotein translocase complex of the outer mitochondrial membrane. *J. Biol. Chem.* **277**, 42197–42204.
- Lazarou, M., McKenzie, M., Ohtake, A., Thorburn, D. R., and Ryan, M. T. (2007). Analysis of the assembly profiles for mitochondrial- and nuclear-dna-encoded subunits into complex I. *Mol. Cell. Biol.* **27**, 4228–4237.
- Lazarou, M., Thorburn, D. R., Ryan, M. T., and McKenzie, M. (2009). Assembly of mitochondrial complex I and defects in disease. *Biochim. Biophys. Acta* **1793**, 78–88.
- McKenzie, M., Lazarou, M., Thorburn, D. R., and Ryan, M. T. (2006). Mitochondrial respiratory chain supercomplexes are destabilized in Barth Syndrome patients. *J. Mol. Biol.* **361**, 462–469.
- McKenzie, M., Lazarou, M., Thorburn, D. R., and Ryan, M. T. (2007). Analysis of mitochondrial subunit assembly into respiratory chain complexes using Blue Native polyacrylamide gel electrophoresis. *Anal. Biochem.* **364**, 128–137.
- Mick, D. U., Wagner, K., van der Laan, M., Frazier, A. E., Perschil, I., Pawlas, M., Meyer, H. E., Warscheid, B., and Rehling, P. (2007). Shy1 couples Cox1 translational regulation to cytochrome c oxidase assembly. *EMBO J.* **26**, 4347–4358.
- Nijtmans, L. G., Taanman, J. W., Muijsers, A. O., Speijer, D., and Van den Bogert, C. (1998). Assembly of cytochrome c oxidase in cultured human cells. *Eur. J. Biochem.* **254**, 389–394.
- Ogilvie, I., Kennaway, N. G., and Shoubridge, E. A. (2005). A molecular chaperone for mitochondrial complex I assembly is mutated in a progressive encephalopathy. *J. Clin. Invest.* **115**, 2784–2792.
- Pagliarini, D. J., Calvo, S. E., Chang, B., Sheth, S. A., Vafai, S. B., Ong, S. E., Walford, G. A., Sugiana, C., Boneh, A., Chen, W. K., Hill, D. E., Vidal, M., *et al.* (2008). A mitochondrial protein compendium elucidates complex I disease biology. *Cell* **134**, 112–123.

- Saada, A., Edvardson, S., Rapoport, M., Shaag, A., Amry, K., Miller, C., Lorberboum-Galski, H., and Elpeleg, O. (2008). C6ORF6 Is an Assembly Factor of Mitochondrial Complex I. *Am. J. Hum. Genet.* **82**, 32–38.
- Schagger, H. (2002). Respiratory chain supercomplexes of mitochondria and bacteria. *Biochim. Biophys. Acta* **1555**, 154–159.
- Schagger, H., de Coo, R., Bauer, M. F., Hofmann, S., Godinot, C., and Brandt, U. (2004). Significance of respirasomes for the assembly/stability of human respiratory chain complex I. *J. Biol. Chem.* **279**, 36349–36353.
- Schagger, H., and Pfeiffer, K. (2000). Supercomplexes in the respiratory chains of yeast and mammalian mitochondria. *EMBO J.* **19**, 1777–1783.
- Schagger, H., and von Jagow, G. (1987). Tricine-sodium dodecyl sulfate-polyacrylamide gel electrophoresis for the separation of proteins in the range from 1 to 100 kDa. *Anal. Biochem.* **166**, 368–379.
- Schagger, H., and von Jagow, G. (1991). Blue native electrophoresis for isolation of membrane protein complexes in enzymatically active form. *Anal. Biochem.* **199**, 223–231.
- Skladal, D., Halliday, J., and Thorburn, D. R. (2003). Minimum birth prevalence of mitochondrial respiratory chain disorders in children. *Brain* **126**, 1905–1912.
- Smeitink, J. A., Zeviani, M., Turnbull, D. M., and Jacobs, H. T. (2006). Mitochondrial medicine: A metabolic perspective on the pathology of oxidative phosphorylation disorders. *Cell Metab.* **3**, 9–13.
- Thorburn, D. R., Sugiana, C., Salemi, R., Kirby, D. M., Worgan, L., Ohtake, A., and Ryan, M. T. (2004). Biochemical and molecular diagnosis of mitochondrial respiratory chain disorders. *Biochim. Biophys. Acta* **1659**, 121–128.
- Wallace, D. C. (1999). Mitochondrial diseases in man and mouse. *Science* **283**, 1482–1488.

MEASURING REDOX CHANGES TO MITOCHONDRIAL PROTEIN THIOLS WITH REDOX DIFFERENCE GEL ELECTROPHORESIS (REDOX-DIGE)

Thomas R. Hurd,^{*} Andrew M. James,^{*} Kathryn S. Lilley,[†] and Michael P. Murphy^{*}

Contents

1. Introduction	344
2. Overview of Redox-Dige	345
3. Experimental Design	347
4. Protein Labeling and Sample Preparation	348
4.1. Thiol blocking	348
4.2. Reduction of redox-modified thiols	348
4.3. Labeling of redox-modified thiols with fluorescent maleimides	349
5. 2-D Gel Electrophoresis of Fluorescently Labeled Samples	351
6. Imaging of Fluorescently Labeled Protein on Gels	351
7. Analysis of Multiple Gels to Determine Statistical Significance of Redox Changes on Individual Proteins	353
8. Spot Excision From 2-D Gels	354
9. Protein Spot Identification by Mass Spectrometry	355
10. Limitations to Redox-Dige and Future Possible Adaptations	356
11. Comparison of Redox-Dige With Other “Redox Proteomic” Techniques	357
12. Concluding Remarks	358
References	358

^{*} The Medical Research Council Mitochondrial Biology Unit, Cambridge, United Kingdom

[†] Department of Biochemistry, Cambridge System Biology Centre, University of Cambridge, Cambridge, United Kingdom

Abstract

Low levels of reactive oxygen and nitrogen species (ROS and RNS) produced by the mitochondrial respiratory chain and ROS and RNS from other sources act as redox signals by oxidizing thiols on specific proteins. Because these thiol modifications occur on a relatively small number of proteins in the absence of bulk thiol changes, it is necessary to use sensitive methods to discover them. Recently, a number of methods have been developed to help facilitate the identification and characterization of redox-sensitive thiol proteins. In this chapter we describe one such method, redox difference gel electrophoresis (redox-DIGE), in which oxidized thiol proteins in redox-challenged samples are labeled with a thiol-reactive fluorescent tag and compared with those in control samples labeled with a different tag on the same 2-D gel. This enables the sensitive detection of redox-sensitive thiol proteins by measuring changes in the relative fluorescence of the two tags within a single protein spot, followed by protein identification by mass spectrometry. With this method we have been able to identify several mitochondrial proteins whose thiol state and activity are altered by low levels of ROS from the respiratory chain, which may be an important and unexplored mode of mitochondrial redox signaling. Importantly, this method is not only applicable to studies in isolated mitochondria but can also be applied to more complicated systems such as intact cells and perhaps even whole organisms.

1. INTRODUCTION

Posttranslational modification of proteins through the oxidation of cysteinyl thiols is important in the regulation of proteins during redox signaling and in the protection of proteins from oxidative damage (Finkel, 2003; Hurd *et al.*, 2005; Rhee, 2006; Thomas *et al.*, 1995). Not all protein thiols are involved in these processes, because most do not react appreciably with ROS and RNS at physiologically relevant concentrations (Winterbourn and Hampton, 2008). Only specific protein thiols, generally those that are accessible and have low pK_as, are thought to play a role (Rhee, 2006). Many different oxidative modifications can form on protein thiols; some are reversible, such as intra- and intermolecular disulfides, glutathionylation, sulfenylamide linkages, and S-nitrosation, whereas others, such as sulfonic acids, are not (Beltran *et al.*, 2000; Poole *et al.*, 2004; Salmeen *et al.*, 2003; Stamler, 1994; Thomas *et al.*, 1995). The method described in this chapter is concerned with the identification of reversible oxidative modifications.

The mitochondrial respiratory chain is a major source of ROS in most cells (Cadenas and Davies, 2000; Chance *et al.*, 1979; Murphy, 2009). The proximity of mitochondrial protein thiols to the major ROS source and the

high mitochondrial matrix pH (~ 8.0) makes mitochondrial thiol proteins particularly susceptible to oxidation by ROS and RNS (Lin *et al.*, 2002). Some mitochondrial proteins undergo ROS-dependent thiol oxidation: peroxiredoxin III (Chang *et al.*, 2004), NADP⁺-dependent isocitrate dehydrogenase, (Kil and Park, 2005), and complex I (Beer *et al.*, 2004; Cochemé and Murphy, 2008; Dahm *et al.*, 2006; Hurd *et al.*, 2008; Taylor *et al.*, 2003). Although methods exist to measure changes in thiol state on specific mitochondrial proteins of known identity, identification of new mitochondrial thiol proteins involved in redox regulation and antioxidant defense has been difficult, in part because of the lack of robust methods for the detection of redox-induced changes in thiol state of proteins in complex protein mixtures (Eaton, 2006).

The method described in this chapter is a global proteomic technique aimed to facilitate the identification of new ROS-sensitive thiol proteins in isolated organelles, intact cells, and whole organisms. It involves labeling protein thiols in control and redox-challenged samples with two different fluorescent dyes containing thiol-reactive maleimide groups, followed by detection of changes in the relative fluorescence on a single 2-D gel and protein identification by mass spectrometry. This method was adapted from the difference gel electrophoresis (DIGE) technique (Lilley and Friedman, 2004; Unlu *et al.*, 1997), which was originally developed to quantify changes in protein expression. DIGE improves reproducibility and significantly reduces gel-to-gel variability that considerably hampers comparison of samples run on different 2-D gels (Alban *et al.*, 2003; Unlu *et al.*, 1997). Thus instead of the use of these dyes to monitor changes in protein expression (their intended application), they are used to identify proteins containing thiols susceptible to oxidation (Chan *et al.*, 2005; Hurd *et al.*, 2007). In combination with the DIGE approach and to improve the sensitivity of this method, we have used a labeling strategy that measures protein thiol oxidation on exposure to ROS (Baty *et al.*, 2005; Gitler *et al.*, 1997). Because most thiols are maintained in a reduced state by the glutathione and thioredoxin systems, measuring protein thiol oxidation is often far more sensitive than measuring thiol loss (Baty *et al.*, 2005). A complete description of this technique, which we call redox-DIGE, is provided in the following sections.

2. OVERVIEW OF REDOX-DIGE

An overview of the redox-DIGE technique is given in Fig. 19.1. A control sample is compared with one that has been redox-challenged, for example, by exposure to ROS or RNS. *N*-Ethylmaleimide (NEM) is then added to both samples to block exposed thiols, and mitochondria are lysed and proteins denatured with SDS. After removing the NEM, oxidized

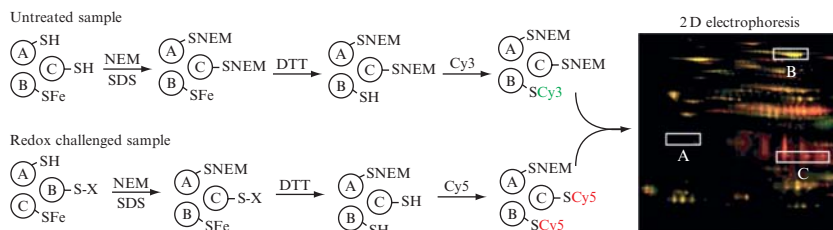


Figure 19.1 The redox-DIGE technique. Upper left, in control mitochondria, free protein thiols (A and C) are blocked with NEM, treated with DTT, and labeled with Cy3 maleimide (green). Lower left, in mitochondria exposed to a redox challenge, free protein thiols may become oxidized (C) and unreactive with NEM. The modified thiols can then be reduced with DTT and tagged with Cy5 maleimide (red). Both samples, control and redox challenged, are pooled, resolved by 2-D electrophoresis on the same gel, and fluorescently scanned. Protein spots that appear red on the superimposed images have undergone redox-sensitive thiol modifications (C). Spots that appear yellow (B) represent proteins containing occluded thiols, such as iron-sulfur centers (SFe). Proteins that contain oxidant-insensitive reduced thiols (A) are not seen.

thiols are reduced with DTT and are then labeled with either Cy3 or Cy5 maleimide for control or redox-challenged samples, respectively. The differentially labeled samples are pooled and resolved on the same 2-D gel, which is then scanned sequentially for Cy3 and Cy5 fluorescence (Cy3 and Cy5 being spectrally distinct). Most proteins with cysteine residues that are fully reduced in both conditions will not be labeled (Fig. 19.1, protein A). Proteins with equally oxidized or occluded thiols in both samples will have identical Cy3 and Cy5 fluorescence, and because they have been pseudo-colored green and red, respectively, they will appear yellow in the superimposed gel images (Fig. 19.1, protein B). However, protein with thiols that have been oxidized on redox challenge will appear red on the superimposed fluorographs (Fig. 19.1, protein C).

With this approach, only proteins containing oxidative modifications that are reducible with DTT, such as disulfides, sulfenic acids, S-nitrosothiols, and sulfonylamide linkages will be observed. Although we have focused on the identification of reversible thiol modifications, because we are interested in redox signaling, irreversibly modified thiol proteins can also be investigated with a similar DIGE approach in which the samples have been labeled differently. Alternately, our labeling strategy can also be altered, for example, by use of different thiol reducing agents to investigate specific types of protein modification, such as glutathionylation (for more information see section 10). Regardless of the way in which the samples are labeled it is important to confirm that when a change in fluorescence is observed, that it is, indeed, due to alterations in protein thiol state and not just protein amount. All our studies have been conducted on isolated mitochondria over short periods of time, where we do not expect to see changes in protein expression, turnover,

or amount. However, in many situations this will not be true. Therefore, experiments should also be conducted to confirm the amount of protein in samples being compared is the same, or at least the changes observed in any particular protein spot are not solely due to alterations in protein amount.

3. EXPERIMENTAL DESIGN

When planning any DIGE experiment, experimental design needs to be carefully considered from the start as the type of analysis required will influence the way in which samples are labeled. DIGE experiments are usually conducted by a biological variance analysis (BVA), which allows comparison of samples across several gels by using one internal standard on all gels (Alban *et al.*, 2003; Van den Bergh *et al.*, 2003). The internal standard is normally a pooled sample comprising equal amounts of each of the samples to be compared (Box 19.1). This ensures that all proteins occurring in the samples are represented, allowing both inter-gel and intra-gel matching. Alternately, DIGE experiments can be conducted by difference in-gel analysis (DIA), where each possible pair of samples is compared directly with one another within a single gel instead of across two or more gels as in BVA (Gharbi *et al.*, 2002; Hu *et al.*, 2003; Van den Bergh *et al.*, 2003; Yan *et al.*, 2002). Although the BVA approach is recommended as the inclusion of an internal standard has been demonstrated to improve the accuracy of relative protein quantification between samples (Alban *et al.*, 2003), BVA is not always appropriate because of the required cost, labor, time, and the requirements for greater amounts of sample. In many situations, a pairwise comparison with DIA can be used with a threshold above which a change is considered significant (Karp *et al.*, 2004). In our initial preliminary investigations with redox-DIGE, we used DIA (Hurd *et al.*, 2007). Although we were able to identify mitochondrial proteins containing thiols sensitive to low concentrations of ROS, the high confidence thresholds, which were required to reduce false positives, decreased the sensitivity, and, therefore, a BVA approach is strongly recommended.

Box 19.1 Recommended experimental design for a redox-DIGE experiment with an internal standard

The pooled standard comprises equal amounts of each sample (unstressed controls 1 to 3 and redox-challenged 1 to 3) labeled with Cy3-maleimide. This pooled standard is then compared with three biologic replicates (1 to 3) for control and redox-challenged samples, which are each labeled with Cy5-maleimide. Six gels in total are required to compare thiol proteins between the two conditions.

4. PROTEIN LABELING AND SAMPLE PREPARATION

All our experiments to date have been conducted on isolated mitochondria prepared from rat hearts with an Ultraturrax blender followed by differential centrifugation (Chappell and Hansford, 1972); however, this method should be easily adapted to other starting materials such as whole cells and even whole organisms such as flies and nematodes.

4.1. Thiol blocking

After incubating mitochondria (0.5 mg protein) under various conditions of oxidative stress, 25 to 50 mM NEM is added to each mitochondrial incubation to prevent thiol-disulfide exchange during subsequent mitochondrial isolation, which is done by centrifugation (15,000g, 2 min). Mitochondrial pellets are then resuspended in 50 μ l SHE buffer (250 mM sucrose, 10 mM HEPES-NaOH, 1 mM EGTA, pH 7.4) containing 50 mM NEM for 5 min at 37 °C. NEM, which permeates phospholipid membranes, is added before mitochondria are lysed to prevent spontaneous oxidation that occurs to some proteins, such as peroxiredoxin 2, on membrane lysis (Low *et al.*, 2007). It is important to check the pH of all solutions, and after NEM addition, adjust the pH or increase buffering capacity, because addition of high NEM concentrations tends to lower pH, which can slow the rate of reaction between thiols and NEM (Gregory, 1955). SDS (1% w/v) is then added and the samples are incubated for 5 min at 37° to expose any buried thiols that were initially inaccessible to NEM. In our hands a NEM concentration of 50 mM blocked more than 99% of the free thiols in our mitochondrial samples (Fig. 19.2). Depending on the thiol content of the sample to be analyzed and the buffer composition, different concentrations of NEM may be necessary to fully alkylate all free protein thiols. However, care should be taken as we find that not all protein oxidative modifications are stable under these alkylation conditions. For example, we have observed in our laboratory that the intraprotein disulfide on thioredoxin 2 can be labile (unpublished data), perhaps due to the denaturation of the protein by SDS rendering the disulfide bond more easily lysed. Therefore, it is advisable to incubate with NEM for the shortest period of time required to block most protein thiols.

4.2. Reduction of redox-modified thiols

The next step is to reduce reversibly oxidized thiols with DTT. Because high NEM concentrations interfere with DTT reduction of oxidized protein thiols, we use gel filtration columns (Micro Bio-Spin 6 Chromatography column; Bio-Rad) to remove NEM from our samples before reduction.

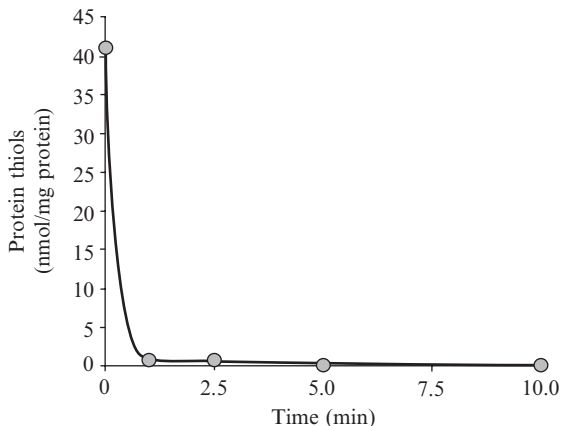


Figure 19.2 Optimization of thiol blocking. Rat heart mitochondria (10 mg protein/ml) were incubated with 50 mM NEM in 1% SDS (w/v) and SHE buffer at 37 °C for various periods of time. NEM and low-molecular-weight thiols were removed from the samples by gel filtration (Micro Bio-Spin 6 Chromatography column preequilibrated with SHE buffer containing 1% SDS [w/v]). To determine the free protein thiol concentration, samples (150 µg protein) were incubated in buffer (80 mM sodium phosphate, 1 mM EDTA, pH 8.0) containing 0.5 mM DTNB for 20 min at 23 °C. Absorbance (412 nm) was then read in a spectrophotometric plate reader (Spectra max Plus 384; Molecular Devices). Free protein thiols were quantified with respect to standard solutions of a known glutathione concentration.

Preferably columns are preequilibrated in SHE buffer containing 1% SDS (w/v); however, columns in the buffer supplied (10 mM TRIS-HCl, pH 7.4) have also been successfully used to remove NEM so it does not interfere with thiol reduction. If columns are not preequilibrated in SHE buffer containing SDS, then SDS should be added to the samples after gel filtration to maintain a concentration of 1% (w/v) throughout the sample preparation. To reduce oxidized protein thiols in our samples, 2.5 mM DTT is added, and they are incubated for 10 min at room temperature. A range of DTT concentrations have been tested and maximal free thiol concentrations observed when 2.5 mM DTT or higher is used (Fig. 19.3). Other reductants have not been thoroughly tested; however, preliminary experiments with TRIS(2-carboxyethyl)phosphine (TCEP) have demonstrated that it too can be used, in place of DTT, to identify oxidant-sensitive thiol proteins (data not shown).

4.3. Labeling of redox-modified thiols with fluorescent maleimides

So as not to interfere with Cy-maleimide labeling, it is important to remove DTT before labeling. This can be done by passage through one or two Micro Bio-Spin 6 Chromatography columns preequilibrated in SHE buffer containing SDS; however, it is advisable to use as few column steps as

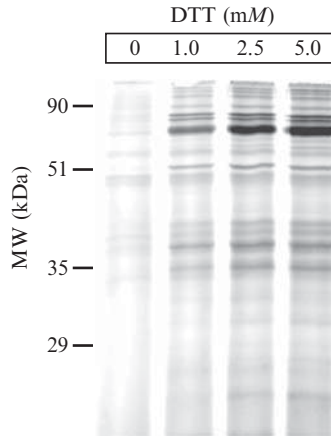


Figure 19.3 Optimization of the reduction of redox-modified thiols. Rat heart mitochondria (20 mg protein/ml) were incubated with 250 μM H_2O_2 in SHE buffer to oxidize protein thiols. Mitochondria were then denatured with SDS, free thiols were blocked with NEM, and NEM was removed as described in Fig. 19.2. To determine the concentration that best reduced oxidized thiols, samples were then incubated with various amounts of DTT (0, 1.0, 2.5, and 5.0 mM) for 10 min at 23°. DTT was removed, as in Fig. 19.2, with two gel filtration columns (preequilibrated with SHE buffer containing 1% SDS [w/v]), and free thiols were labeled with 40 μM CyDyeTM DIGE Fluor CyTM5 saturation dye (GE Healthcare) for 30 min at 37° in the dark. An equal volume of buffer (100 mM TRIS-HCl, pH 6.8, 200 mM DTT, 4% [w/v] SDS, 20% [w/v] glycerol, 0.2% [w/v] bromophenol blue) was added to quench the reaction, the samples were resolved by 12.5% SDS-PAGE and scanned fluorescently (see section 6).

necessary, because each step leads to less sample recovery. DTT-free protein samples are then labeled in the dark with 40 μM CyDyeTM DIGE Fluor CyTM3 saturation dye (GE Healthcare) or CyDyeTM DIGE Fluor CyTM5 saturation dye (GE Healthcare). After 30 min at 37° the reaction is quenched with 2.5 mM DTT and equal amounts of the Cy3- and Cy5-maleimide-labeled samples are pooled and resolved by 2-D electrophoresis. For each sample type, careful control experiments should be performed to optimize the labeling reaction so that complete alkylation of thiols occurs. Although maleimides exhibit a high degree of specificity with thiol groups (Gregory, 1955), they can react slowly with other amino acids (Smyth *et al.*, 1960); therefore, it is also important to minimize side reactions with other amino acids. This can be achieved by making sure the pH of the reaction does not exceed 8.0 during Cy-maleimide labeling. Although GE Healthcare recommends conducting the labeling reaction at pH 8.0, we have had successful results with pH as low as 7.4. Last, reducing the concentration of SDS to 0.25% (w/v) during labeling reaction is recommended, because it does not seem to affect protein solubility and improves subsequent isoelectric focusing.

5. 2-D GEL ELECTROPHORESIS OF FLUORESCENTLY LABELED SAMPLES

2-D electrophoresis of protein extracts is a standard technique and is, therefore, only briefly described here; for further information see [Gorg *et al.* \(2004\)](#) and [Issaq and Veenstra \(2008\)](#). To the samples prepared previously add equal volumes of $2\times$ sample buffer (7 M urea, 2 M thiourea, 2% [w/v] amidosulfobetaine-14 [ASB-14], 20 mg/ml DTT, and 2% [v/v] immobilized pH gradient [IPG] buffer 3-10 nonlinear [NL]), and incubate for 15 min at room temperature. We use amidosulfobetaine-14 (ASB-14) to solubilize proteins during isoelectric focusing, because it improves the resolution of hydrophobic membrane proteins, which are often absent on 2-D gels ([Henningsen *et al.*, 2002](#)). Cy3-labeled protein sample (12.5 μ g protein) is pooled with an equal amount of Cy5-labeled protein sample and rehydration buffer (7 M urea, 2 M thiourea, 2% [w/v] ASB-14, 2 mg/ml DTT and 1% [v/v] IPG buffer 3-10 [NL]) is added to make the volume up to 250 μ l before isoelectric focusing. IPG strips (13 cm, pH 3 to 10 NL; GE Healthcare) are next rehydrated with the samples for 10 h at 20° at 20 V with the IPGphor II apparatus following the manufacturer's instructions (GE Healthcare). IEF is performed at 20° at 50 μ A with the following stepwise gradient: 500 V for 500 volt hours (Vhr); 1000 for 1000 Vhr; and 8000 V for 40 000 Vhr. Before SDS-PAGE, the strips are equilibrated with rocking for 15 min in 100 mM TRIS-HCl, pH 6.8, 30 % (v/v) glycerol, 8 M urea, 1% (w/v) SDS, and 5 mg/ml DTT. The strips are loaded onto a 12% (w/v), 1 mm acrylamide gel and overlaid with 1% (w/v) agarose in SDS running buffer (25 mM TRIS, pH 8.3, 192 mM glycine, and 0.1 % (w/v) SDS) containing 0.2 mg/ml bromophenol blue. The gels are kept at 15° with a Multitemp III (Pharmacia) cooling system and run at 20 mA for 15 min and then at 40 mA until the bromophenol blue dye front runs off the bottom of the gels.

6. IMAGING OF FLUORESCENTLY LABELED PROTEIN ON GELS

After 2-D electrophoresis, gels are transferred to a TyphoonTM 9410 imager (GE Healthcare), and fluorescent spots viewed with 532-nm and 633-nm lasers in conjunction with 580-nm and 670-nm emission filters (band pass 30 nm), respectively. If general protein staining is required, the gels can also be stained with Deep PurpleTM total protein stain (GE Healthcare) and the protein spots imaged with a 457-nm laser in conjunction with a 610-nm band pass emission filter. Gels are usually scanned at

100 μm pixel size and the photomultiplier tube set to ensure a maximum pixel intensity between 40,000 and 80,000 (arbitrary units) to avoid saturation.

Examples of typical fluorescent gel images from our studies with isolated rat heart mitochondria are shown in Fig. 19.4. As can be observed, most proteins are present as multiple spots aligned horizontally in charge trains. Two protein charge trains in the control appear bright yellow, indicating that they contain proteins with oxidized or occluded thiols in control and stressed mitochondria (Fig. 19.4, control gel, yellow boxes). These proteins did not become further oxidized on redox-challenge with low concentrations of H_2O_2 or endogenous ROS, because neither train of spots turned red (Fig. 19.4, 2.5 μM H_2O_2 and endogenous ROS gels, yellow boxes). In contrast, however, one protein train does turn red on redox-challenge, indicating that a protein in these spots has a redox-sensitive thiol or thiols (Fig. 19.4, 2.5 μM H_2O_2 and endogenous ROS gels, red box). No fluorescence for this charge train is observed in the control gel, demonstrating that this thiol protein is largely reduced under control conditions (Fig. 19.4, control gel, red box).

It is important to note that it can be difficult to identify thiol modifications on proteins with many already occluded or oxidized thiols such as the

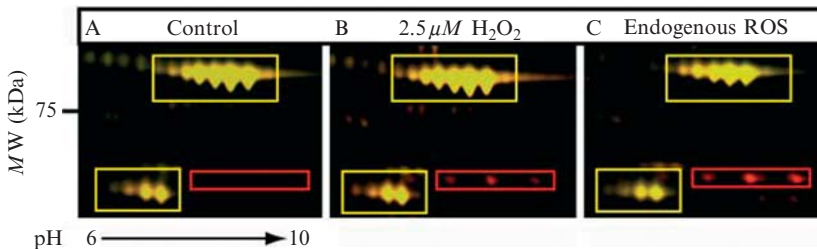


Figure 19.4 Effect of oxidants on mitochondrial protein thiols determined by Redox-DIGE. (A) Superimposed fluorescent scans of a redox-DIGE gel in which unstressed mitochondrial labeled with Cy3-maleimide (green) are compared with similar unstressed mitochondrial labeled with Cy5-maleimide (red). Before sample preparation and analysis, rat heart mitochondria (1 mg protein/ml) were incubated in standard assay medium (250 mM sucrose, 5 mM HEPES, 1 mM EGTA, pH 7.4) with 5 mM glutamate/5 mM malate for 1 min at 37°. (B) Superimposed fluorescent scans of a redox-DIGE gel comparing mitochondria treated as in A and labeled with Cy3-maleimide with mitochondria incubated with 2.5 μM H_2O_2 in standard assay medium for 1 min at 37° and labeled with Cy5-maleimide. (C) Superimposed fluorescent scans of a redox-DIGE gel comparing unstressed Cy3-labeled mitochondrial proteins with mitochondrial proteins exposed to endogenously generated ROS and then labeled with Cy5-maleimide. The Cy3-labeled mitochondria were incubated with succinate (10 mM) and carbonyl cyanide-p-(trifluoromethoxy)phenyl-hydrazone (FCCP; 400 nM) in standard assay medium for 5 min at 37°C before sample preparation and Cy3-labeling. The Cy5-labeled mitochondria were incubated in the same way except antimycin (2.5 μM) was included in the incubation to generate ROS endogenously within mitochondria.

bright yellow spots in Fig. 19.4. This is because changes in thiol state are identified by alterations in the ratio of Cy5 to Cy3 fluorescence. If a protein has one thiol that becomes oxidized on treatment but also has many thiols that are already oxidized or occluded, then the ratio of Cy5 to Cy3 fluorescence will not be as great as a protein that does not have already oxidized or occluded thiols. Although we can see in the gel images in Fig. 19.4 that a protein becomes oxidized on treatment with H_2O_2 or endogenous ROS, a result from a single gel is in itself not enough to assign a redox modification with any certainty because of inherent variability. Therefore, to determine whether this oxidative modification is significant, it is necessary that a number of gels be analyzed in a rigorous manner with one of many commercially available software packages. Our use of GE Healthcare's DeCyder software to identify statistically significant thiol modifications on mitochondrial proteins is described in the next section.

7. ANALYSIS OF MULTIPLE GELS TO DETERMINE STATISTICALLY SIGNIFICANCE OF REDOX CHANGES ON INDIVIDUAL PROTEINS

As mentioned earlier, gels can be analyzed in two different ways by BVA or DIA. Although BVA is recommended, if for preliminary studies a DIA approach is preferred, then we support the use of an approach where significance thresholds are applied (Karp *et al.*, 2004). To determine significance thresholds, a DIA experiment is performed in which spots are code-ctected between the two fluorescence images from a single gel. Spots with a volume less than 0.01% of the total fluorescence or a slope (the change in fluorescent intensity versus pixel width) greater than 1 are excluded, because they are likely to be contaminated with dust particles (Karp *et al.*, 2004). The DeCyderTM program then generates a frequency histogram of the log volume ratios and normalizes the Cy3 fluorescent image (V_1) and Cy5 fluorescent image (V_2) by adjusting the spot volume of the Cy3 fluorescent image (V_1') such that the frequency histogram of the log volume ratios centers on zero (i.e., a Cy5/Cy3 fluorescence ratio of 1), and a normal distribution is fitted to the main peak of the histogram with a standard least squares gradient descent. Outliers are excluded from the model curve fitting procedure by discarding spots below 10% of the top of the main peak in the frequency histogram of the log volume ratios. The calculated normalized log volume ratios are then converted into E ratios with the equation: $E = (V_2/V_1')$. E ratios from control versus control gels can then be used to empirically establish confidence thresholds that encompass a high percentage (normally 95% or greater) of spots and allow one to identify statistically significance redox changes on individual proteins.

In our analysis we established confidence thresholds that encompassed 99% of the spots on 6 control vs control gels. Only spots that had E ratios that fell outside these confidence thresholds on three or more control versus redox-challenged gels were taken as significant.

This normalization method is based on the assumption that the majority of protein spots in the two samples are not different and are labeled with the Cy-maleimides to similar extents. However, if the majority of proteins in the two samples being compared are different and labeled with different amounts of the Cy-maleimides, then this assumption may not hold true and some E ratios may be underestimated. Alternately, gels can be normalized with absolute standards by spiking the samples with known amounts of Cy3- and Cy5-labeled proteins. Here a known amount of a standard protein or proteins that resolve to a different position on the 2-D gel from the proteins within the samples under consideration is added to every sample.

The E ratios obtained from traditional DIGE experiments are quantitative; they tell one exactly how much the amount of protein in the samples being compared varies. For example, if a protein spot has an E ratio of 2, then the amount of the protein has doubled. Although redox-DIGE E ratios can give one a sense of the degree of modification, their quantitation is less straightforward. This is because of two factors: first, proteins may contain a number of redox-sensitive thiols; and second, the initial redox state of the thiols is also often uncertain. Therefore, although for any given protein spot comparing E ratios between different conditions will indicate whether the thiols on that protein have become more or less oxidized, the extent of this modification is more difficult to assess.

8. SPOT EXCISION FROM 2-D GELS

Unlike traditional DIGE where the fluorescent gel images closely match protein staining patterns because all (or nearly all) proteins are labeled, in redox-DIGE fluorescent images generally do not closely resemble protein-staining patterns (Fig. 19.5, compare “endogenous ROS” and “protein stain” panels). Therefore, it is difficult to align protein-stained gels with fluorescent gel images accurately by eye, and thus we recommend excising spots for mass spectrometry robotically. To do this, we use an Ettan Spot Picker (GE Healthcare) to pick spots from our 2-D gels, which we immobilize on glass plates to ensure that they do not distort during the spot-picking process. Before gel casting, 2 to 4 ml of Bind Silane solution (0.1% [v/v] PlusOne™ Bind Silane [GE Healthcare], 80% [v/v] ethanol, 2% [v/v] acetic acid) is pipetted over the surface of gel plates (low fluorescence, GE Healthcare) and wiped dry with a lint-free tissue (Kimwipe). The plates are

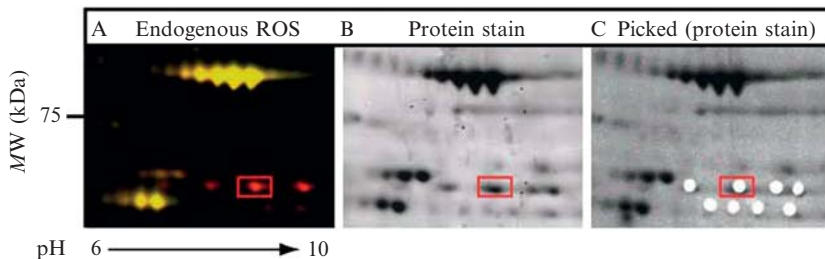


Figure 19.5 Protein staining and spot excision from redox-DIGE gels. (A) Same as C in Fig. 4, 19. (B) Image of gel in A stained with Deep Purple™, a fluorescent protein staining reagent. (C) Image of B after protein spots had been excised robotically.

covered to protect from dust, left to dry for 1.5 h to allow excess silane to evaporate, and two plastic fluorescent reference marker stickers (GE Healthcare) are attached to each plate. The plates are then washed with water extensively before they are used for gel casting. After electrophoresis, glass plate-backed 2-D gels are scanned (see earlier), and each spot is assigned x and y coordinates on the basis of its position relative to the two reference markers with DeCyder™ software. The coordinates of selected protein spots are then exported to an Ettan Spot Picker robot (GE Healthcare), which detects the reference markers on the gel and then excises the spots (1.4-mm-diameter plugs).

Images from a redox-DIGE gel in which several protein spots were picked are provided in Fig. 19.5. The spot in the red box contains a redox-sensitive thiol protein. The protein in this spot can also be visualized with the protein stain Deep Purple™, and after the spot has been excised, the gel can then be rescanned (Fig. 19.5, Picked) to ensure that the robot had successfully removed the selected protein spot from the gel.

9. PROTEIN SPOT IDENTIFICATION BY MASS SPECTROMETRY

Protein identification by tandem mass spectrometry was conducted on excised protein spots with a standard “in-gel” cleavage procedure (Wilm *et al.*, 1996). More specifically, protein spots are incubated at 37° with 12.5 ng/ml sequencing grade trypsin (Roche) in 3 to 7 μ l of buffer containing 20 mM TRIS-HCl, pH 8.0, and 5 mM CaCl₂. Peptides are then extracted from the gel with 3 to 7 μ l of 4% (v/v) ARISTAR-grade formic acid, 60% (v/v) acetonitrile (Romil) solution. All digests are examined in a MALDI-TOF-TOF mass spectrometer (4700 Proteomics Analyzer, Applied

Biosystems) with α -cyano-4-hydroxy-trans-cinnamic acid as the matrix. Normally, we identify proteins primarily on the basis of peptide mass fingerprints with the MASCOT search engine (<http://www.matrixscience.com>, Perkins *et al.*, 1999). In addition, protein identification is corroborated by tandem mass spectrometry sequencing of peptides, which often itself is sufficient to give a statistically significant identification of a protein. Generally, unambiguous protein identifications are reported when only one protein is identified in any given spot. Despite this, it is difficult to entirely exclude the possibility that we sometimes identify an abundant comigrating protein instead of the thiol protein of interest. Specific sites of redox modification can be searched for in MASCOT to definitively identify the thiol protein; however, our attempts to identify the exact cysteines modified by including Cy3- and Cy5-maleimide modifications in MASCOT have to date yielded negative results, perhaps partly because of the behavior of the Cy3- and Cy5-adducts in our MALDI-TOF-TOF spectrometer. As with any large proteomics screen, it is important to verify changes by a different method. Our experience investigating thiol modifications on several mitochondrial proteins has shown us that much more directed analysis is often necessary to pinpoint the exact ROS-sensitive cysteines on many proteins. For example, to identify which of the 17 thiol moieties on the 75-kDa subunit of complex I are ROS sensitive by mass spectrometry, it was necessary to purify the protein and digest it with two different enzymes, trypsin and Asp-N (Hurd *et al.*, 2008).



10. LIMITATIONS TO REDOX-DIGE AND FUTURE POSSIBLE ADAPTATIONS

The method described in this chapter focuses on detecting changes in the amounts of oxidized thiols between two or more samples. Others, however, have used DIGE to measure changes in the amounts of reduced thiols between samples (Chan *et al.*, 2005; Fu *et al.*, 2008). Although measuring changes in oxidized thiols is more sensitive than measuring changes in reduced ones (Baty *et al.*, 2005), assaying thiol loss allows for the identification of irreversibly oxidized thiols. Our technique, on the other hand, is restricted only to investigating DTT-reversible thiol modifications. If one is interested in going in the opposite direction and narrowing the screen to search for specific types of thiol modifications, instead of broadening it to look for all types of thiol modification, different reductants can be used instead of DTT. For example, if glutathione and glutaredoxin are used instead of DTT, glutathionylated thiol proteins may be preferentially identified, or alternately, if thioredoxin and thioredoxin reductase are used in place of DTT, protein-protein disulfides may be preferentially reduced.

Another limitation to our studies with redox-DIGE is that thiol changes on hydrophobic membrane proteins may be missed, because these proteins are difficult to resolve by conventional 2-D gel electrophoresis (Braun *et al.*, 2007). To search for redox-sensitive thiol proteins different types of gel electrophoresis can be used. For example, if mitochondrial membrane proteins are of interest, proteins can be separated by 2-D blue-native gel electrophoresis, a charge shift method used to separate individual membrane proteins, protein complexes, and super complexes (Wittig and Schagger, 2008) instead of standard 2-D electrophoresis. Reactive thiols on extremely hydrophobic proteins could also be investigated by isolating these protein with organic solvents (Carroll *et al.*, 2007) followed by separation by SDS-PAGE and DIGE imaging and analysis.

11. COMPARISON OF REDOX-DIGE WITH OTHER “REDOX PROTEOMIC” TECHNIQUES

In the past few years several other comparative proteomic techniques have been developed to help identify redox-sensitive thiol proteins. Perhaps most prominent of these uses tags called isotope-coded affinity tags (ICAT; (Gygi *et al.*, 1999), which differ in mass instead of fluorescence. Similar to traditional DIGE, ICAT were originally developed to measure changes in protein expression (not thiol state) and also like DIGE, ICAT derivatize proteins by reacting specifically with thiols. ICAT differs from DIGE in that the samples need necessarily not be separated on 2-D gels. Instead, labeled proteins are usually digested with trypsin, and the labeled cysteine-containing peptides are then purified (ICAT also contain biotin moieties to facilitate this) before peptide masses are measured by mass spectrometry. Redox-ICAT methods provide some distinct advantages over redox-DIGE. First, because the peptides that contain the redox-sensitive thiols are directly analyzed and identified by this method, the specific site of thiol oxidation can be determined. Furthermore, because the peptide that is modified is being directly measured, in most cases the identity of the protein is much more certain than it is in redox-DIGE. Although for proteins that contain multiple isoforms, analysis of one peptide might not be enough to determine which isoform is modified. Second, because hydrophobic proteins are often lost during 2-D electrophoresis, redox-ICAT approaches may be preferable to redox-DIGE for the identification of thiol modifications on hydrophobic proteins. Recently, Fu and colleagues have directly compared redox-DIGE with redox-ICAT, and found that both methods complemented each other (Fu *et al.*, 2008). Several proteins were identified with both methods, but interestingly some proteins were only identified with redox-DIGE, whereas others were only identified with redox-ICAT. Therefore, to maximize the probability of identifying proteins containing

redox-sensitive cysteinyl thiols in complex biology systems, both methods should be used.

12. CONCLUDING REMARKS

Increasingly the regulation of proteins by ROS and RNS through oxidation and reduction of cysteinyl thiols is being recognized as an important mode of cellular signaling. Consequently, there has been a push to identify proteins that are involved in thiol-based redox signaling. The method outlined in this chapter, redox-DIGE, has been developed to facilitate this. In this method thiol proteins from mitochondria that have become oxidized during a redox challenge are reduced and labeled with a fluorescent tag. For comparison, thiol proteins from unstressed mitochondria are also reduced and labeled with a different fluorescent tag. These samples are then pooled, resolved on the same 2-D gel, and changes in relative fluorescence are detected on a single 2-D gel. Fluorescence changes on redox-DIGE gels are indicative of thiol oxidation, and proteins with reactive thiols can be then identified by mass spectrometry. We have demonstrated from studies in mammalian mitochondria that redox-DIGE is, indeed, a sensitive method for the identification of ROS-sensitive thiol proteins. We have used redox-DIGE to identify a number of candidate proteins that may be involved in the redox signaling within mitochondria. Although our studies, to date, have all been conducted on isolated mammalian mitochondria, redox-DIGE should also be useful for the identification of thiol modifications on proteins in intact cells and whole organisms. Recently, other differential methods, such as redox-ICAT, have been developed that can be used in parallel with redox-DIGE to help further identify proteins involved in redox signaling.

REFERENCES

- Alban, A., David, S. O., Bjorkestén, L., Andersson, C., Sloge, E., Lewis, S., and Currie, I. (2003). A novel experimental design for comparative two-dimensional gel analysis: Two-dimensional difference gel electrophoresis incorporating a pooled internal standard. *Proteomics* **3**, 36–44.
- Baty, J. W., Hampton, M. B., and Winterbourn, C. C. (2005). Proteomic detection of hydrogen peroxide-sensitive thiol proteins in Jurkat cells. *Biochem. J.* **389**, 785–795.
- Beer, S. M., Taylor, E. R., Brown, S. E., Dahm, C. C., Costa, N. J., Runswick, M. J., and Murphy, M. P. (2004). Glutaredoxin 2 catalyzes the reversible oxidation and glutathionylation of mitochondrial membrane thiol proteins: Implications for mitochondrial redox regulation and antioxidant defense. *J. Biol. Chem.* **279**, 47939–47951.
- Beltran, B., Orsi, A., Clementi, E., and Moncada, S. (2000). Oxidative stress and S-nitrosylation of proteins in cells. *Br. J. Pharmacol.* **129**, 953–960.

- Braun, R. J., Kinkl, N., Beer, M., and Ueffing, M. (2007). Two-dimensional electrophoresis of membrane proteins. *Anal. Bioanal. Chem.* **389**, 1033–1045.
- Cadenas, E., and Davies, K. J. (2000). Mitochondrial free radical generation, oxidative stress, and aging. *Free Radic. Biol. Med.* **29**, 222–230.
- Carroll, J., Altman, M. C., Fearnley, I. M., and Walker, J. E. (2007). Identification of membrane proteins by tandem mass spectrometry of protein ions. *Proc. Natl. Acad. Sci. USA* **104**, 14330–14335.
- Chan, H. L., Gharbi, S., Gaffney, P. R., Cramer, R., Waterfield, M. D., and Timms, J. F. (2005). Proteomic analysis of redox- and ErbB2-dependent changes in mammary luminal epithelial cells using cysteine- and lysine-labelling two-dimensional difference gel electrophoresis. *Proteomics* **5**, 2908–2926.
- Chance, B., Sies, H., and Boveris, A. (1979). Hydroperoxide metabolism in mammalian organs. *Physiol. Rev.* **59**, 527–605.
- Chang, T. S., Cho, C. S., Park, S., Yu, S., Kang, S. W., and Rhee, S. G. (2004). Peroxiredoxin III, a mitochondrion-specific peroxidase, regulates apoptotic signaling by mitochondria. *J. Biol. Chem.* **279**, 41975–41984.
- Chappell, J. B., and Hansford, R. G. (1972). Subcellular components: Preparation and Fractionation, *In* (G. D. Birnie, ed.), pp. 77–91. Butterworths, London.
- Cochemé, H. M., and Murphy, M. P. (2008). Complex I is the major site of mitochondrial superoxide production by paraquat. *J. Biol. Chem.* **283**, 1786–1798.
- Dahm, C. C., Moore, K., and Murphy, M. P. (2006). Persistent S-nitrosation of complex I and other mitochondrial membrane proteins by S-nitrosothiols but not nitric oxide or peroxyxynitrite: Implications for the interaction of nitric oxide with mitochondria. *J. Biol. Chem.* **281**, 10056–10065.
- Eaton, P. (2006). Protein thiol oxidation in health and disease: Techniques for measuring disulfides and related modifications in complex protein mixtures. *Free Radic. Biol. Med.* **40**, 1889–1899.
- Finkel, T. (2003). Oxidant signals and oxidative stress. *Curr. Opin. Cell Biol.* **15**, 247–254.
- Fu, C., Hu, J., Liu, T., Ago, T., Sadoshima, J., and Li, H. (2008). Quantitative analysis of redox-sensitive proteome with DIGE and ICAT. *J. Proteome Res.* **7**, 3789–3802.
- Gharbi, S., Gaffney, P., Yang, A., Zvelebil, M. J., Cramer, R., Waterfield, M. D., and Timms, J. F. (2002). Evaluation of two-dimensional differential gel electrophoresis for proteomic expression analysis of a model breast cancer cell system. *Mol. Cell. Proteomics* **1**, 91–98.
- Gitler, C., Zarmi, B., and Kalef, E. (1997). General method to identify and enrich vicinal thiol proteins present in intact cells in the oxidized, disulfide state. *Anal. Biochem.* **252**, 48–55.
- Gorg, A., Weiss, W., and Dunn, M. J. (2004). Current two-dimensional electrophoresis technology for proteomics. *Proteomics* **4**, 3665–3685.
- Gregory, J. D. (1955). The stability of N-ethylmaleimide and its reaction with sulfhydryl groups. *J. Am. Chem. Soc.* **77**, 3922–3923.
- Gygi, S. P., Rist, B., Gerber, S. A., Turecek, F., Gelb, M. H., and Aebersold, R. (1999). Quantitative analysis of complex protein mixtures using isotope-coded affinity tags. *Nat. Biotechnol.* **17**, 994–999.
- Henningsen, R., Gale, B. L., Straub, K. M., and DeNagel, D. C. (2002). Application of zwitterionic detergents to the solubilization of integral membrane proteins for two-dimensional gel electrophoresis and mass spectrometry. *Proteomics* **2**, 1479–1488.
- Hu, Y., Wang, G., Chen, G. Y., Fu, X., and Yao, S. Q. (2003). Proteome analysis of *Saccharomyces cerevisiae* under metal stress by two-dimensional differential gel electrophoresis. *Electrophoresis* **24**, 1458–1470.

- Hurd, T. R., Costa, N. J., Dahm, C. C., Beer, S. M., Brown, S. E., Filipovska, A., and Murphy, M. P. (2005). Glutathionylation of mitochondrial proteins. *Antioxid. Redox. Signal* **7**, 999–1010.
- Hurd, T. R., Prime, T. A., Harbour, M. E., Lilley, K. S., and Murphy, M. P. (2007). Detection of reactive oxygen species-sensitive thiol proteins by redox difference gel electrophoresis: Implications for mitochondrial redox signaling. *J. Biol. Chem.* **282**, 22040–22051.
- Hurd, T. R., Raquejo, R., Filipovska, A., Brown, S., Prime, T. A., Robinson, A. J., Fearnley, I. M., and Murphy, M. P. (2008). Complex I within oxidatively-stressed bovine heart mitochondria is glutathionylated on Cys-531 and Cys-704 of the 75-kDa subunit: Potential role of Cys residues in decreasing oxidative damage. *J. Biol. Chem.* **283**, 24801–24815.
- Issaq, H., and Veenstra, T. (2008). Two-dimensional polyacrylamide gel electrophoresis (2D-PAGE): Advances and perspectives. *Biotechniques* **44**, 697–700.
- Karp, N. A., Kreil, D. P., and Lilley, K. S. (2004). Determining a significant change in protein expression with DeCyder during a pair-wise comparison using two-dimensional difference gel electrophoresis. *Proteomics* **4**, 1421–1432.
- Kil, I. S., and Park, J. W. (2005). Regulation of mitochondrial NADP⁺-dependent isocitrate dehydrogenase activity by glutathionylation. *J. Biol. Chem.* **280**, 10846–10854.
- Lilley, K. S., and Friedman, D. B. (2004). All about DIGE: Quantification technology for differential-display 2D-gel proteomics. *Expert Rev. Proteomics* **1**, 401–409.
- Lin, T. K., Hughes, G., Muratovska, A., Blaikie, F. H., Brookes, P. S., Darley-USmar, V., Smith, R. A., and Murphy, M. P. (2002). Specific modification of mitochondrial protein thiols in response to oxidative stress: A proteomics approach. *J. Biol. Chem.* **277**, 17048–17056.
- Low, F. M., Hampton, M. B., Peskin, A. V., and Winterbourn, C. C. (2007). Peroxiredoxin 2 functions as a noncatalytic scavenger of low-level hydrogen peroxide in the erythrocyte. *Blood* **109**, 2611–2617.
- Murphy, M. P. (2009). How mitochondria produce reactive oxygen species. *Biochem. J.* **417**, 1–13.
- Perkins, D. N., Pappin, D. J., Creasy, D. M., and Cottrell, J. S. (1999). Probability-based protein identification by searching sequence databases using mass spectrometry data. *Electrophoresis* **20**, 3551–3567.
- Poole, L. B., Karplus, P. A., and Claiborne, A. (2004). Protein sulfenic acids in redox signaling. *Annu. Rev. Pharmacol. Toxicol.* **44**, 325–347.
- Rhee, S. G. (2006). Cell signaling. *H₂O₂, a necessary evil for cell signaling.* *Science* **312**, 1882–1883.
- Salmeen, A., Andersen, J. N., Myers, M. P., Meng, T. C., Hinks, J. A., Tonks, N. K., and Barford, D. (2003). Redox regulation of protein tyrosine phosphatase 1B involves a sulphenyl-amide intermediate. *Nature* **423**, 769–773.
- Smyth, D. G., Nagamatsu, A., and Fruton, J. S. (1960). Some Reactions of N-ethylmaleimide. *Anal. Biochem.* **82**, 4600–4604.
- Stamler, J. S. (1994). Redox signaling: Nitrosylation and related target interactions of nitric oxide. *Cell* **78**, 931–936.
- Taylor, E. R., Hurrell, F., Shannon, R. J., Lin, T. K., Hirst, J., and Murphy, M. P. (2003). Reversible glutathionylation of complex I increases mitochondrial superoxide formation. *J. Biol. Chem.* **278**, 19603–19610.
- Thomas, J. A., Poland, B., and Honzatko, R. (1995). Protein sulfhydryls and their role in the antioxidant function of protein S-thiolation. *Arch. Biochem. Biophys.* **319**, 1–9.
- Unlu, M., Morgan, M. E., and Minden, J. S. (1997). Difference gel electrophoresis: A single gel method for detecting changes in protein extracts. *Electrophoresis* **18**, 2071–2077.

- Van den Bergh, G., Clerens, S., Vandesande, F., and Arckens, L. (2003). Reversed-phase high-performance liquid chromatography prefractionation prior to two-dimensional difference gel electrophoresis and mass spectrometry identifies new differentially expressed proteins between striate cortex of kitten and adult cat. *Electrophoresis* **24**, 1471–1481.
- Wilm, M., Shevchenko, A., Houthaeve, T., Breit, S., Schweigerer, L., Fotsis, T., and Mann, M. (1996). Femtomole sequencing of proteins from polyacrylamide gels by nano-electrospray mass spectrometry. *Nature* **379**, 466–469.
- Winterbourn, C. C., and Hampton, M. B. (2008). Thiol chemistry and specificity in redox signaling. *Free Radic. Biol. Med.* **45**, 549–561.
- Wittig, I., and Schagger, H. (2008). Features and applications of blue-native and clear-native electrophoresis. *Proteomics* **8**, 3974–3990.
- Yan, J. X., Devenish, A. T., Wait, R., Stone, T., Lewis, S., and Fowler, S. (2002). Fluorescence two-dimensional difference gel electrophoresis and mass spectrometry based proteomic analysis of *Escherichia coli*. *Proteomics* **2**, 1682–1698.

EFFECTS OF HEPATITIS C CORE PROTEIN ON MITOCHONDRIAL ELECTRON TRANSPORT AND PRODUCTION OF REACTIVE OXYGEN SPECIES

Roosevelt V. Campbell,^{*} Yuanzheng Yang,^{*} Ting Wang,[†] Aparna Rachamalla,^{*} Yanchun Li,[‡] Stanley J. Watowich,[§] and Steven A. Weinman[¶]

Contents

1. Introduction	364
2. Materials and Model Systems	365
2.1. Materials	365
2.2. Plasmid design and core protein isolation	366
2.3. Mitochondrial isolation and cellular model systems	368
3. HCV Core Protein Effects on Mitochondria <i>In Vitro</i>	369
3.1. Effects of core protein on mitochondrial respiration	369
3.2. Direct effect of core on mitochondrial GSH/GSSG	370
3.3. Measurement of core effects on calcium uptake in isolated mitochondria	371
4. Mitochondrial Effects of Viral Proteins in Cellular Systems	373
4.1. Measurement of mitochondrial depolarization by JC-1 flow cytometry	374
4.2. Measurement of core protein effects on live cell mitochondrial Ca ²⁺	374
4.3. Core protein effects on mitochondrial ROS production	377
5. Conclusion	378
Acknowledgments	378
References	379

^{*} Department of Neuroscience and Cell Biology, University of Texas Medical Branch, Galveston, Texas, USA

[†] Department of Microbiology and Immunology, University of Texas Medical Branch, Galveston, Texas, USA

[‡] Department of Neurology, Baylor College of Medicine, Houston, Texas, USA

[§] Department of Biochemistry and Molecular Biology, University of Texas Medical Branch, Galveston, Texas, USA

[¶] Department of Internal Medicine, University of Kansas Medical Center, Kansas City, Kansas, USA

Abstract

Viral infections frequently alter mitochondrial function with suppression or induction of apoptosis and enhanced generation of reactive oxygen species. The mechanisms of these effects are varied, and mitochondria are affected by both direct interactions with viral proteins and by secondary effects of viral-activated signaling cascades. This chapter describes methods used in our laboratory to assess the effects of the hepatitis C virus core protein on mitochondrial ROS production, electron transport, and Ca^{2+} uptake. These include measurements of the effects of *in vitro* incubation of liver mitochondria with purified core protein and assessment of the function of mitochondria in cells and tissues expressing core and other viral proteins. These methods are generally applicable to the study of viral-mitochondrial interactions.

1. INTRODUCTION

In addition to their roles in respiration and ATP production, mitochondria are key regulators of apoptosis and cell survival. It is, therefore, not surprising that many viruses regulate mitochondrial function for suppression of apoptosis, enhancement of viral replication, or modulation of the host environment (Boya *et al.*, 2004). Several pathologically relevant examples include HIV, human T-cell leukemia virus, hepatitis B and C viruses, and herpesviruses (D'Agostino *et al.*, 2005; Galluzzi *et al.*, 2008).

In some cases, viral proteins are known to bind directly to mitochondrial outer membrane components (Hickish *et al.*, 1994; Rahmani *et al.*, 2000), but in others the mechanisms of the viral mitochondrial effects seem to be secondary to other cellular events. Viral infection often leads to changes in mitochondrial function, including inhibition of mitochondrial electron transport and ATP production, increased mitochondrial superoxide production, suppression or enhancement of apoptosis, alterations in mitochondrial structure, and alterations in mitochondrially based signaling processes (Loo *et al.*, 2006).

To determine the mechanisms of virally mediated mitochondrial changes and assess their relevance to viral life cycle and host pathogenesis, it is necessary to develop methods to analyze viral effects on mitochondria. Because viral effects may be direct results of interactions of viral proteins with mitochondrial targets or indirect effects of viral changes in signaling events, different cellular and subcellular systems are required. In this chapter we describe methods used in our laboratories to assess the direct and indirect effects of HCV core protein on mitochondrial electron transport, calcium uptake, and redox status. These methods should be generally applicable to the broader study of virus-mitochondrial interactions as well.

Hepatitis C virus is a hepatotropic positive-strand RNA virus that causes chronic hepatitis, cirrhosis, and hepatocellular carcinoma (Thomson and Finch, 2005). After infection, the viral proteins form an ER-based replication complex associated with mitochondria and lipid droplets (Moradpour *et al.*, 2007). The HCV core protein is synthesized as a 23-kDa protein (core 1-191) and then cleaved to a mature 21-kDa form (core 1-179) lacking the signal peptide. Core protein contains both basic and hydrophobic regions and, in addition to serving as the viral nucleocapsid protein, it has been shown to alter transcription, cell cycle control, mitochondrial electron transport, and ER stress pathways (Irshad and Dhar, 2006). Transgenic mice that express core protein have mitochondrial electron transport defects and develop hepatocellular carcinoma. Core protein's effects on the mitochondria are both direct and indirect. Although work from our laboratory has shown that core directly stimulates the mitochondrial Ca^{2+} uptake uniporter (Li *et al.*, 2007), others have shown mitochondrial effects secondary to ER stress (Benali-Furet *et al.*, 2005). Both pathways seem important. Even though the specific consequences of these HCV-mitochondria interactions are still under investigation, it is clear that virally induced effects on the mitochondria can have profound effects in the host cell intracellular environment.

To study the effects of core protein on mitochondria we have used multiple model systems both *in vitro* and *in vivo*. All of the model systems described here have their respective advantages and disadvantages, but the use of alternate approaches allows us to confirm and validate different results. This chapter describes methods that we have used to examine the effects of core protein on mitochondrial function.

2. MATERIALS AND MODEL SYSTEMS

2.1. Materials

Instruments: Branson Sonifier 450 (VWR, West Chester, PA); Respirometry system with respirometer cell (MT200A) and Clark-type Oxygen electrode (model 1302) and meter (model 782) (Strathkelvin, North Lanarkshire, Scotland); FLUOstar OPTIMA plate reader (BMG LABTECH, Durham, NC) (Ex/Em 544/590 nm); Becton-Dickinson FACScan Flow Cytometer (BD Bioscience, San Jose, CA); Confocal (fluorescence) microscope or fluorescence microscope such as TE200-IUC Quantitative Fluorescence Live-Cell Imaging System (Nikon, Melville, NY).

Chemicals and Kits: Sodium glutamate was from Fisher (Pittsburgh, PA); 5-sulfosalicylic acid, sodium malate, sodium succinate dibasic, adenosine 5'-diphosphate sodium salt (ADP), cyclosporin A, nicotinamide adenine dinucleotide phosphate (NADPH), and carbonyl cyanide 4-trifluoromethoxy phenylhydrazone (FCCP) were all purchased from

Sigma-Aldrich (St. Louis, MO); Rhod-2 AM (Molecular probes, Eugene, OR) was prepared freshly as a 1.0 mM stock solution in dry DMSO each time; tert-butyl hydroperoxide (Sigma-Aldrich) was diluted in water to 2 mM solution; Ru360 and Thapsigargin (TG) were from CalBiochem (Gibbstown, NJ); JC-1 (5,5',6,6'-tetrachloro-1,1',3,3'-tetraethylbenzimidazolcarbocyanine iodide) (Molecular probes) was diluted in dry DMSO to 5 mg/ml; glutathione reductase (2.2 units/ml), glutathione peroxidase (200 U/ml), and valinomycin (10 μ M stock solution in DMSO) were from Sigma-Aldrich. MitoSOXTM Red (Invitrogen, Carlsbad, CA), 2',7'-dichlorodihydrofluorescein diacetate (DCFDA) (Molecular Probes) was dissolved at a concentration of 5 mM in dry DMSO.

Ratiometric pericam-mt cDNA expression plasmid was kindly provided by Dr. Atsushi Miyawaki (Wako, Saitama, Japan) (Nagai *et al.*, 2001).

GSH/GSSG-412TM kit and GSH 400TM kit were from Oxis Research (Foster City, CA).

2.2. Plasmid design and core protein isolation

To perform detailed and controlled *in vitro* experiments, it is necessary to express and purify the protein of interest in its native conformation. The following section describes a robust method to obtain HCV core protein that contains amino acids 1 to 179, inclusive (Kunkel and Watowich, 2004).

HCV core protein (HCVC179), residues 1 to 179, derived from the AG94 isolate of genotype 1a sequence, was amplified by polymerase chain reaction (PCR) with the sense primer 5'-GGGAAATCCATATG-AGCACGAATCCTAAACCTCAAAGAAAA-3' and the antisense primer 5'-CCGGAATTCTCATTACAGAAGGAAGATAGAGAAA-GAGCAACC. Sequence of the cloned PCR fragment was confirmed by DNA sequencing, and the fragment was then subcloned into a pET30a expression vector (Novagen, Gillstown, NJ).

The preceding HCVC179/pET30a expression vector was transformed into *Escherichia coli* BL21 (DE3) cells, and the bacterial cultures were maintained in 2 \times YT medium for core protein expression. When the optical density, OD_{600nm}, of the culture reached 1.0, 1 mmol/L isopropyl- β -D-thiogalactopyranoside (IPTG) was added to induce HCVC179 expression. Bacterial cultures were maintained for an additional 4 h at 25 $^{\circ}$, and then centrifuged at 5000g for 30 min to pellet the cells. For HCVC179 protein purification, the bacterial pellet was sequentially resuspended in ice-cold lysis buffer (20 mM TRIS-HCl, pH 7.0, 2 mM DTT), urea lysis buffer (8 M urea, 20 mM NA phosphate (NaH₂PO₄; pH 7.0), and urea/salt lysis buffer (8 M urea, 500 mM NaCl, 20 mM (NaH₂PO₄), pH 6.5). Each time the pellet was sonicated with ten 30-sec cycles of sonication and cooling, followed by centrifugation at 50,000g for 20 min at 4 $^{\circ}$ in an SS-34 rotor.

The supernatants remaining after each centrifugation were saved and stored at 4°. Ten microliters of each of the supernatants obtained previously (lysis supernatant, urea lysis supernatant, and urea/salt lysis supernatant) and the urea/salt pellet were treated with sample buffer (75 mM TRIS, pH 6.8, 2% SDS, 5% glycerol, 0.003% bromophenol blue, 0.9% β-mercaptoethanol), and incubated at 37° for 30 min and run on 16% SDS-PAGE. The sample containing the most enriched HCVC179 was determined by staining the gel with Gel Code Blue Stain (Rockford, IL) for 2 h to overnight. If the most HCVC179-enriched fraction occurred in the lysis supernatants and/or the urea lysis supernatants, these fractions were pooled and loaded directly on the HPLC column; if the most HCVC179-enriched fraction occurred in the urea/salt supernatant, the sample needed to be diluted with equal volume of 8 M urea (pretreated with Dowex MR-3 resin, 1 g resin/100ml urea) containing dithiothreitol (DTT) to a final concentration of 50 mM (stock 1.0 M) and incubated overnight at 4°. The HCVC179-containing supernatant was then loaded on a cation-exchange HPLC column (e.g., Poros 20 CM) preequilibrated with cation column equilibration buffer (50 mM HEPES, pH 7.0, 8 M urea, 150 mM NaCl). Fractions were eluted from the column with a linear gradient of NaCl (from 150 to 750 mM) and identified by 16% SDS-PAGE for HCVC179 expression. Fractions containing HCVC179 were pooled and concentrated by centrifugation with Centriplus 10KD at 3000g 4° (typically concentrated by 10- to 15-fold). A reverse-phase HPLC column (e.g., YMC-ODS) was preequilibrated with reverse phase column equilibration buffer (20 mM NaH₂PO₄, pH 3.0, 1% MeOH). Two milliliters of the concentrated samples (12.5 μl concentrated H₃PO₄ per every ml was added before loading) were loaded on the reverse-phase HPLC column and eluted with a linear gradient of 20 mM sodium-phosphate-methanol, pH 3.0 (1% MeOH to 96% MeOH). HCVC179 elutes as a single peak approximately 90% MeOH. Fractions containing HCVC179 were pooled and dialyzed overnight at 4° against refolding buffer (20 mM TRIS, pH 7.0, 100 mM NaCl plus protease inhibitor cocktail [leupeptin 0.05 mM, pepstatin A 0.001 mM, PMSF 0.5 mM]) and dialyzed with fresh refolding buffer plus protease inhibitor cocktail for an additional 6 h. The dialyzed samples were concentrated by use of Centriplus 10KD, 3000g at 4° (typically concentrated by tenfold). The homogeneity and identity of purified HCVC179 was confirmed by SDS-PAGE (typically 98%) and immunoblot with a mouse monoclonal antibody to HCV core protein (Affinity BioReagents).

This method allows efficient and rapid purification of full-length folded HCV core protein and typically produces ~2 mg of purified protein (>95% homogeneity as visualized by SDS-PAGE and Gel Code blue staining) per liter of bacterial culture. Elution conditions will need to be optimized if different cation exchange and reverse-phase columns are used. An example of purity of the core obtained by this method is shown in Fig. 20.1.

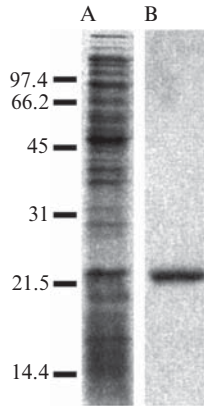


Figure 20.1 HCV core 179 expression and purification. Samples were resolved on an SDS-16% polyacrylamide gel under reducing conditions and visualized by Coomassie blue stain. Lanes: A, expression of HCVC179 in bacterial cell pellets; B, HCVC179 after purification by cation exchange and reverse-phase HPLC. Sizes are indicated in kilodaltons.

2.3. Mitochondrial isolation and cellular model systems

2.3.1. Mitochondrial isolation

Four hundred milligrams of mouse liver tissue was rinsed in ice-cold $1\times$ PBS (137 mM NaCl, 2.7 mM KCl, 4.3 mM Na_2HPO_4 , 1.47 mM KH_2PO_4 , pH 7.4) immediately after animal sacrifice and minced on ice in 4 ml of mitochondria isolation buffer (250 mM sucrose, 10 mM HEPES, 0.5 mM EGTA, 0.1% BSA, pH 7.4). Minced tissue was gently homogenized (3 to 4 strokes) with a Dounce homogenizer with a loose-fitting pestle, and the homogenate was centrifuged at 500g for 5 min at 4°. The supernatant was collected and kept on ice, and the pellet was resuspended again in mitochondria isolation buffer and centrifuged at 500g for 5 min at 4°. The supernatants obtained previously were combined and centrifuged at 7800g for 10 min at 4° to obtain crude mitochondrial pellets. To wash the mitochondria, crude mitochondrial pellets were resuspended in mitochondria wash buffer (250 mM sucrose, 10 mM HEPES, pH 7.4), and centrifugation at 7800g for 10 min at 4° was repeated. The washed mitochondria were resuspended in suitable mitochondria resuspension buffer, and an aliquot of suspension was taken to measure protein concentration.

2.3.2. Cellular model systems

In studying mitochondrial function we have taken advantage of several model systems. These model systems are in general use in the field and have been described in detail elsewhere. Cellular model systems for studying HCV include simple expression systems for viral proteins (Ray *et al.*, 2000), tetracycline repressor-based inducible expression systems (Li *et al.*, 2002;

Otani *et al.*, 2005), replicon cell lines autonomously replicating viral RNA (Blight *et al.*, 2000; Ikeda *et al.*, 2002), cell culture infectious virus (Lindenbach *et al.*, 2005; Wakita *et al.*, 2005; Zhong *et al.*, 2005), and transgenic mice expressing one or more viral proteins in either constitutive or inducible fashion (Honda *et al.*, 1999; Lerat *et al.*, 2002; Moriya *et al.*, 1998).

3. HCV CORE PROTEIN EFFECTS ON MITOCHONDRIA *IN VITRO*

The simplest way to demonstrate a direct mitochondrial effect of a viral protein is to demonstrate that *in vivo* observations can be reproduced *in vitro* through direct interaction of purified viral proteins with isolated mitochondria. The following methods are described for the effect of HCV core on mouse liver mitochondria.

3.1. Effects of core protein on mitochondrial respiration

Freshly isolated mitochondria were resuspended in respiration buffer (130 mM sucrose, 50 mM KCl, 5 mM MgCl₂, 5 mM KH₂PO₄, 0.05 mM EDTA, 5 mM HEPES, pH 7.4) and incubated in the presence or absence of core protein (1 to 10 ng/mg mitochondrial protein) for 5 min at 4°. Immediately after incubation, 1 to 1.5 mg of mitochondria were transferred to a respiration chamber prefilled with 1 ml of respiration buffer, mixed well with magnetic stirring, and allowed to equilibrate at 25°. Complex I-supported state 4 respiration was initiated by adding 5 mM glutamate and 5 mM malate to the sample chamber. Complex I-supported state 3 respiration was initiated by adding 100 nmol of ADP. Maximum oxygen consumption (uncoupled respiration) was measured after returning to state 4 respiration with the addition of 5 μM FCCP. Complex II-supported state 3 and 4 respiration was measured in a similar manner by adding 5 mM succinate instead of glutamate and malate. P:O ratios and FCCP-induced consumption rates were calculated as described by Estabrook (1967).

The advantage of this method is that it allows direct effects of core on mitochondria to be observed in the absence of more complex cellular signaling networks. As illustrated in Fig. 20.2, brief incubations with core protein in the range of 1 to 10 ng/mg mitochondrial protein produce a selective inhibition of complex I-associated electron transport reflected as reduced P:O ratio and uncoupled O₂ consumption from glutamate-malate substrate (Korenaga *et al.*, 2005).

Further details about core protein effects on mitochondrial respiratory complexes can also be obtained by incubating mitochondria with the viral protein as described previously and then measuring respiratory complex activity in submitochondrial particles as previously shown (Korenaga *et al.*, 2005).

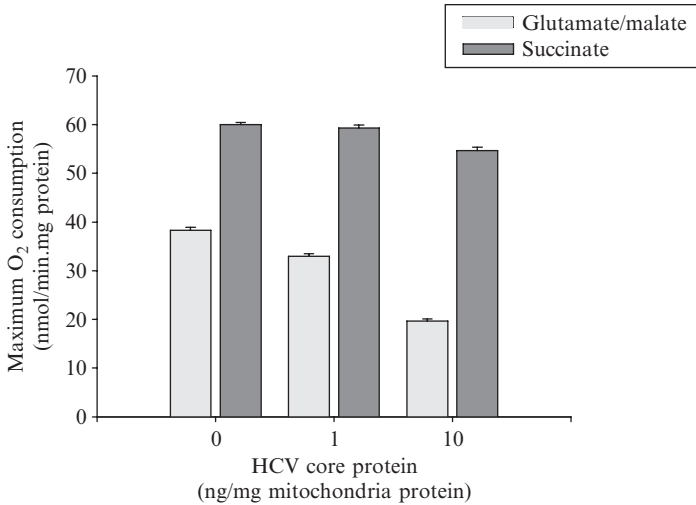


Figure 20.2 Effects of core protein on mitochondrial respiration. Mouse liver mitochondria were incubated with core protein as described. Maximum respiratory rate after addition of FCCP is presented. Note that core protein inhibits respiration with glutamate/malate but not succinate.

3.2. Direct effect of core on mitochondrial GSH/GSSG

The measurement of glutathione in tissue extracts can be performed by multiple assays, including colorimetric assays of thiol reaction products that measure reduced glutathione (GSH), a “recycling” assay in which the rate of glutathione dependent reduction of 5,5'-dithiobis(2-nitrobenzoic acid) or DTNB is proportional to total glutathione (GSH + GSSG) concentration (Anderson, 1989) and several HPLC assays. In mouse liver mitochondria we have found the DTNB recycling assay to accurately measure total glutathione, but attempts to first derivatize GSH to remove it for the measurement of the oxidized fraction were not successful, possibly because of poor penetration of the derivatizing reagent into intact mitochondria. When used for mitochondria, the reactive thiol assays all suffer from some degree of reactivity with nonglutathione thiols and, therefore, tend to overestimate the total GSH content. We solved this problem by use of a commercially available thiol assay for GSH and measuring GSH under three conditions: (1) untreated, (2) after quantitative reduction of the glutathione pool with glutathione reductase and NADPH, and (3) after quantitative oxidation of the glutathione pool with glutathione peroxidase (GPx) and tertiary butyl hydroperoxide (tBOOH). We found this to be the most reliable biochemical assay of GSH in the context of intact mouse liver mitochondria.

After preparing crude mitochondria as described previously, mitochondrial pellets were resuspended in 1.5 ml of PBS alone or in 1.5 ml of PBS containing HCV core protein (50 to 500 ng/mg of mitochondrial protein) and incubated for 5 min at 4°. The contents of each tube were then divided into three equal aliquots of 500 μ l each. One aliquot was used to directly measure both GSH and GSH + GSSG. The second aliquot was used to measure GSH after reduction with glutathione reductase and NADPH. To do so, the sample was first freeze-thawed twice in a dry ice/ethanol bath to release GSH from mitochondria and then treated with 5 μ l of glutathione reductase and 50 μ l of NADPH, mixed by vortex, and incubated for 10 min at 25°. The third aliquot was used to measure reduced thiols after oxidation with GPx and tBOOH. To do so, the sample was first freeze-thawed as described previously and then treated with 5 μ l of GPx and 50 μ l 2 mM tBOOH, mixed by vortex, and incubated for 10 min at 25°. After their respective treatments, the aliquots were placed on ice and acidified with 10% SSA, sonicated for 15 sec, and centrifuged at 10,000g for 10 min at 4°. Glutathione measurements were performed on the supernatants obtained after the centrifugation. We used the DTNB recycling assay for total glutathione (GSH + GSSG), and GSH-400TM thioester method for reduced glutathione (GSH). The recycling assay was performed only on the first aliquot. The thioester method was performed on all three samples. We used the previously referenced commercial kits, but the assays can be done by directly obtaining the individual reagents as well.

For calculation of total glutathione (GSH + GSSG) the DTNB recycling assay result is accurate. For GSH, the thioester result overestimates GSH because of contribution of non-GSH thiols. The magnitude of this nonspecific background is determined after GPx/tBOOH oxidation, and the validity of the thiol method is confirmed by comparing the result from the reduced sample, after background subtraction, to the value obtained with the recycling assay. In our hands these results agree to within 5 to 10%. An example of the use of this method for the determination of the effect of *in vitro* core protein on mitochondrial glutathione is presented in Fig. 20.3.

3.3. Measurement of core effects on calcium uptake in isolated mitochondria

Mitochondria were resuspended in mitochondrial isolation buffer and incubated on ice in the presence or absence of HCV core protein for 30 min. The concentration of core protein used in these experiments ranged from 100 to 600 ng core protein/mg mitochondrial protein. After incubation with core protein, mitochondria were loaded with the Ca²⁺ indicator Rhod-2 AM at a final concentration of 4 μ M and incubated for an additional 1 h at 4°. After this, mitochondria were pelleted by centrifugation at

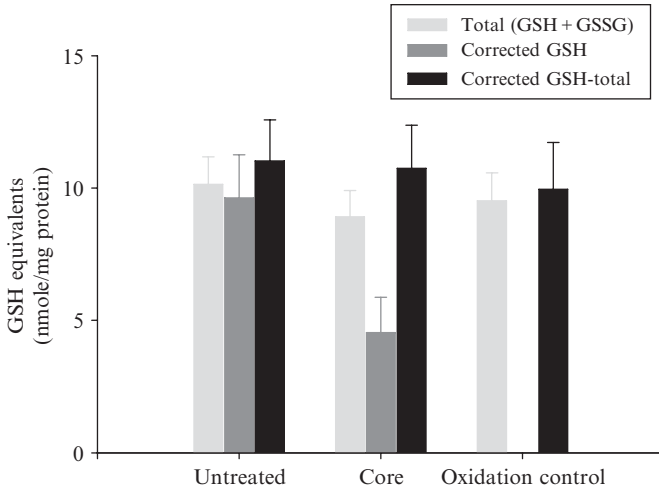


Figure 20.3 Effects of *in vitro* core protein incubation on mitochondrial glutathione. Total glutathione was measured by the DTNB recycling assay. GSH thiol was measured as described either before (dark grey bar) or after (black bar) reduction with glutathione reductase and NADPH. The non-GSH component of the thiol reaction was measured by oxidation of the sample with tBOOH and glutathione peroxidase (oxidation control).

7800g for 10 min at 4° and washed twice in wash buffer. Finally, washed mitochondria were resuspended in respiration buffer (final protein concentration 0.33 mg/ml). Depending on the protocol to be tested, mitochondria could be further treated with various inhibitors (e.g., Ca²⁺ transport inhibitor Ru-360 (125 nM) and/or permeability transition inhibitor cyclosporin A [1 μM]). We recommend carrying out these incubations at 4° for 30 min. Once this was done, the mitochondrial suspension was aliquoted into 96-well plates with at least triplicates for each condition. The plate was incubated at room temperature for 30 min in the dark. After the incubation, 25 μl of Ca²⁺ containing respiration buffer (250 μM Ca²⁺ final concentration) was added to each well with a multichannel pipette, and the plate was immediately placed on the plate reader. Rhod-2 fluorescence (Ex/Em 544/590 nm) was recorded every 30 sec for 60 min.

This method first depletes mitochondrial Ca²⁺ by prolonged incubation with EGTA and then suddenly exposes the mitochondria to an inwardly directed Ca²⁺ gradient. As shown in Fig. 20.4, the combination of the Ca²⁺ uniport inhibitor Ru-360 and the permeability transition pore inhibitor cyclosporin A (CSA) effectively eliminated all Ca²⁺ uptake in this system. *In vivo*, the chemical Ca²⁺ gradient is outward, and thus potential driven uniport is the only significant mechanism for Ca²⁺ entry. Opening of the

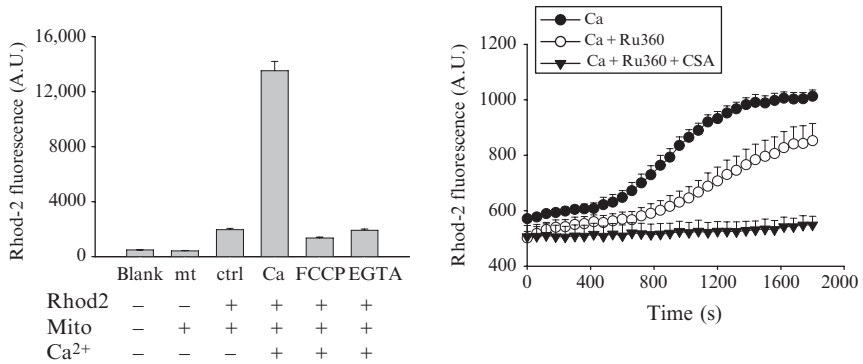


Figure 20.4 Characteristics of Ca²⁺ uptake in isolated mitochondria. Left panel, Confirmation of the intramitochondrial source of the Rhod-2 fluorescence signal. Liver mitochondria were loaded with Rhod-2 and incubated with FCCP (50 nM) or EGTA (10 mM) as indicated. Ca²⁺ (250 μM) was added 30 min before measurement of fluorescence. Note that the Ca²⁺-induced Rhod-2 signal can be completely prevented by mitochondrial depolarization with FCCP. This indicates that it results from mitochondrial uptake of Ca²⁺ and not from Rhod-2 leakage out of the mitochondria. Right panel, Time course of mitochondrial Ca²⁺ uptake. Note that the combination of cyclosporin A and Ru360 was required to completely inhibit uptake under these conditions (see text). Reprinted with permission from FASEB Journal (Li *et al.*, 2007).

permeability transition pore results in Ca²⁺ efflux from the matrix. However, in this *in vitro* system, the Ca²⁺ gradients are reversed, and mitochondrial permeability transition becomes a second mechanism for Ca²⁺ entry. For this reason we found it necessary to conduct all experiments in the presence of CSA. The use of CSA allowed us to measure calcium uptake exclusively because of the calcium uniporter, known to be the only significant source of calcium entry into mitochondria *in vivo*. Preincubation of mitochondria with 100 ng of recombinant core protein increased the initial rate of calcium uptake and the plateau value for steady-state Ca²⁺ content (Fig. 20.4). As expected, the presence of Ru360 completely blocked the effect of core protein (Li *et al.*, 2007).

4. MITOCHONDRIAL EFFECTS OF VIRAL PROTEINS IN CELLULAR SYSTEMS

Viral effects on mitochondria that result as a consequence of signaling events, ER stress, or replication complexes are not likely to occur in the reconstituted *in vitro* systems described in the previous section. It is thus important to measure viral effects on mitochondrial function in cellular systems and compare to direct effects. This section describes methods useful

for measurement of mitochondrial function in cellular and animal model systems for hepatitis C virus infection.

4.1. Measurement of mitochondrial depolarization by JC-1 flow cytometry

Several methods exist to measure mitochondrial membrane potential. JC-1 is a cationic fluorophore with a concentration-dependent fluorescence spectral shift that allows it to be used in a ratiometric fashion to differentiate polarized from depolarized mitochondria. This has some advantages over single wavelength methods, such as rhodamine 123, in which depolarization is marked by a decrease in fluorescence intensity that may be less specific. Use of this method has been described previously (Otani *et al.*, 2005).

For measurement of mitochondrial membrane potential, Huh-7 hepatoma cells with tetracycline-regulated expression of core protein (Li *et al.*, 2002) were grown in 10-mm dishes to 50 to 70% confluence (approximately 1×10^6 cells per dish.) As a positive control for depolarization, one dish was first treated with valinomycin, final concentration 500 nM for 30 min before cell harvesting. Medium was then removed, cells were washed once with PBS, and trypsinized by adding 100 μ l of trypsin solution for 3 min. Cells were then suspended in 5 ml culture medium and centrifuged at 500g for 5min at room temperature. Cell pellets were resuspended in 5 ml of 0.5% BSA in PBS containing 10 μ l of 5 mg/ml JC1 solution for 10min in the dark. JC-1 loaded cells were then centrifuged at 500g for 5 min, washed once with 0.25% BSA in PBS, and resuspended in 1 ml of PBS before immediate analysis by flow cytometry.

This method has proven useful for demonstrating the effect of HCV core protein expression on oxidant and Ca^{2+} -induced mitochondrial depolarization. As shown in Fig. 20.5, control cells cluster with high red fluorescence and submaximal green fluorescence. On depolarization there is first an increase of green fluorescence followed by a loss of red fluorescence. Suitable controls to validate the depolarization are essential. We have found that valinomycin works well for this purpose. We have used this method with core-expressing and non-core-expressing cells, as well as HCV subgenomic and genome-length replicons. These studies demonstrate that core protein expression sensitizes mitochondria to oxidant-induced depolarization (Otani *et al.*, 2005).

4.2. Measurement of core protein effects on live cell mitochondrial Ca^{2+}

In many cases, viral proteins do not alter baseline mitochondrial properties but do alter response to stimuli. An important example of this is mitochondrial Ca^{2+} uptake in response to ER Ca^{2+} release. These processes can be

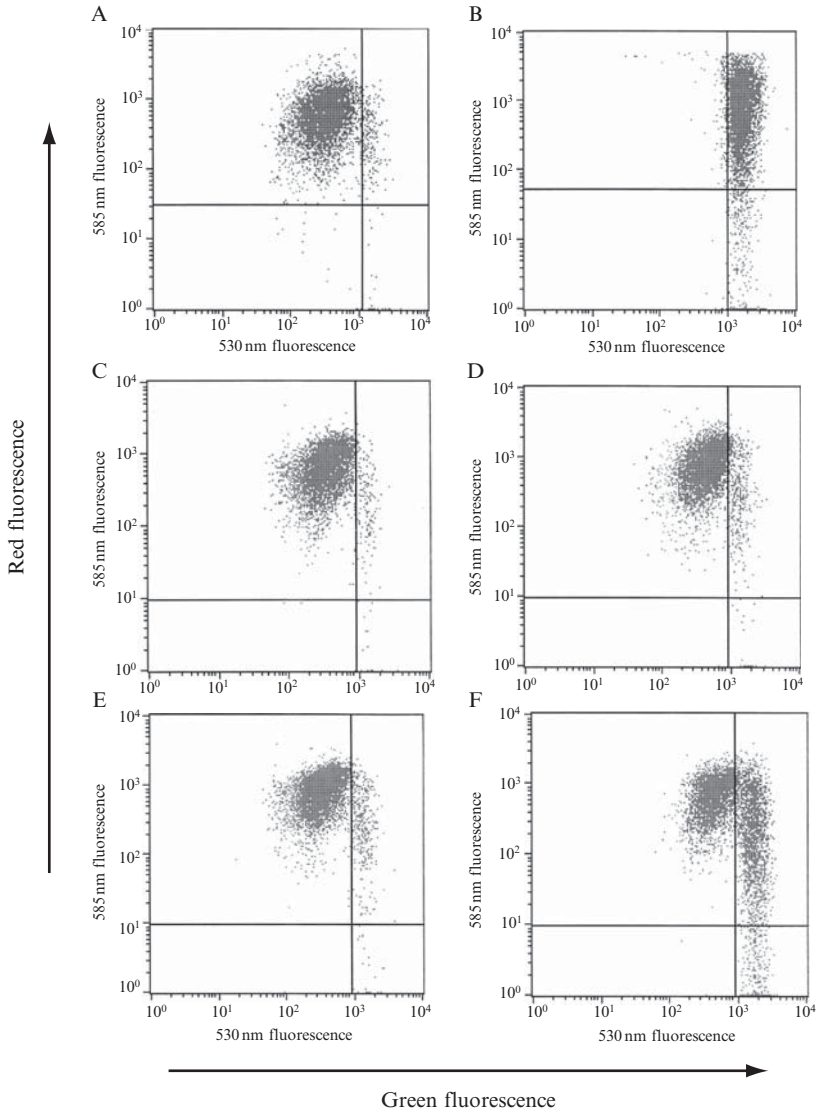


Figure 20.5 Core-induced mitochondrial depolarization measured with JC-1 flow cytometry. Measurements of JC-1 red and green fluorescence were performed as described. (A) Control Huh7 cells. (B) Huh7 treated with valinomycin as a positive control for depolarization. (C) L-14 cells with tet-off regulated core protein expression, in the presence of doxycycline (no core expression). (D) L-14 cells in the presence of doxycycline (no core expression) after incubation with 100 μ M tBOOH. E. L-14 cells in the absence of doxycycline (core expression induced). F. L-14 cells in the absence of doxycycline (core expression induced) after incubation with 100 μ M tBOOH.

measured with targeted protein reporter probes in live cells. The use of ratiometric pericam-mt to measure the effects of core protein on mitochondrial Ca^{2+} uptake in response to ER Ca^{2+} release is described. Ratiometric pericam-mt is a Ca^{2+} -dependent fluorescent protein developed by Miyawaki and colleagues (Nagai *et al.*, 2001) and targeted with a mitochondrial sequence encoding the N-terminal 12-aa presequence of subunit IV of cytochrome *c* oxidase. Dual fluorescence excitation allows Ca^{2+} measurement independently of reporter concentrations or cell geometry.

To measure mitochondrial matrix Ca^{2+} , Huh-7 cells were seeded onto coverslips in 6-well plates and incubated overnight. Cells were then rinsed and transfected with the mitochondrial-targeted Ca^{2+} indicator protein (ratiometric-pericam-mt) cDNA plasmid. After 48 h, coverslips were rinsed and mounted in Ca^{2+} -free buffer in a fluorescence microscope system for quantitative imaging. Pericam-transfected cells were recognized by the presence of fluorescence in a cytoplasmic, perinuclear location typical for mitochondria (Fig. 20.6). Fluorescence emission images at 510 nm were acquired every 2 sec after sequential excitation at 405 and 490 nm. Data analysis was performed with MetaMorph software. Fluorescence intensity at

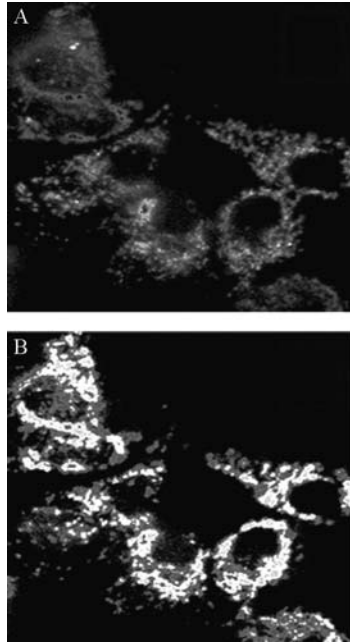


Figure 20.6 Thapsigargin-induced increases in mitochondrial calcium measured with mitochondrially targeted pericam. The images were obtained as described either before (A) or after (B) thapsigargin exposure. The images represent a ratio-mapped image where pixel intensity corresponds to fluorescence ratio.

each wavelength was determined in the mitochondrial region and corrected by subtraction of background fluorescence. Mitochondrial Ca^{2+} was represented as the $F_{495/405 \text{ nm}}$ ratio.

Efficiency of cell transfection can be monitored by the green fluorescence of ratiometric-pericam and is usually approximately 30 to 50% in Huh7 cells transfected with lipofectamine 2000. We have used this method to compare the response of core protein-expressing cells and control cells to thapsigargin-induced ER Ca^{2+} release. Very distinct patterns were observed (Li *et al.*, 2007). Similar to the results seen with isolated mitochondria, expression of core protein caused a rapid increase in mitochondrial Ca^{2+} uptake, in this case after the release of Ca^{2+} from ER induced by thapsigargin.

4.3. Core protein effects on mitochondrial ROS production

Well-established fluorescence methods can be readily used in the HCV cellular model systems for measurement of mitochondrial ROS production. The commercially available fluorescent probes, mitoSOXTM Red and 2',7'-dichlorodihydrofluorescein diacetate (DCFDA) (Molecular Probes) are cell permeable and become highly fluorescent in the presence of ROS (mitoSOXTM being specifically sensitive to superoxide). Both of these probes were used in our cell system to assess the specific effect of core protein on mitochondrial ROS production (Li *et al.*, 2007; Okuda *et al.*, 2002; Otani *et al.*, 2005).

Live cell imaging was used to measure ROS production in response to ER Ca^{2+} release in HCV core-expressing cells or control cells. Cells were grown on glass coverslips, culture medium was aspirated, and cells incubated in phenol red-free medium containing 2.5 μM mitoSOXTM Red for 30 min at 37°. Cells were then washed briefly with Ca^{2+} -free Hanks balanced salt solution and mounted in a microscope chamber containing Ca^{2+} -free buffer solution. Calcium release from the ER was induced by adding thapsigargin to a final concentration of 200 μM . Alternately, cells can be exposed to DCFDA at final concentration of 500 nM immediately before imaging. Fluorescence images (Ex/Em 510/570 nm for mitoSOX; Ex/Em 488/530 nM for DCFDA) were then obtained with a confocal or fluorescence microscope at various time points (generally 1-min intervals). Mitochondrial ROS production was quantified by analysis of cell fluorescence intensity in a perinuclear mitochondrial-rich region.

Similar assays were performed with a plate reader method obviating the need for imaging and cell selection. Cells were first seeded in 96-well plates and incubated for 12 to 24 h followed by incubation with 2.5 μM mitoSOXTM Red or 5 μM DCFDA for 30 min at 37° in the dark. After washing with Ca^{2+} -free buffer, cells were exposed to 10 μM thapsigargin for 2 h. Fluorescence was measured in a plate reader (Ex/Em 510/570 nm for

mitoSOX; Ex/Em 488/530 nm for DCFDA) and raw fluorescence intensity values were normalized to cell numbers plated on each well.

These methods describe the use of simple fluorescence probes for ROS determination in live cells. MitoSOX is an ethidium derivative that is specifically oxidized by superoxide to form a product that intercalates in DNA where it becomes fluorescent. Because of its DNA association, it is retained well in cells and is suitable for flow cytometry measurements as well. DCFDA is somewhat more problematic. Although its fluorescent product is a result of oxidation, this reaction requires enzymatic conversion, and the fluorescent product is somewhat membrane permeant and is only partially retained in the cells. Both oxidation and cell retention can be variable, and these characteristics have made it difficult to use for flow cytometry. In our hands it is best suited for short-term imaging-based measurements before the variable cell retention properties become relevant. Both methods have confirmed that core protein increases mitochondrial ROS production in a Ca^{2+} -dependent fashion (Li *et al.*, 2007; Okuda *et al.*, 2002).

MitoSOXTM measurements showed that TG treatment on core-expressing cells resulted in greater mitochondrial superoxide production compared with that observed in non-core-expressing cells. This effect was specifically induced by Ca^{2+} uptake by the mitochondria; DCFDA measurements also showed results similar to those seen with mitoSOXTM, demonstrating that core protein could sensitize cells to oxidative stimulus. The primary site of ROS production in response to the ROS donor was shown to be the mitochondria (Otani *et al.*, 2005).

5. CONCLUSION

Because viruses have both direct and indirect effects on mitochondrial function, a series of methods that examine mitochondria in live cells and reconstitution systems are required. In the case of HCV core protein, similar effects on electron transport and ROS production have been observed *in vitro* and *in vivo*, and this has allowed the identification of direct interaction of the viral protein with the Ca^{2+} uptake mechanism. These methods are generally applicable to the study of viral protein control of mitochondrial function.

ACKNOWLEDGMENTS

We thank M. Korenaga, K. Otani, M. Okuda, and D. Boehning for help in developing assays. We also thank S. Lemon, K. Li, M. Yi, J. Sun, and T. Chan for helpful advice and providing the model systems for some of the work described here. This work was supported in part by NIH Grant AA12863 from the National Institute on Alcohol Abuse and Alcoholism.

REFERENCES

- Anderson, M. E. (1989). Enzymatic and chemical methods for the determination of glutathione. In "Glutathione: Chemical, Biochemical and Medical Aspects. Part. A." (D. Dolphin, R. Poulson, and O. Avramovic, eds.). pp. 339–365. John Wiley and Sons, New York.
- Benali-Furet, N. L., Chami, M., Houel, L., De, G. F., Vernejoul, F., Lagorce, D., Buscaïl, L., Bartenschlager, R., Ichas, F., Rizzuto, R., and Paterlini-Brechot, P. (2005). Hepatitis C virus core triggers apoptosis in liver cells by inducing ER stress and ER calcium depletion. *Oncogene* **24**, 4921–4933.
- Blight, K. J., Kolykhalov, A. A., and Rice, C. M. (2000). Efficient initiation of HCV RNA replication in cell culture. *Science* **290**, 1972–1974.
- Boya, P., Pauleau, A. L., Poncet, D., Gonzalez-Polo, R. A., Zamzami, N., and Kroemer, G. (2004). Viral proteins targeting mitochondria: Controlling cell death. *Biochim. Biophys. Acta* **1659**, 178–189.
- D'Agostino, D. M., Bernardi, P., Chieco-Bianchi, L., and Ciminale, V. (2005). Mitochondria as functional targets of proteins coded by human tumor viruses. *Adv. Cancer Res.* **94**, 87–142.
- Estabrook, R. W. (1967). Mitochondrial respiratory control and the polarographic measurements of ADP/O ratios. *Methods Enzymol.* **10**, 41–47.
- Galluzzi, L., Brenner, C., Morselli, E., Touat, Z., and Kroemer, G. (2008). Viral control of mitochondrial apoptosis. *PLoS Pathog.* **4**: e1000018.
- Hickish, T., Robertson, D., Clarke, P., Hill, M., di Stefano, F., Clarke, C., and Cunningham, D. (1994). Ultrastructural localization of BHRF1: An Epstein-Barr virus gene product which has homology with bcl-2. *Cancer Res.* **54**, 2808–2811.
- Honda, A., Arai, Y., Hirota, N., Sato, T., Ikegaki, J., Koizumi, T., Hatano, M., Kohara, M., Moriyama, T., Imawari, M., Shimotohno, K., and Tokuhisa, T. (1999). Hepatitis C virus structural proteins induce liver cell injury in transgenic mice. *J. Med. Virol.* **59**, 281–289.
- Ikeda, M., Yi, M., Li, K., and Lemon, S. M. (2002). Selectable subgenomic and genome-length dicistronic RNAs derived from an infectious molecular clone of the HCV-N strain of hepatitis C virus replicate efficiently in cultured Huh7 cells. *J. Virol.* **76**, 2997–3006.
- Irshad, M., and Dhar, I. (2006). Hepatitis C virus core protein: An update on its molecular biology, cellular functions and clinical implications. *Med. Princ. Pract.* **15**, 405–416.
- Korenaga, M., Wang, T., Li, Y., Showalter, L. A., Chan, T., Sun, J., and Weinman, S. A. (2005). Hepatitis C virus core protein inhibits mitochondrial electron transport and increases reactive oxygen species (ROS) production. *J. Biol. Chem.* **280**, 37481–37488.
- Kunkel, M., and Watowich, S. J. (2004). Biophysical characterization of hepatitis C virus core protein: Implications for interactions within the virus and host. *FEBS Lett.* **557**, 174–180.
- Lerat, H., Honda, M., Beard, M. R., Loesch, K., Sun, J., Yang, Y., Okuda, M., Gosert, R., Xiao, S. Y., Weinman, S. A., and Lemon, S. M. (2002). Steatosis and liver cancer in transgenic mice expressing the structural and nonstructural proteins of hepatitis C virus. *Gastroenterology* **122**, 352–365.
- Li, K., Prow, T., Lemon, S. M., and Beard, M. R. (2002). Cellular response to conditional expression of hepatitis C virus core protein in Huh7 cultured human hepatoma cells. *Hepatology* **35**, 1237–1246.
- Li, Y., Boehning, D. F., Qian, T., Popov, V. L., and Weinman, S. A. (2007). Hepatitis C virus core protein increases mitochondrial ROS production by stimulation of Ca²⁺ uniporter activity. *FASEB J.* **21**, 2474–2485.
- Loo, Y. M., Owen, D. M., Li, K., Erickson, A. K., Johnson, C. L., Fish, P. M., Carney, D. S., Wang, T., Ishida, H., Yoneyama, M., Fujita, T., Saito, T., *et al.* (2006).

- Viral and therapeutic control of IFN-beta promoter stimulator 1 during hepatitis C virus infection. *Proc. Natl. Acad. Sci. USA* **103**, 6001–6006.
- Moradpour, D., Penin, F., and Rice, C. M. (2007). Replication of hepatitis C virus. *Nat. Rev. Microbiol.* **5**, 453–463.
- Moriya, K., Fujie, H., Shintani, Y., Yotsuyanagi, H., Tsutsumi, T., Ishibashi, K., Matsuura, Y., Kimura, S., Miyamura, T., and Koike, K. (1998). The core protein of hepatitis C virus induces hepatocellular carcinoma in transgenic mice. *Nat. Med.* **4**, 1065–1067.
- Nagai, T., Sawano, A., Park, E. S., and Miyawaki, A. (2001). Circularly permuted green fluorescent proteins engineered to sense Ca^{2+} . *Proc. Natl. Acad. Sci. USA* **98**, 3197–3202.
- Okuda, M., Li, K., Beard, M. R., Showalter, L. A., Scholle, F., Lemon, S. M., and Weinman, S. A. (2002). Mitochondrial injury, oxidative stress and antioxidant gene expression are induced by hepatitis C virus core protein. *Gastroenterology* **122**, 366–375.
- Otani, K., Korenaga, M., Beard, M. R., Li, K., Qian, T., Showalter, L. A., Singh, A. K., Wang, T., and Weinman, S. A. (2005). Hepatitis C virus core protein, cytochrome P450 2E1, and alcohol produce combined mitochondrial injury and cytotoxicity in hepatoma cells. *Gastroenterology* **128**, 96–107.
- Rahmani, Z., Huh, K. W., Lasher, R., and Siddiqui, A. (2000). Hepatitis B virus X protein colocalizes to mitochondria with a human voltage-dependent anion channel, HVDAC3, and alters its transmembrane potential. *J. Virol.* **74**, 2840–2846.
- Ray, R. B., Meyer, K., and Ray, R. (2000). Hepatitis C virus core protein promotes immortalization of primary human hepatocytes. *Virology* **271**, 197–204.
- Thomson, B. J., and Finch, R. G. (2005). Hepatitis C virus infection. *Clin. Microbiol. Infect* **11**, 86–94.
- Zhong, J., Gastaminza, P., Cheng, G., Kapadia, S., Kato, T., Burton, D. R., Wieland, S. F., Uprichard, S. L., Wakita, T., and Chisari, F. V. (2005). Robust hepatitis C virus infection *in vitro*. *Proc. Natl. Acad. Sci. USA* **102**, 9294–9299.

PARAQUAT-INDUCED PRODUCTION OF REACTIVE OXYGEN SPECIES IN BRAIN MITOCHONDRIA

Derek A. Drechsel *and* Manisha Patel

Contents

1. Introduction	382
2. Methods	383
2.1. Isolation of rat brain mitochondria	383
2.2. Measurement of PQ-induced mitochondrial H ₂ O ₂	384
3. Discussion	388
Acknowledgments	391
References	391

Abstract

Paraquat (PQ) is a prototypical redox cycling agent commonly used experimentally to generate reactive oxygen species and oxidative stress. Recently, PQ has also come under investigation as a potential environmental neurotoxin associated with increased risk for neurodegenerative disease developing after chronic exposure. The interactions of PQ with mitochondria remain an important aspect of its toxicity, particularly in the brain, although the underlying mechanisms are relatively uncharacterized. Here, we describe the basic measurement of PQ-induced hydrogen peroxide (H₂O₂) production in isolated brain mitochondria by use of two independent methods, polarography and fluorometry. The advantages of the use of these two independent methods include the capability to validate results and overcoming limitations in the use of either method exclusively. These simplified *in vitro* techniques for measurement of mitochondrial-generated H₂O₂ can be easily applied to other tissues and models.

Department of Pharmaceutical Sciences, University of Colorado, Denver, Aurora, Colorado, USA

Methods in Enzymology, Volume 456
ISSN 0076-6879, DOI: 10.1016/S0076-6879(08)04421-2

© 2009 Elsevier Inc.
All rights reserved.

1. INTRODUCTION

Paraquat (PQ), a member of the widely used bipyridyl herbicides, is a prototypical agent for the experimental generation of reactive oxygen species (ROS), particularly superoxide (O_2^-) and subsequently hydrogen peroxide (H_2O_2). Accordingly, PQ has been used extensively to test the response and sensitivity of oxidative stress in numerous models. PQ has also been intensely investigated for its potential as a toxic environmental agent. Particular attention has been focused on the brain, where significant damage has been observed in individuals exposed to lethal doses of PQ (Grant *et al.*, 1980; Hughes, 1988). Furthermore, epidemiologic studies suggest an increased risk for Parkinson's disease developing after chronic exposure to PQ (Hertzman *et al.*, 1990; Liou *et al.*, 1997). As a result, cell and animal models with PQ have become increasingly popular for understanding the mechanisms that underlie environmentally-induced parkinsonism (Brooks *et al.*, 1999; McCormack *et al.*, 2002; Shimizu *et al.*, 2003; Thiruchelvam *et al.*, 2000).

The toxicity of PQ is related to its ability to redox cycle, a process in which the parent dication (PQ^{2+}) accepts one electron from an appropriate donor (Fig. 21.1). Subsequent reaction with O_2 ($k \sim 7.7 \times 10^8 \text{ M}^{-1}\text{s}^{-1}$) produces O_2^- while also regenerating the parent compound (Bus and Gibson, 1984). Supporting the role of O_2^- as a key mediator in PQ toxicity are studies demonstrating protection against PQ with superoxide dismutase (SOD) overexpression (Thiruchelvam *et al.*, 2005) or administration of SOD mimetics (Day and Crapo, 1996; Day *et al.*, 1995; Mollace *et al.*, 2003; Patel *et al.*, 1996; Peng *et al.*, 2005), whereas SOD deficiencies exacerbate PQ's effects (Kirby *et al.*, 2002; Van Remmen *et al.*, 2004). The initial reduction of PQ may arise from a number of tissue-specific cellular sources, including enzymes identified in microsomal, plasma membrane, cytosolic, and mitochondrial components (Drechsel and Patel, 2008).

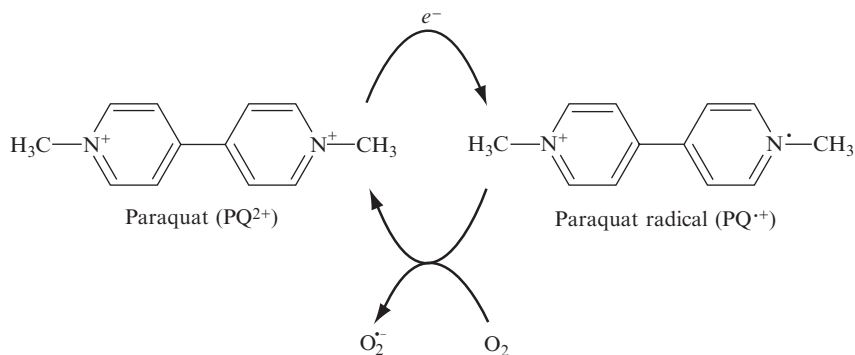


Figure 21.1 Redox cycling mechanism of PQ. e^- represents an appropriate electron source for the reduction of PQ^{2+} .

The interaction of PQ with mitochondria remains an important aspect of its toxicity, particularly in the brain, where mitochondrial dysfunction contributes to numerous neurologic disorders. We have previously demonstrated that mitochondria represent a major subcellular source of ROS generated by PQ in the brain (Castello *et al.*, 2007). Although a number of proposed sites for PQ redox cycling exist within the mitochondria, including components of the electron transport chain (ETC), the relative contributions of these sites remain relatively uncharacterized in brain tissue.

The techniques presented herein describe the measurement of H₂O₂ generated by PQ in isolated brain mitochondria. These techniques provide useful means for examining the involvement of cellular mechanisms in PQ-induced ROS production in brain mitochondria and protection by potential therapeutic agents. The advantages of using two independent methods to measure ROS include the capability to validate results and overcome limitations that may arise with one method exclusively.

2. METHODS

2.1. Isolation of rat brain mitochondria

The recovery of highly purified, respiring mitochondria from brain tissue with conventional isolation techniques presents a challenge to researchers. Application of differential centrifugation alone yields a crude mitochondrial fraction heavily contaminated with synaptosomes and myelin, whereas sucrose gradient differential centrifugation produces mitochondria with poorly preserved metabolic properties (Clark and Nicklas, 1970). However, the use of discontinuous Percoll gradients has been applied to the isolation of mitochondria from rat brain tissue to yield mitochondrial fractions displaying high rates of respiratory activity and limited contamination by synaptosomal and cytosolic components. Protocols for the isolation of mitochondria from rat brain by means of Percoll density gradient centrifugation have been well described (Sims and Anderson, 2008) and, therefore, are only briefly detailed here.

Male Sprague-Dawley rats, age 2 to 3 months, were killed by decapitation under CO₂ anesthesia. Whole forebrains were excised and placed in ice-cold isolation buffer (70 mM sucrose, 210 mM mannitol, 5 mM TRIS-HCl, 1 mM EDTA, pH 7.4) with all subsequent steps performed rapidly on ice. Forebrains were homogenized with a Dounce tissue grinder (Wheaton Science, Millville, NJ) and diluted 1:1 with 24% Percoll followed by centrifugation at 30,700g for 10 min. The upper half of material in the tube was discarded, and the remaining material subjected to Percoll gradient (19% on 40%) and centrifuged at 30,700g for 10 min. The material located at the interface of the lowest two layers (containing the enriched

mitochondrial fraction) was collected, transferred to a new tube, diluted 1:4 with isolation buffer, and centrifuged at 16,700g for 10 min. The pellet was resuspended in isolation buffer containing 1 mg/ml bovine serum albumin and centrifuged at 6700g for 10 min to obtain a final pellet consisting of purified mitochondrial fraction. Protein concentration was measured with Coomassie Plus protein assay reagent (Pierce, Rockford, IL).

With whole forebrain as starting material, this procedure typically recovers approximately 10% of total mitochondria, corresponding to 2.5 to 3.5 mg of protein for use in subsequent experiments. Immunoblots used to assess mitochondrial purity showed undetectable levels of lactate dehydrogenase, a marker of cytosolic/synaptosomal contamination and high levels of the mitochondrial marker cytochrome *c* oxidase subunit IV. Mitochondria integrity was assessed by means of respiratory activity with a Clark-type oxygen electrode (YSI Life Sciences, Yellow Springs, OH). With malate and glutamate as metabolic substrates, respiratory control ratios (state 3 respiration/state 4 respiration) averaged greater than 6, indicating highly coupled, intact mitochondria.

2.2. Measurement of PQ-induced mitochondrial H₂O₂

The following methods used to measure PQ-induced mitochondrial ROS production are based on the detection of extramitochondrial H₂O₂. PQ generates O₂^{•-} in the mitochondria, where it is rapidly converted to H₂O₂ through the actions of manganese superoxide dismutase (MnSOD) and/or spontaneous dismutation. In addition, O₂^{•-}-induced inactivation of iron-sulfur proteins, such as aconitase, may also yield H₂O₂ (Patel, 2004). Unlike O₂^{•-} that is largely impermeable to cellular membranes, H₂O₂ can diffuse into the extramitochondrial space, where it can be measured by the detection methods described (Fig. 21.2). For this reason, the measurement of H₂O₂ release is generally preferred when studying ROS from intact isolated mitochondria (Freeman and Crapo, 1982; Turrens and Boveris, 1980). As expected, the addition of exogenous SOD to isolated mitochondria had no effect on rates of H₂O₂ production induced by PQ, whereas exogenous catalase scavenges any H₂O₂ released in the medium, thus preventing the measurement of the radical species (Fig. 21.3). These data confirm the intramitochondrial nature of PQ-induced O₂^{•-} production in this system.

2.2.1. Polarographic measurement

Polarography that uses Clark-type electrodes has commonly been applied to the measurement of O₂ and NO and recently extended to include detection of H₂O₂ in biological systems. The basic construction of the Clark-type electrode consists of a selective membrane enclosing a sensor that contains the working electrode at a set poise voltage for the reactive species of interest. The reactive species passes through the selective membrane

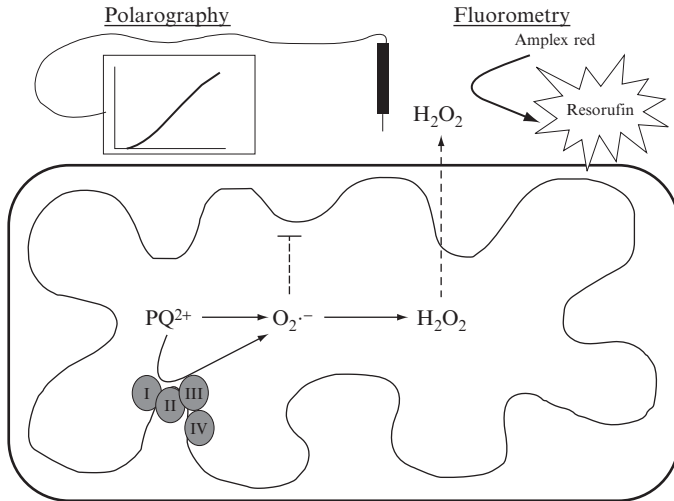


Figure 21.2 Measurement of PQ-induced H₂O₂ from isolated mitochondria. PQ generates O₂^{•-} in the mitochondria where it is converted to H₂O₂ by MnSOD and/or spontaneous dismutation. O₂^{•-} is largely impermeable to cellular membranes, whereas H₂O₂ is able to diffuse out of the mitochondria, where it can be measured by polarographic or fluorometric techniques as described in the text.

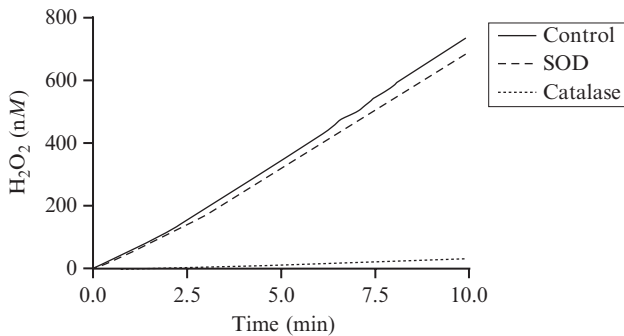


Figure 21.3 Effect of exogenous SOD and catalase on PQ-induced H₂O₂ production in isolated mitochondria. Fluorometric measurement of H₂O₂ in isolated brain mitochondria supplemented with respiration substrates (malate + glutamate) in the presence of 250 μ M PQ (solid line). Addition of exogenous SOD (500 U/ml) had no effect on PQ-induced H₂O₂ production (dashed line). Catalase (40 U/ml) scavenges H₂O₂ released from the mitochondria and decreases its extracellular concentration (dotted line). These data suggest that PQ generates ROS within the mitochondria.

where it can be oxidized at the electrode, generating an electrical (redox) current that is proportional to the concentration of the reactive species in the sample. The main advantage of the use of polarography is the ability to detect real-time steady-state changes in H₂O₂ concentrations that takes into account the contributions of both production and removal of H₂O₂ in

the system. Also, other radical species such as O_2 or NO can be simultaneously measured in the same chamber with the appropriate electrode(s). Finally, if production of the reactive species is temperature dependent, as in the case of NO , a temperature-sensitive electrode can be simultaneously used.

2.2.1.1. Procedure H_2O_2 production in isolated rat brain mitochondria was measured with an Apollo 4000 Free Radical Analyzer equipped with a $100\ \mu m$ H_2O_2 electrode (World Precision Instruments, Sarasota, FL) at the following settings: sampling rate of 5 readings per sec, range of 100 nA, and poise voltage of 400 mV for H_2O_2 . All measurements were conducted in a thermostated open chamber (World Precision Instruments) at 30° in a final reaction volume of 2 ml. The H_2O_2 electrode was immersed in respiration buffer (100 mM KCl, 75 mM mannitol, 25 mM sucrose, 10 mM TRIS-HCl, 10 mM KH_2PO_4 , pH 7.4) approximately 2 h before performing experiments to provide sufficient time for the electrode to polarize.

Each sample run was started by adding ~ 2 ml of respiration buffer to the chamber and allowing the output signal to reach stable baseline (~ 3 min); $20\ \mu l$ of $100\times$ stocks of one or more respiration substrates (250 mM malate, 1 M glutamate, 500 mM pyruvate, or 1 M succinate) were added, followed by 100 μg of isolated mitochondria (0.1 mg/ml final concentration). PQ was then added from 10 mM stock at the indicated concentration and the linear output signal recorded for 2 to 3 min.

The rapid and robust production of H_2O_2 upon addition of PQ increases at a consistent rate over several minutes, during which time the effect of stimulatory/inhibitory agents on H_2O_2 production can be examined. Alternate substrates, inhibitors of the ETC such as rotenone (complex I) or antimycin A (complex III), inhibitors of other mitochondrial systems, or specific agent(s) of interest can be tested for their effects with this system. The agent(s) should be added at appropriate concentration only after obtaining a steady rate of H_2O_2 production after the addition of PQ. Previous work has tested the effect of ETC inhibitors, antioxidant enzymes, and catalytic antioxidants in this system (Castello *et al.*, 2007, 2008).

Rates of H_2O_2 production were determined on the basis of the slope (Δ pA/sec) after the addition of PQ adjusted to the prior baseline and converted to nmol H_2O_2 /mg protein \times min with a predetermined standard curve for H_2O_2 (Fig. 21.4). The effect of any agent of interest can also be determined by comparing rates of PQ-induced H_2O_2 production before and after the addition of the agent.

Proper care of the H_2O_2 electrode is critical to achieve accurate and reproducible results. Contact with the sensor tip should be avoided, since the integrity of the selective membrane can be compromised. To check membrane integrity, immerse the electrode in a 1-M saline solution.

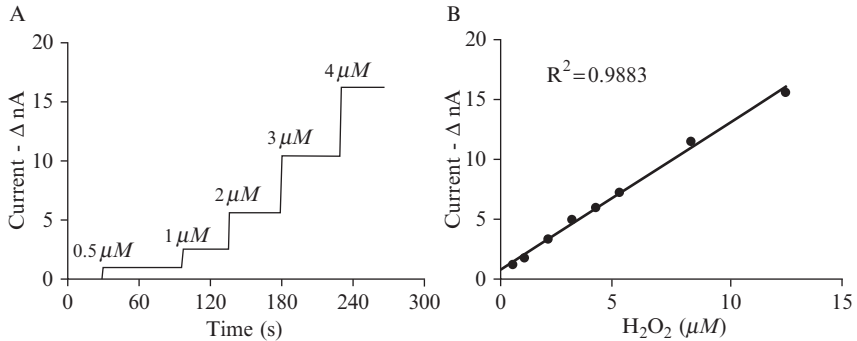


Figure 21.4 H₂O₂ standard curve measured by polarography. (A) Polarographic measurement of H₂O₂ aliquots at indicated concentrations. (B) Change in current (Δ nA) was measured for each aliquot of H₂O₂ and used to generate the standard curve. Linear fit trendline calculated with Prism 5.01 software (GraphPad Software Inc., La Jolla, CA).

The output signal should reflect a low and stable current. After each experiment, the H₂O₂ electrode was immersed in dH₂O for several minutes, and the incubation chamber was washed thoroughly with isopropanol and dH₂O. In addition, the H₂O₂ electrode should periodically be immersed in dH₂O and enzymatic detergent cleaner to remove deposited salts and protein, respectively. This is best performed after the completion of experiments and before storage of the electrode. Furthermore, the electrode is extremely sensitive to pH, temperature, and interference by a number of chemicals, including organic solvents such as ethanol. Several agents may also sensitize or dampen the H₂O₂ response. Therefore, it is critical to test the compatibility of all chemicals and agents under study with the H₂O₂ electrode while maintaining consistent experimental conditions.

2.2.2. Fluorometric measurement

Fluorometric and spectrophotometric methods can also be used to accurately measure and quantitate PQ-induced H₂O₂ production in isolated mitochondria. In addition, this allows independent validation of results obtained by polarography. Although several techniques and reagents exist on the basis of the fluorescent detection of H₂O₂, the fluorogenic probe Amplex Red (10-acetyl-3,7-dihydroxyphenoxazine), in combination with horseradish peroxidase (HRP) serves as a reliable and sensitive means for the detection of H₂O₂ release in biological samples, including isolated mitochondria. In the presence of peroxidase, Amplex Red reacts stoichiometrically 1:1 with H₂O₂ to produce the red-fluorescent oxidation product, resorufin (Zhou *et al.*, 1997). The method described in the following has

been adapted for use with 96-well plates and a fluorescent microplate reader that provides an ideal high-throughput system.

2.2.2.1. Procedure Amplex UltraRed reagent (Molecular Probes, Eugene, OR) (1 mg) contained in a single vial was dissolved in 66.7 μl of DMSO to achieve a fresh 50 mM stock for each set of experiments. HRP (Sigma, St. Louis, MO) is stored frozen at -20° as a 10 U/ml stock. Reaction buffer was prepared by diluting Amplex UltraRed and HRP in 10 ml respiration buffer to concentrations of 50 μM and 0.1 U/ml, respectively. One or more respiration substrates were added directly to wells of a 96-well microtiter plate from 100 \times stocks: 250 mM malate, 1 M glutamate, 500 mM pyruvate, or 1 M succinate. At this point, additional agents (and/or vehicle) may be applied to the plate to test for inhibitory/stimulatory effects on PQ-induced H_2O_2 production. Alternate substrates and inhibitors of the ETC (e.g., rotenone or antimycin A) can be varied for examination of each ETC complex, whereas other agent(s) of interest can be used to test the contributions of other mitochondrial systems; 100 μg of isolated mitochondria was added to reaction buffer (0.1 mg protein/ml final concentration), and 100 μl was aliquoted to wells of plate. PQ was added from 10 mM stock to achieve the indicated concentration. All solutions and plate were kept on ice before fluorescence reading.

Fluorescence of resorufin was measured immediately after addition of PQ by fluorescence microplate reader (Molecular Devices, Sunnyvale, CA) at excitation/emission of 530/590 nm. Fluorescence was monitored over a 10-min period in which H_2O_2 production increased linearly. PQ-induced H_2O_2 production rates over this time course were measured as increase in fluorescence (Δ relative fluorescence units/sec) and adjusted to nmol H_2O_2 /mg protein \times min on the basis of a predetermined standard curve.

3. DISCUSSION

This chapter describes the basic measurement of PQ-induced H_2O_2 production in isolated mitochondria with polarography and fluorometry, including important aspects to consider when these techniques are used. The brain is unique in the context of measuring mitochondrial PQ-induced H_2O_2 , because the isolation of mitochondria from brain tissue requires adaptation of density gradient centrifugations to yield functional mitochondria with minimal contamination compared with conventional techniques commonly applied to other tissues. In addition, despite extensive literature examining aspects of PQ-dependent redox cycling and ROS generation, there are surprisingly limited data suggesting potential mechanisms of PQ toxicity in the brain. The role of mitochondria in the neurotoxicity of PQ is

particularly relevant because (1) the recognition of PQ as a potential environmental neurotoxicant and (2) the association of several neurodegenerative disorders with mitochondrial oxidative damage and dysfunction, including Parkinson's disease, Alzheimer's disease, and amyotrophic lateral sclerosis (Lin and Beal, 2006).

A multitude of methods exist for the measurement of reactive species from isolated mitochondrial preparations in various models. Although the application of these techniques have proved invaluable for identifying critical aspects and sites of mitochondria ROS production, the measurement of H_2O_2 has remained the preferred method, because it allows the use of intact, respiring mitochondria and H_2O_2 is relatively stable compared with other reactive species. In particular, the use of HRP-linked fluorescent products such as scopoletine (Loschen *et al.*, 1971), homovanillic acid (Herrero and Barja, 1997), and p-hydroxyphenylacetic acid (Beckman and Koppenol, 1996) to detect H_2O_2 have been well described. Here, we present a polarographic method to measure H_2O_2 release from isolated mitochondria in conjunction with an established fluorometric method, HRP-linked fluorescence of resorufin.

The fundamental difference between these two methods is the manner in which H_2O_2 production is detected. In contrast to fluorescence methods that measure total H_2O_2 production from a system, polarography is dynamic and is based on continuous real-time measurement of H_2O_2 concentrations in the system. Polarography measures net H_2O_2 production as the steady-state concentration resulting from processes of H_2O_2 production and removal, as opposed to H_2O_2 resulting from production alone. This is best demonstrated in comparing the traces of PQ-induced H_2O_2 production in isolated mitochondria between these two methods (Fig. 21.5). In the case of the fluorometric assay, H_2O_2 is released from the mitochondria and detected by the Amplex Red/HRP system producing resorufin, the fluorescence of which remains stable in the system. Thus, H_2O_2 production increases linearly and consistently over the time course. When polarography is used, however, the H_2O_2 signal is less robust and levels off several minutes after the addition of PQ until reaching equilibrium. Respiring brain mitochondria are also capable scavengers of exogenous H_2O_2 at rates comparable to baseline H_2O_2 production (Zoccarato *et al.*, 2004). Therefore, because H_2O_2 is generated in mitochondria exposed to PQ, it is detected by the electrode but also removed by mitochondrial systems at the same time with a decrease in signal. Removal is an important aspect to consider when using polarographic means to measure H_2O_2 not only in isolated mitochondria but any biological system.

The process of H_2O_2 removal also has a significant effect on the sensitivity of each of these methods to PQ-induced H_2O_2 production. Table 21.1 shows that significant increases in mitochondrial H_2O_2 production can be detected with fluorescence changes with 30 μM PQ. Whereas, significant increases are

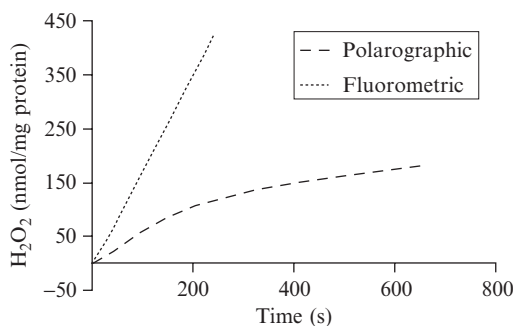


Figure 21.5 PQ-induced H₂O₂ production in isolated brain mitochondria. Polarographic (dashed line) and fluorometric (dotted line) methods were used to measure H₂O₂ production in isolated brain mitochondria supplemented with respiration substrates (2.5 mM malate + 10 mM glutamate) in the presence of 300 μ M PQ.

not seen with polarography until PQ reaches 100 μ M. This difference in sensitivity can be attributed to the measurement of H₂O₂ production by distinctive fluorometric and polarographic means as described previously. However, this aspect of PQ-induced H₂O₂ production should not be confused with sensitivity to H₂O₂ with each method. In fact, the polarographic method may be more sensitive to H₂O₂ concentrations alone than the fluorometric method described (data not shown).

The methods described are for the measurement of PQ-induced H₂O₂ production in brain mitochondria. However, they are readily adaptable to a variety of models, including tissue-specific mitochondrial fractions, assuming that proper isolation techniques are implemented. In addition, other inducers of oxidative stress can be assessed in place of PQ. Our laboratory has adopted these methods to gain insight into mitochondrial mechanisms of H₂O₂ generation by PQ, in particular the role of each ETC complex (Castello *et al.*, 2007), and to assess the potential therapeutic effectiveness of catalytic antioxidant compounds (Castello *et al.*, 2008). The polarographic and fluorometric techniques described provide simplified independent *in vitro* systems for measuring H₂O₂ production in isolated brain mitochondria in response to PQ that can be tailored for use in other models and applications.

Each method and system described has its inherent advantages and disadvantages toward use in the measurement of PQ-induced mitochondrial H₂O₂ production. Polarography allows for real-time detection of dynamic steady-state H₂O₂ concentrations in conjunction with the measurement of other reactive species, although rigorous care of the electrode is necessary to achieve consistent, reproducible results. The fluorometric method is better adapted for high-throughput analysis and shows greater sensitivity to PQ-induced H₂O₂ production in isolated mitochondria. The detection of H₂O₂ by each method can be hampered through interference

Table 21.1 Rates of PQ-induced mitochondrial H₂O₂ production^a

	Fluorometry	Polarography
Control	2.63 ± 0.43	2.60 ± 1.82
30 μM	5.96 ± 0.38*	3.26 ± 1.27
100 μM	21.40 ± 1.29*	15.66 ± 1.17*
300 μM	105.64 ± 5.89*	33.54 ± 4.79*

^a Isolated rat brain mitochondria were assayed for H₂O₂ production in the presence of PQ with polarographic or fluorometric methods as described in text. Malate (2.5 mM) and glutamate (10 mM) were supplied as respiration substrates. All values expressed as nmol H₂O₂/mg protein × min (mean ± S.D., *n* = 3).

* *p* < 0.05, one-way analysis of variance.

by several compounds, including strong reducing agents and trace metals (fluorometry) or organic solvents (polarography). However, such limitations can be overcome with these two validated independent methods.

ACKNOWLEDGMENTS

This work supported by National Institutes of Health grants RO1NS45748 (M.P.), RO1NS039587 (M.P.), and 1F31NS06438-01 (D.A.D.). We thank Dr. Pablo Castello for helpful suggestions.

REFERENCES

- Beckman, J. S., and Koppenol, W. H. (1996). Nitric oxide, superoxide, and peroxynitrite: The good, the bad, and ugly. *Am. J. Physiol.* **271**, C1424–C1437.
- Brooks, A. I., Chadwick, C. A., Gelbard, H. A., Cory-Slechta, D. A., and Federoff, H. J. (1999). Paraquat elicited neurobehavioral syndrome caused by dopaminergic neuron loss. *Brain Res.* **823**, 1–10.
- Bus, J. S., and Gibson, J. E. (1984). Paraquat: Model for oxidant-initiated toxicity. *Environ. Health Perspect* **55**, 37–46.
- Castello, P. R., Drechsel, D. A., Day, B. J., and Patel, M. (2008). Inhibition of mitochondrial hydrogen peroxide production by lipophilic metalloporphyrins. *J. Pharmacol. Exp. Ther.* **324**, 970–976.
- Castello, P. R., Drechsel, D. A., and Patel, M. (2007). Mitochondria are a major source of paraquat-induced reactive oxygen species production in the brain. *J. Biol. Chem.* **282**, 14186–14193.
- Clark, J. B., and Nicklas, W. J. (1970). The metabolism of rat brain mitochondria. Preparation and characterization. *J. Biol. Chem.* **245**, 4724–4731.
- Day, B. J., Shawen, S., Liochev, S. I., and Crapo, J. D. (1995). A metalloporphyrin superoxide dismutase mimetic protects against paraquat-induced endothelial cell injury, *in vitro*. *J. Pharmacol. Exp. Ther.* **275**, 1227–1232.
- Day, B. J., and Crapo, J. D. (1996). A metalloporphyrin superoxide dismutase mimetic protects against paraquat-induced lung injury *in vivo*. *Toxicol. Appl. Pharmacol.* **140**, 94–100.

- Drechsel, D. A., and Patel, M. (2008). Role of reactive oxygen species in the neurotoxicity of environmental agents implicated in Parkinson's disease. *Free Radic. Biol. Med.* **44**, 1873–1886.
- Freeman, B. A., and Crapo, J. D. (1982). Biology of disease: Free radicals and tissue injury. *Lab. Invest.* **47**, 412–426.
- Grant, H., Lantos, P. L., and Parkinson, C. (1980). Cerebral damage in paraquat poisoning. *Histopathology* **4**, 185–195.
- Herrero, A., and Barja, G. (1997). Sites and mechanisms responsible for the low rate of free radical production of heart mitochondria in the long-lived pigeon. *Mech. Ageing Dev.* **98**, 95–111.
- Hertzman, C., Wiens, M., Bowering, D., Snow, B., and Calne, D. (1990). Parkinson's disease: A case-control study of occupational and environmental risk factors. *Am. J. Ind. Med.* **17**, 349–355.
- Hughes, J. T. (1988). Brain damage due to paraquat poisoning: A fatal case with neuropathological examination of the brain. *Neurotoxicology* **9**, 243–248.
- Kirby, K., Hu, J., Hilliker, A. J., and Phillips, J. P. (2002). RNA interference-mediated silencing of Sod2 in *Drosophila* leads to early adult-onset mortality and elevated endogenous oxidative stress. *Proc. Natl. Acad. Sci. USA* **99**, 16162–16167.
- Lin, M. T., and Beal, M. F. (2006). Mitochondrial dysfunction and oxidative stress in neurodegenerative diseases. *Nature* **443**, 787–795.
- Liou, H. H., Tsai, M. C., Chen, C. J., Jeng, J. S., Chang, Y. C., Chen, S. Y., and Chen, R. C. (1997). Environmental risk factors and Parkinson's disease: A case-control study in Taiwan. *Neurology* **48**, 1583–1588.
- Loschen, G., Flohe, L., and Chance, B. (1971). Respiratory chain linked H₂O₂ production in pigeon heart mitochondria. *FEBS Lett.* **18**, 261–264.
- McCormack, A. L., Thiruchelvam, M., Manning-Bog, A. B., Thiffault, C., Langston, J. W., Cory-Slechta, D. A., and Di Monte, D. A. (2002). Environmental risk factors and Parkinson's disease: Selective degeneration of nigral dopaminergic neurons caused by the herbicide paraquat. *Neurobiol. Dis.* **10**, 119–127.
- Mollace, V., Iannone, M., Muscoli, C., Palma, E., Granato, T., Rispoli, V., Nistico, R., Rotiroti, D., and Salvemini, D. (2003). The role of oxidative stress in paraquat-induced neurotoxicity in rats: Protection by non peptidyl superoxide dismutase mimetic. *Neurosci. Lett.* **335**, 163–166.
- Patel, M. (2004). Mitochondrial dysfunction and oxidative stress: Cause and consequence of epileptic seizures. *Free Radic. Biol. Med.* **37**, 1951–1962.
- Patel, M., Day, B. J., Crapo, J. D., Fridovich, I., and McNamara, J. O. (1996). Requirement for superoxide in excitotoxic cell death. *Neuron* **16**, 345–355.
- Peng, J., Stevenson, F. F., Doctrow, S. R., and Andersen, J. K. (2005). Superoxide dismutase/catalase mimetics are neuroprotective against selective paraquat-mediated dopaminergic neuron death in the substantia nigra: Implications for Parkinson disease. *J. Biol. Chem.* **280**, 29194–29198.
- Shimizu, K., Matsubara, K., Ohtaki, K., and Shiono, H. (2003). Paraquat leads to dopaminergic neural vulnerability in organotypic midbrain culture. *Neurosci. Res.* **46**, 523–532.
- Sims, N. R., and Anderson, M. F. (2008). Isolation of mitochondria from rat brain using Percoll density gradient centrifugation. *Nat. Protoc.* **3**, 1228–1239.
- Thiruchelvam, M., Brockel, B. J., Richfield, E. K., Baggs, R. B., and Cory-Slechta, D. A. (2000). Potentiated and preferential effects of combined paraquat and maneb on nigrostriatal dopamine systems: Environmental risk factors for Parkinson's disease? *Brain Res.* **873**, 225–234.
- Thiruchelvam, M., Prokopenko, O., Cory-Slechta, D. A., Richfield, E. K., Buckley, B., and Mirochnitchenko, O. (2005). Overexpression of superoxide dismutase or glutathione peroxidase protects against the paraquat + maneb-induced Parkinson disease phenotype. *J. Biol. Chem.* **280**, 22530–22539.

- Turrens, J. F., and Boveris, A. (1980). Generation of superoxide anion by the NADH dehydrogenase of bovine heart mitochondria. *Biochem. J.* **191**, 421–427.
- Van Remmen, H., Qi, W., Sabia, M., Freeman, G., Estlack, L., Yang, H., Mao Guo, Z., Huang, T. T., Strong, R., Lee, S., Epstein, C. J., and Richardson, A. (2004). Multiple deficiencies in antioxidant enzymes in mice result in a compound increase in sensitivity to oxidative stress. *Free Radic. Biol. Med.* **36**, 1625–1634.
- Zhou, M., Diwu, Z., Panchuk-Voloshina, N., and Haugland, R. P. (1997). A stable nonfluorescent derivative of resorufin for the fluorometric determination of trace hydrogen peroxide: Applications in detecting the activity of phagocyte NADPH oxidase and other oxidases. *Anal. Biochem.* **253**, 162–168.
- Zoccarato, F., Cavallini, L., and Alexandre, A. (2004). Respiration-dependent removal of exogenous H₂O₂ in brain mitochondria: Inhibition by Ca²⁺. *J. Biol. Chem.* **279**, 4166–4174.

THE UPTAKE AND INTERACTIONS OF THE REDOX CYCLER PARAQUAT WITH MITOCHONDRIA

Helena M. Cochemé^{*,†} and Michael P. Murphy[†]

Contents

1. Introduction	396
1.1. Paraquat (PQ) as a redox cycler	396
1.2. PQ and mitochondria	397
1.3. PQ and Parkinson's disease	398
2. Detection of the PQ ^{•+} Radical	399
2.1. Detection of the PQ ^{•+} radical by EPR	399
2.2. Detection of the PQ ^{•+} radical by spectrophotometry	400
3. Detection of PQ	401
3.1. Radioactive [¹⁴ C]-PQ	401
3.2. Detection of PQ indirectly by EPR	402
3.3. Construction of a PQ-selective electrode	402
4. Assays for PQ-Associated Superoxide (O ₂ ⁻) Production	404
4.1. Aconitase inactivation	404
4.2. Coelenterazine (CLZ) chemiluminescence	407
4.3. Amplex Red fluorescence	408
5. Uptake of PQ into Mitochondria	409
5.1. Measurement of PQ uptake with an ion-selective electrode	409
5.2. Measurement of PQ uptake by EPR	410
5.3. Measurement of PQ uptake from the distribution of radiolabeled [¹⁴ C]-PQ	412
6. PQ Toxicity Screens in Yeast Deletion Libraries	413
7. Conclusions	414
Acknowledgments	415
References	415

* Institute of Healthy Ageing, University College London, London, United Kingdom

† The Medical Research Council Mitochondrial Biology Unit, Cambridge, United Kingdom

Abstract

Paraquat (1,1'-dimethyl-4,4'-bipyridinium dichloride) is widely used as a redox cyler to stimulate superoxide production in organisms, cells, and mitochondria. Paraquat is also used to induce symptoms of Parkinson's disease in experimental models of this neurodegenerative disorder. Paraquat causes extensive mitochondrial oxidative damage, and in mammalian systems, complex I of the respiratory chain has been identified as the major site of superoxide production by paraquat. Although much progress has been made at explaining how paraquat interacts with mitochondria, several aspects remain to be clarified—most notably the pathway of paraquat uptake into mitochondria. This chapter describes methods for further investigating the interaction of paraquat with mitochondria and also provides practical information for the general use of paraquat as a superoxide generator and agent of oxidative stress. The techniques covered include the detection and quantitation of the paraquat dication and the paraquat monocation radical (by electron paramagnetic resonance, spectrophotometry, and with an ion-selective electrode); assays for measuring paraquat-induced superoxide production by intact mitochondria or mitochondrial membranes (including aconitase inactivation, and coelenterazine chemiluminescence); methods for assessing paraquat uptake by mitochondria; and screens for identifying paraquat sensitivity or resistance in yeast mutants.

1. INTRODUCTION

1.1. Paraquat (PQ) as a redox cyler

Paraquat (1,1'-dimethyl-4,4'-bipyridinium dichloride; PQ) is a powerful redox cycling agent (Fig. 22.1A). The paraquat dication (PQ^{2+}) accepts an electron from a reductant to form the paraquat monocation radical ($\text{PQ}^{\bullet+}$), which subsequently reacts rapidly with O_2 ($k \sim 7.7 \times 10^8 \text{ M}^{-1} \cdot \text{s}^{-1}$; Hassan, 1984) to produce superoxide ($\text{O}_2^{\bullet-}$). The parent compound PQ^{2+} is thus regenerated and able to catalyze further $\text{O}_2^{\bullet-}$ production.

The reduction potential of $\text{PQ}^{2+}/\text{PQ}^{\bullet+}$ is $E^0 = -446 \text{ mV}$ (Mayhew, 1978). This very negative value has several implications: first, it explains why PQ is such an effective redox cyler ($\text{O}_2/\text{O}_2^{\bullet-}$ $E^0 = -160 \text{ mV}$ at pH 7 for a standard state of 1 M O_2 ; Sawyer and Valentine, 1981), and second, it severely limits the pool of possible intracellular reductants, which have a sufficiently low reduction potential to donate an electron to PQ^{2+} . Biological systems capable of catalyzing $\text{PQ}^{\bullet+}$ formation are typically flavin-containing oxidoreductase enzymes, which use NAD(P)H as electron donors.

PQ has important agricultural applications as a herbicide, whereas in a biochemical context, PQ is widely used as a redox cyler to increase

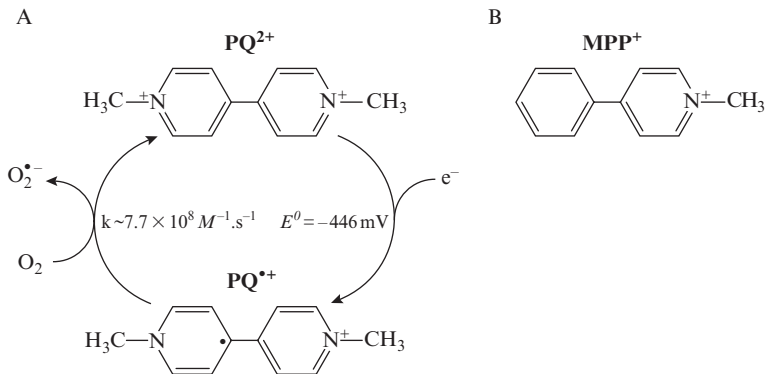


Figure 22.1 Paraquat structure and redox cycling mechanism. (A) The paraquat dication (PQ²⁺) undergoes univalent reduction to generate the paraquat radical (PQ^{•+}), which then reacts rapidly with O₂ to produce superoxide (O₂^{•-}). (B) Structure of the neurotoxin 1-methyl-4-phenylpyridinium (MPP⁺).

O₂^{•-} flux, whereby causing oxidative stress. PQ has been used to generate O₂^{•-} in systems ranging from isolated mitochondria and cultured cells to whole organisms, including yeast, worms, flies, and rodents (e.g., Bonilla *et al.*, 2006; Sturtz and Culotta, 2002; Vanfleteren, 1993; Van Remmen *et al.*, 2004). Redox cycling by PQ is a proximal cause of its toxicity, as indicated by the protection against PQ by superoxide dismutase (SOD) overexpression (e.g., Krall *et al.*, 1988; Thiruchelvam *et al.*, 2005) or administration of SOD mimetics (e.g., Day *et al.*, 1995; Mollace *et al.*, 2003; Peng *et al.*, 2005), and by the PQ hypersensitivity caused by SOD deficiency (Kirby *et al.*, 2002; Sturtz and Culotta, 2002; Van Remmen *et al.*, 2004).

1.2. PQ and mitochondria

Mitochondria have been implicated as a target of oxidative damage by PQ in many studies. For example, mitochondrial expression of a transgenic antioxidant enzyme is more protective against PQ than cytosolic expression (Mockett *et al.*, 2003; Tien Nguyen-nhu and Knoops, 2003); deficiency of MnSOD (the isoform of superoxide dismutase located in the mitochondrial matrix) results in hypersensitivity to PQ (Kirby *et al.*, 2002; Van Remmen *et al.*, 2004); PQ causes an increase in mitochondrial DNA deletions and point mutations in yeast cultures (Cochemé and Murphy, 2008); and mitochondrial swelling is one of the earliest ultrastructural changes on PQ exposure *in vivo* (Hirai *et al.*, 1992; Wang *et al.*, 1992). Therefore, the interaction of PQ with mitochondria is an important component of

its toxicity, and, consequently, there is considerable interest in investigating these mechanisms.

In mitochondria, reported sites of PQ^{2+} reduction include NADH-cytochrome b_5 oxidoreductase and NADH-coenzyme Q oxidoreductase of the mitochondrial outer membrane (Hirai *et al.*, 1992; Shimada *et al.*, 1998) and complex I of the mitochondrial inner membrane (Cochemé and Murphy, 2008; Fukushima *et al.*, 1993).

1.3. PQ and Parkinson's disease

Mitochondrial dysfunction has been implicated in the pathogenesis of Parkinson's disease (Mizuno *et al.*, 1995; Schapira, 2008). PQ treatment is used in some experimental models of Parkinson's disease, and, indeed, there is an epidemiological correlation between the incidence of sporadic Parkinson's disease and environmental exposure to PQ as a herbicide (Dinis-Oliveira *et al.*, 2006). This is supported by the fact that PQ treatment in mice causes selective degeneration of nigral dopaminergic neurons (McCormack *et al.*, 2002), as well as upregulation and aggregation of α -synuclein (Manning-Bog *et al.*, 2002).

Although PQ is structurally similar to the neurotoxin 1-methyl-4-phenylpyridinium (MPP^+ ; Fig. 22.1B), which is widely used as a model of Parkinson's disease, the compounds have different modes of toxicity despite their structural similarity. Most notably, unlike PQ, MPP^+ does not function as a redox cyler. However, both compounds accumulate inside mitochondria, albeit by different mechanisms; MPP^+ accumulates into mitochondria by direct passage across the mitochondrial inner membrane driven by the membrane potential (Davey *et al.*, 1992; Fig. 22.4D), whereas recent work from our laboratory suggests that PQ may be taken up into mitochondria by a low-affinity carrier-mediated process (Cochemé and Murphy, 2008). Once inside mitochondria, both compounds stimulate mitochondrial O_2^- production from complex I: MPP^+ by inhibiting complex I directly (Richardson *et al.*, 2005), and PQ^{2+} by accepting electrons from complex I for redox cycling (Cochemé and Murphy, 2008). Because complex I is the major site of O_2^- production within mitochondria exposed to PQ, and complex I damage is a major factor in idiopathic Parkinson's disease, this supports PQ toxicity as a useful model for investigating how complex I damage might contribute to Parkinson's disease, although the origin of the complex I defect involved is still unclear.

Here we describe techniques for the detection and quantitation of PQ, assays for measuring PQ-induced O_2^- production by mitochondria and methods for assessing PQ uptake by mitochondria.

2. DETECTION OF THE $\text{PQ}^{\bullet+}$ RADICAL

The $\text{PQ}^{\bullet+}$ radical is blue-violet; hence, methyl viologen is often used as an alternative name for $\text{PQ}^{\bullet+}$. The $\text{PQ}^{\bullet+}$ radical can be detected either by electron paramagnetic resonance (EPR) or spectrophotometrically. Because the $\text{PQ}^{\bullet+}$ radical reacts rapidly with O_2 (rate constant of $\sim 7.7 \times 10^8 \text{ M}^{-1}\cdot\text{s}^{-1}$; Hassan, 1984), it is only stable under strictly anaerobic conditions, so buffers and samples must be purged with argon or nitrogen to render them anaerobic.

2.1. Detection of the $\text{PQ}^{\bullet+}$ radical by EPR

The $\text{PQ}^{\bullet+}$ radical has a distinctive EPR spectrum because of the delocalization of the unpaired electron across the conjugated ring system (Fig. 22.2A, trace a). For EPR experiments, we use an EMX 10/12 EPR spectrometer and an AquaX cell (Bruker, Germany) at room temperature with the following instrument settings: microwave frequency, 9.85 GHz;

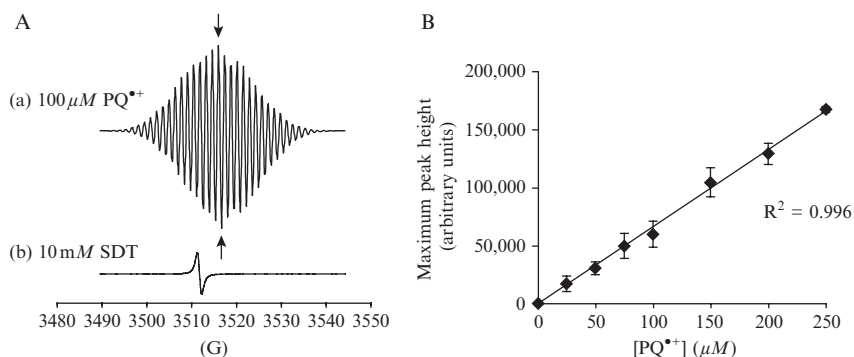


Figure 22.2 Detection and quantification of the $\text{PQ}^{\bullet+}$ radical by EPR spectroscopy. (A) Typical EPR spectrum of the $\text{PQ}^{\bullet+}$ radical (100 μM ; trace a) generated *in vitro* by reduction of PQ^{2+} with a two-fold excess of sodium dithionite. EPR signal of the $\text{SO}_2^{\bullet-}$ radical present in the dithionite solution (10 mM; trace b). (B) Standard curve for the quantification of $\text{PQ}^{\bullet+}$ by EPR on the basis of the height of the maximum peak (arrows in A), which gives a linear relationship for the range tested (0 to 250 μM). Data are the means \pm SD of three measurements.

^a General notes on the handling of PQ: PQ is highly toxic, and appropriate precautions should be taken during handling (consult the safety sheet provided by the manufacturer). PQ is readily soluble in aqueous solutions but is sparingly soluble in organic solvents. A stock at 1 M concentration is routinely prepared in either water or aqueous buffer and aliquots stored at -20° .

microwave power, 10 mW; modulation frequency, 100 kHz; modulation amplitude, 0.8 G; sweep time, 83.886 sec; time constant, 163.84 msec; receiver gain, 6.32×10^4 .

The height of the maximum (i.e., central) peak is proportional to the $\text{PQ}^{\bullet+}$ concentration (Fig. 22.2B). A standard curve can be prepared by generating the $\text{PQ}^{\bullet+}$ radical *in vitro* from known amounts of PQ^{2+} by reduction with freshly prepared sodium dithionite and is linear in the range tested (0 to 250 μM). The EPR signal of the $\text{SO}_2^{\bullet-}$ radical present in the dithionite solution overlaps with the $\text{PQ}^{\bullet+}$ radical spectrum (Fig. 22.2A, trace b). However, importantly this overlap does not affect the intensity of the central peak and, therefore, does not interfere with quantification of the $\text{PQ}^{\bullet+}$ radical.

2.2. Detection of the $\text{PQ}^{\bullet+}$ radical by spectrophotometry

The $\text{PQ}^{\bullet+}$ radical has a distinctive visible absorbance spectrum associated with a local maximum at 603 nm ($\epsilon_{603} = 13,600 \text{ M}^{-1} \cdot \text{cm}^{-1}$; Mayhew, 1978) (Fig. 22.3D). $\text{PQ}^{\bullet+}$ radical formation in anaerobic mitochondria can be followed by an increase in absorbance at 603 nm (Fig. 22.3A), and at sufficiently high concentrations, the blue color formation is strong enough to be detected by eye. For these experiments, mitochondria^b were added to buffer prepurged with either nitrogen or argon in a 3-ml quartz cuvette and supplemented with PQ and other compounds as required. The incubations were then repurged to render them fully anaerobic, and the cuvette was sealed with an airtight stopper. The absorbance was followed over ~ 10 min in a spectrophotometer (DW-2000 SLM-Aminco) with stirring and thermostated to the desired temperature.

Mitochondrial preparations are complex with considerable absorbance in the 500 to 700 nm range because of cytochromes and other chromophores that vary with mitochondrial state (in contrast, EPR detection is specific for $\text{PQ}^{\bullet+}$). To confirm that the increase in absorbance at 603 nm is due to the $\text{PQ}^{\bullet+}$ radical, we scan the absorbance of the sample in the range 500 to 700 nm under anaerobic conditions and again after exposure to O_2 by removing the cuvette stopper and introducing a brief pulse of compressed air (Fig. 22.3B). This exploits the fact that the $\text{PQ}^{\bullet+}$ radical is extremely sensitive to O_2 and will rapidly be converted back to PQ^{2+} . The difference spectrum $\pm \text{O}_2$ should eliminate any absorbance because of mitochondria and give a profile similar to that of the pure $\text{PQ}^{\bullet+}$ radical (Fig. 22.3C,D). Note that $\text{PQ}^{\bullet+}$ radical

^b General notes on mitochondria: Mitochondria from yeast (*Saccharomyces cerevisiae*) and rat heart were isolated by homogenization and differential centrifugation as described previously (Chappell and Hansford, 1972; Glick and Pon, 1995). Incubations with yeast mitochondria were performed in mannitol buffer (0.6 M mannitol, 10 mM TRIS maleate, 5 mM KPi , 0.5 mM EDTA; pH 6.8, KOH) at 30°. Rat heart mitochondria were incubated in KCl buffer (120 mM KCl, 10 mM HEPES, 1 mM EGTA; pH 7.2, KOH) at 37°.

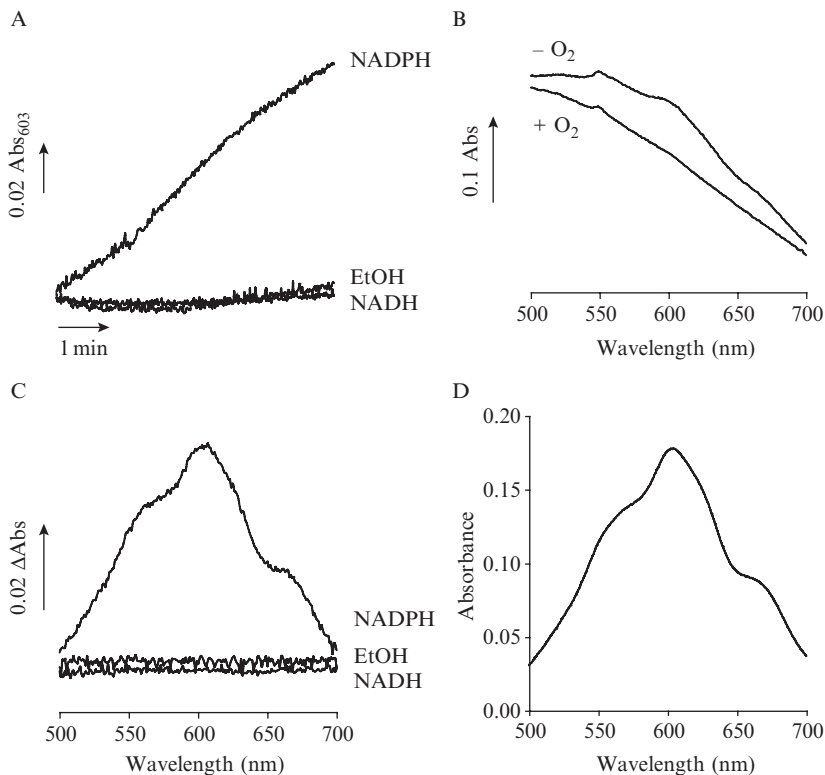


Figure 22.3 Spectrophotometric detection of $\text{PQ}^{\bullet+}$ radical formation by anaerobic yeast mitochondria. (A) Time course at 603 nm showing $\text{PQ}^{\bullet+}$ radical formation by anaerobic yeast mitochondria (0.4 mg protein/ml), incubated for 5 min at 30° in the presence of 1 mM PQ \pm ethanol (5 mM), NADH (1 mM), or NADPH (1 mM). (B) At the end of the incubation, samples were subjected to absorbance scans (500 to 700 nm), first while still under anaerobic conditions and then after exposure to air. The traces shown are for the incubation with NADPH. (C) Difference spectra \pm O_2 to diagnose $\text{PQ}^{\bullet+}$ radical formation. (D) Typical absorbance spectrum of the $\text{PQ}^{\bullet+}$ radical generated *in vitro* by reduction of PQ^{2+} with excess sodium dithionite.

formation in aerobic mitochondria is essentially impossible to detect because of its rapid disappearance in the presence of O_2 .

3. DETECTION OF PQ

3.1. Radioactive [^{14}C]-PQ

Radiolabeled [^{14}C]-PQ is commercially available (e.g., American Radio-labeled Chemicals, Inc. (St Louis, MO, USA); specific activity 55 mCi/mmol, 0.1 mCi/ml) and can be measured by scintillation counting (see section 5.3).

3.2. Detection of PQ indirectly by EPR

Besides the use of EPR to quantify the $\text{PQ}^{\bullet+}$ radical directly, the concentration of PQ in a sample can be measured indirectly by converting all the PQ^{2+} present to $\text{PQ}^{\bullet+}$ (see section 5.2). As previously mentioned, the $\text{PQ}^{\bullet+}$ radical can be generated *in vitro* from PQ^{2+} by reduction with excess sodium dithionite. Anaerobic conditions must first be established by purging samples with nitrogen or argon.

3.3. Construction of a PQ-selective electrode

PQ-selective electrodes were constructed and used as described for electrodes selective for related aromatic cations (Davey *et al.*, 1992; Kamo *et al.*, 1979), except that the plasticizer dioctyl phthalate was replaced by 2-fluoro-2'-nitrodiphenyl ether (Watanabe *et al.*, 1992), which greatly improved membrane selectivity for PQ. Similar ion-selective electrodes are routinely used to measure the concentration of lipophilic cations in real time in mitochondrial incubations to measure the mitochondrial membrane potential (Brand, 1995) or to follow the membrane potential-dependent uptake of lipophilic cations into mitochondria (Murphy and Smith, 2007).

To prepare the ion-exchange membrane, mix in a glass test tube or small (~5 ml) beaker 1 ml of 5% [w/v] polyvinyl chloride (PVC) dissolved in tetrahydrofuran, 300 μl of 10 mM tetraphenylborate in tetrahydrofuran, and 150 μl of 2-fluoro-2'-nitrodiphenyl ether. Pour the solution into a small glass container with a flat base (such as a 35-mm Petri dish or a 25-ml beaker) and evaporate overnight at room temperature to give a uniform clear, rubbery membrane ~0.2- to 0.5-mm thick. To assemble the electrodes, cut the membrane into ~1-cm squares with a scalpel and glue to the end of thin-walled PVC tubing (4-mm diameter, used for electrical shielding; e.g., part number 404-174 from RS Components Ltd., UK) cut to ~5- to 7-cm pieces. To do this, dip one end of the tubing in tetrahydrofuran (~1-mm deep) to create an adhesive surface, and fix the membrane in place gently with tweezers. After drying (typically overnight), check that the seal is airtight by lightly applying pressure to the open end of the tubing with a fingertip and observing a slight bulging of the membrane at the other end. Then carefully trim any residual membrane with a razor blade or fine scissors. Electrodes were characterized for PQ by filling and soaking in a 10 mM aqueous PQ solution overnight (or use 10 mM MPP⁺ in the case of an MPP⁺-selective electrode). When filling the electrode sleeves, it is important to avoid introducing air bubbles into the tubing and to make sure that the filling solution is in contact with the ion-selective membrane.

To set up the PQ-electrode, insert a 0.38-mm diameter platinum wire soldered to a shielded coaxial cable into the internal solution of the electrode sleeve and seal with Parafilm. The PQ-electrode and a reference Ag/AgCl

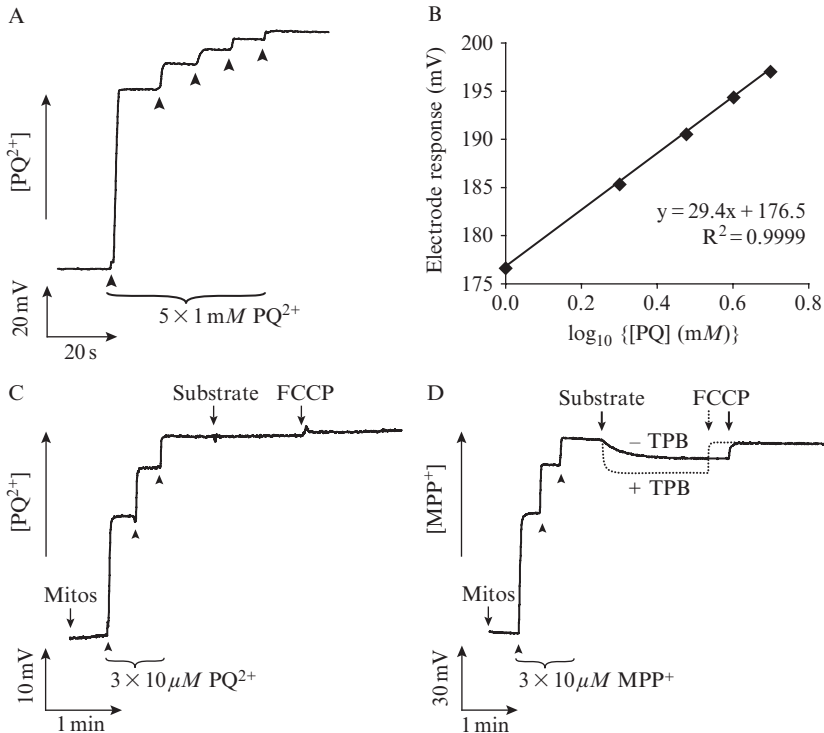


Figure 22.4 Detection of PQ with an ion-selective electrode. (A) Standard curve showing the typical response of a PQ-electrode at 30° to five sequential additions of 1 mM PQ^{2+} (arrowheads). (B) Calibration curve from the previous trace plotted as the electrode response (mV) against the \log_{10} of PQ^{2+} concentration (mM). The slope of the linear trendline is $\sim 30 \text{ mV/decade}$, consistent with the Nernst equation for a dication species at 30° . (C) Using a PQ-electrode to show the lack of bulk PQ^{2+} uptake by isolated mitochondria. The PQ-electrode was calibrated with three successive additions of $10 \mu\text{M PQ}^{2+}$ (arrowheads). Wild-type yeast mitochondria ($0.4 \text{ mg protein/ml}$) were incubated in mannitol buffer, energized with respiratory substrate (5 mM ethanol), and then uncoupled with FCCP ($1 \mu\text{M}$). The presence of TPB^- had no effect (data not shown). (D) Positive control showing membrane potential-dependent uptake of the structurally similar compound MPP^+ by yeast mitochondria. Conditions were as for C, except with an MPP^+ -electrode. The presence of TPB^- ($5 \mu\text{M}$; dashed line) both accelerates and increases the extent of MPP^+ uptake, which is consistent with direct passage of MPP^+ across the mitochondrial inner membrane.

electrode (World Precision Instruments) were connected to a Powerlab data acquisition system by means of a front-end pH amplifier, and the output was recorded with Chart software (all from AD Instruments, Australia). Both the reference and PQ electrodes were inserted into a stirred thermostated buffer solution and the output measured in real time (Fig. 22.4A). The PQ-electrode response was linear with the $\log_{10}[\text{PQ}^{2+}]$ in the range tested

(1 to 5 mM) (Fig. 22.4B). The slope per decade should be ~ 30 mV (at 30°) as predicted by the Nernst equation for a dication species. Note that for ion-selective electrodes against MPP^+ or other monocations, the slope per decade is ~ 60 mV (at 30°).

4. ASSAYS FOR PQ-ASSOCIATED SUPEROXIDE ($\text{O}_2^{\bullet-}$) PRODUCTION

Methods are described here to measure $\text{O}_2^{\bullet-}$ production induced by PQ in isolated intact mitochondria (from yeast and mammals) and mitochondrial membranes generated therefrom. As with all assays for reactive oxygen species, these methods are prone to subtle artefacts; therefore, it is strongly recommended that several orthogonal techniques be applied in parallel before definitively inferring $\text{O}_2^{\bullet-}$ production. For instance, we have compared the results for the aconitase inactivation assay with that of the coelenterazine (CLZ) assay in yeast mitochondria (Fig. 22.5A,B), and the data from the Amplex Red assay and the aconitase inactivation assay for rat heart mitochondria (Fig. 22.6C,D).

4.1. Aconitase inactivation

The enzyme aconitase contains an iron-sulfur cluster at its active site, which is highly sensitive to inactivation by $\text{O}_2^{\bullet-}$ (Gardner, 2002). Levels of $\text{O}_2^{\bullet-}$ production can, therefore, be inferred from the rate of aconitase inactivation during mitochondrial incubations. This assay has several advantages—first, aconitase is an endogenous enzyme and, therefore, there is no requirement to add any exogenous probes; second, mitochondrial aconitase is located in the matrix and, therefore, reports specifically on matrix $\text{O}_2^{\bullet-}$.

Aconitase activity is measured spectrophotometrically by a coupled enzyme assay, linking isocitrate production by aconitase to NADPH formation by isocitrate dehydrogenase (Gardner, 2002). To perform time courses, mitochondria (supplemented with PQ, substrate, uncoupler, or other compounds as required) were incubated in a shaking waterbath at a volume of 0.5 to 1 ml in 15-ml tubes under the appropriate conditions (0.3 mg protein/ml in mannitol buffer at 30° for yeast mitochondria or 2 mg protein/ml in KCl buffer supplemented with 0.1% (w/v) BSA at 37° for rat heart mitochondria). Take an aliquot (typically ~ 50 to $75 \mu\text{l}$) at $t = 0$ to give the initial level of aconitase activity and snap freeze in a 0.5-ml tube on dry ice (we use a prechilled aluminium block with a metal surface complementary to the tubes to give good thermal contact and to ensure rapid freezing). Continue taking aliquots at subsequent time points during the incubation, typically at 1- to 5-min intervals, depending on whether the anticipated rate of inactivation is

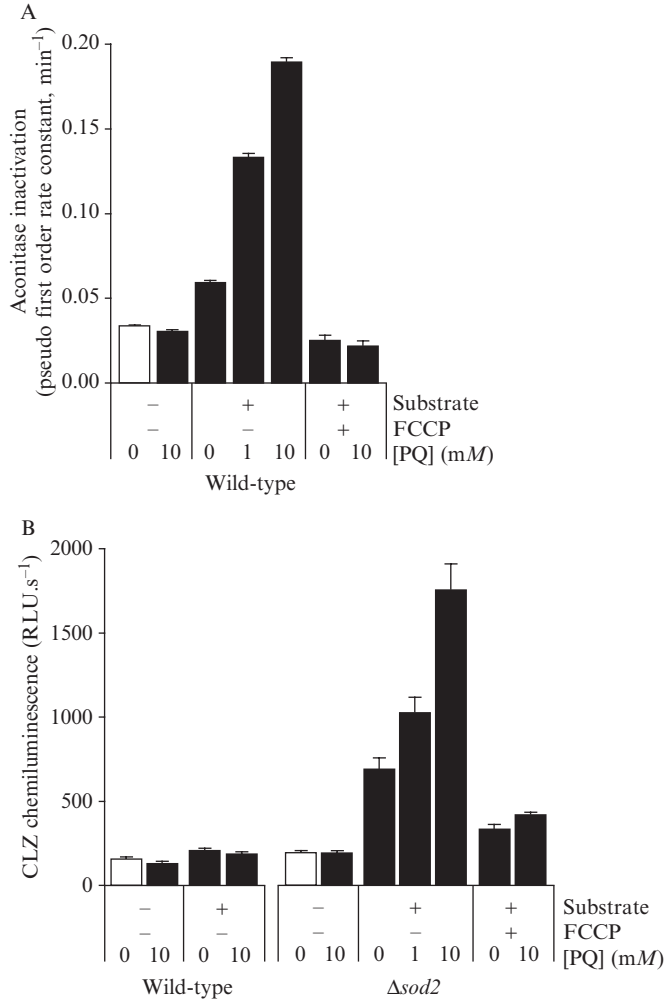


Figure 22.5 Production of $O_2^{\cdot -}$ by PQ in yeast mitochondria—effect of respiratory substrate and uncoupler. (A) Example data for $O_2^{\cdot -}$ production inferred from the aconitase inactivation assay. Wild-type mitochondria (0.3 mg protein/ml) were energized with substrate (5 mM ethanol), treated with PQ (1 or 10 mM) and uncoupled with FCCP (1 μM) as indicated, and incubated at 30°. (B) Example data for $O_2^{\cdot -}$ production measured by the coelenterazine (CLZ) chemiluminescence assay in either wild-type or $\Delta sod2$ mitochondria (50 μg protein/ml). Data are the means \pm SD of four determinations.

high or low, until all the desired time points have been collected. At this stage, the samples can be stored on dry ice or at -80° while incubations under other conditions are performed. However, aconitase is extremely susceptible to inactivation, and, therefore, it is important to only thaw the samples

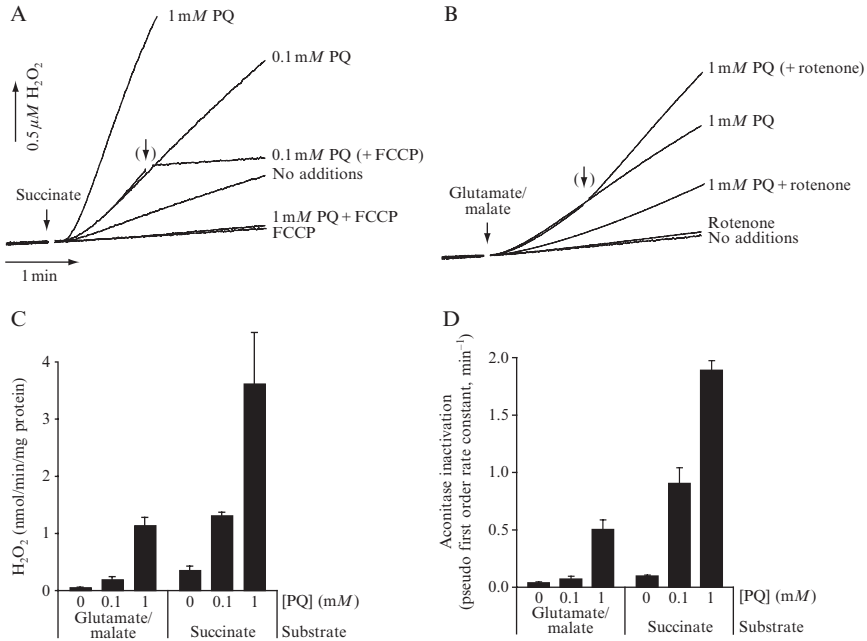


Figure 22.6 Production of H₂O₂ and O₂⁻ by PQ in mammalian mitochondria—effect of respiratory substrate, uncoupler, and respiratory inhibitors. (A to B) Example traces from the Amplex Red assay. Rat heart mitochondria (0.2 mg protein/ml) were incubated at 37° in KCl buffer supplemented with 0.01% [w/v] BSA. Substrate (5 mM succinate or 5 mM glutamate/malate), PQ (0.1 or 1 mM), the uncoupler FCCP (1 μM), and the complex I inhibitor rotenone (4 μg/ml) were added as indicated. (C) Rates of H₂O₂ efflux determined from the above traces. Data are the means ± SD of three-four determinations. (D) O₂⁻ production in rat heart mitochondria determined by the aconitase inactivation assay. Heart mitochondria (2 mg protein/ml) were incubated for 10 min at 37° in KCl buffer supplemented with 0.1% [w/v] BSA. Substrate (5 mM succinate or 5 mM glutamate/malate) and PQ (0.1 or 1 mM) were present as indicated. Data are the means ± SD of three determinations.

immediately before assaying, to work rapidly during the actual assaying process, and to treat all samples identically.

For the inactivation assay, we typically process half a 96-well plate at a time, sufficient for a single condition (i.e., the sequence of ~5 to 8 time points from an incubation). Rapidly thaw the frozen aliquots at 30° and dispense 10-μl volumes of each time point (in 4 to 6 replicates) into a 96-well plate. Then overlay with 190 μl of aconitase assay buffer (50 mM TRIS-HCl [pH 7.4], 0.6 mM MnCl₂, 5 mM sodium citrate, 0.2 mM NADP⁺, 0.4 units/ml isocitrate dehydrogenase, 0.1% [v/v] Triton X-100) preequilibrated to 30° with a multichannel pipette, taking care to avoid creating detergent bubbles during dispensing. Measure the increase in

absorbance at 340 nm in a microplate reader (e.g., SpectraMax Plus384, Molecular Devices) over 7 min with shaking and readings at 15-sec intervals.

To process the data, first plot the level of aconitase activity (A_{340}/min) against time for the duration of the time course. Convert the enzyme activity to a natural logarithm, which should give a straight line when plotted against time, because the inactivation is a pseudo-first order process, and fit with a linear trendline. The slope obtained corresponds to the rate constant of aconitase inactivation and is a measure of steady-state $\text{O}_2^{\bullet-}$ production (Fig. 22.5A).

As a control, exogenous SOD (~ 50 to 100 units/ml) can be added to the incubations to confirm that the $\text{O}_2^{\bullet-}$ production is occurring inside mitochondria (SOD is unable to cross the mitochondrial inner membrane and, therefore, should have no effect on the rate of aconitase inactivation in the matrix). Fluorocitrate ($100 \mu\text{M}$), a competitive inhibitor of aconitase, can be used to determine the background rate of NADPH formation. Note that fluorocitrate is highly toxic and, therefore, for practical reasons was not added routinely for the microplate assay, but we find that the background rate is typically $<10\%$ of the uninhibited rate. We have also performed Western blots to show that the amount of aconitase protein during the incubation is constant, and, therefore, loss of activity is due to enzyme inactivation rather than protein degradation.

4.2. Coelenterazine (CLZ) chemiluminescence

Coelenterazine (CLZ; 2-(*p*-hydroxybenzyl)-6-(*p*-hydroxyphenyl)-8-benzyl-imidazo[1,2-*a*]pyrazin-3-(7*H*)-one, available from Calbiochem) is a membrane-permeant probe, which emits light on reaction with $\text{O}_2^{\bullet-}$ (Lucas and Solano, 1992; Rees *et al.*, 1998). CLZ chemiluminescence can be measured in a luminometer (e.g., AutoLumatPlus LB 953, Berthold), and this method has been applied to assay $\text{O}_2^{\bullet-}$ production from whole isolated mitochondria (Cochemé and Murphy, 2008), mitochondrial membrane fractions (Cochemé and Murphy, 2008; Hurd *et al.*, 2008), and purified enzymes such as complex I (Dahm *et al.*, 2006; Esterhazy *et al.*, 2008).

We have found that the CLZ assay is not effective in the presence of endogenous MnSOD, because CLZ cannot compete for $\text{O}_2^{\bullet-}$ against MnSOD ($k \sim 10^5$ and $10^9 \text{ M}^{-1}\cdot\text{s}^{-1}$ respectively) (Fridovich, 1989; Rees *et al.*, 1998), and, therefore, CLZ is unable to detect matrix $\text{O}_2^{\bullet-}$ production in intact wild-type mitochondria (Fig. 22.5B; Cochemé and Murphy, 2008). However, the CLZ assay can be used reliably in the absence of endogenous MnSOD, for instance in MnSOD-deficient whole mitochondria (e.g., isolated from a Δsod2 yeast mutant strain; Fig. 22.5B), in purified mitochondrial membranes (where the matrix fraction, containing MnSOD, has been removed), and in isolated enzyme preparations.

Resuspend the sample to be assayed in 1 ml of the appropriate buffer, preequilibrated to the desired temperature in a tube suitable for the luminometer. Add substrate, PQ, and any other compounds as required, then mix by gently flicking the base of the tube. Finally add 2 μM CLZ (from a 1 mM stock in MeOH), mix briefly again, and follow the chemiluminescence over the next 5 min starting immediately. We assay chemiluminescence in batches of three samples, measuring the cumulative chemiluminescence over 5 sec every 30 sec. Readings are typically stable during the 5-min period and, therefore, representative of steady state $\text{O}_2^{\bullet-}$ production. Results were averaged and expressed as relative light units (RLU)/sec. Note that BSA, used as a supplement in certain buffers and preparations, interferes with the assay by causing an artefactual increase in CLZ chemiluminescence and should, therefore, be avoided.

Diphenyleneiodonium (DPI) is a flavoprotein inhibitor that is a useful tool for studying PQ metabolism, because most biologic systems capable of catalyzing $\text{PQ}^{\bullet+}$ formation are flavoenzymes. DPI can be used with isolated enzymes and mitochondrial membranes (Cochemé and Murphy, 2008), although the interaction of DPI with whole mitochondria is more complicated (Lambert *et al.*, 2008).

4.3. Amplex Red fluorescence

Mitochondrial $\text{O}_2^{\bullet-}$ generation can also be inferred indirectly by assaying its dismutation product H_2O_2 as it effluxes from mitochondria with the probe Amplex Red (Molecular Probes). H_2O_2 efflux from mitochondria was assayed in a 3-ml quartz cuvette with a fluorimeter (Shimadzu RF-5301). Mitochondria were incubated in a stirred 2.5 ml volume at the desired temperature with 5 units/ml horseradish peroxidase and 50 μM Amplex Red. Results were calibrated against a standard curve with known amounts of H_2O_2 .

A significant advantage of this method is that H_2O_2 levels are followed in real time, and it is simple to make additions (e.g., of a respiratory inhibitor or uncoupler) midway through the incubation (Fig. 22.6A,B). This technique was particularly useful for distinguishing the requirement of a membrane potential for both the uptake of PQ into mitochondria and its redox cycling at complex I once inside the matrix. For instance, note how the presence of rotenone at the start of the incubation prevents $\text{O}_2^{\bullet-}$ generation by PQ in mitochondria respiring on glutamate/malate, whereas addition of rotenone midway through actually enhances the rate (Fig. 22.6B). We explain this by the fact that a membrane potential is initially required for PQ uptake into mitochondria—hence, addition of a respiratory inhibitor from the start blocks PQ-induced $\text{O}_2^{\bullet-}$ production. By adding rotenone midway through the incubation, a proportion of PQ is first allowed to accumulate into the matrix, and subsequent inhibition of complex I by rotenone results in

increased $\text{PQ}^{\bullet+}$ formation from the reduced FMN cofactor. By contrast, in mitochondria respiring on succinate, the uncoupler FCCP inhibits PQ-induced $\text{O}_2^{\bullet-}$ production equally when added either at the start or midway through the incubation (Fig. 22.6A). In this case, uncoupling prevents the membrane potential–dependent uptake of PQ into mitochondria and also reverse electron transport into complex I, which is the source of electrons for $\text{PQ}^{\bullet+}$ radical formation.

5. UPTAKE OF PQ INTO MITOCHONDRIA

PQ uptake by mitochondria can be investigated with an ion-selective electrode specific for PQ or by quantifying the amount of PQ in the mitochondrial pellet after an incubation (either by use of radiolabeled PQ, or by assaying PQ with the EPR technique after *in vitro* conversion to $\text{PQ}^{\bullet+}$).

5.1. Measurement of PQ uptake with an ion-selective electrode

An ion-selective electrode (see section 3.3) works by measuring the effective concentration of the target compound in the incubation medium. A decrease in signal corresponds to uptake of the compound into an internal compartment, in this case mitochondria, as the compound “disappears” from the external buffer.

Incubations were performed in a 3-ml chamber, with stirring, and thermostated to the desired temperature. Resuspend the mitochondria (0.5 to 2 mg protein/ml) in a 3-ml volume and allow the ion-selective electrode to equilibrate and stabilize. Then calibrate the electrode response with consecutive additions of PQ. The response of the electrode to PQ is typically logarithmic, and the signal should be stable after each incremental PQ addition. A respiratory substrate such as succinate can then be added to initiate respiration and to generate a mitochondrial membrane potential. The occurrence of membrane potential–dependent uptake is manifested as a decrease in the concentration of PQ. To confirm that uptake is due to the membrane potential, then add uncoupler (e.g., FCCP) to abolish the membrane potential. If the compound is released from inside the mitochondria, the PQ concentration measured by the electrode should increase back to the original baseline. Tetraphenylborate (TPB^-) lowers the activation energy barrier for passage of lipophilic cations across the lipid bilayer and, therefore, can be used to increase the uptake rate of cations across the mitochondrial membrane (Fig. 22.4D).

With an ion-selective electrode, we recently showed that there is no bulk uptake of PQ into mitochondria by direct passage across the mitochondrial inner membrane driven by the membrane potential, unlike the structurally similar compound MPP^+ (Cochemé and Murphy, 2008, Fig. 22.4C,D). The reason for this marked difference is likely to be the double charge on PQ^{2+} relative to MPP^+ , which will cause a four-fold increase in the Born energy for its movement across the membrane, and thereby result in a far larger activation energy for the movement of PQ^{2+} through biological membranes relative to MPP^+ (Ross *et al.*, 2005).

An interesting point that remains to be addressed is the putative uptake of the $PQ^{\bullet+}$ radical across the mitochondrial inner membrane. Because the $PQ^{\bullet+}$ radical has a single positive charge, it is theoretically possible that it could be accumulated inside mitochondria in an analogous manner to MPP^+ . Because the electrode also recognizes $PQ^{\bullet+}$, as well as PQ^{2+} (although the response is quantitatively different because of the charge differences between the species), the ion-selective electrode system described could, in principle, be used to test the direct uptake of the $PQ^{\bullet+}$ radical into mitochondria. However, this hypothesis is technically challenging to investigate because of the extreme instability of the $PQ^{\bullet+}$ radical under aerobic conditions and the difficulty of maintaining strictly anaerobic conditions with an ion-selective electrode system. Furthermore, because the amount of $PQ^{\bullet+}$ present under aerobic conditions is expected to be negligible, this uptake mechanism of PQ as the monocation radical may not be physiologically relevant.

5.2. Measurement of PQ uptake by EPR

Isolated mitochondria (~ 1 mg protein/ml) were incubated in a 1.5-ml tube with PQ, respiratory substrate, and uncoupler as required, for the desired time (typically 0 to 15 min) and at the appropriate temperature. At this point the mitochondria were isolated by centrifugation (2 min at 16,000g) and the supernatant removed by rapid aspiration without disturbing the pellet. The tube is subjected to a pulse spin to collect any residual supernatant, and the fine tip of a rolled-up tissue paper can then be used to absorb any final droplets. It is critical to remove all the supernatant, so that the measurement of PQ present in the pellet is not overestimated. Resuspend the pellet in 1 ml PBS and vortex vigorously to disrupt the mitochondria and release any PQ. Transfer the entire suspension to a glass test tube and purge with argon or nitrogen to render it anaerobic. Because overpurging can potentially lead to evaporation of the sample, thereby modifying the final concentration, it is important that the timing of the purging procedure is identical for all the samples. While continuing to gently purge the sample, excess sodium dithionite ($10 \mu\text{l}$ of a 1 M solution freshly prepared in PBS) is added, and the suspension will turn blue as any PQ^{2+} is converted to $PQ^{\bullet+}$. The flow of

gas should ensure adequate mixing of the sample. While still under anaerobic conditions, transfer the suspension from the test tube to the EPR cell with a syringe. The intensity of the $\text{PQ}^{\bullet+}$ signal is measured by EPR (section 2.1), and the original PQ concentration is calculated by comparison against a standard curve (0 to 250 μM ; Fig. 22.2B).

Note that even under conditions in which no uptake by isolated mitochondria occurs (e.g., in the absence of a membrane potential, either because of the presence of uncoupler or lack of respiratory substrate), some PQ will be present in the extramitochondrial spaces of the pellet. It is, therefore, important to prepare controls with mitochondria and PQ alone to account for this baseline level of PQ, where PQ is added immediately before pelleting the mitochondria. Any increase in the pellet concentration of PQ above this baseline level corresponds to mitochondrial uptake (Fig. 22.7A). The effective concentration of PQ in the matrix can then be estimated from the mitochondrial matrix volume (see section 5.3), and the membrane potential dependence of uptake can be verified by parallel incubations in the presence of uncoupler (e.g., FCCP).

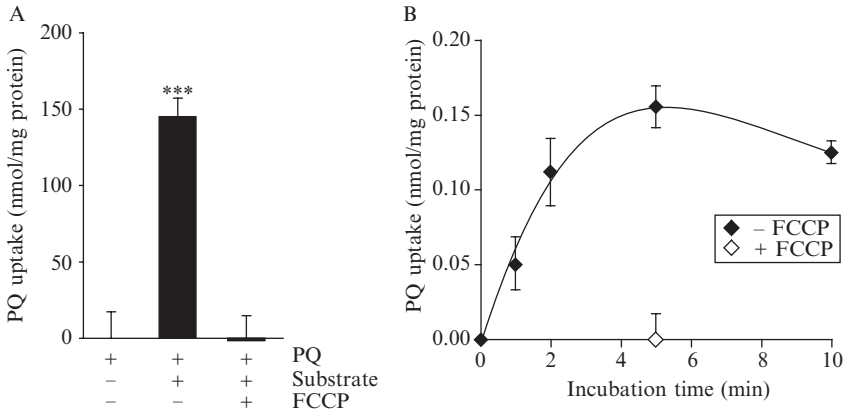


Figure 22.7 PQ Uptake into yeast and mammalian mitochondria. (A) Uptake of PQ by yeast mitochondria, obtained by endpoint measurements with the EPR quantification method. Wild-type yeast mitochondria (0.4 mg protein/ml) were incubated for 10 min at 30° in the presence of 10 mM PQ \pm substrate (5 mM ethanol) \pm 1 μM FCCP. Data were corrected for the $t = 0$ control and are the means \pm SD of four determinations. Statistical significance was calculated with a Student's two-tailed t test. ***, $P < 0.001$. (B) Time course of PQ uptake by mammalian mitochondria, measured by scintillation counting of [^{14}C]-PQ. Rat heart mitochondria (1 mg protein/ml) in KCl buffer + 0.01% [w/v] BSA were energized with 5 mM glutamate/malate and incubated in the presence of 0.1 mM PQ for 0 to 10 min at 37°. To test the membrane potential-dependence of PQ uptake, controls were performed in the presence of 1 μM FCCP. Data were corrected for the $t = 0$ control and are the means \pm range of duplicate determinations.

5.3. Measurement of PQ uptake from the distribution of radiolabeled [^{14}C]-PQ

Alternately, uptake of PQ by mitochondria can be measured with radiolabeled [^{14}C]-PQ (Fig. 22.7B). Incubations are performed as for the EPR method, except that the PQ added is spiked with 100 nCi/ml [^{14}C]-PQ. After incubation, the mitochondrial pellet is isolated by centrifugation as before and after drying with a tissue the pellet is resuspended in 40 μl of 20% [v/v] Triton X-100. The base of the tube containing the resuspended pellet is then cut with clippers into a scintillation vial, which is then filled with 3 ml of scintillant (Fluoran-Safe 2, BDH) and counted in a liquid scintillation analyser (Tri-Carb 2800TR, Perkin Elmer), with appropriate quench corrections. A control in which the PQ is added to unenergized mitochondria just before centrifugation should be performed to calculate the amount of radioactivity associated nonspecifically with the pellet.

An important caveat to measuring the membrane potential-driven uptake of PQ is that at high concentrations it tends to disrupt mitochondria, lowering the membrane potential, and thereby decreasing the driving force for uptake. Therefore, it is important to ensure that a decrease in PQ uptake is not the result of a decrease in membrane potential. A significant advantage of the radioactive method is the possibility of measuring the mitochondrial membrane potential and PQ uptake simultaneously by dual isotope counting ($[^3\text{H}]$ and [^{14}C]) in the same mitochondrial incubation.

The mitochondrial membrane potential is measured from the uptake of [^3H]-methyl triphenylphosphonium (TPMP $^+$; from American Radiolabeled Chemicals, Inc. (St Louis, MO, USA); specific activity 60 Ci/mmol, 1 mCi/ml) (Brand, 1995). The previous mitochondrial incubations containing [^{14}C]-PQ were supplemented with 1 μM TPMP $^+$ spiked with 25 nCi/ml [^3H]-TPMP $^+$. After pelleting the mitochondria, remove an aliquot of the supernatant (400 μl) to a scintillation vial and resuspend the pellet as earlier. A parallel control incubation in the presence of uncoupler (1 μM FCCP) gives the amount of TPMP $^+$ nonspecifically associated with the mitochondrial pellet. The membrane potential value ($\Delta\Psi_{\text{m}}$) is derived from the Nernst equation (Brand, 1995) on the basis of the ratio of TPMP $^+$ in the pellet and the supernatant:

$$\Delta\Psi_{\text{m}}(\text{at } 30^\circ) = 60.1 \log_{10}([\text{TPMP}]_{\text{pellet}}/[\text{TPMP}]_{\text{supernatant}})$$

$$\Delta\Psi_{\text{m}}(\text{at } 37^\circ) = 61.5 \log_{10}([\text{TPMP}]_{\text{pellet}}/[\text{TPMP}]_{\text{supernatant}})$$

$$\text{where } [\text{TPMP}]_{\text{pellet}} = 0.4^c \times (\text{dpm}_{\text{pellet}(-\text{FCCP})} - \text{dpm}_{\text{pellet}(+\text{FCCP})}) / V_{\text{matrix}}^d$$

$$[\text{TPMP}]_{\text{supernatant}} = \text{dpm}_{\text{supernatant}} / V_{\text{supernatant}}$$

Dual isotope scintillation counting of [¹⁴C]-PQ and [³H]-TPMP was used to test putative competitive inhibitors of PQ uptake into mitochondria, controlling for any effects of membrane potential (Cochemé and Murphy, 2008).

6. PQ TOXICITY SCREENS IN YEAST DELETION LIBRARIES

Another approach to investigate the mechanism of PQ toxicity to mitochondria is to measure the effect of PQ on growth of various yeast mutants from a gene deletion library. This method can be used to identify strains that are sensitive or resistant to PQ, and knowledge of the gene deletion involved allows us to infer how PQ is disrupting the cells. We used this approach to test the hypothesis that PQ was being accumulated into mitochondria by a member of the mitochondrial carrier family, thus deletion of the putative PQ carrier would render the deleted strain relatively less sensitive to PQ.

For screening small numbers of mutants, growth assays in liquid culture were set up of yeast from the *S. cerevisiae* deletion library (Open Biosystems). Typically, 10-ml cultures containing a range of PQ concentrations (0.01 to 10 mM) were inoculated at an initial density of $A_{600} \sim 0.1$, incubated at 30° with shaking at 250 rpm, and the A_{600} measured after 24 to 48 h (Fig. 22.8A). Yeast were cultured either in the fermentable glucose medium YPD (1% [w/v] yeast extract, 2% [w/v] peptone, 2% [w/v] glucose), or with the nonfermentable glycerol medium YPG (1% [w/v] yeast extract, 2% [w/v] peptone, 3% [v/v] glycerol).

For larger scale screens, a solid phase method was developed to facilitate higher throughput. Yeast medium containing a concentration gradient of PQ was prepared in 10-cm-square Petri dishes (Sarstedt). A slant of YPG + 1 mM PQ was first poured by placing the Petri dish at an angle. Once this layer had set, the plate was then returned to a horizontal position and covered with standard YPG to form a flat surface containing a gradient of PQ. Yeast suspensions were then spotted (~30,000 cells) in rows along the PQ concentration gradient (0 to 1 mM), and incubated for 1 wk at 30°. Growth was compared against a wild-type control on each plate

^c 0.4 is a correction factor to account for 60% of TPMP⁺ assumed to be membrane-bound (Brand, 1995).

^d The matrix volume of yeast mitochondria was assumed to be 1.8 μl/mg protein (Esteves *et al.*, 2004) and that of rat heart mitochondria 0.5 μl/mg protein (Halestrap and Quinlan, 1983).

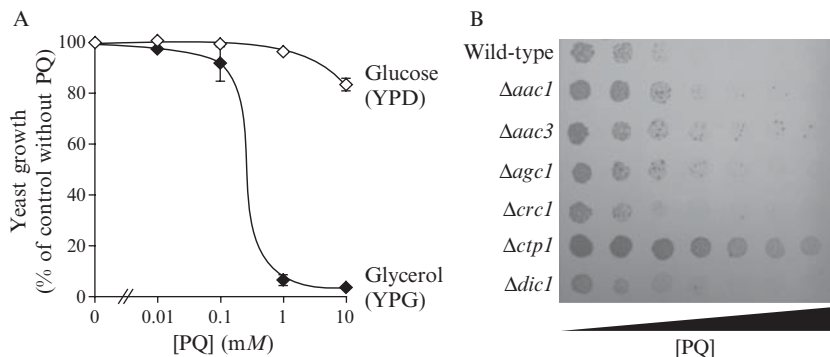


Figure 22.8 Effect of PQ on yeast cultures. (A) Wild-type yeast are more sensitive to PQ during respiratory metabolism, rather than fermentation. Wild-type yeast were cultured in either YPD (glucose) or YPG (glycerol) medium, with a range of PQ concentrations (0.01 to 10 mM). The initial cell density was adjusted to $A_{600} \sim 0.1$, and growth was measured spectrophotometrically after 48 h. Data are expressed as a percentage of the appropriate controls without PQ and are the means \pm range of two independent experiments. (B) Screening for PQ resistance in mitochondrial carrier mutants from a yeast deletion library. Wild-type and mutant strains were spotted in rows onto YPG agar containing a 0 to 1 mM PQ gradient. Photograph of a typical plate after incubation at 30° for 7 days.

(Fig. 22.8B). This screening method is a useful procedure for testing the impact of various gene products on PQ toxicity.

7. CONCLUSIONS

PQ is extensively used as a redox cycling agent to induce oxidative stress in a wide range of experimental systems, from isolated organelles to whole organisms, as well as a tool to induce complex I damage in models of neurodegenerative disease. Although the mechanisms by which PQ interacts with the cell remain to be fully clarified, PQ is known to cause mitochondrial oxidative damage, and complex I of the mammalian respiratory chain has been identified as the major site of $O_2^{\bullet -}$ production by PQ (Cochemé and Murphy, 2008). The methods described in this chapter will be useful to further investigate the interaction of PQ with mitochondria and also provide practical information for the general use of PQ as an experimental tool to generate $O_2^{\bullet -}$ in other systems.

ACKNOWLEDGMENTS

This work was supported by the Medical Research Council (UK) and Research into Ageing (UK). We thank Angela Logan and Thomas Hurd for their helpful comments.

REFERENCES

- Bonila, E., Medina-Leendertz, S., Villalobos, V., Molero, L., and Bohorquez, A. (2006). Paraquat-induced oxidative stress in *Drosophila melanogaster*: Effects of melatonin, glutathione, serotonin, minocycline, lipoic acid and ascorbic acid. *Neurochem. Res.* **31**, 1425–1432.
- Brand, M. D. (1995). Measurement of mitochondrial protonmotive force. In “Bioenergetics—A Practical Approach.” (G. C. Brown, and C. E. Cooper, eds.), pp. 39–62. IRL Press, Oxford.
- Chappell, J. B., and Hansford, R. G. (1972). Preparation of mitochondria from animal tissues and yeast. In “Subcellular Components: Preparation and Fractionation.” (G. D. Birnie, ed.), pp. 77–91. Butterworths, London.
- Cochemé, H. M., and Murphy, M. P. (2008). Complex I is the major site of mitochondrial superoxide production by paraquat. *J. Biol. Chem.* **283**, 1786–1798.
- Dahm, C. C., Moore, K., and Murphy, M. P. (2006). Persistent S-nitrosation of complex I and other mitochondrial membrane proteins by S-nitrosothiols but not nitric oxide or peroxynitrite: Implications for the interaction of nitric oxide with mitochondria. *J. Biol. Chem.* **281**, 10056–10065.
- Davey, G. P., Tipton, K. F., and Murphy, M. P. (1992). Uptake and accumulation of 1-methyl-4-phenylpyridinium by rat liver mitochondria measured using an ion-selective electrode. *Biochem. J.* **288**, 439–443.
- Day, B. J., Shawen, S., Liochev, S. I., and Crapo, J. D. (1995). A metalloporphyrin superoxide dismutase mimetic protects against paraquat-induced endothelial cell injury, *in vitro*. *J. Pharmacol. Exp. Ther.* **275**, 1227–1232.
- Dinis-Oliveira, R. J., Remiao, F., Carmo, H., Duarte, J. A., Navarro, A. S., Bastos, M. L., and Carvalho, F. (2006). Paraquat exposure as an etiological factor of Parkinson’s disease. *Neurotoxicology* **27**, 1110–1122.
- Esterhazy, D., King, M. S., Yakovlev, G., and Hirst, J. (2008). Production of reactive oxygen species by complex I (NADH: Ubiquinone oxidoreductase) from *Escherichia coli* and comparison to the enzyme from mitochondria. *Biochemistry* **47**, 3964–3971.
- Esteves, T. C., Echtay, K. S., Jonassen, T., Clarke, C. F., and Brand, M. D. (2004). Ubiquinone is not required for proton conductance by uncoupling protein 1 in yeast mitochondria. *Biochem. J.* **379**, 309–315.
- Fridovich, I. (1989). Superoxide dismutases. An adaptation to a paramagnetic gas. *J. Biol. Chem.* **264**, 7761–7764.
- Fukushima, T., Yamada, K., Isobe, A., Shiwaku, K., and Yamane, Y. (1993). Mechanism of cytotoxicity of paraquat. I. NADH oxidation and paraquat radical formation via complex I. *Exp. Toxicol. Pathol.* **45**, 345–349.
- Gardner, P. R. (2002). Aconitase: Sensitive target and measure of superoxide. *Methods Enzymol.* **349**, 9–23.
- Glick, B. S., and Pon, L. A. (1995). Isolation of highly purified mitochondria from *Saccharomyces cerevisiae*. *Methods Enzymol.* **260**, 213–223.
- Halestrap, A. P., and Quinlan, P. T. (1983). The intramitochondrial volume measured using sucrose as an extramitochondrial marker overestimates the true matrix volume determined with mannitol. *Biochem. J.* **214**, 387–393.

- Hassan, H. M. (1984). Exacerbation of superoxide radical formation by paraquat. *Methods Enzymol.* **105**, 523–532.
- Hirai, K., Ikeda, K., and Wang, G. Y. (1992). Paraquat damage of rat liver mitochondria by superoxide production depends on extramitochondrial NADH. *Toxicology* **72**, 1–16.
- Hurd, T. R., Requejo, R., Filipovska, A., Brown, S., Prime, T. A., Robinson, A. J., Fearnley, I. M., and Murphy, M. P. (2008). Complex I within oxidatively stressed bovine heart mitochondria is glutathionylated on Cys-531 and Cys-704 of the 75-kDa subunit: potential role of CYS residues in decreasing oxidative damage. *J. Biol. Chem.* **283**, 24801–24815.
- Kamo, N., Muratsugu, M., Hongoh, R., and Kobatake, Y. (1979). Membrane potential of mitochondria measured with an electrode sensitive to tetraphenyl phosphonium and relationship between proton electrochemical potential and phosphorylation potential in steady state. *J. Membr. Biol.* **49**, 105–121.
- Kirby, K., Hu, J., Hilliker, A. J., and Phillips, J. P. (2002). RNA interference-mediated silencing of Sod2 in *Drosophila* leads to early adult-onset mortality and elevated endogenous oxidative stress. *Proc. Natl. Acad. Sci. USA* **99**, 16162–16167.
- Krall, J., Bagley, A. C., Mullenbach, G. T., Hallelwell, R. A., and Lynch, R. E. (1988). Superoxide mediates the toxicity of paraquat for cultured mammalian cells. *J. Biol. Chem.* **263**, 1910–1914.
- Lambert, A. J., Buckingham, J. A., Boysen, H. M., and Brand, M. D. (2008). Diphenyleneiodonium acutely inhibits reactive oxygen species production by mitochondrial complex I during reverse, but not forward electron transport. *Biochim. Biophys. Acta* **1777**, 397–403.
- Lucas, M., and Solano, F. (1992). Coelenterazine is a superoxide anion-sensitive chemiluminescent probe: Its usefulness in the assay of respiratory burst in neutrophils. *Anal. Biochem.* **206**, 273–277.
- Manning-Bog, A. B., McCormack, A. L., Li, J., Uversky, V. N., Fink, A. L., and Di Monte, D. A. (2002). The herbicide paraquat causes up-regulation and aggregation of α -synuclein in mice: paraquat and α -synuclein. *J. Biol. Chem.* **277**, 1641–1644.
- Mayhew, S. G. (1978). The redox potential of dithionite and SO_2^- from equilibrium reactions with flavodoxins, methyl viologen and hydrogen plus hydrogenase. *Eur. J. Biochem.* **85**, 535–547.
- McCormack, A. L., Thiruchelvam, M., Manning-Bog, A. B., Thiffault, C., Langston, J. W., Cory-Slechta, D. A., and Di Monte, D. A. (2002). Environmental risk factors and Parkinson's disease: Selective degeneration of nigral dopaminergic neurons caused by the herbicide paraquat. *Neurobiol. Dis.* **10**, 119–127.
- Mizuno, Y., Ikebe, S., Hattori, N., Nakagawa-Hattori, Y., Mochizuki, H., Tanaka, M., and Ozawa, T. (1995). Role of mitochondria in the etiology and pathogenesis of Parkinson's disease. *Biochim. Biophys. Acta.* **1271**, 265–274.
- Mockett, R. J., Bayne, A. C., Kwong, L. K., Orr, W. C., and Sohal, R. S. (2003). Ectopic expression of catalase in *Drosophila* mitochondria increases stress resistance but not longevity. *Free Radic. Biol. Med.* **34**, 207–217.
- Mollace, V., Iannone, M., Muscoli, C., Palma, E., Granato, T., Rispoli, V., Nistico, R., Rotiroti, D., and Salvemini, D. (2003). The role of oxidative stress in paraquat-induced neurotoxicity in rats: Protection by non peptidyl superoxide dismutase mimetic. *Neurosci. Lett.* **335**, 163–166.
- Murphy, M. P., and Smith, R. A. (2007). Targeting antioxidants to mitochondria by conjugation to lipophilic cations. *Annu. Rev. Pharmacol. Toxicol.* **47**, 629–656.
- Peng, J., Stevenson, F. F., Doctrow, S. R., and Andersen, J. K. (2005). Superoxide dismutase/catalase mimetics are neuroprotective against selective paraquat-mediated dopaminergic neuron death in the substantia nigra: Implications for Parkinson disease. *J. Biol. Chem.* **280**, 29194–29198.

- Rees, J. F., de Wergifosse, B., Noiset, O., Dubuisson, M., Janssens, B., and Thompson, E. M. (1998). The origins of marine bioluminescence: Turning oxygen defence mechanisms into deep-sea communication tools. *J. Exp. Biol.* **201**, 1211–1221.
- Richardson, J. R., Quan, Y., Sherer, T. B., Greenamyre, J. T., and Miller, G. W. (2005). Paraquat neurotoxicity is distinct from that of MPTP and rotenone. *Toxicol. Sci.* **88**, 193–201.
- Ross, M. F., Kelso, G. F., Blaikie, F. H., James, A. M., Cochemé, H. M., Filipovska, A., Da Ros, T., Hurd, T. R., Smith, R. A., and Murphy, M. P. (2005). Lipophilic triphenylphosphonium cations as tools in mitochondrial bioenergetics and free radical biology. *Biochemistry (Mosc)* **70**, 222–230.
- Sawyer, D. T., and Valentine, J. S. (1981). How super is superoxide? *Acc. Chem. Res.* **14**, 393–400.
- Schapira, A. H. (2008). Mitochondria in the aetiology and pathogenesis of Parkinson's disease. *Lancet Neurol.* **7**, 97–109.
- Shimada, H., Hirai, K., Simamura, E., and Pan, J. (1998). Mitochondrial NADH-quinone oxidoreductase of the outer membrane is responsible for paraquat cytotoxicity in rat livers. *Arch. Biochem. Biophys.* **351**, 75–81.
- Sturtz, L. A., and Culotta, V. C. (2002). Superoxide dismutase null mutants of baker's yeast, *Saccharomyces cerevisiae*. *Methods Enzymol.* **349**, 167–172.
- Thiruchelvam, M., Prokopenko, O., Cory-Slechta, D. A., Richfield, E. K., Buckley, B., and Mirochnitchenko, O. (2005). Overexpression of superoxide dismutase or glutathione peroxidase protects against the paraquat + maneb-induced Parkinson disease phenotype. *J. Biol. Chem.* **280**, 22530–22539.
- Tien Nguyen-nhu, N., and Knoops, B. (2003). Mitochondrial and cytosolic expression of human peroxiredoxin 5 in *Saccharomyces cerevisiae* protect yeast cells from oxidative stress induced by paraquat. *FEBS Lett.* **544**, 148–152.
- Van Remmen, H., Qi, W., Sabia, M., Freeman, G., Estlack, L., Yang, H., Mao Guo, Z., Huang, T. T., Strong, R., Lee, S., Epstein, C. J., and Richardson, A. (2004). Multiple deficiencies in antioxidant enzymes in mice result in a compound increase in sensitivity to oxidative stress. *Free Radic. Biol. Med.* **36**, 1625–1634.
- Vanfleteren, J. R. (1993). Oxidative stress and ageing in *Caenorhabditis elegans*. *Biochem. J.* **292**, 605–608.
- Wang, G. Y., Hirai, K., and Shimada, H. (1992). Mitochondrial breakage induced by the herbicide paraquat in cultured human lung cells. *J. Electron Microsc. (Tokyo)*. **41**, 181–184.
- Watanabe, K., Okada, K., and Katsu, T. (1992). Construction of a paraquat-sensitive membrane electrode and its application to forensic chemistry. *Jap. J. Toxicol. Environ. Health* **38**, 142–148.

QUANTIFICATION OF SUPEROXIDE PRODUCTION BY MOUSE BRAIN AND SKELETAL MUSCLE MITOCHONDRIA

Dominika Malinska,^{*,†} Alexei P. Kudin,^{*}
Grazyna Debska-Vielhaber,^{*,‡} Stefan Vielhaber,[‡]
and Wolfram S. Kunz^{*}

Contents

1. Evaluation of Quantitative Methods for Detecting ROS Production	420
1.1. Determination of hydrogen peroxide production	420
1.2. Determination of superoxide production	423
2. The Application of Quantitative Methods for Measurement of ROS Production to Identify the Contribution of Individual Sites to the Superoxide Production of Isolated Brain and Skeletal Muscle Mitochondria	428
2.1. Brain and skeletal muscle preparations used in the study	429
2.2. Quantification of superoxide production of rat brain SMP	430
2.3. Relationship between maximal respiration and complex I-related ROS generation of different brain subcellular preparations	431
2.4. Tissue dependency of mitochondrial superoxide generation rates—comparison of mouse brain and skeletal muscle mitochondria	432
Acknowledgments	436
References	436

Abstract

The production of reactive oxygen species (ROS) has been implicated for numerous pathologic alterations, including neurodegeneration and aging. They are formed to a considerable extent by mitochondria by single electron reduction of molecular oxygen by competent electron donors like flavoproteins and semiquinone species. In this chapter, we evaluate quantitative methods for the

* Division of Neurochemistry, Department of Epileptology and Life & Brain Center, University Bonn, Bonn, Germany

† Laboratory of Intracellular Ion Channels, Nencki Institute of Experimental Biology, Warsaw, Poland

‡ Department of Neurology, University Magdeburg, Magdeburg, Germany

detection of hydrogen peroxide and superoxide production. Applying these methods we compared the ROS production of isolated mitochondria of mouse brain and skeletal muscle. We substantiated previous evidence that most mitochondrial ROS are produced at complexes I and III of the respiratory chain and that the contribution of individual complexes to ROS production is tissue dependent.

1. EVALUATION OF QUANTITATIVE METHODS FOR DETECTING ROS PRODUCTION

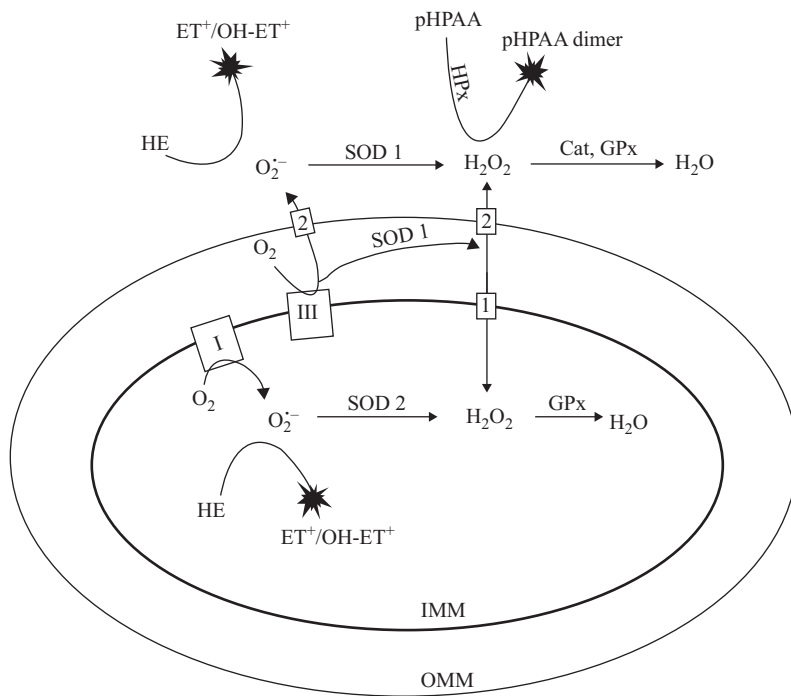
The reactive oxygen species: $O_2^{\bullet-}$, H_2O_2 , and the OH^- radical are products of the single electron reduction of oxygen. The lifetime of these species is limited because of their high reactivity and the high capacity of radical scavenging reactions, thus to detect them in cells, tissue samples, and isolated organelles, very sensitive methods are required. Because ROS production strongly depends on oxygen concentration, in all experiments we used oxygen-saturated media to increase the sensitivity of the applied methods.

1.1. Determination of hydrogen peroxide production

Hydrogen peroxide is formed essentially as a product of dismutation of the superoxide anion by both the cytosolic Cu/Zn superoxide dismutase (SOD1) and the mitochondrial Mn superoxide dismutase (SOD2). Fluorimetric assays for quantitative determination of hydrogen peroxide formation in biological samples like isolated mitochondria usually take advantage from the peroxidase-coupled oxidation of a probe substance resulting in the formation of a fluorescent product (cf. [Scheme 23.1](#)). Typical examples are *p*-hydroxyphenylacetate and 10-acetyl-3,7-dihydroxyphenoxazine (Amplex red). Because hydrogen peroxide is very likely passing all biological membranes by means of aquaporin channels ([Dynowski *et al.*, 2008](#)), the total formation of this ROS species can be accurately assessed, and no specific compartmentation effects have to be taken into consideration (cf. [Scheme 1](#)).

1.1.1. Fluorimetric determination of hydrogen peroxide by peroxidase mediated oxidation of *p*-hydroxyphenylacetate (pHPAA)

A typical calibration experiment of the fluorescence signal with a defined hydrogen peroxide solution is shown in [Fig. 23.1A](#). In the absence of catalase (CAT) within a certain range of hydrogen peroxide concentrations, a linear increase of fluorescence at $\lambda_{ex} = 317$ nm and $\lambda_{em} = 390$ nm is detected. This method is very specific for production of hydrogen peroxide,



Scheme 23.1 Fluorescent probes applied for detection of mitochondrially produced superoxide and hydrogen peroxide. Cat, Catalase; ET^+ , ethidium; OH-ET^+ , 2-hydroxyethidium; GPx, glutathione peroxidase; HE, hydroethidine; HPx, horseradish peroxidase; IMM, inner mitochondrial membrane; OMM, outer mitochondrial membrane; pHPAA, *p*-hydroxyphenylacetic acid; SOD, superoxide dismutase; 1, aquaporin channel; 2, VDAC. I, Respiratory chain complex I; III, respiratory chain complex III.

because xanthine + xanthine oxidase in the absence of superoxide dismutase (SOD) led to a much lower fluorescence increase compared with the same experiment in presence of SOD (Fig. 23.1B, compare traces +SOD and -SOD). The excellent linearity and high specificity toward hydrogen peroxide of this particular method is also demonstrated in the titration experiments with xanthine oxidase shown in Fig. 23.1C.

1.1.2. Fluorimetric determination of hydrogen peroxide by peroxidase-mediated oxidation of Amplex red to resorufin

A typical calibration experiment of the fluorescence signal with a defined hydrogen peroxide solution is shown in Fig. 23.2A. In the absence of catalase (-CAT) within a certain range of hydrogen peroxide concentrations, a linear increase of resorufin fluorescence at $\lambda_e = 560$ nm and $\lambda_{em} = 590$ nm is detected. This method is, however, not specific for production of

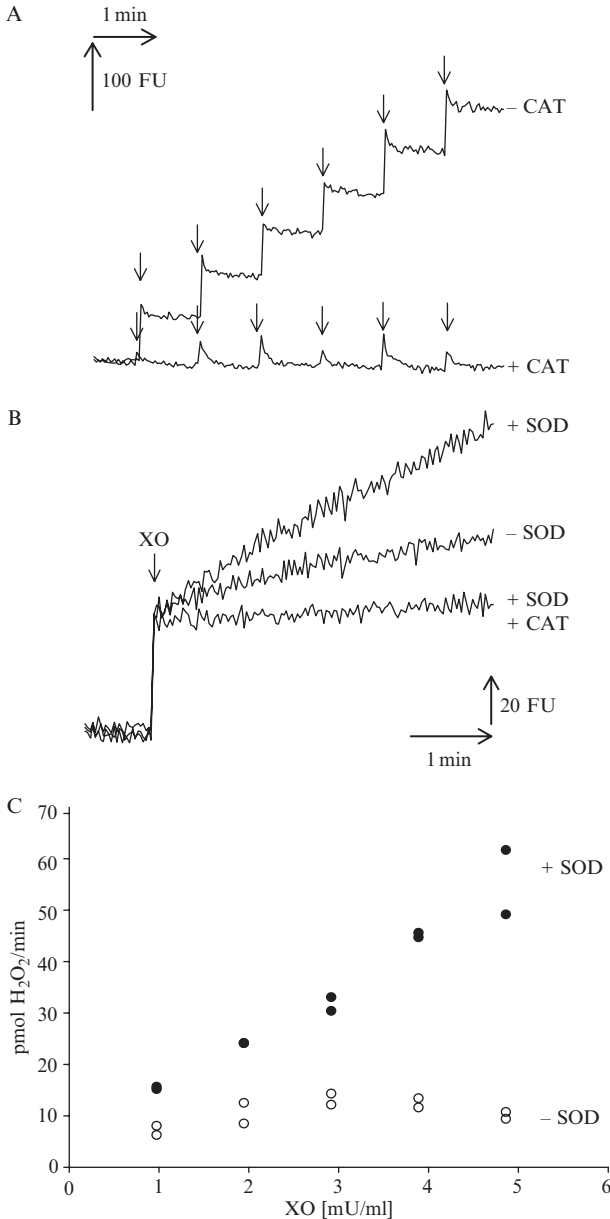


Figure 23.1 Hydrogen peroxide detection with *p*-hydroxyphenylacetate (pHPAA). The fluorescence measurements were performed at $\lambda_{ex} = 317$ nm and $\lambda_{em} = 390$ nm, in the presence of 200 μ M pHPAA, 20 U/ml horseradish peroxidase and, where indicated, 35 U/ml SOD, in oxygen-saturated measurement medium, containing 10 mM KH_2PO_4 , 60 mM KCl, 60 mM TRIS-HCl, 110 mM mannitol, 5 mM $MgCl_2$, and 0.5 mM EDTA (pH 7.4). (A) Calibration of the pHPAA fluorescence signal with hydrogen peroxide

hydrogen peroxide, because xanthine + xanthine oxidase in the absence of superoxide dismutase (SOD) led to a considerable fluorescence increase compared with the same experiment in presence of SOD (Fig. 23.2B, compare traces +SOD and -SOD). The excellent linearity and sensitivity, but rather low specificity toward hydrogen peroxide (cf. filled circles +SOD and open circles -SOD) of this particular method is demonstrated in the titration experiments with xanthine oxidase shown in Fig. 23.2C.

1.1.3. Artifacts of fluorimetric methods for measurement of hydrogen peroxide

Because the steady-state amounts of ROS in biologic systems are extremely low (10^{-10} M for the superoxide anion and 5×10^{-9} M for hydrogen peroxide, Cadenas and Davies [2000]), very sensitive and, therefore, artefact-prone methods are required. A further problem is the low substrate specificity of horseradish peroxidase. A typical artifact is obtained in the presence of NADH. As shown in Fig. 23.3, the addition of 50 to 500 μ M NADH to the measurement medium containing Amplex red, horseradish peroxidase, and superoxide dismutase causes in the absence of biologic systems a catalase-sensitive (cf. trace 500 + CAT) increase in fluorescence, reminiscent of a hydrogen peroxide production. This reaction, which has been already described by Votyakova and Reynolds (2004), is clearly dependent on the concentration of NADH applied (cf. traces in the presence of 50 μ M, 200 μ M and 500 μ M NADH). Similarly, ketoacids, like α -ketoglutarate and pyruvate, cause substantial artifact in the horseradish peroxidase containing measurement medium (Kudin *et al.*, 2005).

1.2. Determination of superoxide production

The superoxide anion is the original reactive oxygen species formed by the one electron reduction of oxygen. The lifetime of this initial species is rather short, because it rapidly dismutates to hydrogen peroxide and molecular oxygen or rapidly reacts with NO. Therefore, the detection and quantification of $O_2^{\cdot -}$ in biological systems has remained a challenge. The superoxide anion can be detected and quantified with its SOD-sensitive reactions, with certain probes forming easily detectable and relatively stable compounds,

titration. Arrows indicate a 140 nM increase in H_2O_2 concentration. The presence of catalase (13,800 U/ml) prevented an increase in pHPAA fluorescence observed on H_2O_2 addition. (B) Selectivity of the method to hydrogen peroxide. An increase in pHPAA fluorescence was monitored after an addition of 1.94 mU/ml of xanthine oxidase (XO) in the presence 500 μ M xanthine (X). The experiment was performed in presence or in absence of SOD, and in presence of both SOD and catalase. (C) Linearity of the pHPAA response. CAT, Catalase; XO, xanthine oxidase.

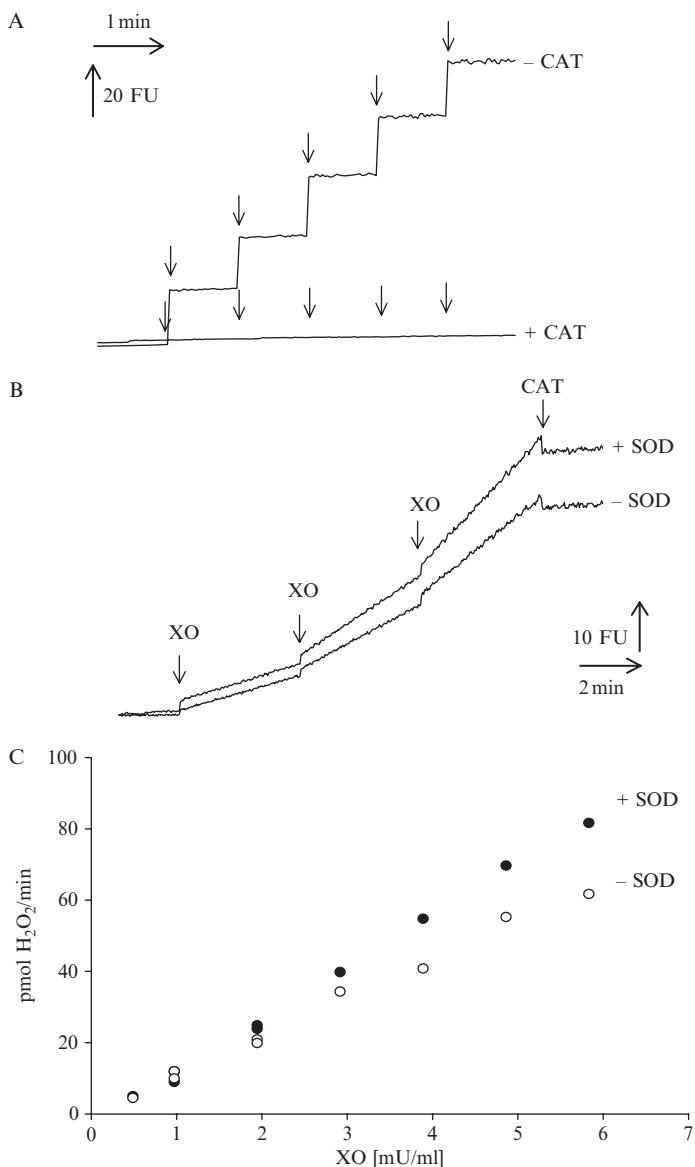


Figure 23.2 Hydrogen peroxide detection with Amplex red. The fluorescence measurements were performed at $\lambda_{\text{ex}} = 560 \text{ nm}$ and $\lambda_{\text{em}} = 590 \text{ nm}$ in oxygen-saturated measurement medium (cf. Fig. 23.1 legend), in the presence of $1 \mu\text{M}$ Amplex red, 20 U/ml horseradish peroxidase, and 35 U/ml SOD. (A) Calibration of the Amplex red fluorescence signal with hydrogen peroxide titration. Arrows indicate a 140 nM increase in H_2O_2 concentration. The presence of catalase ($13,800 \text{ U/ml}$) prevented the increase of Amplex red fluorescence observed on H_2O_2 addition. (B) Selectivity of the method to hydrogen peroxide. An increase in Amplex red fluorescence was monitored after an

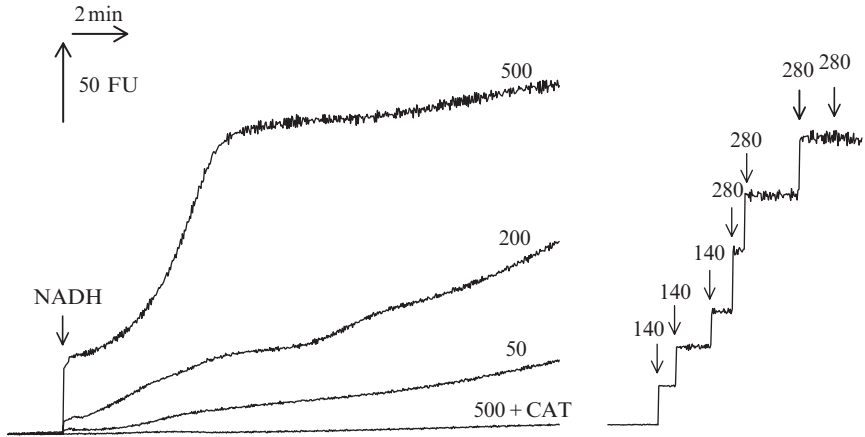


Figure 23.3 NADH-related artefacts of the Amplex red method. The measurement was performed as described in Fig. 23.2. legend. The numbers above the traces indicate the concentration (in μM) of added NADH. CAT, Measurement in additional presence of catalase (13,800 U/min). For comparison a hydrogen peroxide titration experiment is presented (right trace). The numbers above the arrows indicate the amount of H_2O_2 added (in nM).

such as the reduction of acetylated ferricytochrome c , oxidation of epinephrine to adrenochrome, spin trapping with cyclic nitrones, and oxidation of hydroethidine. Because of its high sensitivity and easy application for most biological systems, the fluorimetric detection of hydroethidine oxidation products has remained the method of choice (cf. [scheme 23.1](#)).

1.2.1. Fluorimetric detection of superoxide production with oxidation of hydroethidine

It has been reported that hydroethidine (HE), which has been widely used for the detection of intracellular O_2^- ([Bindokas et al., 1996](#); [Budd et al., 1997](#)), apart from being completely oxidized to ethidium (ET^+) can also form 2-hydroxyethidium (OH-ET^+)—the direct reaction product with the superoxide anion ([Zhao et al., 2005](#)). Because both oxidation products of HE have distinct fluorescence characteristics ([Zhao et al., 2005](#)), we decided to record the fluorescence excitation and emission spectra of the reaction products of hydroethidine with superoxide formed by xanthine/xanthine oxidase, rat brain submitochondrial particles, or rat brain mitochondria. These spectra are presented in [Fig. 23.4A,B](#). Very clearly, both the excitation ([Fig. 23.4A](#)) and

addition of xanthine oxidase (XO, 0.97, 1.94, and 2.91 mU/ml) in the presence of 500 μM xanthine. The experiment was performed in presence or in absence of SOD. At the end of each experiment 13,800 U/ml of catalase was added. (C) Linearity of the pHPAA response. CAT, Catalase; XO, xanthine oxidase.

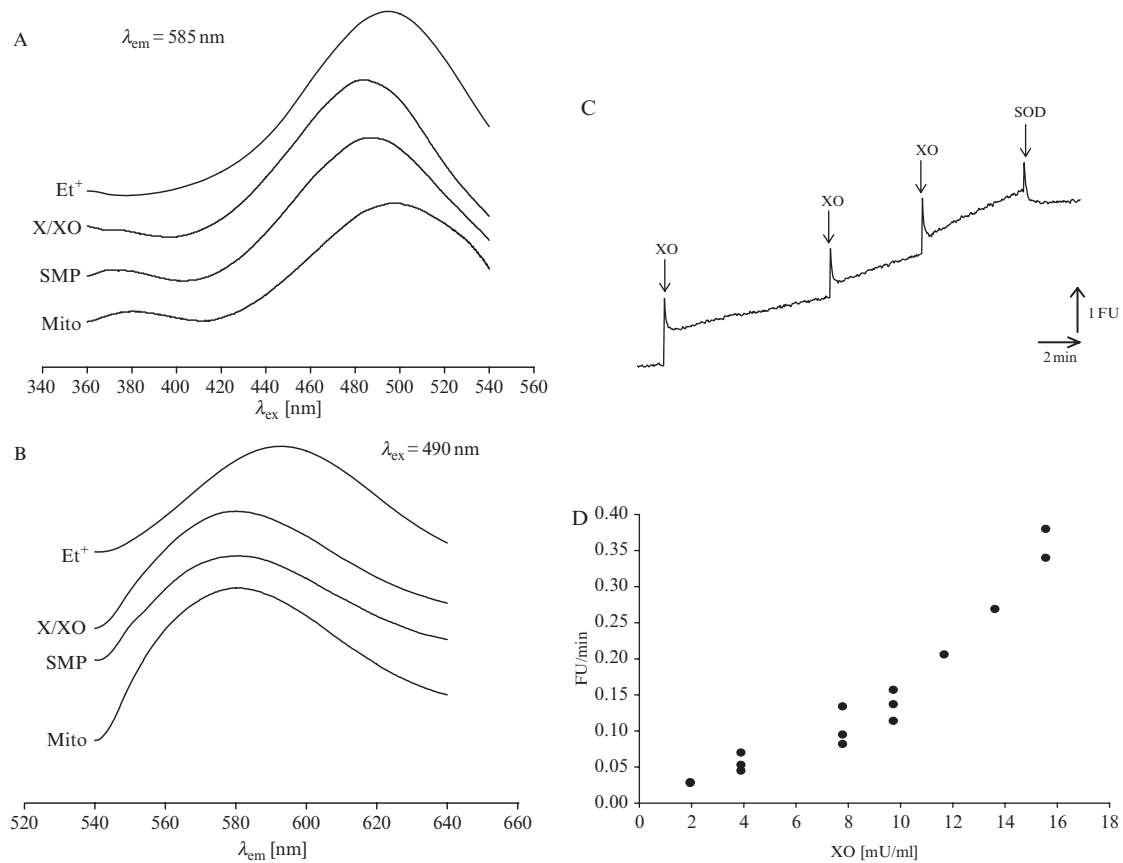


Figure 23.4

emission spectra (Fig. 23.4B) of the fluorescent product of hydroethidine oxidation formed in the presence of xanthine and xanthine oxidase (X/XO) of rat brain submitochondrial particles (RB-SMP) and of rat brain mitochondria (RB-Mito) are, with respect to ethidium (ET⁺), blue shifted but not identical to the spectrum of 2-hydroxyethidium (cf. Zhao *et al.*, 2005). This is very likely the result of the presence of both ET⁺ and OH-ET⁺. The fluorescence responses are within a certain range linearly, depending on the amount of xanthine oxidase added (Fig. 23.4D) and completely sensitive to excess of SOD (Fig. 23.4C). With defined xanthine/xanthine oxidase concentrations, it is possible to calibrate the fluorescence signals to hydrogen peroxide equivalents (cf. Kudin *et al.*, 2008). Similarly, it is possible to express the signals directly in produced superoxide performing a calibration of the xanthine oxidase caused fluorescence increase with the photometric reduction of acetylated cytochrome *c* (see next paragraph).

1.2.2. Photometric detection of superoxide by reduction of acetylated cytochrome *c*

The SOD-sensitive reduction of acetylated cytochrome *c* by superoxide anion has been widely applied to study superoxide production by simple enzyme systems (like xanthine/xanthine oxidase), mitochondrial fragments, and in submitochondrial particles (Azzi *et al.*, 1975). This method relies on the fact that the acetylation of some lysyl residues of ferricytochrome *c* destroys its ability to undergo enzymatic reduction and oxidation. The advantage of this method is a relatively high sensitivity (the extinction coefficient of ferrocycytochrome *c* is at 550 nm $\epsilon = 27.7 \text{ cm}^{-1} \text{ mM}^{-1}$) and that it is, therefore, possible to directly quantify the superoxide production. However, it is problematic to apply this method to intact mitochondria, because the molecular weight of cytochrome *c* is too high to allow an effective permeation of VDAC in the mitochondrial outer membrane.

Figure 23.4 Measurement of superoxide formation with hydroethidine (HET). In the panels (A) and (B) the fluorescence excitation and emission spectra of hydroethidine (3.17 μM) oxidation products are shown, respectively. The applied superoxide producing systems were xanthine/xanthine oxidase (X/XO), antimycin-treated, succinate-oxidizing rat brain submitochondrial particles (SMP), and mitochondria (Mito). (C) Dependency of the HET-fluorescence change slope on the amount of xanthine oxidase. The fluorescence changes were recorded at $\lambda_{\text{ex}} = 470 \text{ nm}$ and $\lambda_{\text{em}} = 585 \text{ nm}$, in the presence of 3.17 μM HET and 500 μM xanthine. Where indicated, xanthine oxidase (to final concentrations 7.8, 11.7, and 15.6 mU/ml) and SOD (35 U/ml) was added. All measurements were performed in an oxygen-saturated medium (cf. legend to Fig. 23.1). (D) Linearity of the fluorescence signal of HET oxidized by xanthine/xanthine oxidase.

1.2.3. Artifacts in the detection of superoxide

The fluorimetric method of superoxide detection with hydroethidine, despite its high selectivity to superoxide, is relatively artefact prone and is difficult for quantification because of nonlinear responses. These problems are very likely related to excitation light-driven photooxidation of hydroethidine and the strong effects of DNA binding on the quantum yield of hydroxyethidium and ethidium.

The photometric method with acetylated cytochrome *c* has a much lower sensitivity than the fluorimetric method. In addition, in the presence of cytochrome *c* reductase and cytochrome *c* oxidase activities, the results may be biased because of contaminating amounts of nonacetylated cytochrome *c*. Therefore, rigorous control experiments in the initial presence of SOD excess are required.

Similar to what has been shown with the Amplex red method (cf. 1.1.3), both superoxide detection methods are affected by the presence of NADH, which at 200 μM results in 1.2- and twofold decrease of slope observed in presence of xanthine/xanthine oxidase for photometric and fluorimetric methods, respectively.

2. THE APPLICATION OF QUANTITATIVE METHODS FOR MEASUREMENT OF ROS PRODUCTION TO IDENTIFY THE CONTRIBUTION OF INDIVIDUAL SITES TO THE SUPEROXIDE PRODUCTION OF ISOLATED BRAIN AND SKELETAL MUSCLE MITOCHONDRIA

The particular impact of the potential sites relevant for the mitochondrial superoxide generation and its influence on mitochondrial metabolism is still a matter of dispute (Grivennikova *et al.*, 2008; Komary *et al.*, 2008; Kudin *et al.*, 2008). Molecular oxygen is a triplet species that can accept only single electrons from potential donors (Naqui *et al.*, 1986). This prevents oxygen (the midpoint potential of the O_2/O_2^- couple is -0.33 V ; Wood [1988]) from spontaneously oxidizing reduced biomolecules with appropriate redox potentials, such as NAD(P)H, which are obligate two-electron donors. Potential single-electron donor sites with matching redox potentials for the reduction of molecular oxygen are located within the mitochondrial respiratory chain, which transfers electrons to oxygen. Within the respiratory chain complex I, the FMN moiety (Kudin *et al.*, 2004; Liu *et al.*, 2002), iron sulfur clusters (Genova *et al.*, 2001; Votyakova and Reynolds, 2001) and semiquinones (Lambert and Brand, 2004), all of which are competent for univalent redox reactions, have been suggested to be responsible for mitochondrial superoxide production. For respiratory chain complex III, the semiquinone anion at center “o” of the Q-cycle being stabilized by antimycin A treatment has been identified as an additional site of

mitochondrial superoxide production (Boveris *et al.*, 1976; Cape *et al.*, 2007), which in contrast to complex I releases superoxide to the intermembrane space (Kudin *et al.*, 2005; St-Pierre *et al.*, 2002). In addition to the respiratory chain, several flavoproteins in the mitochondrial matrix space, like the α -lipoamide dehydrogenase moiety of the α -ketoglutarate dehydrogenase complex (Starkov *et al.*, 2004; Tretter and Adam-Vizi, 2004), the electron transfer flavoprotein of the β -oxidation pathway (St-Pierre *et al.*, 2002), and α -glycerophosphate dehydrogenase (Tretter *et al.*, 2007) are possible candidate sites for mitochondrial ROS production.

2.1. Brain and skeletal muscle preparations used in the study

Rat, mouse, and human brain homogenates were prepared according to the following procedure (Kunz *et al.*, 1999). One male Wistar II rat (~80 days old) or one C57BL6 mouse (~50 days old) was euthanized, and the brain was rapidly removed. Tissue samples from human parahippocampal gyrus were obtained from five patients (three female and two male) with therapy-resistant temporal lobe epilepsy, who underwent epileptic surgery. The whole rat or mouse brain or the human brain tissue was washed and rapidly placed into ice-cold MSE medium (225 mM mannitol, 75 mM sucrose, 1 mM EGTA, 5 mM HEPES, and 1 mg/ml essentially fatty acid free BSA, pH 7.4). After isolation of the subsequent brain areas (rat hippocampus, total mouse brain, or human parahippocampal gyrus), approximately 200 mg wet tissue was homogenized twice for 20 sec at 11,000 rpm with an ultra-turrax homogenizer T 25 (IKA, Staufen, Germany) in 1 ml ice-cold MSE medium and stored on ice.

Rat, mouse, and human brain mitochondria were isolated as described previously (Kudin *et al.*, 2004; 2005). One rat brain, two mouse brains (from C57BL6 mouse or C57BL/6-Tg(SOD1)10Cje/J mouse overexpressing SOD1-The Jackson Laboratory, Bar Harbor, USA), or human brain tissue was minced and homogenized in an ice-cold MSE medium containing 0.5 mg/ml of nagsarse. The homogenate was centrifuged for 4 min at 2000g. The supernatant was decanted and centrifuged at 12,000g for 9 min. The resulting pellet was homogenized in MSE medium containing 0.2 mg/ml of digitonin, centrifuged for 11 min at 12,000g, and the obtained mitochondrial pellet was suspended in MSE medium. All procedures were carried out at 4 °C. The respiratory control index with 10 mM glutamate and 5 mM malate as respiratory substrates with all preparations was routinely better than 6.

Mouse skeletal muscle mitochondria were prepared as previously described (Debska *et al.*, 2002; Wisniewski *et al.*, 1993); 3 C57BL6 mice or C57BL/6-Tg(SOD1)10Cje/J mice were sacrificed by decapitation and the hindlimb muscles were rapidly removed and transferred into ice-cold isolation medium (180 mM KCl, 10 mM EDTA- Na_2 , 7.7 mM EGTA, pH 7.4). Muscles were minced with scissors, trimmed clean of visible fat and

connective tissue, and placed in isolation medium supplemented with 0.08 mg/ml trypsin (10 ml medium per 1 g of tissue). After 30 min, the tissue was homogenized with a motor-driven Teflon-glass Potter homogenizer. The homogenate was centrifuged at 750g for 6 min. The supernatant was decanted and centrifuged at 4,300g for 10 min. The final mitochondrial pellet was once washed (2 min at 23,700g) and then resuspended in medium containing 180 mM KCl and 1 mg/ml essentially fatty acid free BSA (pH 7.4). All procedures were carried out at 4 °C.

Rat brain submitochondrial particles (SMP) were prepared according to [Cino and Del Maestro \(1989\)](#) with following modifications. Isolated mitochondria from eight rat brains were pooled and stored in liquid nitrogen before use (usually 1 or 2 days). After thawing on ice, the mitochondrial suspension was centrifuged at 10,000g for 10 min, and the pellet was resuspended in isolation medium A containing 15 mM MgCl₂ and 50 mM potassium phosphate (pH 7.4) to a final volume of 10 ml. After sonication (70 W, 3 times 15 sec) a centrifugation at 25,000g for 10 min was performed. The supernatant was centrifuged at 48,400g for 87 min. The resulting pellet was resuspended in MSE medium without BSA and centrifuged again at 48,400g for 87 min. The pellet was again resuspended in isolation medium A and centrifuged at 25,000g for 15 min. The SMP in supernatant were washed twice in medium A with after centrifugation at 48,400g for 87 min. The final pellet was suspended in medium A to a concentration of 8 to 10 mg protein/ml, divided into aliquots, and frozen in liquid nitrogen before use. Every aliquot was used only during 1 day; refreezing and repeated use of the SMP aliquots led to lowered rates of superoxide generation.

2.2. Quantification of superoxide production of rat brain SMP

The submitochondrial particle preparation consists of purified mitochondrial inner membranes. Therefore, this is the ideal preparation to study the contributions of the individual respiratory chain-associated ROS-producing sites located in complex I and complex III in almost complete absence of the superoxide dismutases SOD1 and SOD2. In [Table 23.1](#) the specific superoxide production rates of purified rat brain submitochondrial particles are given for two conditions: (1) in the presence of succinate and antimycin, when superoxide is produced nearly exclusively by the center “o” of Q cycle and (2) in the presence of NADH and rotenone, when superoxide is produced by complex I, presumably by the FMNH₂ moiety. To quantitatively compare the data of two different methods the values determined by oxidation of hydroethidine and by reduction of acetylated cytochrome *c* are given. The values determined in the presence of 200 μM NADH have been corrected to account for the effects of NADH on the superoxide detection systems (cf. 1.2.2). Similarly, as previously reported for rat brain mitochondria ([Kudin *et al.*, 2004, 2005](#)), in rat brain

Table 23.1 Generation of superoxide by rat brain submitochondrial particles

	Acetylated cytochrome <i>c</i>	Hydroethidine ^a
NADH + rotenone ^b	1295 ± 545 (<i>n</i> = 7)	1169 ± 247
Succinate + antimycin A	712 ± 280 (<i>n</i> = 4)	891 ± 90

^a The values obtained by hydroethidine oxidation are the average of four measurements performed with one SMP preparation.

^b To correct for unspecific side effects of NADH, the values obtained in the presence of 200 μM NADH were multiplied by 1.2 (acetylated cytochrome *c*) and by 2 (hydroethidine). Correction parameters were determined in the experiments with the use of xanthine + xanthine oxidase system.

All data are presented as mean values ±SD and are expressed in pmol H₂O₂ equivalents/min/mg protein. *n*, Number of independent SMP preparations.

submitochondrial particles the contribution of complex I–driven superoxide generation is higher than the complex III–dependent production rate. This result is in accordance with previous work of [Barja and Herrero \(1998\)](#) and [Kudin *et al.* \(2008\)](#). It clearly excludes for brain mitochondria a considerable contribution of other ROS–producing sites suggested by [Grivennikova *et al.* \(2008\)](#) and [Tretter and Adam-Vizi \(2004\)](#).

2.3. Relationship between maximal respiration and complex I–related ROS generation of different brain subcellular preparations

To quantitatively compare the maximal ROS production rates of different isolates from rat, mouse, and human brain (brain homogenates, isolated brain mitochondria, and submitochondrial particles from rat brain) we plotted the maximal oxygen consumption rates, which is a measure of the content of mitochondrial inner membranes, versus the complex I–dependent ROS–generation rates of subcellular preparations containing mitochondrial inner membranes at different levels of purity. A putative linear relationship between ROS generation and the maximal oxygen consumption rate would strengthen the evidence from [section 2.2](#) that complex I is an important contributor to ROS generation in brain tissue. As shown in [Fig. 23.5](#), all data appear within experimental error compatible with a linear relationship, despite different methods of ROS generation measurements (in homogenates the Amplex red method and in isolated mitochondria the pHPAA method was used). For rat brain SMP (data point 7), we determined superoxide generation by measuring the SOD–sensitive reduction of acetylated cytochrome *c*. To compare ROS production of SMP with the H₂O₂ generation rates of the other preparations with succinate as substrate, we calibrated the assay in H₂O₂ equivalents with defined activities of xanthine oxidase (in presence of xanthine), which was reassayed with the pHPAA method in presence of excess SOD activity (cf. [Kudin *et al.*, 2008](#)).

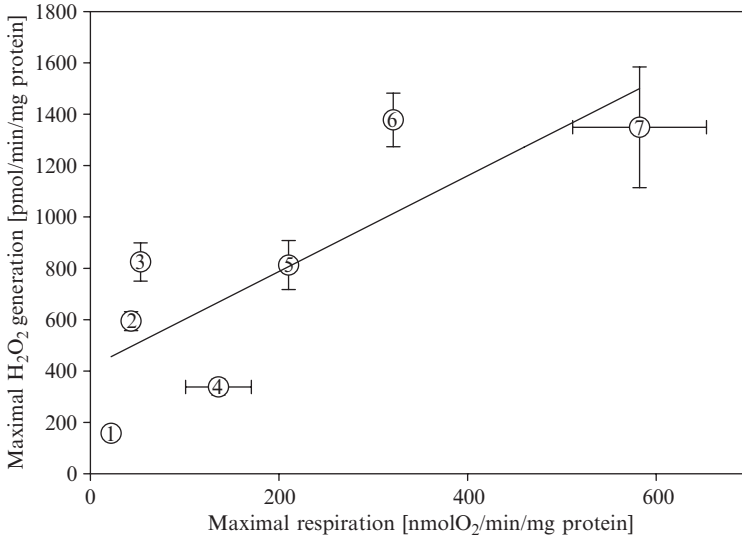


Figure 23.5 Dependency of maximal hydrogen peroxide production rate on mitochondrial inner membrane purity. The maximal ROS generation rates of human brain homogenates from grey matter (1), of rat hippocampal homogenates (2), of mouse whole brain homogenates (3), of human (4), rat (5), and mouse (6) brain mitochondria, and of rat brain SMP (7) were plotted versus the maximal respiration rates (a measure of inner mitochondrial membrane purity). The maximal respiration rates of rat brain SMP were measured after addition of 200 μM NADH. The maximal respiration rates of digitonin-treated brain homogenates and of isolated mitochondria were measured after addition of 250 μM ADP in the presence of 10 mM succinate. The maximal H₂O₂ generation (in the presence of 10 mM succinate) was measured by pHPAA/HRP-coupled method in isolated mitochondria (4, 5, 6), or by Amplex red/HRP-coupled method in digitonin-treated brain homogenates (1, 2, 3). In rat brain SMP superoxide generation was measured by reduction of acetylated cytochrome *c*. This superoxide generation was expressed in H₂O₂ equivalents after calibration experiments with xanthine/xanthine oxidase with cytochrome *c* and pHPAA-based methods. Number of independent experiments: human brain homogenates from grey matter (1) 5; rat hippocampal homogenates (2) 13; mouse whole brain homogenates (3) 5; human brain mitochondria (4) 4; rat brain mitochondria (5) 4; mouse brain mitochondria (6) 5; rat brain SMP (7) 6. The presented data are averages \pm SEM.

2.4. Tissue dependency of mitochondrial superoxide generation rates – comparison of mouse brain and skeletal muscle mitochondria

Because previous work (Barja and Herrero, 1998; Kudin *et al.*, 2005) suggested a considerable tissue dependency of mitochondrial ROS production, we decided to apply the previously described methods to study the difference between mouse skeletal muscle and brain in greater detail.

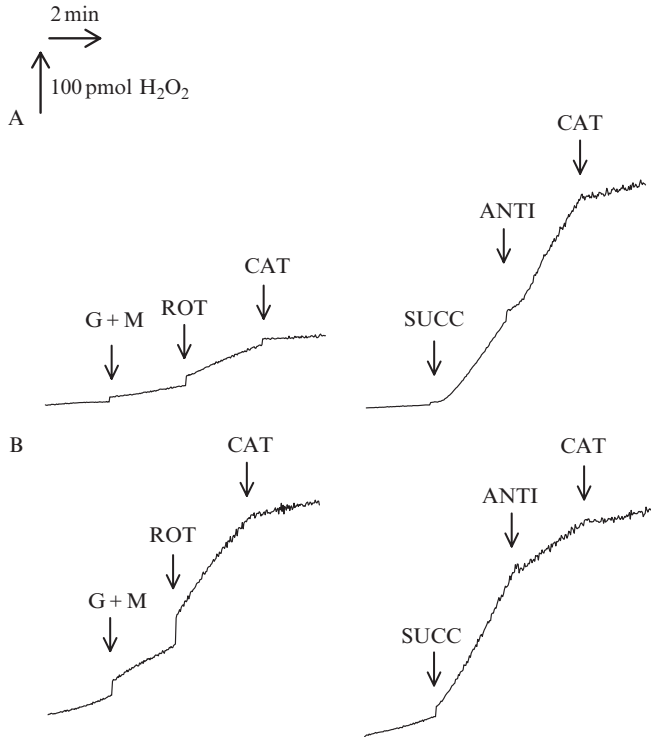


Figure 23.6 Experimental traces of measurements of H₂O₂ generation in mouse skeletal muscle (A) and brain mitochondria (B). The measurements were performed in the presence of 0.1 mg mitochondrial protein/ml and 35 U/ml SOD with the Amplex red–peroxidase method as described in legend to Fig. 23.2. For quantification the catalase-insensitive slope was subtracted. Additions: G + M, 10 mM glutamate + 5 mM malate; ROT, 6.7 μ M rotenone; SUCC, 10 mM succinate; ANTI, 0.5 μ M antimycin A; CAT, 13,800 U/ml catalase.

Fig. 23.6 presents the experiments for the determination of hydrogen peroxide production of mouse skeletal muscle (A) and brain mitochondria (B) at a comparable protein concentration and with the Amplex red method. Mouse brain mitochondria showed elevated rates of hydrogen peroxide production compared with skeletal muscle mitochondria both in the presence of glutamate plus malate plus rotenone and in succinate alone. This indicates a higher complex I–dependent ROS production in brain mitochondria. In contrast, skeletal muscle mitochondria showed a higher succinate + antimycin caused hydrogen peroxide production, which is suggesting a higher complex III–dependent contribution in skeletal muscle mitochondria. Table 23.2 summarizes the quantitative results of hydrogen peroxide generation rates of isolated mouse brain and skeletal muscle mitochondria with the substrates glutamate + malate and succinate,

Table 23.2 Hydrogen peroxide generation rates (in nmol H₂O₂/min/mg protein) of mouse brain and skeletal muscle mitochondria determined with Amplex red

	Brain mitochondria	Muscle mitochondria
Succinate	1338 ± 486 (<i>n</i> = 6)	911 ± 155 (<i>n</i> = 5)
Succinate + TTFB	85 ± 76 (<i>n</i> = 3)	202 ± 145 (<i>n</i> = 4)
Succinate + antimycin	274 ± 168 (<i>n</i> = 6)	953 ± 248 (<i>n</i> = 4)
Glutamate + malate	205 ± 73 (<i>n</i> = 6)	92 ± 33 (<i>n</i> = 4)
Glutamate + malate + TTFB	205 ± 156 (<i>n</i> = 4)	85 ± 17 (<i>n</i> = 3)
Glutamate + malate + rotenone	657 ± 178 (<i>n</i> = 4)	188 ± 35 (<i>n</i> = 3)

The hydrogen peroxide generation rates were determined in the presence of 35 U/ml SOD with the Amplex red-peroxidase method, as described in legend to Fig. 23.2. The substrates and inhibitors were used at the following concentrations: 10 mM glutamate, 5 mM malate, 6.7 μM rotenone, 10 mM succinate, 0.5 μM antimycin A, and the uncoupler TTFB (4,5,6,7-tetrachloro-2-trifluoromethylbenzimidazole): 0.5 μM. *n*, Number of independent experiments. The presented data are averages ±SD.

determined with the Amplex red method. Importantly, in accordance with the traces in Fig. 23.6, two quantitative differences can be seen. First, the complex I-dependent hydrogen peroxide generation by reverse and forward electron flow in mouse brain mitochondria is approximately 1.5- to 3.5-fold larger than in mouse skeletal muscle mitochondria. This can be evaluated by comparing the differences in complex I-dependent hydrogen peroxide generation rates by reverse electron flow (succinate alone) and forward electron flow (glutamate + malate + rotenone). Second, the complex III-dependent hydrogen peroxide formation in skeletal muscle mitochondria is approximately three times larger than in brain mitochondria. This is visible from the big differences in the hydrogen peroxide formation rates in presence of succinate and the complex III inhibitor antimycin or succinate and the uncoupler TTFB. Because Amplex red is detecting both superoxide and hydrogen peroxide (cf. 1.1.2), these experiments were performed in the presence of SOD excess, and, therefore, no information can be obtained about the potential amount of superoxide escaping dismutation reactions. To address this issue we have repeated some of these experiments (with succinate and succinate + antimycin) applying hydroethidine and *p*-hydroxyphenylacetate as more specific fluorescent probes for superoxide and hydrogen peroxide detection, respectively. pHPAA measurements were performed both in the presence and absence of SOD (cf. 1.1.1). In addition, we have tried to confirm the experimental results in mitochondria from mice overexpressing Cu/Zn superoxide dismutase (mouse strain C57BL/6-Tg(SOD1)10Cje/J). The quantitative results of these experiments are summarized in Table 23.3. These data confirm the differences between brain and skeletal muscle

Table 23.3 Hydrogen peroxide and superoxide production of brain and skeletal muscle mitochondria from control and Cu/Zn-SOD overexpressing (TG) mice, determined with *p*-hydroxyphenylacetate (\pm SOD) and hydroethidine

	Brain mitochondria		Muscle mitochondria	
	SUCC	SUCC+ANTI	SUCC	SUCC+ANTI
H ₂ O ₂	805 \pm 411 (<i>n</i> = 18)	63 \pm 47 (<i>n</i> = 11)	661 \pm 428 (<i>n</i> = 16)	513 \pm 322 (<i>n</i> = 18)
O ₂ ^{•-}	94 \pm 51 (<i>n</i> = 15)	238 \pm 87 (<i>n</i> = 15)	136 \pm 61 (<i>n</i> = 11)	221 \pm 111 (<i>n</i> = 12)
H ₂ O ₂ (+SOD)	1249 \pm 573 (<i>n</i> = 5)	259 \pm 93 (<i>n</i> = 5)	1061 \pm 703 (<i>n</i> = 4)	1396 \pm 575 (<i>n</i> = 5)
H ₂ O ₂ TG	1305 \pm 181 (<i>n</i> = 6)	157 \pm 30 (<i>n</i> = 6)	481 \pm 113 (<i>n</i> = 6)	651 \pm 210 (<i>n</i> = 6)
O ₂ ^{•-} TG	63 \pm 9 (<i>n</i> = 6)	178 \pm 42 (<i>n</i> = 6)	112 \pm 41 (<i>n</i> = 6)	273 \pm 115 (<i>n</i> = 6)

The data are expressed in nmol H₂O₂/min/mg protein or in nmol H₂O₂ equivalents/min/mg protein. Experimental conditions as in Table 23.2. The measurements of hydrogen peroxide generation were performed as described in legend to Fig. 23.1 and calibrated by the additions of defined H₂O₂ amounts. The superoxide generation measurements were performed as described in the legend to Fig. 23.4, and calibrated with the xanthine/xanthine oxidase (X/XO) system: The slope of hydroethidine fluorescence changes was determined in presence of X/XO and the same amount of xanthine and xanthine oxidase was used in pHPAA measurements performed both in presence and in absence of SOD. For calculations the SOD-insensitive slope of pHPAA was subtracted. The presented data are averages \pm SD.

mitochondria, concerning the individual contributions of complexes I and III. Moreover, it is visible from the data that substantial amounts of superoxide are formed by complex III only. In mouse brain mitochondria this superoxide visible in presence of succinate + antimycin is nearly exclusively formed at the outer site of inner mitochondrial membrane, because the hydrogen peroxide formation in absence of SOD is low, but SOD addition or the transgenic overexpression of SOD1 in the intermembrane space convert this ROS species to hydrogen peroxide. In contrast, in mouse skeletal muscle mitochondria, approximately 50% of complex III-dependent ROS is produced already as hydrogen peroxide, indicating either more effective intermembrane space dismutation or partial complex III-dependent superoxide release to the matrix space. Interestingly, although there is an effect of the external SOD addition on the hydrogen peroxide production rates of skeletal muscle mitochondria, there seems to be no visible effect of transgenic overexpression of SOD1 in skeletal muscle. This is very likely related to the lower increase of total SOD activities in transgenic skeletal muscle mitochondria in comparison with transgenic brain mitochondria: control brain mitochondria—11.7 \pm 2.5 U/mg; transgenic brain mitochondria—17.8 \pm 4.3 U/mg; control skeletal muscle mitochondria—9.0 \pm 3.0 U/mg; transgenic skeletal muscle mitochondria—10.3 \pm 2.9 U/mg (the values are means \pm SD of four independent mitochondrial preparations).

In previous work we have suggested that a possible reason for the tissue specificity of contribution of the different sites to mitochondrial superoxide production could be the difference in the coenzyme Q content of brain and skeletal muscle mitochondria (Kamzalov *et al.*, 2003; Kudin *et al.*, 2005). Since brain mitochondria contain approximately two-fold less coenzyme Q, the relative contribution of the complex III-dependent ROS producing site is in brain mitochondria very likely lower. On the other hand, differences in activities of ROS converting enzymes are additional possible reasons for this tissue dependency.

ACKNOWLEDGMENTS

This study was supported by grants of the Deutsche Forschungsgemeinschaft (KU-911/15-1, the SBF TR3-A11, and TR3-D12) and the BMBF (01GZ0704) to W. S. K.

REFERENCES

- Azzi, A., Montecucco, C., and Richter, C. (1975). The use of acetylated ferricytochrome *c* for the detection of superoxide radicals produced in biological membranes. *Biochem. Biophys. Res. Commun.* **65**, 597–603.
- Barja, G., and Herrero, A. (1998). Localization at complex I and mechanism of the higher free radical production of brain nonsynaptic mitochondria in the short-lived rat than in the longevous pigeon. *J. Bioenerg. Biomembr.* **30**, 235–343.
- Bindokas, V. P., Jordan, J., Lee, C. C., and Miller, R. J. (1996). Superoxide production in rat hippocampal neurons: Selective imaging with hydroethidine. *J. Neurosci.* **16**, 1324–1336.
- Boveris, A., Cadenas, E., and Stoppani, A. O. (1976). Role of ubiquinone in the mitochondrial generation of hydrogen peroxide. *Biochem. J.* **156**, 435–444.
- Budd, S. L., Castilho, R. F., and Nicholls, D. G. (1997). Mitochondrial membrane potential and hydroethidine-monitored superoxide generation in cultured cerebellar granule cells. *FEBS Lett.* **415**, 21–24.
- Cadenas, E., and Davies, K. J. (2000). Mitochondrial free radical generation, oxidative stress, and aging. *Free Radic Biol. Med.* **29**, 222–230.
- Cape, J. L., Bowman, M. K., and Kramer, D. M. (2007). A semiquinone intermediate generated at the Qo site of the cytochrome *bc*₁ complex: Importance for the Q-cycle and superoxide production. *Proc. Natl. Acad. Sci. USA* **104**, 7887–7892.
- Cino, M., and Del Maestro, R. F. (1989). Generation of hydrogen peroxide by brain mitochondria: The effect of reoxygenation following postdecapitative ischemia. *Arch Biochem. Biophys.* **269**, 623–638.
- Debska, G., Kicinska, A., Skalska, J., Szweczyk, A., May, R., Elger, C. E., and Kunz, W. S. (2002). Opening of potassium channels modulates mitochondrial function in rat skeletal muscle. *Biochim. Biophys. Acta* **1556**, 97–105.
- Dynowski, M., Schaaf, G., Loque, D., Moran, O., and Ludewig, U. (2008). Plant plasma membrane water channels conduct the signaling molecule H₂O₂. *Biochem. J.* **414**, 53–61.
- Genova, M. L., Ventura, B., Giuliano, G., Bovina, C., Formiggini, G., Parenti Castelli, G., and Lenaz, G. (2001). The site of production of superoxide radical in mitochondrial Complex I is not a bound ubisemiquinone but presumably iron-sulfur cluster N2. *FEBS Lett.* **505**, 364–368.

- Grivennikova, V. G., Cecchini, G., and Vinogradov, A. D. (2008). Ammonium-dependent hydrogen peroxide production by mitochondria. *FEBS Lett.* **582**, 2719–2724.
- Kamzalov, S., Sumien, N., Forster, M. J., and Sohal, R. S. (2003). Coenzyme Q intake elevates the mitochondrial and tissue levels of coenzyme Q and alpha-tocopherol in young mice. *J. Nutr.* **133**, 3175–3180.
- Komary, Z., Tretter, L., and Adam-Vizi, V. (2008). H₂O₂ generation is decreased by calcium in isolated brain mitochondria. *Biochim. Biophys. Acta* **1777**, 800–807.
- Kudin, A. P., Bimpong-Buta, N. Y., Vielhaber, S., Elger, C. E., and Kunz, W. S. (2004). Characterization of superoxide-producing sites in isolated brain mitochondria. *J. Biol. Chem.* **279**, 4127–4135.
- Kudin, A. P., Debska-Vielhaber, G., and Kunz, W. S. (2005). Characterization of superoxide production sites in isolated rat brain and skeletal muscle mitochondria. *Biomed. Pharmacother.* **59**, 163–168.
- Kudin, A. P., Malinska, D., and Kunz, W. S. (2008). Sites of generation of reactive oxygen species in homogenates of brain tissue determined with the use of respiratory substrates and inhibitors. *Biochim. Biophys. Acta* **1777**, 689–695.
- Kunz, W. S., Kuznetsov, A. V., Clark, J., Tracey, I., and Elger, C. E. (1999). Metabolic consequences of the cytochrome *c* oxidase deficiency in brain of copper-deficient Movbr mice. *J. Neurochem.* **72**, 1580–1585.
- Lambert, A. J., and Brand, M. D. (2004). Inhibitors of the quinone-binding site allow rapid superoxide production from mitochondrial NADH: Ubiquinone oxidoreductase (complex I). *J. Biol. Chem.* **279**, 39414–39420.
- Liu, Y., Fiskum, G., and Schubert, D. (2002). Generation of reactive oxygen species by the mitochondrial electron transport chain. *J. Neurochem.* **80**, 780–787.
- Naqui, A., Chance, B., and Cadenas, E. (1986). Reactive oxygen intermediates in biochemistry. *Annu. Rev. Biochem.* **55**, 137–166.
- Starkov, A. A., Fiskum, G., Chinopoulos, C., Lorenzo, B. J., Browne, S. E., Patel, M. S., and Beal, M. F. (2004). Mitochondrial alpha-ketoglutarate dehydrogenase complex generates reactive oxygen species. *J. Neurosci.* **24**, 7779–7788.
- St-Pierre, J., Buckingham, J. A., Roebuck, S. J., and Brand, M. D. (2002). Topology of superoxide production from different sites in the mitochondrial electron transport chain. *J. Biol. Chem.* **277**, 44784–44790.
- Tretter, L., and Adam-Vizi, V. (2004). Generation of reactive oxygen species in the reaction catalyzed by alpha-ketoglutarate dehydrogenase. *J. Neurosci.* **24**, 7771–7778.
- Tretter, L., Takacs, K., Hegedus, V., and Adam-Vizi, V. (2007). Characteristics of alpha-glycerophosphate-evoked H₂O₂ generation in brain mitochondria. *J. Neurochem.* **100**, 650–663.
- Votyakova, T. V., and Reynolds, I. J. (2001). DeltaPsi(m)-dependent and -independent production of reactive oxygen species by rat brain mitochondria. *J. Neurochem.* **79**, 266–277.
- Votyakova, T. V., and Reynolds, I. J. (2004). Detection of hydrogen peroxide with Amplex Red: Interference by NADH and reduced glutathione auto-oxidation. *Arch. Biochem. Biophys.* **431**, 138–144.
- Wisniewski, E., Kunz, W. S., and Gellerich, F. N. (1993). Phosphate affects the distribution of flux control among the enzymes of oxidative phosphorylation in rat skeletal muscle mitochondria. *J. Biol. Chem.* **268**, 9343–9346.
- Wood, P. M. (1988). The potential diagram for oxygen at pH 7. *Biochem. J.* **253**, 287–289.
- Zhao, H., Joseph, J., Fales, H. M., Sokoloski, E. A., Levine, R. L., Vasquez-Vivar, J., and Kalyanaraman, B. (2005). Detection and characterization of the product of hydroethidine and intracellular superoxide by HPLC and limitations of fluorescence. *Proc. Natl. Acad. Sci. USA* **102**, 5727–5732.

QUANTIFICATION, LOCALIZATION, AND TISSUE SPECIFICITIES OF MOUSE MITOCHONDRIAL REACTIVE OXYGEN SPECIES PRODUCTION

Aaron M. Gusdon,^{*} Jing Chen,^{*} Tatyana V. Votyakova,[†]
and Clayton E. Mathews^{*}

Contents

1. Introduction	440
2. Materials and Procedures for Isolation of Mouse Mitochondria	442
2.1. Brain mitochondria	442
2.2. Liver mitochondria	443
2.3. Submitochondrial particles (SMPs)	444
3. Materials and Procedures for Quantification of Reactive Oxygen Species (ROS) Production by Mouse Mitochondria	446
3.1. ROS production by intact mitochondria	446
3.2. ROS production by alamethicin-permeabilized mitochondria	447
3.3. ROS production by SMP	449
4. Reagents and Procedures for Evaluating Ros Production by Beta Cells	450
4.1. Beta cell mitochondria isolation	451
4.2. Reactive oxygen species production (ROS) and quantification from isolated beta cell mitochondria	452
4.3. Reactive oxygen species production from intact beta cells	452
5. Concluding Remarks	453
Acknowledgments	453
References	454

^{*} Department of Pathology, Immunology, and Laboratory Medicine, College of Medicine, The University of Florida, Gainesville, Florida, USA

[†] Department of Pediatrics, School of Medicine, University of Pittsburgh, Pennsylvania, USA

Abstract

Mitochondria play a critical role in many different pathologic conditions. Increasing evidence has shown that mitochondrial reactive oxygen species (ROS) production may provide an etiologic link between mitochondria and pathologies. The widespread use of laboratory mice as models for a host of human diseases makes the quantification and localization of ROS production from mice an important endeavor. This chapter presents approaches to the quantification and localization of ROS from mouse brain, liver, and beta cell mitochondria. Techniques for the isolation of mitochondria and mitochondrial fractions and the subsequent quantification of ROS with Amplex Red or a FACS-based method on intact cells are described.

1. INTRODUCTION

The laboratory mouse plays an indispensable role in biomedical research. Mouse models have become the choice for basic and applied research because of both adaptability and the presence of highly genetically standardized inbred strains. In addition, the ability to genetically manipulate mice through transgenic, knock-out, knock-in, and tissue-specific deletion adds significant flexibility and depth to experimental design. Yet, most experiments studying mitochondrial physiology have been performed with isolated organelles from rat models. This is likely to change because of the presence of hundreds of spontaneous or genetically manipulated mouse strains with traits that are relevant to human disease.

Mitochondria have a central role in diabetes (Anunciado-Koza *et al.*, 2008; Mathews *et al.*, 2005), aging (Coussens *et al.*, 2008; Katic *et al.*, 2007), apoptosis (Katoh *et al.*, 2008; Kujoth *et al.*, 2005), cancer (Maximo *et al.*, 2008), and neurodegenerative disorders (Fukui and Moraes, 2008; Junn *et al.*, 2008; Ohsawa *et al.*, 2008). A common link shared by the aforementioned pathologic conditions is reactive oxygen species (ROS) and specifically ROS produced by the mitochondria. Although the source of mitochondrial ROS production may differ for each disease, it is likely that the mitochondrial electron transport chain (ETC) is a major contributor. Mutations or sequence variation in the mitochondrial DNA (mtDNA) can modify both the site and quantity of ROS produced by the ETC (Gusdon *et al.*, 2007, 2008; Moreno-Loshuertos *et al.*, 2006).

Complexes I and III have been identified as sites of ROS production by the ETC. Inhibitors of the ETC can be effective in determining the site of ROS production by isolated mitochondria. Rotenone, an inhibitor of the quinone binding site of complex I (Fendel *et al.*, 2008; Lambert and

Brand, 2004), is useful in assessing complex I–derived ROS production. In intact mitochondria, rotenone has contrasting effects comparing liver mitochondria to brain and beta cell mitochondria. Rotenone slightly inhibits complex I–derived ROS in liver (Gusdon *et al.*, 2008) yet increases ROS production in brain (Muller *et al.*, 2008; Votyakova and Reynolds, 2001). Complex I produces superoxide primarily into the mitochondrial matrix (Miwa and Brand, 2003; Muller *et al.*, 2004). Permeabilization of the inner membrane with the antibiotic alamethicin (Qian *et al.*, 2008) allows for a more direct measurement of complex I ROS production when assessed with Amplex Red. The production of submitochondrial particles further simplifies the system by eliminating soluble antioxidants. Complex III, the other main site of ROS production, can be readily assessed by the inhibitors antimycin A and myxothiazol (Chen *et al.*, 2003; Tretter *et al.*, 2007). Several reports have shown that antimycin A and myxothiazol increase brain mitochondrial ROS production (Chen *et al.*, 2003; Young *et al.*, 2002). However, myxothiazol and antimycin A decrease complex III ROS production from liver mitochondria from several mouse strains (Gusdon *et al.*, 2008). Complex III produces ROS on both sides of the inner mitochondrial membrane (Muller *et al.*, 2004); therefore, analysis of complex III ROS production with alamethicin permeabilized is also useful. In nonphosphorylating submitochondrial particles, electron flow from complex I to complex III is drastically inhibited (Hoppel and Cooper, 1969; Malviya *et al.*, 1968; Racker and Horstman, 1967); therefore, the use of submitochondrial particles in the analysis of complex III ROS production is not informative (Gusdon *et al.*, 2008).

It has long been considered that diseases resulting from mutations in the mitochondrial DNA (mtDNA) are rare genetic disorders. However, alterations or natural sequence variants in the mitochondrial DNA recently have been recognized to play important roles in the pathogenesis of common diseases. Although some attention has been focused on the accumulation of mitochondrial DNA mutations in somatic cells, inheritance of specific disease associated loci in the nuclear genome in combination with common polymorphisms in the mtDNA may contribute to the development of common pathologic conditions such as cancer, cardiovascular disease, diabetes, and aging. Recently, we have published that a diabetes-associated mtDNA mutation modifies ROS generation from the ETC, but that nuclear genes clearly contribute to the ROS signal. It is likely that mouse models will be exploited to better understand the role of mitochondrial ROS production in specific disease states in the near future. This chapter outlines the methods for isolating mitochondria from mouse brain, liver, and beta cells and provides experimental techniques for the quantification and localization of mitochondrial ROS production with the fluorescent dye Amplex Red and a FACS-based approach.

2. MATERIALS AND PROCEDURES FOR ISOLATION OF MOUSE MITOCHONDRIA

2.1. Brain mitochondria

Several methods have been used for the isolation of rodent brain mitochondria. Although differential centrifugation can be used to produce enriched mitochondria from many types of cells and tissues (Pallotti and Lenaz, 2007), this method produces a very crude brain mitochondrial preparation contaminated with synaptosomes and myelin (Sims, 1990; Stahl *et al.*, 1963). Therefore, other methods must be used to obtain a more pure preparation of functional brain mitochondria. Early studies used sucrose gradient centrifugation, yet this method produces mitochondria with poor metabolic parameters given the prolonged exposure to hypertonic conditions (Neidle *et al.*, 1969; Salganicoff and De Robertis, 1965). Improved techniques have used a discontinuous Ficoll gradient (Lai and Clark, 1979; Tanaka and Abhood, 1963). Recently, Sims and Anderson published a protocol that used a discontinuous Percoll gradient resulting in significant enrichment of highly functional mitochondria largely separated from synaptosomes and myelin (Sims and Anderson, 2008). This protocol can also yield distinct myelin and synaptosome bands (Sims and Anderson, 2008). The protocol outlined in the following, based on the work of Sims (Sims, 1991), used a discontinuous Percoll gradient; however, with fewer distinct Percoll concentrations. It allows for the rapid preparation of highly functional and pure mouse mitochondria yet without distinct bands for myelin and synaptosomes.

2.1.1. Materials

Mannitol, sucrose, HEPES potassium salt, fatty acid-free BSA, EDTA, and potassium hydroxide were all purchased from Sigma-Aldrich (St. Louis, MO). Percoll was from Thermo Scientific (Waltham, MA), and the BCA Protein Assay Kits were from Pierce Biotechnology (Rockford, IL).

2.1.2. Procedure for the isolation of mouse brain mitochondria

Percoll was diluted with isolation buffer I (IBI: 225 mM mannitol, 75 mM sucrose, 10 mM HEPES potassium salt, 0.10% fatty acid-free BSA, 1 mM EDTA, pH 7.4 [with KOH]) to produce stocks of 12% v/v, 24% v/v, and 42% v/v. Percoll gradients were prepared in 50 ml Oak Ridge polycarbonate high-speed centrifuge tubes (Nalgene [Thermo Scientific]) by adding 10 ml 24% Percoll, then with a 6-inch long, 18-gauge blunt-ended needle (Popper & Sons, Inc. [New Hyde Park, NY]) fitted to a 10-ml syringe (Becton Dickinson & Co [Franklin Lakes, NJ]) to layer 10 ml 42% Percoll beneath the 24% Percoll. The brain was excised (2 or more for a substantial

yield) and placed in 25 ml cold isolation buffer II (IBII: 225 mM mannitol, 75 mM sucrose, 10 mM HEPES potassium salt, 0.1 mM EDTA, pH 7.4 [with KOH]). The brain was washed once with 25 ml cold 12% Percoll. These organs were then homogenized in 15 ml 12% Percoll with a Kontes Dounce homogenizer with pestles A then B (Kimble-Chase [Vineland NJ]). With a 2-inch-long, 18-gauge blunt-ended needle (Popper & Sons, Inc.) fitted to a 10-ml syringe (Becton Dickinson & Co), the brain homogenate was gently layered on top of the Percoll gradient with the centrifuge tube tilted at a 45° angle on ice. The gradient was centrifuged in a Sorvall SS-34 rotor (Thermo Scientific) at 27,000g (15,000 rpm) for 10 min in a Sorvall RC-6 Plus (Thermo Scientific). After centrifugation, the mitochondrial fraction will be located between the 24% and 42% Percoll layers. A 2-inch-long, 18-gauge blunt-ended needle fitted to a 10-ml syringe was used to remove the waste above the mitochondrial fraction. With a clean blunt-ended needle and syringe, the mitochondrial fraction was extracted, placed in a clean 50-ml centrifuge tube, and then the 50-ml tube was filled with IBI. Mitochondria were pelleted at 10,000g (9150 rpm) for 10 min in a SS-34 rotor with a Sorvall RC-6 Plus Centrifuge. Supernatant was removed with care to not disturb the pellet, and then the pellet was suspended in 300 μ l of IBII. The resuspended pellet was then transferred to a 1.5-ml conical bottom microcentrifuge tube and pelleted again in a tabletop centrifuge at 10,000g for 5 min. The supernatant was then pipetted off and the pellet resuspended in 100 μ l IBII. Mitochondrial protein concentration was determined with the BCA protein assay. Two mouse brains typically yield greater than 3 mg of mitochondrial protein.

2.2. Liver mitochondria

The isolation of mitochondria from mouse liver presents fewer obstacles than brain and can be accomplished effectively by differential centrifugation based on the protocol outlined by Pallade and colleagues (Hogeboom *et al.*, 1948). However, contamination by small particles such as lysosomes and peroxisomes will be present to a varying extent resulting in mitochondrial preparation that is unlikely to exceed 90% purity (Graham, 2001). This mitochondrial preparation exhibits a high respiratory control ratio and functions longer than 4 h after isolation. In differential centrifugation, the initial low-speed spin pellets intact cells, cell debris, and nuclei (Pallotti and Lenaz, 2007). The second, higher speed spin pellets the mitochondria (Pallotti and Lenaz, 2007). The protocol outlined in the following uses the conventional differential centrifugation method with minor modifications. Mannitol is used in this procedure given the previously reported ability of such monosaccharides to increase mitochondrial coupling (Siess, 1983a,b). This protocol can also be applied in principle to skeletal muscle and cultured cells (Frezza *et al.*, 2007).

2.2.1. Reagents

Mannitol, sucrose, HEPES potassium salt, fatty acid-free BSA, EDTA, and potassium hydroxide were all purchased from Sigma-Aldrich (St. Louis, MO). The BCA Protein Assay Kits were from Pierce Biotechnology (Rockford, IL).

2.2.2. Procedure for the isolation of mouse liver mitochondria

The liver was excised and placed in cold IBII (225 mM mannitol, 75 mM sucrose, 10 mM HEPES potassium salt, 0.1 mM EDTA, pH 7.4 [with KOH]) in a 100-ml polypropylene beaker (Thermo Scientific). The organ was washed with 25 ml of IBI (225 mM mannitol, 75 mM sucrose, 10 mM HEPES potassium salt, 0.10% fatty acid-free BSA, 1 mM EDTA, pH 7.4 [with KOH]) and transferred into a beaker with 15-ml IBI. Blunt-ended scissors were then used to cut the liver into small pieces. These pieces were transferred into a Dounce homogenizer and homogenizer with pestles A then B, 5 strokes with each pestle. Homogenate was moved to a 50-ml Oak Ridge polycarbonate high-speed centrifuge tube (Nalgene [Thermo Scientific]) and centrifuged at 1300g for 10 min in a Sorvall SS-34 rotor with a Sorvall RC-6 Plus centrifuge. While decanting the supernatant into a 50-ml Oak Ridge polycarbonate high-speed centrifuge tube, care was taken to not disturb the pellet. The supernatant was subjected to centrifugation, 1300g (3300 rpm) in an SS-34 rotor (Sorvall) for 3 min. Afterwards, the supernatant was decanted into a clean 50-ml Oak Ridge polycarbonate high-speed centrifuge tube. This tube was then centrifuged to pellet the mitochondria at 10,000g for 10 min. The supernatant was discarded and the pellet resuspended in IBII and then transferred to a clean centrifuge tube and centrifuged at 10,000g for 5 min. The supernatant was then removed with a pipette and the pellet resuspended in 100 μ l IBII. Mitochondrial protein concentration was determined with the BCA protein assay. One liver typically yields more than 8 mg of mitochondrial protein.

2.3. Submitochondrial particles (SMPs)

Several different techniques exist for the subfractionation of mitochondria into submitochondrial particles (SMPs). The preparation of coupled or uncoupled, as well as inverted or noninverted SMPs, is possible. Typically, inverted SMPs are produced with mild sonication, whereas noninverted SMPs are produced by treatment with digitonin (Hoppel and Cooper, 1969; Malviya *et al.*, 1968; Racker and Horstman, 1967). Malviya *et al.* have published electron micrographs showing that sonicated SMPs have inverted inner membrane subunits, whereas SMPs prepared with digitonin do not, but both types of SMPs seemed to be vesicular (Malviya *et al.*, 1968).

Digitonin SMPs are believed to have the same orientation as intact mitochondria because both can establish a pH gradient and lower the pH of incubation media (Mitchell, 1966). It has been reported that a loss of bound divalent cation during the preparation of inverted, sonically prepared SMPs is responsible for some of their properties, including a lack of nucleotide specificity for ADP and ATP (Hoppel and Cooper, 1969). Indeed, it has been shown that Mg^{2+} concentrations are significantly lower in sonic particles than in digitonin particles (Cooper, 1960). However, with more vigorous sonication techniques, it is possible to prepare inverted, uncoupled SMPs. These particles are very useful when attempting to characterize the kinetic aspects of complex I (Estornell *et al.*, 1993; Pallotti and Lenaz, 2007). The submitochondrial preparation that follows is based on the procedure used by Gregg and, more recently, by Lesnefsky and colleagues (Chen *et al.*, 2003; Gregg, 1967). It involves rather drastic sonication and produces SMPs that are inverted and uncoupled. These SMPs are ideal for the purpose of ROS quantification and site localization because of their phenotypic differences from intact mitochondria and facile detection of complex I-generated ROS.

2.3.1. Reagents

4-Morpholinepropanesulfonic acid (MOPS), mannitol, sucrose, HEPES potassium salt, fatty acid-free bovine serum albumin (BSA), EDTA, and potassium hydroxide were all purchased from Sigma-Aldrich (St. Louis, MO). The BCA Protein Assay Kits were from Pierce Biotechnology (Rockford, IL).

2.3.2. Procedure for the production of SMPs

SMPs can be prepared with either fresh or frozen mitochondria. After preparation of intact brain or liver mitochondria, these organelles should be subjected to freeze and thaw. The samples should then be diluted to a concentration between 10 and 20 mg of mitochondrial protein/ml with 10 mM MOPS. In most cases the initial concentration of intact mitochondria will be low, and, therefore, several samples may need to be pooled together.

A salt-ice water bath was prepared in a Fisher Sonic Dismembrator (Thermo Scientific) to make the temperature -4° . The samples were sonicated for 20 sec at 60% maximal output and then allowed to rest for 2 min. This cycle was repeated a total of nine times. Afterwards, the samples were centrifuged at 16,000g for 10 min. Supernatants were decanted into clean centrifuge tubes and centrifuged at 150,000g for 45 min. The pellet was resuspended in IB II and the protein concentration established with the BCA protein assay.

3. MATERIALS AND PROCEDURES FOR QUANTIFICATION OF REACTIVE OXYGEN SPECIES (ROS) PRODUCTION BY MOUSE MITOCHONDRIA

Several fluorescent dyes have been used to assess the production of ROS from isolated mitochondria. Given its stability, the detection of hydrogen peroxide is very convenient and allows for real-time quantification. Scopoletin has been used for this purpose and fluoresces while reduced but loses its fluorescence after being oxidized by peroxide and horseradish peroxidase (HRP) (Boveris *et al.*, 1977; Corbett, 1989; Loschen *et al.*, 1971). More recently the use of Amplex Red has gained popularity. In contrast to scopoletin, its reduced form is not fluorescent, but after oxidation by peroxide and HRP, it becomes strongly fluorescent. The methods of ROS quantification outlined in the following uses Amplex Red-based model systems. Indeed, Amplex Red has been demonstrated to possess several advantages over scopoletin. These include increased sensitivity and a linear response over a broader range of hydrogen peroxide concentrations (Votyakova and Reynolds, 2004).

3.1. ROS production by intact mitochondria

The production of ROS by intact mitochondria is readily accomplished with Amplex Red and HRP (Votyakova and Reynolds, 2001, 2004). With intact mitochondria, substrates can be chosen that support either complex I- or complex II-mediated ROS production. NADH itself cannot be used as a complex I substrate given that it is not able to pass through the mitochondrial innermembrane. Instead, the mitochondrial glutamate-aspartate shuttle must be used to carry NADH into the matrix (Quagliariello *et al.*, 1965). To this end, glutamate and malate have been widely used.

Complex II, succinate dehydrogenase, can be assayed for ROS production with the substrate succinate. Succinate dehydrogenase is a member of the electron transport chain and also the only membrane-bound enzyme in the tricarboxylic acid cycle. Succinate dehydrogenase delivers electrons directly to the quinone pool after succinate oxidation (Cecchini, 2003; Sun *et al.*, 2005). Therefore, complex II can be directly assayed by the addition of succinate given its unique dual function. Without addition of the complex I inhibitor rotenone, reverse electron flow from complex II to complex I stimulates high levels of ROS production (Capel *et al.*, 2005; Votyakova and Reynolds, 2001). Therefore, when assessing complex II respiration, rotenone should be added to prevent a 30 to 40% underestimate

of respiratory flux because of the accumulation of oxaloacetate (Capel *et al.*, 2005; Ernster and Nordenbrand, 1967).

3.1.1. Reagents

Stocks of Amplex Red (40 mM, Fluka), rotenone (25 mM [Calbiochem]), diphenyleneiodonium chloride (DPI) (15 mM [Sigma]), myxothiazol [20 mM [Sigma]] were all prepared in dimethyl sulfoxide (DMSO) (Sigma). A 10 mM stock of 4-(hydroxymercuri)benzoic acid (CMB) (Sigma) was prepared in 0.1 M KOH, pH 8.0. Horseradish peroxidase (HRP) (Cayman) was diluted to 2500 U/ml with H₂O, and antimycin A (Sigma) was diluted to 5 mg/ml in ethanol. The incubation media for these experiments was: 125 mM KCl, 2 mM K₂HPO₄, 5 mM MgCl₂, 10 mM HEPES, 10 μM EGTA, pH 7.4, all from Sigma-Aldrich Co. Glutamate, malate, and succinate were all purchased from Sigma-Aldrich Co.

3.1.2. Procedure for assessing ROS production from intact mitochondria

Measurements of ROS production by intact mitochondria were made with a RF-5301 spectrofluorometer (Shimadzu) in a quartz cuvette with the reaction chamber heated to 37° and constantly stirred. To study electron transport from complex I or complex II the incubation media were supplemented with either 5 mM L-glutamate and 5 mM L-malate or 5 mM succinate, respectively. Amplex Red (2 μg/ml) and HRP (1 U/ml) were added to the cuvette containing incubation media and the substrates of choice. Each reaction was initiated with the addition of 0.2 mg/ml freshly isolated mitochondria. Fluorescence was measured kinetically with an excitation wavelength of 560 nm (slit 1.5 nm) and an emission wavelength of 590 nm (slit 3 mM). After the data were acquired, the slopes of the linear portions of each trace were determined. These rates were converted into pmol H₂O₂/min/mg by constructing a H₂O₂ standard curve as described (Votyakova and Reynolds, 2004).

3.2. ROS production by alamethicin-permeabilized mitochondria

Alamethicin is an antibiotic isolated from *Trichoderma viride* and consists of 20 amino acids (Mueller and Rudin, 1968) and is unusually rich in α-aminoisobutyric acid, which greatly reduces its backbone flexibility (Marshall, 1972). The membrane-altering properties of alamethicin have been widely studied in both model lipid membrane systems and physiologic systems. The effect of alamethicin on isolated mitochondria has been often studied in the context of providing a positive control for permeability

transition pore experiments. Indeed, it has been demonstrated that alamethicin increases ROS production from isolated mitochondria as does the formation of the permeability transition pore (Hansson *et al.*, 2008).

The sites and directionality of mitochondrial superoxide production have been studied in detail. It has been demonstrated that mitochondrial complex I produces superoxide exclusively into the mitochondrial matrix, whereas complex III produces superoxide at two distinct sites—generating ROS into the matrix and into the intermembrane space (St-Pierre *et al.*, 2002). The redox-sensitive dye Amplex Red does not pass through the inner membrane and enter the mitochondrial matrix (Kristian and Fiskum, 2004). Therefore, superoxide produced into the matrix must be converted into hydrogen peroxide by manganese superoxide dismutase and diffused into the intermembrane space before being detected by Amplex Red. Total ROS production detected in intact isolated mitochondria can thus be altered by the matrix concentrations of antioxidant enzymes.

Alamethicin can be used to obtain a direct reading of total mitochondrial ROS production. Treating mitochondrial with alamethicin allows for the rapid detection of complex I-derived ROS, as well as the ROS produced into the matrix by complex III (Gusdon *et al.*, 2008). Furthermore, permeabilizing mitochondria with alamethicin allows NADH to have access to its binding site within complex I. Thus, the use of substrate combinations such as glutamate and malate or pyruvate to produce NADH can be bypassed. This allows for a more direct assessment of electron transport chain-generated ROS in the context of whole mitochondria rather than isolated membrane fractions. However, NADH itself has been reported interact with HRP and produce enough peroxide by means of a free radical-mediated mechanism to substantially oxidize Amplex Red (Votyakova and Reynolds, 2004). However, the addition of superoxide dismutase (SOD) completely eliminates this reaction, perhaps because of the inhibition of a superoxide-dependent propagation step in a free radical chain reaction (Votyakova and Reynolds, 2004).

3.2.1. Reagents

Amplex Red (40 mM, Fluka), rotenone (25 mM [Calbiochem]), diphenyleneiodonium chloride (DPI) (15 mM [Sigma]), myxothiazol (20 mM [Sigma]) were all prepared in dimethyl sulfoxide (DMSO) (Sigma). A 10 mM stock of 4-(hydroxymercuri)benzoic acid (CMB) (Sigma) was prepared in 0.1 M KOH, pH 8.0. Horseradish peroxidase (HRP) (Cayman) was diluted to 2500 U/ml with H₂O. Antimycin A (5 mg/mL [Sigma]) and alamethicin (25 mg/ml [Sigma]) stocks were diluted to in ethanol. A stock of NADH (10 mM [Sigma]) was prepared in H₂O fresh before each experiment. Superoxide dismutase (SOD) (10 kU/ml [Sigma]) was

prepared in H₂O. The incubation media for these experiments was: 125 mM KCl, 2 mM K₂HPO₄, 5 mM MgCl₂, 10 mM HEPES, 10 μM EGTA, pH 7.4, all from Sigma-Aldrich Co.

3.2.2. Procedure for quantifying ROS production by alamethicin-permeabilized mitochondria

Measurements of ROS production by alamethicin-permeated mitochondria were made with a RF-5301 spectrofluorometer (Shimadzu) in a quartz cuvette with the reaction chamber heated to 37° and constantly stirred. Amplex Red (2 μg/ml), HRP (1 U/ml), and SOD (40 U/ml) were added to the cuvette containing incubation media. Each reaction was initiated with the addition of 0.2 mg/ml freshly isolated mitochondria. For control reactions, ROS production was measured for at least 2 min without added substrates followed by the addition of 80 μM NADH. Afterwards, ROS production was measured for an additional 2 min. For experimental traces, mitochondrial ROS production was first assessed in the presence of alamethicin (30 μg/ml) with no added substrates for 2 min. NADH (80 μM) was then added, and ROS production was assessed for an additional 2 min. ROS production was also measured after the addition of mitochondrial electron transport complex inhibitors to study sites of ROS production. In each case, the fluorescence was measured for 2 min after the addition of each inhibitor or combination of inhibitors. For these studies each inhibitor (rotenone [10 μM], rotenone and CMB [10 μM, each], or myxothiazol [10 μM]) was added individually or in specified combinations. Fluorescence was measured kinetically with an excitation wavelength of 560 nm (slit 1.5 nm) and an emission wavelength of 590 nm (slit 3 nm), slopes determined over the linear portions of each trace, and the rate converted into pmol H₂O₂/min/mg by constructing a H₂O₂ standard curve as described (Votyakova and Reynolds, 2004).

3.3. ROS production by SMP

The use of SMPs for the study of ROS production offers a slightly different experimental system than either intact mitochondria or alamethicin-permeabilized mitochondria. SMPs prepared by sonication have been shown to be vesicular; however, electron micrographs have indicated that the inner membrane subunits are oriented outward, whereas digitonin-treated SMPs seem to retain inward-oriented inner membrane subunits (Malviya *et al.*, 1968). Also, SMPs have been shown to be largely devoid of matrix antioxidant enzymes such as MnSOD (Raha *et al.*, 2000). Therefore, the complex I ROS signal, which is directed into the matrix, can be much more readily detected in SMPs (Chen *et al.*, 2003). Hence, SMPs

offer a similar advantage as alamethicin-permeabilized mitochondria but differ by their lack of antioxidant enzymes.

3.3.1. Reagents

Amplex Red (40 mM, Fluka), rotenone (25 mM [Calbiochem]), diphenyleneiodonium chloride (DPI) (15 mM [Sigma]), myxothiazol (20 mM [Sigma]) were all prepared in dimethyl sulfoxide (DMSO) (Sigma). A 10 mM stock of 4-(hydroxymercuri)benzoic acid (CMB) (Sigma) was prepared in 0.1 M KOH, pH 8.0. Horseradish peroxidase (HRP) (Cayman) was diluted to 2500 U/ml with H₂O. Antimycin A (5 mg/ml [Sigma]) was diluted to in ethanol. A stock of NADH (10 mM [Sigma]) was prepared in H₂O fresh before each experiment. Superoxide dismutase (SOD) (10 kU/ml [Sigma]) was prepared in H₂O. The incubation media for these experiments was: 125 mM KCl, 2 mM K₂HPO₄, 5 mM MgCl₂, 10 mM HEPES, 10 μM EGTA, pH 7.4, all from Sigma-Aldrich Co.

3.3.2. Procedure to measure ROS production by SMPs

Measurements of ROS production by alamethicin-permeated mitochondria were made with a RF-5301 spectrofluorometer (Shimadzu) in a quartz cuvette with the reaction chamber heated to 37° and constantly stirred. Amplex Red (2 μg/ml), HRP (1 U/ml), and SOD (40 U/ml) were added to the cuvette containing incubation media with either 5 mM succinate or no substrates. Each reaction was started by the addition of 0.05 mg/ml to 0.2 mg/ml SMPs and the rate of ROS production recorded for at least 2 min. For reactions without substrates, 80 μM NADH was added and the rate of ROS production recorded for an additional 2 min. At this time ETS inhibitors were added (rotenone [10 μM], rotenone and CMB [10 μM, each], or myxothiazol [10 μM]) record the rate of ROS production obtained for at least an additional 2 min. The slopes of the linear portions of each trace were determined and converted into pmol H₂O₂/min/mg by constructing a H₂O₂ standard curve as described (Votyakova and Reynolds, 2004).

4. REAGENTS AND PROCEDURES FOR EVALUATING ROS PRODUCTION BY BETA CELLS

Beta cell mitochondrial ROS production has been implicated in the pathogenesis of type 1 and 2 diabetes. An increase in mitochondrial ROS production induced by hyperglycemia has been implicated as the link between elevated blood glucose and pathologic damage (Rolo and Palmeira, 2006). Indeed, mitochondrial ROS production has been shown

to cause DNA damage leading to poly(ADP-ribose) polymerase activation and subsequently GAPDH inhibition. This leads to increased flux through the hexosamine pathway, advanced glycation end-product formation, polyol pathway flux, and increased activation of PKC isoforms—the main pathways of hyperglycemia-induced pathosis (Du *et al.*, 2003).

Recently, our group has demonstrated that an allele of *mt-Nd2* associated with resistance against type 1 diabetes causes decreased mitochondrial ROS production in mice (Gusdon *et al.*, 2007, 2008). However, isolation of mitochondria from primary islet cells would require the use of far too many mouse islet donors for practical purposes. However, the pancreatic beta cell line (NIT-1) derived from the non-obese diabetic (NOD) mouse has been in use for more than 15 y (Hamaguchi *et al.*, 1991). Use of flow cytometry with the mitochondrial superoxide specific dye MitoSOX red is an effective way to determine ROS production from beta cell lines. In the following, we outline a protocol based on the work of Mukhopadhyay *et al.* (2007) with minor modifications for use of MitoSOX Red and flow cytometry to detect beta cell ROS production.

4.1. Beta cell mitochondria isolation

Characterizing the physiology of isolated beta cell mitochondria is an important question in type 1 and 2 diabetes. However, considering that the mouse pancreas contains somewhat more than 1000 islets and each islet contains 1000 cells (Takahashi *et al.*, 2007), isolation of a usable quantity of mitochondria from primary islets would require far too many mouse donors for practical purposes. The use of cell lines as a source of mitochondria represents a practical alternative. In the following, a differential centrifugation procedure for the isolation of mitochondria from beta cell lines is outlined.

4.1.1. Reagents

Mannitol, sucrose, HEPES potassium salt, fatty acid-free BSA, EDTA, and potassium hydroxide were all purchased from Sigma-Aldrich (St. Louis, MO). Percoll was from Thermo Scientific (Waltham, MA) and the BCA Protein Assay Kits were from Pierce Biotechnology (Rockford, IL). Hanks' balanced salt solution (HBSS) was purchased from BioWhittaker (Lonza, Basel, Switzerland). For these experiments, as well as those described previously, two isolation buffers were used: isolation buffer I (IBI): 225 mM mannitol, 75 mM sucrose, 10 mM HEPES potassium salt, 0.1% fatty acid-free BSA, 1 mM EDTA, pH 7.4 (with KOH), and isolation buffer II (IBII): 225 mM mannitol, 75 mM sucrose, 10 mM HEPES potassium salt, 0.1 mM EDTA, pH 7.4 (with KOH).

4.1.2. Procedure for isolating mitochondria from beta cell lines

For the following techniques we have used the NOD insulinoma tumor 1 (NIT-1) cell line. NIT-1 cells were grown to confluence in 15 75-cm² cell culture filter flasks. Media were aspirated and cells washed with 5 ml HBSS. Cells were scraped in 5 ml HBSS until all were dissociated. Cells were then collected in 50-ml conical tubes. Each flask was washed with another 5 ml HBSS and collected in the same conical tubes. Cells were pelleted at 1200 rpm for 10 min in a Sorvall Legend RT. Pellets were saved, resuspended in IBI, and transferred into a Dounce homogenizer. Cells were homogenized with pestles A then B, 5 strokes per pestle. Homogenate was then transferred to 50-ml polycarbonate centrifuge tubes (Nalgene Oak Ridge High-Speed) and centrifuge at 1300g (3300 rpm) in an SS-34 rotor (Sorvall) for 10 min. Supernatant was decanted into a clean centrifuge tube and centrifuged at 10,000g for 10 min. Afterward the supernatant was discarded and the pellet resuspended in IBII. The suspension was then transfer to a 1.5-ml Eppendorf tube and centrifuged at 10,000g for 5 min. Pellets were then resuspended in 100 μ l IBII. Protein concentration was determined with the BCA protein assay. Fifteen confluent flasks typically yield more than 2 mg of mitochondrial protein.

4.2. Reactive oxygen species production (ROS) and quantification from isolated beta cell mitochondria

To assess ROS production from isolated beta cell mitochondria the protocols detailed under [section 3](#) can be used. It is feasible to obtain enough mitochondria to measure ROS from intact and alamethicin-permeated mitochondria. We have never attempted to produce beta cell SMPs because of the amount of starting material necessary to generate enough beta cell SMPs for experimental purposes.

4.3. Reactive oxygen species production from intact beta cells

4.3.1. Reagents

Hanks' balanced salt solution (HBSS) was purchased from BioWhittaker. MitoSox Red, 2',7'-dichlorodihydrofluorescein diacetate (2',7'-dichloro-fluorescein diacetate; H2DCFDA), Sytox Green, and 0.25% trypsin-EDTA were from Invitrogen (Carlsbad, CA), annexin V was obtained from eBioscience (San Diego, CA), and 7-AAD was purchased from BD Bioscience. Annexin V binding buffer (10 mM HEPES, pH 7.4, 140 mM NaCl, 2.5 mM CaCl₂, 2% heat-inactivated FBS).

4.3.2. Procedure for determining ROS production by intact beta cells

In 25-cm² cell culture flasks 1.5×10^6 beta cells were plated. Cells were allowed to adhere for 24 to 48 h. Cells were incubated with 5 μ M MitoSOX Red or 5 μ M H₂DCFDA in the culture media for 1 h or 15 min, respectively, at 37°, whereas control cells were left untreated. Caution: Avoid exposure to light. After the labeling period, media was aspirated and cells washed with 5 ml HBSS. Cells were then dissociated with 1.5 ml 0.25% trypsin-EDTA for approximately 5 min at room temperature. Caution: Use of enzyme-free cell dissociation buffer results in a larger fraction of dead cells. Afterwards 2 ml of culture buffer was added to stop trypsinization. Cells were collected by centrifuging at 1200 rpm for 5 min in a Sorvall Legend RT and washed twice with 1.5 ml annexin V binding buffer. The pellets were resuspended in 1.5 ml of annexin-V binding buffer, and the cells counted with a Fisher Brand Hemocytometer. Cells, 5×10^5 in 500 μ l, were then placed into sterile 12 \times 75-mm polystyrene tubes (BD Falcon). Cells were stained with annexin V (5 μ l) and either Sytox Green (1 μ l) or 7-AAD (5 μ l) for the detection of dead and apoptotic cells. Results were collected with a FACSCalibur (BD Biosciences). With MitoSOX Red we collected events with FL-2 and -3 to collect MitoSOX Red, FL-1 for Sytox Green, and FL-4 for annexin V. With H₂DCFDA we collected events with FL-1 for H₂DCFDA, FL-3 for 7-AAD, and FL-4 for annexin V. *Note:* We have not observed an increase in beta cell ROS production with antimycin A.

5. CONCLUDING REMARKS

Mice are the most widely used models of human disease in biomedical research. The elegant technology available to modify mice genetically coupled with the ability to assemble these genetic modifications with well-described and accepted mouse models presents an effective system to better understand disease mechanisms. Because free radical production has been implicated in a wide variety of pathologic conditions, the attributes of mouse systems make them well suited to better understand the contribution of mitochondrial ROS production in both health and disease. To this end we hope that the techniques and tips described herein will assist researchers to accurately measure the quantity and site of ROS production in their model system.

ACKNOWLEDGMENTS

This work was supported by grants to C. E. M. from the National Institute of Health (DK074656 and AI056374), the Juvenile Diabetes Research Foundation, as well as the Sebastian Family Endowment for Diabetes Research.

REFERENCES

- Anunciado-Koza, R., Ukropec, J., Koza, R. A., and Kozak, L. P. (2008). Inactivation of UCP1 and the glycerol phosphate cycle synergistically increase energy expenditure to resist diet-induced obesity. *J. Biol. Chem.* **283**, 27688–27697.
- Boveris, A., Martino, E., and Stoppani, A. O. (1977). Evaluation of the horseradish peroxidase-scopoletin method for the measurement of hydrogen peroxide formation in biological systems. *Anal. Biochem.* **80**, 145–158.
- Capel, F., Rimbart, V., Lioger, D., Diot, A., Rousset, P., Patureau Mirand, P., Boirie, Y., Morio, B., and Bosoni, L. (2005). Due to reverse electron transfer, mitochondrial H₂O₂ release increases with age in human vastus lateralis muscle although oxidative capacity is preserved. *Mech. Ageing Dev.* **126**, 505–511.
- Cecchini, G. (2003). Function and structure of Complex II of the respiratory chain. *Annu. Rev. Biochem.* **72**, 77–109.
- Chance, B., and Williams, G. R. (1955). Respiratory enzymes in oxidative phosphorylation. I. Kinetics of oxygen utilization. *J. Biol. Chem.* **217**, 383–393.
- Chen, Q., Vazquez, E. J., Moghaddas, S., Hoppel, C. L., and Lesnefsky, E. J. (2003). Production of reactive oxygen species by mitochondria: Central role of complex III. *J. Biol. Chem.* **278**, 36027–36031.
- Cooper, C. (1960). The stimulation of adenosine triphosphate in submitochondrial particles by sulfhydryl reagents. *J. Biol. Chem.* **235**, 1815–1819.
- Corbett, J. T. (1989). The scopoletin assay for hydrogen peroxide. A review and better method. *J. Biochem. Biophys. Methods* **18**, 297–307.
- Coussens, M., Maresh, J. G., Yanagimachi, R., Maeda, G., and Allsopp, R. (2008). Sirt1 deficiency attenuates spermatogenesis and germ cell function. *PLoS ONE* **3**, e1571.
- Du, X., Matsumura, T., Edelstein, D., Rossetti, L., Zsengeller, Z., Szabo, C., and Brownlee, M. (2003). Inhibition of GAPDH activity by poly(ADP-ribose) polymerase activates three major pathways of hyperglycemic damage in endothelial cells. *J. Clin. Invest.* **112**, 1049–1057.
- Ernster, L., and Nordenbrand, K. (1967). Skeletal muscle mitochondria. *Methods Enzymol.* **10**, 86–94.
- Estornell, E., Fato, R., Pallotti, F., and Lenaz, G. (1993). Assay conditions for the mitochondrial NADH: Coenzyme Q oxidoreductase. *FEBS Lett.* **3323**, 127–131.
- Fendel, U., Tocilescu, M. A., Kersch, S., and Brandt, U. (2008). Exploring the inhibitor binding pocket of respiratory complex I. *Biochim. Biophys. Acta* **1777**, 660–665.
- Frezza, C., Cipolat, S., and Scorrano, L. (2007). Organelle isolation: functional mitochondria from mouse liver, muscle and cultured fibroblasts. *Nat. Protoc.* **2**, 287–295.
- Fukui, H., and Moraes, C. T. (2008). The mitochondrial impairment, oxidative stress and neurodegeneration connection: Reality or just an attractive hypothesis? *Trends Neurosci.* **31**, 251–256.
- Gnaiger, E., Méndez, G., and Hand, S. C. (2000). High phosphorylation efficiency and depression of uncoupled respiration in mitochondria under hypoxia. *Proc. Natl. Acad. Sci. USA* **97**, 11080–11085.
- Graham, J. M. (2001). Isolation of mitochondria from tissues and cells by differential centrifugation. *Curr. Protoc. Cell Biol.* **3**, 3.3.1–3.3.15.
- Gregg, C. T. (1967). Preparation and assay of phosphorylating submitochondrial particles: Particles from rat liver prepared by drastic sonication. *Methods Enzymol.* **10**, 181–185.
- Gusdon, A. M., Votyakova, T., Reynolds, I. V., and , E. M. C. (2007). Nuclear and mitochondrial interaction involving *mt-Nd2* leads to increased mitochondrial reactive oxygen species production. *J. Biol. Chem.* **282**, 5171–5179.

- Gusdon, A. M., Votyakova, T. V., and Mathews, C. E. (2008). mt-Nd2a suppresses reactive oxygen species production by mitochondrial complexes I and III. *J. Biol. Chem.* **283**, 10690–10697.
- Hamaguchi, K., Gaskins, H. R., and Leiter, E. H. (1991). NIT-1, a pancreatic β cell line established from a transgenic NOD/Lt mouse. *Diabetes*. **40**, 842–849.
- Hansson, M. J., Månsson, R., Morota, S., Uchino, H., Kallur, T., Sumi, T., Ishii, N., Shimazu, M., Keep, M. F., Jegorov, A., and Elmér, E. (2008). Calcium-induced generation of reactive oxygen species in brain mitochondria is mediated by permeability transition. *Free Radic. Biol. Med.* **45**, 284–294.
- Hogeboom, G. H., Schneider, W. C., and Pallade, G. E. (1948). Cytochemical studies of mammalian tissues. I. Isolation of intact mitochondria from rat liver; some biochemical properties of mitochondria and submicroscopic particulate material. *J. Biol. Chem.* **172**, 619–635.
- Hoppel, C., and Cooper, C. (1969). Studies on the nucleoside specificity of mitochondrial inner membrane particles. *Arch. Biochem. Biophys.* **135**, 184–193.
- Junn, E., Jang, W. H., Zhao, X., Jeong, B. S., and Mouradian, M. M. (2008). Mitochondrial localization of DJ-1 leads to enhanced neuroprotection. *J. Neurosci. Res.* Epub ahead of print.
- Katic, M., Kennedy, A. R., Leykin, I., Norris, A., McGettrick, A., Gesta, S., Russell, S. J., Bluher, M., Maratos-Flier, E., and Kahn, C. R. (2007). Mitochondrial gene expression and increased oxidative metabolism: role in increased lifespan of fat-specific insulin receptor knock-out mice. *Aging Cell* **6**, 827–839.
- Katoh, I., Sato, S., Fukunishi, N., Yoshida, H., Imai, T., and Kurata, S. I. (2008). Apaf-1-deficient fog mouse cell apoptosis involves hypo-polarization of the mitochondrial inner membrane, ATP depletion and citrate accumulation. *Cell Res.* Epub ahead of print.
- Kristian, T., and Fiskum, G. (2004). A fluorescence-based technique for screening compounds that protect against damage to brain mitochondria. *J. Biol. Chem.* **277**, 176–182.
- Kujoth, G. C., Hiona, A., Pugh, T. D., Someya, S., Panzer, K., Wohlgemuth, S. E., Hofer, T., Seo, A. Y., Sullivan, R., Jobling, W. A., et al. (2005). Mitochondrial DNA mutations, oxidative stress, and apoptosis in mammalian aging. *Science* **309**, 481–484.
- Lai, J. C. K., and Clark, J. B. (1979). Preparation of synaptic and non-synaptic mitochondria from mammalian brain. *Methods Enzymol.* **55**, 51–60.
- Lambert, A. J., and Brand, M. D. (2004). Inhibitors of the quinone-binding site allow rapid superoxide production from mitochondrial NADH: Ubiquinone oxidoreductase (complex I). *J. Biol. Chem.* **279**, 39414–39420.
- Lemasters, J. J. (1984). The ATP-to-oxygen stoichiometries of oxidative phosphorylation by rat liver mitochondria. *J. Biol. Chem.* **259**, 13123–13130.
- Loschen, G., Flohé, L., and Chance, B. (1971). Respiratory chain linked H₂O₂ production in pigeon heart mitochondria. *FEBS Lett.* **18**, 261–264.
- Malviya, A. N., Parsa, B., Yodaiken, R. E., and Elliott, W. B. (1968). Ultrastructure of sonic and digitonin fragments from beef heart mitochondria. *Biochim. Biophys. Acta* **162**, 195–209.
- Marshall, G. R. B., and , H. E. (1972). Angiotensin II. Studies on the biologically active conformation. *Circ. Res.* **31**(Suppl 2), 143–150.
- Mathews, C. E., Leiter, E. H., Spirina, O., Bykhovskaya, Y., Gusdon, A. M., Ringquist, S., and Fischel-Ghodsian, N. (2005). mt-Nd2 Allele of the ALR/Lt mouse confers resistance against both chemically induced and autoimmune diabetes. *Diabetologia* **48**, 261–267.
- Maximo, V., Lima, J., Soares, P., Silva, A., Bento, I., and Sobrinho-Simoes, M. (2008). GRIM-19 in Health and Disease. *Adv. Anat. Pathol.* **15**, 46–53.
- Mitchell, P. (1966). Chemiosmotic coupling in oxidative and photosynthetic phosphorylation. *Biol. Rev. Camb. Philos. Soc.* **41**, 445–502.

- Miwa, S., and Brand, M. D. (2003). Mitochondrial matrix reactive oxygen species production is very sensitive to mild uncoupling. *Biochem. Soc. Trans.* **31**, 1300–1301.
- Moreno-Loshuertos, R., Acín-Pérez, R., Fernández-Silva, P., Movilla, N., Pérez-Martos, A. R. d. C. S., Gallardo, M. E., and Enríquez, J. A. (2006). Differences in reactive oxygen species production explain the phenotypes associated with common mouse mitochondrial DNA variants. *Nat. Genet.* **38**, 1261–1268.
- Mueller, P., and Rudin, D. O. (1968). Action potentials induced in biomolecular lipid membranes. *Nature* **217**, 713–719.
- Mukhopadhyay, P., Rajesh, M., Haskó, G., Hawkins, B. J., Madesh, M., and Pacher, P. (2007). Simultaneous detection of apoptosis and mitochondrial superoxide production in live cells by flow cytometry and confocal microscopy. *Nat. Protoc.* **2**, 2295–2301.
- Muller, F., Liu, Y. J., and Van Remmen, H. (2004). Complex III Releases Superoxide to both side of the inner mitochondrial membrane. *J. Biol. Chem.* **47**, 49064–49073.
- Muller, F. L., Liu, Y. J., Abdul-Ghani, M. A., Lustgarten, M. S., Bhattacharya, A., Jang, Y. C., and Van Remmen, H. (2008). High rates of superoxide production in skeletal-muscle mitochondria respiring on both complex I- and complex II-linked substrates. *Biochem. J.* **409**, 491–499.
- Neidle, A., van den Berg, C. J., and Grynbaum, A. (1969). The heterogeneity of rat brain mitochondria isolated on continuous sucrose gradients. *J. Neurochem.* **16**, 225–234.
- Ohsawa, I., Nishimaki, K., Murakami, Y., Suzuki, Y., Ishikawa, M., and Ohta, S. (2008). Age-dependent neurodegeneration accompanying memory loss in transgenic mice defective in mitochondrial aldehyde dehydrogenase 2 activity. *J. Neurosci.* **28**, 6239–6249.
- Pallotti, F., and Lenaz, G. (2007). Isolation and subfractionation of mitochondria. *Methods Cell Biol.* **80**, 3–44.
- Qian, S., Wang, W., Yang, L., and Huang, H. W. (2008). Structure of the alamethicin pore reconstructed by x-ray diffraction analysis. *Biophys. J.* **94**, 3512–3522.
- Quagliariello, E., Papa, S., Saccone, C., Palmieri, F., and Francavilla, A. (1965). The oxidation of glutamate by rat-liver mitochondria. *Biochem. J.* **95**, 742–748.
- Racker, E., and Horstman, L. L. (1967). Partial resolution of the enzymes catalyzing oxidative phosphorylation. *J. Biol. Chem.* **242**, 2547–2551.
- Raha, S., McEachern, G. E., Myint, A. T., and Robinson, B. H. (2000). Superoxides from mitochondrial complex III: The role of manganese superoxide dismutase. *Free Radical Biol. Med.* **29**, 170–180.
- Rolo, A. P., and Palmeira, C. M. (2006). Diabetes. and mitochondrial function: Role of hyperglycemia and oxidative stress. *Toxicol. App. Pharmacol.* **212**, 167–178.
- Salganicoff, L., and De Robertis, E. (1965). Subcellular distribution of the enzymes of the glutamic acid, glutamine and gamma-aminobutyric acid cycles in rat brain. *J. Neurochem.* **12**, 287–309.
- Siess, E. A. (1983a). Different actions of mono- and disaccharides on rat liver mitochondria. *Hoppe Seylers Z. Physiol. Chem.* **364**, 835–838.
- Siess, E. A. (1983b). Influence of isolation media on the preservation of mitochondrial function. *Hoppe Seylers Z. Physiol. Chem.* **364**, 279–289.
- Sims, N. R. (1990). Rapid isolation of metabolically active mitochondria from rat brain and subregions using Percoll density gradient centrifugation. *J. Neurochem.* **55**, 698–707.
- Sims, N. R. (1991). Selective impairment of respiration in mitochondria isolated from brain subregions following transient forebrain ischemia in the rat. *J. Neurochem.* **56**, 1836–1844.
- Sims, N. R., and Anderson, M. F. (2008). Isolation of mitochondria from rat brain using Percoll density gradient centrifugation. *Nat. Protoc.* **3**, 1228–1239.
- St-Pierre, J., Buckingham, J. A., Roebeck, S. J., and Brand, M. D. (2002). Topology of superoxide production from different sites in the mitochondrial electron transport chain. *J. Biol. Chem.* **277**, 44784–44790.

- Stahl, W. L., Smith, J. C., Napolitano, L. M., and Basford, R. E. (1963). Brain mitochondria I. Isolation of brain mitochondria. *J. Biol. Chem.* **19**, 293–307.
- Sun, F., Huo, X., Zhai, Y., Wang, A., Xu, J., Su, D., Bartlam, M., and Rao, Z. (2005). Crystal structure of mitochondrial respiratory membrane protein Complex II. *Cell* **121**, 1043–1057.
- Takahashi, R., Ishihara, H., Takahashi, K., Tamura, A., Yamaguchi, S., Yamada, T., Katagiri, H., and Oka, Y. (2007). Efficient and controlled gene expression in mouse pancreatic islets by arterial delivery of tetracycline-inducible adenoviral vectors. *J. Mol. Endocrinol.* **38**, 127–136.
- Tanaka, R., and Abhood, L. G. (1963). Isolation of rat brain mitochondria devoid of glycolytic activity. *J. Neurochem.* **10**, 571–576.
- Tretter, L., Takacs, K., Hegedus, V., and Adam-Vizi, V. (2007). Characteristics of alpha-glycerophosphate-evoked H₂O₂ generation in brain mitochondria. *J. Neurochem.* **100**, 650–663.
- Votyakova, T. V., and Reynolds, I. J. (2001). DeltaPsi(m)-Dependent and -independent production of reactive oxygen species by rat brain mitochondria. *J. Neurochem.* **79**, 266–277.
- Votyakova, T. V., and Reynolds, I. J. (2004). Detection of hydrogen peroxide with Amplex Red: Interference by NADH and reduced glutathione auto-oxidation. *Arch. Biochem. Biophys.* **431**, 138–144.
- Young, T. A., Cunningham, C. C., and Bailey, S. M. (2002). Reactive oxygen species production by the mitochondrial respiratory chain in isolated rat hepatocytes and liver mitochondria: Studies using myxothiazol. *Arch. Biochem. Biophys.* **405**, 65–72.

ANALYSIS OF ELECTRON TRANSFER AND SUPEROXIDE GENERATION IN THE CYTOCHROME bc_1 Complex

Linda Yu,^{*} Shaoqing Yang,^{*} Ying Yin,^{*} Xiaowei Cen,^{*} Fei Zhou,^{*} Di Xia,[†] and Chang-An Yu^{*}

Contents

1. Introduction	460
2. Materials	461
3. Purification of the Cytochrome bc_1 Complex from Bovine Heart Submitochondrial Particles	462
3.1. Preparation of submitochondrial particles (SMP) from frozen bovine heart muscles	462
3.2. Preparation of succinate: cytochrome c oxidoreductase from SMP	463
3.3. Preparation of cytochrome bc_1 particles from succinate: cytochrome c oxidoreductase	464
3.4. Preparation of cyt bc_1 complex from cyt bc_1 particles	464
4. Electron Transfer Activity in the Purified bc_1 Complex	465
5. Proton Translocation in the Purified bc_1 Complex	466
6. Superoxide Generation by the Purified bc_1 Complex	467
7. Comparison of $O_2^{\bullet-}$ Production by the bc_1 Complexes with Varying Electron Transfer Activities	468
Acknowledgments	470
References	471

Abstract

During the electron transfer through the cytochrome bc_1 complex (ubiquinol-cytochrome c oxidoreductase or complex III), protons are translocated across the membrane, and production of superoxide anion radicals ($O_2^{\bullet-}$) is observed. The bc_1 complex is purified from broken mitochondrial preparation prepared from frozen heart muscles by repeated detergent solubilization and salt

^{*} Department of Biochemistry and Molecular Biology, Oklahoma State University, Stillwater, Oklahoma, USA

[†] Laboratory of Cell Biology, Center for Cancer Research, National Cancer Institute, National Institutes of Health, Bethesda, Maryland, USA

fractionation. The electron transfer of the purified complex is determined spectrophotometrically. The activity depends on the choice of detergent, protein concentration, and ubiquinol derivatives used. The proton translocation activity of $2\text{H}^+/\text{e}^-$ is determined in the reconstituted bc_1 -PL vesicles. The $\text{O}_2^{\bullet-}$ production by bc_1 is determined by measuring the chemiluminescence of the 2-methyl-6-(*p*-methoxyphenyl)-3,7-dihydroimidazol[1,2-1]pyrazin-3-one hydrochloride (MCLA)- $\text{O}_2^{\bullet-}$ adduct during a single turnover of bc_1 complex, with the Applied Photophysics stopped-flow reaction analyzer SX.18MV, by leaving the excitation light source off and registering the light emission. Production of $\text{O}_2^{\bullet-}$ by bc_1 is in an inverse relationship to its electron transfer activity. Inactivation of the bc_1 complex by incubating at elevated temperature (37 °C) or by treatment with proteinase K results in an increase in $\text{O}_2^{\bullet-}$ -generating activity to the same level as that of the antimycin A-inhibited complex. These results suggest that the structural integrity of protein subunits is not required for $\text{O}_2^{\bullet-}$ -generating activity in the bc_1 complex.

1. INTRODUCTION

The mitochondrial electron transport chain is a major intracellular source of superoxide anion radical ($\text{O}_2^{\bullet-}$) production (Chance *et al.*, 1979). The cytochrome bc_1 complex (ubiquinol: cytochrome *c* oxidoreductase, or complex III) has been identified as one of the major $\text{O}_2^{\bullet-}$ production sites in the mitochondrial respiratory chain (McLennan and Esposti, 2000; Turrens and Boeris, 1980; Turrens *et al.*, 1985). The cytochrome bc_1 complex (bc_1) is a multisubunit integral membrane protein complex that catalyzes electron transfer from ubiquinol to cyt *c* with concomitant translocation of protons across the membrane to generate a membrane potential and proton gradient for ATP synthesis (Trumpower and Gennis, 1994). This complex has been purified and its 3-D structure determined (Iwata *et al.*, 1998; Xia *et al.*, 1997, 2007).

The purified bovine bc_1 complex is in a dimeric and oxidized form. Each monomer contains a full complement of all 11 protein subunits (3 redox subunits and 8 supernumerary subunits) with a slight excess of cyt c_1 . Three redox subunits are essential and found in the bc_1 complex from different species: the cyt *b* subunit housing hemes b_L and b_H (low and high potential hemes), the cyt c_1 subunit containing a heme c_1 , and the iron sulfur protein (ISP) housing a high potential 2Fe-2S cluster. All additional subunits, referred to as supernumerary subunits, are believed to contribute to the increased stability of these complexes (Ljungdahl *et al.*, 1987; Yu *et al.*, 1999). The absorption ratio of Soret over UV is approximately 0.95 in the purified preparation compared with that in crystalline form of 0.88 (Yue *et al.*, 1991). The purified complex catalyzes electron transfer from ubiquinol to cyt *c* with a specific activity of 24 μmol cyt *c* reduced per nmol cyt *b* at room

temperature, pH 7.4, with 2,3-dimethoxy-5-methyl-6-(10-bromodecyl)-1,4-benzoquinol ($Q_0C_{10}BrH_2$) as the substrate. When the complex is embedded in phospholipid vesicles, it translocates 2 H^+ per electron transferred. This preparation is very stable; it lasts for days at 0° or months at $-80^\circ C$ without activity loss. Thus, it is suitable for crystallization in the presence or absence of inhibitors. The crystals grown from this preparation diffracted X-rays up to 2.1 Å resolution at best (Esser *et al.*, 2006).

Production of $O_2^{\bullet -}$ during electron transfer through the bc_1 complex is thought to result from leakage of electrons from their normal pathways to react with molecular oxygen. Under normal catalytic conditions, only a very small number of electrons leak from the complex to form $O_2^{\bullet -}$ (Sun and Trumpower 2003; Zhang *et al.*, 1998). This $O_2^{\bullet -}$ -generating activity increases when the electron transfer is blocked by antimycin or when the electron transport chain becomes overreduced (Zhang *et al.*, 1998). The electron leakage (or superoxide production) site has been speculated at ubisemiquinone of the Qp site (Dröse and Brandt, 2008; Muller *et al.*, 2003) or reduced cytochrome b_L (Nohl and Jordan, 1986; Yang *et al.*, 2008), depending on the mechanism by which bifurcation of ubiquinol proceeds in the Q-cycle model (Brandt and Trumpower, 1994; Crofts, 2004; Mitchell, 1976; Yu *et al.*, 2008). If bifurcation of quinol at the Qp site proceeds by the sequential mechanism, semiquinone formed at the Qp site (Cape *et al.*, 2007; De Vries *et al.*, 1981) and reduced heme b_L would both be the electron leakage sites during bc_1 catalysis. If bifurcation of ubiquinol at the Qp site proceeds by the concerted mechanism (Snyder *et al.*, 2000; Zhu *et al.*, 2007), reduced heme b_L would be the only electron leakage site.

This chapter describes methods for measuring the electron transfer, proton translocation, and $O_2^{\bullet -}$ production activities in the cytochrome bc_1 complex. In addition, a large-scale preparation of the cytochrome bc_1 complex from frozen heart muscles is described. A reversed relationship between electron transfer activity and $O_2^{\bullet -}$ production activity in the bc_1 complex is established.

2. MATERIALS

Fresh beef hearts were obtained from Wellington Quality Meat Company at Wellington, Kansas; sodium cholate, deoxycholic acid, cytochrome c (horse heart, type III), superoxide dismutase, antimycin A, valinomycin, and alectin were from Sigma. Proteinase K was from Invitrogen. MCLA was from Molecular Probes Inc. n-Dodecyl- β -D-maltopyranoside (DM) was from Antrace. 2,3-Dimethoxy-5-methyl-6-geranyl-1,4-benzoquinol (Q_2H_2), 2,3-dimethoxy-5-methyl-6-isoprenyl-1,4-benzoquinol (Q_1H_2),

2,3-dimethoxy-5-methyl-6-heptyl-1,4-benzoquinol ($Q_0C_7H_2$), 2,3-dimethoxy-5-methyl-6-decyl-1,4-benzoquinol ($Q_0C_{10}H_2$), and 2,3-dimethoxy-5-methyl-6-(10-bromodecyl)-1,4-benzoquinol ($Q_0C_{10}BrH_2$) were prepared as previously reported (Yu and Yu, 1982). The His₆-tagged four-subunit wild-type complex (Tian *et al.*, 1998), the three-subunit core complex (the complex lacking subunit IV) (Tso *et al.*, 2000), and the [ISP (H131C, H152C)] mutant complex (the complex lacking the iron-sulfur cluster) (Gurung *et al.*, 2005) from *Rhodobacter sphaeroides* were prepared according to methods previously reported. All other chemicals were of the highest purity commercially available.

3. PURIFICATION OF THE CYTOCHROME *bc*₁ COMPLEX FROM BOVINE HEART SUBMITOCHONDRIAL PARTICLES

3.1. Preparation of submitochondrial particles (SMP) from frozen bovine heart muscles

Bovine hearts removed from carcasses of the slaughtered animals were immediately immersed in an ice water bath and transported to the laboratory. The fat tissues and vesicular tubes were trimmed off; chunks of neat muscles approximately 1 to 2 inches in size were put into plastic bags, 10 pounds each, and placed in a -20° freezer. A bag of frozen meat was taken out from the freezer and thawed by placing it at room temperature for 2 h and then in the cold room overnight. The thawed meat was passed through a meat grinder in a cold room. The ground meat was divided into portions of 600 g each. Each portion was mixed with 1.8 L of 10 mM K_2HPO_4 in a Warren blender and homogenized at high speed for two 30-sec periods. A 6 to 10 ml amount of 6 N NaOH was added during blending to maintain the pH at 6.8 to 7.0. The blended mixtures were combined and centrifuged at 1600g for 15 min and the supernatant was poured through an eight-layer cheesecloth. The pellets were resuspended in half of the volume of 20 mM K/Na-phosphate buffer, pH 7.4, and centrifuged at 1600g for 15 min. The supernatants were again collected in the same manner as the first centrifugation step, and all supernatants were combined and divided into two portions. The supernatants were acidified to pH 5.5 with 2 N acetic acid and centrifuged immediately at 3300g for 20 min. The precipitates were immediately washed with a half volume of 20 mM K/Na-phosphate buffer and centrifuged at 3300g for 25 min. The precipitates, referred to as the submitochondrial particles (SMP) or broken mitochondria, were homogenized in 0.1 M phosphate-borate buffer, pH 7.8, to a cyt *b* concentration of approximately 11 μM (4 to 5 L) and stored in a cold room 3 to 4 days before proceeding to the preparation of succinate: cytochrome *c* oxidoreductase.

3.2. Preparation of succinate: cytochrome *c* oxidoreductase from SMP

SMP, aged for 3 to 4 days, were stirred in a cold room for 20 h before 45 ml of a 20% sodium cholate solution was slowly added for every liter of SMP. Pulverized ammonium sulfate (AS), 21.2 g/100 ml of solubilized SMP (37.5% saturation), was slowly added under constant stirring and, after the addition, the stirring continued for another 20 min. The mixture was then centrifuged at 14,000g for 90 min. While the precipitates were saved and stored in a deep freezer (−80 °C) for the preparation of cyt *c* oxidase (Yu *et al.*, 1975), the supernatant solutions were combined, and ammonium sulfate (8.9 g/100 ml) was slowly added under constant stirring. To maintain the pH of the mixture, 5 μl of concentrated ammonium hydroxide was added concurrently for every gram of ammonium sulfate used. The stirring was continued for 20 min before the mixture was centrifuged at 14,000g for 20 min. The resulting precipitates containing crude succinate–cytochrome *c* oxidoreductase (complexes II and III) were dissolved in PES (50 mM phosphate buffer, pH 7.4, containing 1 mM EDTA and 0.25 M sucrose) buffer (~1/6 vol of the SMP used) to a protein concentration of 25 to 30 mg/ml and stored at 0° for 8 h followed by another centrifugation at 96,000g for 40 min. The precipitates, containing mostly cyt *c* oxidase, were discarded. The supernatants were combined and dialyzed overnight with one change of buffer against 50 mM Na/K phosphate buffer, pH 7.4, containing 1 mM EDTA. The crude succinate: cyt *c* oxidoreductase appearing as precipitates in the dialysates were recovered by centrifuging at 28,000g for 30 min and homogenized in 50 mM Tris-HCl buffer, pH 7.2, to a protein concentration of 20 mg/ml. Protein concentration was estimated by optical absorption at 278 nm in 1% SDS using a converting factor of $1\text{OD}_{280} = 0.75 \text{ mg/ml}$. This crude succinate cyt *c* oxidoreductase can be stored at −80 °C for future use or subjected to further purification.

The crude preparation, under constant stirring, was slowly mixed with deoxycholate solution (10%) to 0.35 mg/mg protein. The pH of the mixture was maintained at 7.3 to 7.4 with 1 N NaOH or HCl. The mixture was then subject to ammonium acetate fractionation with a 50% saturated solution. The mixture was brought up to 8.3, 12, 15, and 33% saturation, in steps, by slowly adding saturated ammonium acetate solution. Each fractionation step was followed by stirring for 10 min before the solution was centrifuged for 15 min at 28,000g to remove unwanted precipitates. Purified succinate: cyt *c* oxidoreductase was recovered in the precipitates of the final fractionation step by centrifuging at 96,000g for 30 min with 40% yield. The purified succinate: cyt *c* oxidoreductase was dissolved in 50 mM Na/K phosphate buffer, pH 7.4, containing 0.25 M sucrose and 1 mM EDTA to a protein concentration of approximately 20 mg/ml. The preparation was then

dialyzed against the same buffer extensively over 2 days with two changes of buffer and stored at -80°C .

3.3. Preparation of cytochrome bc_1 particles from succinate: cytochrome c oxidoreductase

The extensively dialyzed, frozen succinate: cyt c oxidoreductase was thawed and diluted with an equal volume of 50 mM Na/K phosphate buffer, pH 7.4, and centrifuged at 158,000g for 60 min. The precipitates were collected and homogenized under an argon atmosphere in 50 mM borate-phosphate buffer, pH 7.8, containing 20 mM succinate. The pH of the suspension was adjusted to 10 with 1 N NaOH and stirred for further 10 min under argon before it was centrifuged at 96,000g for 45 min. The supernatant solution was saved for the preparation of succinate dehydrogenase (Yu and Yu, 1980), and the precipitates were homogenized in borate-phosphate buffer, and the preceding pH 10 treatment was repeated. The precipitates (cyt bc_1 particles, yield >90%) were collected and homogenized in 50 mM Tris-HCl buffer, pH 8.0, to a protein concentration of approximately 20 mg/ml.

3.4. Preparation of cyt bc_1 complex from cyt bc_1 particles

The bc_1 particles as prepared previously were partially reduced. To purify a fully oxidized bc_1 complex, the homogenate was treated with active cyt c oxidase (1% w/w, Yu *et al.*, 1975) and cyt c ($2\ \mu\text{M}$) at 4°C overnight (or until all cyt c/c_1 was oxidized). Potassium deoxycholate (10% solution) was slowly added to the mixture under constant stirring to a ratio of 0.35 mg/mg protein. The solution was centrifuged at 28,000g for 20 min to remove any formed precipitate. The supernatant was then subject to a 10-step ammonium acetate fractionation with 50% saturated solution. The volumes of ammonium acetate solution used for each step were 10, 10, 5, 4, 3.5, 3, 2, 1, 1, and 12% (v/v) of the protein solution, respectively. After each addition, the mixture was stirred continuously at 4°C for 30 min before it was centrifuged to remove any precipitates. The solutions of the first two fractionation steps were centrifuged at 96,000g for 30 min to remove both floating, unwanted fat and precipitates. For steps 3 through 9, the mixtures were centrifuged at 28,000g for 20 min, and for the final step it was centrifuged at 96,000g for 30 min. The purified bc_1 complex was recovered in the precipitates with a yield of approximately 40%. The precipitates were dissolved in 50 mM Tris-HCl buffer, pH 8.0, containing 0.66 M sucrose and stored at -80°C until use. This preparation is suitable for protein crystallization. The crystals obtained diffract X-rays to 2.9 Å resolution in the absence of inhibitor (Xia *et al.*, 1997) and improved to 2.1 Å in the presence of inhibitor (Esser *et al.*, 2006).

4. ELECTRON TRANSFER ACTIVITY IN THE PURIFIED bc_1 COMPLEX

The ubiquinol oxidation activity in purified bc_1 is determined by following the reduction of cyt c spectrophotometrically. The assay mixture contains 50 mM Na/K-phosphate buffer, pH 7.4, 100 μ M cyt c , 1 mM EDTA, and 25 μ M ubiquinol. Diluted cyt bc_1 complex (3 to 5 μ l) containing 0.1 μ M cyt b in the presence of 0.01% DM is added to start the reaction after an initial scan of the mixture for 10 sec at 550 nm for the nonenzymatic reduction of cyt c by the substrate. A difference millimolar extinction coefficient of 18.5 is used for the calculation of cyt c reduction. The substrate, ubiquinol, is prepared by hydrogenation of ubiquinone with Pt-C as catalyst. The ubiquinol stock solution (5 mM) is made in 95% ethanol containing 1 mM HCl. The diluted HCl is used to slow down the autooxidation of substrate. The determination of cyt bc_1 activity depends heavily on the physical state of the complex. Proper dilution of the complex in the presence of the right amount of detergent is the key to obtaining the best activity. Fig. 25.1 shows the activity determined under different protein concentrations. As indicated in Table 25.1, ubiquinol and its derivatives give rise to different activities; of all the derivatives tested; $Q_0C_{10}BrH_2$ shows the best activity.

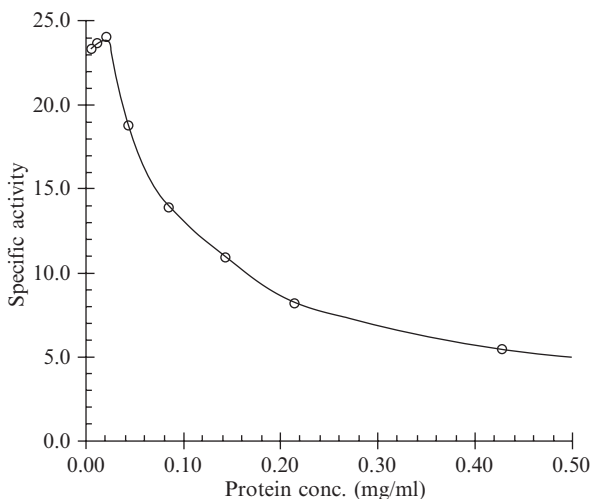


Figure 25.1 Effect of protein concentration on the electron transfer activity measurement of cyt bc_1 complex. Cytochrome bc_1 complex preparation was dissolved in 50 mM Tris-HCl buffer, pH 8.0, containing 0.66 M sucrose and 0.01% DM at indicated protein concentrations. Three- to five-microliter aliquots were used for activity determination at room temperature. Specific activity is expressed as μ moles cytochrome c reduced/nmol cytochrome b /min.

Table 25.1 Relative effectiveness of ubiquinol derivatives in the electron transfer reaction of cyt bc_1 complex

Substrate	Relative activity, %
Q ₂ H ₂	100
Q ₁ H ₂	35
Q ₀ C ₇ H ₂	65
Q ₀ C ₁₀ H ₂	105
Q ₀ C ₁₀ BrH ₂	120

5. PROTON TRANSLOCATION IN THE PURIFIED bc_1 COMPLEX

Phospholipid (PL) vesicles embedded with cyt bc_1 complex were prepared essentially according to the cholate dialysis method (Gurung *et al.*, 2005; Kagawa and Racker, 1971). Asolectin micellar solution was prepared by sonicating 200 mg of acetone-washed asolectin in 4 ml of 50 mM sodium phosphate buffer, pH 7.4, containing 2% sodium cholate and 100 mM KCl in an ice-water bath under an anaerobic environment maintained by continuously passing argon into the vessel. The cyt bc_1 complex (1.25 mg) was mixed with 1 ml of asolectin micellar solution to give an asolectin/protein ratio of 40. The bc_1 complex-PL mixtures were incubated at 0° for 30 min before overnight dialysis at 4 °C against 100 × volumes of 50 mM sodium phosphate buffer, pH 7.4, containing 100 mM KCl with three changes of buffer. The mixture was then dialyzed against 100 × volume of 150 mM KCl (without buffer) for 3 to 4 h.

Proton translocation coupled to electron flow through the bc_1 complex-PL vesicles is measured at room temperature with an Accumet Model 10 pH meter and a Model 13-620-96 combination pH electrode. Twenty-five nmol of Q₀C₁₀BrH₂ were added to 1.6 ml reaction mixture containing 150 mM KCl, 4 μM ferricytochrome *c*, 1 μM valinomycin, and an appropriate amount of bc_1 -PL vesicles (30 to 50 μl). Electron flow is initiated by the addition of 5 nmol of ferricyanide, which oxidized cyt *c*, and thus provided an electron acceptor for the complex. Electron flow is also measured in an identical manner except for the presence of the protonophore, *m*-chloro carbonyl cyanide phenylhydrazone (CCCP), at a concentration of 2 μM, under which the vesicles are permeable to protons and no cross-membrane ΔpH exists. Proton-pumping stoichiometry (H⁺/e⁻) of 2 is calculated as the ratio of the decrease in pH on ferricyanide addition to bc_1 -PL vesicles before and after treatment with CCCP (Fig. 25.2 A, also Gurung *et al.*, 2005). When proton-pumping activity is determined with PL-vesicles coembedded with bovine bc_1 and a *R. sphaeroides* mutant

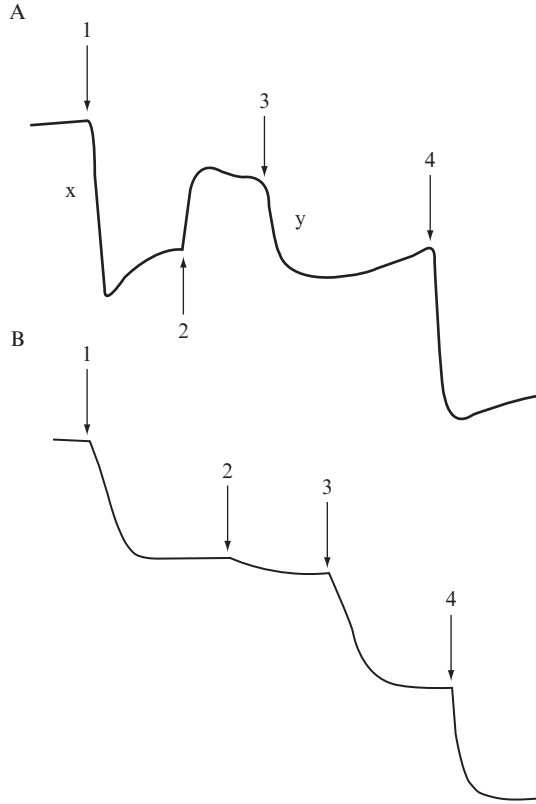


Figure 25.2 Proton-pumping of cyt bc_1 complexes embedded in PL vesicles. Measurement of pH change as an indicator for the proton-pumping activity of PL vesicles embedded with (A) mitochondria bc_1 complex only, (B) with mitochondrial bc_1 complex and the 2Fe-2S cluster lacking mutant complex, H131C-H152C, with ubiquinol as the substrate. Arrows indicate the points of addition of 5 nmol of ferricyanide (1), 3 μ M CCCP (2), 5 nmol of ferricyanide (3), and 5 nmol HCl (4). Note: proton-pumping ratio (H^+/e^-) = x/y .

complex lacking the iron-sulfur cluster [ISP (H131C-H152C)] (Fig. 25.2B), a H^+/e^- of 1 is obtained, indicating that a proton leakage channel is provided by this mutant complex (Gurung *et al.*, 2005).

6. SUPEROXIDE GENERATION BY THE PURIFIED bc_1 COMPLEX

Although the rate of $O_2^{\cdot -}$ production by the cyt bc_1 complex can be determined by measuring the decrease in rate of cyt c reduction in the presence of superoxide dismutase under conditions of continuous turnover of the bc_1 complex (Muller *et al.*, 2002), the small rate of $O_2^{\cdot -}$ formation, compared with

the normal rate of cyt *c* reduction, compromises the accuracy of this method. MCLA has a high sensitivity for $O_2^{\bullet -}$ in the neutral pH range (Nakano, 1990). The MCLA- $O_2^{\bullet -}$ chemiluminescence method has been widely used to detect $O_2^{\bullet -}$ (Midorikawa *et al.*, 2001; Uehara *et al.*, 1993; Zhang *et al.*, 1998). However, when the MCLA- $O_2^{\bullet -}$ chemiluminescence method was adopted to determine the $O_2^{\bullet -}$ production during continuing turnover of the bc_1 complex (in the presence of ubiquinol and cytochrome *c*) with Lumac/3M Biocounter (model 2110A), a high background of $Q_2^{\bullet -}$ production, resulting from the nonenzymatic oxidation of ubiquinol by cytochrome *c*, was encountered. This makes it difficult to accurately measure $O_2^{\bullet -}$ production by the cyt bc_1 complex.

This difficulty has finally been overcome by measuring the chemiluminescence of the MCLA- $O_2^{\bullet -}$ adduct during a single turnover of bc_1 complex, with Applied Photophysics stopped-flow reaction analyzer SX.18MV (Leatherhead, England). By leaving the excitation light source off, the chemiluminescence of MCLA- $O_2^{\bullet -}$ generated when cyt bc_1 complex is mixed with ubiquinol and MCLA is registered in light emission (Denicola *et al.*, 1995). Because the system contains no cytochrome *c*, chemiluminescence of MCLA- $O_2^{\bullet -}$, resulting from nonenzymatic oxidation of ubiquinol by cytochrome *c*, is eliminated. This method enables us to unambiguously compare $O_2^{\bullet -}$ production by various bc_1 complexes.

Experimentally, the reaction is carried out at 25° by mixing solutions A and B in a 1:1 ratio. Solution A contains 100 mM Na^+/K^+ phosphate buffer, pH 7.4, 1 mM EDTA, 1 mM KCN, 1 mM NaN_3 , 0.1% bovine serum albumin, 0.01% DM, and an appropriate concentration of bovine cyt bc_1 or other systems. Solution B contains 125 μM $Q_0C_{10}BrH_2$ and 4 μM MCLA in the same buffer. Once the reaction starts, the produced chemiluminescence, in voltage, is consecutively monitored for 2 sec. $O_2^{\bullet -}$ generation is expressed in xanthine oxidase (XO) units. One XO unit is defined as chemiluminescence (maximum peak height of light intensity) generated by 1 unit of XO, which equals 2.0 V from an Applied photophysics stopped-flow reaction analyzer SX.18MV, when solution A containing 100 mM Na^+/K^+ phosphate buffer, pH 7.4, 100 μM hypoxanthine, 4 μM MCLA, and 1 mM NaN_3 is mixed with solution B containing 100 mM Na^+/K^+ phosphate buffer, pH 7.4, 1 mM NaN_3 and 1 unit of XO.

7. COMPARISON OF $O_2^{\bullet -}$ PRODUCTION BY THE bc_1 COMPLEXES WITH VARYING ELECTRON TRANSFER ACTIVITIES

Under normal catalytic conditions only a very small number of electrons leak from the bovine complex to form $O_2^{\bullet -}$ (Fig. 25.3A). The $O_2^{\bullet -}$ production significantly increases (fivefold) when the electron transfer reaction is blocked

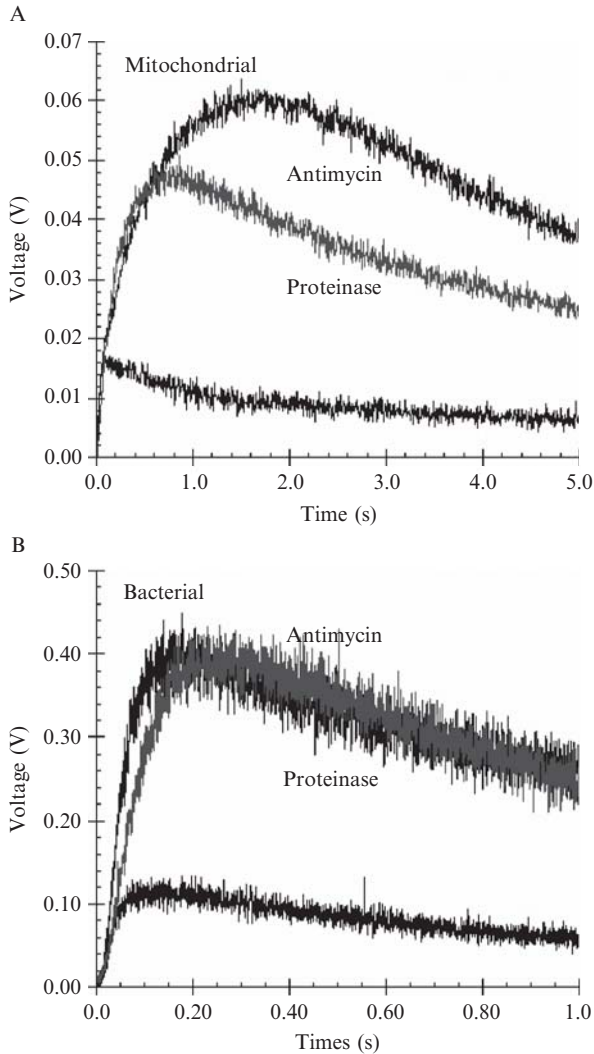


Figure 25.3 Generation of $O_2^{\bullet-}$ in intact, antimycin A-inhibited and proteinase K-treated cytochrome bc_1 complexes. (A) Data for the mitochondrial bc_1 complex and (B) for *R. sphaeroides* four-subunit, wild-type bc_1 complex. The concentrations of bovine and *R. sphaeroides* bc_1 complexes in solution A were $5 \mu M$. Detailed experimental conditions are given in Methods for determining superoxide generation. To digest subunits of the *cyt* bc_1 complex, the bc_1 solution was diluted with 50 mM Tris-HCl buffer, pH 7.4, containing 0.01% DM, to a protein concentration of 20 mg/ml and incubated with 0.4 mg/ml of proteinase K at room temperature. The electron transfer activity and superoxide generation activity were followed during the course of incubation. When electron transfer activity was completely lost, the incubated mixture was subjected to SDS-PAGE to confirm the protein digestion and to determine $O_2^{\bullet-}$ production.

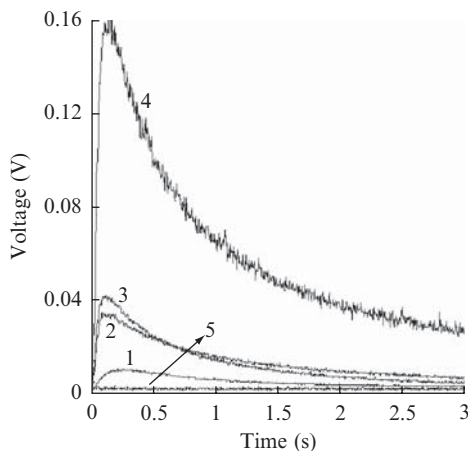


Figure 25.4 Time traces of $O_2^{\bullet-}$ production by various bc_1 complexes. Curves 1 to 4 represent the bovine and *R. sphaeroides* complexes of wild-type, reconstituted, and three-subunit core, respectively. Reconstituted complex refers to the complex reconstituted from the core complex and recombinant wild-type subunit IV. The concentrations of bc_1 complexes used in solution A were $3 \mu M$. Curve 5 is for control experiment when no bc_1 complexes nor $Q_0C_{10}BrH_2$ is present in the system. A similar curve was obtained when 300 unit/ml superoxide dismutase was added to the complete system.

by antimycin A (Fig. 25.3A). This inhibitor effect is also observed in the bacterial complex (Fig. 25.3B). Because no ubisemiquinone can be detected in antimycin A-inhibited complexes in the presence of ubiquinol and such systems feature an increase in the reduction level of cyt b_L , the reduced cyt b_L is most probably the electron source for the superoxide generation.

When $O_2^{\bullet-}$ productions in cyt bc_1 complexes with varying electron transfer activities, a reversed relationship between electron transfer activity and $O_2^{\bullet-}$ production is revealed (Fig. 25.4). The specific activities, μmol cyt c reduced/min/nmol b , for the bovine complex, the four subunit, wild-type, reconstituted, and the three-subunit core complexes of *R. sphaeroides* are 24, 2.2, 2.0, and 0.6., respectively, whereas the $O_2^{\bullet-}$ production, XO unit/nmol b , by these four complexes are 0.03, 0.063, 0.067, and 0.25, respectively (calculated from Fig. 25.4). Inactivation of the bc_1 complex by incubating at elevated temperature ($37^\circ C$) or treatment with proteinase k results in an increase in superoxide production to the same level as that of the antimycin A-inhibited complex (Fig. 25.3). These results suggest that the structural integrity of protein subunits is not required for superoxide generating activity.

ACKNOWLEDGMENTS

This research was supported in part by an NIH grant (GM 30721) to C. A. Y. by the Oklahoma Agricultural Experiment Station (Projects #1819 and #2372), Oklahoma State University, and by the Intramural Research Program of National Cancer Institute, Center for Cancer Research, NIH.

REFERENCES

- Brandt, U., and Trumpower, B. (1994). The proton-motive Q cycle in mitochondria and bacteria. *Crit. Rev. Biochem. Mol. Biol.* **29**, 165–197.
- Cape, J. L., Bowman, M. K., and Kramer, D. M. (2007). A semiquinone intermediate generated at the Qo site of the cytochrome bc_1 complex: Importance for the Q-cycle and superoxide production. *Proc. Natl. Acad. Sci. USA* **104**, 7887–7892.
- Chance, B., Sies, H., and Boveris, A. (1979). Hydroperoxide metabolism in mammalian organs. *Physiol. Rev.* **59**, 527–605.
- Crofts, A. R. (2004). The cytochrome bc_1 complex: Function in the context of structure. *Ann. Rev. Physiol.* **66**, 689–733.
- Denicola, A., Souza, J. M., Gatti, R. M., Augusto, O., and Radi, R. (1995). Desferrioxamine inhibition of the hydroxyl radical-like reactivity of peroxynitrite: Role of the hydroxamic groups. *Free Radic. Biol. Med.* **19**, 11–19.
- De Vries, S., Albracht, S. P., Berden, J. A., and Slater, E. C. (1981). A new species of bound ubisemiquinone anion in QH2: Cytochrome c oxidoreductase. *J. Biol. Chem.* **256**, 11996–11998.
- Dröse, S., and Brandt, U. (2008). The mechanism of mitochondrial superoxide production by the cytochrome bc_1 complex. *J. Biol. Chem.* **283**, 21649–21654.
- Esser, L., Gong, X., Yang, S., Yu, L., Yu, C. A., and Xia, D. (2006). Surface-modulated motion switch: Capture and release of iron-sulfur protein in the cytochrome bc_1 complex. *Proc. Natl. Acad. Sci. USA* **103**, 13045–13050.
- Gurung, B., Yu, L., Xia, D., and Yu, C. A. (2005). The iron-sulfur cluster of the rieske iron-sulfur protein functions as a proton-exiting gate in the cytochrome bc_1 complex. *J. Biol. Chem.* **280**, 24895–24902.
- Iwata, S., Lee, J. W., Okada, K., Lee, J. K., Iwata, M., Rasmussen, B., Link, T. A., Ramaswamy, S., and Jap, B. K. (1998). Complete structure of the 11-subunit bovine mitochondrial cytochrome bc_1 complex. *Science* **281**, 64–71.
- Kagawa, Y., and Racker, E. (1971). Partial resolution of the enzymes catalyzing oxidative phosphorylation. XXV. Reconstitution of vesicles catalyzing ^{32}P adenosine triphosphate exchange. *J. Biol. Chem.* **246**, 5477–5487.
- Ljungdahl, P. O., Pennoyer, J. D., Robertson, D. E., and Trumpower, B. L. (1987). Purification of highly active cytochrome bc_1 complexes from phylogenetically diverse species by a single chromatographic procedure. *Biochim. Biophys. Acta* **891**, 227–241.
- McLennan, H. R., and Esposti, M. D. (2000). The contribution of mitochondrial respiratory complexes to the production of reactive oxygen species. *J. Bioenerg. Biomembr.* **32**, 152–162.
- Mitchell, P. (1976). Possible molecular mechanisms of the protonmotive function of cytochrome systems. *J. Theor. Biol.* **62**, 327–367.
- Midorikawa, J., Maehara, K., Yaoita, H., Watanabe, T., Ohtani, H., Ushiroda, S., and Maruyama, Y. (2001). Continuous observation of superoxide generation in an *in-situ* ischemia-reperfusion rat lung model. *Jpn. Circ. J.* **65**, 207–212.
- Muller, F., Crofts, A. R., and Kramer, D. M. (2002). Multiple Q-cycle bypass reactions at the Qo site of the cytochrome bc_1 complex. *Biochemistry* **41**, 7866–7874.
- Muller, F., Roberts, A. G., Bowman, M. K., and Kramer, D. M. (2003). Architecture of the Qo site of the cytochrome bc_1 complex probed by superoxide production. *Biochemistry* **42**, 6493–6499.
- Nakano, M. (1990). Determination of superoxide radical and singlet oxygen based on chemiluminescence of luciferin analogs. *Methods Enzymol.* **186**, 585–591.
- Nohl, H., and Jordan, W. (1986). The mitochondrial site of superoxide formation. *Biochem. Bioph. Res. Co.* **138**, 533–539.

- Snyder, C.H., Gutierrez-Cirlos, E. B., and Trumpower, B. L. (2000). Evidence for a concerted mechanism of ubiquinol oxidation by the cytochrome bc_1 complex. *J. Biol. Chem.* **275**, 13535–13541.
- Sun, J., and Trumpower, B. L. (2003). Superoxide anion generation by the cytochrome bc_1 complex. *Arch. Biochem. Biophys.* **419**, 198–206.
- Tian, H., Yu, L., Mather, M. W., and Yu, C.-A. (1998). Flexibility of the neck region of the rieske iron-sulfur protein is functionally important in the cytochrome bc_1 complex. *J. Biol. Chem.* **273**, 27953–27959.
- Tso, S. C., Shenoy, S. K., Quinn, B. N., Yu, L., and Yu, C. A. (2000). Subunit IV of cytochrome bc_1 complex from *Rhodobacter sphaeroides*: Location of regions essential for interaction with the three-subunit core complex. *J. Biol. Chem.* **275**, 15287–15294.
- Trumpower, B. L., and Gennis, R. B. (1994). Energy transduction by cytochrome complexes in mitochondrial and bacterial respiration: The enzymology of coupling electron transfer reactions to transmembrane proton translocation. *Annu. Rev. Biochem.* **63**, 675–716.
- Turrens, J. F., and Boveris, A. (1980). Generation of superoxide anion by the NADH dehydrogenase of bovine heart mitochondria. *Biochem. J.* **191**, 421–427.
- Turrens, J. F., Alexandre, A., and Lehninger, A. L. (1985). Ubisemiquinone is the electron donor for superoxide formation by complex III of heart mitochondria. *Arch. Biochem. Biophys.* **237**, 408–414.
- Uehara, K., Maruyama, N., Huang, C. K., and Nakano, M. (1993). The first application of a chemiluminescence probe, 2-methyl-6-[p-methoxyphenyl]-3,7-dihydroimidazo[1,2-*b*]pyrazin-3-one (MCLA), for detecting $O_2^{\cdot -}$ production, *in vitro*, from Kupffer cells stimulated by phorbol myristate acetate. *FEBS Lett.* **335**, 167–170.
- Xia, D., Yu, C. A., Kim, H., Xia, J. Z., Kachurin, A. M., Zhang, L., Yu, L., and Deisenhofer, J. (1997). Crystal structure of the cytochrome bc_1 complex from bovine heart mitochondria. *Science* **277**, 60–66.
- Xia, D., Esser, L., Yu, L., and Yu, C. A. (2007). Structural basis for the mechanism of electron bifurcation at the quinol oxidation site of the cytochrome bc_1 complex. *Photosyn. Res.* **92**, 17–34.
- Yang, S., Ma, H-W., Yu, L., and Yu, C. A. (2008). On the mechanism of quinol oxidation at Q_p site in cytochrome bc_1 complex: Studied by mutants without cytochrome b_L or b_H . *J. Biol. Chem.* **283**, 28767–28776.
- Yu, C. A., Yu, L., and King, T. E. (1975). Studies on cytochrome oxidase. Interactions of the cytochrome oxidase protein with phospholipids and cytochrome *c*. *J. Biol. Chem.* **250**, 1383–1392.
- Yu, C. A., and Yu, L. (1980). Resolution and reconstitution of succinate-cytochrome *c* reductase: Preparations and properties of high purity succinate dehydrogenase and ubiquinol-cytochrome *c* reductase. *Biochim. Biophys. Acta* **591**, 409–420.
- Yu, C. A., and Yu, L. (1982). Synthesis of biologically active ubiquinone derivatives. *Biochemistry* **21**, 4096–4101.
- Yu, C. A., Cen, X., Ma, H-W., Yin, Y., Yu, L., Esser, L., and Xia, D. (2008). Domain conformational switch of the iron-sulfur protein in cytochrome bc_1 complex is induced by the electron transfer from cytochrome b_L to b_H . *Biochim. Biophys. Acta* **1777**, 1038–1043.
- Yu, L., Tso, S. C., Shenoy, S. K., Quinn, B. N., and Xia, D. (1999). The role of the supernumerary subunit of *Rhodobacter sphaeroides* cytochrome bc_1 complex. *J. Bioenerg. Biomembr.* **31**, 251–257.
- Yu, L., Tso, S. C., Shenoy, S. K., Quinn, B. N., and Xia, D. (1999). The role of the supernumerary subunit of *Rhodobacter sphaeroides* cytochrome bc_1 complex. *J. Bioenerg. Biomembr.* **31**, 251–258.

- Yue, W. H., Zou, Y. P., Yu, L., and Yu, C. A. (1991). Crystallization of mitochondria ubiquinol-cytochrome c reductase. *Biochemistry* **30**, 2303–2306.
- Zhang, L., Yu, L., and Yu, C. A. (1998). Generation of superoxide anion by succinate-cytochrome c reductase from bovine heart mitochondria. *J. Biol. Chem.* **273**, 33972–33976.
- Zhu, J., Egawa, T., Yeh, S. R., Yu, L., and Yu, C. A. (2007). Simultaneous reduction of iron-sulfur protein and cytochrome b_L during ubiquinol oxidation in cytochrome bc_1 complex. *Proc. Natl. Acad. Sci. USA* **104**, 4864–4869.

MEASUREMENT OF SUPEROXIDE FORMATION BY MITOCHONDRIAL COMPLEX I OF *YARROWIA LIPOLYTICA*

Stefan Dröse,^{*} Alexander Galkin,[†] and Ulrich Brandt^{*}

Contents

1. Introduction	476
2. Materials, Sample Preparation, and Purification of Complex I from <i>Yarrowia Lipolytica</i>	477
2.1. Materials	477
2.2. Cell growth and preparation of mitochondrial membranes	478
2.3. Purification of complex I, lipid-activation, and reconstitution into proteoliposomes	478
3. Detection of Superoxide (O ₂ ^{•-}) by Acetylated Cytochrome c	479
3.1. Superoxide production by mitochondrial membranes of <i>Y. lipolytica</i>	480
3.2. Superoxide production by reconstituted complex I	481
3.3. pH profile for ubiquinone reduction and superoxide formation	483
4. Detection of Hydrogen Peroxide by the Amplex Red/HRP Assay	484
4.1. Spectral properties of resorufin	484
4.2. Parallel measurement of NADH oxidation, H ₂ O ₂ generation, and buildup of a membrane potential by reconstituted complex I	484
5. Conclusions	487
References	488

Abstract

Complex I (NADH: ubiquinone oxidoreductase) is generally regarded as one of the major sources of mitochondrial reactive oxygen species (ROS). Mitochondrial membranes from the obligate aerobic yeast *Yarrowia lipolytica*, as well as the purified and reconstituted enzyme, can be used to measure complex I-dependent

^{*} Molecular Bioenergetics Group, Cluster of Excellence Frankfurt "Macromolecular Complexes," Medical School, Johann Wolfgang Goethe-University, Frankfurt am Main, Germany

[†] The Wolfson Institute for Biomedical Research, The Cruciform Building, University College London, London, United Kingdom

generation of superoxide ($O_2^{\cdot-}$). The use of isolated complex I excludes interference with other respiratory chain complexes and matrix enzymes during superoxide dismutase-sensitive reduction of acetylated cytochrome *c*. Alternately, hydrogen peroxide formation can be measured by the Amplex Red/horseradish peroxidase assay. Both methods allow the determination of complex I-generated ROS, depending on substrates (NADH, artificial ubiquinones), membrane potential, and active/deactive transition. ROS production by *Yarrowia* complex I in the “forward mode” is essentially independent of catalytic turnover, membrane potential, and the presence of inhibitors or the active/deactive transition.

1. INTRODUCTION

Within the respiratory chain, complex I (NADH: ubiquinone oxidoreductase) and the cytochrome *bc*₁ complex (complex III, ubiquinol: cytochrome *c* oxidoreductase) have been identified as the main sources of “reactive oxygen species” (ROS; Fridovich, 1978; Turrens, 2003). While complex III produces superoxide *in vitro* preferably under conditions of “oxidant-induced reduction” (i.e., in the presence of the specific center N inhibitor antimycin A, sufficient amounts of reducing equivalents, and an oxidized downstream respiratory chain), complex I has been shown to generate superoxide under various conditions at high rates and also in the absence of inhibitors. For this reason, most groups working in the ROS field regard complex I as the more important mitochondrial source of ROS as either a signaling or a deleterious agent. Over the years, all major cofactors involved in the electron transfer chain of complex I have been proposed as sites for superoxide production: flavine-mononucleotide (Galkin and Brandt, 2005; Kussmaul and Hirst, 2006; Liu *et al.*, 2002; Vinogradov and Grivennikova, 2005), iron-sulfur clusters N2 (Genova *et al.*, 2001) and N1a (Kushnareva *et al.*, 2002), and a semiquinone radical formed on ubiquinone reduction (Lambert and Brand, 2004; Ohnishi *et al.*, 2005b). Although contributions from other redox centers still cannot be excluded entirely, it now seems clear that reduced FMN is the major source of electrons for superoxide formation in mitochondrial complex I (Galkin and Brandt, 2005; Kussmaul and Hirst, 2006). Bacterial complex I seems to produce mainly H_2O_2 by direct reduction of O_2 with two electrons from FMNH₂ (Esterhazy *et al.*, 2008). This variation may be due to the marked difference in the redox potential of iron-sulfur cluster N1a, which is much more negative in the mitochondrial enzyme.

In mitochondrial membranes superoxide production by complex I can be measured under two different conditions (Kushnareva *et al.*, 2002; Lambert and Brand, 2004; Liu *et al.*, 2002; Votyakova and Reynolds, 2001): when mitochondria respire on NADH-generating substrates (e.g., malate/glutamate or malate/pyruvate), superoxide production is low

and is stimulated by the addition of inhibitors blocking electron transfer. This is due to increased reduction of upstream components of the respiratory chain, including the redox cofactors of complex I. The highest rates of superoxide production are measured under conditions of succinate-supported reverse electron transfer from complex II via of ubiquinone and complex I onto NAD^+ (Hinkle *et al.*, 1967; Vinogradov and Grivennikova, 2005; Votyakova and Reynolds, 2001). Under these conditions FMN and the other redox centers of complex I become even more reduced. This state and, therefore, ROS formation is highly sensitive to even a small drop in the protonmotive force.

This chapter describes methods to measure the superoxide and hydrogen peroxide (H_2O_2) production by purified complex I from the obligate aerobic yeast *Yarrowia lipolytica*, an organism that was established in our laboratory as a convenient model for the structural and functional analysis of mitochondrial complex I (Kerscher *et al.*, 2002).

2. MATERIALS, SAMPLE PREPARATION, AND PURIFICATION OF COMPLEX I FROM *YARROWIA LIPOLYTICA*

This section summarizes the materials and the methods that are required to obtain a highly pure and active preparation of complex I from *Y. lipolytica*. The use of purified complex I for the investigations of ROS production excludes interference with other respiratory chain complexes and mitochondrial matrix enzymes.

2.1. Materials

Asolectin (total soy bean extract with 20% lecithin) phosphatidylethanolamine (purified from egg yolk), and phosphatidylcholine (purified from egg yolk) were purchased from Avanti Polar Lipids (Alabaster, AL). *n*-dodecyl- β -D-maltoside was obtained from Glycon (Luckenwalde, Germany), and octyl- β -D-glucopyranoside was from Biomol (Hamburg, Germany). Oxonol VI (bis-(3-propyl-5-oxoisoxazol-4-yl)pentamethine oxonol) and Amplex Red (*N*-acetyl-3,7-dihydrophenoxazine) were purchased from Invitrogen/Molecular Probes (Eugene, OR), and decylubiquinone (DBQ) was from Alexis Biochemicals (Lausen, Switzerland). Superoxide dismutase (SOD, from bovine liver), horseradish peroxidase (HRP), cytochrome *c* (from horse heart), deamino-NADH (dNADH), cardiolipin (sodium salt, from bovine heart), and all other chemicals were from Sigma. Acetylated cytochrome *c* was prepared by treatment with acetic anhydride as described (Galkin and Brandt, 2005; Kakinuma

and Minakami, 1978). DQA (2-*n*-decyl-quinazolin-4-yl-amine, SAN 549) was obtained from AgrEvo (Frankfurt, Germany). DBQ, rotenone, DQA, stigmatellin, and Amplex Red were dissolved in DMSO. Bio-Beads SM-2 (20 to 50 mesh) were from Bio-Rad Laboratories (München, Germany) and activated by methanol as described (Dröse *et al.*, 2005). Superoxide and H₂O₂ production were determined with either a diode array spectrophotometer (MultiSpec 1501, Shimadzu) or a Spectra Max PLUS³⁸⁴ plate reader spectrophotometer (Molecular Devices, München). The diode array spectrophotometer was generally used when different activities (e.g., NADH-oxidation, ROS-production, generation of $\Delta\psi$) were to be measured simultaneously. After optimization of the assay with a conventional spectrophotometer, routine measurements can be performed with a microplate reader setup, which consumes less material and saves time because multiple samples can be analyzed in parallel.

2.2. Cell growth and preparation of mitochondrial membranes

The *Y. lipolytica* strain PIP0 was grown overnight at 27° in a 10-L Biostat E fermenter (Braun, Melsungen) in modified YPD medium (2.5% glucose, 2% Bacto peptone, 1% yeast extract). This strain contains a chromosomal copy of the modified *NUGM* gene, encoding a C-terminally his-tagged version of the 30-kDa subunit of complex I (Kerscher *et al.*, 2002). Mitochondrial membranes were prepared following the protocol of Kerscher *et al.* (1999) with the modification detailed in Kashani-Poor *et al.* (2001).

2.3. Purification of complex I, lipid-activation, and reconstitution into proteoliposomes

Purification of *n*-dodecyl- β -D-maltoside solubilized complex I was achieved by Ni-affinity chromatography, followed by gel-filtration as detailed before (Kashani-Poor *et al.*, 2001). Chromatography and gel filtration removes most phospholipids and endogenous Q₉ from the protein (Dröse *et al.*, 2002): only between 26 and 66 mol “organic” (i.e., chloroform/methanol extractable) phosphate per mol complex I and stoichiometric amounts of Q₉ (0.2 to 0.4 mol/mol) remain bound to the enzyme. Delipidation results in a concomitant loss of the NADH: ubiquinone oxidoreductase activity, which can be fully reversed by adding back the phospholipids either as detergent-solubilized micelles (Dröse *et al.*, 2002) or by reconstitution into proteoliposomes (Dröse *et al.*, 2005). A comparable dependence between lipid content and ubiquinone reductase activity was reported later for purified complex I from bovine heart (Sharpley *et al.*, 2006) and *Escherichia coli* (Sinagina *et al.*, 2005; Stolpe and Friedrich, 2004).

For the preparation of lipid-activated complex I that was used for superoxide detection by acetylated cytochrome *c*, 0.5 mg/ml complex I

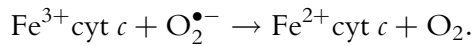
were mixed with 10 mg/ml lipids (76% phosphatidyl-choline/19% phosphatidyl-ethanolamine/5% cardiolipin in 2.3% octylglucoside; Dröse *et al.*, 2002) and dialyzed for 24 h against measuring buffer (50 mM Na⁺/MOPS, pH 7.0, 1 mM EDTA, 20 mM NaCl). Alternately, for reconstitution of complex I into proteoliposomes, 0.3 to 0.5 mg/ml complex I was mixed with 10 mg/ml asolectin and 1.6% octylglucoside and dialyzed under the same conditions (Galkin and Brandt, 2005). To compensate for ubiquinone depletion of the complex I preparations, natural ubiquinone (Q₉ in the case of *Y. lipolytica*) can be added to the lipid/protein/detergent mixture during reconstitution of the enzyme. Q₉ retention can be checked spectrophotometrically at 275 nm after solubilization of the final suspension of the proteoliposomes and reduction by sodium borohydride.

For the parallel measurement of NADH oxidation, H₂O₂ generation and the buildup of a membrane potential by reconstituted complex I, tightly coupled proteoliposomes were prepared with Bio-Beads for removal of detergents (Dröse *et al.*, 2005); 10 mg/ml asolectin solubilized in 16 mg/ml octylglycoside (resulting in “total solubilization” of lipids) was mixed at a protein/lipid ratio of 1:50 (w/w) with purified complex I (usually 200 to 400 μg) in 20 mM K⁺/MOPS, pH 7.2, 50 mM KCl. The mixture was incubated at 4° on an Eppendorf Mixer 5432, and the detergents were removed by the stepwise addition of a 20-fold excess of Bio-Beads (by weight) in four equal aliquots at 30-min intervals. We recently observed a decrease in complex I activity with some batches of Bio-Beads when the proteoliposomes were in prolonged contact with the beads. Therefore, the original protocol (Dröse *et al.*, 2005) was optimized by minimizing the incubation time with Bio-Beads while retaining the tightness of the proteoliposomes formed. Proteoliposomes were collected by centrifugation (90,000g for 1 h) and resuspended in a small volume of 20 mM K⁺/MOPS, pH 7.2, 50 mM KCl (usually 1 μl/μg of protein applied). After ultracentrifugation, the resuspended proteoliposomes were incubated for at least 2 h on ice to allow for sedimentation of aggregated protein and bead fragments. Then the supernatant was carefully removed and used for subsequent measurements. This procedure usually resulted in proteoliposomes with a respiratory control ratio of ~4 that was stable for more than 24 h at 4°.

3. DETECTION OF SUPEROXIDE (O₂⁻) BY ACETYLATED CYTOCHROME *c*

Superoxide detection was based on the acetylated cytochrome *c* assay (Azzi *et al.*, 1975). Reduction of ferricytochrome *c* can be followed spectrophotometrically at 550 nm ($\epsilon_{550-539 \text{ nm}} = 21.5 \text{ mM}^{-1} \text{ cm}^{-1}$) to

measure rates of superoxide formation (overview in [Tarpey and Fridovich, 2001](#)):



Cytochrome *c* is not a specific agent for superoxide detection, because it can also become reduced by cellular components like ascorbate, glutathione, or cellular reductases that enzymatically catalyze cytochrome *c* reduction ([Tarpey and Fridovich, 2001](#)). However, if the contribution by such side reactions is not too high, the superoxide-dependent rate can be deduced as the difference between the cytochrome *c* reduction rates in the absence and presence of superoxide dismutase. A high rate constant ($10^6 \text{ M}^{-1}\text{s}^{-1}$) of the reaction with superoxide anion and the marked decrease of enzymatic reduction and oxidation rates by respiratory chain complexes III and IV on acetylation of cytochrome *c* greatly improve the sensitivity of the assay. In general, AcCyt *c*, as is the case for HRP and Amplex Red (see [section 4](#)), have to be in excess so that the rates of reduction and oxidation can be treated as zero order and depend only on the rate of superoxide production.

3.1. Superoxide production by mitochondrial membranes of *Y. lipolytica*

For the measurement of complex I activity in mitochondrial membranes from *Y. lipolytica* (0.1 to 0.2 mg protein/ml in the assay), deamino-NADH (dNADH) was supplied as electron donor, because this yeast also contains an alternative NDH2-type NADH: ubiquinone oxidoreductase that can use NADH but not its deamino-form ([Kerscher *et al.*, 2008](#)). It should be noted that strains lacking the NDH2-type enzyme are also available ([Kerscher *et al.*, 1999](#)). dNADH oxidation was followed spectrophotometrically at 340 to 400 nm in 40 mM Na⁺/MOPS, pH 7.0, 0.2 mM EDTA, and 20 mM NaCl at 28°. The oxidation of 100 μM dNADH was determined in the absence or presence of 60 μM *n*-decyl-ubiquinone (DBQ), 1 μM stigmatellin, and 10 mM sodium azide. In the first case, dNADH oxidation relies on the presence of endogenous Q₉ and the ubiquinol-oxidating activities of the downstream respiratory chain complexes III and IV. In the second case, the complex I-dependent activity depends on the presence of the substrate analog DBQ, whereas the activities of complexes III and IV are blocked by the specific inhibitors stigmatellin and cyanide, respectively. Note that DBQ forms micelles in aqueous solutions above a concentration of ~100 μM (log partition coefficient cyclohexane/water ~7; [Fato *et al.*, 1996](#)). As typically observed for fragmented membrane preparations of mitochondria, the dNADH oxidation rate was two to three times lower than the dNADH: DBQ oxidoreductase activity

(Table 26.1). This was largely due to loss of endogenous cytochrome *c* during membrane preparation. The measurement of the dNADH-dependent superoxide formation was monitored as the SOD-sensitive (15 U/ml) reduction of 27 μM acetylated cytochrome *c* dissolved in the aforementioned buffer, with a SpectraMax PLUS³⁸⁴ plate reader at 28°. Prior to our experiments, our detection system was tested by monitoring cytochrome *c* reduction by xanthine oxidase (15 mU/ml of enzyme and 50 μM of hypoxanthine). In such conditions addition of 5 U/ml of SOD completely inhibited the reduction of the cytochrome. In *Yarrowia* membranes, the SOD-insensitive production of superoxide was $\sim 50\%$ of the total rate, whereas the superoxide formation rate was $\sim 0.15\%$ of the dNADH oxidation rate in the absence of inhibitors and increased sevenfold on addition of 0.9 μM of the complex III Q_i site (center N) inhibitor antimycin A. Under these conditions, superoxide is formed at the Q_o site (center P) of complex III and at complex I. A block of center P by 1 μM stigmatellin, the ubiquinone binding site of complex I by 2.2 μM DQA or cytochrome oxidase by 10 mM sodium azide resulted in a twofold to threefold increase in superoxide generation. It can be concluded that a higher reduction level of the redox centers in complex I was responsible for the increase of the superoxide production, regardless of whether the electron-transfer chain was blocked at its own ubiquinone binding site or at downstream respiratory chain complexes. Note that stigmatellin inhibition excluded any contribution of complex III to superoxide generation.

3.2. Superoxide production by reconstituted complex I

Detection of the superoxide generated by reconstituted complex I can be carried out with a multiplate reader. Under the conditions described (27 μM acetylated cytochrome *c* and 10 $\mu\text{g/ml}$ proteoliposomes) one measurement takes approximately 4 to 5 min and only 5% of the rate of cytochrome *c* reduction is SOD insensitive. The rates of the NADH-dependent activities catalyzed by complex I-containing proteoliposomes are shown in Table 26.2. Superoxide generation in the absence of any acceptor was only 0.15% of the NADH: DBQ reductase reaction (accounted as 2 e⁻-transfer). It should be noted that DBQ is a much more reliable substrate for complex I (i.e., for the determination of the catalytic activity and for ROS measurements) than the more hydrophilic Q₁. Addition of hydrophobic ubiquinone analogs does not significantly affect the superoxide generation rates; however, hydrophilic Q₁ increases the production eightfold. Presumably, Q₁ acts as a redox mediator between molecular oxygen and the enzyme, mostly at a nonphysiologic site in the hydrophilic domain of complex I (Galkin and Brandt, 2005). It seems most likely that in this case the source of superoxide is the autooxidation of reduced or semireduced Q₁ formed by complex I turnover (James *et al.*, 2005).

Table 26.1 dNADH-dependent activities of *Y. lipolytica* mitochondrial membranes^a

dNADH oxidation			O ₂ ⁻ generation				
HAR ^b	O ₂	DBQ ^b	No additions	Antimycin	DQA	Stigma tellin	Azide
$\mu\text{mol dNADH} \cdot \text{min}^{-1} \cdot \text{mg}^{-1}$			$\text{nmol AcCyt c} \cdot \text{min}^{-1} \cdot \text{mg}^{-1}$				
1.2 ± 0.2	0.17 ± 0.20	0.42 ± 0.13	0.25 ± 0.09	1.74 ± 0.33	0.70 ± 0.21	0.65 ± 0.26	0.57 ± 0.21

^a Data from [Galkin and Brandt \(2005\)](#).^b In the presence of sodium-azide and stigmatellin.**Table 26.2** NADH-dependent activities of complex I-containing proteoliposomes^a

	NADH oxidation			O ₂ ⁻ generation		
	HAR	DBQ	Q ₁	No quinone	DBQ	Q ₁
	$\mu\text{mol NADH min}^{-1} \text{mg}^{-1}$			$\text{nmol AcCyt c min}^{-1} \text{mg}^{-1}$		
Proteoliposomes	21.0 ± 0.3	6.3 ± 0.2	4.3 ± 0.3	16 ± 3	22 ± 2	125 ± 10
Proteoliposomes + Q ₉	22.1 ± 1.0	6.5 ± 0.3	4.1 ± 0.2	16 ± 2	20 ± 3	113 ± 12

^a Data from [Galkin and Brandt \(2005\)](#).

This reaction occurs in the aqueous phase and, therefore, is less pronounced with hydrophobic ubiquinone derivatives. In fact, it was shown that the rate correlates with ubiquinol hydrophilicity and is greatly reduced in the presence of phospholipid membranes (James *et al.*, 2005). Consequently, the addition of phospholipids or the reconstitution into proteoliposomes not only recovers the maximal catalytic activity of purified complex I but also reduces unwanted side reactions. Enrichment of proteoliposomes by ubiquinone Q₉ (~60 mol/mol enzyme) does not affect any of the complex I activities.

All NADH-dependent activities of complex I, including superoxide generation, can be inhibited effectively by diphenyleneiodonium (DPI)—a covalent inhibitor of flavoproteins. Because DPI reacts only with reduced FMN, proteoliposomes have to be incubated with inhibitor (20 mol DPI per mol of the enzyme for ~90% inhibition) on ice for at least 60 min in the presence of a reductant such as NADH in micromolar concentrations. If incubated with oxidized enzyme, DPI does not inhibit complex I at concentrations up to 5 μM . It should be noted that during long incubations in the reduced state, the activity of complex I always decreases, probably because of dissociation of the reduced flavine from the enzyme (Gostimskaya *et al.*, 2007).

3.3. pH profile for ubiquinone reduction and superoxide formation

The absolute NADH: ubiquinone oxidoreductase activity of reconstituted complex I is pH dependent, showing a classical bell-shaped curve with an optimum at approximately pH 7.5 (Fig. 26.1). However, the rate of

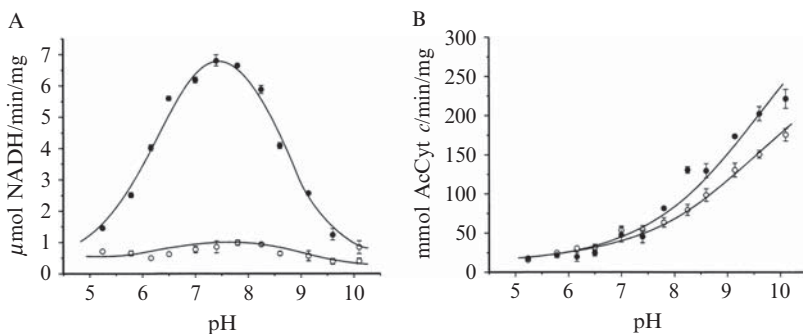


Figure 26.1 pH dependence of ubiquinone reduction and superoxide formation. Complex I was activated by a mixture of 76% phosphatidyl-choline/19% phosphatidyl-ethanolamine/5% cardiolipin. Shown are the pH dependence of the NADH: DBQ oxidoreductase activity (A) and the pH dependence of superoxide generation by complex I (B) in proteoliposomes with (○) and without (●) the addition of 1 μM DQA. Note that the pH profiles for ubiquinone reduction and superoxide formation are different.

superoxide production gradually increases with alkalization of the medium and is 10 times faster at pH 10 than at pH 6.0. This increase is mostly due to a rise in the overall rate of cytochrome *c* reduction, whereas the SOD-insensitive component is increased only slightly. Above pH 9.5 the initial rate can be measured for a short time only, most likely because of the instability of the enzyme in highly alkaline medium. The pH dependence of the superoxide generation rates corresponds to the accumulation of the fully reduced flavine.

4. DETECTION OF HYDROGEN PEROXIDE BY THE AMPLEX RED/HRP ASSAY

With the Amplex Red/HRP assay, the generation of superoxide is detected indirectly by measuring H_2O_2 formation. Superoxide dismutates spontaneously to H_2O_2 , but the reaction is greatly accelerated by superoxide dismutases. In the presence of horseradish peroxidase, H_2O_2 reacts with Amplex Red in a 1:1 stoichiometry to produce the red-fluorescent oxidation product resorufin (Zhou *et al.*, 1997).

4.1. Spectral properties of resorufin

It has to be noted that absorption and fluorescence of resorufin are both pH dependent. Below the pK_a (~ 6.0), the absorption maximum shifts to ~ 480 nm, and the fluorescence quantum yield is markedly lower. In addition, the Amplex Red reagent is unstable at high pH (>8.5). For these reasons the reactions should be performed at pH 7 to 8. For the calculation of H_2O_2 generation the extinction coefficient $\epsilon_{571\text{nm}} = 54 \text{ cm}^{-1} \text{ mM}^{-1}$ can be used, or the assay can be calibrated with known concentrations of H_2O_2 that must be prepared freshly from a 3 to 30% stock solution. The exact H_2O_2 concentrations can be determined by a catalase assay with an oxygen electrode. Note that the excitation/absorption maximum of 563 nm given by Zhou *et al.* (1997) is not correct. We could confirm the maximum given by the manufacturer (571 nm). Nevertheless, if the resorufin formation is followed by fluorescence measurements, the samples should rather be excited at a wavelength of about 560 nm because of the small Stokes shift (absorption and fluorescence emission maxima are 571 nm and 585 nm, respectively). The emission wavelength should be set to ~ 590 nm.

4.2. Parallel measurement of NADH oxidation, H_2O_2 generation, and buildup of a membrane potential by reconstituted complex I

To study the influence of membrane potential and catalytic turnover on superoxide formation, it would be desirable to assay NADH-oxidation (or NADH: DBQ oxidoreductase activity), ROS-production by the Amplex

Red/HRP assay, and generation of a membrane potential by oxonol VI simultaneously in a diode array spectrophotometer. However, we observed an interference of oxonol VI with the Amplex Red/HRP assay (not shown). Therefore, H_2O_2 generation with the Amplex Red/HRP assay and generation of a membrane potential must be measured in parallel (Fig. 26.2). Because HRP has a measurable NADH-oxidase activity and also catalyzes a NADH-dependent oxidation of Amplex Red (see following), these background activities must be determined in the absence of complex I. Approximately 15 μg of reconstituted complex I was added to 20 mM K^+ /MOPS, pH 7.2, 50 mM KCl at 30° for each measurement. To determine the membrane potential formed, 2 μM oxonol VI was present. Subsequently 100 μM NADH, 100 μM DBQ, and 1 μM FCCP were added as indicated in Fig. 26.2. NADH-oxidation was followed at 340 – 400 nm ($\epsilon_{340-400} = 6.1 \text{ mM}^{-1} \text{ cm}^{-1}$), and oxonol VI accumulation in the proteoliposome lumen corresponding to the buildup of a membrane potential was monitored at 623 – 603 nm. The increase in oxonol VI absorption was abolished when the membrane potential was collapsed by the addition of FCCP.

Complex I turnover and membrane potential can be attenuated by the addition of inhibitors of the ubiquinone binding pocket like DQA or rotenone (not shown). Alternately, the active/deactive (A/D) transition of complex I (Vinogradov, 1998) can be used conveniently for this purpose: if complex I is preincubated for 20 min at 30°, it switches to the “deactive”- or D-form that is stabilized by bivalent cations like Ca^{2+} and Mg^{2+} (Kotlyar *et al.*, 1992). Zn^{2+} has been reported to inhibit complex I at even lower concentrations (Sharpley and Hirst, 2006), and we found with *Yarrowia* complex I that this is also due to stabilization of the D-form (Dröse and Brandt, unpublished results). The low concentration needed to inhibit complex I turnover by Zn^{2+} avoided the formation of metal hydroxides that could form at higher concentrations of Ca^{2+} , Mg^{2+} at pH > 7, and disturb the assay by clouding. When the NADH: DBQ oxidoreductase activity was attenuated by incubation of the deactivated complex with increasing concentrations of ZnCl_2 (Fig. 26.2C), a parallel decrease in the membrane potential formed was observed (Fig. 26.2A). For the parallel determination of H_2O_2 production, 20 μM Amplex Red, 0.2 U/ml HRP, 400 U/ml SOD, and the preincubated proteoliposomes were added to the assay buffer. Note that some preparations of SOD have a significant H_2O_2 disproportionating activity because of tiny impurities of highly active catalase. This can easily be checked by oxygen release after adding H_2O_2 to an SOD solution in an oxygraph chamber or by investigating the effect of the SOD on H_2O_2 standards in the Amplex Red/HRP assay. The rather high concentration of SOD was necessary to accelerate the dismutation of superoxide to hydrogen peroxide and to suppress the NADH-dependent oxidation of Amplex Red catalyzed by HRP (Chen and Schopfer, 1999) that causes an unspecific background in the absence of SOD (Votyakova

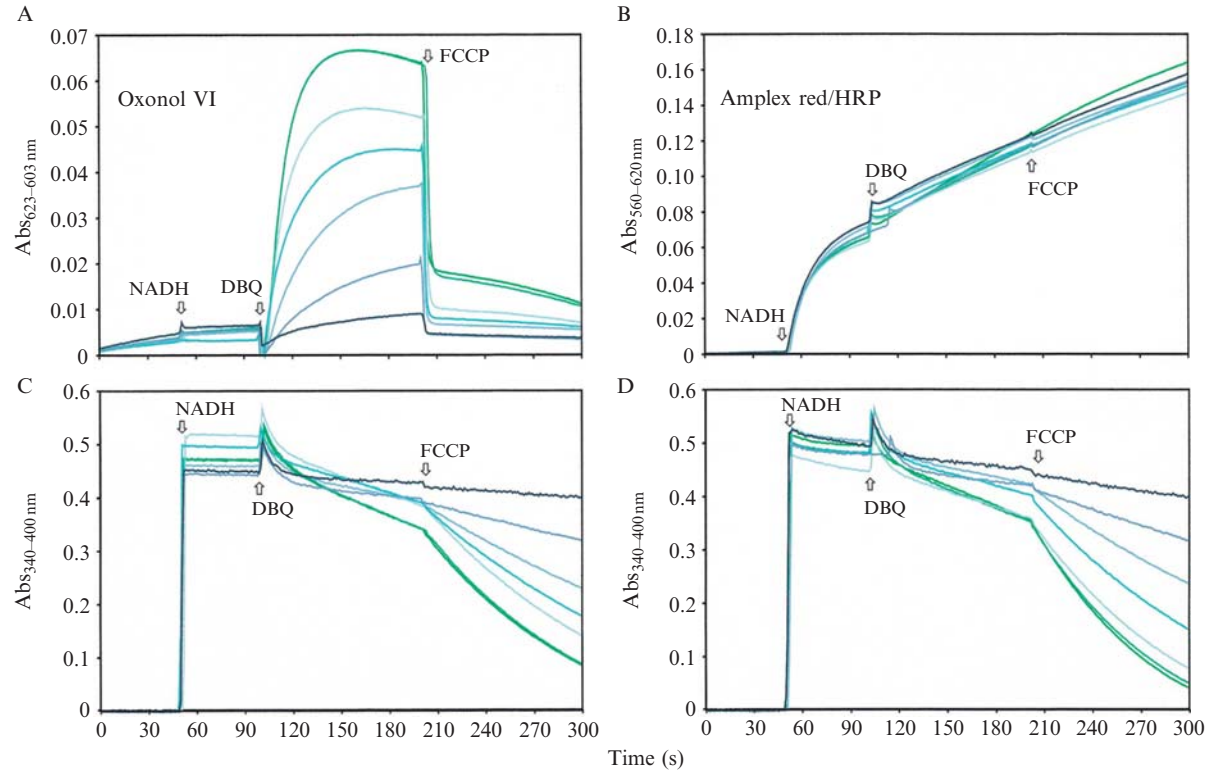


Figure 26.2 Parallel measurement of NADH oxidation, formation of membrane potential, and H₂O₂ generation. By use of proteoliposomes with reconstituted complex I from *Y. lipolytica*, Zn²⁺-ions were applied to inhibit complex I turnover; increasing Zn²⁺ concentrations (0, 1, 5, 10, 20, 50, and 100 μ M) are indicated by different shades of grey. (A) Generation of $\Delta\psi$ as absorbance of oxonol VI; B, rate of H₂O₂ generation measured by the Amplex Red/HRP assay. The rates of NADH oxidation measured simultaneously to the oxonol VI assay are shown in (C) and the rates of NADH oxidation measured simultaneously to the Amplex Red/HRP assay are shown in (D).

and Reynolds, 2004). It must be stressed that H_2O_2 detection by the Amplex Red/HRP assay is highly dependent on the concentration of HRP and Amplex Red and that the “optimal conditions” have to be determined empirically for each experimental setup.

A comparison of the NADH-oxidation rates measured in the Amplex Red/HRP assay (Fig. 26.2C) with those measured with oxonol VI (Fig. 26.2D) revealed that both dyes reduced the coupling ratio of the proteoliposomes somewhat. In the example shown in Fig. 26.2, the addition of Amplex Red already reduced the coupling ratio from 4.9 to 3.8. When oxonol VI was added, it went down further to ~ 2.7 .

Neither the size of the membrane potential nor the catalytic rate of complex I markedly affected the rate of H_2O_2 generation (Fig. 26.2 B). Our observation that ROS production by complex I was essentially independent of catalytic turnover is in good agreement with published measurements with purified complexes from *Yarrowia* (Galkin and Brandt, 2005), bovine heart mitochondria (Kusmaul and Hirst, 2006), and *E. coli* (Esterhazy *et al.*, 2008). However, it is in stark contrast with several reports showing that complex I inhibitors stimulate ROS generation in mitochondrial membranes and intact mitochondria (Lambert and Brand, 2004; Ohnishi *et al.*, 2005a; Votyakova and Reynolds, 2001). There are several possible explanations for this discrepancy: (1) in intact mitochondria, ROS production may be partly due to activity of NAD(P)⁺-dependent matrix enzymes that are stimulated by the increase in nucleotide reduction; (2) the application of hydrophilic analogs of the substrate ubiquinone facilitates nonphysiologic side reactions that do not occur with the endogenous, much more hydrophobic, ubiquinones Q₉ and Q₁₀ (see earlier); (3) fast consumption of NADH by complex I in submitochondrial particles or mitochondrial membranes is prevented by complex I inhibition, thereby affecting ROS production that is controlled by the NADH/NAD⁺ ratio (Kusmaul and Hirst, 2006). Note that the latter effect renders endpoint measurements inadequate for determining the effect of inhibitors on complex I-dependent ROS generation.

5. CONCLUSIONS

Isolated complex I from *Y. lipolytica* generates superoxide during oxidation of NADH in the absence and presence of ubiquinone by direct transfer of an electron from the reduced flavine to oxygen. The generation of superoxide in the forward NADH: ubiquinone oxidoreductase reaction is not sensitive to protonmotive force and essentially is not dependent on catalytic turnover of the enzyme nor on the presence of specific inhibitors.

When measuring NADH-dependent superoxide production by isolated complex I, several factors should be taken into consideration:

- The enzyme has to be reactivated by phospholipids.
- Superoxide generation rates should be given in relation to other NADH-dependent activities of complex I (i.e., NADH: ubiquinone oxidoreductase and NADH: HAR oxidoreductase).
- Superoxide production can be measured directly by superoxide-sensitive probes or indirectly by measuring H₂O₂ formation in presence of excess SOD.
- Concentrations of the components of coupled systems (acetylated cytochrome *c*/SOD or Amplex Red/peroxidase) have to be newly established for any given experimental setup.
- Side reactions of HRP have to be considered when the hydrogen peroxide production is monitored by the Amplex Red/HRP assay.
- For measuring superoxide generation during NADH: ubiquinone oxidoreduction, the use of decylubiquinone is recommended to minimize nonspecific reactions with oxygen.
- Any NADH-dependent activities of complex I including superoxide generation can be blocked by inhibition of the enzyme with diphenyle-neiodonium under reducing conditions.
- Special care should be taken to control the active/deactive transition of complex I in preparations of the eukaryotic enzyme.

REFERENCES

- Azzi, A., Montecucco, C., and Richter, C. (1975). The use of acetylated ferricytochrome *c* for the detection of superoxide radicals produced in biological membranes. *Biochem Biophys Res. Commun.* **65**, 597–603.
- Chen, S. X., and Schopfer, P. (1999). Hydroxyl-radical production in physiological reactions—A novel function of peroxidase. *Eur. J. Biochem.* **260**, 726–735.
- Dröse, S., Galkin, A., and Brandt, U. (2005). Proton pumping by complex I (NADH: ubiquinone oxidoreductase) from *Yarrowia lipolytica* reconstituted into proteoliposomes. *Biochim. Biophys. Acta* **1710**, 87–95.
- Dröse, S., Zwicker, K., and Brandt, U. (2002). Full recovery of the Oxidoreductase activity of complex I (NADH: ubiquinone oxidoreductase) from *Yarrowia lipolytica* by the addition of phospholipids. *Biochim. Biophys. Acta* **1556**, 65–72.
- Esterhazy, D., King, M. S., Yakovlev, G., and Hirst, J. (2008). Production of reactive oxygen species by complex I (NADH: ubiquinone oxidoreductase) from *Escherichia coli* and comparison to the enzyme from mitochondria. *Biochem.* **47**, 3964–3971.
- Fato, R., Estornell, E., Di Bernardo, S., Pallotti, F., Castelli, G. P., and Lenaz, G. (1996). Steady-state kinetics of the reduction of coenzyme Q analogs by complex I (NADH: ubiquinone oxidoreductase) in bovine heart mitochondria and submitochondrial particles. *Biochem.* **35**, 2705–2716.
- Fridovich, I. (1978). The biology of oxygen radicals. *Science* **201**, 875–880.

- Galkin, A., and Brandt, U. (2005). Superoxide radical formation by pure complex I (NADH: ubiquinone oxidoreductase) from *Yarrowia lipolytica*. *J. Biol. Chem.* **280**, 30129–30135.
- Genova, M. L., Ventura, B., Giuliano, G., Bovina, C., Formiggini, G., Parenti Castelli, G., and Lenaz, G. (2001). The site of production of superoxide radical in mitochondrial complex I is not a bound ubisemiquinone but presumably iron-sulfur cluster N2. *FEBS Lett.* **505**, 364–368.
- Gostinskaya, I. S., Grivennikova, V. G., Cecchini, G., and Vinogradov, A. D. (2007). Reversible dissociation of flavin mononucleotide from the mammalian membrane-bound NADH: Ubiquinone oxidoreductase (complex I). *FEBS Lett.* **581**, 5803–5806.
- Hinkle, P. C., Butow, R. A., Racker, E., and Chance, B. (1967). Partial resolution of the enzymes catalyzing oxidative phosphorylation. XV. Reverse electron transfer in the flavin-cytochrome beta region of the respiratory chain of beef heart submitochondrial particles. *J. Biol. Chem.* **242**, 5169–5173.
- James, A. M., Cocheme, H. M., Smith, R. A. J., and Murphy, M. P. (2005). Interactions of mitochondria-targeted and untargeted ubiquinones with the mitochondrial respiratory chain and reactive oxygen species—Implications for the use of exogenous ubiquinones as therapies and experimental tools. *J. Biol. Chem.* **280**, 21295–21312.
- Kakinuma, K., and Minakami, S. (1978). Effects of fatty acids on superoxide radical generation in leukocytes. *Biochim. Biophys. Acta* **538**, 50–59.
- Kashani-Poor, N., Kerschler, S., Zickermann, V., and Brandt, U. (2001). Efficient large scale purification of his-tagged proton translocating NADH: ubiquinone oxidoreductase (complex I) from the strictly aerobic yeast *Yarrowia lipolytica*. *Biochim. Biophys. Acta* **1504**, 363–370.
- Kerschler, S., Dröse, S., Zickermann, V., and Brandt, U. (2008). The three families of respiratory NADH dehydrogenases. *Results Problems Cell Different* **45**, 185–222.
- Kerschler, S., Dröse, S., Zwicker, K., Zickermann, V., and Brandt, U. (2002). *Yarrowia lipolytica*, a yeast genetic system to study mitochondrial complex I. *Biochim. Biophys. Acta* **1555**, 83–91.
- Kerschler, S., Okun, J. G., and Brandt, U. (1999). A single external enzyme confers alternative NADH: ubiquinone oxidoreductase activity in *Yarrowia lipolytica*. *J. Cell Sci.* **112**, 2347–2354.
- Kotlyar, A. B., Sled, V. D., and Vinogradov, A. D. (1992). Effect of Ca^{2+} ions on the slow active/inactive transition of the mitochondrial NADH-ubiquinone reductase. *Biochim. Biophys. Acta* **1098**, 144–150.
- Kushnareva, Y., Murphy, A. N., and Andreyev, A. (2002). Complex I-mediated reactive oxygen species generation: Modulation by cytochrome *c* and NAD(P)^+ oxidation-reduction state. *Biochem. J.* **368**, 545–553.
- Kussmaul, L., and Hirst, J. (2006). The mechanism of superoxide production by NADH: Ubiquinone oxidoreductase (complex I) from bovine heart mitochondria. *Proc. Natl. Acad. Sci. USA* **103**, 7607–7612.
- Lambert, A. J., and Brand, M. D. (2004). Inhibitors of the quinone-binding site allow rapid superoxide production from mitochondrial NADH: ubiquinone oxidoreductase (complex I). *J. Biol. Chem.* **279**, 39414–39420.
- Liu, Y., Fiskum, G., and Schubert, D. (2002). Generation of reactive oxygen species by the mitochondrial electron transport chain. *J. Neurochem.* **80**, 780–787.
- Ohnishi, S. T., Ohnishi, T., Muranaka, S., Fujita, H., Kimura, H., Uemura, K., Yoshida, K., and Utsumi, K. (2005a). A possible site of superoxide generation in the complex I segment of rat heart mitochondria. *J. Bioenerg. Biomembr.* **37**, 1–15.
- Ohnishi, T., Johnson, J. E. Jr., Yano, T., LoBrutto, R., and Widger, W. R. (2005b). Thermodynamic and EPR studies of slowly relaxing ubisemiquinone species in the isolated bovine heart complex I. *FEBS Lett.* **579**, 500–506.

- Sharpley, M. S., and Hirst, J. (2006). The inhibition of mitochondrial complex I (NADH: ubiquinone oxidoreductase) by Zn^{2+} . *J. Biol. Chem.* **281**, 34803–34809.
- Sharpley, M. S., Shannon, R. J., Draghi, F., and Hirst, J. (2006). Interactions between phospholipids and NADH: ubiquinone oxidoreductase (complex I) from bovine mitochondria. *Biochem.* **45**, 241–248.
- Sinegina, L., Wikstrom, M., Verkhovskiy, M. I., and Verkhovskaya, M. L. (2005). Activation of isolated NADH: ubiquinone reductase I (complex I) from *Escherichia coli* by detergent and phospholipids. Recovery of ubiquinone reductase activity and changes in EPR signals of iron-sulfur clusters. *Biochem.* **44**, 8500–8506.
- Stolpe, S., and Friedrich, T. (2004). The *Escherichia coli* NADH: Ubiquinone oxidoreductase (complex I) is a primary proton pump but may be capable of secondary sodium antiport. *J. Biol. Chem.* **279**, 18377–18383.
- Tarpey, M. M., and Fridovich, I. (2001). Methods of detection of vascular reactive species—Nitric oxide, superoxide, hydrogen peroxide, and peroxynitrite. *Circul. Res.* **89**, 224–236.
- Turrens, J. F. (2003). Mitochondrial formation of reactive oxygen species. *J. Physiol.* **552**, 335–344.
- Vinogradov, A. D. (1998). Catalytic properties of the mitochondrial NADH-ubiquinone oxidoreductase (Complex I) and the pseudo-reversible active/inactive enzyme transition. *Biochim. Biophys. Acta* **1364**, 169–185.
- Vinogradov, A. D., and Grivennikova, V. G. (2005). Generation of superoxide-radical by the NADH: ubiquinone oxidoreductase of heart mitochondria. *Biochem. (Moscow)* **70**, 120–127.
- Votyakova, T. V., and Reynolds, I. J. (2001). $\Delta\Psi(m)$ -Dependent and -independent production of reactive oxygen species by rat brain mitochondria. *J. Neurochem.* **79**, 266–277.
- Votyakova, T. V., and Reynolds, I. J. (2004). Detection of hydrogen peroxide with Amplex Red: Interference by NADH and reduced glutathione auto-oxidation. *Arch. Biochem. Biophys.* **431**, 138–144.
- Zhou, M. J., Diwu, Z. J., PanchukVoloshina, N., and Haugland, R. P. (1997). A stable nonfluorescent derivative of resorufin for the fluorometric determination of trace hydrogen peroxide: Applications in detecting the activity of phagocyte NADPH oxidase and other oxidases. *Anal. Biochem.* **253**, 162–168.

AN IMPROVED METHOD FOR INTRODUCING POINT MUTATIONS INTO THE MITOCHONDRIAL CYTOCHROME *b* GENE TO FACILITATE STUDYING THE ROLE OF CYTOCHROME *b* IN THE FORMATION OF REACTIVE OXYGEN SPECIES

Martina G. Ding,^{*} Christine A. Butler,[†] Scott A. Saracco,[†] Thomas D. Fox,[†] François Godard,[‡] Jean-Paul di Rago,[‡] and Bernard L. Trumpower^{*}

Contents

1. Introduction: The Role of Cytochrome <i>b</i> in Superoxide Anion Formation	492
2. Construction of Plasmid pSCSI Containing an ARG8 ^m Cassette Flanked by the Cytochrome <i>b</i> Gene 5'- and 3'-UTR Sequences	494
3. Construction of the Yeast Recipient Strain for Cytochrome <i>b</i> Mutations, YTE31, In which the Cytochrome <i>b</i> Gene is Replaced by Mitochondrially Encoded ARG8	495
4. Construction of the Template Vector, Plasmid pMD2, Containing an Intronless Cytochrome <i>b</i> Gene and COX2	497
5. Introduction of Mutations in the Cytochrome <i>b</i> Gene and Amplifying and Sequencing the Mutated Cytochrome <i>b</i> Genes	498
6. Creation of Yeast Cytochrome <i>b</i> Mutant Strains by Biolistic Transformation of Yeast Strain DFS160 ρ^0 with Plasmids Containing Mutated Versions of the Cytochrome <i>b</i> Gene	498

^{*} Department of Biochemistry, Dartmouth Medical School, Hanover, New Hampshire, USA

[†] Department of Molecular Biology and Genetics, Biotechnology Building, Cornell University, Ithaca, New York, USA

[‡] Institut de Biochimie et Génétique Cellulaires (CNRS), Université Victor Segalen, Bordeaux, France

6.1. Obtaining cytochrome <i>b</i> respiratory-competent mutations in a ρ^+ background	500
6.2. Obtaining cytochrome <i>b</i> respiratory-deficient mutations in a ρ^+ background	502
7. Cytoduction between Recipient Strain YTE31 and MR6, A Derivative of W303-1B	502
8. Creating Recipient Strains FG20 and FG21, Derivatives of W303-1B that Contain the YTE31 Mitochondria	503
References	505

Abstract

Cytochrome *b* is a pivotal protein subunit of the cytochrome *bc*₁ complex and forms the ubiquinol oxidation site in the enzyme that is generally thought to be the primary site where electrons are aberrantly diverted from the enzyme, reacting with oxygen to form superoxide anion. In addition, recent studies have shown that mutations in cytochrome *b* can substantially increase rates of oxygen radical formation by the *bc*₁ complex. It would, thus, be advantageous to be able to manipulate cytochrome *b* by mutagenesis of the cytochrome *b* gene to better understand the role of cytochrome *b* in oxygen radical formation. Cytochrome *b* is encoded in the mitochondrial genome in eukaryotic cells, and introduction of point mutations into the gene is generally cumbersome because of the tedious screening process for positive clones. In addition, previously it has been especially difficult to introduce point mutations that lead to loss of respiratory function, as might be expected of mutations that markedly enhance oxygen radical formation.

To more efficiently introduce amino acid changes into cytochrome *b* we have devised a method for mutagenesis of the *Saccharomyces cerevisiae* mitochondrial cytochrome *b* gene that uses a recoded *ARG8* gene as a “placeholder” for the wild-type *b* gene. In this method *ARG8*, a gene that is normally encoded by nuclear DNA, replaces the naturally occurring mitochondrial cytochrome *b* gene, resulting in *ARG8* expressed from the mitochondrial genome (*ARG8^m*). Subsequently replacing *ARG8^m* with mutated versions of cytochrome *b* results in arginine auxotrophy. Respiratory-competent cytochrome *b* mutants can be selected directly by virtue of their ability to restore growth on nonfermentable substrates. If the mutated cytochrome *b* is nonfunctional, the presence of the *COX2* respiratory gene marker on the mitochondrial transforming plasmid enables screening for cytochrome *b* mutants with a stringent respiratory deficiency (*mit*⁻).

1. INTRODUCTION: THE ROLE OF CYTOCHROME *b* IN SUPEROXIDE ANION FORMATION

Two respiratory enzyme complexes located in the inner mitochondrial membrane, the NADH dehydrogenase complex and the cytochrome *bc*₁ complex, are responsible for the production of superoxide anion by

mitochondria (Muller, 2000). Although there seem to be two sites of superoxide anion formation in the NADH dehydrogenase complex that differ in importance under conditions of forward and reverse electron transfer (Esterhazy *et al.*, 2008), essentially all of the superoxide anion that is formed by the cytochrome *bc*₁ complex originates from the ubiquinol oxidation site at center P. This has been deduced on the basis of the ability of inhibitors that bind at center P or the ubiquinone reduction site at center N to eliminate or promote oxygen radical formation (Muller, 2000).

Center P contains two electron acceptors, the Rieske iron-sulfur cluster and the low potential *b*_L heme of cytochrome *b* (Trumpower, 2004). Structurally, the ubiquinol oxidation pocket at center P is formed by two transmembrane helices (C and F), the *cd1* and *ef* helices, and the conserved PEWY loop of cytochrome *b* (Hunte *et al.*, 2000). Crystal structures of the yeast *bc*₁ complex with stigmatellin bound at center P show that essentially all of the noncovalent interactions responsible for binding of the competitive inhibitor are to amino acids in cytochrome *b* (Lancaster *et al.*, 2007). Likewise, energy minimizations by molecular modeling indicate that interactions between amino acids in cytochrome *b* and the aliphatic side chains of hydroxynaphthoquinones contribute most of the binding energy for these quinoid inhibitors (Kessl *et al.*, 2007).

It had previously been thought that superoxide anion formation at center P results from formation of an unstable, low-potential semiquinone during the ubiquinol oxidation reaction in the Q cycle mechanism at center P and its aberrant reactivity with oxygen instead of the *b*_L heme (Muller, 2000). More recent studies, however, provide compelling evidence that the semiquinone is formed by a reversal of the reaction at center P, in which the *b*_L heme reduces quinone to form the oxygen reactive semiquinone (Drose and Brandt, 2008).

Thus, structural considerations and the redox chemistry of superoxide anion formation at center P suggest that the cytochrome *b* subunit of the *bc*₁ complex is of central importance in this reaction. In addition, several mutations in cytochrome *b* recently have been shown to markedly enhance rates of superoxide anion formation by the yeast *bc*₁ complex (Wenz *et al.*, 2007). To better understand the role of cytochrome *b* in formation of superoxide anion, it would be advantageous to introduce point mutations into the cytochrome *b* subunit and then examine how these affect superoxide anion formation by the isolated enzyme.

Several *S. cerevisiae* strains carrying point mutations in cytochrome *b* have been created in recent years with biolistic bombardment (Kessl *et al.*, 2005, 2007; Wenz *et al.*, 2007). In the previously used methods, the recipient strain contained either a wild-type cytochrome *b* gene or a cytochrome *b* gene with a point mutation (*mit*⁻) impairing mitochondrial respiration. The use of a wild-type recipient strain makes the process very laborious, especially when the mutations of interest have no or only moderate effects on the function of

the *bc₁* complex. This means that hundreds of isolates have to be characterized at the molecular level (e.g., by sequencing) to find the few issued from a recombination between the synthetic ρ^- mtDNA bearing the cytochrome *b* mutation and the wild-type ρ^+ mtDNA of the recipient strain. With the method described here, which is based on the use of a cytochrome *b* deletion strain, all the respiring isolates have the mutation of interest integrated into their mitochondrial genome.

In addition, our method allows the creation of any type of mutation in the cytochrome *b* gene, such as the deletion of a defined segment or the introduction of a combination of several mutations in different regions, something that cannot be easily implemented with a *mit⁻* recipient strain, where most of the coding sequence of the cytochrome *b* gene is still present. Our method provides a simple phenotypic screening approach, revealing in all cases whether a given cytochrome *b* mutation results in a respiratory deficiency or not. In the case of respiratory deficiency, a nonreverting strain lacking a segment of the *COX2* gene is used as a tester strain that is indicative of the presence of the cytochrome *b* encoding plasmid in the mitochondria of the bombarded strain.

2. CONSTRUCTION OF PLASMID pSCSI CONTAINING AN *ARG8^m* CASSETTE FLANKED BY THE CYTOCHROME *b* GENE 5'- AND 3'-UTR SEQUENCES

In the course of this study several new yeast strains were created, and existing yeast strains were used. These are listed in Table 27.1. To create a yeast strain in which the cytochrome *b* gene (“COB”) was replaced by a recoded *ARG8* gene, it was first necessary to create a plasmid capable of making this replacement in the mitochondrial genome. Plasmid pSCSI, which contains an *ARG8^m* cassette in lieu of the cytochrome *b* gene, flanked by 100 bps of *COB* 5'- and 3'-UTR sequences, was generated by PCR with primers containing those flanking sequences and pDS24 (Steele *et al.*, 1996) as a template. The sense primer was COB-ARG8-F, 5'-*gct cta gaT* AAT TAA TAA TAT ATA TTT ATA TAT TTT TTA TTA ATT AAT ATA TAT AAA ATA TTA GTA ATA AAT AAT ATT ATT AAT ATT TTA TAA ATA AAT AAT AAT AAT atg ttc aaa aga tat tta tca tca-3' and anti-sense primer COB-ARG8-R 5'-*gcc tgg agT* TAA AGT ATT ATT ATT ATT AAT AAT TTT ATT TTT ATT TTT ATT ATA TTA TTA ATA ATA ATA ATA TAT ATA TTA TAT CTA TGT ATT AAT TTA ATT ATA TAT aag cat ata cag ctt cga tag c-3'. The underlined base pairs were introduced for improved restriction enzyme cutting. The uppercase letters depict cytochrome *b* 5'- and 3'-UTR sequences, and the lowercase letters are *ARG8^m* sequence capable of binding to pDS24. The letters in

Table 27.1 Genotypes of the *S. cerevisiae* strains used in this study

Strain	Nuclear genotype	mtDNA	Origin
DFS160	<i>Mat</i> α <i>ade</i> 2-101 <i>leu</i> 2 Δ <i>ura</i> 3-52 <i>arg</i> 8 Δ :: <i>URA</i> 3 <i>kar</i> 1-1	ρ^0	Steele <i>et al.</i> , 1996
NB97	<i>Mat</i> <i>a</i> <i>leu</i> 2-3,112 <i>lys</i> 2 <i>ura</i> 3-52 <i>his</i> 3 Δ <i>HinDIII</i> <i>arg</i> 8 Δ :: <i>URA</i> 3	ρ^+ <i>cox</i> 2-60	Bonnefof <i>et al.</i> , 2001
YTMT2	<i>Mat</i> α <i>ade</i> 2 <i>ura</i> 3 <i>leu</i> 2 <i>delta</i> <i>arg</i> 8 Δ :: <i>URA</i> 3 <i>kar</i> 1-1	ρ^+ <i>cox</i> 2-	di Rago lab
YTE31	<i>Mat</i> <i>a</i> <i>ade</i> 2-101 <i>ura</i> 3-52 <i>arg</i> 8 Δ :: <i>hisG</i> <i>kar</i> 1-1	ρ^+ <i>cob</i> Δ :: <i>ARG</i> 8 ^m <i>COX</i> 1 Δ ⁱ ^a	This study
MR6	<i>Mat</i> <i>a</i> <i>ade</i> 2-1 <i>his</i> 3-11,15 <i>trp</i> 1-1 <i>leu</i> 2-3,112 <i>ura</i> 3-1, <i>CAN</i> 1 <i>arg</i> 8 Δ :: <i>HIS</i> 3	ρ^0	Rak <i>et al.</i> , 2007
XPM177-1	<i>Mat</i> <i>a</i> <i>ade</i> 2-101 <i>ura</i> 3-52 <i>arg</i> 8 Δ :: <i>hisG</i> <i>kar</i> 1-1	ρ^- <i>COX</i> 1 Δ <i>i</i>	Fox lab
XPM62a	<i>Mat</i> α <i>lys</i> 2 <i>ura</i> 3-52 <i>his</i> 3 Δ <i>HinDIII</i> <i>arg</i> 8 Δ :: <i>hisG</i>	ρ^+ Δ <i>i</i> <i>cox</i> 1 Δ :: <i>ARG</i> 8 ^m	Fox lab
CK520	<i>Mat</i> <i>a</i> <i>leu</i> 1 <i>canR</i>	ρ^+ Δ <i>i</i>	Labouesse, 1990
SAS1A	<i>Mat</i> <i>a</i> <i>ura</i> 3-52 <i>leu</i> 2-3,112 <i>lys</i> 2 <i>his</i> 3 Δ <i>HinDIII</i> <i>arg</i> 8 Δ :: <i>hisG</i>	ρ^+	Fiumera <i>et al.</i> , 2007

^a Expression of this *COX1* allele does not depend on the *bl4* encoded maturase (Labouesse *et al.*, 1984). Δ *i* indicates intron deleted.

italics depict restriction sites, *Xba*I on the 5'-end, *Xho*I on the 3'-end, by means of which the DNA fragment was cloned into pBS KS, resulting in plasmid pSCS1, shown in Fig. 27.1A.

3. CONSTRUCTION OF THE YEAST RECIPIENT STRAIN FOR CYTOCHROME *b* MUTATIONS, YTE31, IN WHICH THE CYTOCHROME *b* GENE IS REPLACED BY MITOCHONDRIALLY ENCODED *ARG8*

There is only inefficient, if any, mitochondrial transformation when exogenous DNA is delivered directly by bombardment into yeast cells containing ρ^+ mitochondria (Bonnefof and Fox, 2001). This problem is

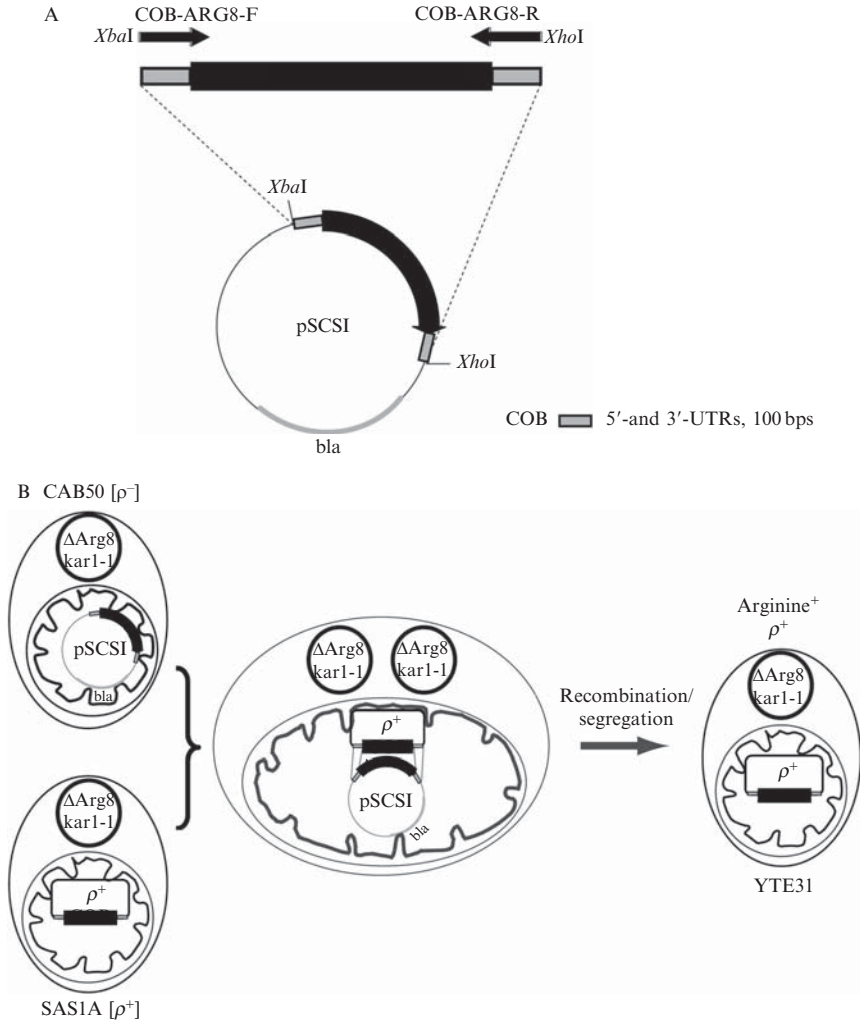


Figure 27.1 Creating the recipient strain containing *ARG8^m* instead of cytochrome *b* in its mitochondria. (A) Creation of a plasmid for biolistic transformation containing an *ARG8^m* cassette flanked by cytochrome *b* 5'- and 3'-UTRs. The template for the *ARG8* gene with mitochondrial codons was plasmid pDS24 (Steele *et al.*, 1996). The primers COB-ARG8-F and COB-ARG8-R were used for the gene amplification, resulting in an *ARG8^m* gene flanked by approximately 100 bps of COB 5'-UTR and 3'-UTR, respectively, encoded by the 5'- ends in both primers. Both primers also contained the restriction sites shown by which the gene was cloned into the pBluescript vector KS to create the vector pSCSI. The plasmid also contains the β -lactamase gene ("bla"). (B) How *ARG8^m* was introduced into the mitochondrial DNA of the recipient strain. The strain used for bombardment was DFS160, which is auxotrophic for leucine and arginine and does not contain mitochondrial DNA. The synthetic ρ^- DFS160-containing the plasmid pSCSI was named CAB50. Replacement of cytochrome *b* by *ARG8^m* can be confirmed by arginine prototrophy.

circumvented by bombarding a suitable strain lacking mtDNA (ρ^0) with a plasmid containing the mutagenic DNA fragment. It is one of the extraordinary aspects of *S. cerevisiae* mitochondria that any plasmid can be replicated and stably propagated as synthetic ρ^- molecules (Fox *et al.*, 1988). When the synthetic ρ^- mtDNA is brought into contact with ρ^+ mtDNA by crossing, homologous recombination can occur at high frequency, leading to the introduction of the mutation of interest into a complete mitochondrial genome.

Plasmid pSCSI was transformed into the mitochondria of the ρ^0 yeast strain DFS160 (Steele *et al.*, 1996) as described previously (Bonnefoy and Fox, 2001), with a biolistic PDS1000/He particle delivery system (Biorad), together with plasmid YEP351 carrying the nuclear selectable *LEU2* marker. Because the efficiency of mitochondrial transformation is rather weak, cotransformation with a nuclear selection marker is performed, such as the *LEU2* gene. *Leu*⁺ transformants originate from cells that have been hit and survived. A few of them (termed CAB50) contain in their mitochondria the plasmid pSCS1. These can confer arginine prototrophy by crossing to a suitable ρ^+ strain, SAS1A (Fiumera *et al.*, 2007), as illustrated in Fig. 27.1B.

The mitochondria of the mated cells fuse, allowing *ARG8^m* to replace the *COB* gene after homologous recombination. Some intermediate steps, not depicted in Fig. 27.1B., were necessary, because the mitochondrial DNA of SAS1A carries the *COX1* gene with introns. For its correct splicing, introns of *COB* are necessary (Labouesse *et al.*, 1985). Because the mutated *COB* genes we wanted to introduce were intronless, the *COX1* introns had to be removed beforehand from the *Arg*⁺ recombinants (CAB52-A) issued from the cross between CAB50 and SAS1A. To this end CAB52-A was crossed with a synthetic ρ^- strain, XPM177-1, bearing an intronless *COX1* gene. CAB52-A recombinants lacking the *COX1* introns were identified by virtue of their ability to recover respiratory competence in crosses with a *cox1* Δ ::*ARG8^m* strain (XPM62a) containing an intronless cytochrome *b* gene. One such cytoductant in which the cytochrome *b* gene was replaced by *ARG8^m* and lacking the *COX1* introns, was retained and named YTE31.

4. CONSTRUCTION OF THE TEMPLATE VECTOR, PLASMID PMD2, CONTAINING AN INTRONLESS CYTOCHROME *b* GENE AND *COX2*

To facilitate the replacement of the *ARG8^m* gene with the mutated *COB* gene, an intronless version of cytochrome *b* was amplified by PCR, with strain CK520 as a template (Labouesse, 1990). The intronless cytochrome *b* gene was cloned into a pBluescript vector by way of *Apa*I and *Hinc*II restriction sites. To be able to screen for cytochrome *b* mutations

leading to respiratory deficiency, the *COX2* gene amplified from strain W303-1B was sequenced and inserted through *Pst*I into the vector, named pMD1. Sequencing the intronless cytochrome *b* gene revealed that it carried a well-characterized mutation at position 252, from glycine to aspartate (Saint-Georges *et al.*, 2002), which had occurred when the intronless mitochondrial genome was created (Seraphin *et al.*, 1987). The mutation was removed with the site-directed mutagenesis kit and the primers listed in Table 27.2, resulting in plasmid pMD2, shown in Fig. 27.2A.

5. INTRODUCTION OF MUTATIONS IN THE CYTOCHROME *b* GENE AND AMPLIFYING AND SEQUENCING THE MUTATED CYTOCHROME *b* GENES

The primers used to introduce mutations with pMD2 as a template and the Stratagene Quikchange II Site-Directed Mutagenesis Kit are listed in Table II. The reaction was performed according to the instruction manual. Because the mitochondrial genome is high in AT content, the amount of primer was varied (i.e., doubled). The extension time/cycle was also doubled compared with the instructions.

Total DNA of the created strains was used as a template in the PCR to verify the presence of the intronless mutated COB gene. Sense primer MD26 starts 78 bps upstream from ATG, 5'- TTT ATA TAT TTT TTA TTA ATT AAT ATA TAT AAA ATA TTA G-3', and anti-sense primer MD27 starts 61 bps downstream of the stop codon, 5'-TTA TTA TAT TAT TAA TAA TAA TAA TAT ATA TAT TAT ATC TAT G -3'. The primer used for sequencing and confirming the mutations was anti-sense primer MD2 5'-CCA TAA TAT AAA CCT TTA GCC ATA TGC-3', located in exon 1. A compilation of the cytochrome *b* mutations created by this new method and the ubiquinol-cytochrome *c* reductase activities of the cytochrome *bc*1 complexes isolated from these yeast mutants are shown in Table 27.3.

6. CREATION OF YEAST CYTOCHROME *b* MUTANT STRAINS BY BIOLISTIC TRANSFORMATION OF YEAST STRAIN DFS160 ρ^0 WITH PLASMIDS CONTAINING MUTATED VERSIONS OF THE CYTOCHROME *b* GENE

A flowchart of the procedure to introduce cytochrome *b* mutations in the mitochondrial genome is shown in Fig. 27.2B. The plasmid pMDx, carrying a cytochrome *b* mutation, *COB_m*, was delivered into the mitochondria of the ρ^0 strain DFS160 by bombardment. Preselection was

Table 27.2 Cytochrome-*b* mutagenesis primers used in this study.

Amino acid change		Primer sequences (5' → 3')
D252G	S	GTA TTC TAT TCA CCT AAT ACT TTA GGT CAT CCT GAT AAC TAT ATT CCT GG
	A	CC AGG AAT ATA GTT ATC AGG ATG ACC TAA AGT ATT AGG TGA ATA GAA TAC
Y9A	S	G GCA TTT AGA AAA TCA AAT GTG GCT TTA AGT TTA GTG AAT AG
	A	CT ATT CAC TAA ACT TAA AGC CAC ATT TGA TTT TCT AAA TGC C
Y9F	S	G GCA TTT AGA AAA TCA AAT GTG TTT TTA AGT TTA GTG AAT AG
	A	CT ATT CAC TAA ACT TAA AAA CAC ATT TGA TTT TCT AAA TGC C
Y9T	S	G GCA TTT AGA AAA TCA AAT GTG ACT TTA AGT TTA GTG AAT AG
	A	CT ATT CAC TAA ACT TAA AGT CAC ATT TGA TTT TCT AAA TGC C
Y16A	S	GTG TAT TTA AGT TTA GTG AAT AGT GCT ATT ATT GAT TCA CCA CAA CC
	A	GG TTG TGG TGA ATC AAT AAT AGC ACT ATT CAC TAA ACT TAA ATA CAC
Y16F	S	GTG TAT TTA AGT TTA GTG AAT AGT TTT ATT ATT GAT TCA CCA CAA CC
	A	GG TTG TGG TGA ATC AAT AAT AAA ACT ATT CAC TAA ACT TAA ATA CAC
Y16I	S	GTG TAT TTA AGT TTA GTG AAT AGT ATT ATT ATT GAT TCA CCA CAA CC
	A	GG TTG TGG TGA ATC AAT AAT AAT ACT ATT CAC TAA ACT TAA ATA CAC
G37A	S	GA AAT ATG GGT TCA TTA TTA GCT TTA TGT TTA GTT ATT CAA ATT GTA ACA GG
	A	CC TGT TAC AAT TTG AAT AAC TAA ACA TAA AGC TAA TAA TGA ACC CAT ATT TC
G37C	S	GA AAT ATG GGT TCA TTA TTA TGT TTA TGT TTA GTT ATT CAA ATT GTA ACA GG
	A	CC TGT TAC AAT TTG AAT AAC TAA ACA TAA ACA TAA TAA TGA ACC CAT ATT TC
R79E	S	GTG CAT AAT GGT TAT ATT TTA GAA TAT TTA CAT GCA AAT GGT GC
	A	GC ACC ATT TGC ATG TAA ATA TTC TAA AAT ATA ACC ATT ATG CAC

(continued)

Table 27.2 (continued)

Amino acid change		Primer sequences (5' → 3')
R79K	S	GTG CAT AAT GGT TAT ATT TTA AAA TAT TTA CAT GCA AAT GGT GC
	A	GC ACC ATT TGC ATG TAA ATA TTT TAA AAT ATA ACC ATT ATG CAC
R79Q	S	GTG CAT AAT GGT TAT ATT TTA CAA TAT TTA CAT GCA AAT GGT GC
	A	GC ACC ATT TGC ATG TAA ATA TTG TAA AAT ATA ACC ATT ATG CAC

S, Sense; A, Antisense. Codons changed are bold.

achieved through the cobombardment of plasmid YEP351 containing the *LEU2* gene (Step 1 in Fig. 27.2B). When the surviving *Leu*⁺ colonies emerged after 5 to 7 days, they were replica-plated on YPDA medium containing a lawn of recipient strain YTE31 and the same medium containing a lawn of a *mit*⁻ *cox2* tester strain, NB97, respectively (Step 2 in Fig. 27.2B). After 2 days, the two mating plates were replica-plated on nonfermentable medium (Step 3 in Fig. 27.2B).

6.1. Obtaining cytochrome *b* respiratory-competent mutations in a ρ^+ background

In case of a cytochrome *b* mutation that supports respiratory growth, respiring colonies emerged on the two replica plates, at the same positions, as shown by the Y16A mutation in Fig. 27.3A, upper panel. The respiring clones issued from the cross with YTE31 resulted from replacement of *ARG8^m* with the mutated, but still functional, cytochrome *b* gene. Those issued from the cross with NB97 originated from a recombination between the *COX2* gene of plasmid pMDx and the mutated *cox2* locus of NB97, schematically depicted in Fig. 27.3B. The only thing that remained to be done was to pick a few respiring clones issued from the cross with YTE31 and to verify them by sequencing for the presence of the cytochrome *b* mutation. Without exception, all of the isolates proved to contain the mutated cytochrome *b* gene properly integrated into a complete mtDNA. It has to be noted that because of the presence of the nuclear *kar1-1* mutation in both DFS160 and YTE31, most of the cells remain haploid after crossing with either the nucleus of DF160 or that of YTE31. In all analyzed cases, >80% of the isolates had the nucleus of YTE31. Thus only a very limited number of colonies (five) need to be analyzed to have the desired cytochrome *b* mutants in the YTE31 nuclear background.

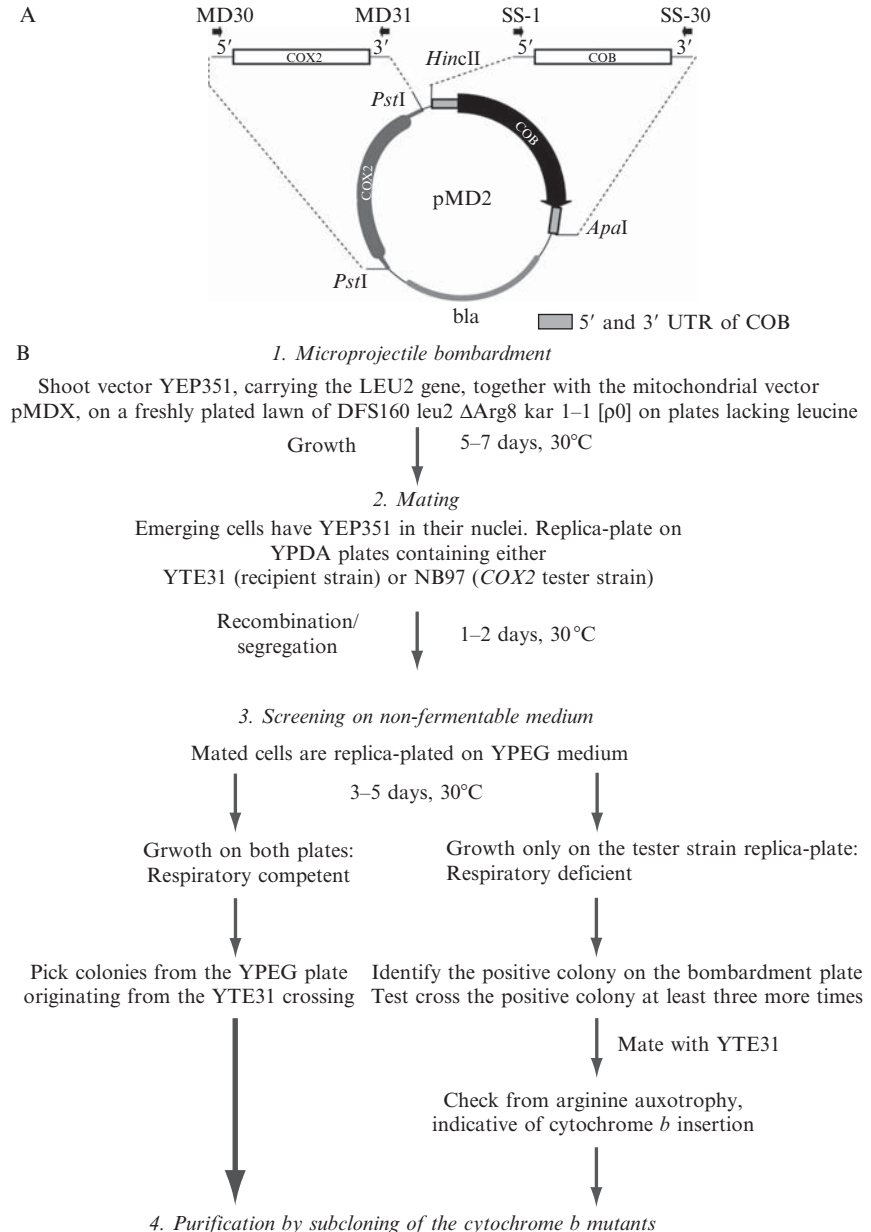


Figure 27.2 Introduction of cytochrome *b* mutations into recipient strain YTE31. (A) Creation of a plasmid containing the cytochrome *b* gene (*COB*) cassette flanked by cytochrome *b* 5'- and 3'-UTRs and a functional *COX2* gene, as a template for primer mutagenesis. The template for the *COB* gene was an intronless version of the cytochrome *b* gene, which was amplified with primers resulting in a *COB* gene flanked by approximately 340 bps of UTRs on each side, and *HincII* and *ApaI* sites for cloning into

6.2. Obtaining cytochrome *b* respiratory-deficient mutations in a ρ^+ background

When the cytochrome *b* mutation seriously impairs the *bc₁* complex, as was the case for the arginine 79 to glutamate exchange, shown in Fig. 27.3A., lower panel, the cross of the synthetic ρ^- *COBm* with YTE31 did not produce clones with good respiratory growth, whereas the cross with the *mit⁻ cox2 strain* (NB97) produced respiratory-competent clones. In that case, further work was needed to isolate the respiratory-deficient cytochrome *b* mutant. If the *Leu⁺* colonies had also received the mitochondrial plasmid, the presence of the plasmid within mitochondria could be confirmed by crossing over of the functional *COX2* on the vector into the NB97 mitochondrial DNA, which contains a functional cytochrome *b* gene.

First, the synthetic ρ^- colonies responsible for the *COX2* rescue (i.e., containing the pMD-R79E plasmid in their mitochondria) had to be carefully located on the original bombardment plate and purified by sub-cloning and repeating the tester strain cross at least three more times. The ρ^- *COBm* was then crossed with the cytochrome *b* deletion strain YTE31. A few percent of the progeny from the crossing consisted of cells where the *ARG8^m* gene had been replaced with the mutated cytochrome *b* gene. These cells could very easily be identified by their inability to grow in the absence of arginine and their ability to recover respiratory competence when crossed with a synthetic ρ^- strain containing the wild-type cytochrome *b* gene.

7. CYTODUCTION BETWEEN RECIPIENT STRAIN YTE31 AND MR6, A DERIVATIVE OF W303-1B

Because most of the laboratory strains we use, including those containing the new center N mutations (Ding *et al.*, 2008), are in the nuclear background of yeast strain W303-1B, we made a cytoduction as described elsewhere (Bonnefoy and Fox, 2001), mating the YTE31 strains carrying respiratory-competent cytochrome *b* mutations with MR6 ρ^0 (Rak *et al.*, 2007), an *arg8* derivative of W303-1B. The mating reaction was spread on

the Bluescript vector, named pCB6. The *COX2* gene, which allows selection of cytochrome *b* mutants that are impaired or respiratory deficient, was amplified with primers that resulted in a PCR product containing the ORF of *COX2* flanked by approximately 250 bps of the 5'- and 3'-UTRs. It was cloned by way of a *PstI* site into vector pCB6, resulting in vector pMD2. (B) Flowchart with the sequence of events needed to introduce plasmid pMDx, containing a cytochrome *b* mutation, into recipient strain YTE31.

Table 27.3 Ubiquinol–cytochrome *c* reductase activities of mitochondrial membranes of the wild-type and mutant yeast strains

Strain	Activity (sec ⁻¹)	% WT
WT	147	100
Y9A	93	63
Y9F	133	90
Y9T	123	84
Y16A	71	48
Y16F	137	93
Y16I	124	84
G37A	95	65
G37C	61	41
R79E	26	18
R79K	129	88
R79Q	98	67

Ubiquinol–cytochrome *c* reductase activities of mitochondrial membranes were measured as described in [Ding et al. \(2008\)](#). “WT” is the wild-type strain where intronless cytochrome *b* was introduced and replaced *ARG8^m*.

YPDA plates such that a countable number of colonies were obtained. This master plate was replica-plated on YPEG after 2 days to select for respiring colonies. Because strain YTE31 carries the *kar1-1* mutation ([Conde and Fink, 1976](#)), which prevents fusion of the nuclei, the desired MR6 nuclear background could be selected for by growth on minimal medium supplied with the needed ingredients.

8. CREATING RECIPIENT STRAINS FG20 AND FG21, DERIVATIVES OF W303-1B THAT CONTAIN THE YTE31 MITOCHONDRIA

To additionally facilitate the process, we created *Mat α* (FG20) and *Mata* (FG21) recipient strains that have the MR6 nuclear background and the YTE31 mitochondria, with the cytochrome *b* gene replaced by *ARG8^m*. The strain FG20 was obtained by mating the *Mat α* MR6 ρ^0 strain ([Rak et al., 2007](#)) with strain YTE31 and selection of Arg⁺ colonies with the nuclear background of MR6. The mating type of FG20 was switched with the HO plasmid to create strain FG21. We also created, by transformation with the HO plasmid, a *MATa* DFS160 strain. Thus, direct screening with the desired W303-1B nuclear background could be performed with DFS160 synthetic petites in either the *a* or α mating type.

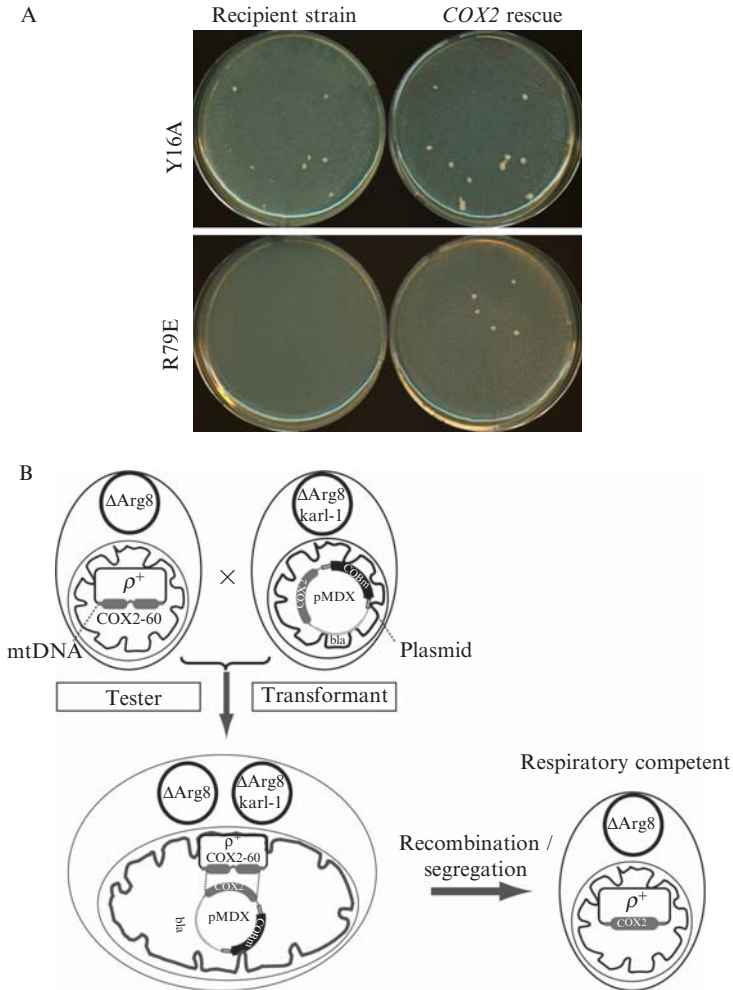


Figure 27.3 Screening for cytochrome *b* mutations. (A) Nonfermentable medium plates (YPEG) carrying the crosses of the synthetic ρ^- with recipient strain YTE31 (left) or the *COX2* rescue strain NB97 (right). The upper half shows the Y16A mutant strain, which is respiratory competent and grows in both crosses. The lower panel shows the R79E mutant strain, the growth of which is only possible with the rescue strain. (B) Schematic of how the *COX2* rescue works. After mating on fermentable medium, the cells are replica-plated on nonfermentable medium. The tester strain, NB97, is ρ^+ but contains a deletion in *COX2* and thus is respiratory deficient unless corrected with a functional *COX2* gene. Hence, the rescue depends on receiving the *COX2* gene on the plasmid that was introduced by biolistic transformation of the bombardment strain and thus confirms the existence of the plasmid in that strain. One has to go back to the original plate to localize the corresponding colony and perform this procedure at least three more times before finally mating the synthetic ρ^- with YTE31.

Strain YTMT2 is the *COX2* tester strain for bombardment in DFS160 Mata. The recipient strains are also necessary to obtain nonfunctional cytochrome *b* mutations in a W303-1B background.

REFERENCES

- Bonnefoy, N., and Fox, T. D. (2001). Genetic transformation of *Saccharomyces cerevisiae* mitochondria. *Methods Enzymol.* **350**, 97–111.
- Conde, J., and Fink, G. R. (1976). A mutant of *Saccharomyces cerevisiae* defective for nuclear fusion. *Proc. Natl. Acad. Sci. USA* **73**, 3651–3655.
- Ding, M. G., Butler, C. A., Saracco, S. A., Fox, T. D., Godard, F., di Rago, J. P., and Trumpower, B. L. (2008). Introduction of cytochrome *b* mutations in *Saccharomyces cerevisiae* by a method that allows selection for both functional and non-functional cytochrome *b* proteins. *Biochim. Biophys. Acta*. In press.
- Drose, S., and Brandt, U. (2008). The mechanism of mitochondrial superoxide production by the cytochrome *bc*₁ complex. *J. Biol. Chem.* **283**, 21649–21654.
- Esterhazy, D., King, M. S., Yakovlev, G., and Hirst, J. (2008). Production of reactive oxygen species by complex I (NADH: ubiquinone oxidoreductase) from *Escherichia coli* and comparison to the enzyme from mitochondria. *Biochemistry* **47**, 3964–3971.
- Fiumera, H.L., Broadley, S. A., and Fox, T. D. (2007). Translocation of mitochondrially synthesized Cox2 domains from the matrix to the intermembrane space. *Mol. Cell Biol.* **27**, 4664–4673.
- Fox, T. D., Sanford, J. C., and McMullin, T. W. (1988). Plasmids can stably transform yeast mitochondria lacking endogenous mtDNA. *Proc. Natl. Acad. Sci. USA* **85**, 7288–7299.
- Hill, P., Kessl, J., Fisher, N., Meshnick, S., Trumpower, B. L., and Meunier, B. (2003). Recapitulation in *Saccharomyces cerevisiae* of cytochrome *b* mutations conferring resistance to atovaquone in *Pneumocystis jiroveci*. *Antimicrob. Agents Chemother.* **47**, 2725–2731.
- Hunte, C., Koepke, J., Lange, C., Rossmannith, T., and Michel, H. (2000). Structure at 2.3 Å resolution of the cytochrome *bc*₁ complex from the yeast *Saccharomyces cerevisiae* co-crystallized with an antibody Fv fragment. *Structure* **8**, 669–684.
- Kessl, J., Ha, K. H., Merritt, A. K., Lange, B. B., Hill, P., Meunier, B., Meshnick, S. R., and Trumpower, B. L. (2005). Cytochrome *b* mutations that modify the ubiquinol-binding pocket of the cytochrome *bc*₁ complex and confer anti-malarial drug resistance in *Saccharomyces cerevisiae*. *J. Biol. Chem.* **280**, 17142–17148.
- Kessl, J. J., Moskalev, N. V., Gribble, G. W., Nasr, M., and Trumpower, B. L. (2007). Parameters determining the relative efficacy of hydroxynaphthoquinone inhibitors of the cytochrome *bc*₁ complex. *Biochim. Biophys. Acta* **1767**, 319–326.
- Labouesse, M. (1990). The yeast mitochondrial leucyl-tRNA synthetase is a splicing factor for the excision of several group I introns. *Mol. Gen. Genet.* **224**, 209–221.
- Labouesse, M., Netter, P., and Schroeder, R. (1984). Molecular basis of the ‘box effect’, a maturase deficiency leading to the absence of splicing of two introns located in two split genes of yeast mitochondrial DNA. *Eur. J. Biochem.* **144**, 85–93.
- Lancaster, C. R. D., Hunte, C., Kelley, J., Trumpower, B. L., and Ditchfield, R. (2007). A comparison of stigmatellin conformations, free and bound to the photosynthetic reaction center and the cytochrome *bc*₁ complex. *J. Mol. Biol.* **368**, 197–208.
- Muller, F. (2000). The nature and mechanism of superoxide production by the electron transport chain: Its relevance to aging. *J. Am. Aging Assoc.* **23**, 227–253.
- Rak, M., Tetaud, E., Godard, F., Sagot, I., Salin, B., Duvézin-Caubet, S., Slonimski, P. P., Rytka, J., and di Rago, J.-P. (2007). Yeast cells lacking the mitochondrial gene encoding

- the ATP synthase subunit 6 exhibit a selective loss of complex IV and unusual mitochondrial morphology. *J. Biol. Chem.* **282**, 10853–10864.
- Saint-Georges, Y., Bonnefoy, N., di Rago, J.-P., Chiron, S., and Dujardin, G. (2002). pathogenic cytochrome *b* mutation reveals new interactions between subunits of the mitochondrial *bc*₁ complex. *J. Biol. Chem.* **277**, 49397–49402.
- S  raphin, B., Boulet, A., Simon, M., and Faye, G. (1987). Construction of a yeast strain devoid of mitochondrial introns and its use to screen nuclear genes involved in mitochondrial splicing. *Proc. Natl. Acad. Sci. USA* **84**, 6810–6814.
- Steele, D. F., Butler, C. A., and Fox, T. D. (1996). Expression of a recoded nuclear gene inserted into yeast mitochondrial DNA is limited by mRNA-specific translational activation. *Proc. Natl. Acad. Sci. USA* **93**, 5253–5257.
- Trumpower, B. L. (2004). The cytochrome *bc*₁ complex. In “Encyclopedia of Biochemistry.” (W. Lennarz and M. D. Lane, eds.), pp. 528–534. Elsevier, New York.
- Wenz, T., Covian, R., Hellwig, P., Macmillan, F., Meunier, B., Trumpower, B. L., and Hunte, C. (2007). Mutational analysis of cytochrome *b* at the ubiquinol oxidation site of yeast Complex III. *J. Biol. Chem.* **282**, 3977–3988.

USE OF RUTHENIUM PHOTOREDUCTION TECHNIQUES TO STUDY ELECTRON TRANSFER IN CYTOCHROME OXIDASE

Lois Geren, Bill Durham, *and* Francis Millett

Contents

1. Introduction	508
2. Preparation of Ruthenium-Labeled Cytochrome <i>c</i> Derivatives	509
2.1. Materials	509
2.2. Preparation of ruthenium-labeled cytochrome <i>c</i>	510
3. Measurement of Intraprotein Electron Transfer in Horse Ru-39-Cc	511
4. Measurement of Electron Transfer from Ru _D -39-Cc to Cytochrome <i>c</i> Oxidase	513
4.1. Measurement of formation and dissociation rate constants for the complex between Ru-Cc and CcO	514
5. Measurement of Electron Transfer and Oxygen Reduction in Cytochrome <i>c</i> Oxidase with Electrostatically Bound Ruthenium Complexes	515
5.1. Measurement of single electron reduction of CcO state P _m to F	516
5.2. Measurement of single electron reduction of F state to O state	517
5.3. Measurement of single electron reduction of state O _H to state E	518
5.4. Measurement of single electron reduction of state E to states R ₂ and P _m	518
Acknowledgment	519
References	519

Abstract

Ruthenium photoreduction methods are described to study electron transfer from cytochrome *c* to cytochrome *c* oxidase and within cytochrome oxidase. Methods are described to prepare a ruthenium cytochrome *c* derivative Ru-39-Cc, by labeling the single sulfhydryl group on horse K39C with (4-bromomethyl-4'-methylbipyridine) (bis-bipyridine)ruthenium(II). The ruthenium complex attached

Department of Chemistry and Biochemistry, University of Arkansas, Fayetteville, Arkansas, USA

Methods in Enzymology, Volume 456
ISSN 0076-6879, DOI: 10.1016/S0076-6879(08)04428-5

© 2009 Elsevier Inc.
All rights reserved.

to Cys-39 on the opposite side of the heme crevice does not interfere with the interaction with cytochrome oxidase. Laser flash photolysis of a 1:1 complex between Ru-39-Cc and bovine cytochrome oxidase results in photoreduction of heme c within 1 μsec , followed by electron transfer from heme c to Cu_A in cytochrome oxidase with a rate constant of $60,000 \text{ s}^{-1}$ and from Cu_A to heme a with a rate constant of $20,000 \text{ s}^{-1}$. A new ruthenium dimer, Ru_2Z , has been developed to reduce Cu_A within 1 μsec with a yield of 60%, followed by electron transfer from Cu_A to heme a and then to the heme a_3/Cu_B binuclear center. Methods are described to measure the single-electron reduction of each of the intermediates involved in reduction of oxygen to water by cytochrome oxidase, including P_m , F, O_H , and E.

1. INTRODUCTION

Cytochrome *c* oxidase (CcO) is the terminal electron transfer complex in the respiratory chains of mitochondria and many prokaryotes (Babcock and Wikstrom, 1992). Electron transfer of four electrons from cytochrome *c* (Cc) to molecular oxygen is coupled to the uptake of four “chemical” protons to form 2 H_2O and the translocation of four “pumped” protons across the membrane. Cc initially transfers an electron to Cu_A located in subunit II, followed by electron transfer to heme a and then to the heme a_3/Cu_B binuclear center located in subunit I, where oxygen is reduced to water. The D-channel containing D-132 is thought to be involved in the uptake of both chemical and pumped protons from the matrix side of the membrane, whereas the K-channel containing K-362 is involved in proton uptake during reduction of the binuclear center (Branden *et al.*, 2006). X-ray crystal structures of bovine (Yoshikawa *et al.*, 1998) *Paracoccus denitrificans* (Ostermeier *et al.*, 1997) and *Rhodocacter sphaeroides* (Qin *et al.*, 2006) CcO have revealed the locations of the redox centers and proton channels in great detail. However, determination of the kinetics of the electron and proton transfer steps and the mechanism of coupling between them remains a challenging problem.

One of the most widely used methods to study rapid electron transfer in CcO involves flash photolysis of CO-bound heme a_3 in reduced CcO, followed by reaction with oxygen (Faxen *et al.*, 2005; Hill, 1991). In another approach, our laboratory has developed a new ruthenium photoreduction technique to inject single electrons into Cc or CcO and measure the subsequent electron transfer reactions on a rapid time scale (Millett and Durham, 2002). To study electron transfer involving cytochrome *c*, a polypyridyl ruthenium complex [Ru(II)] is covalently attached to Cys-39 on Cc to form Ru-39-Cc (Geren *et al.*, 1995). Photoexcitation of Ru(II) to the metal-to-ligand charge-transfer state, Ru(II \star), a strong reductant, leads to rapid reduction of the ferric heme group in Cc. This new technique has

been used to determine that Cc initially transfers an electron into Cu_A of CcO with a rate constant of 60,000 s⁻¹ (Geren *et al.*, 1995). In another approach, several new ruthenium dimers have been developed that bind with high affinity to cytochrome oxidase and can photoreduce Cu_A within 1 μsec (Zaslavsky *et al.*, 1998). This new technique has been used to measure the kinetics for electron transfer from Cu_A to heme a and then to the heme a₃/Cu_B binuclear center, as well as coupled proton pumping.

2. PREPARATION OF RUTHENIUM-LABELED CYTOCHROME C DERIVATIVES

We have developed four different methods for the covalent attachment of a ruthenium complex to a protein (Millett and Durham, 2002). In the method to be described here, a ruthenium bromomethyl reagent is used to label a cysteine sulfhydryl group on the surface of the protein (Geren *et al.*, 1991, 1995). A single free cysteine can be engineered onto the surface of the protein by site-directed mutagenesis to specifically address the goals of the experiment. It is generally desirable to place the ruthenium complex on a surface remote from the binding site with other proteins, so the complex does not interfere with interprotein interactions. It is also important to have a good pathway for electron transfer from the ruthenium complex to the redox center to maximize the rate of electron transfer. Another advantage of this labeling method is that all three chelating ligands can be altered to change the redox potentials of the ruthenium complex, allowing measurement of the reorganization energy and optimization of the rate and yield of photoinduced electron transfer (Fig. 28.1, Table 28.1).

2.1. Materials

The yeast cytochrome *c* mutant H39C, C102T is made as described by Geren *et al.* (1995), and the preparation of horse cytochrome *c* mutant K39C is described in Patel *et al.* (2001). The synthesis of (4-bromomethyl-4'-methylbipyridine) (bis-bipyridine)ruthenium(II) reagent is described by Geren *et al.* (1995), with care being taken to maintain dryness and eliminate metal contamination. The bromination method described in that article has been modified slightly. After reflux in 48% HBr for 3 h, the PF₆ precipitation was eliminated because of the product's poor solubility in water. Instead, the excess HBr was allowed to boil off carefully without allowing any overheating of the dried product, with the final drying done under vacuum and low heat. The dry powder was immediately dissolved in very dry DMF and stored frozen under dry N₂. Extreme care is required to maintain dryness and prevent hydrolysis of the bromine group.

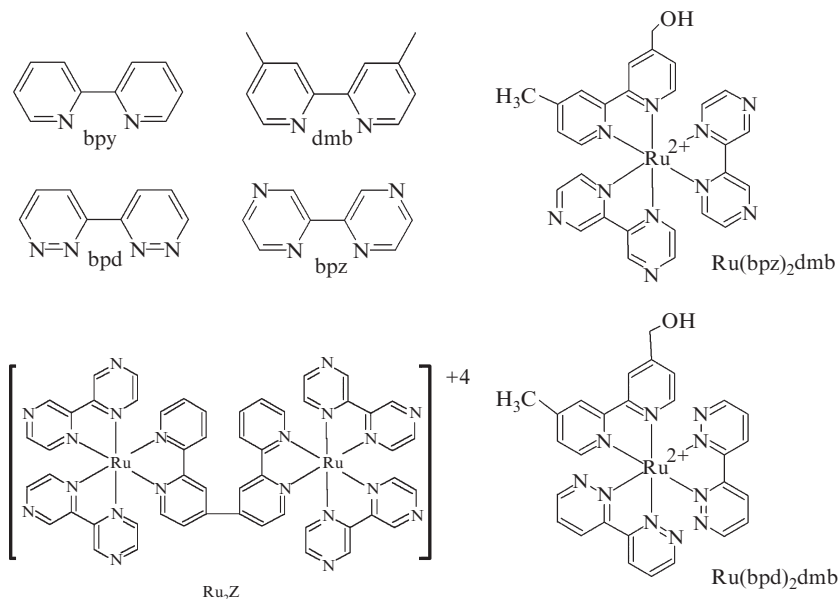


Figure 28.1 Chemical structures of selected ruthenium complexes.

Table 28.1 Standard reduction potentials of ruthenium complexes

Complex	(III)/(II)	(III)/(II*)	(II)/(I)	(II*)/(I)
Ru(bpy) ₃	1.27	-0.87	-1.31	0.83
Ru(bpy) ₂ (dmb)	1.27	-0.83	-1.36	0.79
Ru(bpz) ₂ (dmb)	1.76	-0.25	-0.79	1.22
Ru(bpd) ₂ (dmb)	1.49	-0.49	-1.00	0.98
Ru(bpm) ₂ (dmb)	1.55	-0.30	-0.95	0.90
Ru ₂ C	1.27	-0.87	-1.31	0.83
Ru ₂ Z	1.70	-0.28	-0.82	1.16

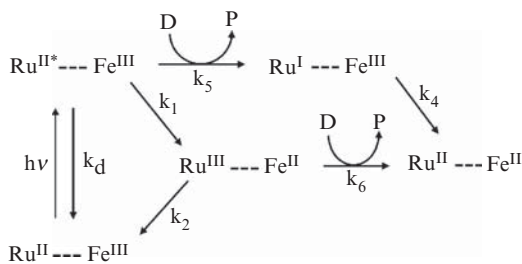
2.2. Preparation of ruthenium-labeled cytochrome *c*

The protein labeling technique is similar for all the bromomethyl ruthenium reagents and is similar to that described in Geren *et al.* (1995) but has been altered somewhat with experience. The protein to be labeled is first treated with a tenfold excess of dithiothreitol for 10 min to reduce any cross-linked disulfide bonds. The sample is then washed two times as quickly as possible with concentrators or a P-2 column into 50 mM sodium borate, pH 9.0, to remove any remaining dithiothreitol. Three to five milligrams of

cytochrome *c* in approximately 300 μl of 50 mM sodium borate, pH 9.0, with a concentration of approximately 1 mM is best. Raising the pH increases the reactivity but decreases the selectivity for cysteines. A pH of 10 to 10.5 will produce labeled lysines as well as cysteines. After degassing under N_2 , a 0.5 equivalent of dithiothreitol is added and stirred 5 min. With a very dry syringe to protect the ruthenium stock solution and continuing to stir, an approximate 3-fold excess (sometimes more, depending on the reactivity of the complex) of the ruthenium reagent is slowly added. The ruthenium reagent is very quickly hydrolyzed by water, and care must be taken to keep the stock dry and use only syringes that have been rinsed with dry ether or dry DMF. After 5 min of stirring, the sample is allowed to react overnight (approximately 18 h) at room temperature, or 3 h at 37°, protected from light. All of the unreacted ruthenium reagent will have hydrolyzed by this time and can then be removed by buffer exchange through dialysis, Amicon concentrators, or Bio-Gel P-2 column. The labeled protein is then purified by ion exchange or HPLC chromatography. The amount of ruthenium reagent used can be adjusted to minimize the amount of unlabeled protein without producing too much multilabeled material. The reaction may be scaled up or down. If the labeling does not cause any disturbance of the protein structure, the absorbance spectra of the ruthenium complex and the protein should be additive. The spectrum of Ru-39-Cc is the same as that of equimolar $\text{Ru}(\text{bpy})_2(\text{dmb})$ and horse Cc. The specific residue on the protein labeled with ruthenium should be confirmed with HPLC separation of a trypsin digest, followed by peptide sequencing as described by [Geren *et al.* \(1991\)](#).

3. MEASUREMENT OF INTRAPROTEIN ELECTRON TRANSFER IN HORSE RU-39-Cc

Internal electron transfer between the ruthenium complex and the heme in a ruthenium-labeled protein is measured with laser flash photolysis ([Durham *et al.*, 1989](#)). The excitation pulse is the third harmonic of a Nd:YAG laser, with a pulse width of 20 nsec and wavelength of 356 nm. The probe source is a pulsed 75 W xenon arc lamp, and the photomultiplier detector has a response time of 10 nsec. Photoexcitation of Ru(II) in 10 μM oxidized horse Ru-39-Cc results in electron transfer from Ru(II*) to Fe(III) to form Ru(III) and Fe(II), followed by reverse electron transfer to form Ru(II) and Fe(III) according to [Scheme 28.1 \(Fig. 28.2\)](#). The reduction of Fe(II) is detected at 550 nm after subtracting a small contribution from Ru(II*) detected at 556 nm, an isobestic for heme *c*. The photoexcitation and recovery of Ru(II) is detected at 434 nm, a heme *c* isobestic. Both transients are fit by use of equations (28.1) and (28.2) based on [Scheme 28.1 \(Durham *et al.*, 1989\)](#).



Scheme 28.1

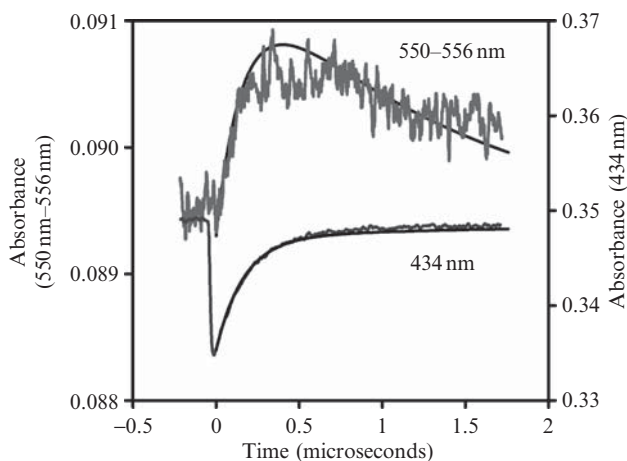


Figure 28.2 Photoinduced electron transfer within horse Ru-39-Cc. A solution containing $10 \mu\text{M}$ Ru-39-horse Cc in 100 mM phosphate buffer, pH 7.0, was excited with a 10-ns 356-nm laser flash, and the transients detected at 550–556 nm and 434 nm. The smooth lines are fitted to Eqs. 28.1 and 28.2 of Scheme 28.1 with $k_1 = 0.6 \times 10^6$, $k_2 = 0.7 \times 10^6$, $k_d = 5.5 \times 10^6$.

$$i(\text{Fe}^{\text{II}}) = \text{Absorbance (550 nm - 556 nm)} = A[e^{-(k_1+k_d)t} - e^{-k_2t}] \quad (28.1)$$

$$i(\text{Ru}^{\text{II}}) = \text{Absorbance (434 nm)} = \Delta\epsilon_{434} C_0 [1 - B e^{-(k_1+k_d)t} + C e^{-k_2t}] \quad (28.2)$$

where $A = k_1 \Delta\epsilon_{550} C_0 / (k_2 - k_1 - k_d)$, $B = (k_2 - k_d) / (k_2 - k_1 - k_d)$, $C = k_1 / (k_2 - k_1 - k_d)$, $\Delta\epsilon_{550} = 18.6 \text{ mM}^{-1}$, and $\Delta\epsilon_{434} = 12 \text{ mM}^{-1}$. The best fit for horse Ru-39-Cc is obtained with $k_1 = (6 \pm 1) \times 10^5 \text{ sec}^{-1}$, $k_2 = (7 \pm 1) \times 10^5 \text{ sec}^{-1}$, and $k_d = (5.5 \pm 1.0) \times 10^6 \text{ sec}^{-1}$ (Fig. 28.2). These rate constants are

independent of protein concentration and are similar to the rates obtained for the yeast Ru-39-Cc (Geren *et al.*, 1995). Residue 39 was chosen for attachment of the ruthenium complex because it is on the back side of Cc remote from the binding site with CcO. There is an efficient electron transfer pathway between the ruthenium complex and the heme consisting of 13 covalent bonds and one hydrogen bond with a total distance of 12.6 Å. The metal-to-ligand charge-transfer excited state Ru(II*) is a strong reducing agent and can rapidly transfer an electron to heme c Fe(III) according to Scheme 28.1. Because the driving forces for k_1 and k_2 of 1.1 and 1.0 eV, respectively, are near the expected reorganizational energy of 0.8 eV, the rate constants k_1 and k_2 should be near the maximum, activationless rate constant (Durham *et al.*, 1989).

The sacrificial electron donor aniline can be used to reduce Ru(III) and lead to the photoreduction of the heme in Ru-39-Cc through k_1 and k_6 steps in Scheme 28.1 with a yield of 5%. Aniline does not have a low enough redox potential to directly reduce Ru(II*). Higher photoreduction yields can be obtained with the Ru(bpd)₂(dmb) complex, which has a redox potential of 0.98 for the Ru(II*)/Ru(I) transition, allowing the sacrificial donor DMAB to directly reduce Ru(II*) to Ru(I) (Table 28.1, Scheme 28.1). The yeast Ru_D-39-Cc is photoreduced through the k_5 and k_4 steps in Scheme 28.1 with a yield of 35%. Reduction potentials for a number of useful ruthenium complexes are listed in Table 28.1.

4. MEASUREMENT OF ELECTRON TRANSFER FROM Ru_D-39-Cc TO CYTOCHROME C OXIDASE

Intracomplex electron transfer from Ru_D-39-Cc to CcO is studied with laser flash photolysis. A Phase R model DL1400 flash lamp-pumped dye laser emitting a 480-nm light flash of <0.5 μsec duration is used as the excitation source (Geren *et al.*, 1995). The sample contains 5 μM yeast Ru_D-39-Cc and 5 μM bovine CcO in 5 mM sodium phosphate, pH 7.0, 5 mM DMAB, and 0.1% dodecyl maltoside at 25°. Under these low ionic strength conditions, Ru_D-39-Cc is tightly bound to CcO, allowing measurement of intracomplex electron transfer according to Scheme 28.2. Excitation of Ru(II) to Ru(II*) with a single laser flash results in rapid photoreduction of heme c, followed by electron transfer to Cu_A and then to heme a. The reaction of heme c is followed at 550 nm, whereas Cu_A and heme a are followed at 830 nm and 605 nm, respectively (Fig. 28.3). The decrease in 830-nm absorbance indicates electron transfer from heme c to Cu_A with a rate constant of 60,000 s⁻¹. The recovery of the 830-nm signal resulting from the reoxidation of Cu_A is matched by the reduction of heme a seen in the 605-nm transient with a rate of $k_b = 2 \times 10^4 \text{ sec}^{-1}$. Both k_a and k_b are independent of protein concentration and ionic strength up to

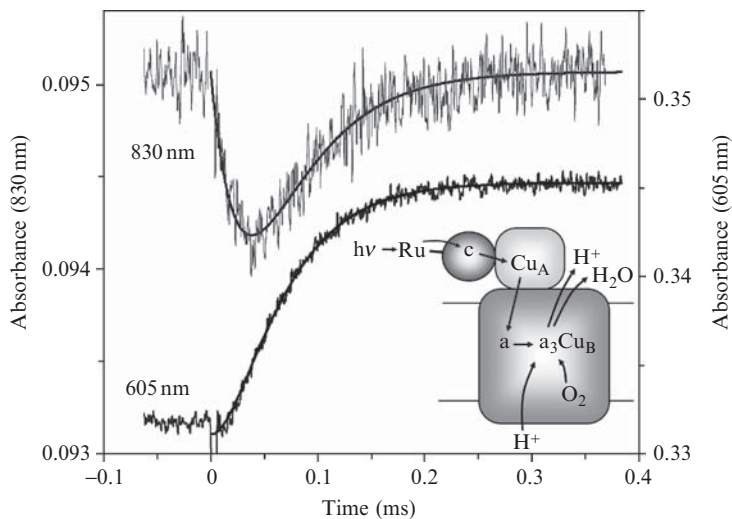
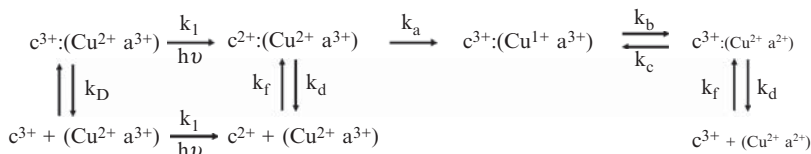


Figure 28.3 Photoinduced electron transfer in Ru_D-39-Cc:CcO complex. A sample containing 5 μM yeast Ru_D-39-Cc and 5 μM bovine CcO in 5 mM sodium phosphate, pH 7.0, 5 mM DMAB, and 0.1% dodecyl maltoside at 25° was excited with a 480-nm laser flash. Cu_A was detected at 830 nm, whereas heme a was detected at 605 nm.

100 mM, indicating intracomplex electron transfer. Site-directed mutagenesis studies have shown that positively charged lysines surrounding the heme crevice of Cc interact electrostatically with negatively charged carboxylates near Cu_A on subunit II of CcO (Wang *et al.*, 1999). A highly conserved tryptophan residue on subunit II mediates electron transfer from the heme group of Cc to Cu_A. Theoretical calculations of the rate of electron transfer based on a computational model of the Cc:CcO complex are in good agreement with the experimental value of $2 \times 10^4 \text{ s}^{-1}$ (Roberts and Pique, 1999; Wang *et al.*, 1999).

4.1. Measurement of formation and dissociation rate constants for the complex between Ru-Cc and CcO

When the ionic strength is increased above 50 mM, the amplitude of the intracomplex phase of electron transfer between Ru-39-Cc and CcO decreases, and a new phase seems to be due to bimolecular electron transfer between the two proteins according to Scheme 28.2. At intermediate ionic strengths between 50 and 100 mM, both intracomplex and bimolecular phases are seen in the kinetics, allowing the fraction *f* of Ru-39-Cc:CcO complex to be determined. With the total concentrations of CcO (*O*_T), and Ru-39-cyt *c* (*C*_T), *K*_D may be calculated from Eq. 28.3.



Scheme 28.2

$$K_D = (1 - f)[(O_t) - f(Cc_t)]/f \quad (28.3)$$

The dissociation constant K_d is given by:

$$K_D = k_{\text{diss}}/k_{\text{form}} \quad (28.4)$$

Because the rate constant k_a is independent of ionic strength up to 100 mM, the presence of two phases indicates the absence of rapid equilibrium, and k_{diss} must be much smaller than k_a . With steady-state assumptions, the bimolecular reaction is given by Eq. 28.5:

$$k_{2\text{nd}} = k_{\text{form}}k_a/(k_{\text{diss}}+k_a) \quad (28.5)$$

Measurement of $k_{2\text{nd}}$ and k_a , along with the calculation of K_D thus also allows the calculation of k_{diss} and k_{form} (Geren *et al.*, 1995). For beef oxidase and yeast Ru-39-C c at 100 mM ionic strength these were found to be $k_a = 6 \times 10^4 \text{ s}^{-1}$, $k_{\text{form}} = 1.8 \times 10^8 \text{ M}^{-1}\text{s}^{-1}$, and $k_{\text{diss}} = 8 \times 10^3 \text{ s}^{-1}$ (Scheme 28.2).

5. MEASUREMENT OF ELECTRON TRANSFER AND OXYGEN REDUCTION IN CYTOCHROME C OXIDASE WITH ELECTROSTATICALLY BOUND RUTHENIUM COMPLEXES

A number of positively charged ruthenium complexes have been developed that bind to CcO and directly photoreduce Cu_A (Fig. 28.1). The ruthenium dimer Ru_2C has a charge of +4 that allows it to bind to the acidic patch on subunit II of CcO (Zaslavsky *et al.*, 1998). The same laser flash photolysis instrumentation described in Section 4 is used to photoreduce CcO by Ru_2C . Laser flash photolysis of 5 μM oxidized bovine CcO and 25 μM Ru_2C in 5 mM TRIS HCl, pH 8.0, with 10 mM aniline and 1 mM 3CP results in electron transfer from the excited state $Ru(II^*)$ of Ru_2C to Cu_A in CcO within 1 μsec , followed by electron transfer from Cu_A to heme a with a rate constant of 20,000 s^{-1} . The mechanism of

photoreduction of Cu_A follows the k_1 and k_6 steps of [Scheme 28.1](#), and the total yield of photoreduced heme a is 6.2%. Another ruthenium dimer, Ru_2Z , has recently been developed that can photoreduce CcO with a yield of 60% ([Brand *et al.*, 2007](#)). Replacement of the bipyridine ligands in Ru_2C with the bipyrazine ligands in Ru_2Z changed all four redox potentials ([Table 28.1](#)). The redox potential of the $\text{Ru}(\text{II}^*)/\text{Ru}(\text{I})$ transition was increased from 0.83 V to 1.16 V, allowing the sacrificial donor aniline to reduce the excited state $\text{Ru}(\text{II}^*)$ to $\text{Ru}(\text{I})$, followed by electron transfer from $\text{Ru}(\text{I})$ to $\text{Cu}_A(\text{II})$ along the k_5 and k_4 steps in [Scheme 28.1](#). Cu_A is 16% reduced and heme a is 52% reduced after electron transfer equilibrium is established between them. The equilibrium constant K for electron transfer between Cu_A and heme a is thus 3.2, and the redox potential of heme a is 30 mV more positive than that of Cu_A ([Brand *et al.*, 2007](#)).

5.1. Measurement of single electron reduction of CcO state P_m to F

A mechanism for the reduction of O_2 by CcO is shown in [Fig. 28.4](#) ([Branden *et al.*, 2006](#)). State O containing a fully oxidized heme a_3/Cu_B binuclear center is reduced by one electron to state E and then by a second electron to state R_2 , which rapidly binds oxygen to form state A. State A is reduced to state P_m in a rapid 4–electron reaction in which electrons come from heme a_3 , Cu_B , and a neighboring tyrosine. The tyrosine radical in state P_m is reduced to form state F, and then oxyferryl heme a_3 is reduced to form state O. There is growing agreement that each of the one–electron transfers to the heme a_3/Cu_B binuclear center is coupled to pumping one proton

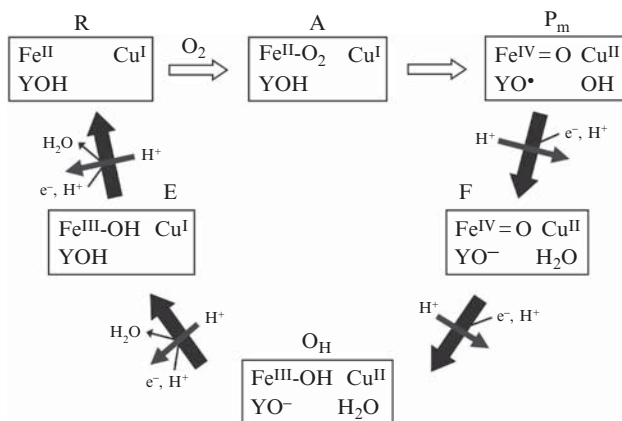


Figure 28.4 Cytochrome *c* oxidase catalytic cycle showing states of the heme a_3/Cu_B binuclear center and conserved tyrosine. Reactions steps indicated by solid arrows are coupled to proton pumping.

across the membrane, as indicated in Fig. 28.4 (Bloch *et al.*, 2004; Verkhovsky *et al.*, 2006). Methods have been developed to study each of the one-electron reduction steps in the mechanism with the ruthenium photoreduction technique.

The P_m state is formed by treating resting state CcO with CO under aerobic conditions (Siletsky *et al.*, 2006). A solution containing 10 μM oxidized bovine CcO and 30 μM Ru_2C in 5 mM TRIS HCl, pH 8.0, is gently bubbled with CO under aerobic conditions for 60 sec and incubated until the difference spectrum indicates formation of P_m . The yield of the P_m state is calculated from $\Delta\epsilon_{607-630} = 11 \text{ mM}^{-1} \text{ cm}^{-1}$, and is typically approximately 75%. After the P_m state is completely formed, 10 mM aniline and 1 mM 3CP are added as sacrificial donors, followed by laser flash photolysis. Photoreduced Cu_A transfers an electron to heme a, followed by electron transfer from heme a to the tyrosine radical near the binuclear center with a rate constant of $4,000 \text{ s}^{-1}$ (Siletsky *et al.*, 2006). The reduction and reoxidation of heme a is followed at 650 nm, whereas the reduction of the binuclear center is followed at 580 nm. Measurement of transmembrane voltage generation under the same conditions indicated two phases of electrogenic proton transfer with rate constants of 3300 s^{-1} and 770 s^{-1} (Siletsky *et al.*, 2006). The fast phase of proton transfer is coincident with electron transfer to the tyrosine radical and is associated with proton delivery to Cu_B bound hydroxide to form water. The slow phase of proton transfer could be due to proton translocation across the membrane.

5.2. Measurement of single electron reduction of F state to O state

The F state is generated by treating resting CcO with 4 mM H_2O_2 (Fabian and Palmer, 1995). A solution containing 8 μM bovine CcO and 22 μM Ru_2C in 5 mM TRIS HCl, pH 8.0, with 10 mM aniline and 1 mM 3CP is treated with 4 mM H_2O_2 and incubated for 5 min to form state F. The yield of F is determined from the peak in the difference spectrum (F – O) at 583 nm with extinction coefficients of $\Delta\epsilon_{583-630} = 5.3 \text{ mM}^{-1} \text{ cm}^{-1}$ and $\Delta\epsilon_{436-414} = 67 \text{ mM}^{-1} \text{ cm}^{-1}$ (Fabian and Palmer, 1995). Laser flash photolysis results in photoreduction of Cu_A , followed by electron transfer to heme a with a rate constant of $20,000 \text{ s}^{-1}$, and electron transfer from heme a to oxyferryl heme a_3 to form state O with a rate constant of 470 s^{-1} . The reduction and reoxidation of the heme a is followed at 605 nm, whereas the reduction of oxyferryl heme a_3 is followed at 580 nm (Zaslavsky *et al.*, 1998). A deuterium isotope effect of 4.3 indicates a proton-transfer rate-limiting step. Measurement of transmembrane voltage generation indicated two phases of electrogenic proton transfer with rate constants of 830 s^{-1} and 220 s^{-1} in a 1:3 ratio (Konstantinov, 1998). The fast phase is coincident with reduction of oxyferryl heme and is associated with proton transfer to

the oxygen on the oxyferryl heme to form water. The slow phase of proton transfer is associated with proton translocation (Konstantinov, 1998). A fast phase of proton release is also observed coincident with reduction of oxyferryl heme (Zaslavsky *et al.*, 2004).

5.3. Measurement of single electron reduction of state O_H to state E

There are several forms of the fully oxidized state of CcO, including the resting state O (Moody, 1996), and the state O_H that is formed immediately after fully reduced state R₄ reacts with oxygen (Bloch *et al.*, 2004). If an additional electron is not injected into the O_H state within approximately 30 sec, then it relaxes back to the resting state O. It has been reported that reduction of state O_H is coupled to proton pumping, whereas reduction of state O is not (Belevich *et al.*, 2007; Bloch *et al.*, 2004; Verkhovsky *et al.*, 2006). A stopped-flowflash technique is used to study 1-electron reduction of state O_H (Brand *et al.*, 2007); 5 μM bovine CcO is anaerobically reduced with 2 mM ascorbate and 1 μM PMS in 5 mM HEPES buffer, pH 7.9, in one syringe of the stopped-flow and then rapidly mixed with oxygenated buffer containing 20 μM Ru₂Z, 10 mM aniline, and 1 mM 3CP. State R₄ reacts with oxygen within 5 msec to form state O_H, and then the laser is fired to excite Ru₂Z to the Ru(I) state, which injects a single electron into Cu_A. An electron is transferred from Cu_A to heme a with a rate constant of 20,000 s⁻¹, followed by biphasic electron transfer from heme a to Cu_B with rate constants of 750 s⁻¹ and 110 s⁻¹ and relative amplitudes of 25% and 75% (Brand *et al.*, 2007). There is no change in absorbance at 436 nm, indicating that the electron acceptor in the binuclear site is Cu_B rather than heme a₃. One electron reduction of *P. denitrificans* CcO state O_H has been studied by Belevich *et al.* (2007) with Ru(bpy)₃ as photoreductant. Correlation of the kinetics of electron transfer and transmembrane voltage generation led to a mechanism for coupling between electron transfer and proton translocation.

5.4. Measurement of single electron reduction of state E to states R₂ and P_m

The one-electron reduction of state E is studied by a stopped-flowflash technique; 5 μM bovine CcO and 5 μM horse heart cytochrome *c* mutant K13E is anaerobically reduced with 2 mM ascorbate and 1 μM PMS in 5 mM HEPES, pH 8.0, 0.1% LM in one syringe of the stopped-flow. This syringe is then mixed rapidly with the other syringe of the stopped-flow containing 20 μM Ru₂Z, 10 mM aniline, and 1 mM 3CP in buffer. After mixing, the reduced CcO that is fully oxidized to the O_H state within 5 m sec, is then reduced by the ferrous K13E Cc within 10 m sec. The laser

is flashed 20 m sec after mixing to excite R_{U_2Z} and inject a single electron into Cu_A , which transfers an electron to heme a. Biphasic electron transfer from heme a to heme a_3 to form state R_2 then occurs with rate constants of 1100 s^{-1} and 90 s^{-1} , and relative amplitudes of 11% and 89%. The 436-nm transient indicates that O_2 rapidly binds to state R_2 to form state P. Additional laser flashes result in transients with a rate constant of 3000 s^{-1} , consistent with the sequential P_M to F transition (Siletsky *et al.*, 2006), demonstrating the advantage of the use of higher yield photoreductants.

ACKNOWLEDGMENT

Supported by NIH grants GM20488 and NCRR COBRE RR15569.

REFERENCES

- Babcock, G. T., and Wikstrom, M. (1992). Oxygen activation and the conservation of energy in cell respiration. *Nature* **356**, 301–309.
- Belevich, I., Bloch, D. A., Belevich, N., Wikström, M., and Verkhovsky, M. I. (2007). Exploring the proton pump mechanism of cytochrome *c* oxidase in real time. *Proc. Natl. Acad. Sci. USA* **104**, 2685–2690.
- Bloch, D., Belevich, I., Jasaitis, A., Ribacka, C., Puustinen, A., Verkhovsky, M. I., and Wikström, M. (2004). The catalytic cycle of cytochrome *c* oxidase is not the sum of its two halves. *Proc. Natl. Acad. Sci. USA* **101**, 529–533.
- Brand, S. E., Rajagukguk, S., Ganesas, K., Geren, L., Fabian, M., Han, D., Gennis, R., Durham, B., and Millett, F. (2007). A new ruthenium complex to study single-electron reduction of the pulsed OH state of detergent-solubilized cytochrome oxidase. *Biochemistry* **46**, 14610–14618.
- Branden, G., Gennis, R. B., and Brzezinski, P. (2006). Transmembrane proton translocation by cytochrome *c* oxidase. *Biochim. Biophys. Acta* **1757**, 1052–1063.
- Durham, B., Pan, L. P., Long, J., and Millett, F. (1989). Photoinduced electron-transfer kinetics of singly labeled ruthenium Bis-(bipyridine) dicarboxybipyridine cytochrome *c* derivatives. *Biochemistry* **28**, 8659–8665.
- Fabian, M., and Palmer, G. (1995). The interaction of cytochrome oxidase with hydrogen peroxide: The relationship of compounds P and F. *Biochemistry* **34**, 13802–13810.
- Faxen, K., Gilderson, G., Adelroth, P., and Brzezinski, P. (2005). A mechanistic principle for proton pumping by cytochrome *c* oxidase. *Nature* **437**, 286–289.
- Geren, L. M., Beasley, J. R., Fines, B. R., Saunders, A. J., Hibdon, S., Pielak, G. J., Durham, B., and Millett, F. (1995). Design of a ruthenium-cytochrome *c* derivative to measure the electron transfer to the initial acceptor in cytochrome *c* oxidase. *J. Biol. Chem.* **270**, 2466.
- Geren, L., Hahn, S., Durham, B., and Millett, F. (1991). Photoinduced electron transfer between cytochrome *c* peroxidase and yeast cytochrome *c* labeled at Cys 102 with (4-bromomethyl-4'-methylbipyridine)[bis(bipyridine)]ruthenium²⁺. *Biochemistry* **30**, 9450.
- Hill, B. (1991). The reaction of the electrostatic cytochrome *c*-cytochrome oxidase complex with oxygen. *J. Biol. Chem.* **266**, 2219–2226.
- Konstantinov, A. A. (1998). Cytochrome *c* oxidase as a proton-pumping peroxidase: Reaction cycle and electrogenic mechanism. *J. Bioenerg. Biomembr.* **30**, 121–130.

- Millett, F., and Durham, B. (2002). Design of photoactive ruthenium complexes to study interprotein electron transfer. *Biochemistry* **41**, 11315–11324.
- Moody, A. J. (1996). As-prepared forms of fully oxidised haem/Cu terminal oxidases. *Biochim. Biophys. Acta* **1276**, 6–20.
- Ostermeier, C., Harrenga, A., Ermler, U., and Michel, H. (1997). Structure at 2.7 Å resolution of the *Paracoccus denitrificans* two-subunit cytochrome *c* oxidase complexed with an antibody F_V fragment. *Proc. Nat. Acad. Sci. USA* **94**, 10547–10553.
- Patel, C. N., Lind, M. C., and Pielak, G. J. (2001). Characterization of horse cytochrome *c* expressed in *Escherichia coli*. *Protein Expr. Purif.* **22**, 220–224.
- Qin, L., Hiser, C., Mulichak, A., Garavito, R., and Ferguson-Miller, S. (2006). Identification of conserved lipid/detergent-binding sites in a high-resolution structure of the membrane protein cytochrome *c* oxidase. *Proc. Natl. Acad. Sci. USA* **103**, 16117–16122.
- Roberts, V. A., and Pique, M. E. (1999). Definition of the interaction domain for cytochrome *c* on cytochrome *c* oxidase. III. Prediction of the docked complex by a complete systematic search. *J. Biol. Chem.* **274**, 38051–38060.
- Siletsky, S. A., Han, D., Brand, S., Morgan, J. E., Fabian, M., Geren, L., Millett, F., Durham, B., Konstantinov, A. A., and Gennis, R. B. (2006). Single-electron photoreduction of the PM intermediate of cytochrome *c* oxidase. *Biochim. Biophys. Acta* **1757**, 1122–1132.
- Verkhovsky, M. I., Belevich, I., Bloch, D. A., and Wikstrom, M. (2006). Elementary steps of proton translocation in the catalytic cycle of cytochrome oxidase. *Biochim. Biophys. Acta* **1757**, 401–407.
- Wang, K., Zhen, Y., Sadoski, R., Grinnell, S., Geren, L., Ferguson-Miller, S., Durham, B., and Millett, F. (1999). Definition of the interaction domain for cytochrome *c* on cytochrome *c* oxidase: II. Rapid kinetic analysis of electron transfer from cytochrome *c* to *Rhodobacter sphaeroides* cytochrome oxidase surface mutants. *J. Biol. Chem.* **274**, 38042–38050.
- Yoshikawa, S., Shinzawa-Iroh, K., Nakashima, R., Yaono, R., Yamashita, E., Inoue, N., Yao, M., Fei, M. J., Libeu, C. P., Mizushima, T., Yamagichi, H., Tomizaki, T., *et al.* (1998). Redox-coupled structural changes in bovine heart cytochrome *c* oxidase. *Science* **280**, 1723–1729.
- Zaslavsky, D., Sadoski, R. C., Wang, K., Durham, B., Gennis, R. B., and Millett, F. (1998). Single electron reduction of cytochrome *c* oxidase compound f: resolution of partial steps by transient spectroscopy. *Biochemistry* **37**, 14910–14916.
- Zaslavsky, D., Sadoski, R. S., Rajagukguk, S., Geren, L., Millett, F., Durham, B., and Gennis, R. B. (2004). Direct measurement of proton release by cytochrome *c* oxidase in solution during the F to O transition. *Proc. Natl. Acad. Sci. USA* **101**, 10544–10547.

Author Index

A

Abhood, L. G., 442
Abrahams, J. P., 136
Acin-Perez, R., 322
Adam, A. C., 211
Adam-Vizi, V., 429, 431
Agar, J. N., 272
Ahlers, P. M., 59
Akey, C. W., 5
Alban, A., 345, 347
Altman, M. C., 111–31
Amchenkova, A. A., 288, 297
Amr, S., 235
Amutha, B., 247–66
Anderson, M. E., 370
Anderson, M. F., 383, 442
Anderson, S., 112
Anunciado-Kiza, R., 440
Arrondo, J. L. R., 56
Asmann, Y. W., 234
Azzi, A., 427, 479

B

Babcock, G. T., 508
Balaban, R. S., 282
Ballou, D. P., 77, 85
Bamber, L., 196
Barja, G., 389, 431, 432
Barquera, B., 312, 314
Bartesaghi, A., 47
Barth, A., 65
Bason, J. V., 118
Baty, J. W., 345, 356
Beal, -, 389
Beattie, D. S., 304
Beckman, J. S., 389
Beer, S. M., 345
Beinert, H., 248, 268
Belasco, J. G., 212
Belevich, I., 518
Belevich, N. P., 75–93
Bellon, P. L. S., 15
Beltran, B., 344
Benali-Furet, N. L., 365
Benard, G., 288
Berger, R. L., 78
Berry, E. A., 184

Biagini, G. A., 303–20
Biederbeck, A., 211, 213, 215, 216, 217, 218, 226
Bilsel, O., 77
Bindokas, V. P., 425
Birch-Machin, M. A., 226
Birmingham, A., 213, 216
Blight, K. J., 369
Bloch, D., 517, 518
Boekema, E. J., 183–90, 194
Bonilla, E., 397
Bonnefoy, M., 495, 496, 502
Bostina, M., 4
Böttcher, B., 9
Boumans, H., 184
Bouwer, J. C., 39
Boveris, A., 384, 429, 446, 460
Boxma, B., 296
Boya, P., 364
Brainan, T., 57
Brand, M. D., 402, 428, 440–1, 476, 487
Brand, S. E., 516, 518
Branden, G., 508, 516
Brandner, K., 326
Brandon, M., 134
Brandt, U., 59, 137, 170, 171, 212, 461, 475–90, 493
Braun, H. P., 183–90, 194
Braun, R. J., 357
Bretaudiere, J. P., 12
Breton, J., 57
Brittain, T., 56
Brock, R., 290, 295, 297, 298
Brooks, A. I., 382
Brummelkamp, T. R., 212, 213
Buchanan, S. K., 117
Burgos, J., 172
Burie, J.-R., 56
Bus, J. S., 382
Buse, G., 121
Butler, C. A., 491–506
Buzy, A., 124
Bych, K., 212, 222

C

Cadenas, E., 344, 423
Calvaruso, M. A., 144
Campbell, R. V., 363–80
Cape, J. L., 429, 461

Capel, F., 446
 Carazo, J. M., 5
 Cardone, G., 41
 Carroll, J., 54, 111–31, 134, 170, 171, 357
 Carrozzo, R., 165
 Carson, J. H., 290, 298
 Castello, P. R., 383, 386, 390
 Cavadini, P., 211
 Cecchini, G., 225, 446
 Cen, X., 459–73
 Chan, H. L., 345
 Chance, B., 268, 344, 460
 Chang, T. S., 345
 Chappell, J. B., 347
 Chatterjee-Kishore, M., 216
 Chaudhuri, T., 265
 Chen, J., 439–57
 Chen, Q., 449
 Chen, R., 112
 Chen, S. X., 485
 Chen, X. J., 195
 Cherepanov, A. V., 76, 78, 79, 80, 85
 Chomyn, A., 324, 331
 Chretien, D., 171
 Chu, G., 213
 Cino, M., 430
 Clark, J. B., 383, 442
 Clarke, S., 326
 Clason, T., 21, 22
 Clason, T. A., 4
 Claypool, S. M., 194
 Cluzel, P., 297
 Cochemé, H. M., 345, 395–417
 Coenen, M. J., 221
 Colca, J. R., 234, 235
 Cole, S. T., 305
 Conde, J., 503
 Cooper, C., 441, 444, 445
 Corbett, J. T., 446
 Coussens, M., 440
 Cox, M. M., 184
 Craig, E. A., 211
 Crapo, J. D., 382, 384
 Crofts, A. R., 461
 Crowther, R. A., 16, 41
 Cruciat, C. M., 184, 185
 Cullen, B. R., 216
 Culotta, V. C., 397

D

DaCruz, S., 113
 D'Agostino, D. M., 364
 Dahm, C. C., 345, 407
 Daily, J. P., 308
 Daldal, F., 97
 Dancis, A., 247–66
 Darrouzet, E., 97

Davey, G. P., 398, 402
 Davies, K. J., 344, 423
 Dawson, R. M. C., 312
 Day, B. J., 382, 397
 De la Torre-Ruix, M. A., 211
 De Robertis, E., 442
 De Vries, D. D., 172
 De Vries, S., 76, 78, 79, 80, 85, 461
 De Wit, A., 169–81
 De Wit L. E. A., 172, 179
 Deans, S. R., 15
 Debska-Vielhaber, G., 419–37
 Degli Esposti, M., 171
 Del Maestro, R. F., 430
 Denicola, A., 468
 Devenish, R. J., 194
 Devonshire, A. L., 171
 Dhar, I., 365
 di Rago, J-P., 491–506
 Diday, E., 6, 13
 Diekert, K., 273, 275
 Dienhart, M. K., 188, 194, 196–7, 199, 205, 206
 Dieteren, C. E. J., 133–51
 Ding, M. G., 491–506
 Dinis-Oliveira, R. J., 398
 Dixon, J. E., 233–46
 Doench, J. G., 217
 Dong, C., 314
 Dooijewaard, G., 171
 Drechsel, D. A., 381–93
 Drgon, T., 195
 Dröse, S., 461, 475–90, 493
 Du, X., 451
 Duby, G., 261
 Duchon, M. R., 288
 Dunning, C. J., 135, 170, 323
 Durham, B., 95–109, 507–20
 Duszyński, J., 197
 Dynowski, M., 420

E

Eaton, P., 345
 Edwards, C. A., 268
 Eliss, R. J., 288
 Elly, L., 169–81
 Elson, E. L., 289
 Enderlein, J., 289, 290, 297
 Engelhardt, P., 36, 45, 46
 Engstrom, G., 97, 99, 105, 107
 Ernster L., 447
 Esposti, M. D., 460
 Esser, L., 107, 461, 464
 Estabrook, R. W., 369
 Esterhazy, D., 407, 476, 487, 493
 Esteves, T. C., 413
 Estornell, E., 445
 Euro, L., 55

F

Fabian, M., 517
 Fahmy, K., 57
 Fang, J., 304
 Fato, R., 480
 Faxen, K., 508
 Fearnley I. M., 111–31
 Felger, P. L., 239
 Fendel, U., 440
 Fernandez-Vizarra, E., 221
 Finch, R. G., 365
 Fink, G. R., 503
 Finkel, T., 344
 Fischer, J. C., 171
 Fisher, N., 303–20
 Fiumera, H. L., 496
 Flemming, D., 57, 58
 Fontanesi, F., 197, 226
 Fontecave, M., 249
 Former, F., 113, 114
 Forster, F., 5
 Fosset, C., 211, 218
 Fox, T. D., 491–506
 Frangakis, A. S., 41
 Frank, J., 5, 8, 10, 12, 46, 47, 187
 Frearson, J. A., 318
 Freeman, B. A., 384
 Frey, T. G., 29–52, 288
 Frezza, C., 443
 Fridovich, I., 407, 476, 480
 Friedman, D. B., 345
 Friedrich, T., 23, 55, 57, 114, 134, 171, 478
 Fry, M., 306
 Fu, C., 357
 Fu, J., 6
 Fukui, H., 440
 Fukushima, T., 398

G

Gaietta, G., 33
 Galante, Y. M., 171
 Galkin, A., 114, 475–90
 Galkin, A. S., 86
 Galluzzi, L., 364
 Gao, X., 107
 Gardner, M. J., 305
 Gardner, P. R., 404
 Garduno, E., 47
 Gaucher, S. P., 113, 114
 Gavrikova, E. V., 21
 Gawehn, K., 223
 Gennerich, A., 296, 297
 Gennis, R. B., 96, 460
 Genova, M. L., 194, 428, 476
 George, S. J., 57
 Gerbeth, C., 222, 228

Geren, L., 507–20
 Geren, L. M., 98
 Gerloff, D. L., 304
 Gerwert, K., 57
 Gharbi, S., 347
 Ghelli, A., 171
 Gibson, B. W., 114
 Gibson, J. E., 382
 Ginter, J. M., 123
 Gitler, C., 345
 Glerum, D. M., 194
 Glick, B. S., 273, 400
 Godard, F., 491–506
 Goldstein, J. C., 31, 33
 Goormaghtigh, E., 56, 57, 58, 67
 Gordon, D. M., 247–66
 Gorg, A., 351
 Gostimskaya, I. S., 483
 Gottlieb, E., 288
 Graham, J. M., 443
 Grant, H., 382
 Gregg, C. T., 445
 Gregory, J. D., 347
 Gremlich, H.-U., 56
 Grgic, L., 89, 224
 Grigorieff, N., 4
 Grivennikova, V. G., 21, 428, 431, 476, 477
 Grotyohann, L. W., 288
 Guénebaut, V., 4
 Günzler, H., 56
 Gurung, B., 462, 466
 Gusdon, A. M., 439–57
 Gygi, S. P., 357

H

Hackenbrock, C. R., 184
 Haggie, P. M., 288, 289, 291
 Haile, D. J., 272
 Halestrap, A. P., 288, 413
 Hamaguchi, K., 451
 Hampton, M. B., 344
 Hansford, R. G., 347
 Hansson, M. J., 448
 Hartl, F. U., 268
 Hartzell, C. R., 268
 Hassan, H. M., 396
 Hatefi, Y., 171, 184, 225
 Hausteiner, E., 289, 290, 291, 294, 298
 Heberle, J., 58
 Hegerl, R., 41
 Heinemeyer, J., 184, 185, 187, 188
 Helliwig, P., 57, 62, 65, 69
 Henningsen, R., 351
 Henze, K., 272
 Herrero, A., 389, 431, 432
 Herrero, E., 211

Herrmann, J. M., 199
 Hertzman, C., 382
 Heymann, J. B., 41
 Hickish, T., 364
 Hiernerwadel, R., 57
 Hill, B., 519
 Hinchliffe, P., 21, 54, 136, 137, 212
 Hink, M. A., 287–301
 Hinkle, P. C., 477
 Hirai, K., 397, 398
 Hirst, J., 54, 59, 175, 476, 485, 487
 Hofhaus, G., 4
 Hofmann, C. A., 234
 Hogeboom, G. H., 443
 Holmes-Hampton, G., 267–85
 Honda, A., 369
 Hong, S., 97
 Hoogenraad, N. J., 322
 Hoppe, W., 5
 Hoppel, C., 441, 444, 445
 Horstman, L. L., 441, 444
 Hou, X., 234
 Hsieh, C. E., 36
 Hu, Y., 347
 Hudder, N., 270, 276, 281–2
 Hughes, J. T., 382
 Humphries, A. D., 331
 Hunte, C., 97, 188, 493
 Hurd, T. R., 343–61, 407

I

Ikeda, M., 369
 Ingledew, W. J., 54, 55
 Inglese, J., 318
 Irshad, M., 365
 Issaq, H., 351
 Iversen, P. W., 318
 Iwaki, M., 58, 59, 62, 65
 Iwasaki, T., 184
 Iwata, S., 97, 107, 113, 136, 460

J

Jackson, A. L., 216
 Jakobs, S., 288, 289
 James, A. M., 343–61, 481, 483
 Janssen, A. J. M., 171, 172
 Janssen, R. J., 134
 Jensen, J. B., 308
 Jewess, P. J., 171
 Ji, Q., 47
 Jiang, M., 47
 Johnson, D. C., 249
 Johnson, K. A., 77
 Johnston, A. J., 331
 Jordan, W., 461
 Junn, E., 440

K

Kagawa, Y., 466
 Kakinuma, K., 477–8
 Kalnin, N. N., 65
 Kamo, N., 402
 Kamzalov, S., 436
 Kao, M. C., 22
 Karp, N. A., 347, 353
 Kashani-Poor, N., 137, 478
 Katan, M. B., 268
 Katic, M., 440
 Katoh, I., 440
 Kelleher, N. L., 123
 Kerscher, S., 478, 480
 Kerscher, S. J., 304
 Kessl, J., 493
 Kil, I. S., 345
 Kiley, P. J., 248
 Kim, H., 97
 Kirby, K., 382, 397
 Kispal, G., 211, 268
 Knauer, V., 5
 Knight, S. A. B., 265
 Knoops, B., 397
 Ko, Y. H., 196
 Kohonen, T., 5
 Komary, Z., 428
 Konstantinov, A. A., 517–18
 Koopman, W. J. H., 133–51, 287–301
 Koppenol, W. H., 389
 Korenaga, M., 369
 Kotlyar, A. B., 21, 485
 Kouril, R., 183–90
 Krall, J., 397
 Kudin, A. P., 419–37
 Kujoth, G. C., 440
 Kunkel, M., 366
 Kunz, W. S., 419–37
 Kushnareva, Y., 476
 Kusmaul, L., 476, 487
 Kutik, S., 194

L

Labouesse, M., 495, 496
 Laemmlli, U. K., 201
 Lai, J. C. K., 442
 Lambert, A. J., 407, 428, 440–1, 476, 487
 Lambros, C., 308
 Lancaster, C. R. D., 493
 Lange, C., 188
 Lange, H., 259
 Lanzavecchia, S., 15
 Lapidus, R. G., 236
 Lawrence, A., 39, 42, 46
 Lazarou, M., 135, 148, 170, 321–39
 Lebart, L., 5, 12
 Lee, F. S., 211

Lemma-Gray, P., 114
 Lemon, D. D., 57
 Lenaz, G., 194, 442, 443, 445
 Leonard, K., 4
 Lerat, H., 369
 Leschziner, A. E., 5
 Lesnefsky, E. J., 239, 445
 Levin, M. K., 290, 298
 Li, K., 368
 Li, Y., 363–80
 Lill, R., 209–31, 248, 249, 250, 268, 272, 273
 Lilley, K. S., 343–61
 Lin, -, 389
 Lin, J., 241
 Lin, T. K., 345
 Lin, Y., 78, 79, 81, 85
 Lindahl, P. A., 267–85
 Lindenbach, -, 369
 Liou, H. H., 382
 Lippincott-Schwartz, J., 290, 291
 Liu, Y., 428, 476
 Lizana, L., 288
 Ljungdahl, P. O., 460
 Loeffen, J. L., 170
 Lok, C. N., 219
 Loo, J. A., 123
 Loo, Y. M., 364
 Loschen, G., 389, 446
 Low, F. M., 348
 Lowell, B. B., 234
 Lucas, M., 407
 Ludwig, B., 226

M

McCormack, A. L., 382, 398
 McDonald, T., 113, 114
 McKenzie, M., 321–39
 McLafferty, F. W., 123
 McLennan, H. R., 460
 Maechler, P., 234
 Magnitsky, S., 55
 Mainanski, N. A., 173
 Majander, A., 171, 174
 Makarov, A., 124
 Maklashina, E., 21
 Malinska, D., 419–37
 Malviya, A. N., 441, 444, 449
 Mamedova, A. A., 70
 Mannella, C. A., 49, 288
 Manning-Bog, A. B., 398
 Măntele, W., 56, 57
 Marabini, R., 5
 Marco, S., 12, 36
 Marko, M., 36
 Marshall, D., 53–74
 Marshall, G. R. B., 447
 Martin, W., 272

Mashevich, G., 194
 Mathews, C., 439–57
 Mattevi, A., 304
 Maximo, V., 440
 Mayhew, S. G., 396
 Meisinger, C., 185
 Meldrum, R. A., 215
 Melo, A. M., 304, 305
 Meyer, B., 155, 167
 Miao, R., 267–85
 Mick, D. U., 194, 197, 326
 Midorikawa, J., 468
 Miller, C. P., 216
 Millet, F., 95–109, 507–20
 Minakami, S., 477–8
 Mitchell, P., 445, 461
 Miwa, S., 441
 Miyawaki, A., 366, 376
 Mizuno, Y., 398
 Mockett, R. J., 397
 Mollace, V., 382, 397
 Montgomery, M. G., 118
 Moody, A. J., 518
 Mootha, V. K., 113, 114
 Moradpour, D., 365
 Moraes, C. T., 440
 Morales, J. G., 267–85
 Moreno-Loshuertos, R., 440
 Morgan, D. G., 5
 Morgner, N., 128
 Moriya, K., 369
 Moser, C. C., 305
 Moss, D., 57
 Mueller, P., 447
 Mühlhoff, U., 210–11, 248, 249, 250, 256,
 257, 272
 Mukhopadhyay, P., 451
 Muller, F., 441, 461, 467, 493
 Müller, M., 298
 Münck, E., 269
 Munnich, A., 222
 Murakami, H., 251
 Murphy, M. P., 343–61, 395–417
 Murray, J., 113
 Musatov, A., 121
 Myers, A. M., 268

N

Nabedryk, E., 57
 Nagai, T., 366, 376
 Nakamaru-Ogiso, E., 54, 55, 114
 Nakano, M., 468
 Nakashima, Y., 174
 Naqui, A., 428
 Narasimha, R., 47
 Neidle, A., 442
 Nelson, D. L., 184

Nemoto, S., 282
 Netz, D. J., 211
 Nguyen, H., 47
 Nicklas, W. J., 383
 Nijtmans, L. G. J., 133–51, 335
 Noguchi, T., 57
 Nohl, H., 461
 Nomura, Y., 298
 Nordenbrand, K., 447
 Noske, A. B., 40
 Nübel, E., 153–68
 Nury, H., 196

O

Ogilvie, I., 135, 170, 323
 Ohnishi, S. T., 487
 Ohnishi, T., 54, 55, 86, 170, 486
 Ohsawa, I., 440
 Okuda, M., 377, 378
 Ollagnier-de-Choudens, S., 249, 272
 Ostermeier, C., 508
 Otani, K., 369, 374, 377, 378
 O'Toole, E. T., 36

P

Paddock, M. L., 234, 241, 242, 243, 245
 Pagliarini, D. J., 113, 135, 170, 236, 237, 239, 323
 Pain, D., 247–66
 Pallade, G. E., 443
 Pallotti, F., 442, 443, 445
 Palmeira, C. M., 450
 Palmer, G., 517
 Palsson, B. O., 268
 Park, J. W., 345
 Partikian, A., 288, 289, 291
 Patel, C. N., 509
 Patel, M., 381–93
 Pebey-Peyroula, E., 195, 196
 Penczek, P. A., 41
 Peng, J., 382, 397
 Perkins, D. N., 356
 Perkins, G. A., 29–52
 Petersen, K. F., 234
 Petronilli, G., 52
 Pfeiffer, K., 154, 155, 159, 164, 184, 185, 197, 322
 Pickova, A., 221
 Pie, Y., 213
 Pique, M. E., 514
 Pocsfalvi, G., 113, 114
 Pohl, T., 70
 Pon, L. A., 273, 400
 Pondarré, C., 211
 Ponka, P., 218, 219
 Poole, L. B., 344
 Puccio, H., 211

Q

Qian, S., 441
 QuagliarIELLO, E., 446
 Quinlan, P. T., 413

R

Rachamalla, A., 363–80
 Racker, E., 441, 444, 466
 Radermacher, M., 3–27
 Radon, J., 15
 Ragan, C. I., 171
 Ragan, U., 268
 Raha, S., 449
 Rahmani, Z., 364
 Rahmelow, K., 65
 Rak, M., 502
 Rardin, M. J., 233–46
 Ray, R. B., 368
 Redfeam, E., 172
 Rees, J. F., 407
 Regenfuss, P., 78
 Remington, S. J., 227
 Reynolds, I. J., 423, 428, 441, 446, 448, 449, 450, 476, 477, 485, 487
 Rhee, S. G., 344
 Rias, I., 155, 156
 Rich, P. R., 53–74, 304
 Richardson, D. R., 218, 219
 Richardson, J. R., 398
 Ritov, V. B., 234
 Ritter, M., 57
 Roberts, V. A., 514
 Robinson, G., 118
 Roder, H., 77
 Rolo, A. P., 450
 Ross, M. F., 410
 Rossignol, R., 288
 Rötig, A., 211
 Rouault, T. A., 226, 248
 Ruchira, M. A., 295
 Rudin, D. O., 447
 Ruiz, T., 5, 16, 17, 23
 Runswick, M. J., 118, 128
 Rustin, P., 222
 Ryan, M. T., 321–39

S

Saada, A., 135, 170, 171, 323
 Saddar, S., 188, 194
 Sadoski, R. C., 97, 105, 106
 Saint-Georges, Y., 497
 Saito, K., 298
 Saleh, A., 308
 Salerno, J. C., 170
 Salganicoff, L., 442
 Salmeen, A., 344

- Sandberg, K., 46
 Sands, R. H., 268
 Sandy, P., 212
 Saracco, S. A., 491–506
 Saraste, M., 193
 Sawyer, D. T., 396
 Saxena, S., 217
 Sazanov, L. A., 21, 54, 117, 118, 136, 137, 212
 Scaduto, R. C. Jr., 288
 Scalettar, B. A., 288
 Schäfer, E., 170, 194
 Schägger, H., 144, 153–68, 184, 185, 194, 197, 200, 201, 218, 219, 220, 322, 326, 331–2, 357
 Schapira, A. H., 398
 Scheffler, I. E., 210
 Scheres, S. H. W., 6
 Schild, D., 296, 297
 Schilling, B., 113
 Schmid, R., 304
 Schneider, D., 311
 Schopfer P., 485
 Schulman, H. M., 218
 Schuster, R., 81
 Schwille, P., 289, 290, 291, 294, 297, 298
 Scorrano, L., 49
 Sengupta, P., 295, 297
 Sepuri, N. B. V., 260
 Seraphin, B., 497
 Sharpley, M. S., 59, 478, 485
 Shastry, M. C., 77
 Sheftel, A. D., 209–31
 Sherwood, S., 175
 Shi, L., 307
 Shimada, H., 398
 Shimizu, K., 382
 Shinkarev, V. P., 106
 Shulman, G. I., 234
 Siess, E. A., 443
 Siletsky, S. A., 517, 519
 Sims, N. R., 383, 442
 Sinegina, L., 86–7, 478
 Skladal, D., 323
 Slater, E. C., 171
 Sled, V. D., 55
 Sluiter, W., 169–81
 Smeitink, J. A., 193, 323
 Smith, A. L., 155
 Smith, M. H., 79
 Smith, R. A., 402
 Snyder, C. H., 461
 Sokolove, P. M., 236
 Solano, F., 407
 Sonar, S., 67
 Sone, N., 184
 Song, D., 211
 Sottocasa, G. L., 239
 Srere, P. A., 227
 Srivastava, S., 134
 St-Pierre, J., 429, 448
 Stahl, W. L., 442
 Stamler, J. S., 344
 Starkov, A. A., 429
 Steele, D. F., 496
 Steffens, G. J., 121
 Stehling, O., 209–31
 Stiggall, D. L., 225
 Stolpe, S., 478
 Stoops, J. K., 16
 Stuart, B., 56
 Stuart, R. A., 188, 191–208
 Sturtz, L. A., 397
 Sugiura, M., 57
 Sun, F., 136, 446
 Sun, J., 461
 Sun, M. G., 29–52
 Sunderhaus, S., 183–90
 Swarts, H. G., 287–301
- T**
- Takahashi, R., 451
 Taminelli, G. L., 235
 Tanaka, M., 76, 81
 Tanaka, R., 442
 Tarpey, M. M., 480
 Tatulian, S. A., 58
 Taylor, E. R., 345
 Taylor, S. W., 113
 Teh, J. S., 304, 306
 Tetsu, O., 235
 Thiruchelvam, M., 382, 397
 Thomas, J. A., 344
 Thomson, B. J., 365
 Thorburn, D. R., 170, 323
 Tian, H., 462
 Tien Nguyen-nhu, N., 397
 Tiranti, V., 174
 Tong, W. H., 226, 248
 Towbin, H., 201
 Toyoshima, C., 9
 Trager, W., 308
 Tretter, L., 429, 431, 441
 Triepels, R. H., 222
 Trounce, I. A., 226
 Trueba, F. J., 297
 Trumpower, B. L., 96, 184, 268, 460, 461, 491–506
 Tso, S. C., 462
 Tsukihara, T., 113, 136, 188
 Turnbull, D. M., 226
 Turrens, J. F., 384, 460, 476
 Tuschl, T., 213
 Typke, D., 9, 38
 Tzagoloff, A., 268

U

Uehara, K., 468
 Ugalde, C., 145
 Unlu, M., 345
 Unwin, N., 9

V

Valentine, J. S., 396
 Van den Bergh, G., 347
 van der laan, M., 194
 van Heel, M., 5, 12, 187
 Van Remmen, H., 382, 397
 Vanderberg, J. P., 308
 Vanfleteren, J. R., 397
 Vanhecke, D., 48
 Veenstra, T., 351
 Venselaar, F., 149
 Venyaminov, S. Y., 65
 Verkhovskaya, M. L., 75–93, 170, 171
 Verkhovsky, M. I., 75–93, 517, 518
 Verkman, A. S., 288, 289, 291
 Vielhaber, S., 419–37
 Vinogradov, A. D., 21, 55, 476, 477, 485
 Visser, A. J., 289, 290, 294, 295, 297
 Vo, T. D., 268
 Vogel, R. O., 134, 135, 145, 146, 149,
 212, 221
 von Jagow, G., 154, 155, 200, 201, 326, 331–2
 von Jagow, J. G., 144
 Vonck, J., 194
 Votyakova, T. V., 423, 428, 439–57, 476, 477,
 485, 487
 Vozza, A., 257, 258
 Vukojević, V., 290, 291

W

Wachsmuth, M., 298
 Wakita, T., 369
 Walker, J. E., 111–31, 171
 Wallace, D. C., 323
 Walz, J., 5
 Wang, G. Y., 397
 Wang, K., 514
 Wang, T., 363–80
 Ward, S. A., 303–20
 Warman, A. J., 303–20
 Watanabe, K., 402
 Watowich, S. J., 363–80
 Weinman, S. A., 363–80
 Weinstein, E. A., 307, 308
 Wenz, T., 493
 Whitelegge, J. P., 124, 125
 Wiedemann, N., 194, 211
 Wiederkehr, A., 234
 Wiegand, G., 227

Wiess, H., 134
 Wikström, M., 86, 608
 Wiley, S. E., 233–46
 Wille, G., 65
 Willems, P. H. G. M., 287–301
 Williams, G. R., 268
 Winterbourn, C. C., 344
 Wisniewski, E., 429
 Wittig, I., 154, 155, 156, 157, 158, 159, 161, 164,
 165, 186, 187, 357
 Woldringh, C. L., 297
 Wollheim, A. N., 234
 Wolpert, M., 65
 Wood, P. M., 428
 Wu, L., 212
 Wumaier, Z., 153–68

X

Xia, D., 97, 136, 459–73
 Xiao, K., 105, 107
 Xiao, Y., 65

Y

Yakolev, G., 54, 55
 Yamaguchi, R., 49
 Yan, J. X., 347
 Yang, S., 459–73
 Yang, Y., 363–80
 Yano, T., 55, 305, 307
 Yin, Y., 459–73
 Yoshikawa, S., 123, 508
 Yoshioka, C., 5, 6
 Young, T. A., 441
 Yu, C. A., 459–73
 Yu, L., 459–73

Z

Zaslavsky, D., 509, 515, 517, 518
 Zeng, Y., 217
 Zerbetto, E., 166, 187, 223
 Zhang, H., 44
 Zhang, L., 461, 468
 Zhang, M., 184
 Zhang, Y., 250, 259, 260, 261
 Zhang, Z., 97, 107
 Zhao, H., 425
 Zheng, L., 211, 218
 Zhong, J., 369
 Zhou, F., 459–73
 Zhou, M., 387, 484
 Zhu, J., 97, 461
 Zick, M., 49
 Zickermann, V., 21, 23
 Zoccarato, F., 389
 Zscherp, C., 58, 65

Subject Index

A

- AAC, *see* ADP/ATP carrier protein
- Aconitase
 - iron–sulfur cluster biogenesis
 - iron–sulfur cluster insertion and nucleotide dependence, 253–255
 - matrix GTP concentration effects, 257–258
 - nucleotide hydrolysis requirement, 255–257
 - superoxide inactivation assay, 404–407
- ADP/ATP carrier protein
 - cytochrome *bc*₁-cytochrome *c* oxidase–TIM23 yeast supercomplex
 - blue-native gel electrophoresis
 - denaturing gel electrophoresis in second dimension, 201
 - protein standard preparation, 200–201
 - running conditions, 201
 - Western blot, 201–203
 - digitonin solubilization
 - concentration, 198–199
 - lysis, 200
 - recrystallization of digitonin, 198
 - mitochondria isolation and storage, 199–200
 - organization, 195–198
 - function, 192
 - histidine-tagged yeast Aac2 protein preparation
 - cloning and expression, 203–204
 - nickel affinity chromatography, 205–206
 - protein features, 206
 - isoforms, 195
- Alamethacin, mitochondria permeabilization for reactive oxygen species assay, 447–449
- Amplex Red
 - Complex I hydrogen peroxide production assay
 - resorufurin spectroscopic properties, 484
 - simultaneous measurement with NADH oxidation and membrane potential, 484–487
 - hydrogen peroxide assay, 421, 423–424
 - superoxide fluorescence assay, 408–409
- Apoptosis, electron tomography of HeLa cell mitochondria, 48–50
- ATPase, *see* Complex V
- Attenuated total reflection Fourier transform
 - infrared spectroscopy, *see* Fourier transform
 - infrared spectroscopy

B

- Beta cell mitochondria
 - diabetes pathophysiology, 450–451
 - isolation, 451–452
 - reactive oxygen species assay in intact cells, 452–453
- Blue-native gel electrophoresis
 - ADP/ATP carrier protein–cytochrome *bc*₁-cytochrome *c* oxidase–TIM23 yeast supercomplex
 - denaturing gel electrophoresis in second dimension, 201
 - protein standard preparation, 200–201
 - running conditions, 201
 - Western blot, 201–203
 - Complex I assembly analysis with green fluorescent protein–tagged human subunits, 144–146
 - cytochrome *c* oxidoreductase, 186–187
 - iron–sulfur cluster assembly studies
 - electrophoresis and autoradiography, 220–221
 - subunit composition assessment by blue-native/denaturing gel electrophoresis, 221–222
 - respiratory chain subunit assembly studies
 - blue-native/denaturing gel electrophoresis, 333–334
 - protein complexes, 331–332
 - processing and analysis, 334–337
 - respiratory chain subunits, 322–323
 - two-dimensional electrophoresis of mitochondrial complexes
 - blue-native/denaturing gel electrophoresis
 - running conditions, 158
 - supercomplex findings, 161–164
 - blue-native/high-resolution clear-native gel electrophoresis
 - processing for denaturing gel electrophoresis, 161
 - running conditions, 159–161
 - supercomplex findings, 164–166
 - final denaturing gel electrophoresis findings, 166–167
 - gel preparation, 156–157
 - materials, 155
 - overview, 154–155
 - sample preparation, 157

C

- Calcium flux, hepatitis C virus core protein effects
 on mitochondria
 cellular model systems, 374, 376–377
 uptake in isolated mitochondria, 371–373
- Citrate synthase, activity assay, 227–228
- Coelenterazine, superoxide chemiluminescence
 assay, 407–408
- Complex I
 absorbance spectroscopy, 55
 activity assays
 gel activity staining, 223–224
 human blood
 fibroblast mitochondria-enriched
 fraction preparation, 174
 linearity, 176
 lymphocyte isolation, 173
 materials, 172–173
 precision, 176–179
 principles, 171–172
 rationale, 170–171
 spectrophotometric assay, 174–175
 spectrophotometric assay, 224
 assembly, *see also* Iron–sulfur cluster
 assembly analysis with green fluorescent
 protein-tagged human subunits
 chloramphenicol treatment and
 accumulation of assembly
 intermediates, 148–149
 expression of fusion proteins
 destination vector, 138
 entry clone creation, 138–140
 expression vector creation, 140
 inducibility analysis, 142–143
 overview, 137–138
 stable transfection, 141–142
 model of assembly, 134–136
 native gel electrophoresis, 144–146
 pulse–chase labeling, 146–148
 subunit selection for labeling, 136–137
 deficiency, 170
 electron microscopy
 angular reconstruction, 5
 overview, 4–5
 prospects for study, 23
 random conical reconstruction
 assumptions, 6
 contrast transfer function correction,
 8–10
 dataset, 6–7
 digitization, 7–8
 particle selection, 10–11
 processing of zero degree images, 11–15
 Radon inversion for three-dimensional
 reconstruction, 15
 refinement, 15–16
Yarrowia lipolytica complex
 data analysis, 17–23
 data collection, 17
 sample preparation, 16
 electron paramagnetic resonance, 55
 Fourier transform infrared spectroscopy
 attenuated total reflection spectroscopy
 electrochemically-induced difference
 spectroscopy, 64
 model compounds and interpretation
 strategies, 64–68
 perfusion-induced difference
 spectroscopy, 62–64
 principles, 58–59
 rehydrated layer preparation, 59–62
Bos taurus complex I, 69–70
 difference spectroscopy, 56–57
 principles, 56
 transmission studies, 57–58
Yarrowia lipolytica complex, 69–70
 freeze-quench electron paramagnetic
 resonance of reduction by NADH,
 85–92
 function, 322
 hydrogen peroxide production assay with
 Amplex Red
 resorufin spectroscopic properties, 484
 simultaneous measurement with NADH
 oxidation and membrane potential,
 484–487
 iron–sulfur clusters, *see* Iron–sulfur cluster
 mass spectrometry, *see* Mass spectrometry
 pH profile for ubiquinone reduction, 483–484
 purification from *Yarrowia lipolytica*
 cell culture, 478
 chromatography, 478
 lipid activation, 478–479
 materials, 477–478
 mitochondrial membrane preparation, 478
 proteoliposome reconstitution, 479
 structure, 4
 subunits, 4
 supercomplex organization, 193–194
 superoxide production assay
 caveats, 488
 cytochrome *c* reduction, 479–480
 mitochondrial membrane assay, 480–482
 pH profile, 483–484
 reconstituted Complex I, 481–483
 X-ray crystallography, 54
 Complex II, *see* Succinate-ubiquinone
 oxidoreductase
 Complex III, *see* Cytochrome *bcl* complex
 Complex IV, *see* Cytochrome *c* oxidoreductase
 Complex V, function, 322
 Confocal microscopy, correlated electron
 microscopy of mitochondria
 cell culture, 31–33
 confocal microscopy, 33–34

- electron microscopy sample preparation
 - dehydration and embedding, 34–35
 - fixation, 34
- identical cell localization
 - sectioning, 35
 - transmission electron microscopy, 35–36
- overview, 30–31
- Cytochrome *b*
 - mutagenesis
 - ARG8 cassette plasmid construction, 494–495
 - biolistic transformation of yeast, 498, 500
 - cytoduction between recipient strain and MR6, 502–503
 - flow chart, 501
 - gene amplification and sequencing, 498
 - primers, 498–500
 - respiratory-competent mutations in
 - ρ + background, 500
 - respiratory-deficient mutations in
 - ρ + background, 502
 - screening, 504
 - template vector plasmid construction, 497
 - yeast recipient strain construction, 495–497, 503, 505
 - superoxide formation role, 492–494
- Cytochrome *bc1* complex
 - ADP/ATP carrier protein–cytochrome *c* oxidoreductase–TIM23 yeast supercomplex
 - blue–native gel electrophoresis
 - denaturing gel electrophoresis in second dimension, 201
 - protein standard preparation, 200–201
 - running conditions, 201
 - Western blot, 201–203
 - digitonin solubilization
 - concentration, 198–199
 - lysis, 200
 - recrystallization of digitonin, 198
 - mitochondria isolation and storage, 199–200
 - organization, 195–198
 - electron transfer
 - assay, 465
 - detection techniques, 97
 - functional overview, 96–97
 - iron–sulfur clusters, *see* Iron–sulfur cluster
 - proton translocation assays, 466
 - purification from bovine heart
 - complex isolation, 474
 - materials, 461–462
 - particle preparation, 464
 - submitochondrial particle preparation, 462
 - succinate:cytochrome *c* oxidoreductase
 - preparation, 463–464
 - ruthenium photooxidation for electron transfer detection
 - flash photolysis, 100–102
 - measurements of electron transfer between proteins
 - cytochrome *bc1* complex, 105–107
 - Ruz–39–Cc and cytochrome *bc1*, 102–105
 - principles, 97–98
 - ruthenium labeling of cytochrome *c*, 99–100
 - structure, 460
 - supercomplex organization, 193–194
 - superoxide generation
 - assay, 467–469
 - electron transfer activity dependence studies, 468, 470
 - mechanism, 461
- Cytochrome *c*
 - electron transfer measurements of ruthenium-labeled derivatives
 - cytochrome *c* oxidase, 513–514
 - electrostatically-bound cytochrome *c* oxidase studies
 - overview, 515
 - single electron reduction of state E to states R2 and Pm, 518–519
 - single electron reduction of state F to state O, 517–518
 - single electron reduction of state OH to state E, 518
 - single electron reduction of state Pm to state F, 516–517
 - intraprotein, 511–513
 - ruthenium-labeled derivatives, *see also* Ruthenium photooxidation
 - cytochrome *c* oxidase-binding studies, 514–515
 - preparation, 509–511
 - reduction potentials, 510
 - structures, 510
 - superoxide assay and reduction, 427, 479–480
- Cytochrome *c* oxidase
 - activity assay, 226–227
 - electron transfer measurements
 - overview, 508
 - ruthenium-labeled electrostatically-bound cytochrome *c* derivatives
 - overview, 513–515
 - single electron reduction of state E to states R2 and Pm, 518–519
 - single electron reduction of state F to state O, 517–518
 - single electron reduction of state OH to state E, 518
 - single electron reduction of state Pm to state F, 516–517
 - techniques for study, 508–509

- Cytochrome *c* oxidoreductase
 cytochrome *bc1* complex–cytochrome *c*
 oxidase–ADP/ATP carrier
 protein–TIM23 yeast supercomplex
 blue–native gel electrophoresis
 denaturing gel electrophoresis in second
 dimension, 201
 protein standard preparation, 200–201
 running conditions, 201
 Western blot, 201–203
 digitonin solubilization
 concentration, 198–199
 lysis, 200
 recrystallization of digitonin, 198
 mitochondria isolation and storage,
 199–200
 organization, 195–198
 electron microscopy, 184, 187–188
 function, 193, 322
 isolation from yeast
 blue–native gel electrophoresis, 186–187
 culture, 184–185
 membrane solubilization, 185
 mitochondria isolation, 185
 sucrose density gradient ultracentrifugation,
 185
 structure, 184
- D**
- Diabetes, beta cell mitochondria pathophysiology,
 450–451
- E**
- Electron microscopy, *see also* Electron
 tomography
 Complex I
 angular reconstruction, 5
 overview, 4–5
 prospects for study, 23
 random conical reconstruction
 assumptions, 6
 contrast transfer function correction,
 8–10
 dataset, 6–7
 digitization, 7–8
 particle selection, 10–11
 processing of zero degree images, 11–15
 Radon inversion for three–dimensional
 reconstruction, 15
 refinement, 15–16
Yarrowia lipolytica complex
 data analysis, 17–23
 data collection, 17
 sample preparation, 16
 correlated light microscopy of mitochondria
 cell culture, 31–33
 confocal microscopy, 33–34
 electron microscopy sample preparation
 dehydration and embedding, 34–35
 fixation, 34
 identical cell localization
 sectioning, 35
 transmission electron microscopy,
 35–36
 overview, 30–31
 cytochrome *c* oxidoreductase, 184, 187–188
 Electron paramagnetic resonance
 Complex I, 55
 freeze–quench of respiratory chain complexes
 calibration, 85
 Complex I reduction by NADH,
 85–92
 principles, 76–79
 transient kinetics overview, 76
 ultra–fast freeze–quench instrumentation
 fast freezing, 81–82
 mixer design, 80–81
 overview, 80
 sample preparation, 82–84
 paraquat detection
 indirect detection, 402
 mitochondria uptake assay, 410–412
 PQ⁺ radical, 399–400
 yeast mitochondria from large–scale
 preparations, 270, 277–279
 Electron tomography
 apoptotic HeLa cell mitochondria, 48–50
 computer and software, 38–39
 databases of mitochondrial data, 48
 electron microscopy, 36–38
 image processing
 enhancement, 48
 tilt series alignment, 45
 tomographic reconstruction, 46
 image recording, 38
 mitochondria *in situ* data collection
 angular increment and tilt range,
 43–44
 cooking area of interest, 42–43
 energy filtering, 39
 fiducial gold particle size and number,
 41–42
 general considerations, 39
 orientation of mitochondrion, 42
 pixel size and magnification, 41
 resolution estimation, 40–41
 serial tomography, 40
 single–tilt versus double–tilt, 43
 movies, 47
 principles, 36
 segmentation of mitochondrial substructure,
 46–47
 tele tomography, 48
 volume measurement, 46
 EPR, *see* Electron paramagnetic resonance

F

- FCS, *see* Fluorescence correlation spectroscopy
- Ferredoxin, iron–sulfur cluster biogenesis
 apoferrredoxin precursor protein expression and purification, 259–260
- GTP-dependent iron–sulfur biogenesis assay, 261–264
- iron–sulfur cluster insertion assay, 260–261
- overview, 258–259
- Flash photolysis, *see* Ruthenium photooxidation
- Flow cytometry
 mitochondrial depolarization by hepatitis C virus core protein, 374–375
- reactive oxygen species assay in intact cells, 452–453
- Fluorescence correlation spectroscopy
 autocorrelation function, 291, 294, 296–297
- ellipsoid volume, 289–290
- mitochondria-targeted enhanced yellow fluorescent protein studies
 baculoviral transfection, 292
- calibration, 292–294
- cell culture, 292
- data analysis, 294–299
- intramatrix protein diffusion overview, 288–289
- recording, 294
- molecular mass estimation, 291
- principles, 289–291
- translational diffusion coefficient, 291
- Fourier transform infrared spectroscopy,
 Complex I
 attenuated total reflection spectroscopy
 electrochemically-induced difference spectroscopy, 64
- model compounds and interpretation strategies, 64–68
- perfusion-induced difference spectroscopy, 62–64
- principles, 58–59
- rehydrated layer preparation, 59–62
- Bos taurus* complex I, 69–70
- difference spectroscopy, 56–57
- principles, 56
- transmission studies, 57–58
- Yarrowia lipolytica* complex, 69–70
- Freeze-quench, respiratory chain complexes
 calibration, 85
- Complex I reduction by NADH, 85–92
- principles, 76–79
- sample preparation, 82–84
- transient kinetics overview, 76
- ultra-fast freeze-quench instrumentation
 fast freezing, 81–82
- mixer design, 80–81
- overview, 80
- FTIR, *see* Fourier transform infrared spectroscopy

G

- Gel electrophoresis, *see* Blue-native gel electrophoresis; Redox difference gel electrophoresis; Two-dimensional gel electrophoresis; Western blot
- GFP, *see* Green fluorescent protein
- Green fluorescent protein
 Complex I assembly analysis with tagged human subunits
 chloramphenicol treatment and accumulation of assembly intermediates, 148–149
- expression of fusion proteins
 destination vector, 138
- entry clone creation, 138–140
- expression vector creation, 140
- inducibility analysis, 142–143
- overview, 137–138
- stable transfection, 141–142
- model of assembly, 134–136
- native gel electrophoresis, 144–146
- pulse-chase labeling, 146–148
- subunit selection for labeling, 136–137
- fluorescence correlation spectroscopy of
 mitochondria-targeted enhanced yellow fluorescent protein
 baculoviral transfection, 292
- calibration, 292–294
- cell culture, 292
- data analysis, 294–299
- intramatrix protein diffusion overview, 288–289
- recording, 294

H

- HAC, *see* Hierarchical ascendant classification
- Hepatitis C virus core protein
 mitochondria interaction studies
 cellular model system studies
 calcium flux, 374, 376–377
- flow cytometry of mitochondrial depolarization, 374–375
- model systems, 368–369
- reactive oxygen species production, 377–378
- isolated mitochondria studies
 calcium uptake assay, 371–373
- glutathione redox status assay, 370–371
- respiration effect assay, 369
- materials, 365–366
- mitochondria isolation, 368
- recombinant protein expression and isolation, 366–367
- synthesis and processing, 365
- Hierarchical ascendant classification, random conical reconstruction, 13–14
- Hydroethidine, superoxide assay, 425–427

Hydrogen peroxide, *see also* Reactive oxygen species
 biological sources, 420
 Complex I production assay with Amplex Red
 resorufin spectroscopic properties, 484
 simultaneous measurement with NADH
 oxidation and membrane potential, 484–487
 mitochondrial production assays
 Amplex Red, 421, 423–424
 fluorometric artifacts, 423
p-hydroxyphenylacetate, 420–422
 paraquat induction in mitochondria
 comparison of assays, 389–391
 fluorometric assay, 387–388
 mitochondria isolation from rat brain, 383–384
 polarographic measurement, 384–387
p-Hydroxyphenylacetate, hydrogen peroxide assay, 420–422

I

Ind1, *see* Iron–sulfur cluster
 Iron–sulfur cluster
 assembly machinery
 iron cofactor incorporation assay
 blue-native gel electrophoresis and autoradiography, 220–221
 iron–55-loaded transferrin preparation and application, 218–219
 membrane preparation, 219–220
 overview, 211
 RNA interference of Nfs1 and Ind1
 efficacy assessment, 215–216
 electroporation, 213, 215
 RNA design, 213
 specificity assessment, 216–218
 vector-based interference, 212
 subunit composition assessment by blue-native/denaturing gel electrophoresis, 221–222
 electron paramagnetic resonance, *see* Electron paramagnetic resonance
 electron transfer role, 210
 mitochondria isolation from yeast for spectroscopic analysis
 absorption spectroscopy, 270, 281
 anaerobic isolation, 272–273
 applications, 281–282
 density gradient centrifugation, 273–275
 electron paramagnetic resonance, 270, 277–279
 homogenization, 273
 iron assay, 276
 iron–omic studies, 269
 large-scale culture, 270–272
 Mössbauer spectroscopy, 269–270, 278–280

overview, 268–269
 packing into spectroscopy holders, 277–281
 protein assay, 276
 nucleotide-dependent biogenesis of mitochondrial apoproteins
 aconitase
 iron–sulfur cluster insertion and nucleotide dependence, 253–255
 matrix GTP concentration effects, 257–258
 nucleotide hydrolysis requirement, 255–257
 ferredoxin
 apoferredoxin precursor protein
 expression and purification, 259–260
 GTP-dependent iron–sulfur biogenesis assay, 261–264
 iron–sulfur cluster insertion assay, 260–261
 overview, 258–259
 mitochondria isolation and purification, 251–252
 model, 249
 nucleotide depletion in isolated mitochondria, 252
 overview, 248–250
 prospects for study, 263, 265
 stock solutions and storage, 250–251
 respiratory complex function assays
 citrate synthase reference activity, 227–228
 Complex I activity
 gel activity staining, 223–224
 spectrophotometric assay, 224
 cytochrome *c* oxidase activity, 226–227
 lactate formation, 222–223
 multiwell plate assay, 224–225
 succinate-ubiquinone oxidoreductase activity, 225

L

Lactate, respiratory complex function assay, 222–223

M

Mass spectrometry, respiratory complex subunits
 bovine mitochondrial-encoded proteins, 112–113
 extraction from mitochondria, 115–117
 high-performance liquid chromatography, 119–120
 isolation of respiratory complexes, 117–118
 mass measurements, 120–123
 prospects for study, 125–126, 128
 proteomics, 113–114
 tandem mass spectrometry, 123–125, 127

- Mitochondria
 Complex I, *see* Complex I
 electron microscopy, *see* Electron microscopy;
 Electron tomography
 electron paramagnetic resonance of respiratory
 chain complexes, *see* Electron
 paramagnetic resonance
 fluorescence correlation spectroscopy, *see*
 Fluorescence correlation spectroscopy
 hepatitis C virus core protein effects, *see*
 Hepatitis C virus core protein
 isolation from yeast for spectroscopic analysis
 absorption spectroscopy, 270, 281
 anaerobic isolation, 272–273
 applications, 281–282
 density gradient centrifugation, 273–275
 electron paramagnetic resonance, 270,
 277–279
 homogenization, 273
 iron assay, 276
 iron-omic studies, 269
 large-scale culture, 270–272
 Mössbauer spectroscopy, 269–270, 278–280
 overview, 268–269
 packing into spectroscopy holders, 277–281
 protein assay, 276
 reactive oxygen species production, *see*
 Reactive oxygen species
 respiratory chain subunit assembly
 crude mitochondria isolation from cultured
 cells, 326
 defects and disease, 323
 gel electrophoresis
 blue-native/denaturing gel
 electrophoresis, 333–334
 blue-native gel electrophoresis of
 complexes, 331–332
 denaturing gel electrophoresis of
 subunits, 331
 processing and analysis, 334–337
 mitochondrial import and assembly assays
 antibody-shift assays, 331
 chase assays, 330
 incubation conditions and gel
 electrophoresis, 329–330
 mitochondrial-encoded subunit assembly
 analysis
 overview, 324
 pulse-chase labeling, 324–325
 sample preparation, 325
 nuclear-encoded subunit *in vitro*
 transcription and translation
 coupled transcription and translation, 328
 template preparation, 327
 transcription, 327–328
 translation, 328
 supercomplexes, *see* Blue-native gel
 electrophoresis; Cytochrome *bcl*
 complex; Cytochrome *c* oxidoreductase;
 Iron–sulfur cluster
 MitoNEET
 absorbance spectroscopy of redox status,
 243–244
 functions, 235
 iron–sulfur cluster pH liability assay, 244–245
 Miner protein homology, 234
 mitochondrial fractionation from rat liver
 differential centrifugation of crude
 mitochondria, 236–237
 highly-purified mitochondria fractionation,
 239–240
 Histodenz gradient purification of
 mitochondria, 237
 Western blot, 240
 pioglitazone interactions, 234
 purification of recombinant proteins
 histidine-tagged protein, 242
 overview, 240–241
 untagged protein, 242–243
 vectors and mutagenesis, 241
 structure, 234–235
 Mössbauer spectroscopy, yeast mitochondria from
 large-scale preparations, 269–270, 278–280
 NADH:quinone oxidoreductase, *see* Complex I;
 Type II NADH:quinone oxidoreductase
 Native gel electrophoresis, *see* Blue-native gel
 electrophoresis
 NDH, *see* Type II NADH:quinone
 oxidoreductase
 Nfs1, *see* Iron–sulfur cluster
 Nucleotide-dependent iron–sulfur cluster
 biogenesis, *see* Iron–sulfur cluster
- P**
- Paraquat
 assays
 electron paramagnetic resonance and
 indirect detection, 402
 ion-selective electrode, 402–404
 PQ⁺ radical
 absorbance spectrophotometry, 400–401
 electron paramagnetic resonance,
 399–400
 radioassay, 401
 mitochondria interactions
 damage mechanisms, 397–398
 hydrogen peroxide production
 comparison of assays, 389–391
 fluorometric assay, 387–388
 mitochondria isolation from rat brain,
 383–384
 polarographic measurement, 384–387
 superoxide production
 aconitase inactivation assay, 404–407
 Amplex Red fluorescence assay, 408–409

- Paraquat (*cont.*)
- coelenterazine chemiluminescence assay, 407–408
 - uptake assays
 - electron paramagnetic resonance, 410–412
 - ion-selective electrode, 409–410
 - radioassay, 412–413
 - Parkinson's disease models, 398
 - redox cycling mechanism, 382, 396–397
 - research applications, 382
 - toxicity
 - overview, 382, 388–389
 - yeast deletion library screening, 413–414
- Parkinson's disease, paraquat models, 398
- R**
- Random conical reconstruction, *see* Electron microscopy
- Reactive oxygen species
- Complex I generation
 - hydrogen peroxide production assay with Amplex Red
 - resorufin spectroscopic properties, 484
 - simultaneous measurement with NADH oxidation and membrane potential, 484–487
 - superoxide assay
 - caveats, 488
 - cytochrome *c* reduction, 479–480
 - mitochondrial membrane assay, 480–482
 - pH profile, 483–484
 - reconstituted Complex I, 481–483
 - hepatitis C virus core protein effects on mitochondrial production, 377–378
 - mouse mitochondria production assays
 - alamethacin-permeabilized mitochondria, 447–449
 - beta cell mitochondria
 - intact cell assay, 452–453
 - mitochondria isolation, 451–452
 - pathophysiology, 450–451
 - biological sources, 420, 440–441
 - brain subcellular preparations, maximal respiration, and Complex I-related species generation, 431
 - Complex-specific production assays in intact mitochondria
 - Amplex Red assay, 447
 - Complex I, 446
 - Complex II, 446–447
 - materials, 447
 - hydrogen peroxide
 - Amplex Red assay, 421, 423–424
 - fluorimetric artifacts, 423
 - p*-hydroxyphenylacetate assay, 420–422
 - mitochondria preparations
 - brain, 442–443
 - liver, 443–444
 - submitochondrial particles, 444–445
 - superoxide
 - artifacts, 428
 - cytochrome *c* reduction, 427
 - hydroethidine, 425–427
 - mouse brain versus skeletal muscle mitochondria, 432–436
 - overview, 423, 425
 - submitochondrial particle assays, 430, 449–450
 - paraquat induction in mitochondria
 - hydrogen peroxide production
 - comparison of assays, 389–391
 - fluorometric assay, 387–388
 - mitochondria isolation from rat brain, 383–384
 - polarographic measurement, 384–387
 - superoxide production
 - aconitase inactivation assay, 404–407
 - Amplex Red fluorescence assay, 408–409
 - coelenterazine chemiluminescence assay, 407–408
- Reactive oxygen species, *see also individual species*
- Redox difference gel electrophoresis
 - comparison with other redox proteomic approaches, 357–358
 - mitochondrial protein thiol analysis
 - experimental design, 347
 - limitations and prospects, 356–357
 - overview, 344–345
 - redox-modified thiols
 - labeling with fluorescent maleimides, 349–350
 - reduction, 348–349
 - thiol blocking, 348
 - two-dimensional gel electrophoresis of fluorescently-labeled samples
 - fluorescence imaging, 351–353
 - mass spectrometry of spots, 355–356
 - multiple gel analysis, 353–354
 - running conditions, 351
 - spot excision, 352–355
 - principles, 345–347
- Resorufin, *see* Amplex Red
- RNA interference, Nfs1 and Ind1 in iron–sulfur cluster assembly
 - efficacy assessment, 215–216
 - electroporation, 213, 215
 - RNA design, 213
 - specificity assessment, 216–218
 - vector-based interference, 212
- ROS, *see* Reactive oxygen species
- Ruthenium photooxidation
 - cytochrome *c* derivatives, *see* Cytochrome *c*
 - ruthenium-labeled protein design and synthesis, 98

- electron transfer detection
 - flash photolysis, 100–102
 - measurements of electron transfer between proteins
 - cytochrome *bc*₁ complex, 105–107
 - Ruz-39-Cc and cytochrome *bc*₁, 102–105
 - principles, 97–98
 - ruthenium labeling of cytochrome *c*, 99–100

S

- SMPs, *see* Submitochondrial particles
- Submitochondrial particles
 - preparation, 444–445
 - reactive oxygen species production assays, 430, 449–450
- Succinate-ubiquinone oxidoreductase
 - activity assay, 225
 - function, 193, 322
 - iron–sulfur clusters, *see* Iron–sulfur cluster supercomplex organization, 193–194
- Sucrose density gradient ultracentrifugation, cytochrome *c* oxidoreductase, 185
- Superoxide, *see also* Reactive oxygen species
 - Complex I production assay
 - caveats, 488
 - cytochrome *c* reduction, 479–480
 - mitochondrial membrane assay, 480–482
 - pH profile, 483–484
 - reconstituted Complex I, 481–483
 - cytochrome *b* role in formation, 492–494
 - cytochrome *bc*₁ complex generation assay, 467–469
 - electron transfer activity dependence studies, 468, 470
 - mechanism, 461
 - mitochondrial production assays
 - artifacts, 428
 - brain submitochondrial particle assay, 430
 - cytochrome *c* reduction, 427
 - hydroethidine, 425–427
 - mouse brain versus skeletal muscle mitochondria, 432–436
 - overview, 423, 425
 - paraquat induction in mitochondria
 - aconitase inactivation assay, 404–407

- Amplex Red fluorescence assay, 408–409
- coelenterazine chemiluminescence assay, 407–408

T

- Two-dimensional gel electrophoresis, redox difference gel electrophoresis analysis of mitochondrial protein thiols
 - fluorescence imaging, 351–353
 - mass spectrometry of spots, 355–356
 - multiple gel analysis, 353–354
 - running conditions, 351
 - spot excision, 352–355
- Type II NADH:quinone oxidoreductase
 - Mycobacterium tuberculosis* enzyme assays
 - endpoint assay for high throughput screening, 315–318
 - Escherichia coli*-based heterologous expression system assay, 311–315, 318
 - function, 305–308
 - Plasmodium falciparum* enzyme assays
 - endpoint assay for high throughput screening, 315–318
 - Escherichia coli*-based heterologous expression system assay, 311–315, 318
 - linked assay, 309–311
 - native assay, 308–309
 - function, 305–308
 - structure and function, 304–305

W

- Western blot
 - ADP/ATP carrier protein–cytochrome *bc*₁–cytochrome *c* oxidase–TIM23 yeast supercomplex, 201–203
 - MitoNEET, 240

X

- X-ray crystallography, Complex I, 54